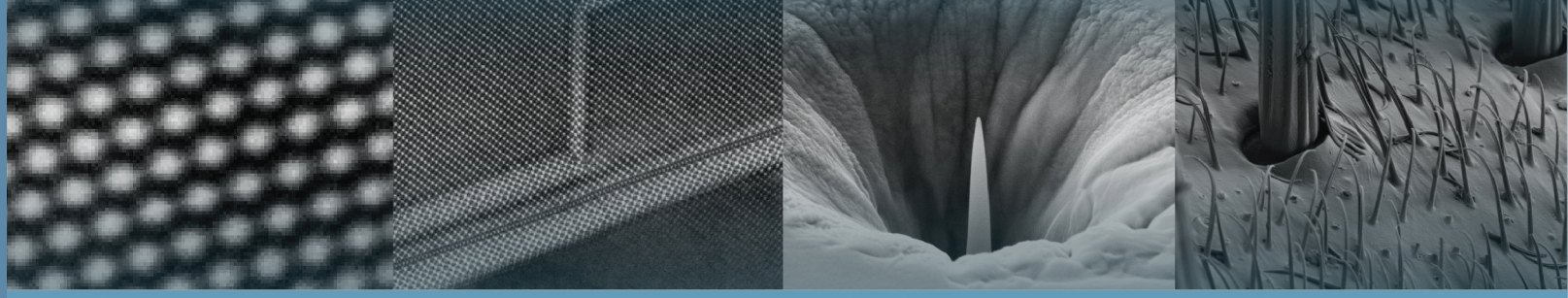


15-18 September 2014, Kraków, Poland

XV International Conference on Electron Microscopy PROGRAMME and ABSTRACTS



EM 2014



AGH University of Science and Technology
International Centre of Electron Microscopy for Materials Science
Faculty of Metals Engineering and Industrial Computer Science



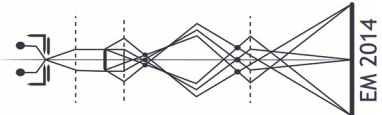
Polish Society for Microscopy



Committee of Materials Science of the Polish Academy of Sciences

EM 2014 15-18 September 2014, Kraków, Poland

| | | | | | | | | | |
|------|----------------------|-------|--|-------|---|-------|---|-------|--|
| time | Sunday 14.09.2014 | time | Monday 15.09.2014 | time | Tuesday 16.09.2014 | time | Wednesday 17.09.2014 | time | Thursday 18.09.2014 |
| | | 9:00 | Bus departure Galaxy Hotel → AGH-UST | 9:00 | HRTEM and electron holography I | 9:00 | HRTEM and electron holography II | 9:00 | Advances in SEM |
| | | 10:00 | Opening ceremony and Plenary session | 10:30 | Coffee break | 10:30 | Coffee break | 10:30 | Coffee break |
| | | 11:30 | Conference photo | 11:00 | Materials science: applications I | 11:00 | Analytical electron microscopy | 11:00 | Materials science: applications III |
| | | 12:00 | Bus departure AGH-UST → Galaxy Hotel | | | | | | |
| | | 13:15 | Lunch | 13:30 | Lunch | 13:15 | Lunch | 13:30 | Closing ceremony |
| | | 14:30 | Instrumentation and computing methods in electron microscopy | 14:30 | Life science: applications | 14:30 | Electron tomography | 14:00 | Lunch |
| | | 16:00 | Exhibition opening | 16:15 | Poster session | 15:45 | Coffee break | | |
| | | 16:30 | Companies presentations | 17:30 | General Assembly of Polish Society for Microscopy | 16:15 | Materials science: applications II | | |
| | | | | | | 18:15 | Bus departure Galaxy Hotel → dinner venue | | |
| | | 19:00 | Welcome reception | 19:00 | Guided tour of the Kazimierz district | 19:00 | Conference dinner | | |
| | | 19:00 | Get together | 20:00 | Dinner | | | | |

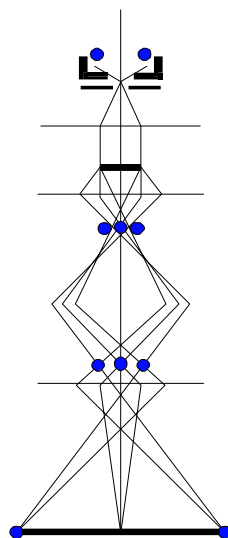


ISBN 978-83-63663-48-3

www.em2014.agh.edu.pl

XV INTERNATIONAL CONFERENCE ON ELECTRON MICROSCOPY

EM2014



PROGRAMME AND ABSTRACTS

Kraków, Poland

15-18 September 2014

© Copyright by AGH University of Science and Technology

Wydanie I, Kraków 2014

ISBN 978-83-63663-48-3

Realizacja wydawnicza:



Wydawnictwo Naukowe Akapit, Kraków
Phone +48 608 024 572; fax +48 12 280 71 51
<http://www.akapit.krakow.pl/>
email: wn@akapit.krakow.pl

CONTENTS

| | |
|--|------|
| International Scientific Committee | v |
| Sponsors | vi |
| Exhibitors..... | vii |
| General information | viii |
| EM2014 programme | xi |
| Abstracts | |
| Oral presentations | 1 |
| Poster presentations | 91 |
| Authors Index | 319 |

XV International Conference on Electron Microscopy

EM2014

organized by

AGH University of Science and Technology
International Centre of Electron Microscopy for Materials Science
Faculty of Metals Engineering and Industrial Computer Science

Polish Society for Microscopy

Committee of Materials Science of the Polish Academy of Sciences

held under the Auspices of the Rector
of AGH University of Science and Technology,
Professor Tadeusz Słomka

Sponsored by



Satellite event of the 18th International Microscopy Congress IMC 2014

ORGANIZING COMMITTEE

Chairperson: Beata DUBIEL
Secretaries: Grzegorz MICHTA, Tomasz MOSKALEWICZ
Members: Władysław OSUCH, Adam KRUK

INTERNATIONAL SCIENTIFIC COMMITTEE

Ludwik Błaż, Poland

Philippe A. Buffat, Switzerland

Jan Cwajna, Poland

Aleksandra Czyrska-Filemonowicz, Poland

Piotr Dłużewski, Poland

Rafał Dunin-Borkowski, Germany

Beata Dubiel, Poland

Jan Dutkiewicz, Poland

Stanisław Dymek, Poland

Ludek Frank, Czech Republic

Maximilian Haider, Germany

Wolfgang Jäger, Germany

Elżbieta Jezierska, Poland

Leopold Jeziorski, Poland

Jerzy Kątki, Poland

Jan Kusiński, Poland

Małgorzata Lewandowska, Poland

Andrzej Marszałek, Poland

Joachim Mayer, Germany

Paul Midgley, Great Britain

Jerzy Morgiel, Poland

Eva Olsson, Sweden

Władysław Osuch, Poland

Magdalena Parlińska-Wojtan, Poland

Maria Richert, Poland

Jan Sieniawski, Poland

Danuta Stróż, Poland

Grzegorz Tylko, Poland

Anna Zielińska-Lipiec, Poland

Paweł Zięba, Poland

Michał Żelechower, Poland

SPONSORS

Financial support from Polish Ministry of Science and Higher Education, Polish Academy of Sciences, European Microscopy Society, FEI and JEOL is gratefully acknowledged



Ministerstwo Nauki
i Szkolnictwa Wyższego

Ministry of Science and Higher
Education



Polish Academy of Sciences



European Microscopy Society



FEI COMPANY
GOLD SPONSOR



JEOL (EUROPE) SAS

EXHIBITORS



UNI-EXPORT INSTRUMENTS POLSKA



International Journal of
MATERIALS RESEARCH



GENERAL INFORMATION

CONFERENCE LOCATION AND VENUE

The conference will take place in Kraków, the second largest city of Poland, regarded as the culture capital and an important centre of science and education.

Kraków, with the population of about 800 000, is a resilient centre of scientific, economic and social life. The city owes its renown not only to the impressive historical heritage, but also to its potential of educated and creative people.

Almost 180 000 students attend the 24 academies and universities in Kraków. The city maintained its original urban layout with the largest European Medieval square. In 1978 the Kraków centre has been inscribed on UNESCO's First List of the World Cultural Heritage.

Conference registration and all sessions, beside opening ceremony and plenary session on Monday 15th September, will be held in the conference centre of the hotel Galaxy, Gęsia 22a St. The hotel Galaxy is located in the city centre near the Vistula river, the Old Town and Kazimierz Jewish District.

Opening ceremony and plenary session will be held in the Aula of AGH University of Science and Technology, A. Mickiewicza 30 Av., on the 1st floor of the main building A0. Organizers will provide shuttle buses for the conference participants on Monday 15th September from Galaxy hotel to AGH-UST at 9:00 and after the plenary session from AGH-UST to Galaxy hotel at 12:00.

WEATHER IN KRAKÓW

September is a beautiful time to travel to Kraków. The weather is usually mild and pleasant. The temperature remains around 15 ÷ 20 °C and sudden rains are common.

REGISTRATION DESK

The conference registration desk will be located on the 1st floor of the hotel Galaxy. It will start on Sunday 14th September at 16:00 and will be available for information/registration throughout conference hours.

BADGES

For security reasons and for catering purposes please ensure that you wear your conference badge throughout the conference and social events.

INFORMATION FOR PRESENTERS

Oral presentations

At conference rooms computers with Windows 7 and Microsoft Office 2010 will be available for speakers. The use of personal computers will also be possible. Presenters will have the opportunity to load their presentation file half an hour before the session.

Poster presentations

Posters will be displayed on special boards corresponding to the poster number. The poster session will take place on the 1st floor of the hotel Galaxy in the Planetarium Terrace on Tuesday 16th September, 16:15 – 17:30.

Poster presenters should check which poster board number has been allocated to them. Adhesive material will be provided for mounting the posters to the boards. The posters should be mounted not later than 11:00 on Tuesday 16th September. The authors should be available by their boards during the poster session for queries and discussion.

There will be also the opportunity to view and discuss the poster presentations during the refreshment breaks.

The posters should be removed by 11:00 on Thursday 18th September.

EXHIBITION

The exhibition of specialized research instrumentation and services will be located in the Gemini Hall at the ground floor of the hotel Galaxy.

Exhibition will be opened on Monday 15th September at 16:00 and will be available for conference participants throughout conference hours.

IMAGE COMPETITION

Beside its scientific value, electron microscopy images show the beauty of the invisible world, which sometimes is both fascinating and intriguing. The images taking part in the competition will be displayed during the conference in the poster room. All the EM2014 participants are kindly asked to vote for the best image award.

SOCIAL EVENTS

During the EM2014 conference few events will be arranged for participants and accompanying persons. We hope that it will be an occasion to meet and network with colleagues in pleasant and friendly atmosphere.

Get together will take place on Sunday 14th September at 19:00 at the 1st floor of the hotel Galaxy in the conference centre.

There will be a Welcome reception on Monday 15th September at 19:00 at the 1st floor of the hotel Galaxy in the Planetarium Terrace.

Guided tour of the Kazimierz district will be arranged on Tuesday 16th September. The guides will gather groups from the front of the hotel at 19:00. The short tour will end at the Stara Zajezdnia (The Old Tram Depot) Św. Wawrzyńca 12 St., where the dinner will be served at 20:00 in unique atmosphere of this place, which was recently renovated and converted for cultural purposes.

The Conference dinner will take place on Wednesday 17th September at 19:00 in the Royal Castle in Niepołomice, located 25 km east of Kraków. Shuttle buses will transfer all participants from the hotel Galaxy at 18:15 to Niepołomice and back after dinner. We hope that EM2014 delegates will enjoy historical interiors of the beautiful 14th century castle and the Polish cuisine.

EM2014 PROGRAMME

SUNDAY 14 SEPTEMBER 2014

16.00 – 19.00 Registration *Galaxy Hotel, 1st floor*
19.00 Get together

MONDAY 15 SEPTEMBER 2014

**OPENING CEREMONY AND
PLENARY SESSION¹** *Aula of the AGH-UST
A0 building 1st floor*

10:00 – 11:00 Opening speeches and welcome
addresses
11:00 – 11:30 Plenary lecture
C Barry Carter (invited): *TEM - it's always in situ*
11:30 – 11:45 Conference photo
12:00 – 13:00 Bus departure AGH-UST → Galaxy
Hotel
13:15 – 14:30 LUNCH

¹ Opening ceremony and plenary session will be held in the Aula of AGH University of Science and Technology, A. Mickiewicza 30 Av., on the 1st floor of the main building A0. All remaining sessions will be held in the conference centre located on the 1st floor of the hotel Galaxy, Gęsia 22a St.

INSTRUMENTATION AND COMPUTING METHODS IN ELECTRON MICROSCOPY

Chairs: Martin Hýtch and Piotr Dłużewski

14:30 - 15:00 Max Haider, Stephan Uhlemann (invited, keynote lecture):
*Instrumental developments for high resolution EM approaching
its physical limitations*
15:00 - 15:15 Sergei Lopatin, Andrey Chuvilin, Dominique Delille: *5th order
aberration correction in the Cs corrected Titan TEM for optimized
HRTEM study of low angle boundaries in graphene-like materials*
15:15 - 15:30 Guillaum Brunetti: *Advanced technology for analytical electron
microscopy by using aberration corrected transmission electron
microscope*

- 15:30 - 15:45 Athanassios S. Galanis: *Advanced electron diffraction applications in TEM based on beam precession: from ultra-fast electron diffraction tomography to orientation imaging & strain mapping*
- 15:45 - 16:00 Hans Dijkstra: *Spectral artifacts with high-efficiency wavelength dispersive spectrometers*
- 16:00 – 16:30 Exhibition opening²
- 16:30 – 17.30 Companies presentations (10 minutes talks)
- 19:00 WELCOME RECEPTION

²Exhibition will be located in the Gemini Hall on the ground floor of the hotel Galaxy.

TUESDAY 16 SEPTEMBER 2014

HRTEM AND ELECTRON HOLOGRAPHY I

Chairs: Aleksandra Czyska-Filemonowicz and Maximilian Haider

- 9:00 - 9:30 Knut Urban (invited, keynote lecture): *Atomic resolution transmission electron microscopy at picometer precision*
- 9:30 - 10:00 Hannes Lichte (invited, keynote lecture): *Electron holography for structures and fields*
- 10:00 - 10:30 Joachim Mayer, Juri Barthel, Lothar Houben, Maryam Beigmohamadi, Knut Urban (invited): *Chromatic aberration corrected TEM and applications in materials science*
- 10:30 - 11:00 COFFEE BREAK

MATERIALS SCIENCE: APPLICATIONS I

Chairs: Eva Olsson and Paweł Zięba

- 11:00 - 11:30 Alexander S. Eggeman, Robert Krakow, Steffen Illig, Henning Siringhaus, Paul A. Midgley (invited): *New developments in electron crystallography: molecular motion and 3D orientation mapping*
- 11:30 - 12:00 Velimir Radmilović (invited): *Planar and zigzag defects in functional oxide nanowires*
- 12:00 - 12:30 Guillermo Solorzano (invited): *Interface diffusion – controlled phase transformations in nanomaterials*
- 12:30 - 13:00 Robert Sinclair, Paul Kempen, Steven Madsen, Richard Chin, Ai Leen Koh (invited): *Recent characterization results on nanoparticles for possible medical applications*

- 13:00 - 13:15 Masahiro Kawasaki, Yuta Nakafushi, Masateru Nose, Tadashi Nobuchi, Makoto Shiojiri: *Two topics from our recent works*
- 13:15 - 13:30 Jan Kusiński, Sławomir Kaç, Kazimierz Kowalski, Beata Dubiel, Stanisław Dymek, Aleksandra Czyrska-Filemonowicz, Sergi Dosta, Emmanuel Georgiou, Paolo Matteazzi: *Microstructural characterization of nanostructured supersonic sprayed Ni-Sn coatings after wear test at elevated temperature*
- 13:30 – 14:30 LUNCH

LIFE SCIENCE: APPLICATIONS

Chairs: Velimir Radmilović and Michał Żelechower

- 14:30 - 15:00 Marta Dubiel, Grzegorz Tylko (invited): *Quantitative analysis of elements in biological materials using energy-dispersive spectrometry and scanning electron microscopy*
- 15:00 - 15:30 Andrzej Marszałek (keynote): *Is electron microscopy still in use for daily medical practice?*
- 15:30 - 15:45 Henryk Kucha, Władysław Osuch, Bogdan Rutkowski, Adam Kruk: *Natural occurrence of graphene and its formation by epitaxial growth on the 001 planes of mica minerals*
- 15:45 - 16:00 Urszula Stachewicz, Russell J. Bailey, Hao Zhang, Corinne A. Stone, Colin R. Willis, Asa H. Barber: *3D and nanoscale investigations of wetting between organic liquids and electrospun nanofibre networks*
- 16:00 - 16:15 Alicja Rapacz-Kmita, Ewa Stodolak-Zych, Magdalena Ziąbka, Agnieszka Różycka, Magdalena Dudek: *The possibility of using SEM and TEM to assess the degree of intercalation of smectite clay with gentamicin*
- 16:15 - 17:30 POSTER SESSION
- 17:30 - 19:00 GENERAL ASSEMBLY OF POLISH SOCIETY FOR MICROSCOPY
- 19:00 GUIDED TOUR OF THE KAZIMIERZ DISTRICT
- 20:00 DINNER

WEDNESDAY 17 SEPTEMBER 2014

HRTEM AND ELECTRON HOLOGRAPHY II

Chairs: Hannes Lichte and Jan Kusiński

- 9:00 - 9:30 Ulrich Dahmen, Abhay Gautam, Colin Ophus, Tamara Radetic (invited): *Observations of atomic mechanisms of interface motion by aberration-corrected microscopy*
- 9:30 - 10:00 Rafal Dunin-Borkowski, Vadim Migunov, Jan Caron, András Kovács, Giulio Pozzi (invited): *Towards quantitative mapping of three-dimensional and weak electrostatic potentials and magnetic fields using electron holography*
- 10:00 - 10:30 Martin Hýtch (invited): *State of the art of strain mapping in nanostructures by dark-field electron holography and aberration-corrected HR(S)TEM*
- 10:30 - 11:00 COFFEE BREAK

ANALYTICAL ELECTRON MICROSCOPY

Chairs: Wolfgang Jäger and Sławomir Kret

- 11:00 - 11:30 Philippe A. Buffat, Aleksandra Czyrska-Filemonowicz (invited, keynote): *EDS quantitative microanalysis and element mapping down to the nanometer scale and beyond*
- 11:30 - 12:00 Ferdinand Hofer, Werner Grogger, Gerald Kothleitner and Franz Schmidt (invited): *Scanning transmission electron microscopy at atomic resolution*
- 12:00 - 12:30 Eva Olsson (invited): *Determining local variation in structure and composition of catalyst particles and barrier layers using imaging and spectroscopy by high resolution analytical transmission electron microscopy*
- 12:30 - 13:00 Cecile Hebert, Simon Schneider (invited): *Angular resolved low loss in EFTEM mode: capturing the whole diffraction pattern*
- 13:00 - 13:15 David Poppitz, Andriy Lotnyk, Jürgen W. Gerlach and Bernd Rauschenbach: *Characterization of epitaxial GaN thin films by aberration-corrected scanning transmission electron microscopy*
- 13:15 - 14:30 LUNCH

ELECTRON TOMOGRAPHY

Chairs: Paul Midgley and Stanisław Dymek

- 14:30 - 15:00 Sara Bals, Bart Goris, Gustaaf Van Tendeloo (invited, keynote): *High resolution 3D imaging of nanomaterials*
- 15:00 - 15:15 Adam Kruk, Grzegorz Cempura, Aleksandra Czyrska-Filemonowicz (invited): *3D imaging of nanoparticles in superalloys by STEM-EDS and FIB-SEM tomography*
- 15:15 - 15:30 Charlotte Hamngren Blomqvist, Annika Altskär, Stefan Gustafsson, Niklas Lorén, Anne-Marie Hermansson and Eva Olsson: *3D imaging of silica gels for correlation between porous nanostructure and mass transport properties*
- 15:30 - 15:45 Piotr Bobrowski, Marek Faryna, Zbigniew Pędzich: *Three-dimensional microstructure analysis of cubic zirconia sinters by FIB-SEM serial sectioning*
- 15:45 - 16:15 COFFEE BREAK

PARALLEL SESSIONS

- 16:15 – 17:30 **MATERIALS SCIENCE: APPLICATIONS II YOUNG SCIENTISTS SESSION**

MATERIALS SCIENCE: APPLICATIONS II

Chairs: Christine Leroux and Maria Richert

- 16:15 -16:30 Elżbieta Jezierska: *Dark-field HRTEM and LACBED images*
- 16:30 - 16:45 Jerzy Morgiel, Małgorzata Pomorska, Rafał Nowak, Natalia Sobczak: *First stages of reaction of molten aluminium with MgO substrate*
- 16:45 - 17:00 Jürgen Gluch, Lars Röntzsch, Ehrenfried Zschech: *EELS characterization of iron oxide nanostructures grown by the steam-iron process*
- 17:00 - 17:15 Boryana Rashkova, Krystina Spiradek-Hahn, Manfred Brabetz, Zaoli Zhang, Helmut Clemens, Svea Mayer: *Microstructure evolution and grain refinement process in an intermetallic titanium aluminide alloy with high molybdenum content*
- 17:15 - 17:30 Anna Kula, Ludwik Błaż, Makoto Sugamata: *Microstructural modifications of Al-Fe based alloys due to magnesium addition and rapid solidification procedure*

YOUNG SCIENTISTS SESSION

Chairs: Maria Sozańska and Agnieszka Kopia

- 15:15 - 16:25 Krishnan Dileep, Boddapati Loukya, Ranjan Datta: *Probing nano scale variation of optical properties of NiCo₂O₄, NiFe₂O₄ and CoFe₂O₄ by high resolution EELS*
- 16:25 - 16:35 Joanna Gryboś, Jan Kaczmarczyk, Juri Barthel, Filip Zasada, Zbigniew Sojka: *Size and shape of cobalt spinel nanocrystals determined by HAADF-STEM and DFT first-principles calculations*
- 16:35 - 16:45 Joanna Karbowniczek, Grzegorz Cempura, Faiz Muhaffel, Huseyin Cimenoglu, Aleksandra Czyrska-Filemonowicz: *Influence of micro-arc oxidation conditions on microstructure and phase composition of hydroxyapatite coatings*
- 16:45 - 16:54 Witold Chromiński, Małgorzata Lewandowska: *In-situ transmission electron microscopy investigations of dislocation structures evolution in severely deformed technical pure aluminium*
- 16:54 - 17:03 Katarzyna Stan-Głowińska, Lidia Lityńska-Dobrzyńska, János L. Lábár: *Microstructural changes in Al-Mn-Fe-Mo melt spun ribbons studied by in-situ heating in a TEM*
- 17:03 - 17:12 Robert Albrecht, Maciej Zubko, Włodzimierz Bogdanowicz, Eleftheria Maria Pechlivani, Jan Sieniawski, Krzysztof Kubiak: *Multi-scale orientation measurement by X-ray and electron diffraction techniques in single crystal superalloy*
- 17:12 - 17:21 Krzysztof Morawiec, Piotr Dłużewski: *Computer methods for Cs corrected TEM images*
- 17:21 - 17:30 Bartosz Chmiela, Adrian Mościcki, M. Sozańska: *Effect of hydrogen on corrosion of Mg-Al alloys in various electrolyte solutions*
- 18:15 BUS DEPARTURE GALAXY HOTEL → DINNER VENUE
- 19:00 CONFERENCE DINNER

THURSDAY 18 SEPTEMBER 2014

ADVANCES IN SEM

Chairs: Cecile Hebert and Marek Faryna

- 9:00 - 9:30 Ludek Frank, Ivo Konvalina, Šárka Mikmeková (invited, keynote): *Scanning electron microscopy with biased samples*
- 9:30 - 10:00 Maria Sozańska, Michał Żelechower (invited): *How to avoid fundamental mistakes and misinterpretations in electron probe X-ray microanalysis (EPMA)*
- 10:00 - 10:15 Tomasz Goryczka, Józef Lełątko, Patrick Ochin: *In-situ study of phase transformation in NiTi shape memory alloys using EBSD technique*
- 10:15 - 10:30 Tomasz Tokarski: *Analysis of measurement conditions for high resolution transmission Kikuchi diffraction*
- 10:30 – 11:00 COFFEE BREAK

MATERIALS SCIENCE: APPLICATIONS III

Chairs: Elżbieta Jezierska and Ludwik Błaż

- 11:00 - 11:30 Christine Leroux, Veronique Madigou, Suzanne Giorgio, Andre-Luis Lopez Moriyama, Carlson Pereira de Souza, Agnieszka Kopia, Łukasz Cieniek, Kazimierz Kowalski (invited): *Nanostructured oxides for gas sensing*
- 11:30 - 12:00 Ana M. Sanchez, Sanfeng Wu, Chunming Huang, Xiandong Xu, David H. Cobden, Jonathan J.P. Peters and Richard Beanland (invited): *Microscopy of two-dimensional nanostructures*
- 12:00 - 12:30 Wolfgang Jäger (invited): *Transmission electron microscopy for defect engineering of high-efficiency solar cells*
- 12:30 - 13:00 Piotr Dłużewski, Sławomir Kret, Kamil Sobczak, Francesco Ivaldi, Jolanta Borysiuk, Tian Li, Dong Tang (invited): *TEM and EELS investigations of crystal and electronic structure of nanomaterials*
- 13:00 - 13:30 Boris Straumal, Askarr R. Kilmametov, Andreia A. Mazilkin, Anna Korneva, Olga A. Kogtenkova, Brigitte Baretzky, Paweł Zięba: *Effective temperature in Cu-based alloys during high pressure torsion*
- 13:30 CLOSING CEREMONY
- 14:00 – 15:00 LUNCH

Poster session

P1

Piotr Bała, Katja Tsyrlin, Heiner Jaksch

3D reconstruction and characterization of carbides in Ni based high carbon alloy in a FIB/SEM system

P2

Piotr Bazarnik, Ewelina Ciecierska, Magda Jurczyk-Kowalska, Małgorzata Lewandowska, Maciej Kowalski, Sławomir Krauze, Andrzej Czulak, Werner Hufenbach

The influence of addition of CNTs, nano-SiO₂ and POSS on the structure of polyurethane foams

P3

Katarzyna Błoch, Paweł Pietrusiewicz, Marcin Nabiałek, Karol Szlązak

SEM and TC in studies of structure and microstructure changes in bulk amorphous materials and their impact on the soft magnetic properties

P4

Magdalena Bieda, Piotr Bobrowski, Katarzyna Berent, Jakub Kawalko, Marek Faryna, Francois Brisset, Krzysztof Sztwiertnia

Microstructure evolution during annealing of 6013 aluminium alloy after complex deformation - advanced SEM studies

P5

Alberto Fabrizi, Giulio Timelli, Stefano Ferraro, Franco Bonollo

Evolution of Fe-rich compounds in a secondary Al-Si-Cu alloy: influence of cooling rate

P6

Jacek Krawczyk, Wojciech Gurdziel, Włodzimierz Bogdanowicz, Grzegorz Dercz

Morphology of tungsten growth forms in quasicrystalline Al₆₅Cu₂₀Fe₁₄W alloys

P7

Izabela Kalemba, Stanisław Dymek, Mateusz Kopyściański

Electron microscopy characterization of friction stir welded 5083-H111 and 7075-T651 aluminum alloys

P8

Janusz Krawczyk, Piotr Bała, Tomasz Tokarski, Łukasz Frocisz, Bogdan Pawłowski

The SEM analysis of hydrogen-assisted cracking in toughened steel

P9

Sabina Lesz, Anna Januszka, Marcin Nabiałek and Ryszard Nowosielski

Fracture morphology and mechanical properties of Fe-Co-B-Si-Nb bulk metallic glass after compression

P10

Krzysztof Miernik

Fractography of the dual phase steels

P11

Wiesława Nocuń-Wczelik, Barbara Trybalska

Scanning electron microscopy as a tool in the studies of hydrated cementitious materials microstructure formed in the presence of some heavy metals containing admixtures

P12

Bożena Sartowska, Oleg Orelovitch, Pavel Apel, Adam Presz

Polymeric track etched membranes – investigations with scanning electron microscopy techniques

P13

Anna Wassilkowska

Application of Peltier cooling device in a variable-pressure SEM

P14

PWJ van Wyk, H. Grobler

Computing methods to enhance out-of-focus images: the scientific acceptability

P15

Cyril Guedj

Measurement of structural and optical properties of monoclinic HfO_2 at the subnanometric level using energy-filtered HRTEM-VEELS

P16

Sławomir Kret, Piotr Wojnar, Elżbieta Janik, Tomasz Wojtowicz

TEM study of catalytic ZnTe/MgZnTe core shell nanowires grown by MBE

P17

Marek Nikiel, Benedykt Jany, Paulina Indyka, Franciszek Krok

Gold nanostructures assembled on Ge(001) surface studied with electron microscopies

P18

Julita Smalc-Koziorowska, Henryk Turski, Czesław Skierbiszewski, George Dimitrakopoulos

Uncommon strain relaxation observed in InGaN/GaN structures – transmission electron microscopy structural studies

P19

Paulina Indyka, Joanna Gryboś, Piotr Legutko, Paweł Stelmachowski, Andrzej Kotarba, Zbigniew Sojka

TEM/STEM/EELS studies of cryptomelane nanorods

P20

Mariusz Andrzejczuk, Agnieszka Teresa Krawczyńska, Piotr Bazarnik, Małgorzata Lewandowska, Monika Michalska, Ludwika Lipińska, Andrzej Czerwiński

STEM characterization of LiMn_2O_4 powder modified by metal oxides

P21

Bożena Sartowska, Ewa Pańczyk, Lech Waliś, Jakub Dudek, Władysław Weker, Maciej Widawski

Elemental composition in micro areas of the medieval Central Europe coins

P22

Bogdan Rutkowski, Aleksandra Czyrska-Filemonowicz

Microstructural investigation of dense ceramic membranes for oxygen separation in coal-fired power plants

P23

Robert Schlegel, Gerald Wagner, Felix Fahrnbauer, Tobias Rosenthal, Philipp Urban, Christina Fraunhofer, Oliver Oeckler

Intrinsic nano- and microstructures in thermoelectric Ge-Sb-Te materials with various dopants

P24

Kamil Sobczak, Piotr Dłużewski

LSPR of Ag nanostructures investigated with TEM and EELS

P25

Ildikó Cora, Péter Pekker, István Dódon, Dóra Janovszky

Structure determination of apatite and Ag-Cu-Zr alloys using PED and diffraction tomography techniques

P26

Mariusz Andrzejczuk, Agata Roguska, Marcin Pisarek, Małgorzata Lewandowska, Krzysztof J. Kurzydłowski

STEM characterization of TiO₂ and Al₂O₃ oxides produced by electrochemical oxidation metallic substrate

P27

Magdalena Bieda, Krzysztof Sztwiertnia

In situ annealing together with orientation mapping in TEM and SEM as a method for complex characterization of recrystallization process

P28

Mariusz Bigaj, Monika Mitka, Sonia Boczkal, Zbigniew Zamkotowicz, Janusz Żelechowski, Maciej Gawlik

Morphology of precipitates in 3xxx alloys with zirconium

P29

Jolanta Borysiuk, Kamil Sobczak, Agata Kamińska, Elżbieta Jezierska, Akio Yamamoto, H.P. David Schenk, Tadeusz Suski

Indium segregation during growth of InAlN layers – TEM observations

P30

Łukasz Cieniek

Effect of electron energy on the structural evolution of functional perovskite La_{0.6}Ca_{0.4}CoO₃ thin films produced by pulsed electron deposition (PED) technique

P31

Miroslav Cieslar, Jan Bajer, Michaela Poková, Mariia Zimina, Jozef Zrník

Microstructure of annealed AA3003 alloy after constrained groove pressing

P32

Tomasz Czeppe, Lidia Lityńska-Dobrzyńska, Anna Sypień, Grzegorz Garzeł, Zbigniew Świątek, Anna Wierzbicka-Miernik, Anna Góral

Phase composition and microstructure of the alloys from Ni₃Al-Ni₃Sn system after rapid quenching and decomposition

P33

Karolina Dudzińska, Julita Smalc-Koziorowska, Emilia Skótek, Wiesław Świątnicki

Identification of phases in bearing steel 67SiMnCr6-6-4 on the basis of the transmission electron microscopy study

P34

Dung Trung Tran, Cheuk-Wai Tai, Gunnar Svensson

TEM-based pair distribution function study of bimetallic nanoparticles

P35

Julita Dworecka, Elżbieta Jezierska, Janusz Rębiś, Krzysztof Rożniatowski, Wiesław Świątnicki

TEM & AFM - complementary techniques for structural characterization of nanobainitic steel

P36

Adam Gołaszewski, Jerzy Szawłowski, Wiesław Świątnicki

The electron microscopic measurements of the multiphase microstructure in 35CrSiMn5-5-4 steel

P37

Anna Góral, Lidia Lityńska-Dobrzyńska, Katarzyna Berent

Effect of dispersed α -Al₂O₃ particles on the morphology and tribological properties of nickel-alumina coatings

P38

Adam Grajcar, Andrzej Kilarski, Krzysztof Radwański, Radosław Swadźba

Microstructural features of strain-induced martensitic transformation in advanced ultra-high strength medium-Mn steels

P39

Barbara Grzegorczyk, Wojciech Ozgowicz, Elżbieta Kalinowska-Ozgowicz

Microstructural features of Cu-Zn single crystals deformed at elevated temperature

P40

Sławomir Kąc, Tomasz Moskalewicz, Grzegorz Szwachta

Microstructure of niobia-stabilized bismuth oxide thin films deposited by PLD technique

P41

Jarosław Konieczny, Krzysztof Labisz

EDS technique appliance for investigation of laser remelted and alloyed aluminium cast alloys

P42

Katarzyna Konopka

Shape, size and distribution of metal particles embedded into ceramic matrix

P43

Agnieszka Kopia, Łukasz Cieniek, Kazimierz Kowalski

Microstructural investigation of Sr doped LaCoO₃ thin films deposited by pulsed laser deposition

P44

Mateusz Kopyściański, Marek Stanisław Węglowski, Stanisław Dymek

Electron microscopy characterization of a multi-run friction stir processing cast AlSi9Mg aluminum alloy

P45

Anna Korneva, Boris Straumal, Paweł Zięba, Askar Kilmametov

Electron microscopy of pressure torsion deformed Cu-10 wt.% In alloy

P46

Joanna Kowalska, Wiktoria Ratuszek, Małgorzata Witkowska, Anna Zielińska-Lipiec

Microstructure and texture evolution during cold rolling in the Fe-23Mn-3Si-3Al alloy

P47

Jacek Krawczyk, Maciej Zubko, Włodzimierz Bogdanowicz, Jan Sieniawski, Krzysztof Kubiak, Marzena Szczepkowska

EBS and X-ray topography in analysis of single-crystalline turbine blades root

P48

Henryk Kucha, Heinz Mali, Władysław Osuch, Oskar Paris

Superstructuring in the garavellite-berthierite solid solution series FeSbBiS₄ – (Fe₂Sb₂Bi₂S₈ - Fe₂Sb₃BiS₈), a TEM and XRD micro diffraction study

P49

Krzysztof Labisz, Tomasz Tański, Jarosław Konieczny

Electron microscope investigation of cast aluminium alloy after laser feeding with ceramic powder

P50

Sonia Boczkal, Marzena Lech-Grega, Janusz Żelechowski

The effect of additions of Zn and Zr on the structure and texture of cast and wrought Mg alloys with different content of Ca

P51

Maria W. Richert, Beata Leszczyńska - Madej, Ilona Nejman, Paulina Zawadzka

Microstructure characterization of ZrO₂ - Y₂O₃ coatings deposited by thermal spraying process

P52

Lidia Lityńska-Dobrzyńska, Joanna Wojewoda-Budka, Anna Góral, Katarzyna Stan-Głowińska, Mikołaj Mitka, Jan Dutkiewicz

Microstructure of rapidly and conventionally solidified quasicrystalline Al-Cu-Fe alloys

P53

Mirosława Pawlyta, Dariusz Lukowiec, Barbara Liszka

Characterization of the high potential carbon supports predicted as efficient materials for hydrogen storage

P54

Łukasz Major, Roman Major, Jurgen M. Lackner, Jerzy Morgiel

Microstructure of novel multilayer nano- composite, protective coatings for medical tools application

P55

Krzysztof Matus, Mirosława Pawlyta, Grzegorz Matula

Characterization of nanometric-sized carbides formed during tempering of carbide-steel cermets

P56

Wojciech Maziarz, Paweł Czaja, Tomasz Czepe, Maciej Szczerba, Anna Wójcik, Katarzyna Wańkowicz, Jan Dutkiewicz

Microstructure and martensitic transformation in $Ni_{48}Mn_{39.5}Sn_{12.5-x}Si_x$ metamagnetic Heusler alloy ribbons

P57

Magdalena Maria Miszczyk, Henryk Paul

Recrystallization nucleation in plane strain deformed Al-Mn-Mg-Sc-Zr aluminium alloy

P58

Tomasz Moskalewicz, Sigrid Seuss, Aldo R. Boccaccini, Grzegorz Cempura, Adam Gruszczyński, Aleksandra Czyrska-Filemonowicz

Microstructure and morphology of composite polymer-based coatings on metallic substrates for medical applications

P59

Tomasz Moskalewicz, Sławomir Zimowski, Ivan Progalskiy, Bogdan Wendler, Aleksandra Czyrska-Filemonowicz

Microstructure and properties of TiN/Si_3N_4 nanocomposite coating on Vanadis 23 HS steel

P60

Grażyna Mrówka-Nowotnik, Małgorzata Wierzbińska, Jan Sieniawski, Andrzej Nowotnik

Intermetallic phases examination in $AlCu_4Ni_2Mg_2$ aluminium alloy

P61

Marcin Nabiątek, Paweł Pietrusiewicz, Katarzyna Błoch, Michał Szota

Effect of isothermal annealing on the structure (XRD), microstructure (SEM, TEM) and magnetic properties of classical and bulk nanocrystalline alloys

P62

Andrzej Nowotnik, Paweł Rokicki, Paweł Pędrak, Sławomir Kotowski, Jan Sieniawski, Grażyna Mrówka-Nowotnik

Dynamic precipitation of nickel based superalloys undergoing sever deformation below solvus temperature

P63

Anita Olszówka-Myalska

An influence of casting procedure on microstructure and properties of Mg alloy-glassy carbon particles composite

P64

Agnieszka Kurc-Lisiecka, Wojciech Ozgowicz, Elżbieta Kalinowska-Ozgowicz, Wojciech Maziarz

The influence of martensite transformation induced by plastic deformation on the microstructure of metastable austenite in X5CrNi18-10 stainless steel

P65

Henryk Paul, Jerzy Morgiel, Marek Faryna, Mariusz Prażmowski

Microstructure and interfacial reactions during explosive bonding of carbon or stainless steels to zirconium

P66

Mirosława Pawlyta, Klaudiusz Gołombek

Characterization of multilayer (Ti,Al,Si)N coating by transmission electron microscopy

P67

Paweł Pietrusiewicz, Marcin Nabiałek, Katarzyna Błoch, Michał Szota

The influence of solidification rate on the structure (XRD) microstructure (SEM, TEM) and magnetic properties of amorphous $Fe_{61}Co_{10}Y_8W_1B_{20}$ alloy

P68

Michaela Poková, Miroslav Cieslar, Mariia Zimina

The influence of equal channel angular pressing on microstructure evolution during in-situ heating in transmission electron microscope

P69

Alina Pruna, Daniele Pullini, Dimitrios Tamvakos, Athanasios Tamvakos, David Busquets-Mataix

Effect of substrate on the morphology of electrodeposited ZnO nanostructures

P70

Agnieszka Radziszewska, Axel Kranzmann, Ilona Dörfel, Maria Mosquera Feijoo, Monika Solecka

The microstructure and chemical composition of stainless steel after high temperature corrosion

P71

Kinga Rodak, Adam Hernas

Microstructural characterization of Laves phase in X10CrMoVNg9-1 and 12CrMoWCuVNb steels after long time exposure

P72

Edyta Roźniata, Dariusz Zasada

Application of scanning electron microscopy and EDS microanalysis for microstructural investigation of hypoeutectoid steels with 1% Ni

P73

Janusz Ryś, Anna Zielińska-Lipiec
Microstructure evolution in duplex stainless steels

P74

Piotr Sagan, Grzegorz Wisz, Mariusz Bester, Marian Kuzma
Electron diffraction study of layers obtained from ZnCrTe target by PLD method

P75

Sayanti Banerjee, Uwe Muehle, Markus Löffler, Andre Heinzig, Jens Trommer, Ehrenfried Zschech
Preparation and characterization of silicon nanowires using SEM/FIB and TEM

P76

Emilia Skołek, Krzysztof Wasiak, Wiesław A. Świątnicki
Changes in the microstructure and phase composition of the steel 35HGSA depending on the quenching and partitioning parameters

P77

Emilia Skołek, Szymon Marciniak, Wiesław A. Świątnicki
Determination of temperature stability of steel X37CrMoV5-1 based on the electron microscopy observations

P78

Magdalena Staszewska, Joanna Lewandowska-Łańcucka, Małgorzata Wierzbińska, Maria Nowakowska
Scanning and transmission electron microscopies as a techniques for the hybrid silica and silicone structures characterization

P79

Anna Sypień, Tomasz Czeppe Zbigniew Świątek, Lidia Lityńska-Dobrzyńska
TEM study of the multistage process of the TiZrCuPd BMG's partially isothermal crystallization

P80

Marzena Szczepkowska, Włodzimierz Bogdanowicz, Robert Albrecht, Józef Lelaćko, Jan Sieniawski, Krzysztof Kubiak
Correlation between withdrawal rate and microstructure of single crystalline superalloys CMSX-4

P81

Jerzy Morgiel, Marta Marszałek, Maciej Szlezzynger, Tomasz Czeppe, Konstanty Marszałek
Investigation of TEM in-situ heating of Ni/Al multilayers

P82

Agnieszka Twardowska, Jerzy Morgiel, Bogusław Rajchel
On the wear of TiB_x/TiSi_yC_z coatings deposited on 316L steel

P83

Vlastimil Vodárek, Jan Holešinský, Anastasia Volodarskaja, Adam Hernas
Microstructural evolution in AISI 316LN + 0.1wt.%Nb steel during creep at 600 and 625°C

P84

Anna Wassilkowska, Rashid Galin
Study of zinc oxide nanopores structure on powder medium for TDG

P85

Piotr Wieciński, Jerzy Smolik, Halina Garbacz, Krzysztof J. Kurzydłowski
Microstructure and stress evolution in multilayered structures under external load

P86

Anna Wierzbicka-Miernik, Krzysztof Miernik, Joanna Wojewoda-Budka, Lidia Lityńska-Dobrzyńska, Anna Korniewa-Surmacz
Morphology and chemical characterization of the Cu/(Sn,Ni) diffusion couples annealed at 220°C

P87

Grażyna Mrówka-Nowotnik, Małgorzata Wierzbińska, Jan Sieniawski, Andrzej Nowotnik
Microstructural evolution of aluminium alloy 2024 during homogenization process

P88

Grzegorz Włoch, Tomasz Skrzekut, Jakub Sobota, Ludwik Błaż
Silver matrix composite reinforced by aluminum-silver intermetallic phases

P89

Joanna Wojewoda-Budka, Lidia Lityńska-Dobrzyńska, Katarzyna Stan, Jerzy Morgiel
TEM microstructures formed due to the reactions in Al/metal oxide couples

P90

Krzysztof Pańcikiewicz, Anna Zielińska-Lipiec
TEM investigations of a microstructure of 7CrMoVTiB10-10 steel weld metal

P91

Mariia Zimina, Michaela Poková, Jozef Veselý, Jan Bohlen, Dietmar Letzig, Gerrit Kurz, Jozef Zrník, Miroslav Cieslar
Effect of aging on twin-roll cast AZ31 magnesium alloy after constrained groove pressing

P92

Maciej Zubko, Krystian Prusik, Irina Galuskina, Joanna Wspaniała-Rak, Danuta Stróż
Precession Electron Diffraction (PED) studies of grossular from the Wiluy River locality, Sakha-Jakutia Republic, Russia

P93

Jagna Karcz, Andrzej Woźnica, Marcin Binkowski, Małgorzata Klonowska-Olejnik, Tytus Bernaś, Jerzy Karczewski, Paweł Migula
*SEM-EDS and X-ray micro computed tomography studies of skeletal surface pattern and body structure in the freshwater sponge *Spongilla lacustris* collected from Goczalkowice reservoir habit (Southern Poland)*

P94

Julia Minicka, Katarzyna Otulak, Grażyna Garbaczewska, Beata Hasiów-Jaroszewska
The ultrastructural comparison of plants infected with different pathotypes of Pepino mosaic virus (PepMV)

P95

Ida-Maria Sintorn, Martin Ryner, Gustaf Kylberg, Rickard Nordström, Mats Uppström, Jan Fulin, Petr Stepan, Vladimir Kolarik, Michal Drsticka, Eva Coufalova
A desk-top low voltage TEM for high quality imaging of biological specimen

P96

Aleksandra Zarzyńska-Nowak, Małgorzata Jeżewska, Beata Hasiów-Jaroszewska
Cytopathology of barley plants infected with Barley stripe mosaic virus (BSMV) different strains

P97

Paweł Czaja, Wojciech Maziarz, Tomasz Czeppe, Maciej Szczerba, Anna Wójcik, Robert Chulist, Jan Dutkiewicz
Influence of grain refinement on microstructure and martensitic transformation in $Ni_{48}Mn_{39.5}Sn_{10.5}Al_2$ metamagnetic shape memory alloy powders

P98

Dagmara M. Fronczek, Joanna Wojewoda-Budka, Lidia Lityńska-Dobrzyńska, Zygmunt Szulc, Paweł Zięba
Transmission electron microscopy characterization of the clads' bonding interfaces manufactured using explosive welding

P99

Marta Gajewska, Jerzy Morgiel
Microstructural investigation of in situ AMCs obtained via reactive sintering of Al with Mg_3N_2

P100

Marta Janusz, Łukasz Major, Jurgen M. Lackner, Jerzy Morgiel
Microstructure characterization of Cr/CrN+ a-C:H/a-C:H:Cr multilayer coatings on Carbon Fiber Composites (CFC)

P101

Jakub Kawałko, Magdalena Bieda, Krzysztof Sztwiertnia
In-situ recrystallization and orientation imaging of commercially pure titanium deformed plastically by complex loading

P102

Barbara Kościelniak, Maria Sozańska, Jan Cwajna
Effect of carbides on creep resistance of master heat ingot of IN-713C nickel superalloy

P103

Katarzyna Kubok, Lidia Lityńska-Dobrzyńska, Anna Wierzbicka-Miernik
TEM study of aged Mg-3Zn-3Ca wt.% alloy for biomedical applications

P104

Mikołaj Mitka, Lidia Lityńska-Dobrzyńska, Anna Góral, Łukasz Rogal
Electron microscopy of quasicrystals in Al-Cu-Fe mechanically alloyed powder

P105

Aldona Mzyk, Roman Major, Juergen M. Lackner, Łukasz Major

Effect of the silicon carbide nanoparticles introduction on the biological properties of porous polymer coatings

P106

Paweł Petrzak, Marek Blicharski, Stanisław Dymek, Monika Solecka

Electron microscopy investigation of Inconel 625 weld overlay on boiler steels

P107

Tomasz Skrzekut, Anna Kula, Ludwik Błaż, Makoto Sugamata

Structural and mechanical features of mechanically alloyed AlMg-CeO₂ composite

P108

Monika Solecka, Paweł Petrzak, Jan Kusiński, Agnieszka Radziszewska

The microstructure of weld overlay Ni-base alloy deposited on carbon steel by CMT method

P109

Tomasz Ratajski, Beata Dubiel, Grzegorz Cempura, Aleksandra Czyrska-Filemonowicz

STEM-EDS and electron diffraction investigation of TCP phases in CMSX-4 single crystal nickel-base superalloy

P110

Klaudia Tembecka, Roman Major, Beata Butruk, Hanna Plutecka, Łukasz Major

Influence of microstructure and mechanical properties of titanium carbonitride stabilized hydrogel coatings on haemocompatible properties

P111

Agnieszka Uniwersał, Tomasz Tokarski, Sebastian Wroński, Mirosław Wróbel, Krzysztof Wierzbanowski

SEM study of the development of local texture and microstructure during asymmetric rolling of copper

P112

Krzysztof Kulawik, Philippe A. Buffat, Aleksandra Czyrska-Filemonowicz

Characterization of γ' and γ'' nanoparticles in Inconel 718 superalloy down to atomic level

P113

Sebastian Krawiec, Łukasz Krawczyk

SEM investigation of cracks in turbine wheels in car engine turbochargers

P114

Tomasz Ratajski, Beata Dubiel, Adam Kruk, Adam Gruszczyński, Aleksandra Czyrska-Filemonowicz

The influence of high temperature annealing on the γ' precipitates morphology in CMSX-4 single-crystalline nickel-base superalloy

P115

Władysław Osuch, Grzegorz Michta, Adam Kruk

The structure of the weld layer on stainless X50CrMnNiNbN21-9 steel

P116

Władysław Osuch, Grzegorz Michta, Adam Kruk

Pad welding of Inconel 625 layer on structural steel used in the power industry

P117

Krzysztof Żaba, Sandra Puchlerska, Michał Kwiatkowski, Tomasz Tokarski, Maciej Nowosielski

Comparative microstructure analysis of the plastically deformed alloy Inconel®718, manufactured by plastic working and direct metal laser sintering

P118

Włodzimierz Bogdanowicz, Robert Albrecht, Jan Sieniawski, Krzysztof Kubiak

Disorientation angles of single-crystal superalloy turbine blades defined by X-ray topography, X-ray and EBSD mapping

P119

Petra Bublíková, Vít Rosnecký, Jan Michalička, Hygreeva Kiran Namburi, Miroslava Ernestová, Eliška Keilová, Jan Kočík

An applied methodology of 1 mm foil preparation for TEM studies on neutron irradiated austenitic stainless steels used in nuclear power plants

P120

Radosław Swadźba, Jerzy Wiedermann, Lucjan Swadźba, Marek Hetmańczyk

Degradation analysis of thermal barrier coatings and modified aluminide coatings using S/TEM

P121

Anna Bukowska, Konrad Gruszka, Marcin Nabiałek, Katarzyna Błoch, Adrian Łukaszewicz, Michał Szota

Structure (XRD) and the microstructure (TEM, SEM, AFM) analysis of bulk amorphous and nanocrystalline alloys based on FeCoB

P122

Anna Sycheva, Adam Radanyi, Zoltan Gacsi

Investigation of pressure induced whisker formation on pure tin electroplated copper and brass surfaces

P123

Virendra Kumar

Applications of electron microscope in infectious diseases

P124

Zaoli Zhang, Rostislav Daniel, Christian Mitterer, Gerhard Dehm

Advanced study of the atomic and electronic structure of the defects in metal nitride films

P125

Bartosz Chmiela, Adrian Mościcki and Maria Sozańska

Effect of hydrogen on corrosion of RE-containing magnesium alloys in sodium sulfate solution

ABSTRACTS
oral presentations

TEM - it's always in situ

C. Barry Carter^{1-3,a}

¹Dept of Chem. & Biomolec. Engng, U. of Connecticut, 191 Auditorium Rd, Storrs, CT USA

²Dept of Mats Sci & Engng, U. of Connecticut, 97 North Eagleville Road, Storrs, CT USA

³Institute of Materials Science, U. of Connecticut, 97 North Eagleville Road, Storrs, CT USA

^acbcarter@engr.uconn.edu

Abstract

The meaning of 'in-situ TEM' will be discussed in relation to past, present and future applications.

Introduction

One of today's most exciting applications of transmission electron microscopy concerns the increasing flexibility for in-situ experimentation. While all TEM imaging is, by definition, in-situ, the term has come to imply carrying out an experiment inside the TEM while observing the specimen. Until recently, almost all such experiments were undertaken in the ambient vacuum of the TEM. The oxygen partial pressure was thus invariably extremely low. Even quite stable oxides would be reduced during observation in the TEM—the extent of this reduction might not be appreciated without careful analysis of EELS data. This paper will present an overview of why insitu studies are now becoming so widespread, what the future may hold and why all TEM users should care about these developments.

The concept of performing experiments inside the TEM has been known since the TEM was first invented and is generally referred to by a phrase like 'in-situ TEM examination' [1]. One challenge encountered in all TEM studies is knowing if, and if so how and how much, the electron beam has changed the specimen. Recently, advances in the design of the specimen holder have allowed specimens to be examined when in a different environment, such as a less-reducing atmosphere or even inside a liquid. It should not be a surprise that the electron beam will then interact with the gas or liquid that then surrounds the specimen, so all the lessons learnt about beam/specimen interactions (e.g., [3]) must still be applied and, in fact, may become even more important.

The principle references providing the background to this talk are two textbooks, namely one on transmission electron microscopy [1] and the other on ceramic materials [2]. The importance and potential for in-situ experiments will be illustrated by examples from the author and his colleagues including simple heating experiments, solid-state reactions, and reactions involving a liquid.

Summary

In-situ TEM studies are becoming ubiquitous. The possibilities are exciting but the challenges will also be significant, particularly because the variables and precise conditions are often so difficult to determine. This determination is so important if the rigorous scientific approach is to be followed wherein an experiment must be reproducible!

References

- [1] D.B. Willias and C.B. Carter: Transmission Electron Microscopy: A Textbook for Materials Science. 2 ed. 2009, New York: Springer.
- [2] C.B. Carter and M.G. Norton: Ceramic Materials: Science and Engineering. 2nd ed. 2013, New York: Springer.
- [3] J. Basu, C.B. Carter, R. Divakar, V.B. Shenoy and N. Ravishankar: Appl. Phys. Lett. 93(13) (2008) p. 133104-1-3.

Instrumental developments for High Resolution EM approaching its physical limitations

Max. Haider^{1,2,a} and Stephan Uhlemann^{1,b}

¹CEOS GmbH, Englerstr. 28, D-69126 Heidelberg, Germany

²Karlsruhe Institute of Technology, LEM, Engesserstr. 7, D-76128 Karlsruhe, Germany

^ahaider@ceos-gmbh.de, ^buhlemann@ceos-gmbh.de

The resolving power of a microscope is one of the most important parameters especially when talking about modern high resolution instruments like TEM or STEM. In contrary, the attainable resolution depends on the resolving power and the object and it can only be measured when imaging a certain object detail. Therefore, resolving power in this context means the object independent capability of an instrument to image a certain minimal size of an ideal object detail only limited by instrumental parameters. And the resolution is the minimal detail of a certain object which can be resolved by a certain instrument.

As it is well known, the resolution depends on:

- the resolving power of the microscope,
- the scattering properties of the object,
- the properties of the transfer function of the camera, the MTF, and
- the environmental conditions of the instrument.

In order to improve the attainable resolution we are concentrating our efforts on an improvement of the resolving power of the microscope. For this purpose we are working on a steady improvement of already existing correctors, on new corrector developments and on the investigation of limitations of electron optical components which were not known before.

After the first successful development of a Cs-corrector [1, 2] the limitations set by instabilities of the base instrument had to be tackled. This task was carried out by the EM manufacturer by setting up new microscopes with improved stability capable of showing atomic resolution on a daily basis. The next big step towards sub-atomic resolving power was the TEAM (Transmission Electron Aberration-corrected Microscopy) project [3] for which the goal on the resolving power was set to 50 pm for TEM as well as for STEM.

The target specification of the TEAM project could be achieved although an increase of an unexplainable image spread in TEM mode was noticed. The understanding of this image spread caused investigations over a 2 - 3 years and finally it could theoretically and experimentally be explained [4]. This image spread is caused by thermal magnetic noise caused by free electrons which are present in any conductive body. This noise depends on the temperature and currently it is unavoidable except by going to very low temperatures of all metal components surrounding the electron bundle within the objective lens as well as in the corrector. At room temperature one possibility is to reduce the disturbances of this magnetic noise by minimizing the beam diameter within the electron optical components. However, there are limits set by the required field strengths for the compensation of the spherical and especially of the chromatic aberration. The magnetic fields are limited by the saturation of the soft iron and the electrostatic fields by the break through voltage of the electrodes. Nevertheless, we could optimize the present Cc-correctors for the PICO project at Jülich [5] and for the SALVE project at Ulm by optimizing the diameters of the multipole elements and increasing the output of the power supplies as much as possible. Due to the increased power supplies strengths we could reduce the beam diameter by about 20% leading to a decreased influence of the thermal noise. This modified CCOR⁺ will be installed at Jülich in spring and for SALVE a new EM manufacturer will join this project because Zeiss stepped out of the TEM/STEM business.

Besides the compensation of the chromatic aberration ultra-high resolution can also be achieved by employing a cold field emission gun, Cs-compensation and very high tension (1.2 MeV). Such a project is in progress at the Advanced Research Laboratory, Tokyo. The current state of this FIRST project [7] will be reported.

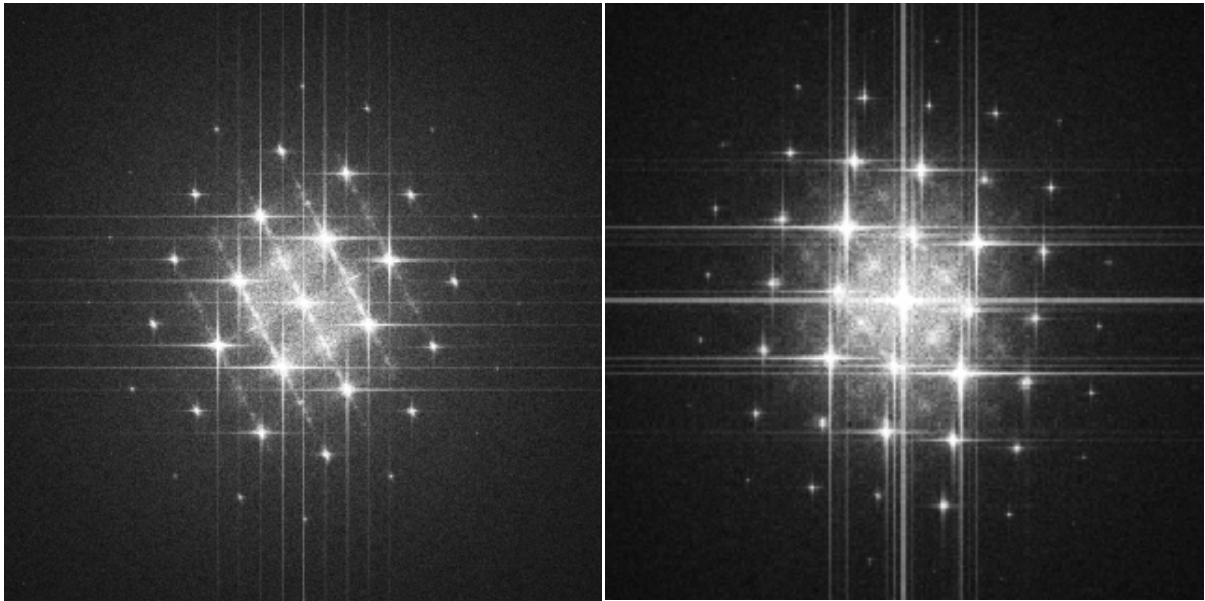


Fig. 1. Diffractograms of oriented Gold in full correction mode (Cs and Cc compensated) acquired in a Titan at 300 kV with a) a CCOR and b) a CCOR+. The scale is the same for a) and b) but with the CCOR+ more reflections at larger scattering angles can be observed. This diffractogram is not a proof of a resolving power of 50 pm but it shows the reduction of image spread by lowering the beam path.

References

- [1] M. Haider et.al.: Nature 392 (1998), p. 768.
- [2] O.L. Krivanek, N. Dellby, A.R. Lupini: Ultramicroscopy 78 (1999), p. 1.
- [3] TEAM: <http://ncem.lbl.gov/TEAM-project/index.html>.
- [4] S. Uhlemann et.al.: Phys. Rev. Lett. 111, 2013.
- [5] PICO: <http://www.er-c.org/centre/micfac/frames/titanp.htm>.
- [6] SALVE: <http://www.salve-project.de/about/index.html>.
- [7] FIRST: <http://www.first-tonomura-pj.net/e/index.html>.

5th order aberration correction in the Cs corrected Titan TEM for optimized HRTEM study of low angle boundaries in graphene-like materials

Sergei Lopatin¹, Andrey Chuvilin² and Dominique Delille^{1*}

¹FEI Company, Achtseweg Noord 5, 5600KA Eindhoven, The Netherlands

²CIC nanoGUNE, Tolosa Hiribidea 76, E-20018, Donostia - San Sebastian, Spain

*Dominique.Delille@fei.com

Introduction

Recent advances in spherical aberration (Cs) correction for transmission electron microscopes (TEM) in combination with electron sources of very low energy spread (use of monochromator) enabled imaging of single- and bi-layer graphene with atomic resolution [1]. Newly developed TEM techniques such as single atom or single atomic column spectroscopy [2,3] and atomic resolution electron tomography [4] recently drove the need for increased electron radiation doses to be applied to samples, while radiation damage started to be the key limitation factor for high resolution TEM [5].

For graphene-like (light element) materials [6] the radiation dose limitation is shown to be particularly severe through several explanations. First, the knock-on damage cross section is higher for low atomic number elements [7]. Second, light elements like Carbon produce less contrast than heavier elements, so that even higher doses are needed to obtain a sufficient signal-to-noise ratio (SNR). Finally, graphene-like materials appear in the form of low dimensional allotropes that have only one or a few atoms in the typical projection of a high-resolution TEM image. While resolution-wise we are not limited any more by modern Transmission Electron Microscopes, a big question mark remains about the sample stability under the beam during the image acquisition.

Optimization of the acquisition parameters of TEM systems allows minimizing electron dose and thus reducing possible sample damage. Here we present an extensive study of TEM tuning to obtain high quality HRTEM images of graphene. FEI Titan Transmission Electron Microscope was used, equipped with a Cs image corrector, a high brightness gun and a monochromator (energy spread of the electron beam better than 0.2 eV). Special attention was paid to optimize the settings of the Cs corrector.

Tuning of Cs corrector is based on measurement of image defocus (df) and astigmatism while recording so-called Zemlin tableau [8]. It will be demonstrated here that accounting for Cs of 3rd and 5th order (C3 and C5 correspondingly) and systematic error of C3 measurement results in more than 2 times increase in contrast, i.e. more than 4 times less electron dose to obtain the same SNR (Fig. 1) in HRTEM pictures.

The optimal settings found using this novel technique will be used in the context of the study of low angle boundaries (LAB) in graphene. LAB is typically a row of edge dislocations, separation of those defining the boundary angle. LABs are not directly observable on the HRTEM images but can be identified using dedicated methods like geometrical phase analysis (GPA), see Fig. 2. Physically speaking, LABs are of strong interest, as they represent a perfect discontinuous layer with periodically spaced singularities.

References

- [1] K.W. Urban: Nat. Mater. 10 (2011), p. 165.
- [2] P.E. Batson: Nature (London) 366 (1993), p. 727.
- [3] D.A. Muller, L.F. Kourkoutis, M. Murfitt, J.H. Song, H.Y. Hwang, J. Silcox, N. Dellby, O.L. Krivanek: Science 319 (2008), p. 1073.
- [4] M. B. Sadan, L. Houben, S. G. Wolf, A. Enyashin, G. Seifert, R. Tenne, and K. Urban: Nano Lett. 8 (2008), p. 891.

- [5] R.F. Egerton, P. Li, and M. Malac: *Micron* 35 (2004), p. 399.
- [6] K.S. Novoselov, A.K. Geim, S.V. Morozov, D. Jiang, Y. Zhang, S.V. Dubonos, I.V. Grigorieva, and A. A. Firsov: *Science* 306 (2004), p. 666.
- [7] F. Banhart: *Rep. Prog. Phys.* 62 (1999), p. 1181.
- [8] F. Zemlin, K. Weiss, P. Schiske, W. Kunath, K. -H. Herrmann: *Ultramicroscopy* 3 (1978), p. 49.

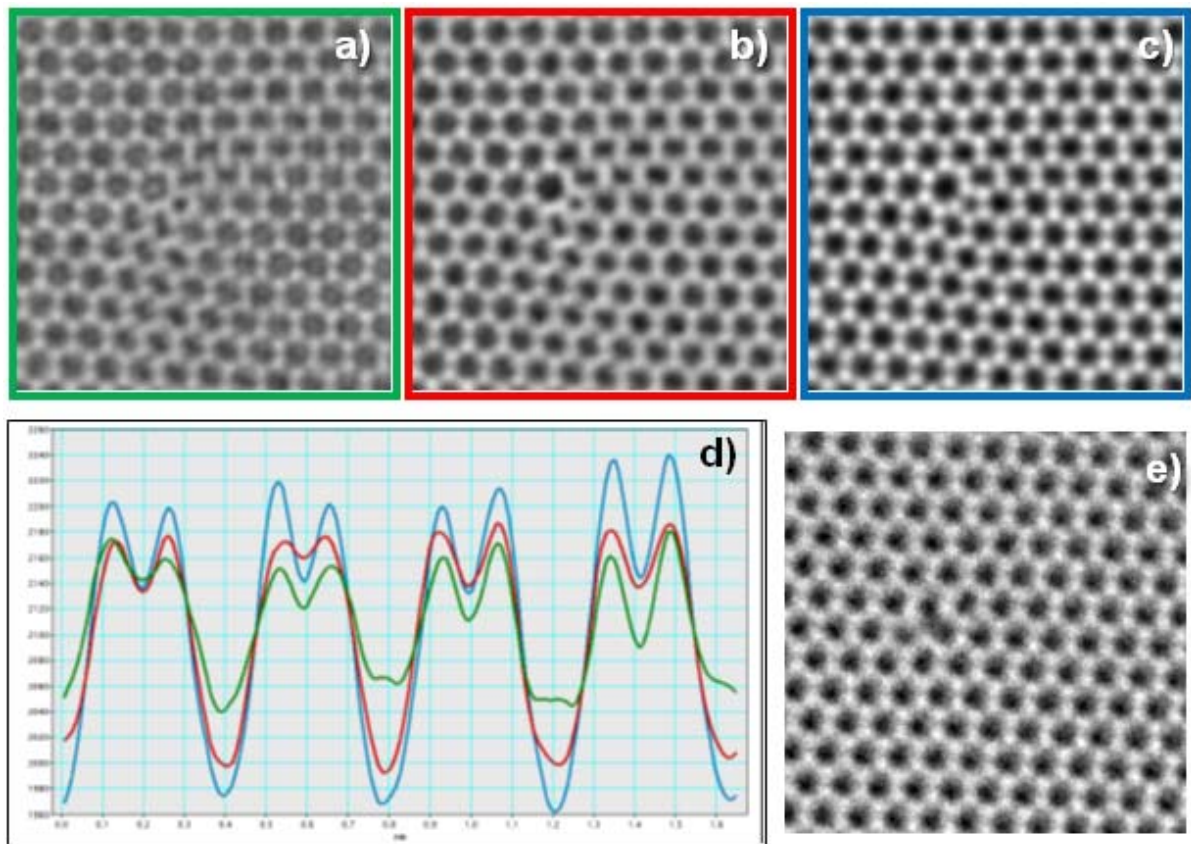


Fig. 1. Simulation verification of the impact of optimum conditions: a) Scherzer conditions optimized for 0.1 nm transfer; b) C5+C3+df conditions optimized for 0.1 nm transfer; c) C5+C3+df conditions optimized for 0.1 nm transfer and systematic error from Zemlin tableau is accounted; d) the intensity profiles across simulated images; e) an experimental image acquired at approximately optimum conditions

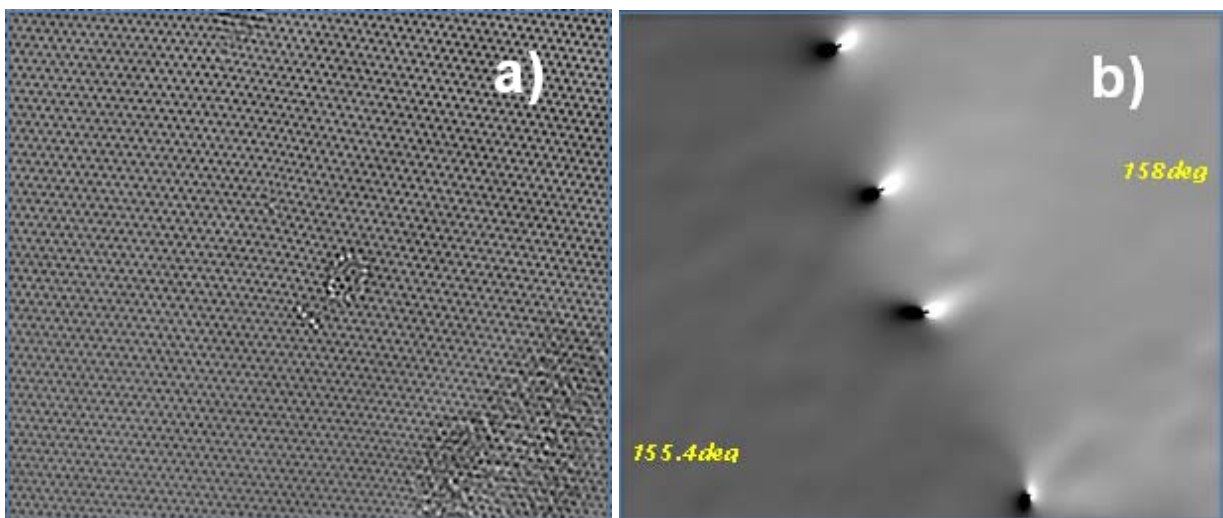


Fig. 2. LAB in graphene: a) original HRTEM image; b) dislocations identification by GPA (rotation map)

Advanced technology for analytical electron microscopy by using aberration corrected transmission electron microscope

Guillaume Brunetti^{1,a}

¹JEOL (EUROPE) SAS, Espace Claude Monet, 1 Allée de Giverny, 78290 Croissy-sur-Seine, France

^abrunetti@jeol.fr

The nanoworld: where individual atoms that constitute substances are directly observed. A TEM equipped with Cold-FEG (Cold Field Emission Gun) realizes this dream. With Cold-FEG, a superb high-quality electron beam is produced that achieved a narrower spread and forms a sharper probe with higher brightness than a conventional Schottky FEG. Many improvements have been developed for the conception of the ARM-200F.

The ARM-200F receives a new design allowing the improvement of the mechanical, electrical stability and the protection against environmental disturbances. Furthermore, the base frame has been designed to the optimum geometry for the accommodation of double TEM/STEM Cs correctors totally integrated. The use of a spherical aberration corrector for electron optic system as standard, has achieved a scanning transmission image (STEM-HAADF) resolution of 0.078 nm, the highest in the world among the commercial transmission electron microscopes.

These improvements coupled with Cold-FEG allow the ARM to perform high level studies for all TEM techniques (HRTEM, HRTEM, EELS, EDS, Annular Bright Field, diffraction ...). Furthermore, the ARM-200F equipped with Cold-FEG and the new Centurio EDS detector (solid angle 1 sr) allows the acquisition of atomic resolution EDS mapping (Figure 1).

Example of application: the use of a Cold-FEG dramatically improves EELS energy resolution. As seen figure 2, the energy resolution is about 0.3eV for a Cold-FEG. This very good energy resolution is a major factor for EELS studies; in particular ELNES (Energy Loss Near Edge Structure) exhibits a characteristic shape depending on the chemical bonding states in a substance. Figure 2 is an example of analysis of rutile and anatase.

JEOL offers “Ultra-high resolution” with this next generation of “improved Cold-FEG”.

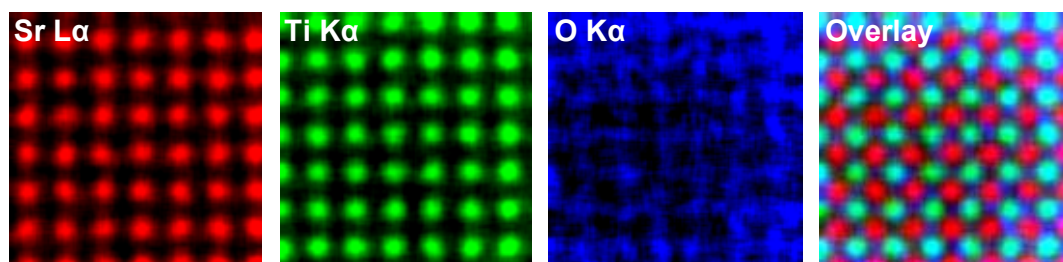


Fig. 1. Atomic resolution EDS mapping on SrTiO₃ sample

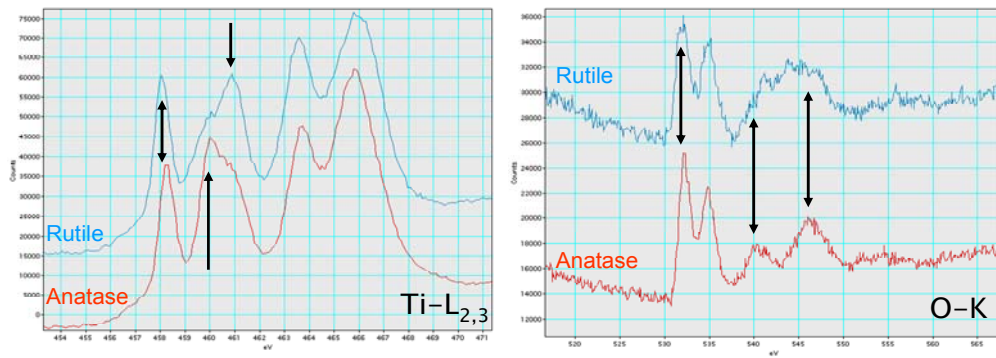


Fig. 2. EELS spectra of rutile and anatase type crystal, which show ELNES obtained from the O-K edge and the Ti-L edge, reveal clear differences in chemical bonding states (indicated by arrows). The higher energy resolution of a Cold-FEG enables clear observation of these differences

Advanced electron diffraction applications in TEM based on beam precession: from ultra-fast electron diffraction tomography to orientation imaging & strain mapping

Athanassios S. Galanis^{1,a}

¹NanoMEGAS SPRL Blvd Edmond Machtens 79 , B-1080 Brussels, Belgium

^atgalanis@nanomegas.com, tgalanis@upatras.gr

Introduction

Precession Electron Diffraction (PED) technique in Transmission Electron Microscope (TEM) has been first reported by the Vincent and Midgley in 1994. Since then, and mainly since the commercial availability of beam precession device into the market ten years after the pioneering work, several TEM applications for nanomaterials are based in PED technique. It is currently well known that precession enhance dramatically the reflections quality (quasi-kinematical, similar to X-ray intensities) and the diffraction data resolution. More than 250 articles (that include PED technique) from various laboratories worldwide and dedicated issues of major scientific microscopy journals have been published the last decade.

Due to precession influence on diffraction patterns data, PED was firstly applied in electron crystallography, that in combination with the 3D diffraction tomography by TEM, consist a critical method for structure determination of various nanocrystals, from complex zeolites and minerals to metals and alloys. Automated orientation and phase mapping analysis of a variety of materials (metals, semiconductors, oxides etc.) by TEM using PED technique consists another successful application, called ASTAR. This technique is very similar to the traditional EBSD method by SEM, but the major benefit compared to EBSD technique, is the high spatial resolution that can be up to 1-3 nm resolution (in case of FEG-TEM). Furthermore, precession diffraction has been recently successfully applied to obtain Strain mapping analysis of several semiconductor materials at 1-4 nm resolution (sensitivity 0.02%), based on comparison of PED-NBD patterns of strained with a reference - non-strained areas.

Methods & Results

Herein, we are presenting the latest methods development for three different applications based on PED technique in TEM. Firstly, an ultra-fast automated precession assisted 3D electron diffraction tomography method is presented, where PED data can be collected about 10-20 times faster compared to hitherto 3D diffraction tomography procedure[1]. In conventional PED tomography method, a series of ED patterns are collected in a TEM every 1degree of tilting around the goniometer axis, but a drawback of the technique is time consuming, mainly due to the time needed for crystal position tracking after every tilt step [2, 3]. By tilting the TEM holder using 3D tomography, the sample is moving along a definite direction for a specific (quite large) tilt range and -as consequence- such crystal movement could be tracked by shifting the beam (instead of tracking the crystal) along the same direction. Towards, we used the ASTAR control unit for TEM [4, 5] where a linear area along the crystal movement direction was scanned, and PED pattern were recorder by a CCD camera, during tilting. Less than 5-6 min is required for data acquisition and the data quality is efficient (as like conventional tomography technique in TEM) for structure determination of variety of material, including beam sensitive compounds, as organic & pharmaceuticals.

The second technique that is presented herein is the automated orientation and phase mapping analysis of several materials using ASTAR method. Recent results of important materials are reported, showing that ASTAR method in TEM is a powerful tool for texturing with resolution up to 1 nm when an FEG-TEM is used. Precession Electron diffraction spot patterns are collected with an external ultra fast CCD camera while the sample area of interest is scanned by the electron beam. Beam scanning is

controlled by an external source, such as the precession device by NanoMEGAS [4]. The orientation/phase identification is next performed off-line [6]. Local crystallographic orientation and / or phases are identified through an original algorithm that compares the recorded ED spot patterns with pre-calculated (simulated) templates for all possible orientations and/or phases. ASTAR method has been successfully applied to several materials as like, metals, alloys, minerals, semiconductors, ceramics, nanowires, ion batteries, organic compounds, etc.

The third application based in PED method that is presented here, is the strain mapping analysis. Strain measurement with high spatial resolution and high precision in semiconductor devices and other materials is critical to monitor the designed and unintended strain distributions. In strain mapping measurement by TEM, spot diffraction patterns with nanobeam illumination is used and data from strained and unstrained regions using a quasi-parallel nanoprobe (<5 nm) are collected. Next, diffraction patterns from strained region are matched against the reference pattern from unstrained region, in order to measure the strain properties of the material. However, the presence of strong dynamical effects in TEM diffraction patterns lead to rapid changes in spot intensities with slight thickness and orientation changes. Thus, precession technique is applied in strain mapping analysis, as the strong dynamical effect is reduced dramatically. Furthermore, when precession is applied, data are insensitive to thickness and orientation small changes and the number of reflections is increased leading to improved data with higher order spot reflections. Strain mapping analysis in TEM by PED technique consist a straightforward method that can be applied at any TEM and provides rapid and accurate data (same order of magnitude as dark field holography) without any requirement to index diffraction patterns.

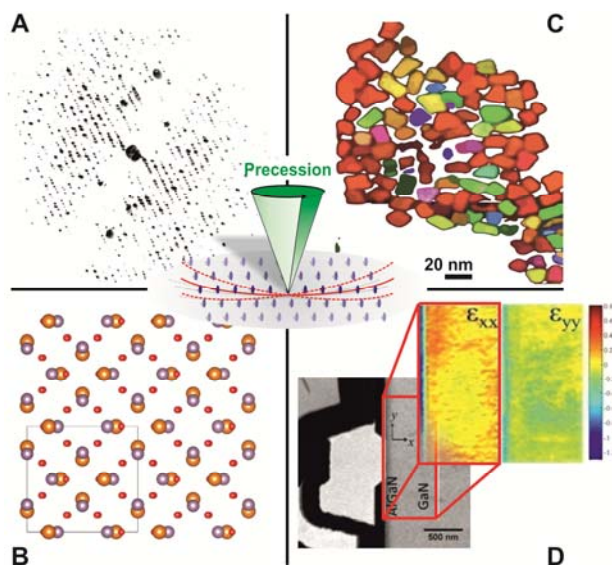


Fig. 1. Crystal structure on MgMoO_4 solved by Ultra-fast Precession Electron Diffraction tomography (B) and the corresponding reconstructed reciprocal space (A). Orientation Map of Au-nanoparticles obtained by ASTAR technique in TEM (C). Strain mapping analysis of AlGaN / GaN system used as High Electron Mobility Transistor (HEMT) (D)

References

- [1] M. Gemmi, A.S. Galanis and S. Nicolopoulos: MC2013, Proceedings Part I, IM1.P30, p. 73, Regensburg, Germany.
- [2] E. Mugnaioli, T. Gorelik and U. Kolb: Ultramicroscopy Vol. 109 (2009), p. 758.
- [3] U. Kolb, T. Gorelik, C. Kübel, M.T. Otten and D. Hubert: Ultramicroscopy Vol. 107 (2007), p. 507.
- [4] NanoMEGAS: www.nanomegas.com.
- [5] E.F. Rauch, J. Portillo, S. Nicolopoulos, D. Bultreys, S. Rouvimov and P. Moeck: Zeitschrift für Kristallographie Vol. 225 (2010), p. 103.
- [6] E.F. Rauch and M. J. Veron: Mater. Sci. Eng. Tech. Vol. 36 (2005), p. 552.

Spectral artifacts with high-efficiency wavelength dispersive spectrometers

Johannes Menso Dijkstra

Thermo Fisher Scientific, Takkebijsters 1, Breda, the Netherlands

hans.dijkstra@thermofisher.com

Modern high-efficiency wavelength dispersive spectrometers (HE-WDS) have shown for many years to be a very useful expansion of the microanalysis capabilities of the analytical scanning electron microscope (SEM), complementing the much more common energy dispersive spectrometers (EDS). The large improvement compared to EDS of energy resolution and thus signal to background ratio, have made the HE-WDS an excellent tool to separate minor elements from overlapping major elements in complex samples, and for the qualitative and quantitative analysis of trace elements.

Since most users of HE-WDS systems have limited or no experience with conventional fully focusing WDS spectrometers, and the built-in ease of use of the HE-WDS system makes them as convenient as EDS systems, often users tend to forget that these are still wavelength dispersive systems, and thus exhibit several of the typical artifacts that experienced WDS users take for granted.

EDS users mainly have to deal with two serious artifacts: Silicon escape peaks and pulse pile-up peaks, caused by the EDS detector and the pulse-processing electronics respectively. Both these artifacts are not present in any WDS spectrum.

In WDS the most common artifacts are higher order reflection peaks and absorption phenomena in either the diffracting crystal or the gas of the proportional counter. Both types of artifacts can be seen in HE-WDS, but their significance varies from the same artifacts in classical WDS systems.

In this presentation these artifacts are properly explained and illustrated, and a direct comparison is made between spectra from a classical WDS and a modern HE-WDS using the same samples and analysis conditions.

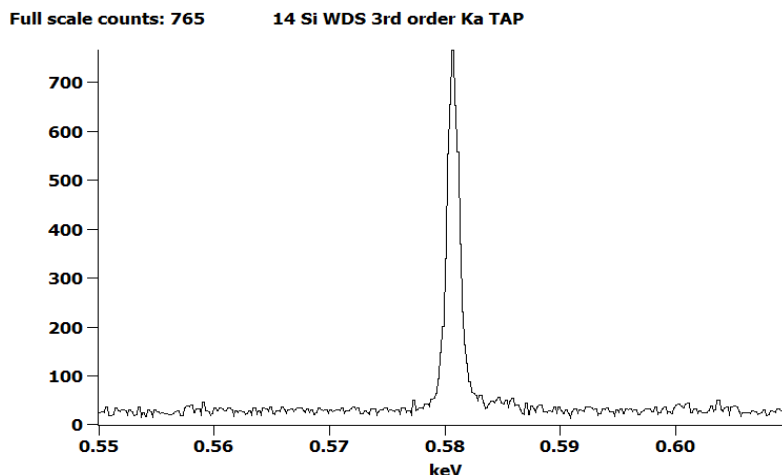


Fig. 1. Third order reflection of Si-Ka using HE-WDS with TAP crystal. Energy resolution of ~ 2 eV !!

Atomic resolution transmission electron microscopy at picometer precision

Knut W. Urban

Ernst Ruska Center & Peter Grünberg Institute, Research Center Jülich, D-52425 Jülich/Germany
k.urban@fz-juelich.de

Introduction

In recent years aberration-corrected transmission electron microscopy (TEM) has demonstrated that the new research opportunities offered by this technique are meeting the growing demand of materials science for atomic-scale characterization of materials [1, 2]. Genuine atomic resolution has become available allowing to measure individual atomic positions and lateral atomic shifts with a precision in the picometer range. In addition exploiting the coherence of the wave field and the subtle phase relations of the electron waves typical for TEM also elemental information can be obtained, e.g. close to boundaries or interfaces [3]. On this basis aberration-corrected TEM has become a unique measurement tool allowing direct correlation of macroscopic physical properties and of the results of *ab-initio* calculations with individual atomic position measurements. However, in order to do so the electron microscopic investigations have to become more quantitative, much beyond the level which appeared to be sufficient in pre-aberration correction times.

Picometer Precision

The goal is to measure the set of individual atom positions in a sample, $\mathbf{X}=\{\mathbf{r}_1, \mathbf{r}_2, \mathbf{r}_3, \dots\}$. This set denotes universal coordinates in the crystallographic sense, i.e. free of joint rotations or displacements. Of course we are not interested to measure the atom positions in a tilted sample since the respective coordinates are not universal. Although this may sound trivial, it is not so in reality: The precision of the new-generation optical instruments is substantially higher than the mechanical precision of even the best sample goniometers. Therefore, it is in general unavoidable that the results are affected by small residual sample tilts. We note that a (uncontrollable) tilting angle of only 0.5 mrad leads to a geometrical shift in a 10 nm thick specimen of 5 pm. For an optical precision in the order of 1 pm this cannot be tolerated. However, this is not all: The atomic contrast maxima are affected by tilt in a quantum-mechanical way. The Bloch states pertaining to two different atom species (different nuclear charge number, different scattering potential) in a crystal are reacting differently to tilt giving rise to artifacts in atom coordinate measurements which cannot be recognized as such without a proper treatment in contrast calculations. As a result positions and distances measured taking the primary, uncorrected atomic intensity maxima data cannot be trusted.

An additional goal in modern transmission electron microscopy is to measure atomic-scale concentrations (occupancies). It has been shown that this is possible on a relative scale [3] and now also on an absolute scale [4]. This requires the measurement of the amplitude of the atomic intensity maxima. However, the values of these intensities are affected by sample thickness, by sample tilt and by aberrations in the optical part of the imaging process. The former two parameters are not known. The aberrations, including those adjusted on purpose for contrast (spherical and defocus aberration) are not known sufficiently accurately either. Detailed measurements have shown that in picometer microscopy one of the critical issues is the drift of the optical parameters [5]. The values measured by the Zemlin tableau technique hours or even minutes before image acquisition may be unreliable. This is clearly an entirely different scenario compared to that defining the (today inadequate) standards of the pre-aberration-correction era. Trustable picometer precision results can only be obtained by a quantitative complete and self-consistent inversion of the imaging process by quantum-mechanical and optical image calculations. While in the past qualitative simulation results were considered sufficient and the problem was considered solved when the exit-plane wave function was retrieved

from a set of images which then was taken (employing in general without further justification the projected potential approximation) as a direct representation of the atomic arrangement, this is no longer adequate.

Absolute Contrast Measurements

Recently the ultimate that can be achieved to date in quantitative transmission electron microscopy was investigated studying the atom relaxations and the elemental intermixing at the interface of a $\text{LaAlO}_3/\text{SrTiO}_3$ heterostructure [5]. A primary set of data was collected by fitting two-dimensional Gaussians to the intensity distributions in images acquired in a TITAN 80-300 transmission electron microscope at 300 keV. A sub-set of these data describing the (known) atomic lattice away from the interface was taken as a 'template' in order to derive the values for the imaging parameters at the time of image acquisition. For this a first-approximation model of the template structure was taken as input for the Schrödinger equation searching for solutions as a function of specimen thickness and tilt. The image intensity distribution (still in the template area) was used as input for a reconstruction of the electron exit plane wave function taking spherical aberration, defocus aberration, two and threefold astigmatism, and coma as parameters. A quantitative fit of the theoretical to the experimental image intensity distribution was achieved. We note that this has to include the diffuse background intensity between the intensity maxima since this is much more sensitive to parameter changes than the maxima.

A critical issue in such calculations is the problem of the so called *Stobbs factor* which describes the fact that the measured image contrast (defined as the standard deviation of the intensity from the image mean intensity, normalized to one) is by typically a factor of three too low when compared to the calculated value. It could be shown that the bulk of the Stobbs factor originates from the particular transfer properties of the CCD camera as expressed by the modulation transfer function [6]. However, it was found that a fully quantitative matching on an absolute scale of the experimental contrast requires a convolution of the simulated image intensity with a Gaussian function in addition. The root-mean square (rms) width of this Gaussian is termed effective image spread, s . The value of s represents the radius of a blurring operation that has to be applied to the simulated image in order to establish an optimum absolute contrast match between simulation and experiment. This value was found to be quite small, i.e. 20 pm. It has to be pointed out that comparing a theoretical contrast calculation with a real experimental situation (with finite electrical lens current stabilities, mechanical vibrations, the effect of electron bombardment, radiation damage etc.) a perfect 1:1 match can hardly be expected without such a phenomenological factor. After the imaging parameters, the actual values of specimen thickness and tilt and all the aberrations prevailing at the time of image acquisition were established, the atomic interdiffusion and picometer-range atom relaxations close to the interface could be measured with optimum precision. This is the first case where absolute-scale contrast matching was achieved. Furthermore absolute occupation data and picometer precision position data could be measured simultaneously in transmission electron microscopy in the same position of the sample for the first time.

References

- [1] K. W. Urban: Science 321 (2008), p. 506.
- [2] K. W. Urban: Nat Mater. 8 (2009), p. 260.
- [3] C.-L. Jia and K. Urban: Science 330 (2004), p. 2001.
- [4] C.-L. Jia et al.: Microsc. Microanal. 19 (2013), p. 310.
- [5] J. Bartel and A. Thust: Ultramicroscopy 111 (2010), p. 27.
- [6] A. Thust: Phys. Rev. Lett. 102 (2009), p. 220801.

Electron holography for structures and fields

Hannes Lichte

Triebenberg Laboratory, Institute of Structure Physics, Technische Universität Dresden, Germany

Hannes.Lichte@Triebenberg.de

Transmission Electron Microscopy is wave optics: The electron wave is modulated both in amplitude and phase by interaction with the object. Usually, however, the detector only records the intensity representing the squared amplitude of the wave, whereas it is blind for the phase modulation. This phase-loss means a considerable loss of information, e.g. about electric and magnetic fields in the object. Furthermore, scrambling of amplitude and phase by the aberrations of the TEM gives rise to a distortion of the image wave with respect to the object wave, and hence to severe problems with interpreting the findings in terms of object properties.

The phase-loss is overcome by electron holography proposed by Gabor [1]. Amongst the 20 forms of electron holography identified by Cowley [2], the most successful method so far is off-axis electron holography. By means of the Moellenstedt electron biprism [3] used as a coherent beam splitter, a reference wave is superimposed to the image wave; this gives rise to an interference pattern (“hologram”), which contains both amplitude and phase in contrast and position of the interference fringes, respectively. By means of a reconstruction procedure, the distributions of amplitude and phase in the field of view are determined quantitatively, i.e. the image wave is revived completely. Details can be found in the review [4]. The uniqueness of holography lies in the fact that, in addition to the amplitude (intensity), it provides the phase distribution from the object. Therefore, most applications of holography evaluate only the reconstructed phase images.

At medium resolution with details larger than 2 nm, the aberrations of the electron lenses can be neglected, and hence the reconstructed wave agrees with the object wave. Thus, the reconstructed phase distribution can directly be interpreted in terms of the object. This is the basis for studying

- Mean Inner Potentials in solids
- Soft Matter: Phase contrast in focus without staining
- Functional potentials: pn-junctions in semiconductors
- Electric Fields controlling growth in biominerals
- Electric potential distribution in charge-modulated structures
- Magnetic fields in and around magnetic structures down to a nanoscale

Examples of such applications are described in detail in [5].

Holographic Tomography.

The phase signal represents the 2D-projection of the object structure integrated along the electron path. To obtain full 3D-information, the methods of holography and tomography are combined: A tilt series of holograms is recorded, from which the corresponding 2D-phase image series is reconstructed. Following tomographic procedures, from these 2D-images the 3D-representation is reconstructed, which allows uniquely determining 3D electric potential distribution [6].

At atomic resolution, because of the aberrations, amplitude and phase of the reconstructed wave differ considerably from the object wave and hence cannot be interpreted directly. First, the aberrations have to be corrected by appropriate processing. Then, both in amplitude and phase, lateral resolution can be achieved as high as determined by the information limit offered by the TEM used for recording the hologram. The resulting phase images allow details of the atomic structure to be revealed, such as

- difference of atomic numbers of different constituents
- number of atoms in an atomic column
- interatomic electric potentials
- potentials across interfaces

Examples and further references are given in [4].

Performance Limits

The optimal reachable lateral resolution is given by the information limit of the microscope, which is close to or better than 0.1nm with a modern TEM. Besides the lateral resolution, however, the signal resolution is likewise essential, because the structures of interest mostly produce only very weak phase modulations. Lateral and signal resolution can be combined in one figure of merit, the Information Content $InfoCont=n_{\phi}n_{rec}$ of a hologram [7]. It is the product of the number n_{ϕ} of phase values distinguishable in the range $(0,2\pi)$, and the number n_{rec} of pixels reconstructed across the field of view. $InfoCont$ depends on the quality of the microscopy system: it is given e.g. by the brightness of the electron emitter, stability of the TEM, the quality of the electron detector used, and the disturbance level of the whole lab. In our case, $InfoCont = 7100$ is routinely achievable. This means for example that, in order to see details of $2\pi/50$ such as fields of single atoms corresponding to $n_{\phi} = 50$, the number of reconstructed pixels is limited to $n_{rec} = 140$. Reachable lateral resolution and field of view are related accordingly: aiming at a lateral resolution of 0.1nm , the reachable field of view is limited to 7nm , because one resolution element is made up by two pixels (Nyquist sampling theorem).

In summary, one can say that, after 40 years of development, electron holography is an established method for comprehensive characterization of solids including their intrinsic electromagnetic fields. The performance, essentially restricted by quantum noise, allows atomic resolution both laterally and in signal. Any improvement of electron microscopy, such as of lateral resolution and of brightness of the electron gun, will enhance the capabilities of this unrivalled method for nanocharacterization. Therefore the new achievements such as the aberration corrector and electron sources with highest brightness will improve also the holographic analysis of smallest details in solids.

References

- [1] D. Gabor: Nature 161 (1948), p. 563.
- [2] J.M. Cowley: Ultramicroscopy 41 (1992), p. 335.
- [3] G. Möllenstedt and H. Düker: Z. Physik 145 (1956), p. 377.
- [4] H. Lichte and M. Lehmann: Rep. Prog. Phys. 71 (2008), p. 016102.
- [5] H. Lichte, P. Formánek, A. Lenk, M. Linck, Ch. Matzeck, M. Lehmann and P. Simon: Annu. Rev. Mater. Res. Vol. 37 (2007), p. 539.
- [6] D. Wolf, A. Lubk, F. Röder and H. Lichte: Curr. Opin. Solid State Mater. Sci. 17 (2013), p. 126.
- [7] H. Lichte: Ultramicroscopy 108 (2008), p. 256.

Chromatic aberration corrected TEM and applications in materials science

Joachim Mayer^{1,2a}, Juri Barthel², Lothar Houben², Maryam Beigmohamadi^{1,2}
and Knut Urban²

¹Central Facility for Electron Microscopy, RWTH Aachen University, 52074 Aachen, Germany

²Ernst Ruska-Centre for Microscopy and Spectroscopy with Electrons, Research Centre Juelich, 52425 Juelich, Germany

^amayer@gfe.rwth-aachen.de

Introduction

The invention of aberration correctors has revolutionized the development of TEM and STEM instrumentation. Only shortly after the development and installation of the first TEM with a corrector for the spherical aberration [1], commercial instruments with aberration correctors are now offered by all major manufacturers. In order to provide a platform for these novel developments and based on the experience with the first aberration corrected TEM [2-4], Research Centre Juelich and RWTH Aachen University have jointly founded the Ernst Ruska-Centre for Microscopy and Spectroscopy with Electrons (ER-C) [5]. Research at the Ernst Ruska-Centre focuses on the development of new quantitative methods in TEM and on their application in materials science and solid state physics.

Instrumentation

At the Ernst Ruska-Centre we have recently installed the FEI Titan 60-300 PICO. PICO is a fourth-generation transmission electron microscope capable of obtaining high-resolution transmission electron microscopy images approaching 50 pm resolution in the C_C - and C_S -corrected mode at 300 keV. It is currently one of only two microscopes in the world capable of chromatic aberration correction.

Experimental Results

In the present contribution we will report on the initial results obtained with the PICO instrument. In the PICO instrument, HRTEM images can be obtained with simultaneous correction of the spherical and the chromatic aberration. Furthermore, a spherical aberration corrector also exists in the illumination system for C_S -corrected STEM imaging.

The benefits of chromatic aberration corrected imaging are particularly large for HRTEM imaging at low accelerating voltages and for energy filtered (EFTEM) imaging with large energy window width. In the present contribution we will focus on these two applications and will present results from our recent work.

Examples for low voltage HRTEM imaging will be presented from our work on graphene and from experiments with beam-sensitive nanoparticles. In these experiments we lowered the accelerating voltage to values as low as 50 kV, in order to keep the electron energy below the displacement threshold.

As example for energy filtered imaging, we will present the first experimental EFTEM images using the C_C - and C_S -corrected optics for a sample of crystalline silicon. Atomic resolution images could be obtained and the contrast formation will be discussed. Quantum mechanical calculations from first principles were performed and are an essential adjunct to elucidating the process of electron propagation and image formation [7].

Further examples which will be discussed will include applications in materials and energy sciences. Specifically, we will report on our investigations of Si/SiO₂ multiple quantum wells for all silicon solar cells. Current concepts which promise a substantial increase in PV efficiency are based on

the use of manifold absorbers consisting of Si/SiO₂ multiple quantum wells (QWs). In the Si/SiO₂ QW material the charge carrier confinement leads to an increase of the energy gap well above the bandgap value of bulk Si (1.1 eV), tunable by the Si quantum well thickness. A double-junction solar cell consisting of a Si wafer and an ideal QW absorber with a band gap of 1.8 eV is predicted to have a theoretical efficiency limit of 40 %. We will report on our studies of such QW structures with layer thicknesses in the range of 1 - 3 nm. EFTEM imaging in the PICO gives valuable insight in the chemical nature of the layer structure at atomic resolution.

References

- [1] M. Haider, H. Rose, S. Uhlemann, E. Schwan, B. Kabius, and K. Urban: Nature 392 (1998), p. 768.
- [2] M. Lentzen, B. Jahnen, C.L. Jia, K. Tillmann, and K. Urban: Ultramicroscopy 92 (2002), p. 233.
- [3] C.L. Jia, M. Lentzen, and K. Urban: Science 299 (2003), p. 870.
- [4] C. L. Jia, K. Urban: Science 303 (2004), p. 2001.
- [5] <http://www.er-c.org>.
- [6] B. Kabius, P. Hartel, M. Haider, H. Müller, S. Uhlemann, U. Loebau, J. Zach, and H. Rose: J. Electron Microsc. 58 (2009), p.147.
- [7] K. Urban, J. Mayer, J. Jinschek, M. J. Neish, N. R. Lugg, and L. J. Allen: PRL 110, (2013), p. 185507.

New developments in electron crystallography: molecular motion and 3D orientation mapping

Alexander S. Eggeman^{1,a}, Robert Krakow^{1,b}, Steffen Illig^{2,c},
Henning Sirringhaus^{2,d} and Paul A. Midgley^{1,e}

¹Department of Materials Science and Metallurgy, University of Cambridge, 27 Charles Babbage Road, Cambridge, CB3 0FS, UK

²Cavendish Laboratory, University of Cambridge, J.J. Thompson Avenue, Cambridge, CB3 0HE, UK

^aase25@cam.ac.uk, ^brk471@cam.ac.uk, ^csi278@cam.ac.uk, ^dshs220@cam.ac.uk, ^epam33@cam.ac.uk

Introduction

Advances in electron microscope hardware, coupled with new algorithms and fast computation, have led to many recent developments in the analysis of materials at the nano- and atomic scale. Whilst high resolution imaging can lead to insights with pm resolution, there are still many situations in which electron diffraction plays an important role. In this paper, we explore two examples where novel information can be retrieved using electron diffraction, which cannot be found with any other technique.

Molecular Motion in Organic Semiconductors

Many of the electrical and optical properties of organic semiconductors are governed by the interaction of electronic excitations with intra- and inter-molecular vibrations. Direct measurements of these interactions are however rare and can be best made through the use of thermal diffuse scattering (TDS) experiments which are sensitive to any correlated motion of the molecular structure. Many of the organic structures of interest, however, are not well suited to x-ray techniques as they can often be in the form of thin films or nanostructures. Electron diffraction offers a way to probe these interactions with high spatial resolution. However, in order to fully interpret any TDS seen in the electron diffraction pattern, simulations, taking into account any dynamical effects, must be undertaken.

Fig. 1(a) shows an experimental electron diffraction pattern recorded parallel to the [001] zone axis of a TIPS-pentacene thin film [1]. The intensity scale has been adjusted in this image to enable the weak diffuse scattering to be seen clearly. Fig. 1(b) shows a best-fit multislice simulation which matches the experimental data remarkably well. Simulations were undertaken using a frozen-phonon approach and by using a large supercell to allow fine sampling of reciprocal space and improved fidelity [2]. Reliable statistics for the atomic displacements were found after 50 iterations. The simulations indicated that the distribution of relative intermolecular distances was best-fit using a Gaussian with a width of $0.08 \pm 0.02 \text{ \AA}$. Molecular dynamics confirmed these results and allowed a quantitative understanding of the electronic properties of this organic semiconductor.

Combining Electron Tomography and Precession Electron Diffraction

Precession electron diffraction (PED), introduced twenty years ago [3], has been used not only to elucidate the crystal structure of an unknown material, but also, with its scanning variant (SPED), to probe the orientation of known structures and particularly polycrystalline metals. The possibility to extract quantitative orientation images in the TEM makes it a complementary technique to that of orientation imaging with EBSD in the SEM. At the nanometer length scale, the resolution offered by SPED, TEM specimens vary both laterally and in depth. The possibility that the morphology, composition or crystal orientation might change in all three dimensions leads one to explore how tomographic methods can be coupled with SPED and to orientation imaging specifically. Whilst there has been work using conical DF imaging to determine 3D orientation information [4], here we present a new method based purely on PED patterns to reconstruct 3D morphology and orientation. By acquiring patterns pixel by pixel using SPED, then sequentially tilting and repeating the acquisition, it

is possible to acquire a full 3D data set to allow real space reconstruction of the sample morphology and more importantly, determine the relative orientation of phases seen in that 3D space. Fig. 2 shows an example from a commercial Ni-base superalloy in which the real space 3D reconstruction shows a metal carbide (MC) particle within a Ni-rich f.c.c. γ matrix. By analyzing the reconstructed 3D reciprocal space from the carbide and neighbouring matrix phase, a new interface relationship was discovered with the $\{531\}$ face of the matrix epitaxially-strained to match the $\{111\}$ surface of the carbide.

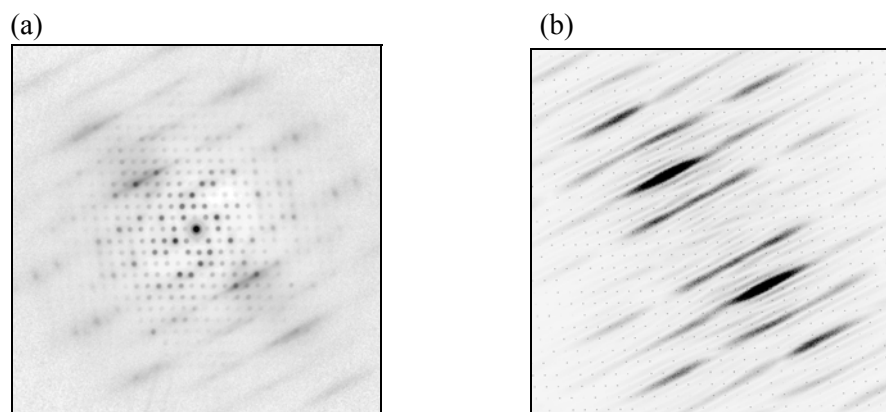


Fig. 1. (a) Experimental [001] diffraction pattern recorded from a thin film of TIPS-pentacene. (b) Best-fit multislice simulation of the pattern in (a)

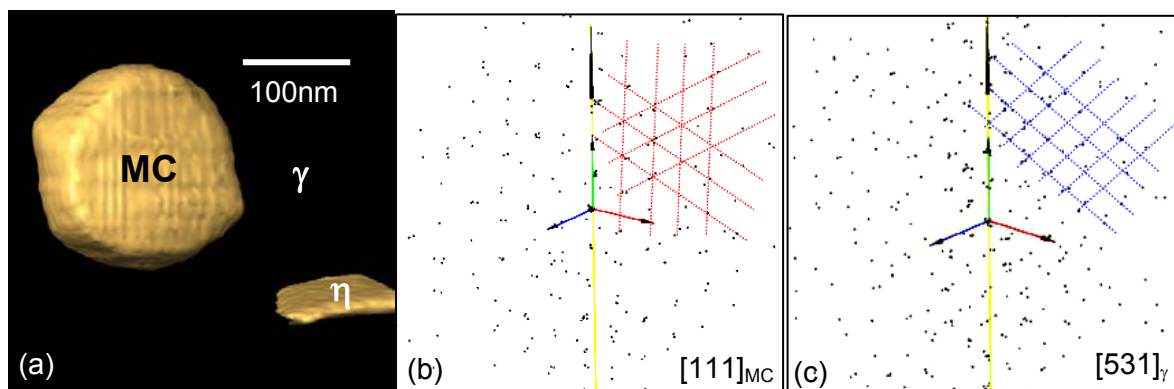


Fig. 2. (a) Real space tomogram reconstructed from a tilt series of SPED patterns with extracted 3D reciprocal space maps indicating the relative orientation between (b) the cubic metal carbide (MC) particle and (c) the f.c.c. γ matrix. The reciprocal space map for the η -phase is not shown here

References

- [1] A.S. Eggeman, S. Illig, A. Troisi, H. Sirringhaus and P.A. Midgley: Nat Mater. 12 (2013), p. 1045.
- [2] A.S. Eggeman, A. London and P.A. Midgley: Ultramicroscopy 134 (2013), p. 44.
- [3] R. Vincent and P.A. Midgley: Ultramicroscopy 53 (1994), p. 271.
- [4] H.H. Liu, S. Schmidt, H.F. Poulsen, A. Godfrey, Z.Q. Liu, J.A. Sharon and X. Huang: Science 332 (2011), p. 833.

Planar and zigzag defects in functional oxide nanowires

Velimir Radmilović

Nanotechnology and Functional Materials Center, Faculty of Technology and Metallurgy, University of Belgrade, Karnegijeva 4, Belgrade, Serbia

We recently discovered a novel method to produce $M_2O_3(ZnO)_n$ polytypoid nanowires (MZO, where M could be various elements, such as In, Ga, Fe), and we demonstrated nanostructured enhancement in both thermal and electrical properties in ZnO-based polytypoid nanowires and study the effect of the atomic structure on performance. Due to the decoupling of certain electrical and thermal properties, these polytypoid nanowires, which contain nanometer-scale periodic compositional and structural features, are promising materials for a variety of applications. This new concept of structure control at atomic level is in agreement with the theoretical prediction that it is possible to increase the material-dependent figure of merit by using low dimensional materials, attributed to electronic band structure changes and enhanced interface phonon scattering. It appeared that control of lattice phonon transport contribution is essential to improve thermoelectric properties of ZnO based nanowires. Atomic resolution high angle annular dark field (HAADF) imaging is used to perform a detailed structural analysis on the $M_2O_3(ZnO)_n$ nanowires, unambiguously determined the location of indium within the structure and to evaluate lattice strain and the presence of defects. Based on this analysis we propose that the superlattice structure is generated through a defect-assisted solid state diffusion. One of the greatest advantages of this novel synthesis is the ability to tune the nanoscale features of the polytypoid wires by simply adjusting the amount of metal precursor. Compare to ZnO nanowires, these new oxide thermoelectric nanostructures exhibited almost three orders of magnitude increase in efficiency, due to hindering of phonon propagation, while preserving good electrical conductivity. This will enable future studies on structure-dependent thermoelectric properties and possibly lead to further enhancements in thermoelectric efficiency.

All TEM has been performed at the National Center for Electron Microscopy, LBNL, Berkeley, supported by the Director, Office of Basic Energy Sciences, Materials Sciences and Engineering Division, of the U.S. Department of Energy under Contract No. DE-AC02-05CH11231. VR acknowledges support by the Ministry of Education and Science of the Republic of Serbia, under project No. 172054.

Interface diffusion–controlled phase transformations in nanomaterials

Guillermo Solórzano

Department of Materials Science and Engineering, PUC-Rio, Rua Marques de sao Vicente 225, Rio de Janeiro,
22453-900 Brazil
guilsol@puc-rio.br

Grain boundary diffusion–controlled transformations are examined. Under this category we consider discontinuous precipitation (DP), discontinuous dissolution (DD) and diffusion induced grain boundary migration (DIGM) phenomena. We briefly describe first the discontinuous mode of precipitation (DP) in metallic polycrystalline systems where, upon aging heat treatments, supersaturated solid solutions decomposes by the action of moving grain boundaries, acting as fast diffusion paths for solute atoms redistribution, leave behind a depleted matrix and a lamellar or rod precipitate product growing in a cooperative fashion. From a fundamental point of view, these are among the most intriguing solid-solid transformations: their full analysis involves consideration of interacting friction, capillary and chemical forces all focused on a moving grain boundary. In this regard, discontinuous transformations products differ from those controlled by volume (lattice) diffusion, most of which can be modeled, at least to first order, on the basis of a local equilibrium hypothesis. In contrast, the non-equilibrium aspects of discontinuous transformation are central to its description. From the experimental point of view, through analysis in different alloy systems, we have concluded that the high–resolution dedicated STEM, in its several modes of operation, is capable of yielding information of value in increasing our understanding of solid-state transformations. In particular, the microanalysis capabilities allows the determination of diffusion data for individual moving grain boundaries and measure the residual super saturation within depleted lamellae in a DP product and thereby to infer the chemical stored energy in the material besides the interfacial and strain energy stored at the high density precipitate/matrix interfaces.

We extend the analysis of the above described phenomena taking place in a submicron grain size material and the resulting interface multiplication in the transformation product which can consume the entire matrix. Moreover we demonstrate that the combination of DP followed by continuous dissolution at high temperatures promotes a dramatic grain refinement effect, achieving a polycrystalline material with 3 orders of magnitude smaller grains.

From the practical point of view, DP in structural materials has been considered as deleterious to mechanical properties as long lived fine coherent precipitates are swept by the grain boundary reaction front. However, starting materials with high super saturation and properly engineering microstructure could develop DP and exhibit interesting physical properties. In particular, we have demonstrated that in some nano-scale grain size magnetic systems an adequate DP volume fraction generates a giant magneto resistance GMR behavior.

Recent characterization results on nanoparticles for possible medical applications

Robert Sinclair, Paul Kempen, Steven Madsen, Richard Chin and Ai Leen Koh

Department of Materials Science and Engineering and Stanford Nanocharacterization Laboratory

Stanford University, Stanford, California 94305, USA

lbobsinc@stanford.edu

Nanotechnology has increasing applications for medical purposes. The group with which we are associated is developing nanoparticle systems for early cancer detection and therapy. Of particular interest is the attachment of nanoparticles to cancer tumors or circulating tumor cells followed by their detection by physical properties such as magnetic signals or surface enhanced Raman spectroscopy (SERS). Our contribution is to analyze the location and attachment of nanoparticles to cancer cells. Because of the dimensions involved, advanced microscopy techniques are required for this research.

In this presentation we will describe several case studies including high resolution SEM on SERS nanoparticles in brain tumors, and a toxicological study on nanoparticles in organ tissue for colorectal cancer using STEM techniques. Recent research using electron beam lithography to manipulate nanoparticle shape for high SERS intensity and the application of FIB for cryo-sectioning of cells will be summarized.

This research is supported by a CCNE-T grant from the National Cancer Institute through Professor Sam Gambhir of the Stanford Medical School.

Two topics from our recent works

Masahiro Kawasaki¹, Yuta Nakafushi², Masateru Nose³, Tadashi Nobuchi⁴,
Makoto Shiojiri^{2,5}

¹ JEOL USA Inc., Peabody, MA 01960, USA

² School of Science and Engineering, University of Toyama, Toyama 930-8555, Japan

³ Faculty of Art and Design, University of Toyama, Takaoka 933-8588, Japan

⁴ Professor emeritus of Kyoto University, Kyoto, Japan

⁵ Professor emeritus of Kyoto Institute of Technology, Kyoto, Japan

The first topic is on the structure of nanocomposite hard coatings fabricated by differential pumping co-sputtering (DPCS). To elucidate the process and mechanism of film growth in a DPCS system, we prepared a Cr(Al)N/38 vol.%SiO_x nanocomposite layer on the under buffer layers that were grown on a Si substrate and examined the structure of these layers by means of analytical electron microscopy, discussing the results of hardness measurements for these coatings. Next, we present an investigation on the structure and biomechanics of culms of *Phragmites australis* used for Japanese double reed wind instrument “Hichiriki”. The structure of culms harvested from different reed beds was examined by means of plant anatomy and the indentation hardness and Young modulus were locally measured on the tissues of different Hichiriki reeds, discussing the relation with music performance of reeds.

Keywords: Hard coating, wind instrument reed, Cr(Al)N/SiO_x, *Phragmites australis*, hardness

Microstructural characterization of nanostructured supersonic sprayed Ni-Sn coatings after wear test at elevated temperature

Jan Kusiński^{1a}, Sławomir Kąc^{1b}, Kazimierz Kowalski^{1c}, Beata Dubiel^{1d}, Stanisław Dymek^{1e}, Aleksandra Czyrska-Filemonowicz^{1f}, Sergi Dosta^{2g}, Emmanuel Georgiou^{3h}, Paolo Matteazzi⁴ⁱ

¹AGH University of Science and Technology 30 Mickiewicza Av. 30-059 Krakow, Poland

²University of Barcelona, Martí i Franques 1, E-08028, Barcelona, Spain

³KU Leuven, Dept. MTM, Kasteelpark Arenberg 44, B-3001 Leuven, Belgium

⁴CSGI and MBN Nanomaterialia, Via Bortolan 42, Vascon di C. (TV), Italy

akusinski@agh.edu.pl, bslawomir.kac@agh.edu.pl, ckkowalsk@agh.edu.pl, dbdubiel@agh.edu.pl, edymek@agh.edu.pl, fczyrska@agh.edu.pl, gsdosta@cptub.org, hemmanuel.georgiou@mtm.kuleuven.be, imatteazzi@mbn.it

Introduction

Coatings are applied to reduce surface degradation caused by a wear, corrosion and oxidation. Nowadays, nanocrystalline coatings, due to their increased hardness, high mechanical strength, enhanced corrosion and oxidation resistance, and/or an improved friction and wear behavior [1-3] are gaining importance in tribology. Actually, with using of modern PVD and CVD techniques is possible to deposit advanced multilayer coatings that permit dry contact of machinery parts or dry machining, eliminating the need to dispose of lubricants and coolants [4]. However, there are limitations of their usage, including relatively low coating thickness (max. 10 μm), reduced size of deposition area, substrate geometry, cost, and complexity of the process. Indeed, among a variety of coating techniques that permit to deposit thicker coatings thermal spray deposition is gaining a lot of attention [5]. The biggest challenge in thermal spraying of nanostructured powders is to retain nanostructuring after thermal spraying by limiting thermal diffusion and grain growth. In recent years, the supersonic cold gas spraying (CGS) deposition has been proved to be an attractive method for depositing thick nanostructured coatings, due to high kinetic energy of deposited particles and relatively low deposition temperature. The basic scientific and technological aim of the conducted research is the generation of nanostructured intermetallic Ni-Sn coatings having low friction coefficient and high wear resistance at elevated temperature. The wear behavior of the CGS coatings was compared to the one of industrial bulk or sprayed coated benchmark materials. Paper describes the microstructural and compositional changes that occur in the coatings during wear testing at 200, 400 and 550°C.

Materials and experimental details

Nanostructured Ni–20wt.% Sn coatings were deposited onto Inconel 725 alloy by supersonic spraying of agglomerated nano-grained Ni-Sn powders (20–50 nm). These powders were produced by the mechanical alloying process by high energy ball milling in an inert atmosphere. All the coating constituents are added to the ball mill and subsequently milled to get a nano-sized powder by a displacement reaction. The nanostructured coatings were then deposited by means of supersonic spraying on the Inconel substrates. The deposition parameters were a gas temperature between 600–800°C, variable pressure between 38 and 40 bars, and a stand-off distance of 20 to 60 mm. Dense coatings having a thickness of about 100 μm were achieved. Reciprocating sliding tests were performed in ambient air, at a normal load of 2 N, displacement amplitude of 200 μm and a sliding frequency of 5 Hz for 10,000 cycles in a high load tribometer. The microstructure and chemical composition of the as-sprayed, as well as after wear test Ni-Sn coatings were analyzed using FEI microscope with connected an energy dispersive X-ray analyzer (EDS) apparatus, and in a 200 kV JEOL JEM-200CX transmission electron microscope. Cross sections of the sprayed coatings were

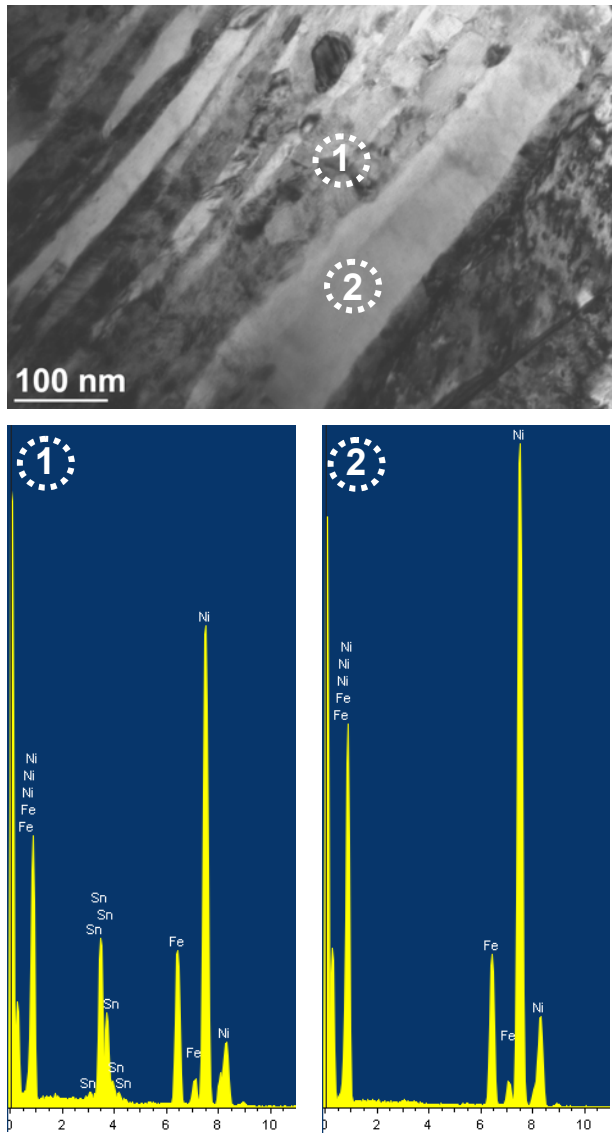


Fig. 1. TEM bright field image of as-deposited Ni-Sn coating and EDS spectrograms recorded in marked areas 1 and 2

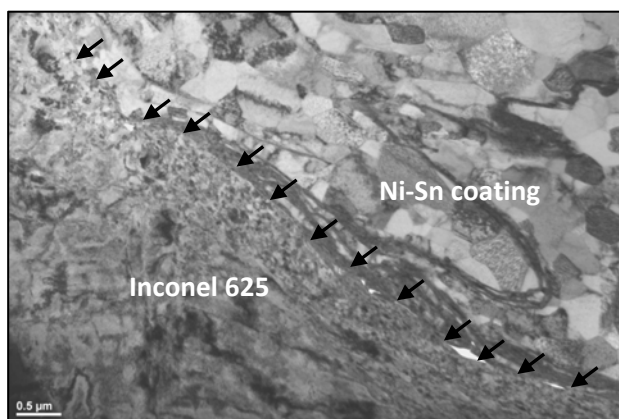


Fig. 2. TEM image showing microstructure at the Inconel 625 and Ni-Sn coating boundary in the sample that was wear tested at 550 °C

prepared by a Duo-Mill focused ion beam (Fig. 1). TEM bright field image showing layered, nanostructural, of as-deposited Ni-Sn coating and EDS spectrograms recorded in marked areas 1 and 2; one may observe that Sn is present only in darker areas. Light grains are rich of Ni. After the wear test thin films for TEM were cut from the oxide based tribo-layer by means of FIB technique. Recrystallisation in the Ni-Sn coating is well visible, due to annealing at 550°C of heavily deformed coating material (Fig. 2). Severe deformation of Ni-Sn powder occurring during mechanical alloying as well as supersonic spraying. Recrystallisation in the Ni-Sn coating is well visible, due to annealing at 550°C of heavily deformed coating material (Fig. 2).

Severe deformation of Ni-Sn powder occurring during mechanical alloying as well as supersonic spraying lowered recrystallisation temperature. Darker paths of fine grains in the coating are areas rich of Ni-Sn phase. During wear testing at 200, 400 and 550°C the Ni-Sn CGS coatings exhibit a wear behavior under reciprocating sliding better than benchmark materials. This is attributed to an appropriate balance of soft (Ni) and hard (Ni₃Sn) phases, and to the nanostructuring of the matrix, as well as to the presence of an oxide based tribo-layer, as confirmed by EDS and XPS analyses.

References

- [1] A.A. Voevodin, J.S. Zabinski, C. Muratore: Surf. Coat. Technol. 10 (2005), p. 665.
- [2] S. Achanta, M. Feuerbacher, A. Grishin, X. Ye, J.-P. Celis: Intermetallics 18 (2010), p. 2096.
- [3] M. Mohanty, R.W. Smith, M. De Bonte, J.-P. Celis, E. Lugscheider: Wear 198 (1996), p. 251.
- [4] E. Vancoille, J.P. Celis, J.R. Roos: Tribol. Int. 26 (1993), p. 115.
- [5] G. Bolelli, B. Bonferroni, J. Laurila, L. Lusvardi, A. Milanti, K. Niemi, P. Vuoristo: Wear 276-277 (2012), p. 29.

Quantitative analysis of elements in biological materials using energy-dispersive spectrometry and scanning electron microscopy

Marta Dubiel^{1,a}, Grzegorz Tylko^{1,b}

¹Department of Cell Biology and Imaging, Institute of Zoology, Jagiellonian University,
Gronostajowa 9, 30-387 Krakow, Poland

^amarta.dubiel@uj.edu.pl, ^bgrzegorz.tylko@uj.edu.pl

Introduction

Biological materials are mainly composed of low-Z number elements. Their organic matrices are classified into carbohydrate- (e.g. plant and fungi cell walls), protein- (e.g. animal soft tissues) and lipid-based (adipose tissue) ones. Thus, to determine element concentration in such specimens, appropriate standards have to be prepared, measured, and their spectra compared to those obtained from the unknown [1]. It is accepted that both standards and unknown biological material must be similar in the weighted sum of Z^2/A for all element present in a specimen (G-factor) to calculate element concentrations accurately. Then, any corrections for Z, A and F are not necessary what eliminates additional computations. It must be pointed out, however, that elemental distribution in some biological specimens is not homogeneous and many structures are mineralized (with high content of Si or Ca) or contain elements with Z number higher than 20 (e.g. Fe, Cu or Zn) [2]. Thus, preparation of standards relevant to the unknown is difficult or not possible. In this study we verified the applicability of several quantitative approaches usually used in biological X-ray microanalysis to determine elements (from sodium to calcium) in different organic and mineralized matrices.

Material and Methods

Monte Carlo simulations with WinX-Ray and CASINO codes [3,4] were chosen for examinations. 25 protein-based matrices with known concentration of elements were defined and their spectra simulated to obtain X-ray intensities or peak-to-background ratios for Na, Mg, P, S, Cl, K and Ca. Then, standard calibration curves were determined in the form of functions of intensities or P/B ratios and element concentrations (Fig. 1). Additionally, single protein standard with known composition and G-factor value of 4.0 was chosen and its spectrum simulated. Further, 30 different virtual carbohydrate-based specimens (the unknowns) with G-factor values between 3.42 and 4.88 were prepared and their spectra simulated to obtain characteristic intensities or P/B ratios for elements of interest mentioned above. Next, the element concentrations were determined using the following methods: 1) intensity- or 2) P/B-based calibration curves, direct comparisons (proportions) of 3) X-ray intensities or 4) P/B ratios between the unknown and the standard as well as 5) the iteration method when P/B ratios only were taken into consideration according to methodology described elsewhere [1,4]. Finally, errors related to nominal values of G-factors as well as element concentrations were computed. The range of errors at the level of $\pm 5\%$ was chosen to treat quantification procedure accurate for element quantification in biological materials.

Results and Discussion

Here, the quantification process was performed using single or group of protein standards in relation to carbohydrate-based unknown specimens. Thus, the difference between carbohydrate and protein G-factor values is insignificant. However, the presence of other elements leads to significant increase of the weighted sum of Z^2/A and sometimes the values of G-factors between a standard and an unknown exceed 25% or more. It might influence results obtained from proportions but should not be the case when the calibration curves are defined. There, a broad range of element concentrations introduced into the set of standards covers the ranges expected in the unknown. However, we found that the calibration curve derived from P/B ratios were not applicable to establish content of elements accurately (Fig. 2). The curves derived from intensities generated more accurate results (Fig. 2) but not for all elements tested, e.g. Mg and Cl were found underestimated whereas S overestimated. The best results were obtained with iterative method where P/B values are taken into account (Fig. 2). Neither matrix composition nor the presence of other elements tested influenced the results significantly.

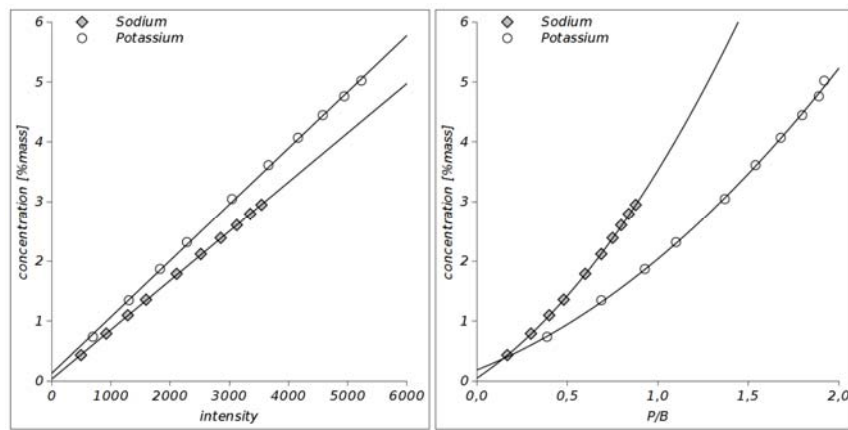


Fig. 1. The representative calibration curves for Na and K obtained on the basis of X-ray intensities (left) and P/B ratio (right) in the function of increasing element concentration

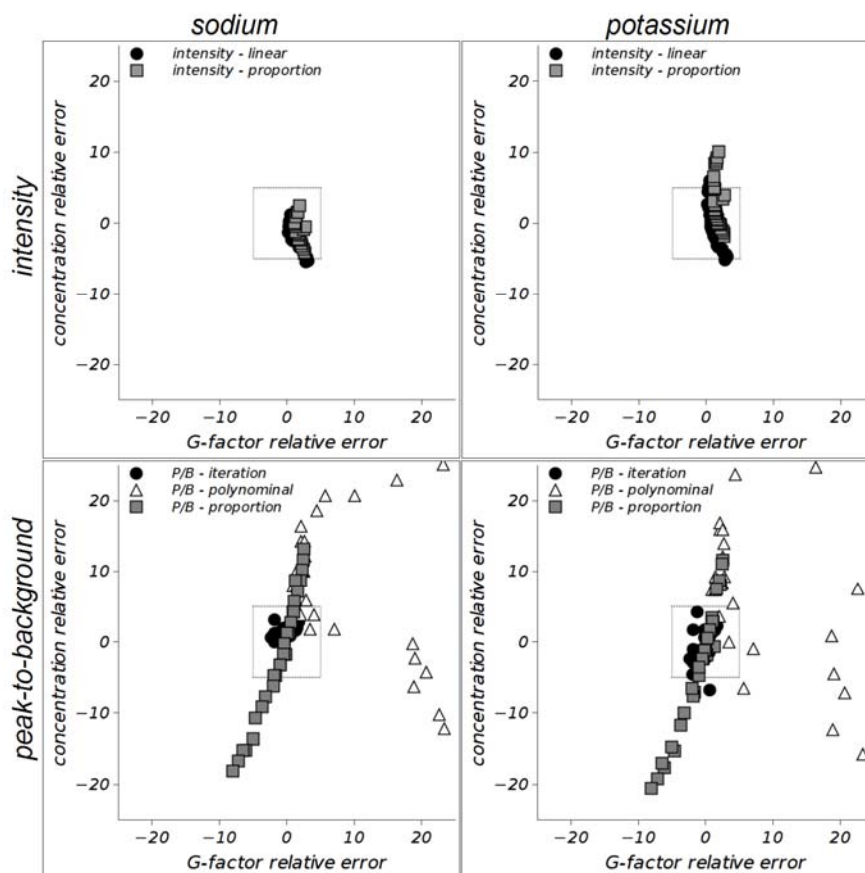


Fig. 2. Distribution of relative errors calculated for Na and K after their quantitative determination in virtual carbohydrate material when compared to protein-based standard. The results were obtained on the basis of X-ray intensities (upper panel) or P/B ratios (lower panel) using the calibration curves, proportion or iterative approaches. Dot-line square in the middle of the chart defines $\pm 5\%$ range of the relative error for G-factor value and element concentrations

References

- [1] A. Warley, in: X-ray microanalysis for biologists, edited by A.M. Glauert, volume 16 of Practical Methods in Electron Microscopy, Portland Press (1997).
- [2] P. Janik, G. Tylko, B. Ostachowicz, K. Turnau: Microsc. Res. Tech. Vol. 73 (2010), p. 1134.
- [3] R. Gauvin, E. Lifshin, H. Demers, P. Horny, H. Campbell: Microsc. Microanal. Vol. 12 (2006), p. 49.
- [4] P. Hovington, D. Drouin, R. Gauvin: Scanning Vol. 19 (1997), p. 1.
- [5] G. Roomans, in: X-ray microanalysis, edited by P.W. Hawkes and U. Valdrè Biophysical Electron Microscopy, London Academic Press (1990).

Is electron microscopy still in use for daily medical practice?

Andrzej Marszałek

¹Department of Oncologic Pathology, Poznan University of Medical Sciences and Greater Poland Oncology Center, Garbary 15, Poland

²Chair and Department of Clinical Pathomorphology, Collegium Medicum in Bydgoszcz, Nicolaus Copernicus University in Torun, Skłodowskiej 9, Bydgoszcz, Poland

amars@ump.edu.pl

At the beginning

The golden era of daily use of electron microscopy in medicine is gone. After 30 years (with peak in 60-ties and 70-ties last century) of blossoming development of TEM as a tool for basic as well diagnostic studies, it was first partially replaced by immunohistochemistry and then by other methods. Nowadays, here comes the era of genetic or molecular biology techniques, and some researchers believe that they will solve majority of problems of diseases development and diagnosis. Nevertheless, in some fields of medicine there is still a place for ongoing use of EM as a tool, that couldn't be replaced by any other technology. The best example is nephrology, in which the diagnosis of glomerulonephritis couldn't be done properly without samples evaluated by transmission electron microscopy. In other cases EM could be used in process of diagnosis of rare diseases or could be helpful in solving unusual presentation of diagnostic entity. This could be well illustrated by the use of TEM in dermatology, infectious disease as well as in oncologic pathology or diagnosis of immotile cilia syndrome. Yet another of present use of EM is utility of this technique for so called basic studies.

Instead of conclusions

To prove the need of keeping electron microscopy as powerful technique, in the presentation there will be introduced some selected clinical cases along with outline the complementary diagnostic procedures. Although around the world, still there are many EM facilities, according to high costs of the equipment as well a need of expertise for proper diagnosis the future is unclear.

Natural occurrence of graphene and its formation by epitaxial growth on the 001 planes of mica minerals

Henryk Kucha, Władysław Osuch, Bogdan Rutkowski, Adam Kruk

AGH University of Science and Technology, al. Mickiewicza 30, 30-059 Kraków, Poland

Introduction

The term *graphene* has been used first in 1987 [1] to describe single sheets of graphite as one of the constituents of Graphite Intercalated Compounds (GIC; i.e. a crystalline salt of the intercalant and graphene). So graphene is, by definition, a 2-dimensional, crystalline allotrope of carbon densely packed in a regular hexagonal pattern. The carbon-carbon bond length in graphene is about 0.142 nm, and the single graphene sheet in graphite has an interplanar spacing of 0.335 nm.

Probably the first note of naturally occurring graphene was related to phyllosilicate (mica, montmorillonite) intercalated graphites from Kupferschiefer black shale [2]. Such GIC's, well visible in reflected light microscope, when studied by TEM diffraction, show two groups of the c_0 value of the phyllosilicate sheet suggesting intercalation of two or three graphene layers.

Materials & methods

Samples from two localities has been studied: 1) Cu-bearing Kupferschiefer black shale from Poland containing illite, montmorillonite and mica intercalated graphite, and 2) Turnagain Ni and Platinum Group Elements deposit in alaskaites containing biotite, antigorite and molybdenite intercalated graphite from BC, Canada.

Samples for TEM were made under control of optical microscope from micro-areas first analysed by microprobe, Raman at 532 nm and SEM. TEM diffractions has been made with a Jeol JEM200CX microscope at 200kV, and a FEI electron microscope.

Kupferschiefer graphene

Graphite intercalated micas are well visible in reflected light microscope. Mica intercalated graphite often shows composite diffraction dots (Fig. 1). They arise from superposition of graphene (usually 2 layers) and mica patterns. TEM diffraction reveals two groups of the c_0 value of the phyllosilicate sheet: a) 1.679 ± 0.017 nm being a sum of phyllosilicate sheet $1.00 + 2$ graphene layers 0.67 nm (2×0.335 nm), and b) 2.240 ± 0.25 nm – 2.48 ± 0.35 nm being a sum of the phyllosilicate sheet 1.00 nm + 3 graphene layers ($0.335 \times 3 = 1.005$ nm).

Raman spectra show that the main peak D^* at 2718 cm^{-1} is distinctly asymmetric and after peak fitting appears to be composed of 3 peaks at 2228, 2660 and 2720, which is a very close to similar pattern from Turnagain (Fig. 4), and suggests the presence of 2 graphene layers [3].

Turnagain graphene

Graphene occurs as spectacular epitaxial intergrowths with biotite, annite or with antigorite (Fig. 3). Increasing magnification on SEM finer and finer intergrowths of graphite-type material with phyllosilicates can be observed.

Raman spectra diagnostic to graphene are shown between $2500 - 2830 \text{ cm}^{-1}$. Performed peak fitting, resolved 3 main peaks (cm^{-1}): main peak at 2720.54, and two subsidiary ones at 2658.95 and 2684.20. This peak structure suggests bi-layer graphene (Ferrari, 2007). TEM diffraction patterns show often superimposed mica and graphene, suggesting intercalated nanostructure.

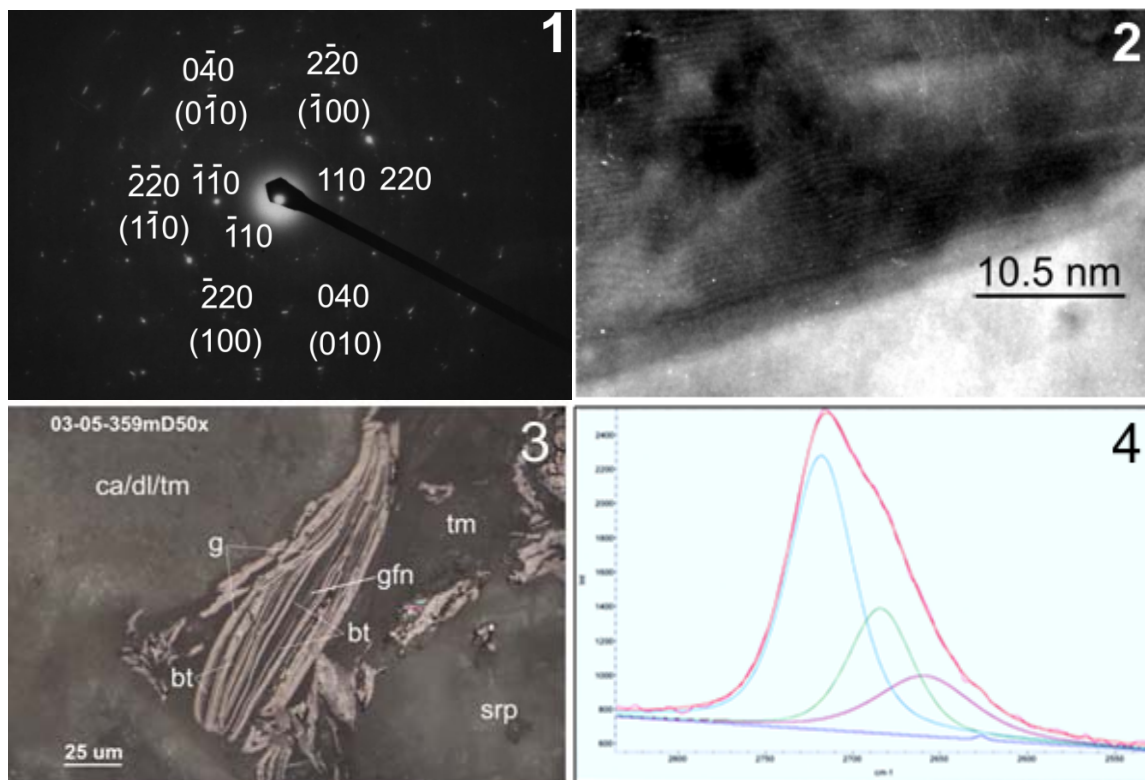


Fig. 1. The 001 TEM diffraction pattern of graphene (indices in brackets) intercalated mica (indices free standing). Diffraction nodes have a complex structure due to overlap of dots from mica and graphene. 220 of graphene may occur due to double diffraction. Sample 45, Lubin Mine

Fig. 2. Parallel fringes of graphene intercalated mica. Ripples may occur due to slight misfit of graphene and mica 001 layers. Diffraction shown on Fig. 1 (Kupferschiefer, Poland)

Fig. 3. Photomicrograph of graphene (graphite) intercalated biotite (bt) mica showing thicker graphite (g) layers, and with nano graphene (gfn) intercalated biotite (bt). Matrix is serpentinite (srp), tremolite (tm), dolomite (dl) and calcite (ca). Reflected light, Sample 03-05-359mD2

Fig. 4. Raman spectrum of nano epitaxial intergrowths of biotite/graphene from Fig. 3 (gfn), Sample 03-05-359mD2 ($\lambda=532$ nm). Performed 2D peak fitting shows 3 peaks suggesting bi-layer graphene. Range 2500 – 2830 cm^{-1}

References

- [1] S. Mouras: Rev. Chim. Miner. Vol. 24 (1987), p. 572.
- [2] H. Kucha, A. Wiczorek: Miner. Deposita Vol. 23 (1988), p. 174.
- [3] A.C. Ferrari: Solid State Commun. 143, (2007), p. 47.

3D and nanoscale investigations of wetting between organic liquids and electrospun nanofibre networks

Urszula Stachewicz^{1*}, Russell J. Bailey¹, Hao Zhang¹, Corinne A. Stone²,
Colin R. Willis² and Asa H. Barber¹

¹Department of Materials, School of Engineering and Materials Science, Queen Mary, University of London, Mile End Road, London E1 4NS, United Kingdom

²Defence Science & Technology Laboratory, Porton Down, Salisbury SP4 0JQ, United Kingdom

*u.stachewicz@qmul.ac.uk

Introduction

The wetting behaviour between fibres and liquids with low surface tension is of critical importance in not only textiles applications but also tissue engineering or filtration. The physical interaction of liquids in contact with fibrous materials is therefore of interest but is poorly understood despite years of experimental and theoretical development. Current difficulties in understanding wetting behaviour at fibrous arrays is perhaps due to the use of wetting theories that do not fully consider the geometry of the wetted surface, such as Wenzel and Cassie-Baxter [1].

Observation of wetting hierarchy, small and large scale droplet wetting on electrospun nanofibre networks, is therefore assisted by 3D imaging obtained with focussed ion beam (FIB) microscopy to section through a sample and high resolution cryo scanning electron microscopy (cryo-SEM) to take 2D images sequentially during sectioning. The results from the cryo-SEM/FIB are compared with individual electrospun fibre wetting experiments using a Wilhelmy balance approach. These observations are important in generally understanding the wetting behaviour between liquid droplets and fibre networks and in designing oleophobic surfaces.

Materials and Methods

Polyamide 6 (PA6, $M_w = 24,000 \text{ g}\cdot\text{mol}^{-1}$, BASF, Ultramid B33 L, Germany) was dissolved in a mixture of acetic acid ($\geq 99.7\%$, Sigma Aldrich, U.S.A.) and formic acid (98%, Sigma Aldrich, U.S.A.) (50/50 mass ratio) to produce a resultant polymer concentration of 12 wt% in solution. The PA6 polymer solution was electrospun into nanofibres using a large scale multi-jet electrospinning setup (NanoSpider, Elmarco, Czech Republic). This fibre spinning was achieved by applying a voltage of 60 kV between a rotating wire cylinder and an aluminium sheet acting as a ground electrode 18 cm above the cylinder [2, 3]. Electrospun PA6 fibre mats were used in their as-manufactured state but also surface modified to provide a more hydrophobic, and potentially oleophobic, material. Surface modification of the PA6 fibre sample was achieved using plasma treatment to add fluoropolymer to the electrospun fibre surfaces.

Droplets of silicone oil (PDMS) were sprayed onto electrospun nanofibre mats and flash frozen under liquid nitrogen. The frozen liquid droplets on the nanofibre mat were sputter coated with Au/Pd and transferred to the cryo-stage of the Small Dual Beam (SDB) microscope (Quanta 3D FEG, FEI Company, E.U./U.S.A.). As samples contained liquid phase, all samples were installed into a cryo-stage (Gatan, UK) incorporated within the SDB. The cryo-stage allows liquid nitrogen to be pumped through a sample holder containing the electrospun fibre mat with droplets, and maintains low temperatures at -160°C in this work. The SDB allows both imaging of surfaces with SEM and removal of the surface layer using FIB to allow further SEM imaging of sub-surface structure. Fig. 1 shows the examples of silicone oil droplets on plasma treated PA6 nanofibres. Collection of 2D SEM images as the FIB mills through samples is used for subsequent 3D reconstruction. Cross-sectional slices of 100 nm in thickness were milled using FIB from the block of the nanofibre sample at 16 kV and a final beam current of 0.5 nA. Resultant SEM images show a surface of the electrospun PA6

mat and silicone oil droplet that are subsequently sectioned progressively using FIB to expose wetting details.

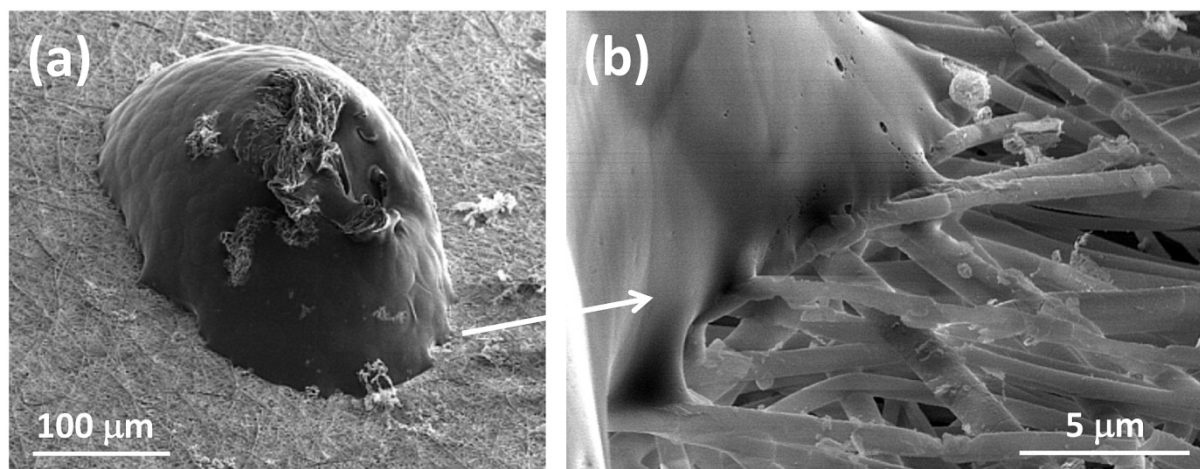


Fig. 1. SEM images of silicone droplets on a plasma treated PA6 mat show (a) a lack of a wetted region around the droplet and (b) partial wetting between the individual electrospun fibres and the silicone oil.

Additionally, individual electrospun fibre wetting experiments using a Wilhelmy balance approach were performed according to previously established method [4, 5]. The plasma treated electrospun fibres exhibited polyethylene glycol and polypropylene glycol liquid repellency and partial wetting with the low surface tension silicone oil.

Summary

SEM imaging in conjunction with FIB-sectioning and cryo-preparation is effective in determining the interaction between liquid probes and electrospun fibre surfaces. Wetting at different length scales is often observed, with partial wetting between individual electrospun fibres and liquid associated with a larger scale non-wetting regime, or sub-surface wetting of the mat occurring when a macroscopic droplet is within a partial wetting regime. Such observations suggest large scale measurements of liquid droplet contact angles may be unreliable in fully understanding the interaction between a liquid and fibrous surface.

References

- [1] G. McHale, *Langmuir* 23, (2007), p. 8200.
- [2] U. Stachewicz, I. Peker, W. Tu, A. H. Barber, *ACS Appl. Mat. Inter.* 3, (2011), p. 1991.
- [3] U. Stachewicz, F. Modaresifar, R. J. Bailey, T. Peijs, A. H. Barber, *ACS Appl. Mat. Inter.* 4, (2012), p. 2577.
- [4] U. Stachewicz, A. H. Barber, *Langmuir* 27, (2011), p. 3024.
- [5] U. Stachewicz, C. A. Stone, C. R. Willis, A. H. Barber, *J. Mater. Chem.* 22, (2012), p. 22935.

The possibility of using SEM and TEM to assess the degree of intercalation of smectite clay with gentamicine

Alicja Rapacz-Kmita^{1,a}, Ewa Stodolak-Zych^{1,b}, Magdalena Ziabka^{1,c},
Agnieszka Różycka^{1,d}, and Magdalena Dudek^{2,e}

¹ AGH University of Science and Technology, Faculty of Materials Science and Ceramics, Mickiewicza 30, 30-059 Cracow, Poland

² AGH University of Science and Technology, Faculty of Energy and Fuels, Mickiewicza 30, 30-059 Cracow, Poland

^akmita@agh.edu.pl, ^bstodolak@agh.edu.pl, ^cziabka@agh.edu.pl, ^dar@agh.edu.pl, ^epotoczek@agh.edu.pl

Introduction

Clays and clay minerals are commonly used in the pharmaceutical industry as excipients or active substances. They can be considered as raw pharmaceutical materials that once evaluated or modified to fulfil regulatory pharmacopoeia requirements, may achieve the status of pharmaceutical substances suitable for use in the manufacture of medicinal products. The technological properties of clays are directly related to their colloidal size and crystalline structure in layers, meaning a high specific surface area, optimum rheological characteristics or excellent sorptive abilities etc. [1,2].

Many studies have been reported on montmorillonite-drug hybrids for controlled drug delivery, for example ibuprofen, vitamin B1, nicotine, and others [3-6]. This paper describes an attempt to intercalate the clay mineral with gentamicin, which is one of the few antibiotics thermally stable, remaining active even after the autoclaving process. The process was monitored by XRD analysis. The possibility of using SEM and TEM to assess the degree of intercalation was also taken under consideration. The study aimed to observe the behaviour of gentamicin in the presence of smectite, and to identify possibilities for gentamicin to fill the emptiness present in the interlayer spaces of smectite.

Materials and methods

The smectite clay (SM), namely magnesium aluminium silicate Veegum®F manufactured by R.T. Vanderbilt Company, Inc., was used in the study as a drug carrier. Gentamicine (G) in a form of gentamicin sulphate (C₂₁H₄₃N₅O₇·H₂SO₄) was purchased from Sigma-Aldrich, USA, and the following procedure was used to intercalate the smectite clay with gentamicin: (1) smectite powder was weighed, and then mixed with distilled water using a magnetic stirrer while heating to 60°C for 24 hours, (2) gentamicin sulphate was added to the suspensions of the powder (ratio SM:G, was thus 4:1), (3) after the addition of gentamicin, the suspension was mixed with a magnetic stirrer at 60°C for 24 hours, (4) thoroughly mixed solution was placed in sterile containers, and then quenched with liquid nitrogen and lyophilized in a freeze dryer Freezone6l Labconco at -51°C at a pressure of 0.3 Pa for 48 hours.

The unmodified smectite clay as well as gentamicin and the gentamicin intercalated smectite were studied by XRD analysis to assess effectiveness of the intercalation process. The XRD analysis was performed using Empyrean X-ray diffractometer produced by PANalytical.

Microstructural observations of the smectite, gentamicin and the gentamicin intercalated smectite were made by the use of a scanning electron microscope Nova NanoSEM 200, FEI, and the transmission electron microscope TEM (JEOL JEM-1011). The EDS analysis was used to investigate effectiveness of the intercalation process in microregions.

Results and discussion

A successful attempt was made to intercalate smectite with gentamicin to confirm the possibility of using of the smectite as a drug carrier. The XRD study reveals, that after the contact with gentamicin the primary reflection shifts from 7.2° to 6.1° of 2θ, value what corresponds to the

increased basal spacing of 14.3 Å. In consequence, the increased basal spacing after the reaction of gentamicin with smectite provides an evidence of the intercalation of the drug into the smectite clay.

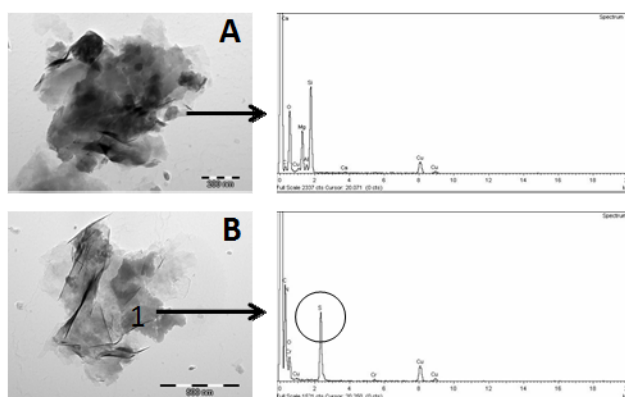


Fig. 1. TEM micrographs and EDS chemical analyses of the smectite before (A) and after (B) intercalation with gentamicin

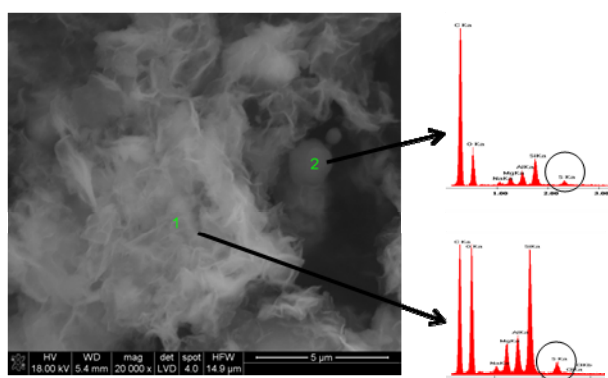


Fig. 2. SEM micrographs and EDS chemical analyses of the smectite after intercalation with gentamicin

XRD analysis can determine if a smectite intercalation process took place, but the use of SEM (Fig. 1) and TEM (Figure 2) with EDS and element mapping allows for more complete identification of the intercalation, since the location of elemental analysis can be accurately monitored. Combination of XRD with SEM and TEM provide a more relevant structural and chemical information, thus it may eventually help to assess whether the drug was built-in into packages of the clay.

Conclusion

The results of the study show the usefulness of SEM and TEM analyses combined with EDS in microregions to evaluate the possibility of using smectite as a drug carrier. They can successfully provide information not only about the intercalation in a bulk but also can monitor the distribution of drug in microregions.

Acknowledgements

This study was performed within the framework of funding for statutory activities of AGH University of Science and Technology in Krakow, Faculty of Materials Science and Ceramics.

References

- [1] A. López-Galindo, C. Viseras, P. Cerezo: *App. Clay Sci.* 36 (2007), p. 51.
- [2] J. Konta: *App. Clay Sci.* 10 (1995), p. 275.
- [3] J.P. Zheng, H.Y. Luan, L.F. Xi, K.D. Yao: *App. Clay Sci.* 36 (2007), p. 297.
- [4] G.V. Joshi, H.A. Patel, B.D. Kevadiya, H.C. Bajaj: *App. Clay Sci.* 45 (2009), p. 248.
- [5] T. Pongjanyakul, W. Khunawattanakul, S. Puttipip: *App. Clay Sci.* 44 (2009), p. 242.
- [6] B.D. Kevadiya, G.V. Joshi, H.M. Mody, H.C. Bajaj: *App. Clay Sci.* 52 (2011), p. 364.

Observations of atomic mechanisms of interface motion by aberration-corrected microscopy

Ulrich Dahmen^{1,a}, Abhay Gautam^{2,b}, Colin Ophus^{1,c}, Tamara Radetic^{2,d}

¹National Center for Electron Microscopy, LBNL, Berkeley, California, USA

²University of Belgrade, Faculty of Technology and Metallurgy, Nanotechnology and Functional Materials Center, Belgrade, Serbia

^aUDahmen@lbl.gov, ^bARGautam@lbl.gov, ^cClphus@lbl.gov, ^dTradetic@lbl.gov

Introduction

The development of aberration correction for electron microscopy has greatly increased our ability to characterize materials at the atomic scale. The TEAM project at the National Center for Electron Microscopy was launched as a collaborative effort between several DOE labs and commercial manufacturers to develop the next generation electron microscope with the goal of reaching a resolution of 0.5Å. This effort has contributed in a number of ways to advances in the field – by developing novel technologies, enabling new science and opening opportunities for innovation. This talk will briefly describe some of the new technologies and highlight their impact on materials characterization with examples of recent applications of the TEAM suite of instruments to dynamic processes in nanomaterials. Although examples will include tomography, liquid cell microscopy, beam-sensitive materials and solid-liquid interfaces, the major focus of this talk will be on the analysis of atomic mechanisms of grain boundary motion.

Structure and motion of steps in grain boundaries

Understanding the mechanisms and dynamics of structural defects at the atomic scale is of key importance for the development of new materials. Whether it is the motion of interfaces during deformation or the evolution of facets during crystal growth, the ability to observe the dynamic changes in atomic structure at high resolution is essential. The spatial and temporal resolution of aberration corrected microscopes and new detectors make it possible to connect experimental observations with atomistic simulations on comparable scales. One of these processes, the motion of grain boundaries in Au bicrystals, will be described in detail, based on observations in both STEM and TEM imaging modes.

Gold films with the mazed bicrystal structure were produced by heteroepitaxial growth on single crystal Ge substrates to produce grain boundaries with 90°<110> tilt character. In the mazed bicrystal geometry the misorientation and tilt character of all grain boundaries is fixed, leaving the boundary inclination as the only free variable. This makes it possible to observe preferred boundary facets and their motion during deformation or thermal migration.

Figure 1 shows a high resolution image of grain boundary in a gold 90° <110> bicrystal from a time series recorded at higher than video rates. The characteristic defect structure of the grain boundary is shown in color to highlight the difference from the periodic structure of the two grains. A detailed statistical analysis of such grain boundaries, based on the hull function approach for the description of incommensurate interfaces, has been used to compare experimental and simulated structures [1]. Used with dynamic observations, such analyses can reveal the mechanism of motion at the atomic scale, which can be related both, to the gliding behavior of this boundary during deformation [2] and the capillary shrinkage of island grains [3], such as that shown in Figure 2. These and similar observations have helped us understand the step mechanism that controls the motion of these interfaces [4].

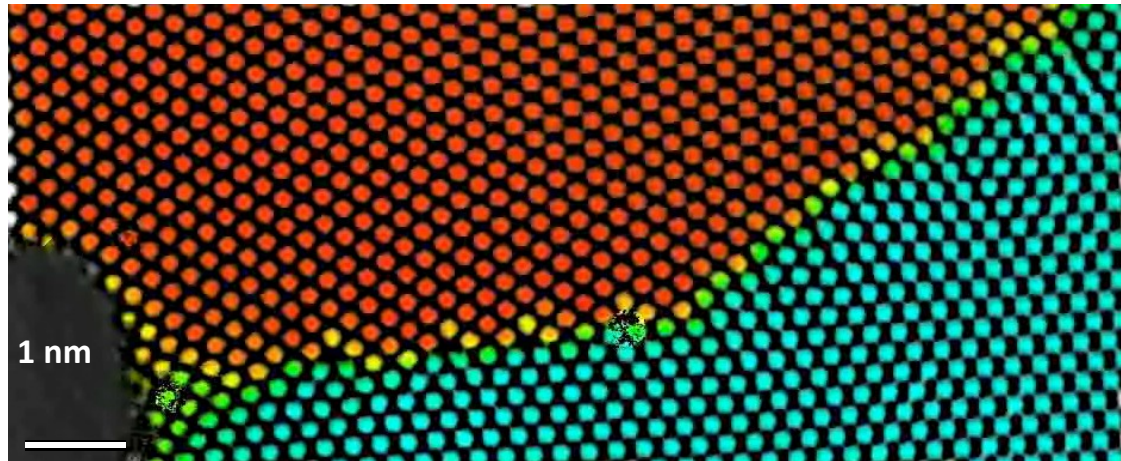


Fig. 1. Atomic resolution image of an incommensurate grain boundary in a $90^\circ\langle 110\rangle$ gold bicrystal observed during beam-induced defect motion. The image represents an average between individual events detected during a dynamic time sequence of 1600 frames at faster than video rate. The two grain orientations are marked in red and blue. Defects outlining facets are visible in green and yellow. The horizontal facet corresponds to the dominant facet controlling boundary motion and grain morphology

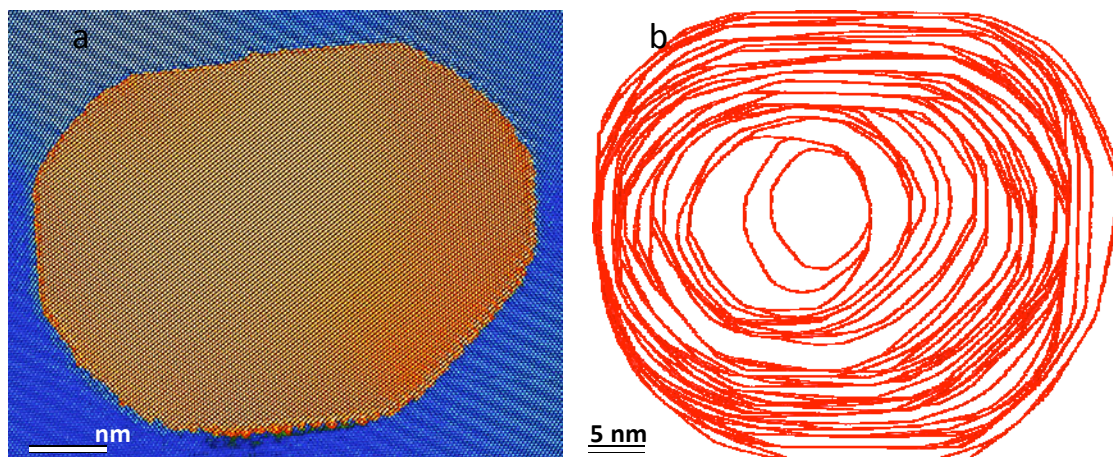


Fig. 2. Island grain in a $90^\circ\langle 110\rangle$ tilt bicrystal of gold during in-situ observation at 206° . Grain shrinkage under a capillary driving force was followed by tracing boundary motion until complete disappearance of the grain after a period of 28 minutes. Boundary motion is controlled by step motion in dominant facets such as that shown in Fig. 1

References

- [1] A. Gautam, C. Ophus, F. Lancon, V. Radmilovic, U. Dahmen: *Acta Mater.* 61 (2013), p. 5078.
- [2] F. Lancon, J. Ye, D. Caliste, T. Radetic, A.M. Minor, U. Dahmen: *Nano Lett.* 10 (2010), p. 695.
- [3] T. Radetic, C. Ophus, D.L. Olmsted, M. Asta, U. Dahmen: *Acta Mater.* 60 (2012), p. 7051.
- [4] The National Center for Electron Microscopy at LBNL is supported by the U.S. Department of Energy under Contract # DE-AC02-05CH11231.

Towards quantitative mapping of three-dimensional and weak electrostatic potentials and magnetic fields using electron holography

Rafal E. Dunin-Borkowski^{1,a}, Vadim Migunov^{1,b}, Jan Caron^{1,c}, András Kovács^{1,d}
and Giulio Pozzi^{2,e}

¹Ernst Ruska-Centre for Microscopy and Spectroscopy with Electrons and
Peter Grünberg Institute, Forschungszentrum Jülich, D-52425 Jülich, Germany

²Department of Physics and Astronomy, University of Bologna, Viale B. Pichat 6/2, Bologna, Italy

^ard@fz-juelich.de, ^bv.migunov@fz-juelich.de, ^cj.caron@fz-juelich.de, ^da.kovacs@fz-juelich.de,
^egiulio.pozzi@unibo.it

Introduction

Off-axis electron holography is a powerful technique that can be used to record the phase shift of the electron wave that has passed through an electron-transparent specimen in the transmission electron microscope (TEM). The phase shift is sensitive to the electrostatic potential and magnetic induction in the specimen. Recent developments in the technique have included the use of specimen holders with multiple electrical contacts to study nanoscale working devices, the application of electron holographic tomography to record three-dimensional potentials with nm spatial resolution and the use of ultra-stable transmission electron microscopes and either phase-shifting electron holography or cumulative hologram acquisition to achieve sub- $2\pi/1000$ -radian phase sensitivity.

Electrostatic potentials

We have applied off-axis electron holography to measure the electrostatic potential and electric field around an electrically-biased Fe atom probe tomography needle, as shown in Figs. 1 and 2. The experiment involved applying a voltage between the needle and a counter-electrode that was placed ~ 400 nm from it. The phase shift recorded using electron holography was analyzed both by fitting the recorded phase distribution to a simulation based on two lines of opposite charge density and by using a model-independent approach involving contour integration of the phase gradient to determine the charge enclosed within the integration contour [1]. In the present study, both approaches required evaluation of the *difference* between phase images acquired for two applied voltages, in order to subtract the mean inner potential and magnetic contributions to the phase. On the assumption of cylindrical symmetry, the three-dimensional potential and field around the needle were determined from the results, as shown in Fig. 1. Charge density profiles along the needle, measured using both approaches, are shown in Fig. 2 and are consistent with each other.

Magnetic fields

We are also working on a model-based approach that can be used to reconstruct the three-dimensional magnetization distribution in a specimen from a series of phase images recorded using electron holography. In order to develop the technique, we have generated simulated magnetic induction maps by projecting three-dimensional magnetization distributions onto two-dimensional Cartesian grids. We use known analytical solutions for the phase shifts of simple geometrical objects to pre-compute contributions to the phase from individual parts of the grids, in order to simulate phase images of arbitrary three-dimensional objects from any projection direction, with numerical discretization performed in real space to avoid artifacts generated by discretization in Fourier space without a significant increase in computation time. This forward simulation approach is used in an iterative model-based algorithm to solve the inverse problem of reconstructing the three-dimensional magnetization distribution in the specimen from a tomographic tilt series of phase images. Such

a model-based approach avoids many of the artifacts that result from using classical tomographic techniques, as well as allowing additional constraints to be incorporated.

Towards improved sensitivity in electron holographic measurements

The need for greater sensitivity in electron holographic measurements is illustrated, for magnetic measurements, by the fact that a single Bohr magneton is associated with a step in phase of $\sim 2\pi/10^5$ radians, while even a 2 nm ferromagnetic particle produces a phase shift of only $\sim 2\pi/1000$ radians. Fortunately, it is possible to measure the magnetic moment of a nanocrystal quantitatively from a phase image by making use of the relationship between the volume integral of the induction and the true magnetic moment [2]. When considering experiments aimed at the retrieval of weak phase shifts, it is important to remember that the sample must remain clean, that electron-beam-induced charging due to secondary electron emission can contribute to the measured electrostatic potential contribution to the phase shift and that the quantitative interpretation of phase shifts measured from crystalline specimens can require comparisons with dynamical simulations, even for a specimen thickness of only a few atoms [3].

References

- [1] M. Beleggia, T. Kasama, R.E. Dunin-Borkowski, S. Hofmann and G. Pozzi: Appl. Phys. Lett. Vol. 98 (2011), p. 243101.
- [2] M. Beleggia, T. Kasama and R.E. Dunin-Borkowski: Ultramicroscopy Vol. 110 (2010), p. 425.
- [3] We are grateful to M. Beleggia, A.H. Tavabi, P. Diehle, A. London, T.F. Kelly, D.J. Larson and M. Farle for valuable contributions to this work.

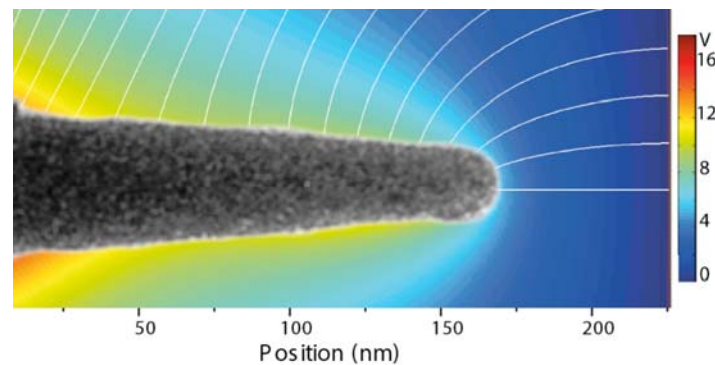


Fig. 1. Central slice of the 3D electrical potential (colors) and electric field (white lines) between an Fe atom probe tomography needle and a Au counter-electrode, determined from the charge density distribution in the needle measured from the *difference* between phase images recorded using off-axis electron holography at applied bias voltages between the needle and the counter-electrode of 0 and 5 V

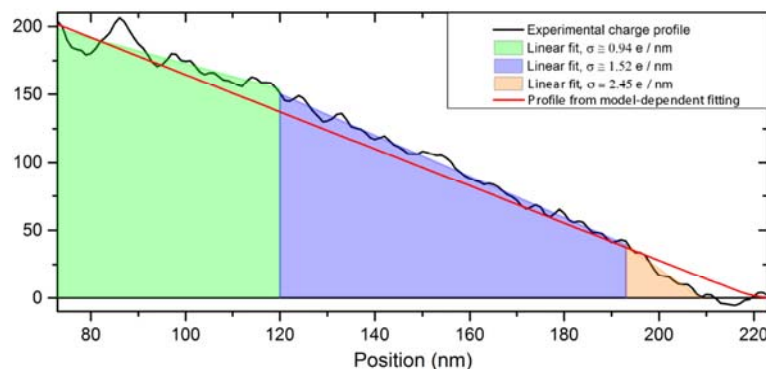


Fig. 2. Cumulative charge profiles along the needle shown in Fig. 1, measured by off-axis electron holography in units of electrons using model-independent (black) and model-dependent (red) methods

State of the art of strain mapping in nanostructures by dark-field electron holography and aberration-corrected HR(S)TEM

Martin Hýtch

CEMES-CNRS, nMat Group, 29 rue Jeanne Marvig, 31055 Toulouse, France

We present the state of the art in strain mapping at the nanoscale using aberration-corrected high-resolution electron microscopy (HRTEM) [1] and dark-field electron holography (DFEH) [2]. The new holographic technique allows strain to be measured to high precision, with nanometre spatial resolution and for micron fields of view. As with any TEM technique the samples are necessarily thin which allows some of the strain to be relaxed: the well-known thin film effect. In addition, dynamical scattering effects the strain information.

Strain mapping at the highest resolution and certain sample geometries is still best carried out by the analysis of high-resolution images, obtained either by aberration-corrected HRTEM or high-angle annular dark-field scanning TEM (HAADF-STEM). Examples of multiferroic materials where the local polarization and strain can be obtained by analyzing the displacements of individual atomic columns [3].

This overview will, in particular, show results from the recently installed I2TEM microscope (Hitachi), an instrument specifically designed for DFEH experiments and aberration-corrected HRTEM over wide fields of view.

References

- [1] M.J. Hýtch, E. Snoeck and R. Kilaas: *Ultramicroscopy* 74 (1998), p. 131.
- [2] M.J. Hýtch, F. Houdellier, F. Hüe, and E. Snoeck: *Nature* 453 (2008), p. 1086.
- [3] A. Lubk, M.D. Rossell, J. Seidel, Y.H. Chu, R. Ramesh, M.J. Hýtch, and E. Snoeck: *Nano Lett.* 13 (2013), p. 1410.

EDS quantitative microanalysis and element mapping down to the nanometer scale and beyond

Philippe André Buffat^{1,2,a} and Aleksandra Czyska-Filemonowicz^{2,b}

¹Centre Interdisciplinaire de Microscopie Electronique, Ecole Polytechnique Fédérale de Lausanne, CH-1015 Lausanne, Switzerland

²International Centre of Electron Microscopy for Materials Science, AGH University of Science and Technology, 30-059 Krakow, Poland

^aphilippe.buffat@epfl.ch, ^bczyrska@agh.edu.pl

Introduction: technical advances

Energy Dispersive X-Ray Spectrometry (EDS) remains the easiest way of chemical microanalysis in the transmission electron microscope (TEM) for a broad range of users thanks to its low number of set-up parameters, mainly accelerating voltage and beam current, and quite straightforward interpretation software.

The advent of larger EDS diodes, or even multiple diodes designs, has improved the raw collection angle from 0.1 sr for the old 10 mm² detectors to near 1sr using one 100 mm² or 4x30 mm² diodes. Some of them have no longer a protective window and raise the collection efficiency beyond one order of magnitude and even more for light elements detection like nitrogen.

In parallel the technology of Silicon Drift Diodes (SDD) withstand input count rates in excess of 100'000 counts/s instead of the former few thousands of Silicon-Lithium drifted diodes (Si-Li). This bright improvement immediately beneficial to bulk sample analysis in the SEM would be lost in high spatial resolution TEM - where low beam current and thin sample combine to give only a weak X-ray emission – if in parallel suppliers didn't develop brighter field emission guns with cold or Schottky cathodes and electron probe forming optics with spherical aberration (C_s) correction.

Nowadays, probes less than 0.2 nm carrying current in excess of 1 nA are available that brings single atom column microanalysis in the line of sight. The actual limitation becomes the sample resistance to irradiation damage under electron flux that may reach a few 10⁶ A/cm². One should also be aware that C_s -corrected probes become strongly converging at the atom scale resolution that reduces the depth of focus and thus the useful sample thickness to some 20nm. Quantification software also requires some new development to take in account some of the new set-up of diodes.

An example: nanoprecipitates investigation in Ni-base superalloy

This example on nickel-base superalloy, Inconel 718, illustrates the present potential and limits of EDS STEM observation at high spatial resolution on a Titan³ 60-300 (FEI) fitted with a DCOR spherical aberration corrector (CEOS) for thin and intense probe forming and ChemiSTEM [1], a Super-X EDS detector with 4 windowless diodes and an X-FEG high brightness electron gun.

The mechanical properties of Inconel 718 are improved by nanoprecipitates γ' (type Ni₃(Al,Ti) ordered fcc) and γ'' (type Ni₃Nb tetragonal ordered bc) in a γ matrix (fcc disordered Ni-Cr-Fe solid solution). TEM dark field and HAADF/STEM give ambiguous images and only EDS maps bring clear phase distribution using Al and Nb as selective elements (Fig. 1).

Even in thin TEM foils, the nanoprecipitates are buried in the matrix and prevent to gather single phase EDS spectra. However, the shape of element distribution profile and atom resolution in EDS maps of different thicknesses samples together with numeric models and atom probe tomography show that Fe and Cr are only belonging to the matrix. The absence of one matrix element in precipitates together with high quality maps makes possible to subtract the Ni contribution of the surrounding matrix and to derive the true γ' and γ'' composition [2].

High-resolution STEM EDS maps of alloys showing distinct atom columns appear significantly more delicate to obtain than for perovskites or semiconductors. On the hand the preparation of foils only a few tens of nanometers, thick and reasonably flat, is trickier in multiphase metal alloys. On the other hand, they seem also more prone to electron beam damaging.

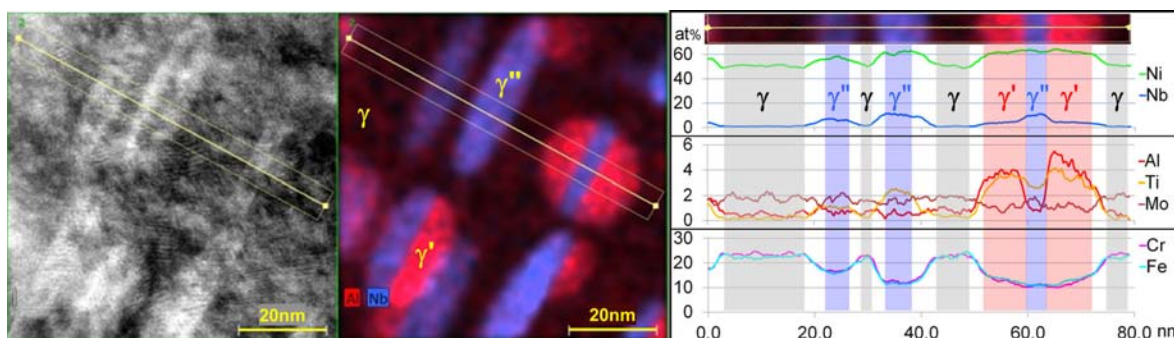


Fig. 1. Left: HAADF/STEM. Centre: raw counts maps (200kV, 430pA, 10mrad, 17min) differentiate the 3 phases: red (Al, γ'), blue (Nb, γ'') and dark (γ). Some γ' and γ'' join on a $(001)_{\gamma'/\gamma''}$ plane to form so-called "co-precipitates". Right: the linescan shows that Nb and Ti are respectively present in γ' and γ'' in substitution to (Al, Ti) and Nb in addition to elements expected in the models

The original EDS map of a γ'/γ'' [010] interface (Fig. 2) was averaged over vertical rows of equivalent atom columns to filter noise while retaining the composition change across that interface. The interface plane contains only Ni. The γ' Al/Ti columns are facing the closest γ'' Nb columns across the interface. The first plane in γ' along the interface exhibits a dark HAADF contrast. It corresponds to a slight reinforcement of the Al atom columns contrast suggesting that Al segregation occurs. Geng has observed a similar effect using atom probe tomography [3].

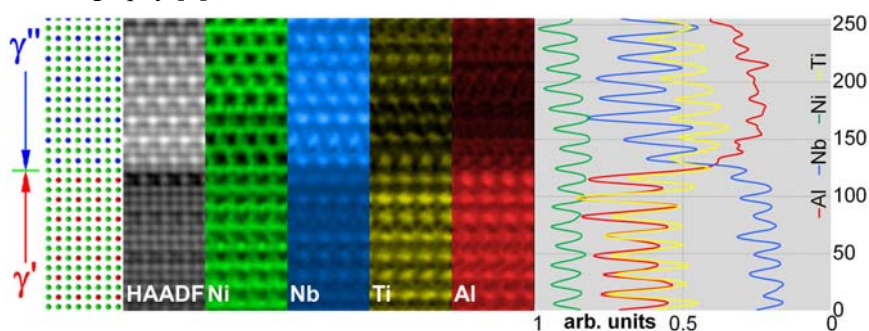


Fig. 2. Left to right: Ball model, HAADF, raw counts element maps and profiles of a γ'/γ'' interface (200kV, 220pA, 16mrad, 330s).

The probe progressively broadens (defocus and de-channeling) along its path through this rather thick foil beyond atom resolution and prevents getting quantitative composition of single columns

Conclusion

Nowadays, EDS supersedes - with exception of the ultra-light elements (Li, Be, B) - the Electron Energy Loss Spectroscopy (EELS) for element mapping down to the nanometer scale (easier to set-up, no "delayed" or "unfavourable" element edges like Al in this example). At the atom resolution level, EELS keeps its advantage of a better signal collection but suffers from spatial resolution loss due to strong interaction delocalization for low energy edges.

The main limits of EDS are nowadays the resistance of the sample to electron irradiation and the need for better quantification software.

Acknowledgements

Part of the study was performed within ESTEEM2 project; financial support from the European Union under FP7 contract for Integrated Infrastructure Initiative, reference 312483 ESTEEM2.

References

- [1] P. Schlossmacher et al.: Microscopy and Analysis 24 7 (2010), p. S5 (EU).
- [2] P.A. Buffat et al.: Scripta Mater. (submitted).
- [3] W.T. Geng: Phys. Rev. B76 (2007), p. 224102.

Scanning transmission electron microscopy at atomic resolution

Ferdinand Hofer^{1,a}, Werner Grogger^{1,b}, Gerald Kothleitner^{1,c} and Franz Schmidt^{2,d}

¹Institute for Electron Microscopy and Nanoanalysis, Graz University of Technology and Graz Centre for Electron Microscopy, A-8010 Graz, Austria

²Institute of Physics, University of Graz, A-8010 Graz, Austria

^aferdinand.hofer@tugraz.at, ^bgerald.kothleitner@felmi-zfe.at, ^cfranz.schmidt@felmi-zfe.at,
^dwerner.grogger@felmi-zfe.at

The new generation of scanning transmission electron microscopes paved the way for imaging and elemental mapping at the atomic scale. The rapid development of STEM was clearly caused by the introduction of aberration corrected STEM probes. Further innovative components such as high-brightness guns combined with monochromators, improved EELS-spectrometers, new X-ray detector concepts and better instrumental stabilities now enable elemental mapping at atomic resolution in many laboratories around the world [1]. In this paper we will highlight two main application fields for STEM imaging and analysis:

- 1) Two important developments enhanced the potential for successful elemental mapping at atomic resolution: First, the introduction of collection-efficient solid state X-ray detectors (SDD) [2] and second, the simultaneous acquisition of EELS and EDS spectrum images with fast scanning rates [3]. In the meanwhile many examples of atomically resolved elemental maps have been published, but we have to realize that the coloured elemental maps only show qualitative information. However, it is extremely important to provide elemental quantification in terms of volumetric densities (i.e. number of atoms per unit volume), as it allows correlating structural and chemical information with each other (“unit cell atom counting”). Using a SrTiO₃ crystal of known thickness and density we show how EELS and EDS elemental maps can be quantified by combining both spectroscopies and including the zeta factor method for X-ray quantification [4]. The results show that it is possible to get the number of atoms in the individual atom columns showing that elastic and thermal scattering effects can severely influence the quantification at atomic resolution [5].
- 2) It is now widely accepted that STEM in combination with EELS can probe the (partial) local density of states of plasmonic modes in noble metal nanoparticles and nanostructures. Using fast electrons, instead of photons, to analyse localized surface plasmons has the advantage of unbeaten high spatial resolution. This enables observation of the electric field distribution of localized surface plasmons even on complex nanostructures at the nanometre scale. In order to demonstrate the power of STEM-EELS we will highlight recent studies of breathing modes in silver nanodiscs [6] and plasmon dispersions in flat silver nanolayers [7].

References:

- [1] K. Kimoto et al.: Nature 450 (2007), p. 702.
- [2] H.S. von Harrach et al.: J. Phys: Conf. Ser. 241 (2010), p. 012015.
- [3] G. Kothleitner et al.: Proc. European Microscopy Conference, Manchester (2012) PS 2.7.
- [4] G. Kothleitner et al.: Microsc. Microanal. (2014) doi: 10.107/S1431927614000130.
- [5] G. Kothleitner et al.: Phys. Rev. Letters 112 (2014) 085501, 1-5.
- [6] F. Schmidt et al.: Nano Lett. 14 (2012), p. 5780.
- [7] F. Schmidt et al.: Nature Comm. 5:3604 (2014), doi: 10.101038/ncomms4604.

This work has received funding from the European Union within the 7th Framework Programme under Grant Agreement no. 312483 [ESTEEM2).

Determining local variation in structure and composition of catalyst particles and barrier layers using imaging and spectroscopy by high resolution analytical transmission electron microscopy

Eva Olsson

Department of Applied Physics, Chalmers University of Technology, 412 96 Gothenburg, Sweden
eva.olsson@chalmers.se

As material synthesis and nanofabrication methods are refined and the control of material structure reaches beyond the nanoscale the role of individual interfaces, defects and atoms is pronounced and can dominate the properties. The strong influence of local atomic structure offers the possibility of designing new components with tailored and unique properties. Electron microscopes provide the possibility of correlating the structure to transport properties with a spatial resolution that reaches the atomic scale. A knowledge platform of how to design new materials by combining experiments and theory can thus be established. In addition, inserting a scanning tunnelling or an atomic force microscope in the electron microscope enables studies of dynamic events.

This talk will address, in particular, two systems to illustrate how information about the active elements of materials and devices are identified and studied. One system concerns the effect of the interface between noble metal particles and oxide supports on the efficiency of the catalysts and on the ageing properties in different gas compositions. The activity, ageing and dispersion measurements are carried out in bench reactors. The other system is superconducting Al/AlO_x/Al tunnel junctions. The insulating tunnel barrier is about 1-2 nm in thickness. Detailed studies show that the thickness varies along the junction. Due to the exponential dependence of the tunnel current on the barrier thickness changes as small as 0.1 nm are of significance importance and affect the performance in terms of, for example, sensitivity. The electron structure and composition of the barrier layers are other crucial parameters. The mechanisms of degradation and the structure of the catalyst particle systems and the tunnel barriers and interfaces are studied using electron microscopy and in particular high resolution transmission electron microscopy (TEM) and scanning TEM (STEM). High angle annular dark field (HAADF) STEM imaging using a probe corrected Titan TEM instrument provides Z-contrast information revealing the distribution of the noble metals on the oxide support with atomic resolution. Complementary information is extracted using monochromated electron energy loss spectroscopy (EELS) in the Titan TEM.

Angular resolved low loss in EFTEM mode: capturing the whole diffraction pattern

Cécile Hébert^{1,a}, Simon Schneider^{1,b}

¹LSME, ICMP, station 12, Ecole Polytechnique Fédérale de Lausanne, Switzerland

^acecile.hebert@epfl.ch

Electron energy-loss spectrometry (EELS) is a powerful and nowadays well-known technique to investigate materials. In the low-loss range, it provides information about the loss function $\text{Im}(-1/\epsilon)$, and, eventually, after Kramers-Kronig analysis of the data, it is possible to retrieve the dielectric function $\epsilon(\omega)$ [1]. Using angular resolved electron energy-loss spectrometry, one can even obtain the whole 4D information $\epsilon(\omega, q)$.

In the following, we will show a special way of performing angular resolved EELS acquisition. A JEOL 2200 FS equipped with an in-column Ω filter, allows us to take advantage of the energy filtered transmission electron microscopy (EFTEM) technique. This mode allows a complete recording of the angular resolved spectra in a “3D” datacube, while keeping a parallel illumination.

To allow increasing the signal, while keeping a parallel illumination and a good energy resolution, we found that the best is to operate the Jeol 2200FS in the “nano beam diffraction” mode. By doing so, and using a 40mm C2 aperture, one can achieve a 200nm illuminated area on the specimen, with parallel illumination and without SA aperture, thus without cutting a large part of the electron beam.

Data have been acquired on a specimen made of a thin film of Ag that had been sputtered on NaCl, and then released and deposited on a Cu grid.

After acquisition, the data have been integrated radially, and corrected for plural scattering. The result is a 2D intensity map that shows the intensity of the EELS spectrum as a function of the momentum transfer’s norm on one axis and energy on the other

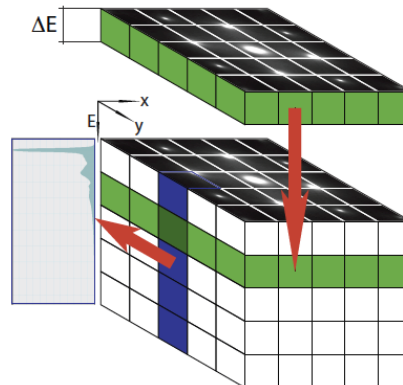


Fig. 1. Sketch of the acquisition procedure in EFTEM. The energy selecting slits allows to acquire a diffraction pattern at a given energy. The patterns are then combined, and a spectrum can be extracted for each pixel in the diffraction plane

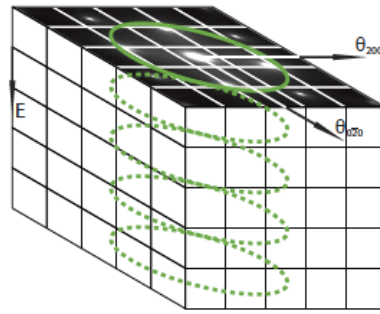


Fig. 2. Sketch of the integration procedure. All the spectra originating from a circle are summed up to give the contribution as a function of q

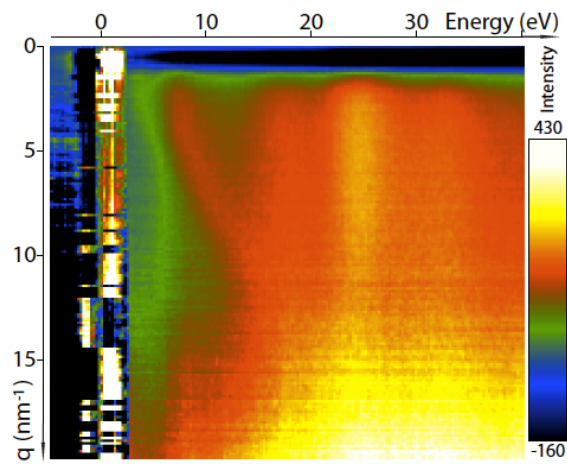


Fig. 3. Angular resolved low loss EELS of Ag obtained after plural scattering correction

References

- [1] A. Alkauskas et al: Ultramicroscopy 110 (2010), p. 1081.

Characterization of epitaxial GaN thin films by aberration-corrected scanning transmission electron microscopy

David Poppitz^{1,a}, Andriy Lotnyk^{1,b}, Jürgen W. Gerlach^{1,c} and Bernd Rauschenbach^{1,d}

¹Leibniz Institute of Surface Modification Leipzig, Germany

^adavid.poppitz@iom-leipzig.de, ^bandriy.lotnyk@iom-leipzig.de, ^cjuergen.gerlach@iom-leipzig.de,

^dbernd.rauschenbach@iom-leipzig.de

Introduction

Gallium nitride (GaN) is a semiconductor material which is widely used in photonics applications due to its optical properties and is also of great interest in material science. To improve the emission efficiency of optoelectronic devices it is necessary to minimize the defect density in GaN thin films.

To achieve this, many different manufacturing processes are being used in research and industry, and GaN layers are produced with different thicknesses and surface topographies. In the present work, we investigate GaN thin films produced by ion-beam assisted molecular-beam epitaxy (IBA-MBE) with thicknesses lower than 250 nm. Different defects in the thin films and at the substrate/film interface are observed by aberration-corrected (Cs-corrected) scanning transmission electron microscopy (STEM).

Experimental

The GaN thin films were grown directly on super-polished 6H-SiC(0001) substrates without any buffer layers by IBA-MBE [1, 2]. GaN thin films with thicknesses of about 45 - 240 nm and a high crystalline quality were produced. The maximum kinetic energy of the nitrogen ions supplied by a hollow-anode ion source was 25 eV. The Ga effusion cell was operated at a temperature of 1010 °C and the substrate was heated to a temperature of 700 °C.

STEM investigations were performed with a Titan3 G2 60-300 probe Cs-corrected S/TEM, equipped with high angle annular dark field (HAADF), bright field (BF), dark field (DF) and annular bright field (ABF) detectors. For analytical TEM work a Gatan imaging filter for electron energy loss spectroscopy (EELS) and energy filtered TEM analysis was used. The microscope was operated at 300 kV accelerating voltage. The TEM samples were prepared by the focused ion beam technique (FIB). After FIB preparation, the TEM lamellae were polished further by using focused low-energy argon ion milling in a NanoMill system. Thereby, the samples were polished in several steps using ion energies in the range from 900 eV down to 200 eV [3]. With these steps, TEM sample thicknesses lower than 20 nm (as measured with EELS) were achieved. In addition, amorphous surface layers and implantations from the FIB process were removed. All FIB lamellae were prepared with the a -axis $[2\bar{1}\bar{1}0]$ as zone axis of the GaN films.

Results

Figure 1b shows an ADF-STEM image of a GaN thin film deposited by IBA-MBE. Various defects were found in the film and close to the GaN-SiC interface. The defects in the film were identified as grain boundaries, stacking faults and dislocations. It was observed that two polytypes, namely the cubic (z-GaN) and the hexagonal GaN (w-GaN) polytype are present in the GaN thin film. The first several nanometers of the GaN film consist of the hexagonal phase with a high density of defects like stacking faults and dislocations, followed by the cubic GaN phase which contains defects like stacking faults. Above the layer with cubic GaN phase a layer containing the hexagonal GaN phase is formed. This layer exhibits a significantly lower density of defects.

In Figure 2b an ADF-STEM image of the GaN/SiC interface is shown. The stress caused by the lattice mismatch of 3.5 % of the GaN and SiC is mainly relaxed within the first three layers of the GaN film. To compensate this mismatch the stacking order of the GaN layers changes as a result of misfit dislocations from ABC to ABAB stacking. Due to the high quality of the TEM sample and the Cs corrected STEM setup it was possible to image also the light elements in the first monolayers of the GaN film by ADF imaging. The local polarity of the epitaxially grown GaN thin film was determined as Ga polar. In addition, the structure of different defects like stacking faults and dislocations was imaged with atomic resolution inside the film as well as at the interface.

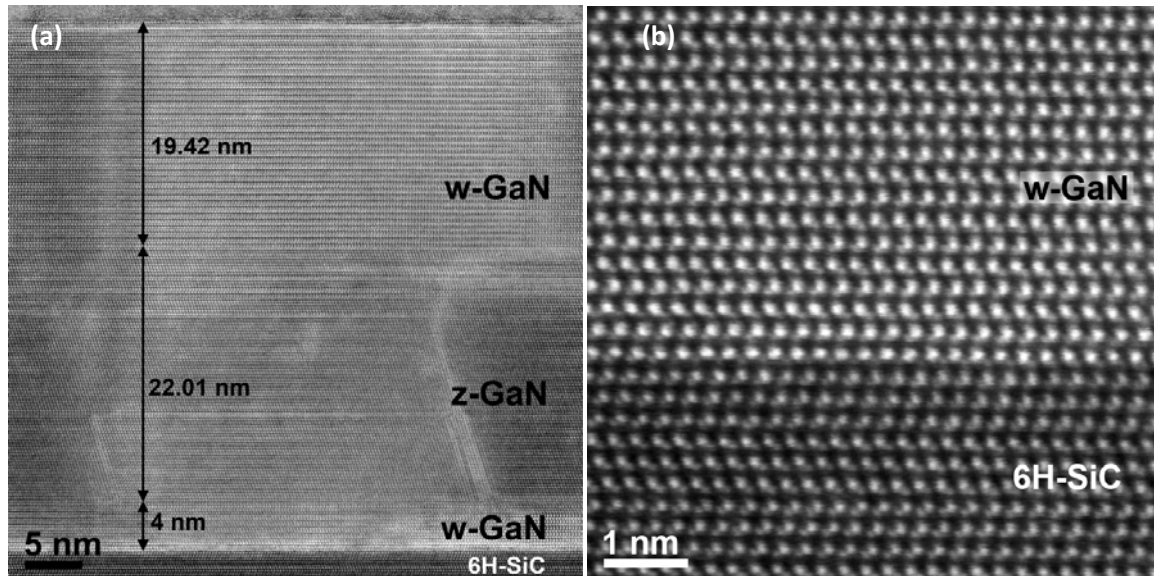


Fig. 1. ADF-STEM image of 45.5 nm thick GaN thin film grown on 6H-SiC substrate. The image shows different polytypes of GaN (a). ADF-HRSTEM image of the GaN/SiC interface (b). Probe forming aperture angle is 20 mrad and detector inner and outer angles are 19.1 and 106.5 mrad, respectively. Viewing direction is $[2\bar{1}\bar{1}0]$ for w-GaN and 6H-SiC

Summary

We have produced GaN thin films with high crystalline quality by IBA-MBE on 6H-SiC substrates. These thin films were characterized by advanced transmission electron microscopy in order to investigate the local structure of GaN thin films and the substrate/film interface. By using ADF imaging in Cs-corrected STEM, it was possible to image real structure of GaN/SiC interface containing both light and heavy elements.

Acknowledgements

The financial support of the European Union and the Free State of Saxony (LenA Project; Project No. 100074065) is greatly acknowledged. Prof. A. Anders, Lawrence Berkeley Laboratory, Berkeley, US, is thanked for providing the hollow-anode ion source.

References

- [1] L. Neumann, J.W. Gerlach and B. Rauschenbach: Thin Solid Films Vol. 520 (2012), p. 3936.
- [2] A. Anders, N. Newman, M. Rubin, M. Dickinson and E. Jones: Rev. Sci. Instrum. Vol. 67 (1995), p. 905.
- [3] D. Poppitz, A. Lotnyk, J. W. Gerlach, B. Rauschenbach: Acta Mater. Vol. 65 (2014), p. 98.

High resolution 3D imaging of nanomaterials

Sara Bals^{1,a}, Bart Goris^{1,b} and Gustaaf Van Tendeloo^{1,c}

¹EMAT-University of Antwerp, Groenenborgerlaan 171, B-2020 Antwerp, Belgium

^aSara.Bals@uantwerpen.be, ^bBart.Goris@uantwerpen.be, ^cStaf.Vantendeloo@uantwerpen.be

Introduction

New developments in the field of nanoscience drive the need for quantitative characterization techniques that yield information down to the atomic scale. Transmission electron microscopy (TEM) and scanning transmission electron microscopy (STEM) are excellent techniques to investigate nanomaterials. Not only structural, but also chemical and even electronic information can nowadays be obtained, atomic column by atomic column. However, TEM and most related techniques actually provide only a two-dimensional (2D) projection of what is a three-dimensional (3D) object. To overcome this problem, 3D electron microscopy or so-called "electron tomography" has been developed [1]. Most results have been achieved at the nanometer level, but recent developments have pushed the resolution of the technique to the atomic level [2-9].

High resolution electron tomography

Recently, a novel approach for high resolution electron tomography, based on compressive sensing, was proposed. Compressive sensing (CS) is a technique specialized in finding a solution that has a sparse representation to a set of linear equations. At the atomic scale, the approach exploits the sparsity of the object since only a limited number of voxels are occupied by atoms. As illustrated in Fig. 1, the approach has been applied to reconstruct the atomic structure of Au nanorods [8]. The surface facets of the Au nanorod in Fig. 1.a are mainly composed of $\{110\}$ and $\{100\}$ facets. However, when inspecting 3D reconstructions of nanorods that were synthesized using a different surfactant, it was determined that $\{520\}$ facets were the most dominant ones (Fig. 1.b). Such information is of crucial importance to interpret the catalytic behaviour of these materials. During the reconstruction process, no prior knowledge about the atomic lattice was used. As a result, small deviations of the positions of the atoms from a perfect lattice can be observed. Fig. 1.c illustrates that surface strain can be measured when applying a 3D extension of the geometrical phase analysis [9].

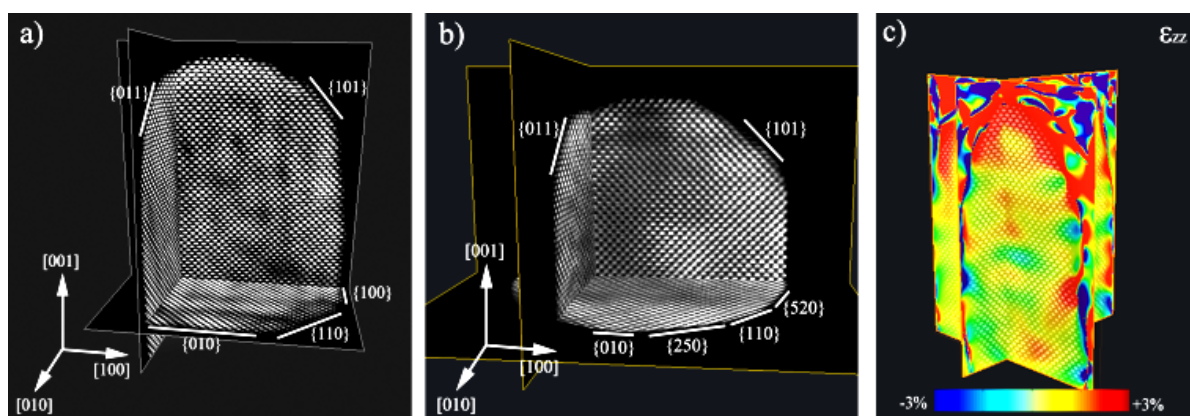


Fig. 1. (a,b) Orthogonal slices through the atomic scale reconstruction of Au nanorods. The side facets of these rods can be clearly recognized. (c) Strain measurement along the major axis of the nanorod

Going further than simply determining the *positions* of atoms, a crucial aim is also identifying the *type* of individual atoms in bimetallic nanoparticles [10]. This information can be obtained from

HAADF STEM tomography due to the dependency of the intensity in the projection images to the atomic number. A detailed analysis of the position and the atom type in a core-shell bimetallic nanorod was performed using orthogonal slices through the 3D reconstruction, as shown in Fig. 2. Individual Ag and Au atoms can be distinguished, even at the metal-metal interface, by comparing their relative intensities. An intensity profile was acquired along the direction indicated by the white arrow in Fig. 2.b. From this intensity profile, also presented in Fig. 2, it is clear that Au and Ag atoms can indeed be identified from their intensities using a threshold value. In this manner, each atom in the cross sections shown in Fig. 2.b and 2.c was assigned to be either Ag or Au. The result is shown in Fig. 2.d and 2.e and leads to correct indexing of the type of interfacial planes.

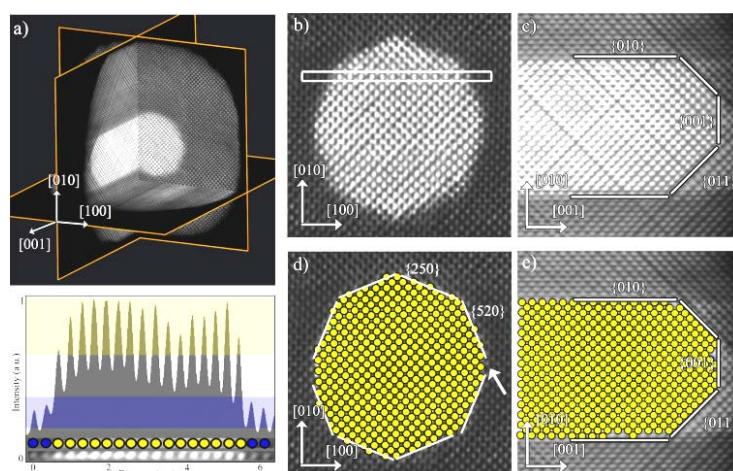


Fig. 2. (a) Orthogonal slices through the reconstruction show the core-shell structure of the nanorod. (b,c) Detailed view of slices through the reconstruction perpendicular and parallel to the major axis of the nanorod. In (c) artefacts are related to (currently) unavoidable remaining scanning noise. An intensity profile was acquired along the direction indicated by the white rectangle in (b). (d,e) Slices corresponding to b) and c), in which each Au atom is indicated by a yellow circle

References

- [1] P. A. Midgley, R. E. Dunin-Borkowski: *Nat. Mater.* 8 (2009), p. 271.
- [2] S. Van Aert, K. J. Batenburg, M. D. Rossell, R. Erni, G. Van Tendeloo: *Nature* 470 (2011), p. 374.
- [3] S. Bals, M. Casavola, M. A. van Huis, S. Van Aert, K. J. Batenburg, G. Van Tendeloo, D. Vanmaekelbergh: *Nano Lett.* 11 (2011), p. 3420.
- [4] D. Van Dyck, F. R. Chen: *Nature* 486 (2012), p. 243.
- [5] M. C. Scott, C. C. Chen, M. Mecklenburg, C. Zhu, R. Xu, P. Ercius, U. Dahmen, B. C. Regan, J. W. Miao: *Nature* 483 (2012), p. 444.
- [6] C. C. Chen, C. Zhu, E. R. White, C. Y. Chiu, M. C. Scott, B. C. Regan, L. D. Marks, Y. Huang, J. Miao: *Nature* 496 (2013), p. 74.
- [7] S. Bals, S. Van Aert, C.P. Romero, K. Lauwaet, M.J. Van Bael, B. Schoeters, B. Partoens, E. Yücelen, P. Lievens, G. Van Tendeloo: *Nat. Commun.* 3 (2012), p. 897.
- [8] B. Goris, S. Bals, W. Van den Broek, E. Carbo-Argibay, S. Gomez-Grana, L. M. Liz-Marzan, G. Van Tendeloo: *Nat. Mater.* 11 (2012), p. 930.
- [9] M. J. Hytch, E. Snoeck, R. Kilaas: *Ultramicroscopy* 74 (1998), p. 131.
- [10] B. Goris, A. De Backer, S. Van Aert, S. Gómez-Graña, L. M. Liz-Marzán, G. Van Tendeloo, S. Bals: *Nano Lett.* 13 (2013), p. 4236.

STEM-EDX and FIB-SEM tomography of Allvac 718Plus superalloy

Adam Kruk^a, Grzegorz Cempura^b, Aleksandra Czyrska-Filemonowicz^c

AGH University of Science and Technology, Al. A. Mickiewicza 30, 30-059 Kraków, Poland

^akruczek@agh.edu.pl, ^bcempura@agh.edu.pl, ^cczyrska@agh.edu.pl

Allvac 718Plus (718Plus) is a high strength, corrosion resistant nickel-chromium-iron based superalloy used for applications in power generation, aeronautics and aerospace [1]. Its typical chemical composition is: Ni-18Cr-10Fe-9Co-5.1(Nb+Ta)-1W-2.7Mo-0.7Ti-1.5Al-0.03C (wt%). The 718Plus microstructure consists of a γ matrix (Ni-based solid solution) with ordered face centred cubic γ' -Ni₃(Al,Ti) type phase, some orthorhombic δ -Ni₃Nb and hexagonal η -Ni₃Ti, η^* -Ni₆AlNb or Ni₆(Al,Ti)Nb particles precipitated at the grain boundaries [2]. The aim of this study was to describe 718Plus microstructure and apply STEM-EDX and FIB-SEM tomography to 3D imaging and metrology of the precipitates. Microstructural investigation and phase chemical compositions of 718Plus superalloy were performed using STEM-EDX tomography using a probe Cs corrected Titan³ G2 60-300 with ChemiSTEM™ system. Detection system allowed to achieve high X-ray signal over a large tilt angle of sample and collect series of 2D elemental maps in the angular range from -60° to +60° with step of 4°. The TEM study was conducted on the lamella prepared by FIB. Tomographic reconstruction of a tilt series images was performed using SIRT method, which allowed visualizing the three-dimensional distribution of selected elements (Al, Cr) in the analysed volume. The other technique used for 3D imaging of 718Plus superalloy microstructure was FIB-SEM tomography [3]. The NEON CrossBeam 40EsB with Ga-ion beam at parameters: 30 kV, 100 pA and aperture of 30 μ m was used to perform a precise in-situ milling. Consequently, the acquired stack of images was transformed directly into a 3D data volume with a voxel resolution of 12×12×12 nm. Repeated removal of layers as thin as a 12 nm allowed exploring a total volume of 10.7×7.2×7.7 μ m. The 3D visualization of reconstructed space for FIB-SEM tomography was performed using ImageJA 1.45b and Avizo Fire 6.3 software. Fig.1. shows the results of 3D visualization of the shape and distribution of γ' particles in 718Plus superalloy and complex particle of η phase at different angle of view using STEM-EDX tomography technique. The chemical composition of this phase was found to be different from orthorhombic Ni₃Nb δ phase, its chemistry was close to Ni₆(Al,Ti)Nb. The volume fraction of γ' phase, and the equivalent average particle diameter in the reconstructed volume were as follows: $V_v = 12.5\%$ and $D_{eq} = 26.0 \pm 8.3$ nm. Fig. 2 shows 718Plus microstructure observed using SEM-EsB detector (Z-contrast imaging). Platelet shaped particles, identified as η phase by EDS analysis, were observed at grain boundaries and occasionally at twin boundaries. It can be seen that precipitates with round-to-blocky morphology are randomly dispersed within the matrix. Fig. 2 shows 3D visualization of the shape and distribution of η phase at γ grain boundary in 718Plus alloy. The results achieved confirm the ability of STEM-EDX and FIB-SEM tomography to reconstruct 3D structures with dimensions in tens of nanometers. Such 3D reconstructions can serve as a basis for quantitative analysis of complex structures in a nanoscale.

References

- [1] R. M. Kearsey, J. Tsang, S. Oppenheimer, E. Mcdevitt: JOM 64 (2)(2012), p. 241.
- [2] E.J. Pickering, H. Mathur, A. Bhowmik: Acta Mater. 60 (2012), p. 2757.
- [3] Kruk, A. Czyrska-Filemonowicz: Arch. Metall. Mater. 58 (2013), p. 387.

Acknowledgement

The authors acknowledge the financial support from EU 7FP under Grant Agreement 312483 - ESTEEM2 and the AGH-UST statutory project (nr 11.11.110. 299).

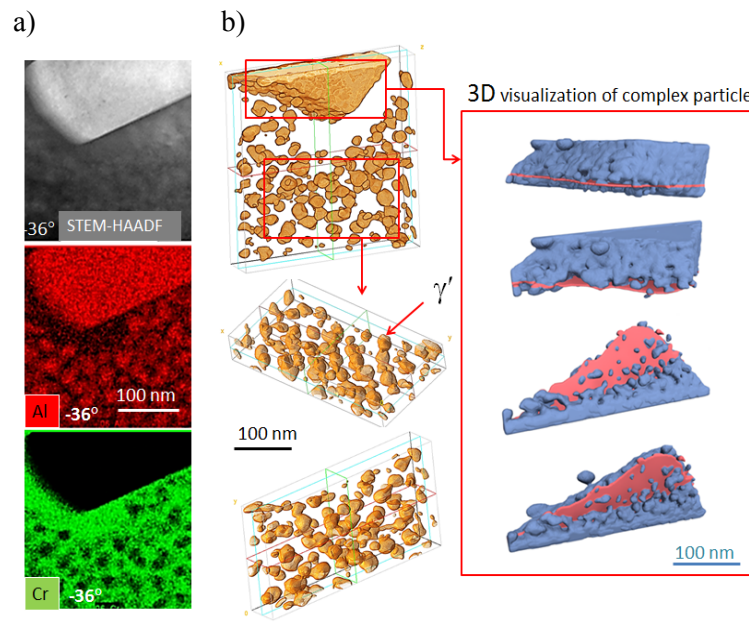


Fig. 1. Visualization of γ' particles in 718Plus superalloy using STEM-EDX tomography technique; a) STEM-HAADF and STEM-EDX elemental Al and Cr map images at -36° tilt angle, selected from the registered tilt series, b) 3D visualization of γ' and complex particle of η phase at different angle of view

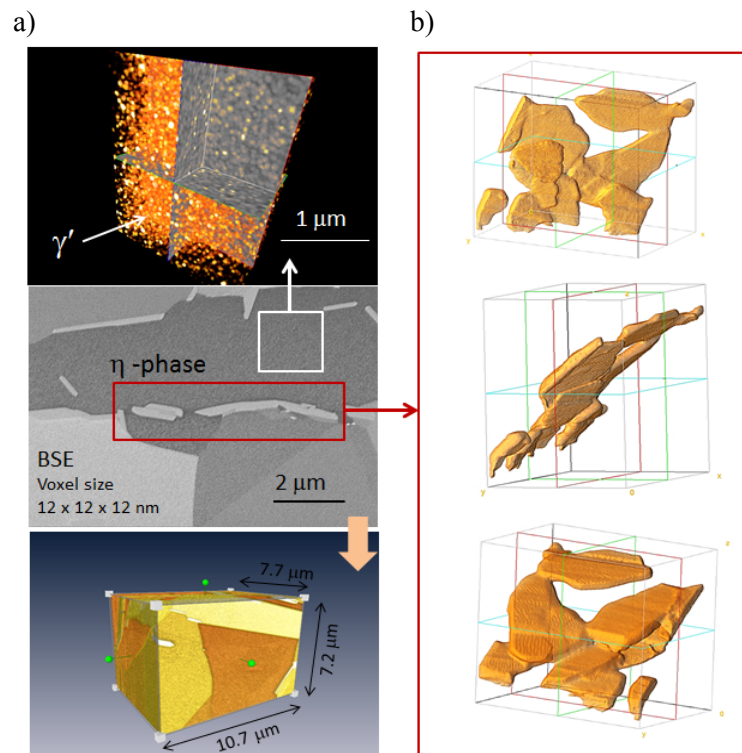


Fig. 2. Microstructure of 718Plus as seen by SEM-EsB detector (middle image on Fig.2a) and three-dimensional visualization of tomographic reconstructed volume of 718Plus superalloy by FIB-SEM tomography technique; a) spatial distribution of spherical γ' precipitates observed inside the analysed volume of the γ matrix, b) morphology at different angle of view of η phase precipitated at the γ grain boundary. Reconstructed volume: $10.7 \times 7.2 \times 7.7 \mu\text{m}$ and voxel size: $12 \times 12 \times 12 \text{ nm}$

3D imaging of silica gels for correlation between porous nanostructure and mass transport properties

Charlotte Hamngren Blomqvist^{1,a}, Annika Altskär^{2,b}, Stefan Gustafsson^{1,c},
Niklas Lorén^{2,d}, Anne-Marie Hermansson^{1,2,e} and Eva Olsson^{1,f}

¹Applied Physics, Chalmers University of Technology, S-412 96 Göteborg, Sweden

²Structure and Material Design, The Swedish Institute for Food and Biotechnology, SIK, Frans Perssons väg 6, S-402 29 Göteborg, Sweden

^acharlotte.hamngren.blomqvist@chalmers.se, ^baa@sik.se, ^cstefan.gustafsson@chalmers.se,
^dniklas.loren@sik.se, ^eamh@sik.se, ^feva.olsson@chalmers.se

Introduction

Soft porous materials are widely used in every-day products, e.g. in foods and medicine. The material structure determines the material properties, for instance the three-dimensional process of mass transport (flow rate and diffusion). Hence – in order to understand how to further optimize different porous soft materials for a variety of purposes – quantitative determination of three-dimensional structural data is crucial for establishing the correlations between structural properties and mass transport on different length scales. Gel structures consisting of particles distributed in three dimensions constitute one category of important soft materials. A characterisation of the transport paths, e.g. the distribution and sizes of pores as well as connectivity between pores is not entirely possible using traditional transmission electron microscopy (TEM), since it creates a two dimensional projection of a three dimensional material. Transmission electron microscope tomography (3D TEM) and scanning TEM (STEM) are powerful and indispensable complementary techniques for determining the three-dimensional structure on the nanometer scale. Careful sample preparation and state of the art equipment are crucial for the work. This work is focused on the direct connection between authentic quantitative nanostructural data and mass transport properties. We aim to quantify nanostructural porous properties of colloidal silica gels, on a length scale where the exact influence of flow versus diffusion is unknown. This approach facilitates the development and optimization of “smart” soft materials, with tailor-made diffusion and mass transport properties. In this talk, I will focus on how we utilized 3D TEM for soft materials on silica nanoparticle gels, working towards understanding mass transport on a nanoscale.

Methodology

We have used 3D STEM to image three colloidal silica nanoparticle gel samples where the porosity properties were controlled. The investigation spans from a porosity scale dominated by flow, to one dominated by diffusion. This approach provides interesting opportunities for understanding the correlation between nanostructure and mass transport.

In 3D STEM, an image series of the sample is collected while tilting the sample holder between two maximum tilt points [1], e.g. from +70° to -70°. In this case, the possible tilt range is either limited by the sample holder or by the sample thickness. The software Xplore3D and Inspect3D (FEI), and IMOD were used for image acquisition, alignment and reconstruction of the sample 3D volume.

The primary nanoparticles of the gels have a diameter of approximately 20 nm and 4 nm, respectively. The gel samples were prepared and embedded in plastic (TAAB LV) resin, using a solvent exchange technique. Prior to the collection of TEM or scanning TEM (STEM) tomography series, the embedded gel samples were segmented in 70-300 nm thin sections using an ultramicrotome. Both the sole primary particles and the gelled samples were characterised in two and three dimensions using 3D (S)TEM.

Results and conclusions

Using image analysis, the volume-weighted mean volumes (VWMV) [2] of the manufactured silica gels were analysed, and found to correspond to pore sizes with diameters of 20 nm, 60 nm and 230 nm, respectively. Digital 3D volumes of the three samples were created from 3D TEM imaging with subsequent reconstruction and visualization (see Figure 1 for an example). This combination of TEM tomography and advanced preparation techniques for high-resolution microscopy provides unique structure information that will generate new knowledge and understanding about structure-transport relationships. This process is also an important step in the general development of 3D TEM for soft materials.

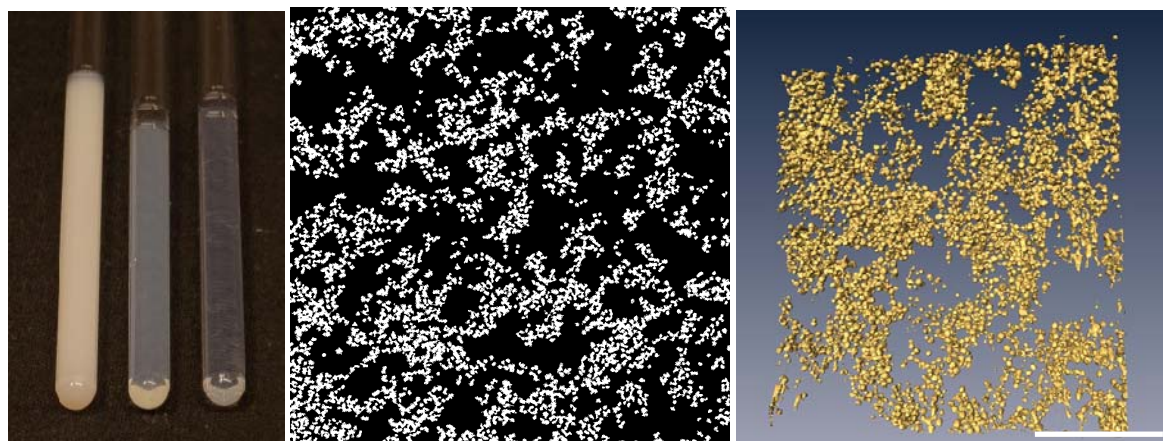


Fig. 1. Left: The three different silica gel samples. The VWMV of the samples from left to right is 230 nm, 60 nm and 20 nm, respectively. Centre: Filtered STEM image of a 70 nm thick section of the courser gel. The white silica nanoparticles are 20 nm in diameter. Right: 3D STEM visualisation of the courser gel. Scalebar is 500 nm

Acknowledgements

This project forms part of the VINN Excellence centre SuMo Biomaterials at Chalmers University of Technology. The centre is a collaboration between academia and several companies. We kindly thank Prof. Sara Bals and Dr. Hamed Heidari (EMAT, Antwerp) for valuable exchange concerning 3D STEM and ESTEEM2 for supporting the collaboration. We thank Dr. Tobias Gebäck (Chalmers University of Technology) for flow simulations. We also thank AkzoNobel for providing the samples and VINNOVA for funding.

References

- [1] P.A. Midgley and M. Weyland: Ultramicroscopy Vol. 96 (2003), p. 413.
- [2] H.J.G. Gundersen and E.B Jensen: J Microsc-Oxford Vol. 138 (1985), p. 127.

Three-dimensional microstructure analysis of cubic zirconia sinters by FIB-SEM serial sectioning

Piotr Bobrowski^{1,a}, Marek Faryna^{1,b}, Zbigniew Pędzich^{2,c}

¹Institute of Metallurgy and Materials Science PAS, 25 Reymonta Str., 30-059 Kraków, Poland,

²AGH University of Science and Technology, Faculty of Materials Science and Ceramics,
30 Mickiewicza Str., 30-059 Kraków, Poland

^abobrowski.piotrek@gmail.com, ^bm.faryna@imim.pl, ^cpedzich@agh.edu.pl

Introduction

The automated analysis of Electron Backscatter Diffraction (EBSD) patterns in the Scanning Electron Microscopy (SEM) for orientation imaging has become an established technique for crystallographic microstructural characterization in materials science. Combination of serial sectioning with a Focused Ion Beam (FIB) and EBSD-based orientation microscopy in dual-beam SEM extends experimental capabilities and gives an opportunity to investigate, not only the surface of the material, but also the bulk of the sample [1]. The FIB-SEM instrument enables tomographic, serial sectioning experiments to be carried out and gives possibility to analyze microstructure in three dimensions (3D).

The 3D EBSD technique is based on sequential removal of material layers and acquisition of orientation maps. Using dedicated software, the maps are stacked together and a 3D reconstruction of microstructure is created. It enables analysis of grain size and orientation distribution as well as full characterization of grain boundaries, what was unachievable by means of standard two dimensional (2D) EBSD analysis. Accurate estimation of the grain size distribution, calculation of number of nearest neighbors and characterization of the grain boundary (GB) network e.g. its geometry and character distribution (GBCD) in the 3D have become available [2]. In this research, a series of yttria stabilized zirconia samples were analyzed using the 3D-EBSD technique. Grain size distribution and number of neighbors were calculated. The results were compared to the ones obtained from the 2D EBSD data.

Experimental

Starting powders were obtained by hydroxides co-precipitation in ammonia solution [3]. A series of four samples, containing cubic zirconia stabilized by 8 mol% addition of yttria, was manufactured at different sintering temperatures, varying in the range from 1500°C to 1650°C. Samples were cylindrical with a diameter of 5 mm and a height of 1 mm. Prior to the FIB-SEM (FEI Quanta 3D FEGSEM) investigations, the specimens were sputter-coated with gold to remove the electron beam induced charge during scanning. Investigations were carried out at the voltages of 20 kV and 30 kV and currents of 3 nA and 5 nA for the electron and ion beams, respectively. The experimental data were processed using TSL OIM Analysis 5 and Dream3D 4.2 software [4].

Results

In the case of each sample the dimensions of the region of interest (ROI) for 3D measurements were 40 x 20 x 10 μm resulting in the analyzed volume of 8000 μm^3 . Samples were scanned with a step size of 200 nm on a square grid pattern. Maps were acquired with a 200 nm distance to obtain a cubic data voxel. For regular 2D analysis, maps were collected from a 50 x 50 μm area with a 250 nm step size. A clean-up procedure was applied to the obtained EBSD data to remove single, misindexed pixels (wild spikes). The minimum grain size was set to 10 adjacent pixels and the maximum orientation difference between two adjacent pixels, attributed to the same grain, was equal to 2°. The number of grains measured in each sample ranged from 214 to 428 and from 64 to 302 for the 3D and 2D data, respectively.

The 3D microstructure was reconstructed based on the stacks of inverse pole figure (IPF) maps. The average grain volume calculated from 3D data varied between $18.7 \mu\text{m}^3$ and $37.4 \mu\text{m}^3$. The average number of nearest neighbors ranged from 8.2 to 10.4. The 2D microstructure analysis was based on maps acquired from the area of $2500 \mu\text{m}^2$. The average grain area varied between $4.83 \mu\text{m}^2$ and $21.83 \mu\text{m}^2$. The average number of nearest neighbors, calculated from the 2D data, was in the range from 5.6 to 6.8.

The obtained values of grain volumes and grain areas, derived from the 3D and the 2D data were converted into equivalent grain diameters. The calculations were based on the assumption that the shape of grains could be approximated by a sphere in the case of 3D and a circle in the case of the 2D data. Such an assumption is acceptable when the investigated material is composed of uniaxial grains, which was true in the case of the investigated cubic zirconia. The calculated values of the average equivalent grain diameter varied from 2.79 to 3.29, and from 2.21 and 4.72 for the 3D and 2D data, respectively.

The analysis of the experimental data confirmed that samples sintered at higher temperature were composed of smaller amount of larger grains. At higher temperatures, the rate of the sintering process is faster leading to the formation of larger grains.

The average number of neighbors, derived from 2D data, oscillates around the value of 6, what is the most energetically favorable configuration. The average number of neighbors, calculated based on the 3D data, is higher than in the case of 2D data. Such a result is the consequence of counting neighbors that are located not only in plane of a single cross-section, but also below and above this plane. The application of 3D EBSD enabled direct calculations of the number of neighboring grains without the need of use of stereological approach.

Summary

The 3D-EBSD technique was applied to microstructure investigations of yttria stabilized cubic zirconia (c-ZrO₂). A series of four samples sintered at different temperatures was analyzed showing that the ones sintered at higher temperatures contained smaller amount of larger grains compared to those sintered at lower temperatures. Application of ion milling enabled a direct determination of various microstructural parameters, such as grain size and number of neighboring crystallites, contrary the 2D experimental data analysis which requires an application of stereological corrections approach.

Acknowledgements

The paper is financed by the Polish National Science Centre upon decision DEC-2012/05/B/ST8/00117. The research is co-financed by the European Union under the European Social Fund, project no. POKL.04.01.01-00-004/10.

References

- [1] S. Zaeferrer, S. Wright, D. Raabe: Metall. Mater. Trans. A 39A (2008), p. 374.
- [2] G. Rohrer: J. Am. Ceram. Soc. 94 (2011), p. 633.
- [3] Z. Pędzich, K. Haberko: Ceram Int. 20 (1994), p. 85.
- [4] dream3d.bluequartz.net.

Probing nano scale variation of optical properties of NiCo₂O₄, NiFe₂O₄ and CoFe₂O₄ by high resolution EELS

Krishnan Dileep^{1,a}, Boddapati Loukya^{1,b} and Ranjan Datta^{1,c}

¹International Center for Materials Science, Jawaharlal Nehru Center for Advanced Scientific Research, Jakkur P.O., Bangalore 560064, India.

^adileep@jncasr.ac.in, ^bloukya@jncasr.ac.in, ^cranjan@jncasr.ac.in

Introduction

CFO, NFO and NCO are magnetic spinel oxides of recent interest for their spintronics applications. These materials, in the thin film form, can show mixed cation and charge state ordering depending on growth method. NFO samples grown at 690°C showed ideal inverse spinel structure. A fundamental indirect band gap of 1.6eV and direct band gaps of 2.4 eV and 2.8 eV were observed in conventional transmittance and reflectance measurements [1]. CFO samples grown at 690 °C show ideal inverse spinel structure, a fundamental indirect band gap of 1.17 ±0.08 and a direct band gap of 2.74 ±0.10 eV [2]. The NCO films grown at higher temperatures (>450°C) show ideal inverse spinel structure and are nonmagnetic (NCO550). NCO films grown at lower temperatures (<450°C) are ferrimagnetic and metallic (NCO250 and NCO350) [3]. They show structural deviation from ideal inverse spinel structure towards mixed cations at A and B cations along with variations in charge state. Along with these types of structural deviations, other structural varieties like anti-phase domains (APDs) and A site cation vacancies are also commonly observed [4]. Such structural diversity has implications in optical and magnetic properties.

In the presented work, we have studied the nanoscale variation of band gaps in NFO (grown at 800°C), CFO (grown at 670°C) and NCO samples (grown at 250°C, 350°C and 550°C) by HREELS. Wien2k based DFT calculations of accurate band gaps were performed using mBJLDA exchange correlation potential.

Experimental details

The NFO and CFO films studied in this report are grown by liquid injection chemical vapor deposition (DLI-CVD) [5]. NCO films are grown by pulsed laser deposition. TEM samples were prepared by mechanical polishing followed by Ar ion milling. High resolution transmission electron microscopy (HRTEM) images and high resolution electron energy loss spectroscopy (HREELS) measurements were done in FEI TITAN 80-300 kV TEM operating with an extraction voltage of 300kV. Gun monochromator was excited during the HREELS experiment which improved the resolution to 210meV at 0.03 eV /channel dispersion. The optical absorption coefficient was calculated from the single scattering distribution (extracted by Fourier-Log deconvolution method). at the low loss region of HREELS by employing kramers-kronig analysis. The indirect and direct band gaps were measured by using the equation for traditional semiconductors like Si where a plots of $(\alpha.E)^{0.5}$ vs E gives indirect band gap and $(\alpha.E)^2$ vs E gives the direct band gap.

Artifacts like the Cerencov radiations are known to limit the measurements of band gaps by EELS. However, previous reports suggest that for direct band gaps, the Cerencov effects can be effectively minimized by acquiring spectra at very low thickness ($< 0.5 \lambda$ for hexagonal GaN) [6]. All the acquisitions in our experiment were done at 0.2λ - 0.4λ . The indirect band gap requires removal of the Cerencov radiation. Cerencov radiation losses are confined to a very small angular dispersion ($< 20 \mu\text{rad}$) [6], so we removed the contribution of Cerencov electrons by digitally removing the contributions from very low scattering angle as shown in Fig 1b. The collection semiangle used for acquisition was 2.7 mrad which included the expected Γ to X indirect transition (~ 1.2 mrad) in the magnetic oxide samples studied. HREELS measurements for NCO samples were done at both 90K and 300K.

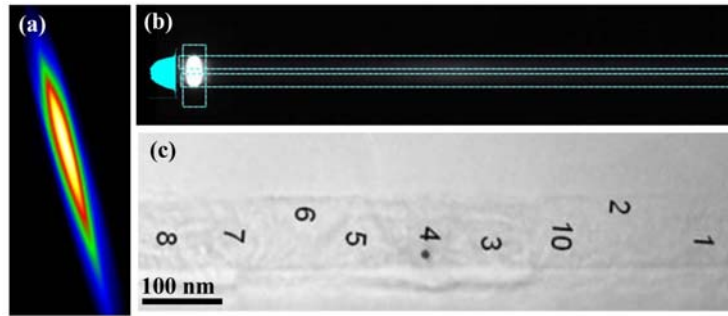


Fig. 1. (a) The beam after monochromator excitation which gives a resolution of 210 meV for 0.03 eV/channel. (b) The spectrum image. The intensity profile across the aperture is shown to the left side of the beam. The spectra are collected from either side of the center of the GIF aperture for indirect band gap measurement to avoid the contribution of Cerencov radiation. (c) Spectra are collected from different areas of the sample

Results and discussions

NFO direct band gap was found to be 2.35 ± 0.02 eV in most areas studied. Also, it showed other two direct band gaps of 2.8 ± 0.1 eV and 2.07 ± 0.02 eV. Indirect band gap varied from as low as 0.6 eV to 4.04 eV from place to place. CFO direct band gap varied from as low as 1.51 eV to 3.53 eV while the indirect band gap varied from 1.08 to 5.94 eV. For the NCO samples grown at $< 450^\circ\text{C}$ (250°C and 350°C) the fundamental band gap was found to be indirect band gap (Γ to X) while for sample grown at 550°C fundamental band gap was direct (Γ to Γ). Fig 2 shows a few selected spectra. Details will be presented at the conference.

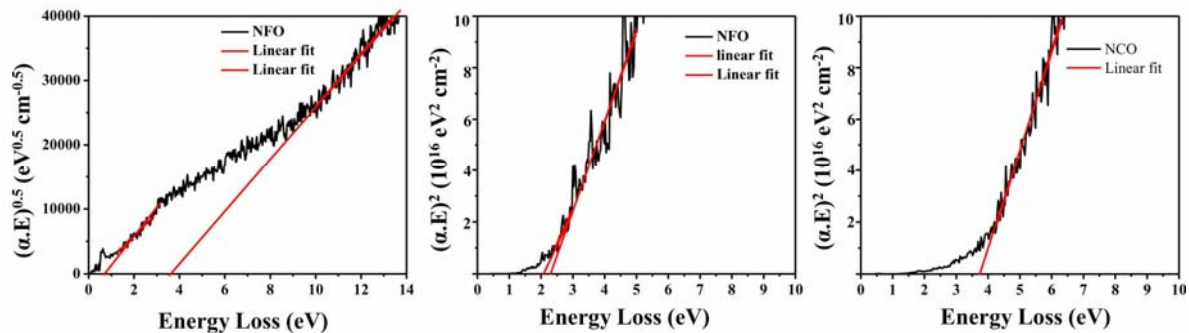


Fig. 2. Examples for optical band gap analysis demonstrated for (a) Indirect band gap of NFO (b) direct band gap for NFO and (c) direct band gap of NCO550

Conclusions

NFO and CFO showed band gap absorptions corresponding to ideal inverse spinel structures but additional absorption edges were present due to different areas with tetrahedral cation vacancies. This observation has been supported by HRTEM images. NCO samples showed a wide range of direct and indirect absorption edges because of mixed A and B cation distribution.

References

- [1] Q.-C. Sun, H. Sims, D. Mazumdar, J. X. Ma, B. S. Holinsworth, K. R. O'Neal, G. Kim, W. H. Butler, A. Gupta and J. L. Musfeldt: Phys. Rev. B Vol. 86 (2012), p. 205106.
- [2] B. S. Holinsworth, D. Mazumdar, H. Sims, Q.-C. Sun, M. K. Yurtisigi, S. K. Sarker, A. Gupta, W. H. Butler and J. L. Musfeldt: Appl. Phys. Lett. Vol. 103 (2013), p. 082406.
- [3] M. N. Iliev, P. Silwal, B. Loukya, R. Datta, D. H. Kim, N. D. Todorov, N. Pachauri and A. Gupta: J Appl. Phys. Vol. 114 (2013), p. 033514.
- [4] R. Datta, S. Kanuri, S. V. Karthik, D. Mazumdar, J. X. Ma and A. Gupta: Appl. Phys. Lett Vol. 97 (2010), p. 071907.
- [5] L. Shen, M. Althammer, N. Pachauri, B. Loukya, R. Datta, M. Iliev, N. Bao and A. Gupta: J. Crys. Growth Vol. 390 (2014), p. 61.
- [6] L. Gu, V. Srot, W. Sigle, C. Koch, P. van Aken, F. Scholz, S. B. Thapa, C. Kirchner, M. Jetter and M. Rühle: Phys. Rev B Vol. 75 (2007), p. 195214.

Size and shape of cobalt spinel nanocrystals determined by HAADF-STEM and DFT first-principles calculations

Joanna Gryboś^{1,a}, Jan Kaczmarczyk^{1,b}, Juri Barthel^{2,c}, Filip Zasada^{1,d}
and Zbigniew Sojka^{1,e}

¹ Faculty of Chemistry, Jagiellonian University, Ingardena 3, Krakow

² Ernst Ruska-Centre, Forschungszentrum Jülich GmbH, D-52425 Jülich, Germany.

^agrybosjo@chemia.uj.edu.pl, ^bj.kaczmarczyk@chemia.uj.edu.pl, ^cju.barthel@fz-juelich.de,
^dzasada@chemia.uj.edu.pl, ^esojka@chemia.uj.edu.pl

Introduction

Many important properties of nanostructured oxides depend on their size, dimensionality, and shape [1]. Being widely used in heterogeneous catalysis, oxide nanocrystals are characterized by a clear-cut structure and substantial surface area. This makes them excellent model systems for experimental and theoretical investigations into the surface related properties at atomic scale. From the thermodynamic point of view, the equilibrium shape of a nanocrystal is determined by the free energies of exposed facets $\gamma_{hkl}(n)$, and can be revealed by the Wulff construction that minimizes the total surface free energy at a fixed volume. In the case when the morphology of a nanocrystal is known from microscopic observations, $\gamma(n)$ can be assessed in an iterative way by inversion of the Wulff construction until the resulting shape matches the observed one. New catalytic materials of enhanced activity and selectivity can be designed by exploiting the phenomenon that faceted polyhedral crystals expose well-defined crystallographic planes, depending on the synthesis method. In such an approach, facets exposing crystallographic planes of high activity or with a higher density of active sites could be intentionally promoted.

Methodology and discussion

Previous attempts to determine the morphology of nanocrystals were mostly based on advanced electron microscopy techniques such as spherical-aberration corrected TEM observations supplemented with an exit-wave restoration [2] or HAADF/ADF STEM [3]. It has been shown that

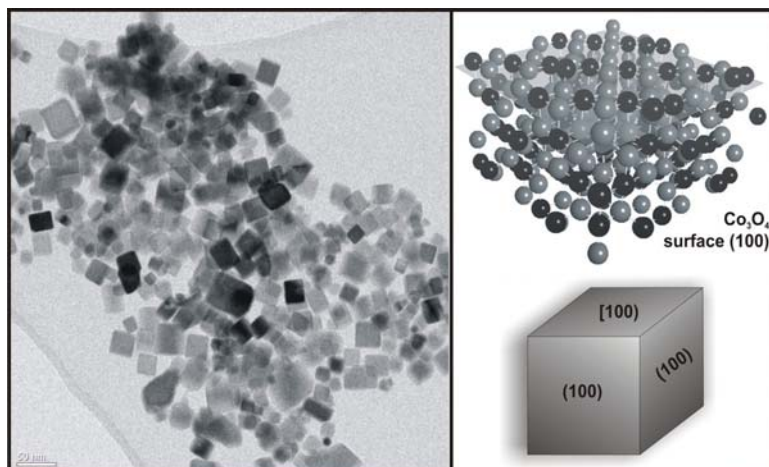


Fig. 1. TEM image of cubic-shaped Co_3O_4 nanocrystals together with calculated morphology and exposed (100) surface structure

HAADF STEM imaging and DFT ab-initio calculations. The validity of our approach is tested with Co_3O_4 nanoparticles with a controlled cubic morphology. Samples were

obtained by microwave assisted hydrothermal synthesis. Owing to a PVP surfactant addition the cubic nanocrystals exposed only (100) facets.

The experimental part of the shape analysis is based on the acquisition of HAADF STEM images with an intentionally increased electron probe size. The high-angle elastic scattering signal is registered as a fraction of the incident probe current by a respectively calibrated detector. Numerical calculations of HAADF STEM images under such a condition show a linear dependency of the recorded signal on the specimen thickness for randomly oriented nanocrystals and for probe diameters larger than the crystal unit cell (Fig. 2)¹.

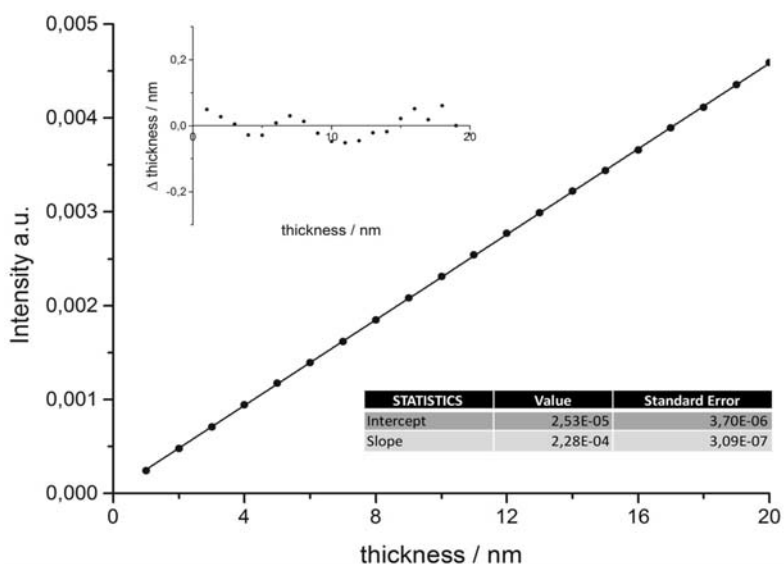


Fig. 2. Simulated HAADF signal for randomly oriented Co_3O_4 nanocrystals. *Insert*: Discrepancies between real and calculated thickness of Co_3O_4 nanocrystals

(100) surface was constructed by cleaving the solid in the normal (100) direction (Fig.1). It is planned to apply this approach for a shape analysis of nano-oxide catalytic materials with lower crystal symmetry, such as t- and m- ZrO_2 .

References

- [1] F. Zasada *et al.*: J. Phys. Chem. C 115 (2011), p. 6423.
- [2] L. Y. Chang, A. S. Barnard, L. C. Gontard, R. E. Dunin-Borkowski: Nano. Lett. 10 (2010), p. 3073.
- [3] D. G. Stroppa *et al.*: Nano. Res. Lett. 8 (2013), p. 475.
- [4] J. M. LeBeau, S. D. Findlay, L. J. Allen, S. Stemmer: Nano Lett 10 (2010), p. 4405.
- [5] H. Katz-Boon, Ch. J. Rossouw, Ch. Dwyer, J. Etheridge: Ultramicroscopy 124 (2013), p. 61.
- [6] J. Hafner: J. Comput. Chem. 29 (2008), p. 2046.

¹ HAADF STEM simulations were performed using the Dr. Probe software, J. Barthel, <http://www.er-c.org/barthel/drprobe/> (February 2014)

Influence of micro-arc oxidation conditions on microstructure and phase composition of hydroxyapatite coatings

Joanna Karbowniczek^{1a}, Grzegorz Cempura^{1b}, Faiz Muhaffel^{2c}, Huseyin Cimenoglu^{2d}, Aleksandra Czyrska-Filemonowicz^{1e}

¹ AGH University of Science and Technology, Al. A. Mickiewicza 30, PL-30059 Kraków

² Istanbul Technical University, 34469 Istanbul, Turkey

^ajkarbow@agh.edu.pl, ^bcempura@agh.edu.pl, ^cmuhaffel@itu.edu.pl,

^dcimenoglu@itu.edu.tr, ^eczyrska@agh.edu.pl

Keywords: electron microscopy, titanium alloys, micro-arc oxidation

Introduction

In regenerative medicine titanium and its alloys are used for dental and joints implants for more than eighty years. During all that time extensive research were done to improve their mechanical properties, corrosion resistance in body fluids and biocompatibility. Good integration between implant and bone is a crucial parameter for long-term implants replacing or complementing bone tissue [1]. Stable connection guarantees functionality of the implant and reduces the risk of loosening that may lead to the necessity of the revision surgery. Interesting possibility of surface modification of Ti alloys for improving biocompatibility is deposition of porous coating containing hydroxyapatite (HA) [2]. HA mimics extracellular matrix naturally present in bone tissue, porous layer enables ingrowth of the osteoblasts, both characteristics enhance bone-implant binding. Micro-arc oxidation (MAO) is one of the possible methods to obtain this type of coating [3].

Materials and methods

HA coatings were deposited on Ti6Al7Nb - two phases ($\alpha + \beta$) titanium alloy by micro-arc oxidation process. The only variable in MAO process was the electrolyte composition, all other parameters were the same for all prepared samples. Electrolytes composition was as-follow:

Solution 1: sodium phosphate (Na_2PO_4) and calcium acetate hydrate ($(\text{CH}_3\text{COO})_2\text{Ca}\cdot\text{H}_2\text{O}$)

Solution 2: β -glycerol phosphate ($\text{C}_3\text{H}_9\text{O}_6\text{PO}_4$) and calcium acetate hydrate

Solution 3: sodium phosphate and calcium glycerol phosphate hydrate ($\text{C}_3\text{H}_7\text{CaO}_6\text{PO}_4\cdot\text{H}_2\text{O}$)

Coatings were investigated by scanning electron microscopy and energy dispersive X-ray spectroscopy (SEM-EDS) as well as analytical- and high resolution transmission electron microscopy (TEM, HRTEM) techniques utilized cross-section lamellae prepared by FIB.

Results and discussion

SEM images of surfaces of three types of the samples showed the diversity between them. The highest porosity and rather smooth surface, typical for MAO process, was observed for sample 2 (Fig. 1b). Samples number 1 and 3 (Figs 1a, c) had much lower porosity, however specific aggregations of platelets were present, they caused much higher surface development. Mean roughness (R_a) for samples number 1, 2 and 3 were measured as 3.8; 1.6 and 3.65, respectively. SEM-EDS analysis of the sample chemical composition showed that all of them contain the same elements: Ti, Ca, P and O, only the concentration of particular element was different.

Investigation of sample cross-sections revealed layered structure of the coatings. Titanium dioxide layer was formed directly at the substrate, then areas rich in Ti, O and Ca were present and the outer layer was consisted of hydroxyapatite (HA). However, the thickness of each phase was different depending on the type of the coating. Fig. 2 presents chemical composition maps from cross-section of sample 1, confirming layered structure of the coating. HRTEM investigation of FIB lamella prepared from the outer layer of the coating showed that platelets were identified as HA (Fig. 3). Further identification of layer phase composition by electron diffraction and TEM-EDS is in progress.

Microscopic investigation proved that just a modification in electrolyte composition, keeping constant all other parameters of MAO process, resulted in significant change in microstructure,

composition and porosity of deposited coatings. To verify which type of the coating would be the best for biomedical applications in vitro cell cultures will be performed.

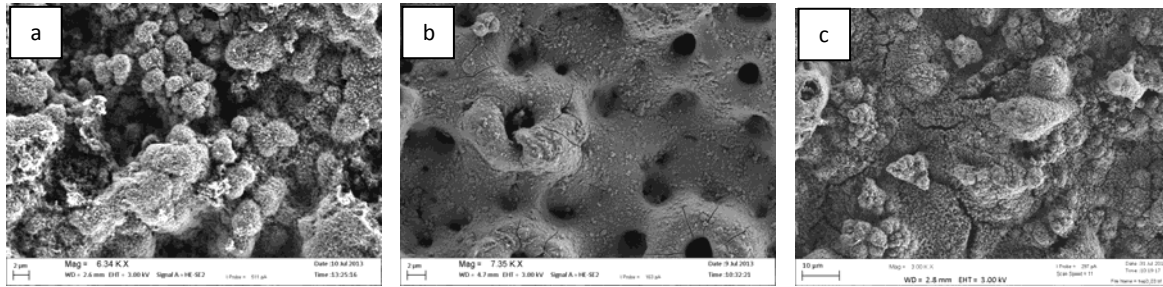


Fig.1. SEM images of the coatings' surface: a) sample 1, b) sample 2, c) sample 3

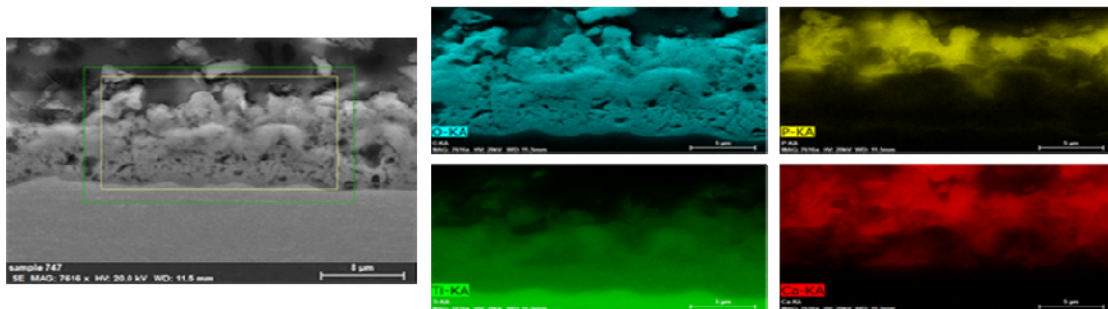


Fig. 2. a) SEM image of cross-section from sample 1, mapped area marked with green rectangle, b) oxygen distribution, c) phosphorus distribution, d) titanium distribution, e) calcium distribution

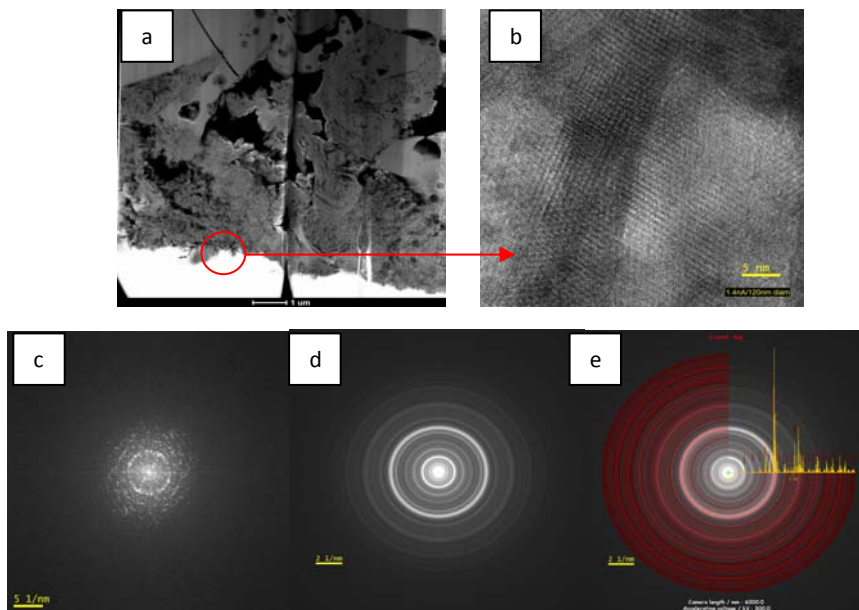


Fig. 3. a) TEM image of the coating outer layer of the sample 1, b) HRTEM image from the area marked by red circle, c) diffraction pattern after FFT, d) diffraction pattern after FFT rotational averaged, e) JEMS match HA

References

- [1] P. Roach, D. Eglin, K. Rohde, C.C. Perry: J. Mater. Sci: Mater. Med. 18 (2007), p. 1263.
- [2] D.Y. Kim, M. Kim, H.E. Kim, Y.H. Koh, H.W. Kim, J.H. Jang: Acta Biomater. 5 (2009), p. 2196.
- [3] H. Cimenoglu, M Gunyuz, G.T. Kose, M. Baydogan, F. Ugurlu, C. Sener: Mater. Char. 62 (2011), p. 304.

Acknowledgement

The study was realized within OPTYMED research project (nr 2013/08/M/ST8/00332) financed by NCN. Authors would like to thank Prof. Philippe Buffat for his significant help with TEM investigations.

In-situ transmission electron microscopy investigations of dislocation structures evolution in severely deformed technically pure aluminium

Witold Chromiński^a, Małgorzata Lewandowska^b

Warsaw University of Technology, Faculty of Materials Science and Engineering, Wołoska 141, 02-507 Warsaw, Poland

^awichr@inmat.pw.edu.pl, ^bmalew@inmat.pw.edu.pl

Development of dislocations structures during plastic deformation has been extensively investigated using TEM. However, conventional TEM observations of the samples exposed to plastic deformation reveal their structure only between different stages and some subtle effects can be unnoticed. On the other hand, in-situ experiment allows to follow the evolution of dislocations structure continuously and is widely use to enhance understanding of dislocation patterning. In this study, plastic deformation of ultrafine grained aluminium obtained via hydrostatic extrusion (with relatively low accumulated strain of $\epsilon=1.8$) was investigated using in-situ experiments in TEM to provide new insights into microstructure development and mechanism of grain size refinement.

The material was investigated in terms of texture (EBSD) and dislocation structures (TEM). EBSD was performed using HITACHI SU70 SEM with accelerating voltage of 20kV. Investigation of dislocation structures were performed on JEOL JEM 1200 EX (120kV) TEM with double tilt holder for full control over diffraction conditions. Weak beam g-3g imaging with deviation parameter s slightly positive was used to show sharp dislocation lines. Burgers vector was determined with invisibility criterion $\mathbf{g} \cdot \mathbf{b} = 0$ by comparison of different images.

In-situ specimens were thin discs electrochemically polished and glued to straining holder grip with conductive epoxy resin. In-situ straining experiment was applied to investigate dislocation sources and evolution of dislocation structures. All observations were done under two-beam condition.

Hydrostatic extrusion of pure aluminium resulted in a non-homogenous structure with two types of grains: $\langle 111 \rangle$ oriented which are significantly refined with the size of about 200 nm and $\langle 001 \rangle$ oriented which are relatively large with well developed dislocation substructure. Diffraction contrast experiment showed that three types of dislocations arrangements form in the recrystallized grains. Two of them were recognized as low energy dislocation structure (LEDS) – screw dislocation square twist network and dislocation walls containing dislocations with at least four different Burgers vectors. Third structure was single Burgers vector dislocation array. In-situ straining experiment showed that LEDS are stable and do not change during plastic deformation whereas non-LEDS are unstable and gliding dislocation interact with them. For low strain, these structures collapse whereas for higher strain, such a structure is a nuclei for LEDS due to efficient dislocation intersections producing jogs.

Microstructural changes in Al-Mn-Fe-Mo melt spun ribbons studied by in-situ heating in a TEM

Katarzyna Stan-Głowińska^{1,a}, Lidia Lityńska-Dobrzyńska^{1,b}
and János L. Lábár^{2,c}

¹Institute of Metallurgy and Materials Science, Polish Academy of Sciences, Krakow 30-059, Reymonta 25, Poland

²Institute for Technical Physics and Materials Science, Research Centre for Natural Sciences, Hungarian Academy of Sciences, H-1121 Budapest, Konkoly-Thege ut 29-33, Hungary

^ak.stan@imim.pl, ^bl.litynska@imim.pl, ^clabar.janos@ttk.mta.hu

Introduction

Aluminium alloys strengthened with quasicrystalline icosahedral particles are a new group of light-weight materials with interesting mechanical properties [1]. Combination of small hard icosahedral particles with a soft aluminium matrix leads to high values of tensile strength of those materials. They also exhibit good thermal stability compared to commercially available aluminium alloys [2, 3]. This stability is connected with the presence of transition metals (e.g. Nb, Ta and Ti) in the quasicrystals. These elements are characterized by very low diffusivity in aluminium [4]. In our previous work it was found that small addition of Mo (1 at.%) into $\text{Al}_{91}\text{Mn}_6\text{Fe}_2\text{Mo}_1$ melt spun ribbons increases the decomposition temperature of quasicrystalline phase by 100 °C compared to the initial $\text{Al}_{91}\text{Mn}_7\text{Fe}_2$ composition [5]. In this work an alloy with higher content of aluminium $\text{Al}_{94}\text{Mn}_4\text{Fe}_1\text{Mo}_1$ was cast to increase plasticity of the ribbon. The stability of the icosahedral phase in the new alloy was investigated by in-situ heating in a TEM and compared to the results obtained for $\text{Al}_{91}\text{Mn}_6\text{Fe}_2\text{Mo}_1$ ribbon. The formation of various crystalline phases after decomposition of both the spherical and the intercellular quasicrystalline phase was analyzed.

Methodology

The alloy of nominal composition $\text{Al}_{94}\text{Mn}_4\text{Fe}_1\text{Mo}_1$ was cast using the melt-spinning technique under argon atmosphere. Thin foil was prepared by electropolishing in electrolyte containing nitric acid and methanol (1:3). The in-situ experiment was carried out using a heating holder in Philips CM20 transmission electron microscope in the temperature range 400 – 550 °C. The microstructure of the sample before and after the heating was examined with FEI transmission electron microscope Tecnai G2 operating at 200 keV, equipped with HAADF-STEM detector, combined with an energy dispersive X-ray (EDX) EDAX spectrometer.

Results

The $\text{Al}_{94}\text{Mn}_4\text{Fe}_1\text{Mo}_1$ ribbon in as spun state exhibit two phase structure: icosahedral quasicrystals (i-phase), with different morphology, embedded in aluminium matrix. Based on TEM studies two observations were made. First, for the higher content of Al in the alloy, i-phase occurs mainly in the form of intercellular particles (Fig. 1a) with small fraction of spherical quasicrystals (contrary to what was observed in the $\text{Al}_{91}\text{Mn}_6\text{Fe}_2\text{Mo}_1$). Second, based on bright field image analysis (using ImageJ program), the fraction of i-phase in the samples decreased by about twice compared to the $\text{Al}_{91}\text{Mn}_6\text{Fe}_2\text{Mo}_1$. For the $\text{Al}_{94}\text{Mn}_4\text{Fe}_1\text{Mo}_1$ ribbon, the part of sample selected for in-situ heating contained three regions: the first with very fine intercellular i-phase, the second with spherical particles and the third with bigger intercellular quasicrystals (Fig. 1a). EDX maps of elements distribution obtained for the investigated area indicated that Mo was not present in the bigger intercellular particles. During in-situ experiment significant changes in the sample microstructure occurred in region 1 and 2 after 30 minutes of heating at 450 °C, and in region 3 after 30 minutes at 500 °C. Tracing of types of phases formed after decomposition of the quasicrystalline phase in

particular regions leads to a conclusion that in the first and second areas fine intercellular quasicrystals and spherical particles decompose into $\text{Al}_{12}(\text{Mn}, \text{Mo})$ phase during heating (Fig. 1b). Analysis of the region containing bigger intercellular particles indicated that Al_3Mn was formed after i-phase decomposition (Fig. 1b). Smaller fraction of i-phase in $\text{Al}_{94}\text{Mn}_4\text{Fe}_1\text{Mo}_1$ ribbon compared to the $\text{Al}_{91}\text{Mn}_6\text{Fe}_2\text{Mo}_1$ caused decrease of microhardness values from 204 ± 15 to 167 ± 6 HV and decrease of Young's modulus by about 30%.

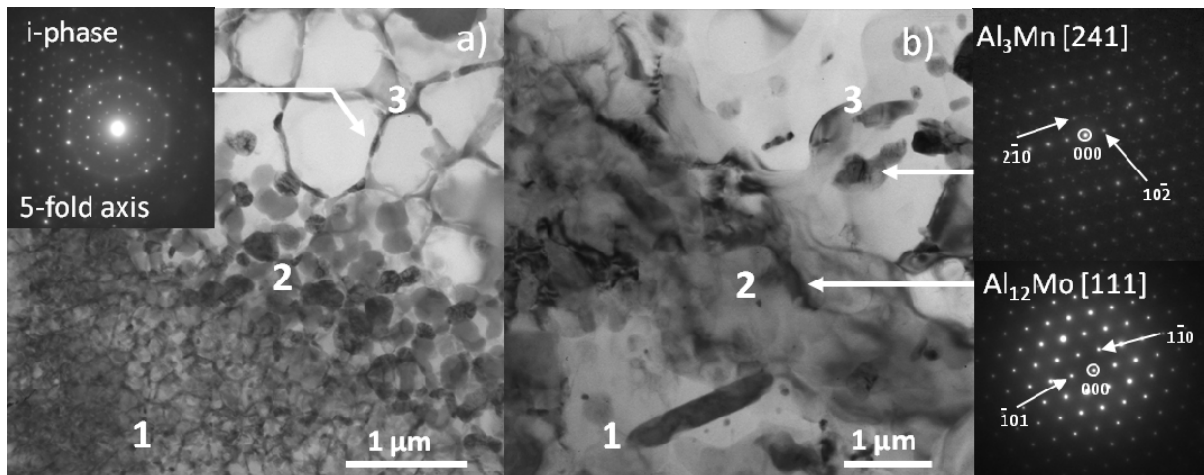


Fig. 1. Bright field image of a) the part of thin foil selected for in-situ heating observations with three distinct regions marked with numbers together with SADP of the intercellular i-phase revealing 5-fold symmetry b) the same part of the sample after heat treatment with SADPs of $\text{Al}_{12}(\text{Mn}, \text{Mo})$ phase formed in the region 1/2 and Al_3Mn phase formed in the region 3

Conclusions

Higher content of Al in the $\text{Al}_{94}\text{Mn}_4\text{Fe}_1\text{Mo}_1$ ribbon compared to $\text{Al}_{91}\text{Mn}_6\text{Fe}_2\text{Mo}_1$ results in the change of morphology and volume fraction of the i-phase. During in-situ heating, the most significant changes in the sample microstructure occur at 450 and 500 °C. Obtained results indicate that the i-phase that is present in the form of primary spherical particles is more thermally stable than the intercellular quasicrystals present in the same sample. Due to changes in the composition of a quasicrystalline phase in different areas of the samples (spherical and intercellular i-phase) decomposition of quasicrystalline leads to formation of different crystalline phases including $\text{Al}_{12}(\text{Mn}, \text{Mo})$ and Al_3Mn .

References

- [1] M. Galano, F. Audebert, A. G. Escorial, I. C. Stone and B. Cantor: J. Alloy. Compd. Vol. 495 (2010), p. 372.
- [2] M. Cavojsky, M. Balog, J. Dvorak, E. Illekova, P. Svec, P. Krizik, D. Janickovic and F. Simancik: Mater. Sci. Eng. A Vol. 549 (2012), p. 233.
- [3] K. Dam, D. Vojtech, and F. Prusa: Mater. Sci. Eng. A Vol. 560 (2013), p. 705.
- [4] K.E. Knippling, D.C. Dunand and D.N. Seidman: Z. Metallkd. Vol. 96 (2006), p. 246.
- [5] K. Stan, L. Lityńska-Dobrzyńska, J.L. Lábár and A. Góral: J. Alloys Compd. Vol. 586 (2014), p. S395.

Multi-scale orientation measurement by X-ray and electron diffraction techniques in single crystal superalloy

Robert Albrecht^{1a}, Maciej Zubko^{1b}, Włodzimierz Bogdanowicz^{1c},
Eleftheria Maria Pechlivan^{2d}, Jan Sieniawski^{3e}, Krzysztof Kubiak^{3f}

¹Institute of Materials Science, University of Silesia, 75 Pułku Piechoty 1A, 41-500 Chorzów, Poland

²Applied Physics Laboratory, Department of Physics, Aristotle University of Thessaloniki, GR 54124 Thessaloniki Greece

³Department of Materials Science, Rzeszów University of Technology, W. Pola 2, 35-959 Rzeszów, Poland

^aralbrecht@us.edu.pl, ^bmaciej.zubko@us.edu.pl, ^cwlodzimierz.bogdanowicz@us.edu.pl, ^depechl@physics.auth.gr, ^ejansien@prz.edu.pl, ^fkrkub@prz.edu.pl

Keywords: X-ray topography, superalloy, EBSD, Precession electron diffraction

Single crystal superalloys are widely used in high temperature applications as they present higher cycle fatigue strength and better thermal resistance especially at elevated temperatures, compared with conventional polycrystalline forms. In recent researches, it has been stated that primary and secondary crystal orientation has a significant impact on high cycle fatigue of single-crystal turbine blades, that could reduce their service life time. Therefore, crystalline quality of turbine blades should be precisely controlled after casting.

In this work the multi-scale orientation measurements were conducted on second generation single crystal nickel based superalloy by applying electron and X-ray diffraction methods. The precise characterization of crystal orientation of the complex microstructure superalloy was investigated by X-ray Laue Diffraction, X-ray Topography, Scanning Electron Microscopy (EBSD) and Transmission Electron Microscopy orientation mapping. Measurements results confirm that the selective characterization methods are complementary, besides the fact that different orientation defects can be visualized using specified ones. The recent work gives a new guide line for checking crystal quality and orientation defects in single crystal superalloys and determine suited characterization techniques.

Computer methods for Cs corrected TEM images

Krzysztof Morawiec^{1,a}, Piotr Dłużewski^{1,b}

¹Institute of Physics PAS

^amorawk@ifpan.edu.pl, ^bdluzew@ifpan.edu.pl

One of the most important problem of the transmission electron microscopy is computer processing of results. The spherical aberration corrected high-resolution images contain a lot of information about the test object, but this information is not available directly. The serie of images recorded under controlled changes of electron optic parameters allow to compute phase and amplitude of exit electron wave function. This problem, known as the Electron Wave Reconstruction (EWR), is intensively developed as a powerful method for detailed characterization of atomic structure of the matter.

Progressing development of both hardware and software gives us the computational ability to solve the EWR problem in the reasonable period of time. The possibility of using the computational performance of GPU (Graphics Processing Unit) is particularly promising. GPU is able to perform large numbers of parallel calculations which can significantly accelerate the analysis of TEM images. Currently the software for the electron wave reconstruction is developed using the CUDA language for GPU programming. Results obtained with this software will be presented and theoretical predictions will be discussed.

Acknowledge

This research was co-financed by the European Regional Development Fund within the Innovative Economy Operational Programme 2007-2013 “Analytical high resolution transmission electron microscope for nanoscience, nanotechnology and spintronics” No POIG.02.01-00-14-032/08.

Effect of hydrogen on corrosion of Mg-Al alloys in various electrolyte solutions

Bartosz Chmiela^{1,a*}, Adrian Mościcki^{2,b} and M. Sozańska^{3,c}

Silesian University of Technology, Faculty of Materials Science and Metallurgy,
Kraśińskiego 8, 40-019 Katowice, Poland

^abartosz.chmiela@polsl.pl, ^badrian.moscicki@polsl.pl, ^cmaria.sozańska@polsl.pl

Keywords: Mg-Al alloys, corrosion, hydrogen

Magnesium alloys are characterized by low density and high specific strength (comparable with steels and titanium alloys) and so are widely used as structural materials in the automotive and aerospace industries. The best known and commonly used are Mg-Al alloys, especially AZ91 alloy (and very similar GA8 alloy). However, the use of these magnesium alloys is hindered by the fact that they offer insufficient corrosion resistance, even in dilute electrolyte solutions. Many investigations show that hydrogen is the main corrosive factor appearing during chemical reactions between magnesium and water in electrolyte solution. The main intermetallic phase in AZ91 and GA8 alloys is $Mg_{17}Al_{12}$ (β phase), which is a hydrogen trap. During the corrosion, magnesium hydride (incoherent with the β phase) would be brittle fractured when the inner stress caused by hydrogen pressure and expansion stress of formation of magnesium hydride was higher than fracture strength. However, another Mg-Al alloy AE44, contains Al and rare-earth elements and its microstructure consists of precipitates of other phases ($Al_{11}RE_3$, Al_2RE , $Al_{10}RE_2Mn_7$) in α -Mg matrix.

The paper presents the corrosion behaviour of AZ91, GA8 and AE44 magnesium alloys in 0.1M sodium sulfate solution and 3.5% sodium chloride solution. Selecting three various Mg-Al alloys allows to analyse the various effects of hydrogen on these materials. The phase identification was performed by XRD and EBSD analysis. Microstructure of the alloys before and after corrosion was observed using scanning electron microscope (SEM) and scanning transmission electron microscope (STEM).

Dark-field HRTEM and LACBED images

Elżbieta Jezierska

Warsaw University of Technology, Faculty of Materials Science and Engineering,
Wołoska 141, 02-507 Warsaw, Poland
ejeziers@inmat.pw.edu.pl

TEM images are very important in understanding phase transformations, defects generation and propagation. Conventional TEM consisting of bright field imaging and SAD pattern are still very useful in materials characterization. Dark-field TEM technique is powerful for investigation of coherent precipitates and twins even in modern nanostructured materials. It is advantageous to use the dark field technique to study features which are of low contrast on a bright-field image. This advantage applies particularly to the detection of very small precipitates in a matrix. Some deviations from the Bragg setting are much more readily detected on the dark-field image than on the bright-field image.

Detailed characterization of early stages of crystallization and precipitation can be performed using HRTEM images. Why do not use HRTEM image in a dark-field mode?

For successful HRTEM experiment we need very thin, flat and well oriented sample, without contaminated layer and multibeam condition to resolve atomic structure. In the case of real sample some interesting features are usually in a wedge-shaped thicker region of the sample. Without objective aperture the contrast is very poor, so it is difficult to obtain a phase-contrast image with atomic resolution. To overcome these difficulties dark-field HRTEM image can be formed with smaller objective aperture to separate chosen diffracted beam. Such image is similar to Z-contrast HAADF on STEM, but can be formed without special equipment.

The Large-Angle Convergent-Beam Electron Diffraction (LACBED) technique was proposed by Tanaka in 1980 to improve the quality of the CBED patterns obtained with a large angle convergent incident beam (Kossel patterns). In this method a specimen is raised (or lowered) from its usual eucentric position in the object plane. The LACBED technique which uses a defocus incident beam has a unique property: the image of the illuminated area of the specimen is superimposed on the diffraction pattern composed of Bragg lines. Therefore, the pattern is a mapping between the direct and the reciprocal spaces and “shadow image” of a defect is visible on the pattern.

TEM investigations were performed on JEM 3010 Jeol equipped with Gatan CCD camera. Conventional TEM studies, HRTEM and LACBED were used to elucidate the structure of $(Al,Mn)_3Ti$ ordered intermetallics, GaN/SiC epilayers, NdFeB magnets. For advanced studies of the nature of antiphase boundaries (APBs) LACBED method in dark-field mode was employed. Perfect symmetry was confirmed from LACBED images and ordering is manifested in superlattice Bragg lines. Any defects breaking the translational symmetry and perfect order can be visible on LACBED lines. For antiphase domain boundaries (APBs) in ordered compound the splitting of superlattice Bragg lines on LACBED images can be observed. The superlattice excess line is split into two lines with equal intensity on bright-field LACBED pattern as well as on dark-field LACBED pattern if the domains are enough large to see the effect. This splitting can be considered as typical and used to identify APBs.

Acknowledgements

The financial support from the Polish Ministry of Science and Higher Education, Faculty of Materials Science & Engineering Warsaw University of Technology is acknowledged.

First stages of reaction of molten aluminium with MgO substrate

Jerzy Morgiel¹, Małgorzata Pomorska¹, Rafał Nowak², Natalia Sobczak²

¹ Institute of Metallurgy and Materials Science, 25 Reymonta st., 30-059 Kraków

² Foundry Research Institute, 73 Zakopianska st., Kraków

Introduction

Interaction between molten aluminium and metal oxides (MO) takes place in many routine industrial processes, but understanding of these phenomena as is still limited. Most of a knowledge in this area was as yet obtained from wetting experiments. They help to establish both the reaction rate documenting itself by thickness of reaction products layer formed at comparable time - temperature ranges and the type of newly formed phases [1]. The high reactivity of molten aluminium with MgO substrates results in a formation of thick reaction products region (RPR) characteristic for most Al/MO couples. It makes Al/MgO couple a preferable model system for studies devoted to understanding of the mechanism responsible for the development of unique interpenetrating metal-ceramic structures formed due to such interaction. However, early experiments on Al/MgO produced conflicting conclusions concerning even the RPR phase content, i.e. either the presence of MgAl_2O_4 spinel or the type of Al_2O_3 phases, as summarized by Morgiel *et al* [2]. The extensive microstructure investigations including optical and electron microscopy observations of RPR formed in Al/MgO couples gave evidence that it is built of two layers, i.e. first - located closer to melt - of coarse dendrite like $\alpha\text{-Al}_2\text{O}_3$ separated by aluminium channels and second of finer - less regular forms - of MgAl_2O_4 spinel also with some aluminium in-between [2, 3]. The first attempts at formulating a mechanism of formation of RPR in Al/MgO included two possible paths, i.e. either starting with a layer of Al_2O_3 or MgAl_2O_4 [3]. In both cases, a direct reaction of MgO to one of these oxides was assumed. The metallic channels in RPR were consider a result of volume difference of MgO and alumina or spinel. The more recent observations of RPR showed that it is always separated from MgO by metallic channel [4]. It suggests, that first liquid aluminium dissolves MgO and then the oxides in RPR grow from the melt. This sharp change in viewing the above processes reopened problem of nucleation and growth of the RPR and especially the beginning of reaction path. However, investigation of the early stages of interaction of liquid aluminium with MgO substrate taking place in vacuum at high temperature calls for infinitesimal times, which practically could not be realized due to technical difficulties. Fortunately, during wetting experiments the aluminium drop placed at MgO substrate moves occasionally leaving in its wake places, which were just touched with liquid metal. In such case, neither duration nor the latter temperature exposure is controlled. Even so, this brief contact of the liquid metal with substrate is the only source of information on the Al/MgO RPR nucleation events.

Therefore, the aim of this paper was to investigate both the microstructure and phase composition of selected areas of the MgO substrate which show only residual or small effects of its interaction with liquid aluminium, i.e. outside of the RPR formed under the drop.

Experimental procedure

The Al/[100]MgO couple was formed during wetting experiment at 1000°C as described in detail elsewhere [2-3]. The microstructure observations were performed using TECNAI G² F20 FEG (200 kV) equipped with integrated EDAX EDS detector. Thin foils were prepared with QUANTA 200 Dual Beam FIB equipped with OmniProbe lift-out system.

Results

The observations showed, that a momentary contact of liquid aluminium with [100] MgO substrate caused the formation of a layer of MgAl_2O_4 . It was built of coarse columnar crystallites of

nearly the same orientations having planar interface with MgO and a chevron-like with the drop side (Fig. 1a, encircled area). Such character of those two interfaces indicates that the layer was nucleated at MgO monocrystalline substrate and next grow into liquid aluminium. It means that the process was controlled by solid state out-diffusion of magnesium and oxygen from the substrate through newly formed spinel layer. Every few microns the layer of spinel brakes down producing local gaps through which, due to capillary phenomenon, the liquid aluminium again comes to direct contact with the substrate. These small openings develop to thin meandering aluminum channels of sides covered with spinel.

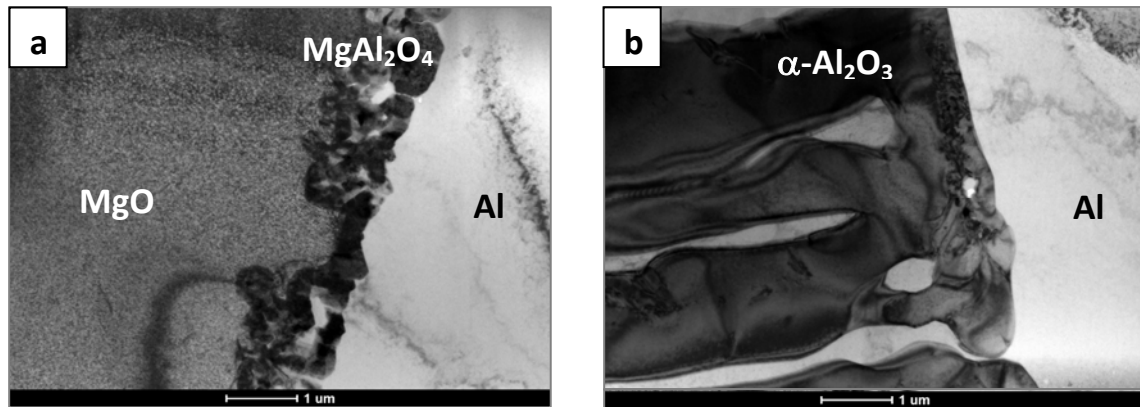


Fig. 1. Products of short (a) and long (b) time exposure of [100] MgO substrate to liquid Al

The nearby area - being in contact with liquid aluminium for slightly longer time - shows only coarse dendrite-like α - Al_2O_3 crystallites (Fig. 1b). The close inspection of these crystallites shows the presence of numerous small voids or magnesium filled pockets at their “roots”. It indicates that the MgAl_2O_4 spinel layer is consumed by subsequently formed α - Al_2O_3 crystallites. Therefore, the formation of MgAl_2O_4 , controlled by out-diffusion of O and Mg from substrate, should be assumed as a first stage of development of the RPR. Next, the spinel serves as nucleation site for α - Al_2O_3 crystallites. Growth of the latter is controlled by dissolution rate of MgO by liquid aluminium and diffusion of O in the latter (Mg is moved out from the RPR to aluminium drop and evaporates), i.e. diffusion in liquid state.

Summary

The microstructure investigation of the areas of [100]MgO substrate, being exposed to liquid aluminium only for short time allowed to prove that it causes growth of a thin layer of MgAl_2O_4 columnar spinel crystallites. Soon after its formation, spinel serves as nucleation site for α - Al_2O_3 , which consumes the former and next grows at expense of MgO. The latter is dissolved by liquid aluminium constantly penetrating along channels between the α - Al_2O_3 .

The growth of MgAl_2O_4 is controlled by solid state diffusion of Mg and O out of MgO substrate and through newly forming phase, while the growth of α - Al_2O_3 is controlled both by dissolution rate of MgO by liquid aluminium and diffusion of the oxygen in the latter.

References

- [1] N. Sobczak: Sol. St. Phenom. 101 (2005), p. 221.
- [2] J. Morgiel et al.: Arch. Metal. Mater. 59 (2013), p. 497.
- [3] R. Nowak, N Sobczak, E. Sienicki, J. Morgiel: Sol. St. Phenom. 172 (2011), p. 1273.
- [4] J. Morgiel et al.: Mater. Eng. (Inżynieria Materiałowa) 34 (2013), p. 162.

Acknowledgements

The research was performed in a frame of the project ZAMAT (Advanced Materials and Technologies for their Production), No POIG.01.01.02-00-015/09-00, task 5.5.2.

EELS characterization of iron oxide nanostructures grown by the steam-iron process

Jürgen Gluch^{1,2,3,a}, Lars Röntzsch² and Ehrenfried Zschech^{3,4}

¹Institute for Materials Science, TU Dresden, 01062 Dresden, Germany

²Fraunhofer Institute for Manufacturing Technology and Advanced Materials (IFAM), Branch Lab Dresden, Winterbergstr. 28, 01277 Dresden, Germany

³Fraunhofer Institute for Ceramic Technologies and Systems - Materials Diagnostics (IKTS-MD), Maria-Reiche-Str. 2, 01109 Dresden, Germany

⁴Dresden Center for Nanoanalysis (DCN), TU Dresden, 01062 Dresden, Germany

^ajuergen.gluch@tu-dresden.de

This study is focused on the different iron oxide structures and their morphologies that evolve during the steam-iron-process: $3 \text{ Fe} + 4 \text{ H}_2\text{O} \leftrightarrow \text{Fe}_3\text{O}_4 + 4 \text{ H}_2$. Due to the use of cheap, non-hazardous and abundant materials this reaction is a possible candidate for modern hydrogen storage technologies. Hydrogen generation results from the reaction of highly reactive nano-sized iron powder with water steam. Hydrogen storage is performed by its reaction with magnetite powder. Since the early use of the steam-iron-process a crucial disadvantage is the decrease of storage capacity after repeated storage cycles, caused by morphology changes of the iron based materials that results in coarsening and loss of active surface. The oxidation of nano-sized pure iron powder at temperatures up to 750 K in a humid atmosphere results in a complex growth pattern of oxides, previously reported for stainless steel [1]. A multi-layer oxide develops at elevated temperatures. This oxide layer exhibits complex structures and microstructures. In tomographic x-ray reconstructions (Carl Zeiss nano XCT 100) this oxide appears to form a closed skin layer around the powder agglomerate particles. This leads to a decrease of the reactivity during repeated cycles of the redox reaction. This oxide skin layer is up to 250 nm thick and it is covered with whisker and platelet like features growing at random at the surface. To investigate the growth mechanism and possible routes for prevention of oxide skin formation we characterized the various oxide structures grown at different temperatures between 520 K and 770 K by FIB/SEM (Carl Zeiss NVision 40) and analytical TEM equipped with EDX and EELS (Carl Zeiss Libra 200 Cs MC). Buried features and cross sections of the oxide skin layer were prepared applying the FIB lift out technique. We used a STEM/EELS based method [2] to measure the relative intensities of the Fe L_3 and L_2 white lines in core electron energy-loss spectra to distinguish the different oxides in the samples. The whiskers are hematite and the shell contains magnetite.

Acknowledgement

This work is funded by the European Union (ERDF) and the Free State of Saxony via the ESF project 100087859 ENano.

References

- [1] R.L. Higginson and G. Green: *Corr. Sci.* 53 (2011), p.1690.
- [2] L. Cavé, T. Al, D. Loomer, S. Cogswell, L. Waever: *Mircon* 37 (2006), p. 301.

Microstructure evolution and grain refinement process in an intermetallic titanium aluminide alloy with high molybdenum content

Boryana Rashkova^{1,a}, Krystina Spiradek-Hahn^{2,b}, Manfred Brabetz², Zaoli Zhang^{3,c}, Helmut Clemens¹ and Svea Mayer¹

¹ Department of Physical Metallurgy and Materials Testing, Montanuniversität Leoben, Roseggerstr. 12, 8700 Leoben, Austria

² Alloy Development Group, Montanuniversität Leoben, c/o Forschungszentrum Seibersdorf, 2444 Seibersdorf, Austria

³ Erich Schmid Institute of Materials Science, Austrian Academy of Sciences, Jahnstr. 12, 8700 Leoben, Austria

^aboryana.rashkova@unileoben.ac.at, ^bkrystina.spiradek-hahn@unileoben.ac.at, ^czaoli.zhang@oeaw.ac.at

Introduction

Intermetallic TiAl alloys are considered for high-temperature applications in automotive and aerospace industries due to their potential of significant component weight saving [1]. At ambient temperatures these alloys consist of γ -TiAl (L1₀ structure), α_2 -Ti₃Al (DO₁₉) and β_0 -TiAl (B2). At certain temperatures, however, α_2 disorders to α -Ti(Al) (A3 structure) and β_0 disorders to β -Ti(Al) (A2). Only the γ -phase keeps its ordered state until dissolution. In order to improve the processing characteristics during hot working further alloy and process development is required. While conventional TiAl alloys are stabilized in the ($\alpha_2 + \gamma$) phase field region, novel alloying concepts have been developed to design so-called β/γ - alloys [2]. These alloys are characterized by a high content of Mo as a strong β -stabilizer [3]. The characterization of the constituent phases and their transition temperatures was the subject of previous studies [2,4-6]. In the present work, the influence of high Mo content on the microstructure evolution and phase transformations has been examined.

Experimental

The actual chemical composition of the model alloy as determined by X-ray fluorescence spectroscopy is Ti-43.94Al-6.78Mo-0.09B (in at.%). The small amount of B is added to refine the microstructure during solidification by the formation of borides. The model alloy was cast by GfE Metalle and Materialien GmbH, Nuremberg, Germany. In order to eliminate casting defects and to provide nearly equilibrium conditions, the material was hot-isostatically pressed (HIP) at 1200°C for 240 min at a pressure of 200 MPa. Afterwards, the alloy was cooled slowly to room temperature. During the heat treatment, the sample was homogenized in the single β -phase field region at 1450°C for 30 min and then cooled to room temperature by water quenching. The next step of the heat treatment included isothermal heating at 1000°C for 168 hours followed by water quenching. The microstructure was studied by TEM using a Philips CM 12 microscope operating at 120kV equipped with an EDAX analytical system as well as by high resolution TEM (HRTEM) using a Philips CM 20 STEM and Tecnai F20 operating at 200kV. Samples were prepared by mechanical thinning followed by twin-jet electro polishing.

Results

TEM studies of the above-mentioned model alloy confirm the prior quantitative SEM analyses, FIB/SEM tomography with 3D image analysis and high-energy X-ray diffraction results from literature [2,4-6], designing so-called β/γ -alloys. Figure 1a shows a BF TEM micrograph of the as-HIPed Ti-44Al-7Mo alloy condition, where only two phases are present, namely γ - and β_0 -TiAl. This

result is also in agreement with neutron diffraction data [5] and revealed that $\alpha_2\text{-Ti}_3\text{Al}$ is completely suppressed at room temperature. Furthermore, the TEM BF micrograph (Fig. 1b) of the long-term annealed sample clearly show that a subsequent annealing at 1000°C for 168 hours leads to a strong grain refining effect, where the microstructure again consists of γ - and β_0 -phase.

HRTEM image recorded along the [111] direction of the β -matrix after homogenization treatment at 1450°C for 30 min (Figure 2a) and corresponding FFT analysis indicates an initial formation of the γ -phase precipitation, i.e. a first stage of γ -phase. Furthermore, geometrical phase analysis (GPA) was used for determining displacement field and lattice distortions around the initially-formed γ -precipitate, which reveals a relative different lattice distortion region in the β_0 -matrix (Figure 2b). According to the previous analysis, it is concluded that the γ -phase transformation cannot be completely suppressed by water quenching in order to have a single β -phase region.

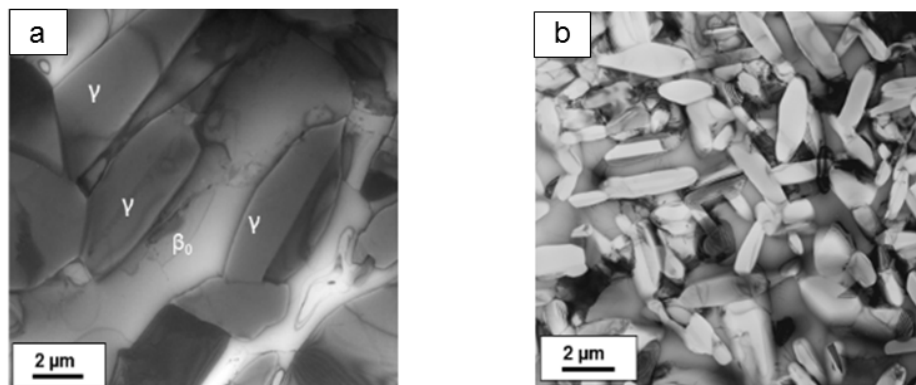


Fig. 1. BF TEM micrographs of the model alloy a) in as-HIPed condition and b) after β -homogenization and additional long-term heat treatment at 1000°C for 168 hours

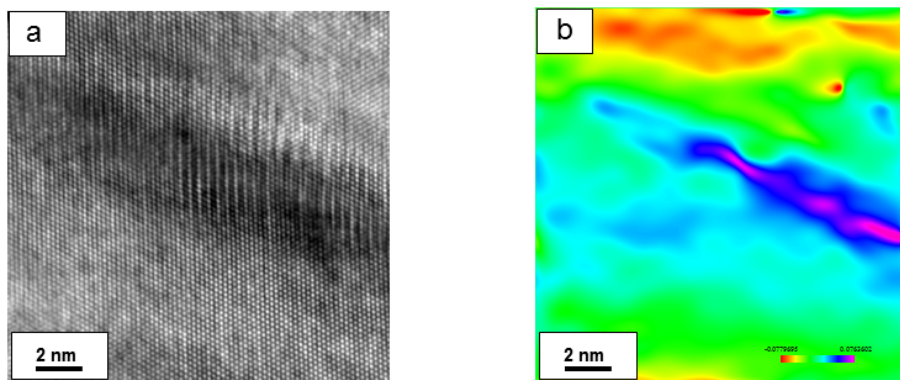


Fig. 2. Microstructure of the alloy after β -homogenization treatment at 1450°C for 30 min a) Wiener filtered HRTEM image showing the lattice strain field of the precipitation of the γ -phase in the β -matrix and b) GPA strain map, ϵ_{yy}

References

- [1] H. Clemens, S. Mayer: *Adv. Eng. Mater.* 15 (2013), p. 191.
- [2] T. Schmoelzer *et al.*: *Adv. Eng. Mater.* 13 (2011), p. 306.
- [3] H. Clemens *et al.*: *Adv. Eng. Mater.* 10 (2008), p. 707.
- [4] S. Mayer *et al.*: *Mater. Res. Soc. Proc.* 1295 (2011), p. 113.
- [5] S. Kabra *et al.*: *Int. J. Mat. Res. (formerly Z. Metallkd.)* 102 (2011), p. 697.
- [6] M. Engstler *et al.*: *Adv. Eng. Mater.* 15 (2013), p. 1225.

Microstructural modifications of Al-Fe based alloys due to magnesium addition and rapid solidification procedure

Anna Kula^{1,a}, Ludwik Blaz^{1,b}, Makoto Sugamata^{2,c}

¹ Faculty of Non – Ferrous Metals, AGH-University of Science and Technology, 30 - 059 Cracow

² Department of Mechanical Engineering, College of Industrial Technology, Nihon University,
1-2-1 Izumi-cho, Narashino Chiba 275 – 8575, Japan

^akula@agh.edu.pl, ^bblaz@uci.agh.edu.pl, ^csugamata@cit.nihon-u.ac.jp

Rapid Solidification (RS) is addressed to broad range of aluminum-based systems containing transition metal (TM) addition. Aluminum-TM alloys represent particularly the great research interest since in the technological practice an improved performance of structural materials at elevated temperatures is required.

The hardening mechanism of Al-TM alloys is based on the high volume fraction of finely distributed intermetallic particles, which are stable at high temperatures due to low diffusivity and limited solubility of alloying elements [1, 2]. Unfortunately, conventional casting and ingot metallurgy processes cannot guarantee effective strengthening of these alloys, since the formation of coarse primary intermetallic phases occurs [3, 4]. On the contrary, rapid solidification technique offers favorable microstructure modifications with uniform dispersion of fine intermetallic compounds crystallized under high cooling rate. This novel approach to Al-TM systems results in development of dispersion-strengthened materials with unique mechanical properties. The strengthening effect can be further enhanced by addition of magnesium to aluminum matrix. It has been already reported that the solid solution strengthening by Mg addition effectively increases mechanical properties of the materials at low and intermediate temperatures [5].

In the present work, the effect of rapid solidification on the microstructure and mechanical properties of Al-Fe based alloys have been investigated. Additionally, the solid solution strengthening by the magnesium addition into aluminum matrix was studied as well.

Rapidly solidified flakes were produced by argon gas atomizing of the molten alloy with subsequent spray deposition on the rotating water-cooled cooper roll. Using typical powder metallurgy (PM) techniques, i.e. cold pressing, vacuum degassing and hot extrusion, the RS-flakes were consolidated to the bulk PM materials. Mechanical properties of as extruded materials were examined by compression tests performed within the temperature range of 293-873K. High strength of as-extruded materials and relatively high ductility of RS-samples were observed. It was noticed that the most effective solid solution strengthening due to Mg-addition is observed at low and intermediate deformation temperatures. It was found that increasing of deformation temperature above ~570K results in negligible hardening related to Mg addition. Microstructural modifications, in particular effective refining of intermetallic compounds has been observed in RS materials.

It was considered that application of RS technique in production process of Al-Fe based alloys leads to formation of materials with unique combination of advantageous properties, which are determined by the novel features of the microstructure and solid solution hardening due to Mg.

References

- [1] J.C. Ehrström, A. Pineau: Mater. Sci. Eng. A Vol. 186 (1994), p.55.
- [2] D. Vojtech, A. Michalcova and P. Novak: Solid St. Phenom. Vol. 138 (2008), p.145.
- [3] A. Kula, L. Blaz, M. Sugamata: Mat. Sci. Forum Vol. 674 (2011), p.165.
- [4] A. Kula, L. Blaz, M. Sugamata: Solid St. Phenom. Vol. 186 (2012), p.279.
- [5] M. Sugamata, J. Kaneko, H. Fujii and M. Kubota: Mat. Sci. Forum Vol. 331-337 (2000), p.1157.

Financial support from National Science Center under grant No: 2011/01/B/ST8/03012 is kindly acknowledged.

Scanning Electron Microscopy with biased samples

Luděk Frank^a, Ivo Konvalina^b and Šárka Mikmeková^c

Institute of Scientific Instruments ASCR, v.v.i., Královopolská 147, 61264 Brno,
Czech Republic

^aludek@isibrno.cz, ^bkimiki@isibrno.cz, ^csarka@isibrno.cz

The arrangement of the scanning electron microscope with the sample biased to a high negative potential is discussed from the point of view of detection of signal electrons both in reflected and transmitted modes.

Introduction

Recent trends in methodological and instrumental developments in scanning electron microscopy (SEM) emphasize detection issues and low energies, in contrast to the previous accent on spot size (although interest remains in aberration correctors). The principle of biasing the sample to a high negative potential in order to retard the primary electrons before they land on the sample was broadly implemented several years ago and opened the way to very low energy SEM. However, the biased sample also provides significantly modified detection conditions.

Collection of signals

Traditionally, samples in the SEM have been situated in a field free space, merely with a front face bias of the secondary electron detector. Fast backscattered electrons (BSE) and, in the case of sufficiently thin samples, elastically transmitted electrons (TE) followed straight trajectories from their points of emission, for which reason the majority of them missed the detectors, particularly those emitted at larger angles from the optical axis. Open objective lenses offer smaller primary spots thanks to the penetration of their magnetic field toward the sample. Signal trajectories from a sample immersed in a magnetic field are significantly modified (Fig. 1a) but electrons backscattered at larger polar angles still return to the sample and are therefore lost for detection, while forward scattered signals are mismatched between TE detector segments. When biasing the sample to a negative potential we not only gain a tool for convenient unlimited adjustment of the landing energy of electrons [1], but also advantageously influence the signal trajectories (Fig. 1b). At a certain combination of the magnetic and electric fields, even the angular distribution of the emission is well acquired (Fig. 1c) in order to distinguish contrast mechanisms behind.

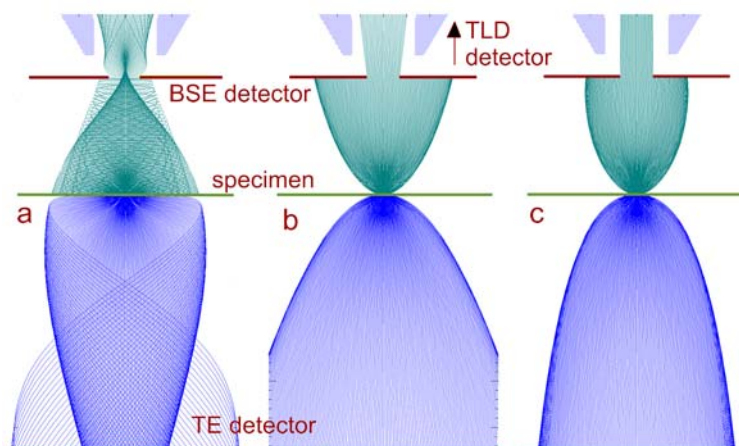


Fig. 1. Trajectories of signal electrons with the specimen immersed in the field of the open objective lens (a), with the biased sample retarding the beam 10 times (b), and with a combination of both (c)

Application examples

The simplest effect of sample biasing consists in considerably more successful collection of the BSE and TE to the respective detectors (Fig. 2). At low landing energies this is combined with acceleration of the signal species and correspondingly higher detector efficiency. If the complete BSE emission is collimated to a detector split into coaxial acquisition rings, the observed contrast progressively passes from topography combined with the edge effect through the local crystallinity of grains back to pure topographic contrast (Fig. 3). The decrease in the landing energy of electrons generally enhances the contrast magnitude owing to more intensive scattering, so that even single atomic layers or internal strain distribution can be distinguished (Fig. 4) [2].

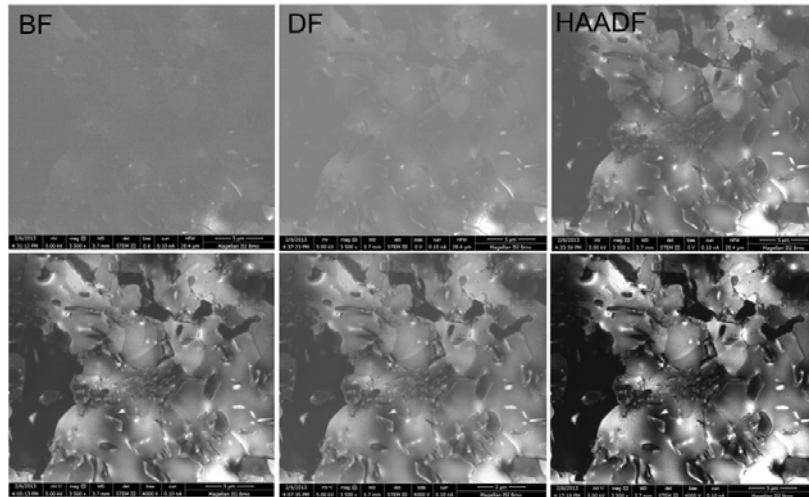


Fig. 2. Section of a complex steel (ferritic matrix with austenite and martensite phases) shown in the TE detector channels by 5 keV electrons without sample bias (top) and with 4 kV bias (bottom)

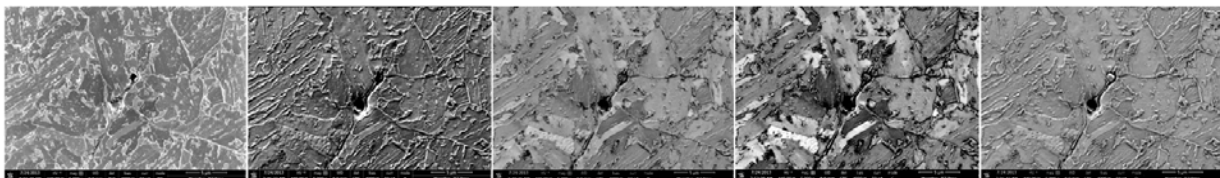


Fig. 3. Surface of a multiphase steel with bainitic-ferritic matrix, imaged at a sample bias of 4 kV with 440 eV BSE from polar angle intervals arranged between 0° and 85° (left to right)

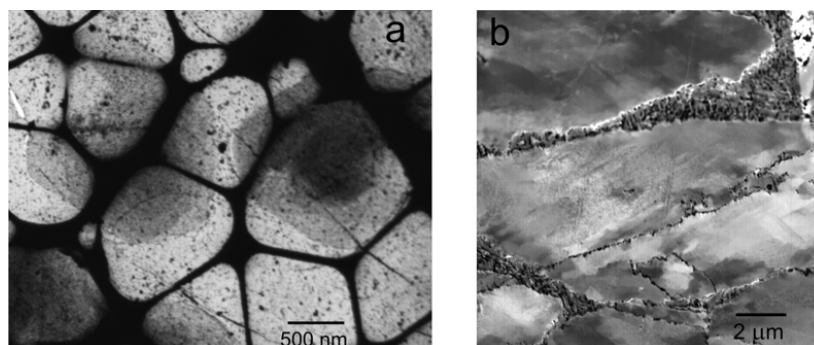


Fig. 4. (a) Multilayer graphene deposited on a carbon lacey (220 eV, BF signal); (b) heavily deformed austenitic grains in chromium steel processed by tixofforming (500 eV, total BSE)

References

- [1] I. Müllerová and L. Frank: Adv. Imaging & Electron Phys. Vol. 128 (2003), p. 309.
- [2] Project supported by the Technology Agency of the Czech Republic under no. TE01201118.

How to avoid fundamental mistakes and misinterpretations in Electron Probe X-Ray Microanalysis (EPMA)

Maria Sozańska^a, Michał Żelechower^b

Silesian University of Technology, Institute of Materials Science, Krasińskiego 8, 40-019 Katowice, Poland

^amaria.sozańska@polsl.pl, ^bmichal.zelechower@polsl.pl

The paper is the author's reaction for striking fundamental mistakes and misinterpretations of EPMA results presented by several people even in high impact factor journals. Hence, the authors would like to remind basic physical and practical principles enabling to avoid similar errors. The principles review comprises sample preparation, an accelerating voltage selection, discussion of EPMA spatial resolution, EDS/WDS X-ray spectrometers resolution effects, light elements analysis conditions, phenomena associated with X-rays attenuation at the absorption edge and standardless quantification. The readers can find in the paper some helpful suggestions and practical recommendations.

In-situ study of phase transformation in NiTi shape memory alloys using EBSD technique

Tomasz Goryczka^{1,a}, Józef Lelątko^{1,b}, Patrick Ochin^{2,c}

¹University of Silesia, Institute of Materials Science, 75 Pulk Piechoty, 40-007 Chorzow, Poland

²CNRS-ICMPE 2 rue Henri Dunant 94320, Thiais, France

^atomasz.goryczka@us.edu.pl, ^bjozef.lelatko@us.edu.pl, ^cochin@icmpe.cnrs.fr,

Introduction

NiTi alloys belong to a large family of the alloys, which reveals shape memory effect. However, this effect bases on the reversible martensitic transformation. Transformation occurs between high temperature phase – so called parent phase with structure B2 and low temperature phase – martensite. In NiTi-base alloys, transformation may go as a one-step ($B2 \leftrightarrow B19$ or $B2 \leftrightarrow B19'$) or multi-step transformation ($B2 \leftrightarrow B19 \leftrightarrow B19'$ or $B2 \leftrightarrow R \leftrightarrow B19'$). It depends on the chemical composition and/or additionally introduced thermo-mechanical treatment [1].

In general, binary NiTi alloy, without additional treatments, martensitic transformation appears as a one-step with sequence $B2 \leftrightarrow B19'$. The crystallographic lattices of the both phases are strictly correlated. During transformation one lattice is transformed into other via *habitus* plane. In consequence of lattice correlation the shape memory effect (SME) can reach up to 9% in single-crystal. Polycrystalline material shows lower value of the SME. However, it can be increase when the amount of properly oriented grains also increases. One of such methods appears to be a rapid solidification realized by twin rolls casting technique.

The present results are focused on crystallographic correlation between both lattices using diffraction of back scattered electrons (EBSP). The EBSD patterns were stored at temperatures characteristic for the martensitic transformation.

Experimental details

The NiTi alloy with nominal chemical composition of 50 at.% Ti and 50 at% Ni was produced with use of the twin rolls casting technique (TRC) [2-3]. The strip was about 30cm long, 4cm wide and 300um thick [3]. In order to study the transformation, the edges of the strip were cut off and from the central part of the strip, the samples were prepared.

Transformation behavior of the alloy was studied with use of the differential scanning calorimeter Perkin Elmer DSC-7 (DSC). Thermograms were measured in a range between -120°C to 125°C with the rate of 10 deg/min.

Observations of surface morphology as well as crystallographic orientation of grains were done with use of scanning electron microscope (SEM) JEOL JSM-6480. The microscope was equipped with electron back scatter detector (EBSD) and hot stage, which enables for temperature increasing up to 700°C.

Results

The first of all, the transformation temperature were determined from the thermograms. Obtained values are presented in Table 1. The symbols for characteristic transformation temperatures are as follows: M_s – start temperature of the martensitic transformation; M_f – finish temperature of the martensitic transformation; A_s – start temperature of the reverse martensitic transformation; A_f – finish temperature of the reverse martensitic transformation; ΔH – enthalpy of the transformation.

Table 1. Transformation temperatures and enthalpy determined from DSC measurements

| | M_s [°C] | M_f [°C] | ΔH_{B2-B19} [J/g] | A_s [°C] | A_f [°C] | $\Delta H_{B19'-B2}$ [J/g] |
|-------|------------|------------|---------------------------|------------|------------|----------------------------|
| Alloy | 21.5 | 13.6 | 28.5 | 41.3 | 50.7 | 28.9 |

In order to get alloy in martensitic state, the sample was cooled down to 10⁰C and then slowly heat up to room temperature. The EBSD patterns were collected at martensitic state (21⁰C). Basing on that pole figures were calculated (Fig. 1). Results proves the presence of the grains oriented in {001}<100> as well as {001}<011> texture components.

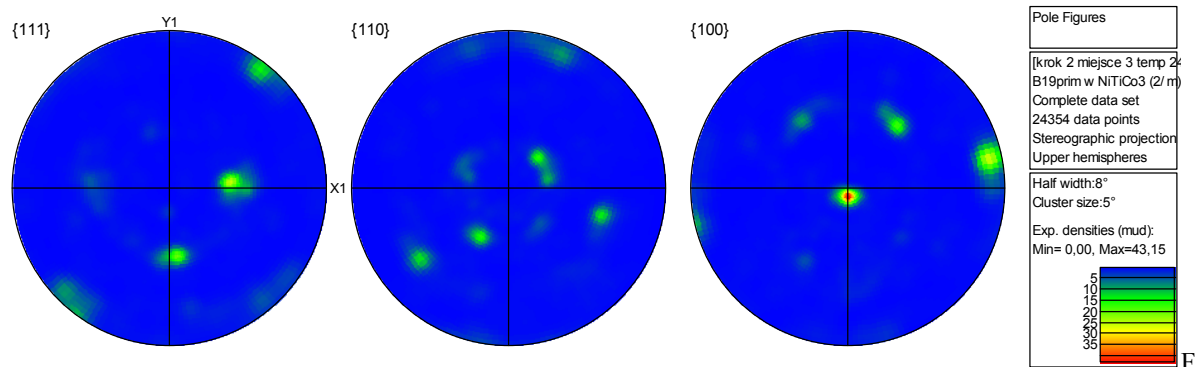


Fig. 1. Pole figure calculated from EBSD collected at 21°C

Then, temperature was rising up to and stabilized at 135°C. The procedure of the EBSD measurements and pole figure calculations was repeated (Fig. 2).

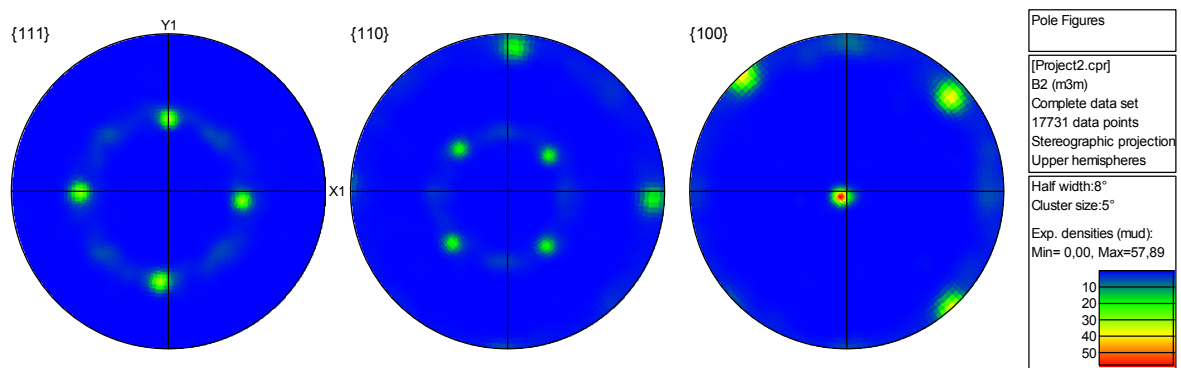


Fig. 2. Pole figure calculated from EBSD collected at 135°C (b)

Conclusions

Basing on the EBSD patterns measured at temperatures, where the parent phase (B2) as well as the monoclinic martensite (B19') exist, it can be proved that both lattices are crystallographically correlated.

References

- [1] K. Otsuka, C. M. Wayman: *Shape Memory Materials* (Cambridge University Press, UK 1998).
- [2] T. Goryczka, P. Ochin: *Sol. St. Phenom.* Vols. 203-204 (2013), p. 101.
- [3] T. Goryczka, P. Ochin: *J. Mat. Proc. Tech.* Vols. 162-163, (2005), p. 178.

Analysis of measurement conditions for high resolution transmission Kikuchi diffraction

Tomasz Tokarski

Faculty of Non-Ferrous Metals, AGH-University of Science and Technology, 30-059 Cracow, Poland
tokarski@agh.edu.pl

Measurements of orientation of crystalline materials play an important role in the novel materials characterization. For this reason, different techniques were developed to analyze special material features such as individual grain orientation, grain boundary character as well as local misorientations. Recently SEM/EBSD technique is commonly used for high resolution orientation imaging. For the conventional EBSD geometry (see Fig. 1), where samples need to be tilted to a high angle, typically 70° , the spatial physical resolution is mainly determined by electron beam interaction volume, which is known to be lower for heavy elements and lower accelerating voltages [1, 2]. It has been already recognized that the achievable spatial resolution of that configuration is ~ 50 nm, in particular for heavy elements such as Cu and accelerating voltage conditions in the range of 5 to 10kV [2]. On the other hand, decreasing of accelerating voltage results in deterioration of overall system performance due to lower camera efficiency and increased sensitivity to sample surface contamination. Problem with poor resolution is more pronounced in the case of light metals such as Al and its alloys, since higher volume interaction of electrons with sample occurs. The achievable spatial resolution of standard EBSD employed to bulk Al specimens is limited to about 50 nm to 250 nm [1]. It has been demonstrated by Keller and Geiss [3] that it is possible to obtain transmitted Kikuchi patterns at thin foils with use of SEM and conventional EBSD camera. It has been shown that lower interaction volume with thin sample is the direct source for improved spatial resolution. Due to different pattern formation in transmission mode of imaging, technique was named t-EBSD (transmission EBSD) [3] or TKD (Transmission Kikuchi Diffraction) [4]. Main difference with comparison to the conventional EBSD is application of thin foil for TKD imaging instead of bulk sample. Thin specimen, the same as in TEM imaging, is placed slightly above the EBSD camera. Incident beam penetrates material near the edge of the foil perforation, which gives simultaneously an image in the dedicated transmitted electron (TE) detector and visible Kikuchi patterns (Fig. 1).

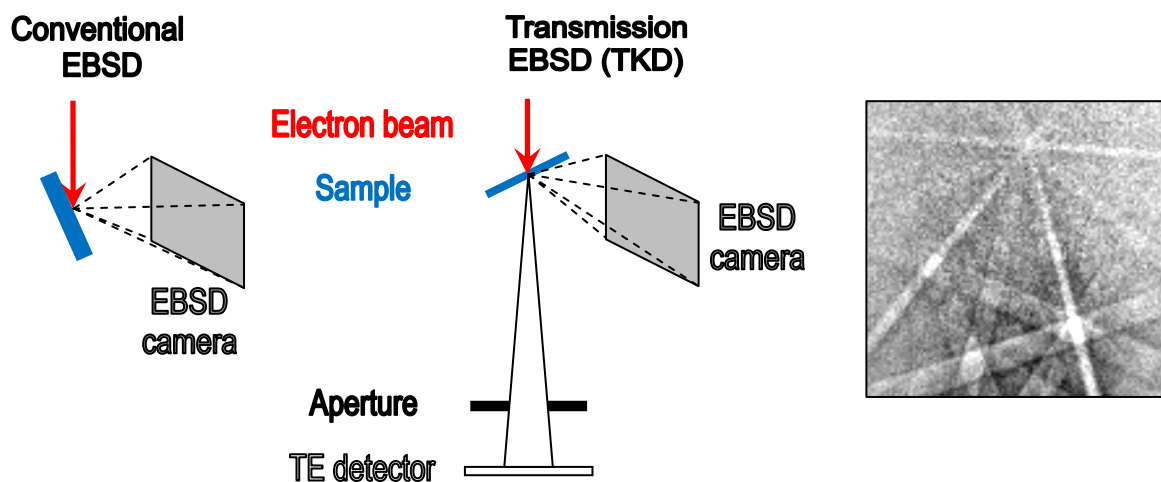


Fig. 1. Schematic of specimen setup in correspondence to incident electron beam and detectors for conventional EBSD and t-EBSD (TKD). Transmission Kikuchi diffraction is also included

Detailed geometry of the specimen setup such as working distance, specimen tilt and camera position is instrument dependent. In the present study, by application of custom made specimen holder it was possible to simultaneous acquisition of transmission image and diffraction pattern in the same sample position. This approach significantly differs from works reported in the literature [3], where to perform complete image and crystallography analysis, separate stage tilt was necessary. Transmission image observations are found to be crucial for proper selection of analysis area at high magnifications. As an example, structure and orientation imaging map for ECAP processed Al specimen acquired at x100k magnification are shown in Figure 2.

In the present work, detailed analysis of the measurement parameters and its influence on the pattern formation and orientation imaging is presented. Different combinations of sample tilt and thickness, accelerating voltage, beam current and camera integration times with respect to different materials (light and heavy elements) were tested and discussed.

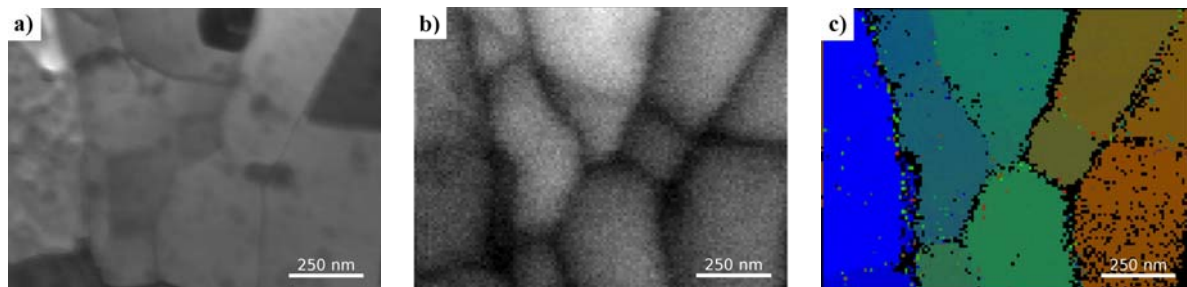


Fig. 2. Simultaneous acquisition of image and orientation mapping of the same area of aluminum sample deformed by ECAP; (a) bright field STEM image acquired by means of the TE detector, (b) pattern quality map, (c) orientation map (image cleaning procedure was not applied)

References

- [1] D.R. Steinmetz and S. Zaeferrer: *Mat. Sci. Technol.* Vol. 26 (2010), p. 640.
- [2] D. Chen, J.C. Kuo, W.T. Wu: *Ultramicroscopy* 111 (2011), p. 1488.
- [3] R.R. Keller, R.H. Geiss: *J. Microsc.* Vol. 245 (2012), p. 245.
- [4] P.W. Trimby: *Ultramicroscopy* 120 (2012), p. 16.

Acknowledgements

Financial support of Structural Funds in the Operational Programme-Innovative Economy (IE OP) financed by the European Regional Development Fund-Project No POIG.01.03.01-00-015/08 (NANOMET) is gratefully acknowledged.

Nanostructured oxides for gas sensing

Christine Leroux^{1,a}, Veronique Madigou^{1,b}, Suzanne Giorgio^{2,c},
Andre-Luis Lopez Moriyama^{3,1,d}, Carlson Pereira de Souza^{3,e}, Agnieszka Kopia^{4,f},
Łukasz Cieniek^{4,g}, Kazimierz Kowalski^{4,h}

¹Université de Toulon, CNRS, IM2NP UMR 7334, 83957 La Garde, France

²Aix-Marseille Université, CNRS, CINaM UMR 7325, 13288 Marseille, France

³Universidade Federal do Rio Grande do Norte, L. Nova, 59072-970 Natal, Brazil

⁴University of Science and Technology AGH, Faculty of Metals Engineering and Industrial Computers Science, 30-059 Cracow, al. Mickiewicza 30, Poland

^aleroux@univ-tln.fr, ^bmadigou@univ-tln.fr, ^csuzanne.giorgio@univ-amu.fr, ^dandre-luis.lopezmoriyama@im2np.fr, ^ecarlson@ufrnet.br, ^fkopia@agh.edu.pl, ^glukasz.cieniek@agh.edu.pl, ^hkazimierz.kowalski@agh.edu.pl

Introduction

Nowadays, measurement and control systems for pollutant and toxic gas emissions gain increasing importance in the frame of sustainable development. Although gas sensors devices are widely commercialized, they still suffer from drawbacks like lack of selectivity and stability. Detecting traces of gas in air requires also new sensing materials. Semiconducting metal oxides sensors have a working temperature of 350-400°C, thus have to be heated, which represent electrical power consumption. Other parameters like time of reaction, time of recovery, reproducibility should also be considered. To overcome some of these disadvantages, nanostructured materials are investigated. The detection function of the sensing material is dependant of a high surface to volume ratio, but also to the exposed crystallographic facets. Nanoparticles present high surface to volume ratio, but tend to agglomerate. One way to overcome to some extent this phenomenon is to build hierarchical and hollow oxide nanostructures [1]. The transduction function of the sensing material is more linked to the composition and structure. It should be possible to tailor the reactivity and sensitivity of the sensing materials by controlling their composition, their structure, phase, shape, size, and size distribution [2]. Hence, we were interested in studying cobalt ferrites and rare earth oxides as nanoparticles or thin films for applications in gas sensors. Ferrite materials have been tested for their gas sensing capability and catalytic activity in oxidation reactions [3-4]. The cobalt ferrite (CoFe₂O₄) attracts considerable attention due to its good chemical stability, mechanical hardness, magnetic behavior and catalytic activity [4-5]. LaFeO₃ and LaCoO₃ perovskites have also very good chemical stability and sensibility to carbon monoxide. [6-7]. Partial substitution by ions Sr²⁺ ions, lead to (SrLa)FeO₃ and (SrLa)CoO₃ with vacancies, thus better transduction properties.

Results

Octahedron-like nanoparticles of CoFe₂O₄ were synthesised using a hydrothermal technique. Several microscopy techniques like SEM, conventional TEM coupled with EDS, high resolution TEM, environmental TEM, were carried out in order to understand the mechanisms involved in the growth of the grains and their reaction under gas. The particles have an octahedral shape, with sizes around 20 nm (Fig. 1). Samples were observed under 1mbar gas pressure and were submitted to H₂ - O₂ cycles, at ambient temperature. The {111} facets became more rounded under oxygen (Fig. 2). Before that, the {100} facets extended which led to truncated octahedra. The same phenomenon was already observed in case of metallic nanoparticles [8].

Thin films of perovskite LaCoO₃ grown by Pulsed Laser Deposition are nanostructured, with lateral grains sizes around 30 nm and a significant roughness (Fig. 3).

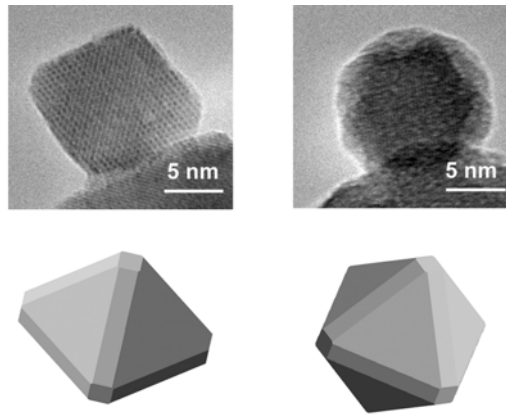


Fig. 1. The same CoFe_2O_4 nanoparticle viewed along a $[110]$ direction, and viewed along a $[111]$ direction after tilting, along with a drawing of the octahedron projection

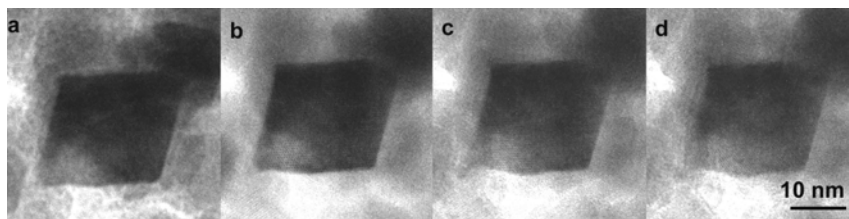


Fig. 2. Evolution of one CoFe_2O_4 nanoparticle under O_2

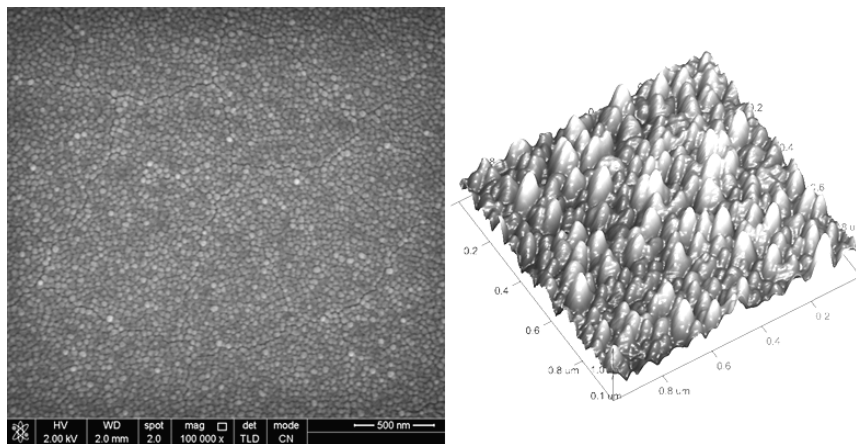


Fig. 3. SEM and AFM image of a LaCoO_3 film

References

- [1] J.-H. Lee: *Sensor. Actuat. B* 140 (2009), p. 319.
- [2] C. Wang, L. Yin, L. Zhang, D. Xiang and R. Gao: *Sensors* 10 (2010), p. 2088.
- [3] C. Xiangfeng, J. Dongli, G. Yu, Z. Chenmou: *Sensor. Actuat. B* 120 (2006), p. 177.
- [4] D.S. Mathew, R.S. Juang: *Chem. Eng. J.* 129 (2007), p. 51.
- [5] L. Ajroudi, S. Villain, V. Madigou, N. Mliki, Ch. Leroux: *J. Cryst. Growth* 312 (2010), p. 2465.
- [6] T. Sathitwitayakul, M. Kuznetsov, I.P. Parkin, R. Binions: *Mat. Lett.* 75 (2012), p. 36.
- [7] Z.G. Mu, L. Zhang, XF Li, JF Hu: *J. Rare Earths* 29 (2011), p. 374.
- [8] M. Cabié, S. Giorgio, C.R Henry, M. Rosa Axet, K Philippot, B. Chaudret: *J. Phys. Chem. C* 114 (2010), p. 2160.

Microscopy of two-dimensional nanostructures

Ana M. Sanchez^{1,a}, Sanfeng Wu², Chunming Huang², Xiandong Xu², David H. Cobden², Jonathan J.P. Peters¹ and Richard Beanland¹

¹Department of Physics, University of Warwick, Gibbet Hill Road, Coventry CV4 7AL, UK

²Department of Physics, University of Washington, Seattle, Washington 98195, USA

^aa.m.sanchez@warwick.ac.uk

Two dimensional transition-metal dichalcogenides have recently emerged due to their spectral gap in the band structure, offering an extensive range of opto-electronic applications. MoSe₂/WSe₂ bilayers has been obtained using Chemical Vapour Deposition. This heterojunction has been analysed using atomic resolution electron microscopy. A stacking with the Se atoms of the WSe₂ layer aligned with the Mo atoms of the MoSe₂ layer has been determined. Superstructure formation has been also observed due to the distortion in the metal.

Introduction

The fascinating mechanical and electrical properties of graphene, absent in bulk graphite[1, 2], have encouraged researchers to look for other two-dimensional (2D) materials. The transition-metal dichalcogenides (TMD) MX₂ have a layered structure, with just van der Waals forces between the layers. The properties of bulk TMD range from insulators (i.e. HfS₂) to metals (i.e. VSe₂)[3]. Monolayers of semiconducting TMD exhibiting a direct band gap, have promise to complement the zero bandgap energy of graphene, offering an extensive range of applications in electronics and optics.

Single layers of these inorganic layered compounds can be obtained by direct exfoliation of the bulk equivalents, both mechanical and chemical, but vapor growth techniques are a promising route to obtaining high optical and excellent electrical performance of TMD monolayers[4-6]. Progress in controlling the growth requires an exhaustive characterization of these 2D materials, and atomic-resolution measurements are critical for both understanding and control of the physical/chemical properties (e.g. bandgap engineering). Here, we examine lateral (monolayer) and vertical (bi-layer) WSe₂/MoSe₂ heterojunctions.

Methods

The samples were grown by physical vapor transport at the Nanoscale Optoelectronics Laboratory at the University of Washington.

The dichalcogenides layers were characterised using atomic resolution electronic microscopy. The imaging and EDX analysis was carried out in a Jeol 2100 LaB6 and a double-corrected ARM200F (80-200kV).

Results

Annular Dark Field imaging of the WSe₂/MoSe₂ heterojunction showed areas with different intensity indicating higher thickness and/or density. An atomic resolution ADF image across the edge of a bilayer/monolayer is shown in Fig. 1(a). The increase in intensity in from left to the right indicates that it goes from a single layer to a bilayer. EDX data confirmed that the bright layer was formed by Mo, Se and W while only the first two elements were observed in the dark area. A detailed analysis of those areas was carried out using atomic resolution imaging in order to understand the stacking of WSe₂/MoSe₂ in this heterojunction. In this bilayer the upper WSe₂ layer follows the same stacking as the lower MoSe₂ layer. The MoSe₂/WSe₂ heterojunction can have different stackings. Four different possibilities have been proposed for MoS₂/WSe₂ heterojunction[7] that can be adapted to our case. The intensity in the image can be better explained if the stacking of the bilayer is C7 type, i.e.,

the Se atoms of the WSe₂ layer are aligned with the Mo atoms of the MoSe₂ layer, and vice versa (see Fig. 1(b)).

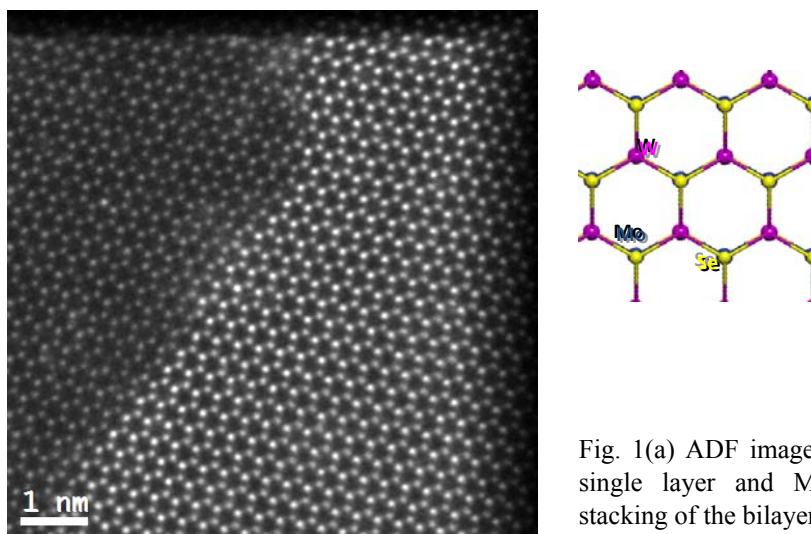


Fig. 1(a) ADF image of the interface between a MoSe₂ single layer and MoSe₂/WSe₂ bilayer. (b) C7 type stacking of the bilayer

A different stacking arrangement of the bilayer was also observed, without a simple rotational or translation orientation relationship. Interestingly, the top layer has a completely different crystal structure in this case. The bright W atoms have a zig-zag chain-like pattern similar to a WTe₂. This has been previously suggested, the presence of a distortion in the metal plane can give rise to superstructure.

Summary

Stacking of MoSe₂/WSe₂ bilayers has been analysed using aberration correction imaging. In this heterojunction Se atoms of the WSe₂ layer are aligned with the Mo atoms of the MoSe₂ layer, constituting a C7 type stacking. Distortion in the metal plane has also been observed, giving rise to superstructure.

References

- [1] A.K. Geim, K.S. Novoselov: Nat. Mater. 6 (2007), p. 183.
- [2] A.H. Castro Neto, F. Guinea, N.M.R. Peres, K.S. Novoselov, A.K. Geim: Rev. Mod. Phys. 81 (2009), p. 109.
- [3] M. Chhowalla, H.S. Shin, G. Eda, L.-J. Li, K.P. Loh, H. Zhang: Nat. Chem. 5 (2013), p. 263.
- [4] J.S. Ross, S. Wu, H. Yu, N.J. Ghimire, A.M. Jones, G. Aivazian, J. Yan, D.G. Mandrus, D. Xiao, W. Yao, X. Xu: Nat. Commun. 4 (2013), p. 1474.
- [5] S. Wu, C. Huang, G. Aivazian, J.S. Ross, D.H. Cobden, X. Xu: Acs. Nano. 7 (2013), p. 2768.
- [6] S. Najmaei, Z. Liu, W. Zhou, X. Zou, G. Shi, S. Lei, B.I. Yakobson, J.-C. Idrobo, P.M. Ajayan, J. Lou: Nat. Mater. 12 (2013), p. 754.
- [7] K. Kosmider, J. Fernandez-Rossier: Phys. Rev. B 87 (2013), p. 075451.

Transmission electron microscopy for defect engineering of high-efficiency solar cells

Wolfgang Jäger

Institute for Materials Science, Christian-Albrechts-University of Kiel, Kaiserstrasse 2, 24143 Kiel, Germany

e-mail: wolfgang.jaeger@tf.uni-kiel.de

Multi-junction solar cells based on III-V compound semiconductor layer systems are of interest for power generation in terrestrial concentration photovoltaics and in space applications. Efficiencies well above 40% have been obtained for concentrator solar cells grown by metal-organic vapor deposition on Ge substrates. Prerequisites for the high conversion efficiency of sunlight into electricity are excellent material quality and low dislocation density of the solar cell layer systems. High-resolution imaging and spectroscopic methods of transmission electron microscopy were applied successfully to supporting the development of novel solar cell concepts. Two application areas will be illustrated: analyses for the control of defect and layer strains in lattice-mismatched epitaxial layer growth on Ge [1,2], and analyses of interfaces after thin layer transfer combined with semiconductor wafer bonding for solar cells on Si substrates [3-5]. Aberration-corrected transmission electron microscopy extends the analytical capabilities as is clearly shown by the analyses of GaAs/Si interfaces in wafer-bonded solar cells [4]. Optimized solar cell concepts result in active cell regions with significantly reduced defect densities. The success of such concept developments led to a GaInP/GaAs/Ge cell with a record efficiency of 41.1 % and a GaInP/GaAs/Si solar cell with an AM1.5g efficiency of 26.1%.

It is a pleasure to acknowledge all contributions of my colleagues from the Microanalysis of Materials Group, CAU Kiel, Germany, of Dr. Frank Dimroth and his colleagues at Fraunhofer Institute for Solar Energy Systems, Freiburg, Germany, and of Dr. Lothar Houben and Professor Rafal Dunin-Borkowski from the Ernst-Ruska Center, Jülich, Germany.

References

- [1] J. Schöne, E. Spiecker, F. Dimroth, A.W. Bett, W. Jäger: Appl. Phys. Lett. 92 (2008), p. 081905.
- [2] J. Schöne, E. Spiecker, F. Dimroth, A.W. Bett, W. Jäger: J. Phys.: Conf. Ser. 471 (2013), p. 012008.
- [3] K. Derendorf, S. Essig, E. Oliva, V. Klinger, T. Roesener, S.P. Philipps, J. Benick, M. Hermle, M. Schachtner, G. Siefert, W. Jäger, F. Dimroth: J. Photovoltaics Vol 3, Issue 4 (2013), p.1423.
- [4] D. Häussler, L. Houben, S. Essig, M. Kurttepli, F. Dimroth, R.E. Duni-Borkowski, W. Jäger: Ultramicroscopy 134 (2013), p. 55.
- [5] F. Dimroth, T. Roesener, S. Essig, Ch. Weuffen, A. Wekkeli, E. Oliva, G. Siefert, K. Volz, T. Hannappel, D. Häussler, W. Jäger, A.W. Bett: J. Photovoltaics, accepted for publication (2014).

TEM and EELS investigations of crystal and electronic structure of nanomaterials

Piotr Dłużewski^{*1}, Sławomir Kret¹, Kamil Sobczak¹, Francesco Ivaldi¹, Jolanta Borysiuk¹, Tian Li¹, Dong Tang²

¹Institute of Physics Polish Academy of Sciences, al. Lotników 32/46, 02-668 Warsaw, Poland

²FEI Co, NL-5600 MD Eindhoven, The Netherlands

*dluzew@ifpan.edu.pl

Nowadays, commercially available transmission electron microscopes offer wide range of measurement possibilities like high efficient electron energy loss spectroscopy (EELS) and energy filtered transmission electron microscopy (EFTEM). That allows, among others, the measurement of surface plasmons resonance (SPR) and the determination of valence states from analysis of electron-energy loss near-edge fine structure (ELNES). The EELS data are comparable with those obtained by X-ray absorption spectroscopy (XAS) but spatial resolution of EELS can be in atomic scale.

The phenomena of electron energy loss can be exploited in both scanning and imaging working mode of TEM. In scanning mode a spectrum is recorded at a given beam position and therefore the spatial resolution is determined by beam size and specimen thickness, which indicate a volume from which the spectrum is collected. The energy resolution depends on monochromaticity of the incident electron beam and the quality of a spectrometer. The instabilities of environment, especially the low frequency magnetic field oscillations, play an important role. The problem of environmental instability in the case of monochromated electron beam will be illustrated on an example of band-gap energy measurement for semiconducting nanostructures.

An example of EELS examination leading to the determination of oxidation state of Mn in GaMnN:Mg nanostructures will be presented. The Mn valence state can be determined from measurement of intensities and energy position of L₂ and L₃ absorption edges. It will be shown that oxidation state of Mn is changed with increasing of Mg doping. Both intensity ratio and distance of energy positions of the L₂ and L₃ absorption edges indicated increasing of oxidation state of Mn from 2⁺ to 3⁺ with increasing Mg doping.

EFTEM technique is to form an image with electrons within a certain kinetic energy range. The EFTEM standard procedure for elemental mapping is based on recording three images: two pre-edge images with electron energy loss window before an absorption edge and one post-edge image with energy window after the absorption edge. The element mapping is obtained by the post-edge image after removing a background extrapolated from two pre-edge images. The intensity of the resulting image is proportional to the concentration of the element for which the absorption edge was used. Figure 1 shows the application of the EFTEM element mapping procedure in the case of AlN/GaN heterostructure.

An interesting application of EFTEM is mapping of electronic properties with a use of plasmon absorption. It is well known that plasmon excitation energy depends on the mobility and density of charge carriers. This fact allows to determined elemental composition of semiconducting structures. It will be shown for CdTe/ZnTe axial nanowires.

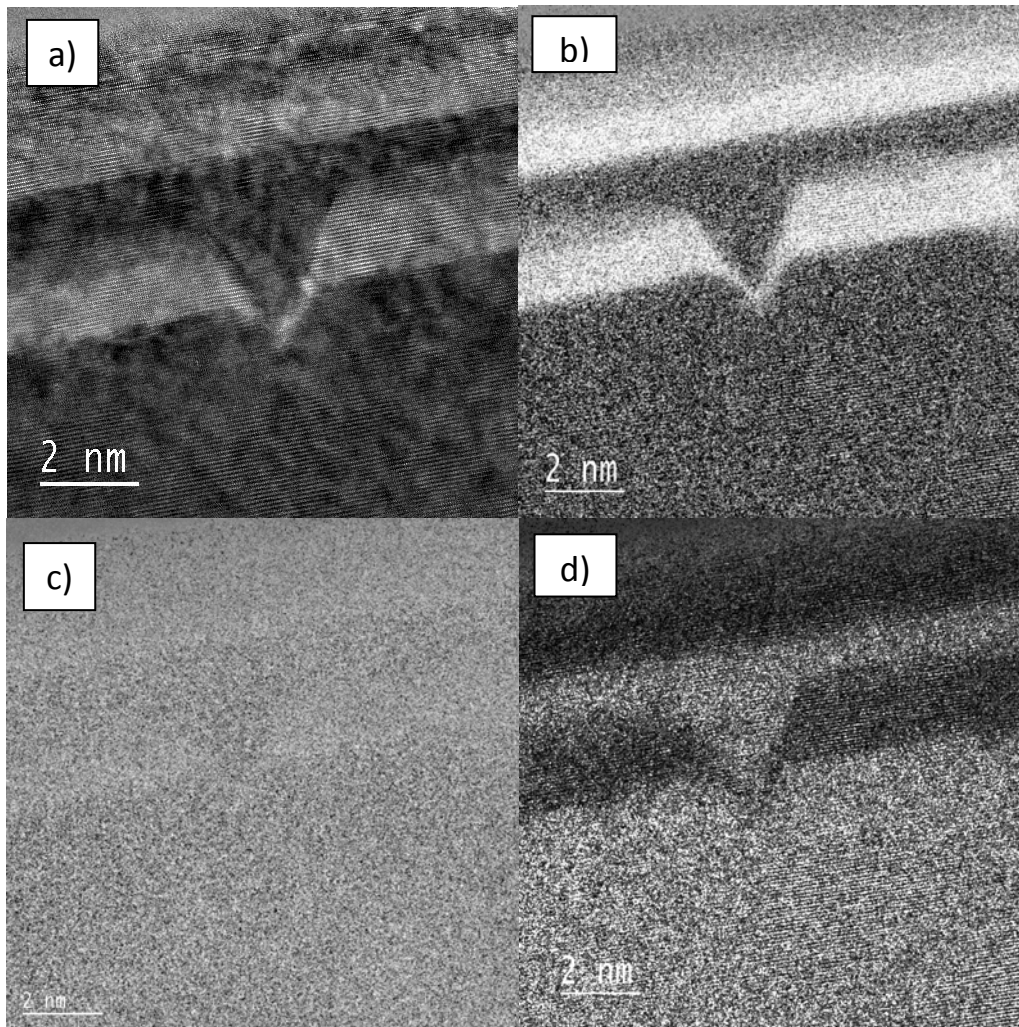


Fig. 1. High-resolution image of AlN/GaN heterostructure a) and results of EFTEM element mapping procedure for Al b), N c), and Ga d) (bright contrast corresponded to higher element concentration)

Another example is a determination of indium concentration x in $\text{In}_x\text{Al}_{1-x}\text{N}$ ternary system from shift of plasmon peak position. Both theoretical and experimental studies have proved the linear relation between shift of plasmon peak energy in respect to atomic concentration x of indium and therefore the quantitative value of x can be easily determined from EELS measurement.

Acknowledge

This research was co-financed by the European Regional Development Fund within the Innovative Economy Operational Programme 2007-2013 “Analytical high resolution transmission electron microscope for nanoscience, nanotechnology and spintronics” No POIG.02.01-00-14-032/08 and National Science Centre (Poland) 2013-2015 No. DEC -2012/05/D/ST3/03161

Structural investigations of SPD-driven phase transformations

**Boris B. Straumal^{1,2}, Askarr R. Kilmametov², Andrela A. Mazilkin¹,
Anna Korneva³, Olga A. Kogtenkova¹, Brigitte Baretzky², Paweł Zięba³**

¹Institute of Solid State Physics, Russian Academy of Sciences, Ac. Ossipyan str. 2, 142432 Chernogolovka, Russia

²Karlsruher Institut für Technologie (KIT), Institut für Nanotechnologie, Hermann-von-Helmholtz-Platz 1, 76344 Eggenstein-Leopoldshafen, Germany

³Institute of Metallurgy and Materials Science, Polish Academy of Sciences, Reymonta St. 25, 30-059 Cracow, Poland

Electron microscopy is the important tool permitting to investigate the phase transformations in the materials. Severe plastic deformation (SPD) induces various phase transformations in the materials like formation or decomposition of a supersaturated solid solution, dissolution of phases, disordering of ordered phases, amorphization of crystalline phases, synthesis of the low-temperature, high-temperature or high-pressure allotropic modifications, and nanocrystallization in the amorphous matrix. Therefore, SPD represents a novel instrument in the hands of materials scientists allowing them to control and to tailor the microstructure and properties of functional and structural materials. SPD is complimentary to the usual methods like heating, quenching, conventional deformation (like rolling or forging), ageing, annealing etc.

Using TEM and HREM we characterized the phases before and after SPD and analyzed the possible structural mechanisms of the SPD-driven phase transformations. The fine instrument for such studies is the investigation of formation and decomposition of solid solutions in the Cu-based binary alloys with various second components (Co, Ag, In, Hf, Cr, Sn, Al). They have different mixing enthalpy with copper. TEM and HREM permitted us to follow the details of the formation of precipitates of a second phase during the decomposition of a supersaturated solid solution, on the one hand, or the destruction of coarse precipitates and their partial dissolution in the undersaturated Cu-based solid solution, on the other hand. We observed in such a way, that the final state after SPD does not depend on the starting state. The composition of Cu-matrix in this *equifinal* state is equal to that which can be reached in *equilibrium* after long annealing at a certain effective temperature T_{eff} . The T_{eff} (called effective temperature) is different in different Cu-based alloys.

ABSTRACTS
poster presentations

3D reconstruction and characterization of carbides in Ni based high carbon alloy in a FIB/SEM system

Piotr Bala^{1,a}, Katja Tsyulin^{2,b}, Heiner Jaksch²

¹AGH University of Science and Technology, Faculty of Metals Engineering and Industrial Computer Science, Av. A. Mickiewicza 30, 30-059 Krakow, Poland

²Carl-Zeiss, Carl-Zeiss-Street 56, 73447 Oberkochen, Germany

^apbala@agh.edu.pl, ^bkatja.tsyulin@zeiss.com

Introduction

In the present work results of investigations of high carbon alloy from the Ni-Ta-Al-Cr system are presented. The alloy has been designed to have a good tribological properties at elevated temperatures. Despite availability of numerous hot work materials there is still a growing need for new alloys showing unique properties, which could be used under heavy duty conditions, i.e. at high temperatures, in a chemically aggressive environment and under wear conditions. The good tribological properties should ensure heterogeneous microstructure consisting of primary carbides surrounding dendrites. The 3D morphology and distribution of primary carbides and determine location and identification the type of secondary carbides after heat treatment were the purpose of the presented paper.

Experimental procedure

The test melt of a mass of approximately 1 kg was made in a vacuum furnace, and cast into a ceramic mould. Samples were cut from the casting foot. The investigation were made on samples in as-cast condition and after heat treatment. Heat treatment consisted of solution heat treatment (1100°C, 1h, water cooling) and ageing at 850°C for four hour. The microstructures of the samples were investigated by use of the scanning electron microscope FIB Zeiss AURIGA CrossBeam. With the sequence of cross-section SE images obtained from the SEM, a 3D reconstruction has been achieved after proper alignment and image processing, from which both qualitative and quantitative analysis can be performed. Based on 1 000 photos has been reconstructed the volume of material of 28x22x22 µm.

Material for investigations

The chemical composition of the new Ni-based alloy (Table 1) was designed in the Laboratory of Phase Transformations, Department of Physical and Powder Metallurgy, AGH University of Science and Technology. Its chemical composition was tailored to obtain the matrix strengthening by precipitation of the γ' phase and minimum 30 vol.% of primary carbides. The presence of a carbide eutectic is crucial. Carbides should remain stable in the microstructure regardless of heat treatment conditions in order to improve the wear resistance. It was decided to use Ni matrix due to the lack of allotropic transformations, which could destabilize the microstructure and properties during the high-temperature exploitation.

Table 1. The chemical composition (wt. %) of the investigated alloy

| C | Cr | Ta | Al | Zr | Ni |
|-------|------|-----|-----|-----|---------|
| 0.834 | 19.4 | 6.1 | 2.8 | 0.2 | balance |

Results

A characteristic, coarse-grained dendritic microstructure occurs in the investigated alloy in the as-cast condition. Primary dendrites with secondary arms were observed. Tantalum carbides of MC type

and chromium carbides of M_7C_3 type are distributed in interdendritic spaces (Fig. 1a,b). Inner dendrites precipitations of a γ phase occurs (volume fraction about 68%). [1]

After heat treatment (Fig. 1c,d) the volume fraction of primary carbides has not changed, but appearance of tantalum and chromium secondary carbides was observed. The secondary chromium carbides of M_7C_3 type precipitate near primary tantalum carbides, but precipitation of secondary tantalum carbide of MC type occur near the primary chromium carbides. Such microstructure is a result of crystallization conditions. During crystallizations both tantalum and chromium atoms were push out from growth dendrites.

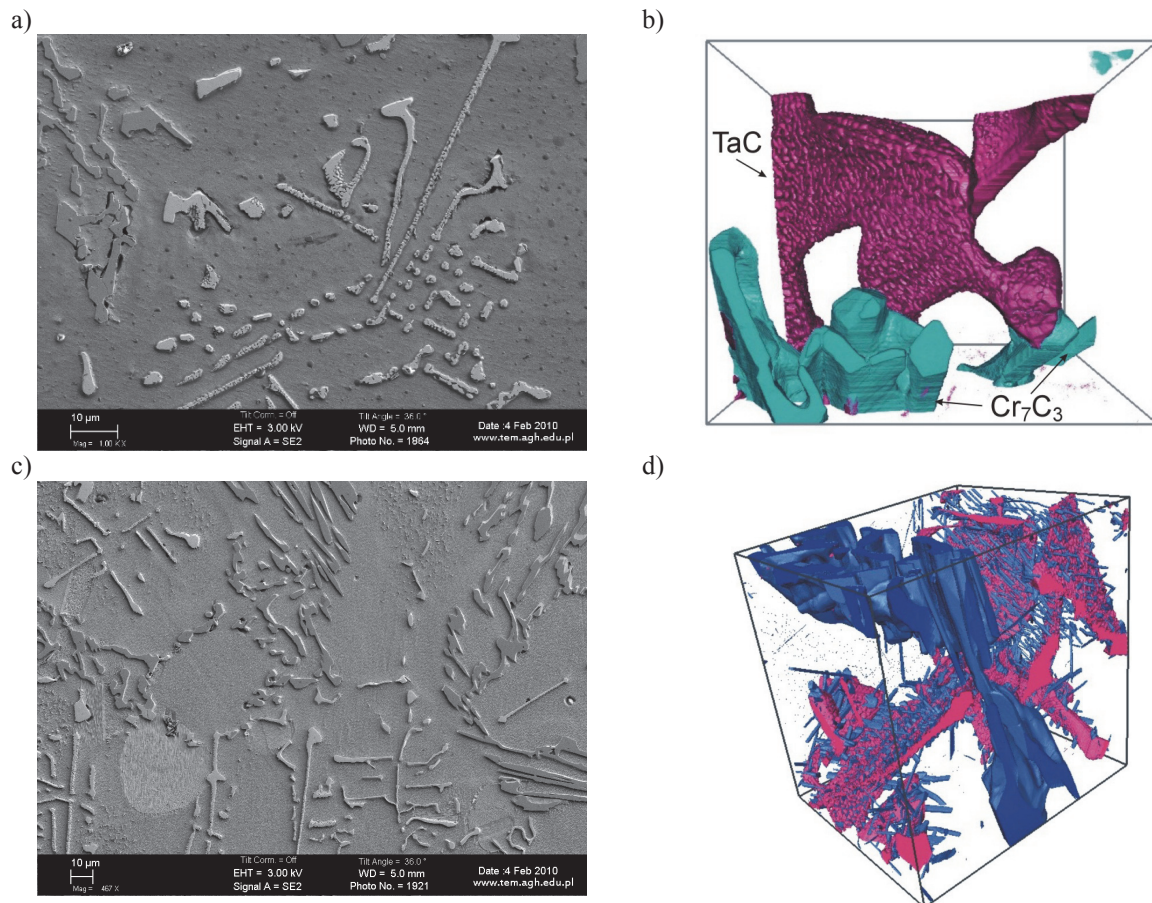


Fig. 1. a) Microstructure of investigated alloy in as-cast state, b) primary carbides 3D reconstruction in as-cast state, c) microstructure of investigated alloy after heat treatment, d) primary and secondary carbides 3D reconstruction after heat treatment

Summary

Primary carbides play an important role in the investigated alloy designed to have a good tribological properties at elevated temperatures. The 3D morphology and distribution of such carbides has been elucidated via a slice & view procedure in a FIB/SEM system. Obtained results show that formed microstructure model consisting of primary carbides surrounding dendrites has been achieved. In addition, it was possible to determine location and define the type of secondary carbides after heat treatment.

Acknowledgements

The authors would like to thank MSc Adam Gruszczyński from AGH University of Science and Technology, Krakow for the valuable help in this research.

References

- [1] P. Bala: Arch. Metall. Mater. Vol. 55 (2010), p. 1053.

The influence of addition of CNTs, nano-SiO₂ and POSS on the structure of polyurethane foams

Piotr Bazarnik^{a,1}, Ewelina Ciecierska¹, Magda Jurczyk-Kowalska¹,
Małgorzata Lewandowska¹, Maciej Kowalski², Sławomir Krauze²,
Andrzej Czulak³, Werner Hufenbach³

¹Warsaw University of Technology, Faculty of Materials Science and Engineering, Woloska 141, 02-507 Warsaw, Poland

²Transport Vehicles Upholstery Manufacturer TAPS - Maciej Kowalski, Solec 3/5, 94-247 Łódź, Poland

³Technische Universität Dresden, The Institute of Lightweight Engineering and Polymer Technology

^abazarnik123@gmail.com

Electron microscopy is a powerful tool to understand and control the properties of nanomaterials. In this study, it was used to investigate the influence of various nano and micro-additives on the structure of polyurethane (PU) rigid foams. PU rigid foam structures are the most effective materials with the best insulation value per unit thickness and thermal energy storage. Its flame redundancy and mechanical properties are often increased by the addition of different fillers. Three types of composite fillers were used: high purity (95%) multi-wall carbon nano-tubes (CNTs), nano-silica and polyhedral oligomeric silsesquioxane (POSS). All three fillers were examined by using scanning and transmission electron microscopy (Fig. 1).

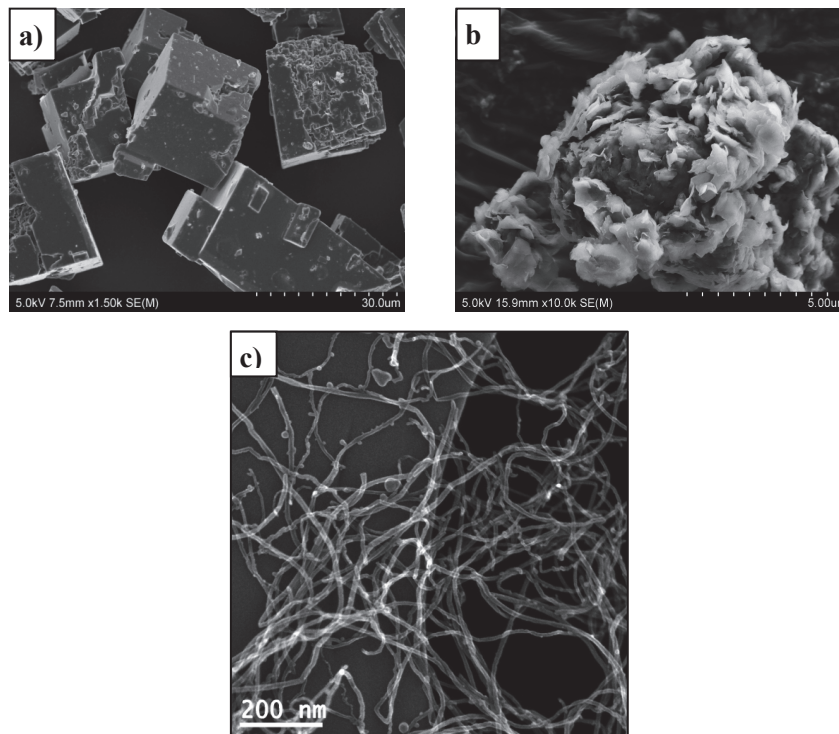


Fig. 1. Secondary electron images of fillers : a) POSS, b) nano-silica agglomerates, c) CNTs

All fillers were dispersed in polyol by using three roll milling machine. Three different concentrations of fillers were examined: 0.1%, 0.05% and 0.01%. The structure of foams and dispersion of fillers was examined by using scanning electron microscopy. Studies have shown that the addition of fillers has a major impact on size and dispersion of big pores in foams matrix. At the same time in samples with CNTs one can observe an increase in the number and size of small pores. In the sample with highest concentration of CNTs there is a large density of CNTs agglomerates.

SEM and TC in studies of structure and microstructure changes in bulk amorphous materials and their impact on the soft magnetic properties

Katarzyna Błoch^{1,a}, Paweł Pietrusiewicz^{1,b}, Marcin Nabiałek^{1,c},
Karol Szlązak^{2,d}

¹Czestochowa University of Technology, Faculty of Production Engineering and Materials Technology, Institute of Physics, 19 Armii Krajowej Av., 42-200 Czestochowa, Poland

²Warszawa, Warsaw University of Technology, Department of Materials Science and Engineering, 141 Woloska Av, 02-507 Warsaw, Poland

^a23kasia1@wp.pl, ^bpietrusiewicz@wip.pcz.pl, ^cnmarcell@wp.pl, ^dkarolszlazak@wp.pl

Properties of metallic alloys depend mainly on their microstructure, which is formed at the time of their manufacture or due to a specific thermal treatment. In the past 30 years, an intense research on new functional material groups, called bulk amorphous materials and nanocrystalline materials are performed. This group should include ferromagnetic alloys with soft magnetic properties that can be designed by changing their atomic structure. Materials of this type is a better alternative to currently used so-called conventional transformer steels with crystal structure (FeSi). Therefore, it is very important to know the exact mechanism of changes in the structure of amorphous materials and know how to design a material in such a way to obtain good nanocrystalline structure with grains of the equal size. The paper presents research results obtained for samples in the form of plates with a thickness of 0.5 mm produced by injection casting. Based on the analysis of these results the changes taking place in the structure of amorphous material can be described as a result of isothermal annealing under strictly defined conditions. Such annealing results in the formation of an amorphous matrix of evenly distributed particles of nanometric dimensions. The structure and microstructure of test samples in amorphous and nanocrystalline state were analyzed through: X-ray diffractometer (XRD), scanning and transmission electron microscope (SEM and TEM) and computed tomography (CT). Impact of structural changes on the magnetic properties was examined using a vibration magnetometer (VSM). Detailed analysis of the microstructure made for the ferromagnetic amorphous and nanocrystalline state alloys in combination with the magnetic studies, enable full description of the impact of microstructure change and influence of imperfections caused by the manufacturing process on the material magnetic properties.

Microstructure evolution during annealing of 6013 aluminium alloy after complex deformation - advanced SEM studies

**Magdalena Bieda^{1,a}, Piotr Bobrowski^{1,b}, Katarzyna Berent^{1,c}, Jakub Kawalko^{1,d},
Marek Faryna^{1,e}, Francois Brisset^{2,f}, Krzysztof Sztwiertnia^{1,g}**

¹ Institute of Metallurgy and Materials Science, Polish Academy of Sciences, 25 Reymonta St., Krakow, Poland

² Institut de Chimie Moléculaire et des matériaux d'Orsay, Université Paris-Sud, Bat. 410-420, 91405 ORSAY, France

^anmbieda@imim-pan.krakow.pl, ^bbobrowski.piotrek@gmail.com, ^ckasia.berent@gmail.com,
^dkuba.kawalko@gmail.com, ^em.faryna@imim.pl, ^ffrancois.brisset@u-psud.fr, ^gk.sztwiertnia@imim.pl

Qualitative and quantitative description of microstructure of crystalline materials are crucial for characterization of many complex processes like e.g. deformation or recrystallization. In this study advanced scanning electron microscope (SEM) techniques such as in situ annealing experiments and automated three-dimensional investigation orientation microscopy, i.e. combination of Electron Backscatter Diffraction (EBSD) and Energy Dispersive Spectrometry (EDS) with Focused Ion Beam (FIB) milling, were used. These methods were chosen to investigate the aluminium alloy 6013 which after thermal treatment posses a relatively uniform bimodal distribution of stable fine ($\ll 1\mu\text{m}$) and coarse ($>1\mu\text{m}$) particles. The alloy samples were subjected to plastic deformation by complex extrusion process by use of the KoBo method (complex extrusion of the ingot on a press with reversibly rotating die) [1]. The presence of large and small particles affects the behaviour of this material during deformation and recrystallization processes [2,3]. Investigations in the regions close to particles are of special interest and, due to application of proper analytical tools, the microstructural characterization of such an alloy was possible.

At first, the EBSD maps acquired from deformed material were analysed. Microstructure was compared with another one recorded from the same material deformed by cold-rolling [4]. Then, the development of microstructure on each step of recrystallization was investigated using combined EBSD maps and in situ heating in the SEM chamber. Simultaneous heating and acquisition of EBSD maps helped to analyse changes in the material during annealing. Such experiments were needed to obtain the relationship between orientation of grains in deformed material and orientation of grains in material during and after annealing, as well as the observations grain boundaries mobility during nucleation, recrystallization and grain growth.

Due to the presence of free surface there are some differences in the annealing of bulk materials, contrary to the samples dedicated to the SEM experiments. By using 3D investigations, in-depth analysis of the samples after heating to requisite temperatures enabled to visualise the shape, distribution and dimensions of the second phase particles and orientation characteristics of the areas near the particles which are of the main interest. Their chemical composition was also analysed at each step of the 3-D sectioning.

Changes in microstructure of the investigated 6013 alloy during annealing emphasised the role of particles of both kinds and their impact on recrystallization and grain growth. The obtained results were confirmed by calorimetric studies.

References

- [1] A. Korbel, W. Bochniak, US Patent No 737, 959 (1998), European Patent No 0711210 (2000).
- [2] H. Jazaeri, F.J. Humphreys: *Acta Mater.* Vol. 11, (2004), p. 3239.
- [3] H. Jazaeri, F.J. Humphreys: *Acta Mater.* Vol. 11, (2004), p. 3251.
- [4] M. Bieda, K. Sztwiertnia, A. Korneva, T. Czeppe, R. Orlicki: *Sol. St. Phenom.* 163 (2010), p.13.

Evolution of Fe-rich compounds in a secondary Al-Si-Cu alloy: influence of cooling rate

Alberto Fabrizi^a, Giulio Timelli^b, Stefano Ferraro^c and Franco Bonollo^d

University of Padua - Department of Management and Engineering, Stradella S. Nicola, 3 - 36100 Vicenza, Italy

^afabrizi@gest.unipd.it, ^btimelli@gest.unipd.it, ^cferraro@gest.unipd.it, ^dbonollo@gest.unipd.it

The influence of cooling rate on the nucleation and growth mechanism of Fe-rich intermetallics in a secondary Al-Si-Cu alloy has been investigated by several analysis methods such as optical microscope (OM), scanning electron microscope (SEM), energy dispersive spectroscopy (EDS) and backscattered electron diffraction (EBSD). Morphological and size evolution of two Fe-rich phases, α -Al(Fe,Mn,Cr)Si and β -Al(Fe,Mn)₂Si, have been observed and characterized under different experimental conditions. Useful information on the 3-D morphology of α -Al(Fe,Mn,Cr)Si phase has been achieved by observing deep etched samples. By varying the cooling rate during solidification, α -Al(Fe,Mn,Cr)Si dodecahedron crystals, as well as Chinese-script, branched structures and dendrites form, while coarse β -Al(Fe,Mn)₂Si needles appear at lower cooling rates.

It is also revealed how the chemical composition of the α -Fe phase varies with the morphology: lower Cr and Mn levels are detected in the Chinese script structures with respect to polyhedral crystal. Elemental EDS maps of α -Fe branched structures show a preferential concentration of Cr and Mn in the center region than to the peripheral arms (Fig. 1). According to these results, the growth mechanisms of the α -Al(Fe,Mn,Cr)Si and β -Al(Fe,Mn)₂Si compounds obtained at different cooling rates have been discussed in terms of morphological evolution and elemental distribution.

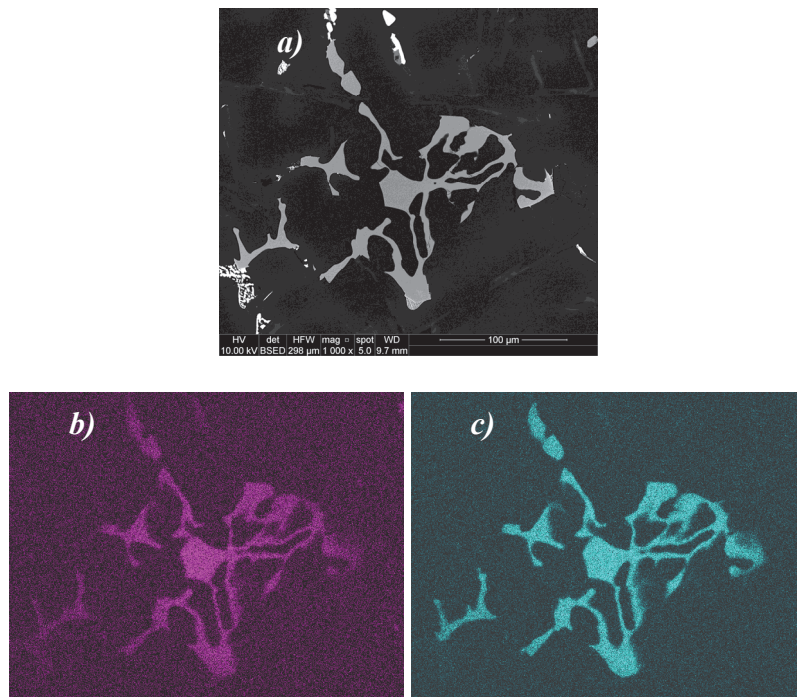


Fig. 1. a) SEM micrograph of a branched α -Fe crystal; Cr and Mn distribution maps (b and c, respectively)

Morphology of tungsten growth forms in quasicrystalline $\text{Al}_{65}\text{Cu}_{20}\text{Fe}_{14}\text{W}$ alloys

Jacek Krawczyk^{1,a}, Wojciech Gurdziel^{1,b},
Włodzimierz Bogdanowicz^{1,c} and Grzegorz Dercz^{1,d}

¹Institute of Material Science, University of Silesia, 40-007 Katowice, Bankowa 12, Poland

^ajacek.krawczyk@us.edu.pl, ^bwojciech.gurdziel@us.edu.pl,
^cwlodzimierz.bogdanowicz@us.edu.pl, ^dgrzegorz.dercz@us.edu.pl

Keywords: Al-Cu-Fe alloy, quasicrystal, growth morphology, tungsten whiskers, nano whiskers

The growth morphology and arrangement of tungsten and β -phase (Al (Fe, Cu)) in Al-Cu-Fe-W alloy was analyzed. The composition of $\text{Al}_{65}\text{Cu}_{20}\text{Fe}_{14}\text{W}$ (at.%) was used for preparation of ingot containing the icosahedral quasicrystalline phase.

The ingots were obtained in a two-stage process. At the first stage, the induction melting of elements and preliminary homogenization using mechanical mixing of melt were carried out. The second stage was realized by vertical Bridgman technique of crystallization. The X-ray phase analysis, optical and scanning electron microscopy (SEM) observations and chemical composition analysis were performed.

It was stated that the whiskers of tungsten were irregularly distributed in the volume of ingots often creating clump agglomerations. Minimal diameter of the whiskers was about 10 – 100 nm and maximal – several dozen micrometers. The whiskers of tungsten formed a clump-like frame (Fig. 1A) on which the β -phase in a form of membrane was stretched out or created a non-planar oval forms (Fig. 1B).

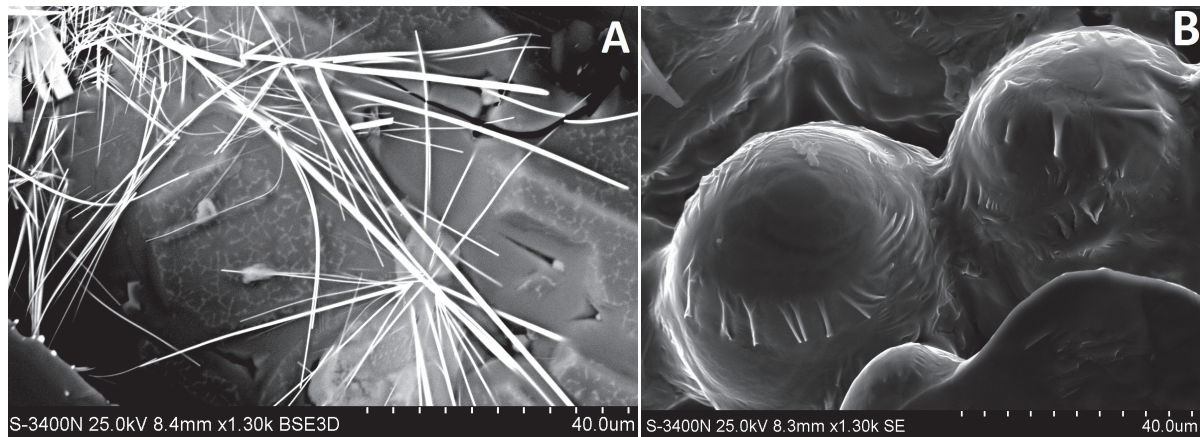


Fig. 1. Sample image of tungsten fibers (Fig.1A) and oval forms based on β -phase (Fig. 1B)

Electron microscopy characterization of friction stir welded 5083-H111 and 7075-T651 aluminum alloys

Izabela Kalemba^a, Stanisław Dymek^b and Mateusz Kopyściański^c

AGH University of Science and Technology, Krakow, Poland

^akalemba@agh.edu.pl, ^bgmdymek@cyfronet.pl, ^cmateusz.kopyscianski@gmail.com

Introduction

Friction stir welding (FSW) is a joining process that already well established in the aerospace, automotive and shipbuilding industries. The one of the most important features of this technology is the potential to join dissimilar-metal combinations that differ in melting points, crystal structure, strength, density etc. Fusion welding of dissimilar metallic alloys, even when possible, often produces large, brittle particles of intermetallic phases during solidification. This suggests that fusion welding of such metals cannot be practically used. Friction stir welding, however, is a solid-state process that exhibits distinct advantages over fusion welding due to the lack of melting and solidification of the materials that are being joined. The friction stir welded joint develops from the action of a rotating tool that is inserted into abutting workpieces and is subsequently displaced along the joining path (Fig. 1). The joint forms from the simultaneous plastic flow and mixing of the materials from each side of the interface as material are transferred from the leading edge of the tool to the trailing edge [1-3]. The primary difference between joining similar and dissimilar alloys is the discontinuity in properties across the butting surfaces, which has a large influence on the patterns of material flow during stirring. Also, an important aspect in the friction stir welding of dissimilar metals is the selection of the appropriate alloys for the advancing and the retreating sides to obtain optimum mixing and weld properties.

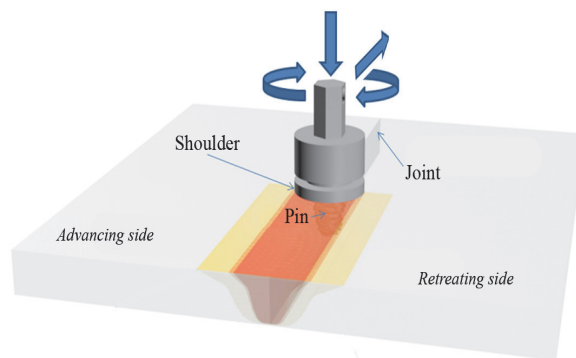


Fig. 1. Schematic illustration of FSW process

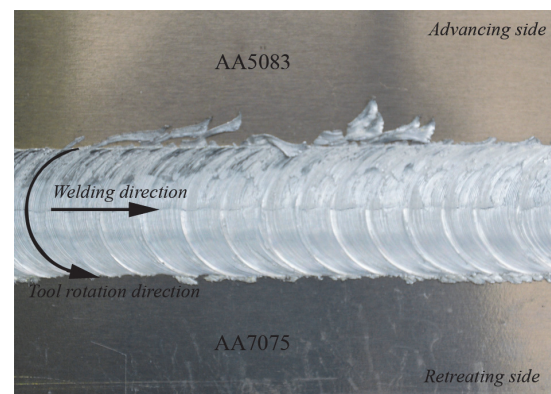


Fig. 2. Dissimilar weld appearance; top surface

The research is focused on microstructural characterization of butt welds of dissimilar aluminum alloys – work-hardenable alloy 5083 and age-hardenable alloy 7075 producing by the friction stir welding. These alloys belong to widely used aluminum alloys in aerospace and shipbuilding, whereby it is often necessary to join these materials. However, studies on FSW process of dissimilar aluminum alloys 5xxx and 7xxx series joints are not numerous. In open literature on FSW, a few papers are only available [4,5].

Methodology

The materials used in this study were aluminum alloys: 5083-H111 (Al-Mg) and 7075-T651 (Al-Zn-Mg-Cu). The alloys were friction stir welded in Welding Institute in Gliwice, Poland. The joining parameters were following: tool rotation speed – 560 RPM and welding speed – 140 mm/min. The

5083 alloy was on the advancing side of the weld while the 7075 alloy was on the retreating side (Fig. 2).

The microstructural characterization of friction stir welds was performed by scanning and transmission electron microscopy. Metallographic samples were prepared from weld cross-sections by initially grinding on sand papers, then polishing and finally etching.

Results

The SEM observation reveals a complex microstructure of the tested dissimilar weld. The microstructure of the stirred zone (Fig.3a) was characterized by bands associated with material flow. The patterns create an vortex-like structure. The creation of vortex structures in solid-state flow testifies to the complexity of material flow during FSW welding. The mutual mixing of dissimilar aluminum alloys was far from complete. Figure 3b shows the EDS maps illustrating a non-uniform distribution of the main constituent elements (aluminum, magnesium, zinc and copper) within the stirred zone.

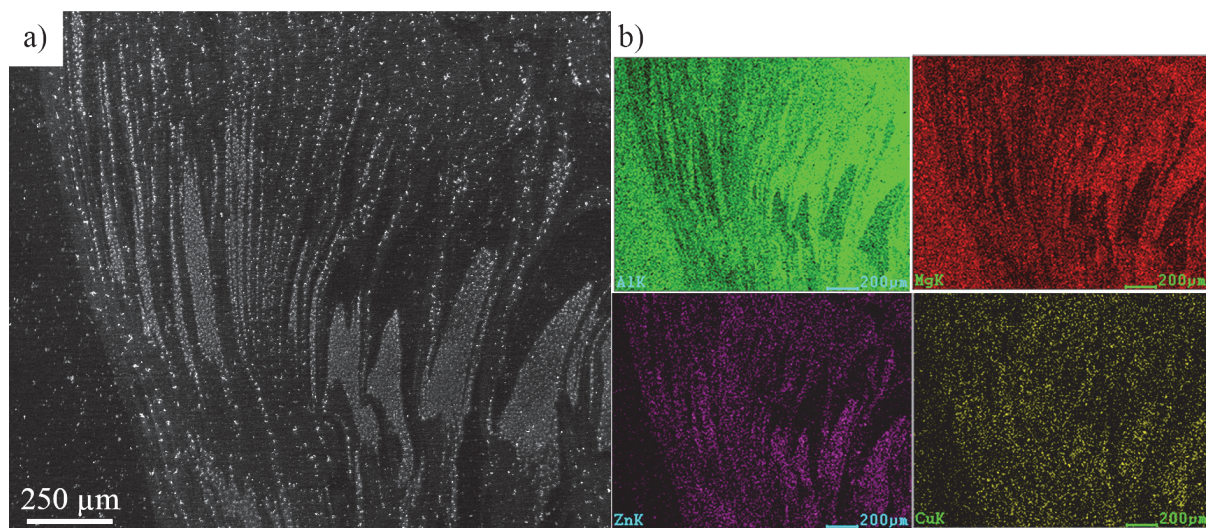


Fig. 3. a) Microstructure of the stirred zone and b) EDS map analysis of the area: distribution of aluminum, magnesium, zinc and copper

Summary

The preliminary results of the research showed that the FSW process makes it possible to produce defect-free joints between dissimilar aluminum alloys 5xxx and 7xxx series. However, the dissimilar weld microstructure is complex and reveals an vortex-like structure.

References

- [1] L.E. Murr: J. Mater. Eng. Perform. Vol. 19 (2010), p. 1071.
- [2] P.L. Threadgill, A.J. Leonard, H.R. Shercliff and P.J. Withers: Int. Mater. Rev. Vol. 54 (2009), p. 2.
- [3] R.S. Mishra, M.W. Mahoney: Friction Stir Welding and Processing (ASM International, Ohio 2007).
- [4] M.H. Shojaeefard, R.A.Behnagh, M. Akbari, M.K.B. Givi and F. Farhani: Mater. Des. Vol. 44 (2013), p. 190.
- [5] V.X. Tran, J. Pan and T. Pan: J. Mater. Proc. Technol. Vol. 209 (2009), p. 3724.

The SEM analysis of hydrogen-assisted cracking in toughened steel

Janusz Krawczyk^{1,a}, Piotr Bała^{1,b}, Tomasz Tokarski^{2,c}, Łukasz Frocisz^{1,d},
Bogdan Pawłowski^{1,e}

¹AGH University of Science and Technology, Faculty of Metals Engineering and Industrial Computer Science, A. Mickiewicza Av. 30, 30-059 Krakow, Poland

²AGH University of Science and Technology, Faculty of Non-Ferrous Metals, A. Mickiewicza Av. 30, 30-059 Krakow, Poland

^ajkrawcz@agh.edu.pl, ^bpbala@agh.edu.pl, ^ctokarski@agh.edu.pl, ^dlukfro@gmail.com, ^ebpawlow@agh.edu.pl

Introduction

Electrolytic zinc coating is one of the easiest way to prevent rust on screws due to its high anti-corrosive properties. However, during galvanic process atomic hydrogen can be absorbed into the steel microstructure which can result in hydrogen embrittlement, sometimes called internal hydrogen assisted cracking [1-3]. The higher the tensile strength of steel, the greater the risk is of this occurring. It was found [4-7] that susceptibility to hydrogen-assisted cracking in toughened steels is connected mainly with the effect of tempering on the solubility of hydrogen in steel microstructure (hydrogen trapping).

This paper analyzes the fracture behaviour of zinc coated screws made of 30MnB4 steel after proper and improper heat treatment followed by baking performed as means of dehydrogenation process.

Materials and research methodology

The material used in this study was a commercial low alloy 30MnB4 steel, widely used for screw fabrication. Quenched and tempered (tempering at 410°C) screws made of this steel was electrolytically zinc coated by Fe/Zn12c1B layer followed by baking at 200°C for 5 h. For the purpose of this work, zinc coating (and further baking) was performed for quenched but not tempered screw. Such samples were loaded to failure by torsion. Following failure, fracture surfaces were examined using scanning electron microscopy (SEM) and microstructure of samples were observed using light microscopy.

Results of investigation

Fig.1 shows the typical features of the fracture surface of quenched and tempered screw electrolytically zinc coated and baked at 200°C for 5 h. Fracture surface of not tempered screw is shown in Fig. 2.

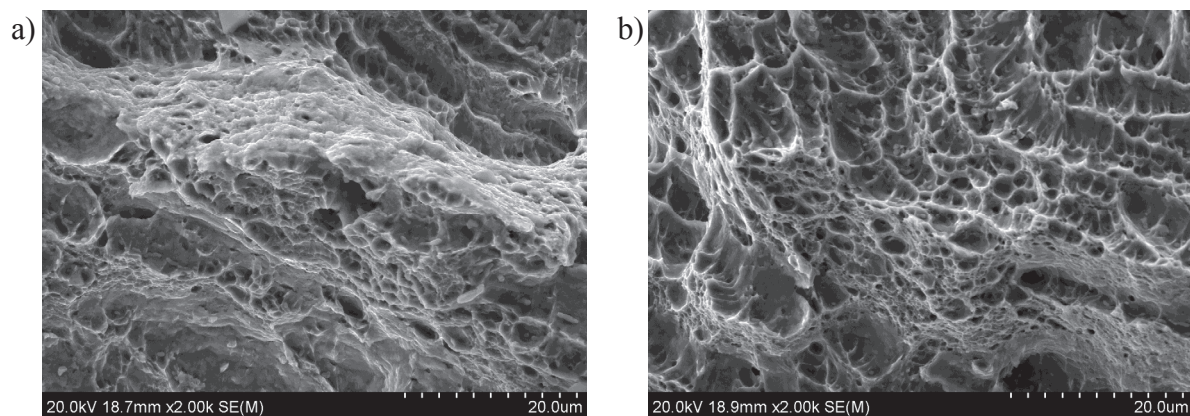


Fig. 1. SEM view of the fracture surface of properly heat treated screw, a) core, b) close to surface

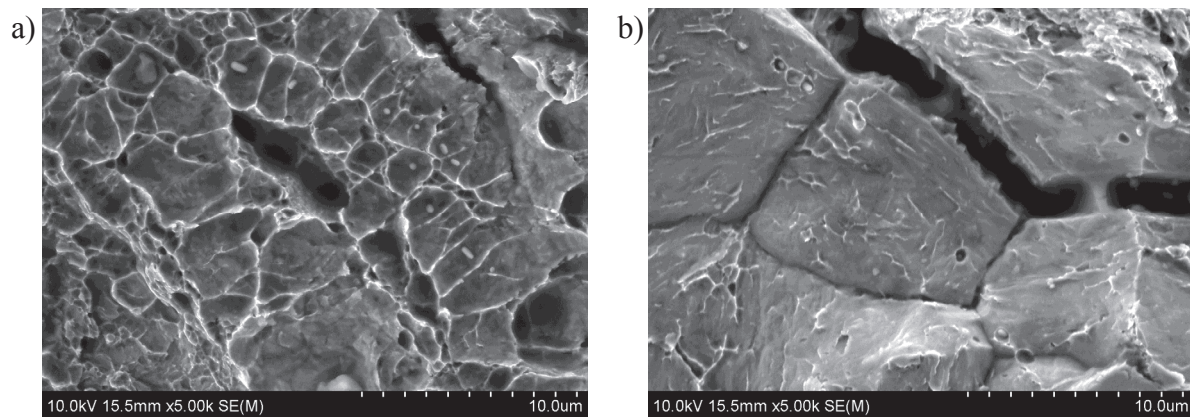


Fig. 2. SEM view of the fracture surface of improperly heat treated screw, a) core, b) close to surface

As it is shown, the whole fracture surface of tempered screw is characterized by overload microvoids (dimple fracture). Such fracture mode was observed only in core region of not tempered screw (Fig. 2a). In close to the surface region of this screw brittle, intergranular fracture mode was observed, typical for hydrogen-assisted cracking. SEM view of the carbides in the microstructure of properly and improperly heat treated screws are shown in Fig. 3

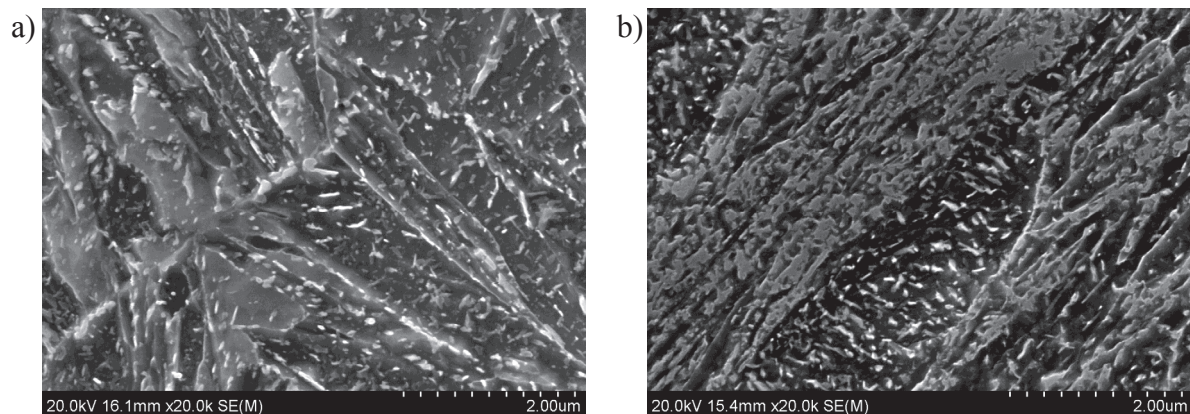


Fig. 3. SEM view of the carbides in the microstructure, a) properly heat treated, b) improperly heat treated screw

Summary

The proper heat treatment (quenching followed by tempering at 410°C) with subsequent baking decreases the hydrogen solubility and prevents brittle fracture mode.

References

- [1] R.P. Gangloff: *Critical Issues in Hydrogen Assisted Cracking of Structural Alloys*, in: Environment Induced Cracking of Metals, Sergei Shipilov, ed., Elsevier Science, Oxford, UK, (2006).
- [2] R.W. Staehle, et al. (Eds.) *Stress Corrosion Cracking and Hydrogen Embrittlement of Iron Base Alloys*, NACE, Houston, TX, (1977).
- [3] *Hydrogen in Metals. Proceedings of the 2nd International Congress*, Pergamon Press, Paris, France, 6-10 June, (1977).
- [4] B. Pawlowski: *Werkstoffe und Korrosion* Vol. 37, iss.8 (1986), p. 448.
- [5] A. Mazur, B. Pawlowski: *Corr. Sci.* Vol. 26, iss. 1 (1986) p. 7.
- [6] B. Pawlowski, A. Mazur, S. Gorczyca: *Corr. Sci.* Vol. 32, iss. 7 (1991), p. 685.
- [7] F. Sanoglu: *Mat. Sci. Eng. A* Vol. 315 (2001), p. 98.

Fracture morphology and mechanical properties of Fe-Co-B-Si-Nb bulk metallic glass after compression

Sabina Lesz^{1,a}, Anna Januszka^{1,b}, Marcin Nabiałek^{2,c}
and Ryszard Nowosielski^{1,d}

¹Institute of Engineering Materials and Biomaterials, Silesian University of Technology,
18a Konarskiego Street, 44-100 Gliwice, Poland

²Czestochowa University of Technology, Institute of Physics, Armii Krajowej Av. 19,
42-200 Czestochowa, Poland

^asabina.lesz@polsl.pl, ^banna.januszka@polsl.pl, ^cnmarcell@wp.pl ^dryszard.nowosielski@polsl.pl

Introduction

Metallic glasses (MGs) are poised to be mainstay materials for the 21st Century due to the unique physical and chemical properties, which offers a great potential for application in industry, medicine, energy systems, microelectronics, aeronautics and many other fields. The first reported scientifically obtained metallic glass (MG) was the alloy Au₇₅Si₂₅ produced at Caltech by Klement, Willens & Duwez in 1960, by extremely rapid cooling of the melted alloy [1]. In the 1960s, Chen and Turnbull developed amorphous alloys of Pd-Si-Ag, Pd-Si-Cu, and Pd-Si-Au [2]. Chen also fabricated an amorphous Pd-Cu-Si alloy with a diameter of up to 1 mm that could be considered to be a bulk metallic glass (BMG) [3]. A study of the mechanical properties of these novel materials was first reported in 1971 by Masumoto and Maddin [4]. In recent years a great expansion in the number of alloy compositions known to give bulk metallic glasses (BMGs) has occurred. The first Fe-based bulk metallic glasses (BMGs) were prepared in 1995 [5], since then, Fe-based bulk metallic glasses have been studied as a novel class of engineering materials, which have a good glass forming ability and soft magnetic properties [6,7]. For example, in 2004, Inoue et al. synthesized [(Fe_xCo_{1-x})_{0.75}B_{0.2}Si_{0.05}]₉₆Nb₄ (x = 0.1 and 0.5 at.%) BMGs exhibit good soft magnetic properties, as well as superhigh fracture strength of 3000–4000MPa and ductile strain of 0.002 [6]. Bulk metallic glasses (BMGs) possess superior mechanical properties such as high strength and great elastic strain making them ideal candidates for structural application. However, the poor ductility and brittle fracture exhibited in nearly all monolithic BMGs limit their structural application. Hence a well understanding fracture morphology and mechanical properties is importance for designing performance BMGs.

Methodology

The purpose of the paper was investigation of the mechanical properties, structure and particularly fracture morphology of the Fe₃₆Co₃₆B₁₉Si₅Nb₄ bulk metallic glasses (BMGs) after compression. The master alloy ingots with above compositions were prepared from the pure Fe, Co, Nb metals and non-metallic elements: Si, B, in an argon atmosphere. The investigated material was cast in form of rods with diameter of 2, 3 and 4 mm. According to Johnson, cooling rate achieved for an as-cast diameter R can be estimated as: $T = 10/R^2$ (cm) [8]. Thus, the achieved cooling rate in the rod-shaped samples with 2, 3 and 4 mm in diameter could be estimated to be 1000, ~444 and 250 K/s. Obviously the smaller the as-cast diameter, the larger the cooling rate is achieved. The rods were prepared by the pressure die casting. The following experimental techniques were used: X-ray diffraction (XRD) phase analysis method to test the structure, scanning electron microscopy (SEM) to investigation of fracture morphologies obtained after decohesion process in compression test. The measurement of mechanical properties, like: Young modulus - E , compression strength - σ_c , elastic strain - ϵ were made in compression test. Compression strength tests for bulk metallic glasses were performed on testing machine ZWICK 100 at room temperature. For each group, five specimens were tested, and averaged data were used.

Results

It was found from the obtained results of structural studies performed by X-ray diffraction that diffraction pattern of surface rods with 2, 3 and 4 mm in diameter of $\text{Fe}_{36}\text{Co}_{36}\text{B}_{19}\text{Si}_5\text{Nb}_4$ alloy consists of a broad-angle peak, which is typical for the amorphous phase. The mechanical properties of samples, including Young's modulus - E , compression strength - σ_c and elastic strain - ε , are listed in Table 1. With the increase of rod's diameter the Young's modulus and strength decrease, suggesting a soft trend. These changes are probably connected with changes structure relaxation. In sample in form of rod with 4mm, where cooling rate of rods during casting is lower, the structure is much relaxation. This indicates that cooling rate plays a significant role in the plasticity of metallic glasses. Fracture morphology of rods have been different on the cross section. Smooth fracture morphology and smooth fracture with areas of vein pattern morphology have been observed.

Table 1. Compressive mechanical properties of samples used in compression test at room temperature

| Rod-shaped samples | Young's modulus, E [GPa] | Compression strength, σ_c [MPa] | Elastic strain, ε [%] |
|-----------------------|----------------------------|--|-----------------------------------|
| with 2 mm in diameter | 78 | 1793 | 1.8 |
| with 3 mm in diameter | 38 | 1117 | 2.6 |
| with 4 mm in diameter | 21 | 789 | 2.9 |

Conclusions

The results of these investigations suggest that the significant factor to control the structure, mechanical properties and fracture morphology of the $\text{Fe}_{36}\text{Co}_{36}\text{B}_{19}\text{Si}_5\text{Nb}_4$ BMGs is cooling rate. Thus these factor has an instructional significance for the optimizing design of the performance materials.

References

- [1] W. Klement, R. H. Willens, P. Duwez: Nature 187 (1960), p. 869.
- [2] H.S. Chen, D. Turnbull: Acta Metall. 17 (1969), p.1021.
- [3] H.S. Chen: Acta Metall. 22 (1974), p.1505.
- [4] T.Masumoto, R.Maddin: Acta Metall. 19 (1971), p. 725.
- [5] A. Inoue: Mater. Trans. JIM Vol. 36, 7 (1995), p. 866.
- [6] B. Shen, A. Inoue: App. Phys. Lett. 85, 21 (2004), p. 4911.
- [7] S. Lesz, R. Babilas, M. Nabialek, M. Szota, M. Dospiał, R. Nowosielski: J. Alloys Compd. 509S (2011), p. S197.
- [8] X. H. Lin, W. L. Johnson: J. Appl. Phys. 78 (1995), p. 6514.

Fractography of the dual phase steels

Krzysztof Miernik

Institute of Materials Engineering, Cracow University of Technology,
37, Jana Pawla II Av., 31-866 Cracow, Poland
kmiernik@mech.pk.edu.pl

Incomplete quenching from the ferrite and austenite ($\alpha + \gamma$) range is the most popular method to produce a mechanical low-carbon steel [1]. Traditionally, low-carbon steels with a two-phase structure of ferrite and martensite are defined in the literature as Dual Phase (DP) steels. These materials in the form of thin sheets with thickness $0.5 \text{ mm} < g < 2 \text{ mm}$ are currently widely used in the automotive industry for example, as a body elements [2]. Little information is found on the mechanical properties and fracture mechanisms of this type of material when sheet thickness is above 2 mm. The presented results concern the mechanical properties of a low carbon structural steel with the chemical composition given in Table 1, subjected to hardening from the two-phase range in order to obtain a ferritic-martensitic structure. The topographic studies were performed on samples after impact and tensile tests using a scanning electron microscope (SEM, Jeol JSM5510LV).

Table 1. Chemical composition of dual phase steel

| Element | C | Mn | Si | Mo | S | P | Cr | Ni | Cu | Al | Nb | Ti |
|-----------------|------|------|------|------|-------|-------|------|------|------|------|-------|--------|
| Content, wt.[%] | 0.15 | 1.03 | 0.31 | 0.23 | 0.013 | 0.025 | 0.85 | 0.12 | 0.21 | 0.02 | 0.004 | 0.0042 |

Different material properties were obtained after the heat treatment shown in Fig. 1. The tensile strength of the tested steels changed from about 800 to more than 1250 MPa with increasing quenching temperature. The increase of the heat treatment temperature also affected the impact strength improvement from 14 to 54 J/cm².

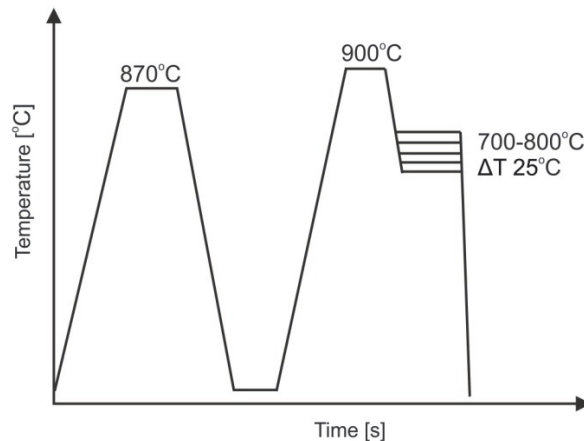


Fig. 1. The scheme of the heat treatment

The SEM fractography results for the samples after the mechanical tests are shown in Fig. 2.

The analyses of the fracture after the impact tests revealed, that a brittle decohesion of the high carbon martensite grains occurred in the ferritic matrix at low temperature intercritical hardening.

The dynamics of brittle crack development in the martensite caused also the spread of a brittle cracking inside the minimally deformed ferrite grains (Fig. 2a). With increasing quenching temperature, the decrease of the martensite hardness and increase of its specific volume in the microstructure appeared and resulted in the gradual change in micromechanisms of decohesion from

brittle to ductile fracture (Fig. 2b). Different decohesion mechanisms depending on hardening temperature of the fracture after tensile tests were observed.

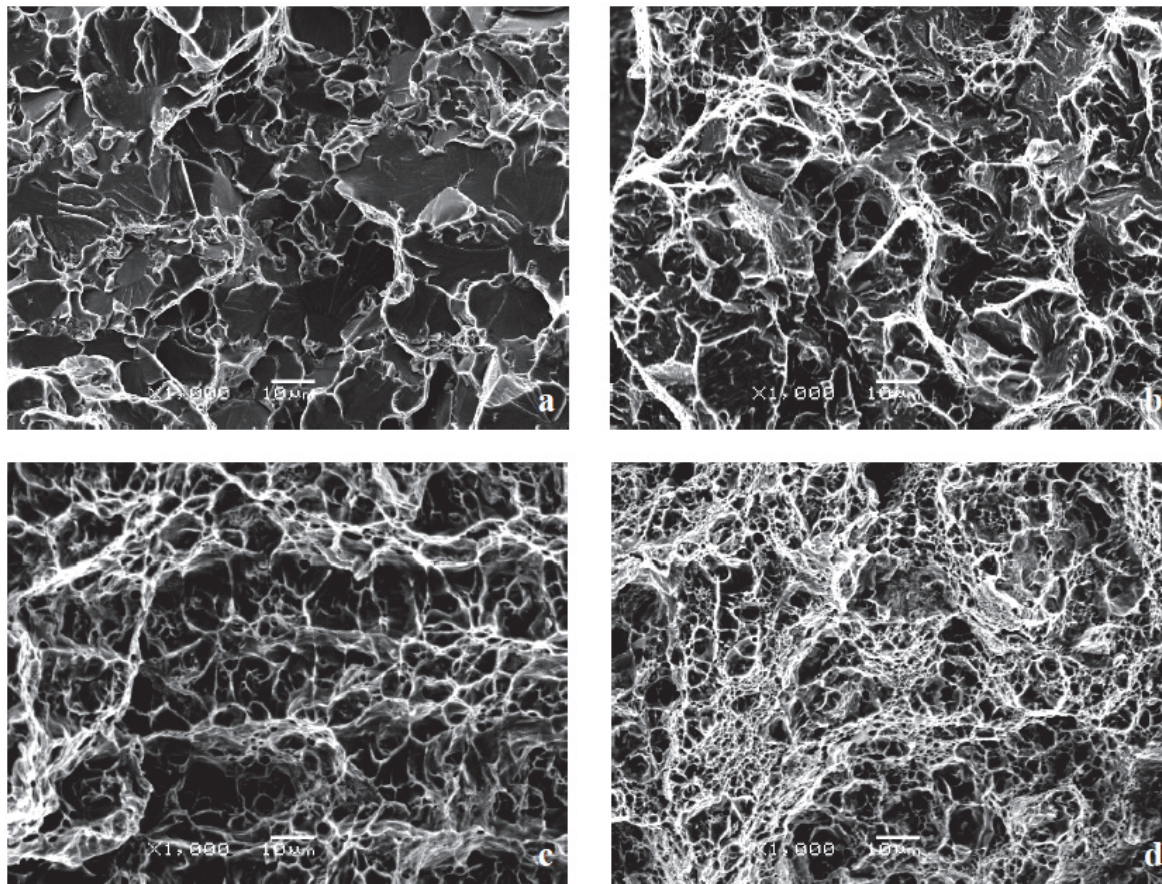


Fig. 2. The fracture of DP steel sample after impact test: a-700°C, b-800°C; The fracture of the sample after tensile test: c-700°C, d-800°C

At low quenching temperature the cracks had a ductile character with small areas of brittle fracture of the hard martensite phase (Fig. 2c). With increasing quenching temperature from the $\alpha + \gamma$ range, a distinct change of decohesion mechanisms was observed. Starting from the hardening temperature of 750 ° C the samples had the features of the ductile fracture with a high degree of plastic deformation on the whole surface observed– Fig. 2d.

The increase of quenching temperature caused the increase of low-carbon martensite content. The reduction of the carbon concentration in the martensite cell brought about the increase of the material ductility despite its higher volume fraction of martensite in the microstructure.

References

- [1] A. Bag, K.K. Ray, E.S. Dwarakadasa: Metall. Mater. Trans. A, Vol. 30A, May 1999.
- [2] G. Fourlaris, R. Ellwood, T.B. Jones: Mater. Des. 28, 2007.

Scanning electron microscopy as a tool in the studies of hydrated cementitious materials microstructure formed in the presence of some heavy metals containing admixtures

Wiesława Nocuń-Wczelik^{1,a}, Barbara Trybalska^{1,b}

¹AGH University of Science and Technology, al. Mickiewicza 30, 30-059 Kraków, Poland

^awiesia@agh.edu.pl, ^bbarbara.trybalska@agh.edu.pl

Introduction

Cement hydration is a heterogeneous process in which the nearly amorphous calcium silicate hydrates are formed, accompanied by crystalline calcium aluminosulfate phases (ettringite) and calcium hydroxide. Basic properties of cement pastes are attributed to these calcium silicates, known as C-S-H gel. The formation of hydrated phases leads to the reduction of distance between the grains and the viscosity of paste is enhanced. At the next stage of this process the rigid skeleton structure is built and this structure reveals ability to transfer some load [1].

The development of investigation techniques, particularly the scanning microscopy, allowed to differentiate the morphological types of the calcium silicate hydrates, depending on the properties of cement, water to cement ratio, time of maturing and additives/admixtures used. The following classification from the morphological point of view have been proposed: C-S-H I of fibrous microstructure, C-S-H II with network structure known as *honeycomb*, C-S-H III occurring in the form of isometric grains and the C-S-H IV occurring as assemblages of spherical particles, corresponding to the “inner” product and visible under the electron microscope as compact gel [2].

In this paper the microscopic observations and analyses relating to the reactions occurring in cement pastes processed with the solutions of heavy metal sulfates and nitrates are reported. The cementitious material mixed with solutions revealed, at low concentrations of admixtures, acceleration of hydration process, as evaluated by calorimetric measurements. The example microstructures are given as figs 1 ÷ 2.

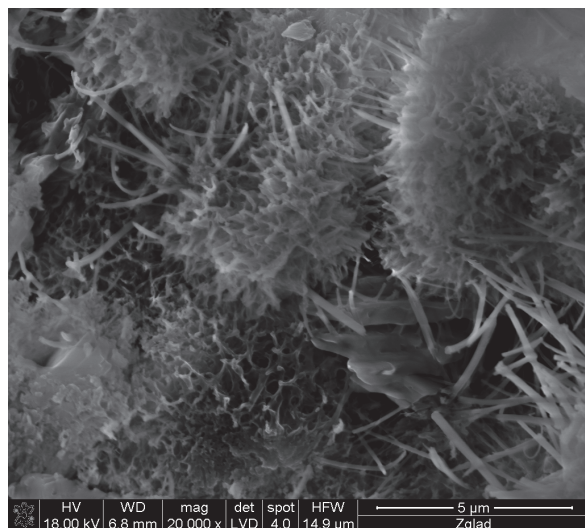


Fig.1. Microstructure of cement paste processed with water; see well developed C-S-H and ettringite needles

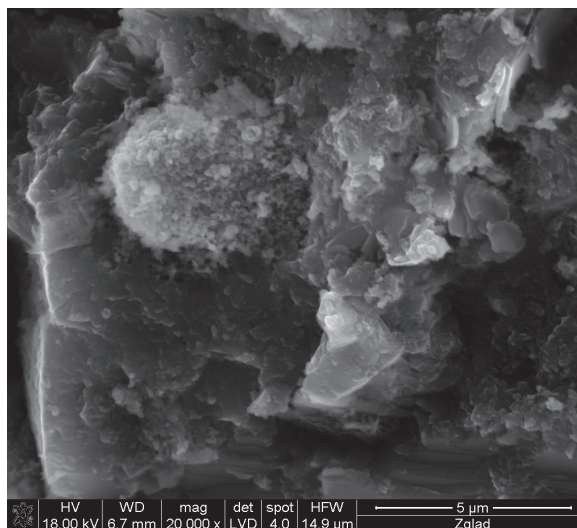


Fig. 2. Microstructure of cement paste processed with $\text{Cd}(\text{NO}_3)_2$; see poorly developed C-S-H

Conclusions

At higher concentrations the more or less retardation of the process was observed. The hydration products reflect very well the kinetics of dissolution/precipitation reactions, controlled by the process occurring in the liquid phase, enriched with admixtures. The morphology and composition of calcium silicate, as well as calcium hydroxide are strongly affected by heavy metal compounds. The amount of ettringite depends on the presence of sulfates; gypsum is observed as a result of calcium ions reaction with sulfate. At the presence of heavy metal compounds the nucleation of the products is generally hindered and formation of calcium silicate well shaped forms is disturbed, as it has been found in some earlier studies [3].

References

- [1] H.F.W. Taylor, *Cement Chemistry*, Thomas Telford Publishing, London (1997).
- [2] S. Diamond, in: *Hydraulic Cement Pastes: their Structure and Properties*, Proc. of Conference, Cement and Concrete Ass., Wexham Springs (1976).
- [3] W. Nocuń-Wczelik, *Struktura i właściwości uwodnionych krzemianów wapniowych*, Prace Komisji Nauk Ceramicznych, Polski Biuletyn Ceramiczny Nr 18, Ceramika 59, Kraków (1999).

Acknowledgement

The financial support from the Faculty of Material Science and Ceramics, University of Science and Technology AGH in Cracow, Poland is greatly acknowledged (grant No 11.11.160.437).

Polymeric track etched membranes – investigations with scanning electron microscopy techniques

Bożena Sartowska^{1,a}, Oleg Orelovitch^{2,b}, Pavel Apel^{2,c}, Adam Presz^{3,d}

¹Institute of Nuclear Chemistry and Technology, Dorodna 16 str., 03-195 Warsaw, Poland

²Flerov Laboratory of Nuclear Reactions, Joint Institute for Nuclear Research, 141980 Dubna, Joliot-Curie 6 str., Moscow region, Russia

³Institute of High Pressure, Sokolowska 29/37 str., Warsaw, Poland

^ab.sartowska@ichtj.waw.pl, ^borel@nrmil.jinr.ru, ^capel@nrmil.jinr.ru, ^dpresz@unipress.waw.pl

Track-etched membranes are porous systems consisting of a polymer foil with thin channels-pores from surface to surface. Polymeric film is irradiated with accelerated heavy ions and then etched in etching solution. The solubility of the track material in certain chemical reagents strongly exceeds the solubility of the initial material. For this reason a hole or a cavity is being etched along the track. As a result the membrane with well defined pore geometry and determined pore density is obtained. Control over pore geometry opens the way to a number of new applications of track-etch membranes. For obtaining other than cylindrical (conical, funnel-like or cigar-like) pores the methods with UV exposure application and surfactant addition to the etching solution was used. The main membrane parameters are: porosity, pores size and shape of channels.

The increasing interest in this kind of material is connected with the development of nanoporous materials with unique properties such as diode-like effects in membranes with highly asymmetrical nanopores. The materials can be used for molecular sensors and atom beam optics, development of nanocapillary bodies for modelling the transport of molecules and ions in constrained volumes.

The aim of presented work was to characterize produced membranes from PET foil and determine their parameters using scanning electron microscopy techniques. The etched samples with high pore density (approximately 10^8 cm^{-2}) were examined using the SEM and HRSEM. Information about pores diameters and pores density were obtained during the observation of the both surfaces of samples. Pores geometry was characterized in details during fractures of the samples observations.

Methods of sample preparation were discussed and SEM images of the surfaces and cleavages of polymeric membranes with different pore shape and geometrical parameters are presented.

Research was supported by the cooperation programme between the Polish scientific institutes with the JINR, Dubna, Russia (04-5-1076-2009/2014) and by the Polish Ministry of Science and Higher Education (2804/ZIBJ Dubna/2013)

Application of Peltier cooling device in a variable-pressure SEM

Anna Wassilkowska

Cracow University of Technology, Faculty of Environmental Engineering,
Warszawska 24, Cracow 31-155, Poland

awassilkowska@pk.edu.pl

Introduction

The use of a scanning electron microscope in geological and biological sciences often requires a variable vacuum to obtain an image of thermodynamically unstable test objects. The studies often involve hydrated and/or non-conductive samples [1]. This work aims to show the use of Peltier cool-stage in the preparation of "natural" specimens for observation using an electron microscope.

Experimental conditions

In conventional SEMs, a special cryo-holder facilitates specimen preparation. The author used a Hitachi S-3400N VP-SEM with a Deben Peltier cool-stage option [2] during the experiment. The electron gun has a tungsten filament. By evacuating the specimen chamber together with the pre-cooled sample, temperatures of up to -30°C at maximum pressure of 270 Pa were obtained using a standard Peltier device. The back-scattered electrons detector (BSE) operates both in high and low pressure with optimal resolution of 10 nm, whereas the secondary electrons detector (SE) shows resolution of 3 nm for 30 kV accelerating voltage and serves only in high-vacuum mode provided by the vacuum system.

Results and discussion

Fig. 1 shows a structure of saline containing *Gardia* oocysts of protozoa. The images were taken at 11 Pa and 10 kV using the BSE detector. The inevitable crystallization of suspensions drying at room-temperature causes many structural artifacts to interfere with specimen analysis in a SEM. Dynamic phase changes of potable water were registered under continuous cooling in a Peltier stage for rather high beam voltage of 15 kV (Fig. 2). The experiment has not been repeated and has probably no meaningful applications for the microscopic studies of organic samples. The experiment on plant-leaf imaging could be more applicable to study organic samples, because of the freeze-dry method applied (Fig. 3). The leaves were held in a specimen chamber at -28°C and 22 Pa overnight and images were taken in high-vacuum mode using the SE detector. The quality of SE images is adequate at magnification of 1.000 x. Lower accelerated voltage could be used in order to record the fine surface topography of beam-sensitive specimens in a relatively short time interval without excessive surface loading or destruction of the structure. The application of Peltier cool-stage is advantageous, when using the EDS technique, because it prevents sputtering on conductive coatings which may hinder the analysis of elements in a specimen.

Acknowledgement

The author would like to thank Prof. Wojciech Dąbrowski from the Institute of Water Supply and Environmental Protection for his support and helpful discussions during the investigation.

References

- [1] M. Polus, A. Wassilkowska, W. Dąbrowski: AWE International Issue March (2012), p. 33.
- [2] Information on <http://www.deben.co.uk>.

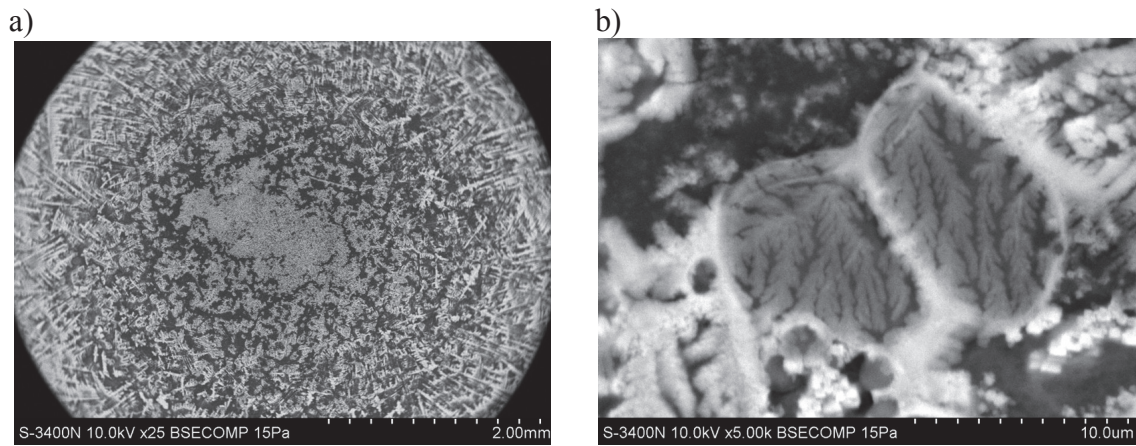


Fig. 1. Gardia oocysts after drying of saline suspension (a) and magnified specimen structure (b)

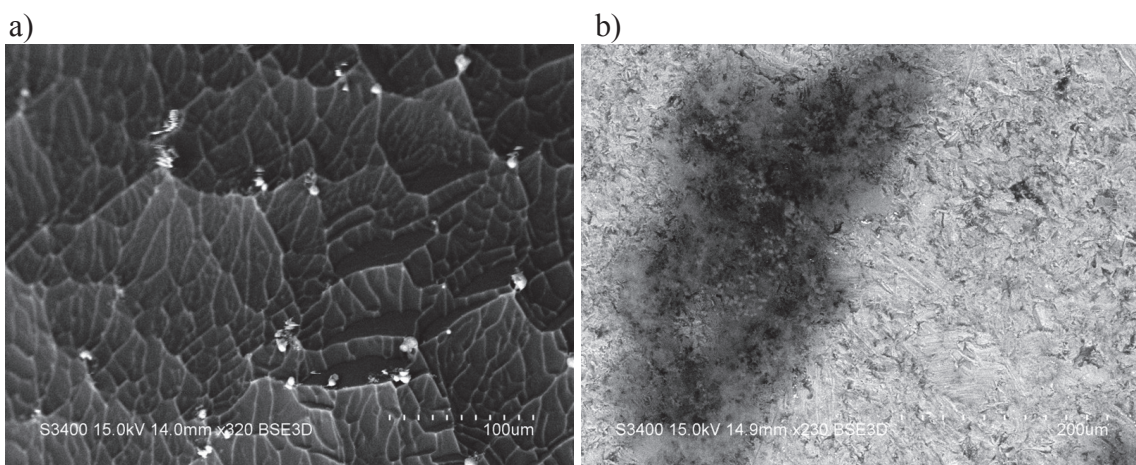


Fig. 2. Structure of tap-water drop at -28°C (a) and *in-situ* sublimation caused by electron beam (b)

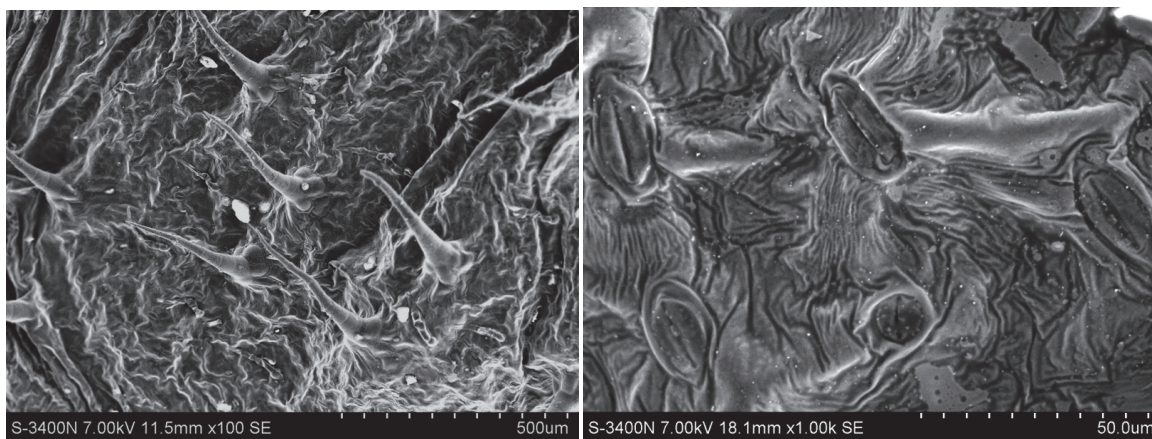


Fig. 3. Plant-leaf pre-cooled in chamber pressure of 22 Pa; SE images for 10 min at 7 kV voltage

Computing methods to enhance out-of-focus images: the scientific acceptability

P.W.J. van Wyk^{1,a}, H. Grobler^{1,b}

¹Centre for Microscopy, University of the Free State, Bloemfontein, South Africa

^avanwykpw@ufs.ac.za, ^bgroblerh@ufs.ac.za

Introduction

Third world countries often encounter funding problems to purchase state-of-the-art equipment and as a result mostly own very basic equipment. Technical problems may be encountered when complex specimens are examined with older and basic types of scanning electron microscopes. Thus, some of the most common problems encountered when examining living organisms and other structures with less expensive electron microscopes, are often poor focus and low image quality. Phenomena causing these problems with the electron microscope may be inherent charging of a specimen and phosphorescence of samples making it difficult to focus the microscope. Phosphorescence may also cause the specimen to produce hazy images no matter what attempts are made to optimise the microscope settings. The question arises if it is scientifically acceptable to use software to improve image quality. In an attempt to clarify this issue, commercially available "deconvolution software" was used to enhance scanning electron microscope digital images without altering the scientific originality of the data. Deconvolution is the recovery of an object from an image that is degraded by blurring and noise [1].

Material and methods

Different types of material were used in an attempt to clarify some of the phenomena that caused poor image quality. Biological samples were prepared by fixing the cells in 3% sodium phosphate buffered (0.1M, pH 7.0) glutardialdehyde for three hours. Samples were rinsed twice in buffer solution for 10 minutes each to remove excess aldehyde, followed by post fixation in 1% osmium tetroxide in the same buffer. The material was dehydrated in an ethanol series (50, 70, 95, 100% and second 100% change) and critical point dried. These samples were mounted on double sided adhesive carbon tape and coated with gold by sputter coating. Yeast cells (*Schizosaccharomyces pompe*) and an unknown natural bacterial biofilm growing on pebbles were respectively prepared according to the above method.

Nanomaterial samples in the form of finely grounded air-dried powders were similarly pasted onto carbon tape excluding any other chemical preparation steps. These types of samples were mainly phosphorescence compounds such as ZnS:Cu and YAG:Ce. The mounted samples were sputter coated with gold.

All samples were examined at 5kV with a Shimadzu SSX-550 (Kyoto, Japan) scanning electron microscope with a tungsten filament electron gun. The probe size settings of this type of microscope has only relative positional values and the probe size in nanometers could neither be determined nor data about the settings found in the operator's manual. All settings were thus adjusted and optimised only to the operator's best visual satisfaction and captured at 960 lines (67 seconds per frame).

Results and discussion

Biological samples are sometimes highly "three dimensional" and the focus depth-of-field presented the greatest problematic area for good quality focus. Some samples were focused using generally a through-focus series of three images for each sample. Figure 1 shows a captured area of a sample of several microns in depth. The out-of-focus deeper parts are prominent. A freeware program was used to combine the three-image series into one image and then enhanced by the deconvolution software in an attempt to remove the inherent charging or glow and improve the

resolution (Fig. 2). The improved image was superimposed over its original image to preserve the scientific originality.

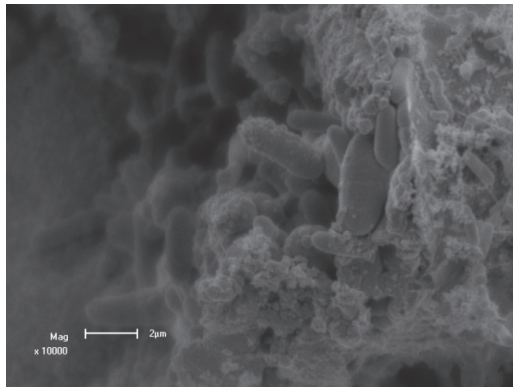


Fig. 1. Original image of biofilm

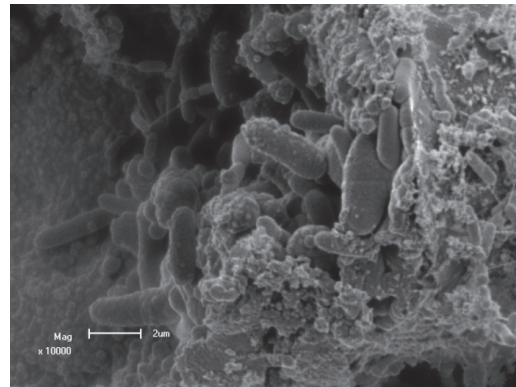


Fig. 2. Enhanced image of similar area

The phosphorescence samples yielded images of very low contrast with poor resolution regardless all attempts to optimise the microscope settings (Fig. 3). The samples were relatively flat compared to the biological specimens and it was thus not necessary to capture images at different focus areas. The images were enhanced by the deconvolution software (Fig. 4).

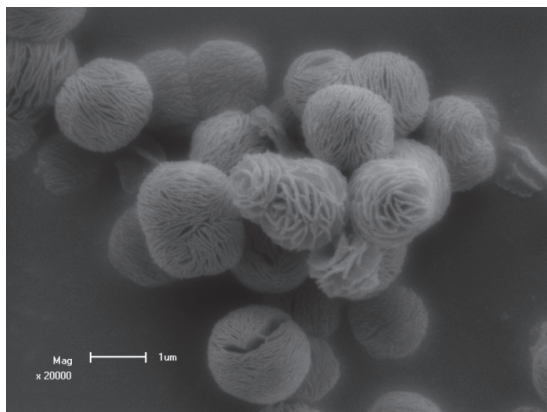


Fig. 3. Original image of Ce compound

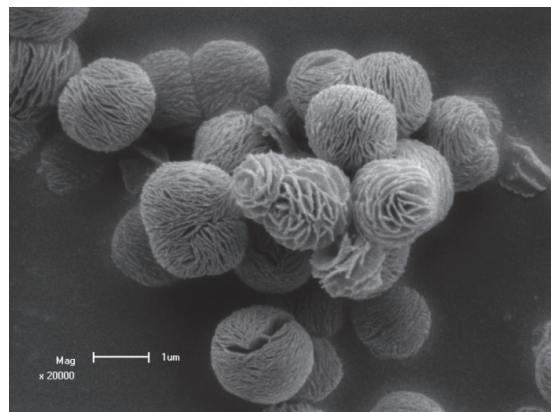


Fig. 4. Enhanced image of similar area

Summary

The growth of biological organisms may take several months. If microscope examinations deliver poor results and low quality images, experiments must be repeated at great cost and loss of time. Enhancing the images delivered excellent results and it is thus time- and cost effective to improve results rather than repeating experiments, which may still again produce poor results. The image enhancements in all cases did not add or remove any data, but only enriched it. Most imaging programs are freely available on the internet. However, even investing in commercial software such as deconvolution software at a negligible cost fraction of an expensive electron microscope, is worth the financial layout.

Reference

[1] Information on <http://www.svi.nl/HomePage>.

Measurement of structural and optical properties of monoclinic HfO₂ at the subnanometric level using energy-filtered HRTEM-VEELS

Cyril Guedj

CEA, LETI, MINATEC Campus, 17 Rue des Martyrs, 38054 Grenoble Cedex 9, France
cguedj@cea.fr

Energy-filtered high-resolution transmission electron microscopy and valence electron energy loss spectroscopy (HRTEM-VEELS) are used to simultaneously map the nanostructural and optical properties of monoclinic hafnia. Exit-wave reconstruction was necessary to validate the structural models unambiguously because of the polymorphism and nanocrystallinity of hafnia. In the low-loss range, the optical absorption displays 9 main spectral features. The pic B appears to be the most affected by the change in lattice orientation. The optical bandgap is significantly reduced when the nanostructure changes from [010]-oriented monoclinic towards polycrystalline.

Introduction

With the downscaling of devices, accurate metrology at the nanoscale has become a crucial objective for the microelectronic and optoelectronic industry. The International Technology Roadmap for Semiconductors [1] outlines that the “measurement of complex material stacks and interface properties including physical and electrical properties” is a “difficult challenge” for sub-16 nm CMOS technology nodes. The characterization of high- κ gate stacks (based for instance on hafnia-based materials) is particularly complicated due to the length scales at which structural and dielectric properties have to be determined. To develop characterization protocols that are independent of materials stacks and integration schemes, more advanced methods are required. To our knowledge, electron energy loss spectroscopy EELS is the only technique capable of measuring dielectric properties [2,3] (complex dielectric permittivity), and chemical properties [4] (composition, atomic bonding) on the same sample with nanometer spatial resolution. In this work, valence electron energy loss spectra of monoclinic hafnia have been measured by HRTEM-VEELS with nanometric spatial resolution. In particular, we show that the monoclinic hafnia oriented [010] optically differs from polycrystalline hafnia.

Results and discussion

The cubic, tetragonal, orthorhombic and monoclinic phases [5] are difficult to distinguish from standard selected-area diffraction patterns. The monoclinic phase (space group P21/c) is the most stable in ambient conditions. Therefore it was necessary to implement advanced exit-wave reconstruction techniques from focal series to validate the structural model unambiguously, using the True Image software [6]. The aberrations from the microscope are numerically corrected from the exit-wave reconstruction algorithm, therefore the atomic-scale model of monoclinic hafnia [010] can be obtained with a significant confidence. The change in crystal orientation markedly changes the optical properties (Fig. 1). The absorption can be satisfactorily described with a model of 9 oscillators labeled from A to I.

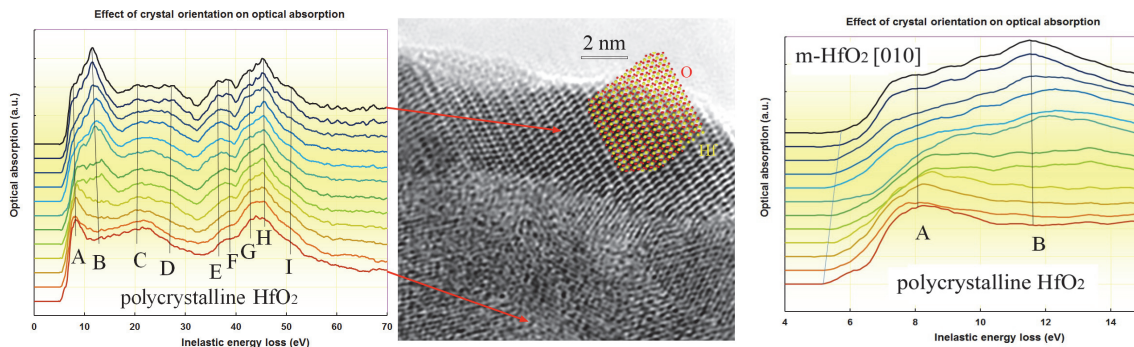


Fig. 1. Relationship between nanostructure and optical properties. The absorption spectra are calculated from the Kramers-Krönig transformation of the energy loss spectra, after subtraction of the zero-loss signal measured in vacuum. The atomic scale model of m-HfO₂ [010] is given in the center

A clear decrease in optical bandgap is observed when the nanostructure evolves from [010]-oriented towards polycrystalline. This important effect should be taken into account in the design of (opto)electronic nanodevices.

Conclusions and perspectives

The effect of nanostructure on the optical properties of hafnia nanocrystals has been measured locally by HRTEM-VEELS. Hence this technique could be a possible solution to the ITRS most difficult characterization challenges [1].

References

- [1] <http://www.itrs.net/>
- [2] M. Stöger-Pollach: *Micron* 39 (2008), pp. 1092.
- [3] P.L. Potapov, H.-J. Engelmann, E. Zschech, M. Stöger-Pollach: *Micron* Vol. 40, 2 (2009), p. 262.
- [4] J. Wang, X.F. Wang, Q. Li, A. Hryciw & A. Meldrum: *Phil. Magazine* 87:1 (2007), p. 11.
- [5] J.M. Léger, A. Atouf, P.E. Tomaszewski, A.S. Pereira: *Phys. Rev. B* 48 (1993), p. 93.
- [6] C. Kübel and A. Thust: *Electron Crystallography*, NATO Science Series II: Mathematics, Physics and Chemistry, Volume 211, Springer, T.E. Weirich et al. (eds.) (2006), p. 373.

Acknowledgements

Measurements were carried out at in the Nanocharacterization Platform (PFNC) of MINATEC (www.minatec.org).

TEM study of catalytic ZnTe/MgZnTe core shell nanowires grown by MBE

Śławomir Kret^{1,a}, Piotr Wojnar^{1,b}, Elżbieta Janik^{1,c} and Tomasz Wojtowicz^{1,d}

¹ Institute of Physics, Polish Academy of Sciences, Al. Lotników 32/46, 02-668 Warsaw,
^akret@ifpan.edu.pl, ^bwojnar@ifpan.edu.pl, ^cjanik@ifpan.edu.pl, ^dwojto@ifpan.edu.pl

Introduction

Nanowires are characterized by a considerable surface to volume ratio. This property can be used to build effective nanosensors. Moreover, properties of semiconductor nanowires attract a great interest because of emerging applications of these structures in the field of nano-photonics [1] and photovoltaics [2]. Te-based nanowires are especially promising in this respect because II-VI semiconductors are characterized by direct energy gaps with values covering the entire visible light spectral range, from 1.6 eV (CdTe) to 3.5 eV (MnTe). On the other hand surface defects may degrade the performance of such devices. In particular, the presence of surface states, which act as a trap for free carriers may affect the electron transport and optical properties of nanowires. This is manifested, for example, as a considerable decrease of the near band edge emission from ZnTe nanowires [3]. A possible method of solving the issue of surface states is adding a ZnMgTe passivation shell which results in unsuccessful recover of the excitonic emission at ZnTe band edge, around 2.39 eV [4]. However, spatially resolved cathodoluminescence investigation clearly shows that not all nanowires are good light emitters. This can be explained by the crystalline structure of a particular nanowire under investigation. The current work is devoted to investigation of the structural properties of ZnTe shells overgrown on ZnTe nanowire cores.

Experimental details and results

ZnTe NWs are grown by molecular beam epitaxy (MBE) on Si or GaAs substrate at various temperatures being in the range of 420-400 °C using gold/Si or gold/Ga droplet as catalyzer in VLS growth regime. The growth of ZnMgTe shells is performed in the same process but at lower temperature around 250-350 °C, similarly as describe in [3,4]. TEM investigation using Cs-HRTEM, HR-STEM, EDS are performed with FEI Titan 80-300 Cube microscope after transferring NWs to a holey carbon film.

The ZnTe NWs cores grow always in the (111) direction and have cubic structure with high density of stacking order defects. The density of SF and twins boundaries highly depend on used substrate, growth temperature and diameter of NW. Various types of the ZnMgTe shell are identified. Type A - continuous epitaxial shell in which ZnMgTe follows crystal structure and lattice orientation of the core. Even, SF present in the core propagate into the shell (fig 1a,b). EDS investigation of such structure confirms that in ZnMgTe shell the Mg/Zn ratio reaches 0.25-0.3 (0.2 in the case of fig 1c). Type-B shell – build from epitaxial nanocrystals which are in crystallographic relation to core but do not take orientation of the core (fig 1e,f) with Mg/Zn ratio in the range of 0.35-0.5. For Mg/Zn ratio > 0.5, type-C poly-crystalline or amorphous shells are observed (fig 1gh). For all type of shells, the strong EDS signal from oxygen indicates the presence of the oxide formed probably in air after the growth. Moreover, all shells have asymmetric thickness. In the case of type-A shell the thickness of the shell for a given individual NW changes from 4 to 20 nm depending of the size of the NW. This asymmetry is probably related to highly directional flows of molecular beams in the growth process and shadowing effect caused by neighboring NWs. The strongest asymmetry is observed for type-C shells which may form only on one side (fig 1 g, h) of NW. The presence of different types of shells and various compositions in the same sample can be explained by different local elemental flux density related to differently oriented surface of NWs core which is critical for the low temperature growth of the shell due to the absence of the long range surface diffusion.

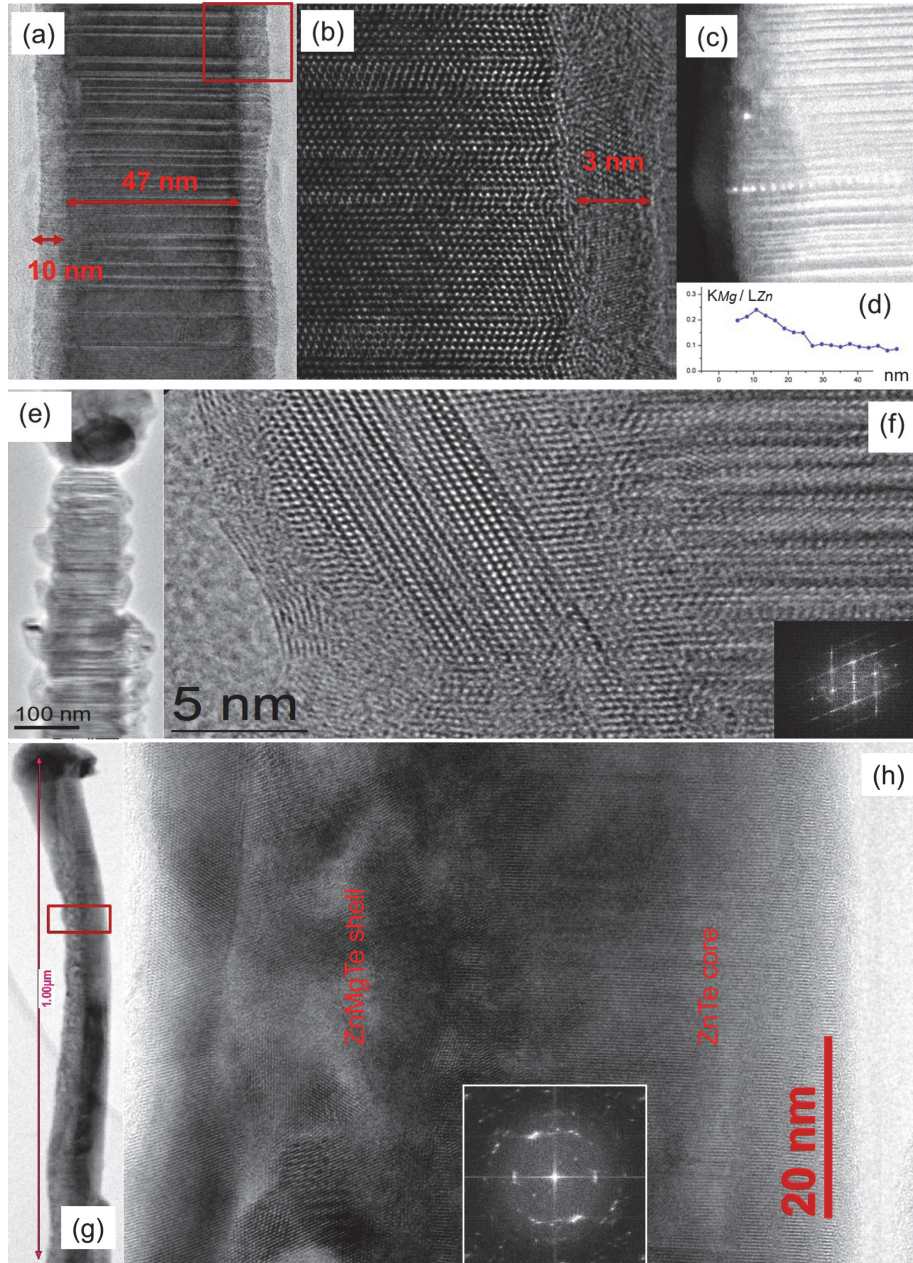


Fig. 1. Various crystalline structures of ZnMgTe shell on ZnTe NWs core. (a,b) Cs-HRTEM of type_A, (c,d) STEM/EDS analysis results (e,f) Cs-HRTEM of type B shell and (g,h) type-C and FFT of shell structure

The research has been supported by the European Union through grants (POIG.01.01.02-00-008/08), POIG.01.01.02-00-008/08) and National Centre of Science (Poland) grant DEC-2011/01/D/ST5/05039.

References

- [1] Y. Huang, X. F. Duan and C.M. Lieber: *Small* 1 (2005) p. 142.
- [2] B. Tian, X. Zheng, T.J. Kempa, Y. Fang, N. Yu, G. Yu, J. Huang: *Nature* 449 (2007), p. 885.
- [3] E. Janik et al: *Appl. Phys. Lett.* 89 (2006), p. 133114.
- [4] P. Wojnar, M Szymura, W. Zaleszczyk, Ł Kłopotowski, E Janik, M. Wiater, L. T. Baczewski, S. Kret, G. Karczewski, J. Kossut and T. Wojtowicz: *Nanotechnology* 24 (2013), p. 365201.

Gold nanostructures assembled on Ge(001) surface studied with electron microscopies

Marek Nikiel^{1,a}, Benedykt Jany¹, Paulina Indyka², Franciszek Krok¹

¹Jagiellonian University, Marian Smoluchowski Institute of Physics, Reymonta 4, 30059 Krakow, Poland

²Jagiellonian University, Faculty of Chemistry, Ingardena 3, 30060 Krakow, Poland

^amarek.nikiel@uj.edu.pl

We report on the nanostructures formation after room temperature deposition of 6 ML of Au on clean, reconstructed Ge(001) surface followed by subsequent *in-situ* annealing to temperatures ranging from 473 K to 770 K. It has been found that the post-annealing leads to formation of metallic islands on the germanium substrate, of a rectangular shape (for annealing temperatures below 650K) or of octagonal shape for the temperatures above 650K. HR-SEM examination of samples annealed in the highest temperature, exhibited that the islands are surrounded by a dark “hallo”. The “hallo” region was identified by mean of STM measurements as a gold-enriched germanium surface with 1D gold nanowires.

To study the island/substrate interface, the lamellas taken across the islands were prepared by using FIB technique and examined with FEI Tecnai Osiris 200 kV TEM. The HR-TEM and the HR-STEM measurements provided that the islands are immersed in substrate, which is in contradiction with the previous studies [1]. It has been found that the Au islands are of not uniformed crystalline structure. Also, the EDX measurements provided that the Au islands are surrounded by subsurface layer, buried 2-3 nm under the surface, which was identified as a gold-rich phase.

References

[1] J. Wang, M. Li and E.I Altman: Surf. Sci. 596 (2005), p. 126.

Uncommon strain relaxation observed in InGaN/GaN structures – transmission electron microscopy structural studies

Julita Smalc-Koziorowska^{1,2,a}, Henryk Turski^{1,b}, Czesław Skierbiszewski^{1,2,c}
and George Dimitrakopoulos^{3,c}

¹Institute of High Pressure Physics PAS, Sokołowska29/37, 01-142 Warszawa, Poland

²TopGaN Ltd., Sokołowska 29/37,01-142 Warszawa, Poland

^ajulita@unipress.waw.pl, ^bturski@unipress.waw.pl, ^cgdim@auth.gr

The InGaN layers are used as active layers in nitride semiconductor lasers emitting light in the green range of wavelengths. Reliable long living green emitters will enable the production of laser projectors offering visualization of images with best color range, highest pixel resolution and best bright-dark contrast of the images[1]. Construction of nitride emitters from this spectral region requires preparation of thin epitaxial layers (down to few nm) of $\text{In}_x\text{Ga}_{1-x}\text{N}$ with $x \approx 0.3$ that is considered as consisting of high In-content. InGaN layers and quantum wells constitute the active regions of optoelectronic devices, such as blue/green light emitting diodes, laser diodes, as well as new-generation photovoltaic cells. First InGaN green lasers have been already achieved in 2010 by Osram[2] and Nichia[3]. However the lifetime and efficiency of these optoelectronic devices still should be improved in order to use them in the mass production. One of the issues, which should be optimized in order to get efficient green emitters, is the high density of structural defects. The defects inside nitride layers with high amount of In deteriorate the performance of the nitride based devices since they act as nonradiative centers and lead to a reduction of the devices lifetime[4]. The presence of the structural defects is mainly caused by the mismatch between subsequent layers in the semiconductor structures, however the introduction of the defects could be also enhanced or minimized by the applied epitaxial growth conditions. In our transmission electron microscopy (TEM) structural studies (Fig. 1) of InGaN layers with nominal 15 to 30% composition of In deposited by molecular beam epitaxy on free-standing GaN substrate we observe that the InGaN layer is itself free of defects, however we observe many defects laying at the both interfaces between InGaN and GaN layers. In the high resolution TEM cross section studies we see presence of dislocations at the GaN/InGaN interface; however we also observe that some defects descend below the interface line. Such a defect configuration has not been reported in the literature yet.

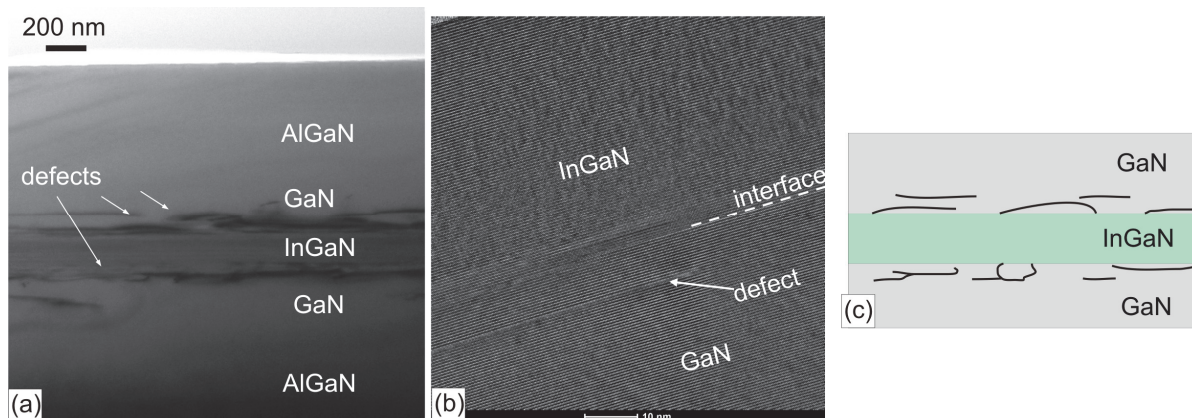


Fig. 1. (a) Bright-field image of the nitride heterostructure containing $\text{In}_{0.2}\text{Ga}_{0.8}\text{N}$ layers taken with $g \parallel 1\bar{1}20$ off $[1\bar{1}00]$ zone axis, showing the distribution of dislocations at the InGaN/GaN interfaces in complex nitride heterostructure; (b) High resolution TEM image of the interface between the InGaN layer on GaN substrate, the defect present below the interface line is indicated; (c) schematic representations of the defect distributions at the InGaN/GaN interfaces in studied layers

Publications on InGaN relaxations mechanisms typically report on the InGaN layers with high density of threading dislocations[5-8]. Srinivasan *et al* [8] or Liu *et al* [7] found that the InGaN layer deposited on GaN (0001) substrate contain mixed type $1/3\langle 11\bar{2}3 \rangle$ dislocation which may slip on the $\{11\bar{2}\bar{2}\}$ plane and contribute in the misfit relaxation. In our studies we also observe dislocations with Burgers vector $b=1/3\langle 11\bar{2}3 \rangle$ in thick InGaN layers deposited on GaN substrates. However in case of InGaN layers embedded in more complex nitride heterostructure consisting of AlGa_N, GaN and InGaN layers (Fig. 1a), the observed dislocations have only the Burgers vector $b=1/3\langle 11\bar{2}0 \rangle$ and are laying on the (0001) planes. In both types of investigated structures, we observed descending of dislocations to adjacent GaN layers. We also observe basal stacking faults probably formed due to dissociation of perfect dislocations present at the interface.

The InGaN/GaN structures were investigated in cross-section and plan-view configuration. The analysis of the dislocations character and their distribution in InGaN/GaN structure was performed using $g\bullet b$ criteria by taking the weak-beam dark field images with various g vectors, and by HRTEM studies. The possible mechanism of the introduction of observed defects into the InGaN/GaN structures will be presented.

References

- [1] U. Strauss, A. Avramescu, T. Lermer, D. Queren, A. Gomez-Iglesias, C. Eichler, J. Müller, G. Brüderl, and S. Lutgen: *phys. status solidi (b)* 248 (2011), p. 652.
- [2] A. Avramescu, T. Lermer, J. Müller, C. Eichler, G. Brüderl, M. Sabathil, S. Lutgen, and U. Strauss: *Appl. Phys. Express* 3 (2010), p. 061003.
- [3] Y. Enya, Y. Yoshizumi, T. Kyono, K. Akita, M. Ueno, M. Adachi, T. Sumitomo, S. Tokuyama, T. Ikegami, K. Katayama, and T. Nakamura: *Appl. Phys. Express* 2 (2009), p. 082101.
- [4] U. Strauss, T. Lermer, J. Mueller, T. Hager, G. Brüderl, A. Avramescu, A. Lell, and C. Eichler: *Phys. Status Solidi a-Applications and Materials Science* 209 (2012), p. 481.
- [5] A. M. Fischer, Z. Wu, K. Sun, Q. Wei, Y. Huang, R. Senda, D. Iida, M. Iwaya, H. Amano, and F. A. Ponce: *Appl. Phys. Express* 2 (2009), p. 0410021.
- [6] J. Mei, R. Liu, F.A. Ponce, H. Omiya, T. Mukai: *Appl. Phys. Lett.* 90 (2007), p. 171922.
- [7] R. Liu, J. Mei, S. Srinivasan, H. Omiya, F. A. Ponce, D. Cherns, Y. Narukawa, and T. Mukai: *Japanese J. Appl. Phys. Part 2: Letters* 45 (2006) p. L549.
- [8] S. Srinivasan, L. Geng, R. Liu, F.A. Ponce, Y. Narukawa, S. Tanaka: *Appl. Phys. Lett.* 83 (2003), p. 5187.

TEM/STEM/EELS studies of cryptomelane nanorods

Paulina Indyka^{1,a}, Joanna Gryboś^{1,b}, Piotr Legutko^{1,c}, Paweł Stelmachowski^{1,d},
Andrzej Kotarba^{1,e} and Zbigniew Sojka^{1,f}

¹ Faculty of Chemistry, Jagiellonian University, Ingardena 3, 30-060 Krakow, Poland

^apaulina.indyka@uj.edu.pl, ^bgrybosjo@chemia.uj.edu.pl, ^cpiotr.legutko@uj.edu.pl,
^dpawel.stelmachowski@uj.edu.pl, ^ekotarba@chemia.uj.edu.pl, ^fsojka@chemia.uj.edu.pl

Introduction

Tunnel-based frameworks based on manganese oxides are used as catalytic materials in various oxidation processes. Among critical factors determining the performance of such materials, the interlayer structure that could facilitate ion insertion and extraction is vital for their catalytic activity [1]. In the particular case of the cryptomelane - a tunneled potassium manganese oxide $\text{KMn}_8\text{O}_{16}$ - the one-dimensional architecture of nanorods may contribute to facilitate potassium ion diffusion and spreading on the activated reactant, which is beneficial for soot combustion. Thus, careful microstructure evaluation with the required spatial and chemical resolution at the length scale of the interest is of fundamental importance for understanding of their catalytic behavior.

Experimental

A cryptomelane potassium manganese oxide $\text{KMn}_8\text{O}_{16}$ was synthesized through a hydrothermal process. The powder sample was dispersed in ethanol, sonicated, and dropped into a holey carbon-coated copper grid. The morphological, structural and chemical investigations of the samples were carried out using analytical high resolution transmission electron microscope (FEI Tecnai Osiris) with X-FEG Schottky field emitter operated at accelerating voltage of 200 kV, equipped with Super-X windowless EDX (Energy Dispersive X-ray) detector system with silicon drift detector (SDD) technology. A High Angle Annular Dark Field (HAADF) detector for Z contrast imaging was used in the scanning transmission electron microscopy (STEM) mode. STEM images coupled with EDS elemental mapping were acquired with applied sample drift correction (Bruker Esprit software) in order to determine elemental composition of the sample and to directly identify the location of the specific elements. Sample was loaded into a beryllium double-tilt low-background holder in order to reduce the production of spurious X-rays. TEM images were recorded by a 2k Gatan CCD camera in a digital format. Complementary in-depth structural details of the sample were further analyzed by means of a GIF (Gatan Image Filtering) system equipped with an EELS spectrometer by performing EFTEM (Energy Filtered) and STEM-EELS (Electron Energy Loss Spectroscopy) experiments.

Results and Discussion

Fig. 1 illustrates the results of the TEM studies of the as-synthesized cryptomelane manganese oxide in the form of nanorods (20-500 nm). Selected area electron diffraction (SAED) pattern taken from a large group of the nanorods consists of sharp rings that can be indexed in accordance with the $\text{KMn}_8\text{O}_{16}$ monoclinic structure. The high resolution TEM image and the corresponding Fast-Fourier-Transform (FFT) pattern, shown as inset in Fig.1b, reveals lattice fringes with the interplanar spacing of 0.49 nm, which correspond well to the (200) plane of the cryptomelane manganese oxide. An in-depth analysis and image simulations showed also that bright contrast in the HR TEM images comes from the K^+ and O^{2-} ions, whereas darker contrast is associated with the planes containing the Mn^{3+} and O^{2-} ions.

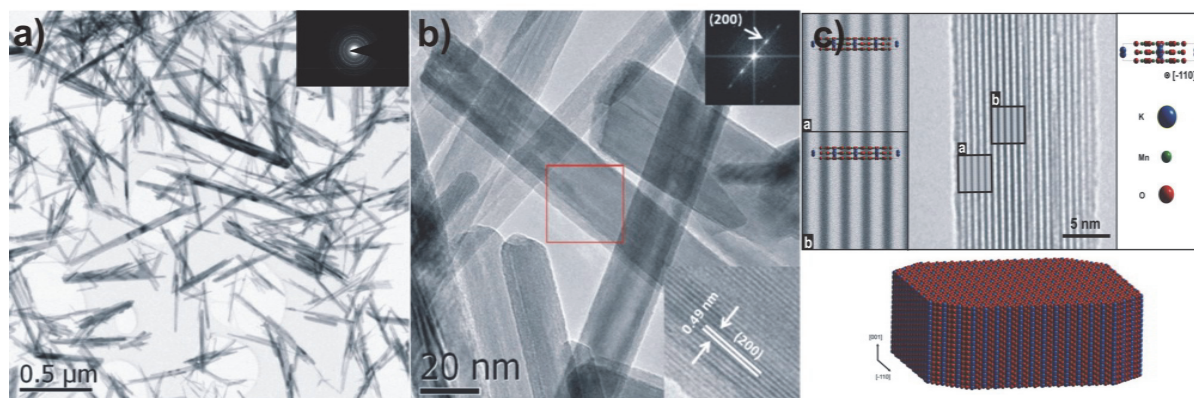


Fig. 1. TEM low magnification image of as-synthesized cryptomelane manganese oxide with the corresponding SAED pattern (a), HRTEM image of nanorods along with an FFT pattern and enlarged bottom insert clearly showing lattice fringes corresponding to the (200) planes indicating high degree of crystal ordering (b), A 3-D model of cryptomelane crystal along with its unit cell matched to the simulated TEM image superimposed on the corresponding TEM projection (c)

The EDS, EELS and EFTEM techniques were employed to determine elemental distribution of potassium, manganese and oxygen within the cryptomelane nanorods. The EELS spectroscopic data were acquired using spectrum imaging technique - at core loss energies the background signal was subtracted to create elemental map and further combined with STEM HAADF image (Fig. 2a). Comparison of the EELS spectra obtained at different areas in the bulk and at the surface of the cryptomelane nanorods, revealed significant variations of the chemical composition, and uneven repartition of potassium. The results provided a nanoscale picture of potassium ion diffusion channels, arrangement of manganese octahedra, and variations in the Mn oxidation states. Spectroscopic results were further complemented by EFTEM (Fig. 2d), and HAADF/STEM/EDS (Fig.2c) elemental imaging, showing local dispersion of the investigated elements. These studies, complemented by species resolved thermal desorption and work function measurements, allow for detailed understanding of potassium ion interlayer and surface diffusion in the cryptomelane tunnel structure.

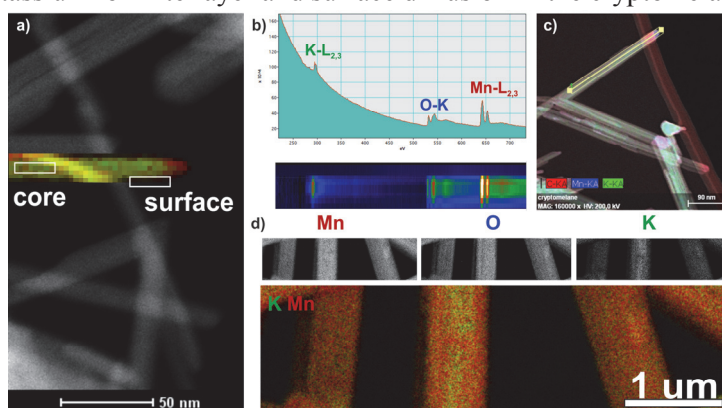


Fig. 2. STEM image combined with EELS chemical composition data (a), typical EELS spectrum and 2D EELS spectrum of $\text{KMn}_8\text{O}_{16}$ with clearly visible core absorption edges (b), HAADF image coupled with EDS elemental composition mapping (c), EFTEM elemental maps of the cryptomelane sample (d), the data for potassium, manganese and oxygen repartition are shown with RGB color coding

Acknowledgements

The project was financed by the Polish National Science Center awarded by decision number DEC-2011/01/B/ST4/00574.

References

- [1] D. Su, H.-Y. Ahn, G. Wang: *J. Mater. Chem. A* 1 (2013), p. 4845.

STEM characterization of LiMn_2O_4 powder modified by metal oxides

Mariusz Andrzejczuk^{1,a}, Agnieszka Teresa Krawczynska^{1,b}, Piotr Bazarnik^{1,c},
Małgorzata Lewandowska^{1,d}, Monika Michalska^{2,e}, Ludwika Lipińska^{2,f},
Andrzej Czerwiński^{3,g}

¹Faculty of Materials Science and Engineering, Warsaw University of Technology, Woloska 141, 02-507 Warsaw, Poland

²Institute of Electronic Materials Technology, Wolczynska 133, 01-919 Warsaw, Poland

³Faculty of Chemistry, University of Warsaw, Pasteura 1, 02-093 Warsaw, Poland

^amandrzejczuk@inmat.pw.edu.pl, ^bakrawczy@inmat.pw.edu.pl, ^cbazarnik123@gmail.com

Lithium manganese oxide LiMn_2O_4 (LMO) is one of the best candidates for a cathode material in lithium-ion batteries due to its low cost and low toxicity. However, capacity fading owing to dissolution of manganese into an electrolyte and Jahn-Teller distortion effect during charge-discharge cycles still limits the practical application of LMO as a positive electrode [1, 2]. To suppress reaction between a positive electrode material and an electrolyte, protective oxides can be added to LMO particles. In this work we present the results of scanning transmission electron microscopy (STEM) characterization of LMO powders after surface modification by oxides. Three types of oxides Al_2O_3 , La_2O_3 and ZrO_2 in various content of 1, 3, 5%wt. were selected for LMO modification. The chemical analyses of particles were performed using electron energy-loss spectroscopy (EELS) and X-ray energy dispersive spectroscopy (EDS) combined with STEM. Phases were identified from nanodiffraction patterns. It is suspected that surface modification of LMO grains using oxides improves cyclic stability and capacity retention. Hence, structure characterization using advanced electron microscopy might be crucial for understanding the influence of the microstructure on electrochemical performance.

References

- [1] M.S. Whittingham: Chem. Rev. 104(10) (2004), p. 4271.
- [2] A.M. Kannan, A. Manthiram: Electrochem. Solid-State Lett. 5(7) (2002), p. A167.

Acknowledgments

This work was supported by The National Centre for Research and Development through the research grant PBS1 (contract no. PBS1/A1/4/2012).

Elemental composition in micro areas of the medieval Central Europe coins

**Bożena Sartowska^{1,a}, Ewa Pańczyk^{1,b}, Lech Waliś^{1,c}, Jakub Dudek^{1,d},
Władysław Weker^{2,e}, Maciej Widawski^{2,f}**

¹Institute of Nuclear Chemistry and Technology, Dorodna 16 str., 03-195 Warsaw, Poland

²National Archeological Museum, Długa 52 str., 00-241 Warsaw, Poland

^a b.sartowska@ichtj.waw.pl, ^b e.panczyk@ichtj.waw.pl, ^c l.walis@ichtj.waw.pl, ^d j.dudek@ichtj.waw.pl,
^e w.weker@pma.pl, ^f m.widawski@pma.pl

The aim of the presented work was to determine the provenance and dating of a few groups of the early medieval Central Europe coins. The widely known and already described types of coins have been chosen for investigations. However, an attribution and chronology of them often constitute a serious problem for historians and numismatists.

The Saxon coins, so called the Otto and Adelheid denarii as well as the Polish ones, the Władysław Herman and Bolesław Śmiały coins, were examined. Totally, about two hundred coins were studied in their many aspects. The ores from selected sources will be also analyzed to determine a provenance of metals used for coins manufacturing. For hundreds years coins were in uncontrolled conditions and in variable environment. Destructed and inhomogeneous surface were one of the effect of corrosion processes.

Electron microscopy with energy dispersive X-ray analysis (SEM-EDS), X-ray fluorescence analysis (EDXRF, TXRF) and laser ablation inductively-coupled plasma mass spectrometry (LA-ICP-MS) were applied. All limitations arisen from a complex structure of the historical artefacts were taken into consideration.

The main goal of SEM using was detailed localization and precise selection of interesting and important micro areas of the coin surface. Elemental analysis were carried out inside small (about 50 µm width) crater after the LA-ICP-MS investigations. Analyses were made at the coin surface and inside – along and across - the crater. The obtained results proved the higher concentration of silver at the surface as compared to silver concentration in the bulk of the samples. Opposite phenomenon was observed for copper concentration. These results were the successive effect of the long time corrosion processes.

The results of these investigations are significant for our knowledge of the history of Central European coinage, especially of Polish coinage. An interpretation of the results of the statistical methods allowed us to differentiate the artefacts in relation to the various production centers (mints), various recipes as well as various raw materials and methods of their purification.

Research was supported by Ministry of Sciences and Higher Education (N N 507 427 239).

Microstructural investigation of dense ceramic membranes for oxygen separation in coal-fired power plants

Bogdan Rutkowski^{1,a}, Aleksandra Czyrska-Filemonowicz^{1,b}

¹AGH University of Science and Technology, International Centre of Electron Microscopy for Materials Science and Faculty of Metals Engineering and Industrial Computer Science, Al. A. Mickiewicza 30, 30-059 Krakow, Poland

^arutkowsk@agh.edu.pl, ^bczyrska@agh.edu.pl

Contemporary, highly-developed countries are struggled by the increasing environmental CO₂ pollution, caused by increasing demand on electrical power. In order to fulfil these exact requirements, conventional coal-fired power plants have to combust increased amount of coal, generating enhanced amount of carbon dioxide and contributing to global warming. In order to decrease the amount of CO₂, released to the atmosphere, a carbon capture and storage (CCS) process has been developed. The most promising CCS technique is OXYFUEL process, in which coal is combusted in the oxygen instead of air, effecting in almost pure CO₂ in flue gas, ready to be captured, compressed into liquid form and stored in natural cavities under the ground in order to avoid its emission to the atmosphere. In order to produce oxygen, a classical cryogenic process [1] or dense ceramic membranes [2] can be used.

In current paper, the results of microstructural investigation of as-received and thermally treated Ba_{0.5}Sr_{0.5}Co_{0.8}Fe_{0.2}O_{3-δ} (BSCF 5582) dense ceramic membrane are presented. Investigated material has one of the best oxygen permeation rates from all so far known perovskite-structured materials [3]. Despite its advantages, this material is unstable under certain conditions (temperature and oxygen pressure) and secondary phase is nucleating at the grain boundaries [4], deteriorating the oxygen flux.

Micro- and nanostructure of the BSCF 5582 was characterised by transmission electron microscopy using advanced probe Cs-corrected S(TEM) Titan³ G2 60-300 of FEI, equipped with a ChemiSTEM system. BSCF 5582 lamellas were prepared by FIB (NEON CrossBeam 40EsB of Zeiss). Phase investigation was performed by STEM-EDS and selected area electron diffraction (SAED) methods. Electron diffraction patterns were interpreted with the help of a JEMS software.

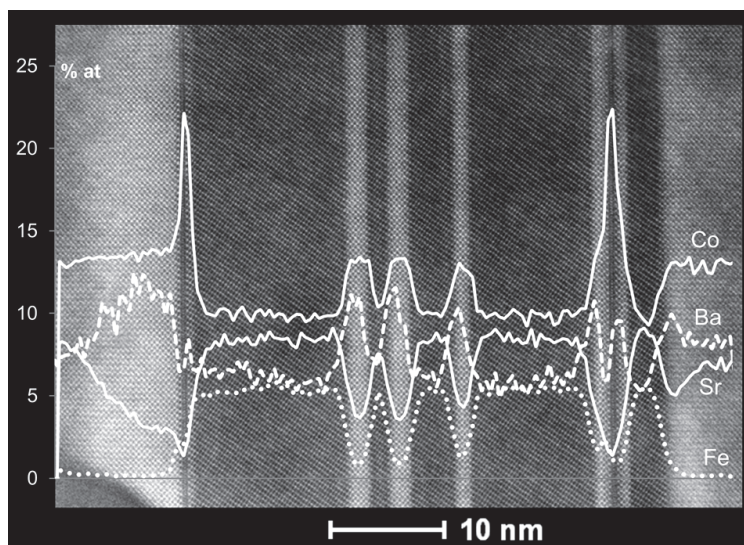


Fig. 1. HRSTEM-HAADF image of secondary phase in as-received BSCF 5582 with EDS-linescan result superimposed

The microstructure of as-received BSCF 5582 consists of cubic perovskite grains. Grain boundaries are decorated by thin precipitates of secondary phase. During heat treatment in the temperature range of ~750-800 °C, secondary phase is growing, decreasing transport properties. Fig. 1 shows a nanostructure of as-received BSCF 5582 membrane material with superimposed result of

EDS linescan. Secondary phase is enriched in Co and Ba, whereas amount of Sr and Fe is decreased; oxygen content of ~70 % (at) is similar for both phases. Additionally, some Co- rich atomic layers are also present.

In Fig. 2a, the microstructure of BSCF 5582 after thermal treatment at 750 °C/336h is shown. Volume fraction of secondary phase (light grey contrast) is increased in comparison to as-received material. Cobalt and iron distribution map, allowing to distinguish two phases, is shown on Fig. 2b.

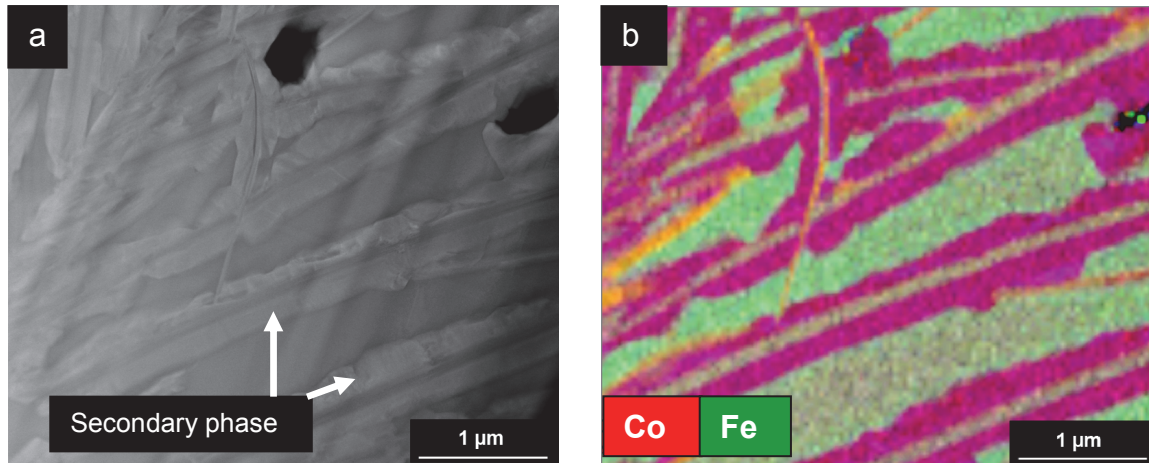


Fig. 2. a) STEM-HAADF image of secondary phase in heat treated (750 °C/336h) BSCF 5582, b) Co- and Fe map, showing distribution of secondary, Co-rich phase

Performed investigation shown that small amount of secondary phase is present even in as-received material. During long-term exposure at temperature range between 750 and 850 °C, BSCF 5582 decomposes. The chemical composition of secondary phase depends on annealing temperature.

Acknowledgement

The support by AGH-UST statutory research project (nr 11.11.110.299) is kindly acknowledged. The authors would like to thank Institute of Energy and Climate Research (IEK-2), Forschungszentrum Juelich, for providing BSCF 5582 material.

References

- [1] R.L. Cornelissen, G.G. Hirs: *Energy Convers. Manage.* Vol. 39 (1998), p.1821.
- [2] J. Kotowicz, S. Michalski: *Energy* Vol. 64 (2014), p. 109.
- [3] S. Baumann, J.M. Serra, M.P. Lobera, S. Escolástico, F. Schulze-Küppers, W.A. Meulenber: *J. Membrane Sci.* Vol. 377 (2011), p. 198.
- [4] B. Rutkowski, J. Malzbender, R.W. Steinbrech, T. Beck, H.J.M. Bouwmeester: *J. Membrane Sci.* Vol. 381 (2011), p. 221.

Intrinsic nano- and microstructures in thermoelectric Ge-Sb-Te materials with various dopants

Robert Schlegel¹, Gerald Wagner¹, Felix Fahrnbauer¹, Tobias Rosenthal², Philipp Urban¹, Christina Fraunhofer² and Oliver Oeckler^{1,*}

¹Leipzig University, Faculty of Chemistry and Mineralogy, Scharnhorststr. 20, 04275 Leipzig, Germany

²LMU Munich, Department of Chemistry, Butenandtstr. 5-13, 81377 Munich, Germany

* oliver.oeckler@gmx.de

In recent years, various approaches to improving thermoelectric materials have been discussed for a broad range of compounds [1]. Among these, there are attempts to create and filling structural voids as well as “top down”, i. e. mechanically induced nanostructures, which are known to decrease the lattice thermal conductivity and thus improve the thermoelectric figure of merit ZT. A simple but efficient way towards intrinsically nanostructured materials involves heterogeneous nanostructures consisting of two thermoelectrically active materials, which may be obtained in situ by phase separation and phase transitions [2]. In the present study, the thermoelectric properties were investigated as a function of composition as well as of nano- and microstructure for three related systems.

Quenching the corresponding melts yields germanium antimony tellurides (GST materials) that form a matrix which is single-crystalline over large sample regions and contains nanoscale skutterudite-type CoSb₃ precipitates. GST can be pseudocubic or trigonal in a metastable state that is characterized by intersecting defect layers which significantly influence the (ZT) value [3]. High-resolution electron microscopy (HRTEM), selected-area electron diffraction (SAED) and an energy dispersive X-ray spectroscopy (EDX) provide information on the relative crystallographic orientation of the phases present, on their unit-cell dimensions, their compositions and their approximate structure. As crystal structure refinement from electron diffraction data is rather imprecise, single-crystalline regions of Ar-ion thinned samples were analyzed with a microfocused synchrotron beam. Suitable crystals with sizes smaller than ~ 2 μm were selected and pre-characterized by means of TEM and EDX. Simulated HRTEM images confirm the atomic structure obtained from synchrotron data. In some samples, oriented intergrowth was occasionally found by SAED. Systematic investigations yield the optimal CoSb₃ content for an enhanced ZT value, which is mainly due to a significant increase of the Seebeck coefficient and a lower thermal conductivity than in “pure” GST materials.

Many research projects have focused on crystalline materials with high electrical conductivities, aiming at the reduction of their thermal conductivity according to the phonon-glass-electron crystal concept. Glasses, on the other hand, exhibit low thermal conductivities and require optimization of the electrical properties. Se analogues of GST, e. g. GeSb₂Se₄, form glasses upon quenching. These are comparable to amorphous (GeSe_{3.5})₈₈Sb₁₂ [4,5] which exhibits an electrical conductivity of about 1300 S/cm. X-ray powder diffraction patterns of such quenched samples exhibit no Bragg reflections and SAED patterns show diffuse rings. Annealing leads to crystallites in an amorphous matrix. Glasses that contain nanoscale crystallites are expected to be promising thermoelectric materials with a pronounced degree of phonon scattering.

The system Sn/Bi/Se presents further unexpected results. Despite the different formula type, the structure of SnBi₄Se₇ corresponds to that of 21R-GeSb₂Te₄ whereas cubic Sn₄Bi₂Se₇ (NaCl type) is similar to the high-temperature phase of GST [6]; HRTEM and SAED show short-range defect ordering in planes perpendicular {111} in a parquet-like arrangement. Annealing of SnBi₄Se₇ leads to unidirectional stacking of defect planes which leads to layers that correspond to those in hypothetical 21R or 15R stacking variants.

References

- [1] J.R. Sootsman, D.Y. Chung, M.G. Kanatzidis: *Angew. Chem. Int. Ed.* Vol. 48 (2009), p. 8616.
- [2] X. Su, H. Li, G. Wang, H. Chi, X. Zhou, X. Tang, Q. Zhang, C. Uher: *Chem. Mater.* Vol. 23 (2011), p. 2948.
- [3] T. Rosenthal, M.N. Schneider, C. Stiewe, M. Döblinger, O. Oeckler: *Chem. Mater.* Vol. 23 (2011), p. 4349.
- [4] A. Giridhar, P.S.L. Narasimham, S. Mahadevan: *J. Non-Cryst. Solids* Vol. 37 (1980), p. 165.
- [5] N. Tohge, T. Minami, Y. Yamamoto, M. Tanaka: *J. Appl. Phys.* Vol. 51 (1980), p. 1048.
- [6] K. Adouby, M.L. Elidrissi Moubtassim, C.P. Vicente, J.C. Jumas, A.A. Touré: *J. Alloys Compd.* Vol. 453 (2008), p. 161.

LSPR of Ag nanostructures investigated with TEM and EELS

Kamil Sobczak^{1,a}, Piotr Dłużewski^{1,b}

¹Institute of Physics Polish Academy of Sciences, al. Lotników 32/46, 02-668 Warsaw, Poland

^aksobczak@ifpan.edu.pl, ^bdłużew@ifpan.edu.pl

It is well known from optical spectroscopy that properties of collective oscillations of conduction electrons in metallic nanostructures are strongly correlated with the size and shape of these structures. These oscillations, known as plasmons, are intensively investigated with Transmission Electron Microscopy (TEM) combined with Electron Energy Loss Spectroscopy (EELS). Joint use of these two techniques allows examination of plasmons coming from a single object with the size less than hundred nanometers, what is not possible in the case of optical methods.

Electron Energy Loss Spectroscopy and Energy Filtered Transmission Electron Microscopy (EFTEM) techniques were applied to investigate the Localized Surface Plasmon Resonance (LSPR) in Ag nanostructures. EELS spectra were collected with a use of monochromated electron beam with energy spread of ~ 0.2 eV. In this work will be presented the results of examination of Ag structures with size of several hundred nanometers and with irregular shapes. The crystal structure and morphology of the Ag objects were determined by High-Resolution Transmission Electron Microscopy. The obtained results will be compared with theoretical predictions.

Acknowledge

This research was co-financed by the European Regional Development Fund within the Innovative Economy Operational Programme 2007-2013 “Analytical high resolution transmission electron microscope for nanoscience, nanotechnology and spintronics” No POIG.02.01-00-14-032/08 and National Science Centre 2013-2015 No. UMO -2012/05/D/ST3/03161.

Structure determination of apatite and Ag-Cu-Zr alloys using PED and diffraction tomography techniques

Ildikó Cora^{1,2,a}, Péter Pekker¹, István Dódony² and Dóra Janovszky¹

¹Hungarian Academy of Sciences-University of Miskolc, Materials Science Research Group, H-3515 Hungary, Miskolc, Egyetemváros

²Eötvös Loránd University, H-1117 Hungary, Budapest, Pázmány P. stny. 1/c

^acoraildiko@gmail.com

Introduction and methodology

The need for characterization and structure determination of nanometer sized materials (like metallic alloys) is rapidly growing. Electron crystallographic methods are promising approaches in characterizing their crystal structures. The recently developed techniques of electron diffraction make it possible to determine the structure of submicron sized single crystals. With precession electron diffraction (PED) technique [1,2,3] the dynamical scattering (as the main disadvantage of electron diffraction) can be drastically reduced producing “quasi-kinematical” intensities. Diffraction tomography enables the mapping of wide volume of the reciprocal space. The reconstruction of the reciprocal space and the extraction of hkl – intensity dataset were produced by ADT3D software [4,5]. For structure determination and refinement we used SIR2011 [6] and SHELXL97 [7] software packages. The examined samples were: CO₃-containing hydroxyl-apatite and two Ag-Cu-Zr alloys.

Results

Hydroxyl-apatite from Erdősmecke (Hungary) contains minor amount of CO₃. The aims were to determine the crystal structure of apatite and the localization of the CO₃-group in the structure. After identifying the space group symmetry using PED relative intensity data and HRTEM images we can start the determination process.

The other Cu-Zr-Ag ternary system belongs to the Cu-based bulk amorphisable alloy systems. In the last three decades intensive research has been carried out on amorphous alloys because of their specific properties (i.e. high strength, good corrosion resistance, good magnetic properties etc.). The aim of our study is to determine and refine the crystal structure of two, unknown Cu-rich compounds of this ternary system: AgCu₄Zr cubic phase and the Ag-containing Cu₁₀Zr₇.

Acknowledgements

The research realized by Ildikó Cora was supported by the European Union and the State of Hungary, co-financed by the European Social Fund in the framework of TÁMOP 4.2.4. A/1-11-1-2012-0001 ‘National Excellence Program’. The infrastructural support of the described work was carried out as part of the TÁMOP-4.2.2/B-10/1-2010-0008 project in the framework of the NewHungarian Development Plan. The realization of this project is supported by the European Union, co-financed by the European Social Fund.

References

- [1] R. Vincent and P.A. Midgley: Ultramicroscopy Vol. 53 (1994), p. 271.
- [2] C.S. Own: System Design and Verification of The Precession Electron Diffraction Technique. (PhD Thesis, Northwestern University 1987).
- [3] A. Avilov, K. Kuligin, S. Nicolopoulos, M. Nickolskiy, K. Boulahya, J. Portillo, G. Lepeshov, B. Sobolev, J.P. Collette, N. Martin, A.C. Robins and P. Fischione: Ultramicroscopy Vol. 107 (2007), p. 431.
- [4] U. Kolb, T. Gorelik, C. Kübel, M.T. Otten and D. Hubert: Ultramicroscopy Vol. 107 (2007), p. 507.
- [5] U. Kolb, T. Gorelik and M.T. Otten: Ultramicroscopy Vol. 108 (2008), p. 763.
- [6] M.C. Burla, R. Caliendo, M. Camalli, B. Carrozzini, G.L. Cascarano, C. Giacovazzo, M. Mallamo, A. Mazzone, G. Polidori, S. Diligi and R. Spagna: J. Appl. Cryst. Vol. 45 (2012), p. 357.
- [7] G. M. Sheldrick: Acta Cryst. Vol. A64 (2008), p. 112.

STEM characterization of TiO₂ and Al₂O₃ oxides produced by electrochemical oxidation metallic substrate

Mariusz Andrzejczuk^{1,a}, Agata Roguska², Marcin Pisarek²,
Małgorzata Lewandowska¹, Krzysztof Jan Kurzydłowski¹

¹Faculty of Materials Science and Engineering, Warsaw University of Technology, Woloska 141, 02–507 Warsaw, Poland

²Institute of Physical Chemistry, Polish Academy of Sciences, Kasprzaka 44/52, 01–224 Warsaw, Poland

^amandrzejczuk@inmat.pw.edu.pl

Metal oxide nanotubes have become very attractive material with potential applications in nanoelectronics, catalysis, energy etc. However, their properties depend on morphology which results from fabrication conditions. Electrochemical oxidation of metal substrate is excellent method for preparation structurally well-defined metal oxide nanotubes with defined diameter and length [1,2]. In this work titania nanotubes 70 nm in diameter and alumina nanotubes 60 nm in diameter were fabricated by electrochemical oxidation of metal at voltage 20 V in electrolyte. Morphology of TiO₂ and Al₂O₃ nanotubes were characterized by scanning transmission electron microscopy – STEM (Fig.1). Metal oxide interfaces were analyzed by X-ray energy dispersive spectrometer (EDS) and electron energy loss spectroscopy (EELS). In order to obtain three-dimensional structure information a high angle annular dark field scanning transmission electron microscopy (HAADF-STEM) tilt series were recorded. As the effect different morphologies of different substrates nanotubes were observed.

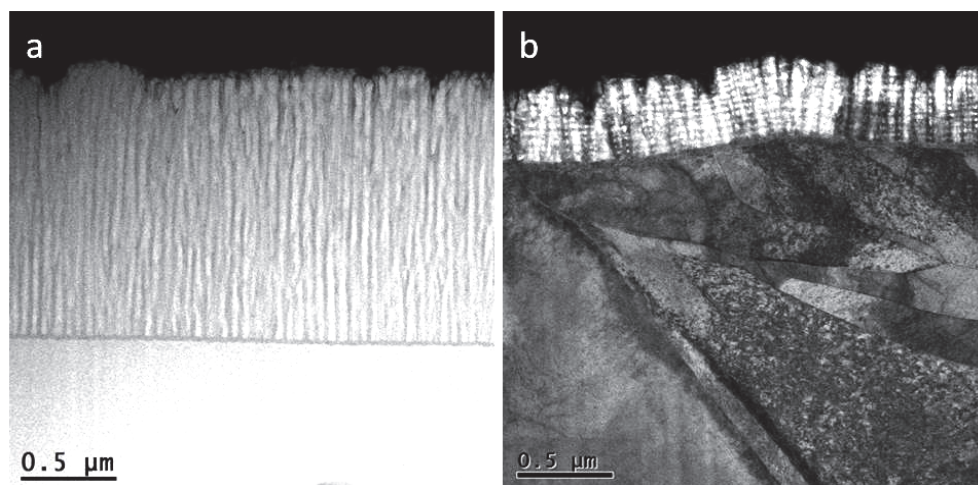


Fig. 1. STEM images of (a) Al₂O₃/Al and (b) TiO₂/Ti interface

References

- [1] A. Roguska, M. Pisarek, M. Andrzejczuk, M. Dolata, M. Lewandowska, & M. Janik-Czachor: *Mat. Sci. Eng. C* 31(5) (2011), p. 906.
- [2] M. Pisarek, A. Roguska, A. Kudelski, M. Andrzejczuk, M. Janik-Czachor, K.J. Kurzydłowski: *Mater. Chem. Phys.* 139 (1) (2013), p. 55.

In situ annealing together with orientation mapping in TEM and SEM as a method for complex characterization of recrystallization process

Magdalena Bieda^{1,a}, Krzysztof Sztwiertnia^{1,b}

¹ Institute of Metallurgy and Materials Science, Polish Academy of Sciences, 25 Reymonta St., Krakow, Poland

^anmbieda@imim-pan.krakow.pl,

^bk.sztwiertnia@imim.pl

Additional equipment in transmission electron microscopes (TEM) and scanning electron microscopes (SEM) as in situ holders and stages give an opportunity for complex investigation of materials during e.g. mechanical tests, heating. In situ devices can be applied for many material studies and what is most important thanks to them unique data can be obtained about phenomena changing in temperature or time.

In situ experiments in electron microscopy were considered difficult and unreliable, mainly because of different conditions of sample preparation and observation which can influence the behaviour of the material. Existence of one (in SEM) or two (in TEM) free surfaces makes it possible to monitor some differences in processes occurred in bulk material then in microscopic sample [1,2]. Fortunately, with taking into account many factors which can influence in situ measurements, there can be assured proper conditions for making them a source of scientific observation [3]. In order to avoid artificial results and confirm observation of the in situ annealing supplementary calorimetric studies should be performed.

New benefits of in situ experiments come from development of Orientation Microscopy in TEM and SEM. Combined in situ study and acquisition of crystallographic data from the chosen areas of the sample can improve the quality and reliability of investigations and supplied interesting results.

For investigation recrystallization processes in material by means of in situ experiments aluminium alloy 6013 was chosen. This material represents a group of materials with characteristic bimodal second phase distribution that can influence material behaviour during annealing. This complicated process can be visualised and characterised step by step investigation in TEM and SEM by combined in situ heating and orientation mapping.

Aluminium alloy 6013 was solution heat treated, aged and reversibly cold-rolled up to 90%. After thermal treatment the uniform bimodal distribution of stable fine ($\ll 1\mu\text{m}$) and coarse ($>1\mu\text{m}$) particles was obtained. The deformed material was investigated by heating holder in TEM and a new in situ stage in SEM (GATAN Murano 525). Orientation measurements were performed by TEM system [4] and SEM EBSD TSL OIM Analysis system. In order to confirm results parallel calorimetric studies were done.

Analysis of the orientations maps were presented. The mobility of grain boundaries and texture on each step of annealing were calculated from orientation maps in TEM and SEM. The orientation relationships between the crystallites from the deformation zones (before annealing) and the new grains appearing in these regions after annealing were obtained. Results from TEM were mainly used for deformation zones characterization because of the grain size in these areas was of nanometres. Investigations in SEM allowed for characterization of larger areas during annealing and obtain better statistical data.

The presented results showed that recrystallization process in the material can be considered as a number of partly overlapping processes that proceed in two stages. In the first stage the deformation zones around large second phase particles act as sites for PSN (particle-stimulated nucleation). This nucleation is accompanied by the growth of nuclei. However, the migration of high angle grain boundaries only occurs in deformation zones. Enlargement of new grains in the matrix was also observed. In the second stage, high angle grain boundaries migrated in the direction of the high

orientation gradient. This migration was limited in normal direction to areas of the deformed matrix between bands of new grain formation in the initial stage of recrystallization.

Joint methods OM and in situ annealing in TEM and SEM confirmed by calorimetric studies were powerful tools to provide complex information about material behaviour during annealing. Transition from SEM measurements to TEM measurements improves the resolution capability down to a few square nanometres. Both instruments can be used for complementary analysis of crystalline materials at the "micro" and "nano" scale. It was possible to obtain information about grain distribution, misorientation between grains, the local orientation distribution function and the misorientation distribution function during stages of recrystallization process.

References

- [1] W.W. Mullins: Acta Metall. 6 (1958), p.414.
- [2] F. J. Humphreys, M. Hatherly: *Recrystallization and Related Annealing Phenomena* Pergamon (2002).
- [3] K. Sztwiertnia, F. Haessner: Mater. Sci. Forum 157-162, (1994), p.1069.
- [4] M. Bieda: Sol. St. Phenom. 186 (2012), p. 53.

Morphology of precipitates in 3xxx alloys with zirconium

Mariusz Bigaj^{1,a}, Monika Mitka^{1,b}, Sonia Boczekal^{1,c}, Zbigniew Zamkotowicz¹,
Janusz Żelechowski¹ and Maciej Gawlik¹

¹Institute of Non-Ferrous Metals in Gliwice Light Metals Division ul. Pilsudskiego 19, 32-050 Skawina, Poland
^ambigaj@imn.skawina.pl, ^bmmitka@imn.skawina.pl, ^csboczekal@imn.skawina.pl

Introduction

The study presents the results of microstructure examinations and phase identification of precipitates in zirconium-containing AlMn alloys after heat treatment and rolling. Chemical composition in microareas was determined by EDX on a scanning electron microscope and by STEM on a transmission electron microscope. Phase identification was carried out using EBSD method, X-ray diffraction and X-ray phase analysis. Studies have shown that due to the decomposition of the solid solution, an Al₆Mn phase was formed in the melt. In the case of an addition of silicon and iron, it was the α-AlFeSi phase. Structure examined by TEM showed the presence of fine-dispersed spherical precipitates of zirconium. In the alloy with an addition of silicon and magnesium, a large number of the precipitates of an Mg₂Si phase was also detected.

Methodology

Tests were performed on the AlMnZr, AlMnMgZr and AlMnMgSiZr alloys after heat treatment and rolling.

The heat treatment consisted in heating the samples at a rate of 50°C/h to 450°C, holding for 12 hours and cooling in water. Samples were rolled with the deformation $\epsilon = 50\%$ (from the thickness of 10 to 5 mm).

Samples for TEM and SEM examinations were prepared by mechanical grinding, polishing, and etching using ion beam milling.

Results and conclusions

The structure of AlMnZr sample observed under SEM and TEM shows the intermetallic phases containing AlFeMn located at grain boundaries, and unevenly distributed fine lamellar precipitates containing AlMnSi and AlMnSiFe (Figure 1a). Inside the grains, fine spherical precipitates of zirconium are present in a size of about 20 nm (Figure 2A). X-ray phase analysis revealed the presence of Al₅₇Mn₁₂ phase identical with the Al₆Mn phase.

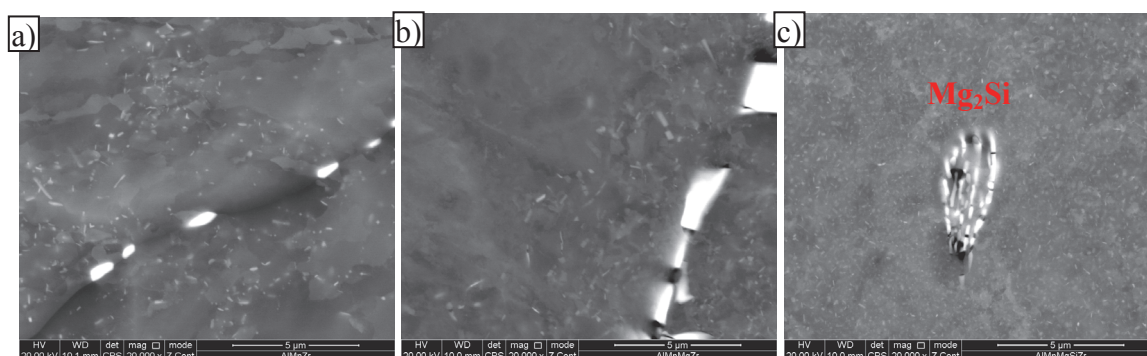


Fig. 1. SEM microstructure observed in CBS mode on samples of the following alloys: AlMnZr (a), AlMnMgZr (b) and AlMnMgSiZr (c)

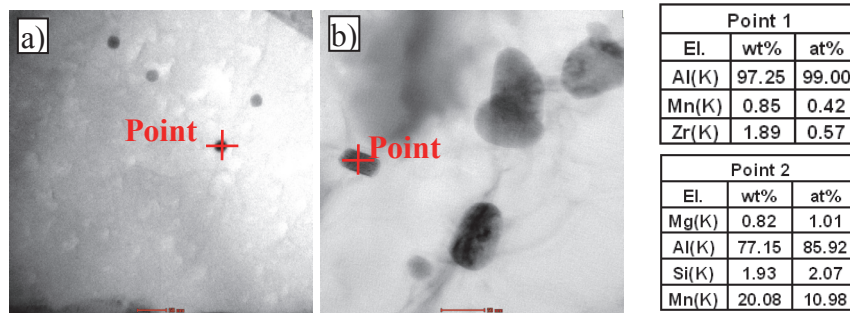


Fig. 2. TEM microstructure with well visible precipitates of zirconium in AlMnZr alloy (a) and lamellar precipitates of nanometric size in the sample of AlMnMgZr alloy (b)

The sample of AlMnMgZr alloy was characterised by an increased concentration of lamellar precipitates at the grain boundaries (Figure 2b). The EBSD phase identification method revealed the presence of $Al_{4.01}MnSi_{0.74}$ phase - cubic (Th) [m3], with lattice parameters $a = b = c = 12.643 \text{ \AA}$, $CI = 0.086$ (Figure 3) [1].

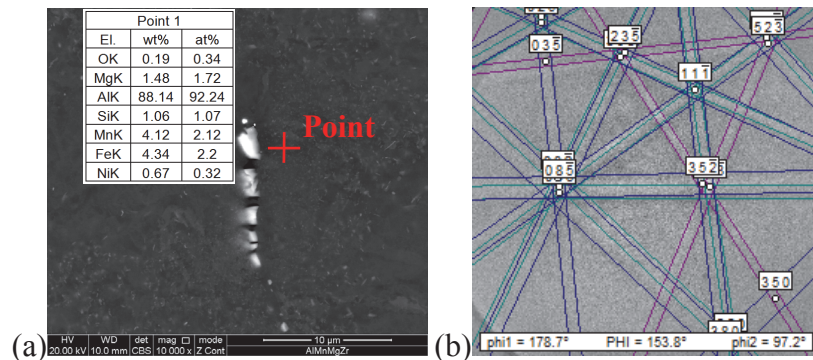


Fig. 3. SEM microstructure with EDX chemical analysis in microregions (a) and Kikuchi line image of $Al_{4.01}MnSi_{0.74}$ phase (b) in AlMnMgZr alloy

Studies carried out on a sample of AlMnMgSiZr alloy additionally showed the presence of a large amount of precipitates containing silicon, which were identified as Mg_2Si phase (Figure 1c). In this alloy, the lamellar precipitates are spread evenly inside the grains.

References

- [1] The International Centre for Diffraction Data, PDF-2 Release 2011, ICDD (2011).

Indium segregation during growth of InAlN layers – TEM observations

Jolanta Borysiuk^{1,2,a}, Kamil Sobczak^{1,b}, Agata Kamińska^{1,c}, Elżbieta Jezierska^{3,d}, Akio Yamamoto^{4,e}, H.P. David Schenk^{5,f} and Tadeusz Suski^{6,g}

¹Institute of Physics, Polish Academy of Sciences, Al. Lotników 32/46, 02-668 Warsaw, Poland

²Faculty of Physics, University of Warsaw, Hoża 69, 00-681 Warsaw, Poland

³Faculty of Materials Science and Engineering, Warsaw University of Technology, Wołoska 141, 02-507 Warsaw, Poland

⁴Department of Electrical and Electronics Engineering, University of Fukui, 3-9-1 Bunkyo, Fukui 910-8507, Japan

⁵SOITEC Specialty Electronics, Place Marcel Rebuffat, Z.A. de Courtaboeuf 7, 91140 Villejust, France

⁶Institute of High Pressure Physics, Polish Academy of Sciences, Sokołowska 29/37, 01-919 Warsaw, Poland

^aborysiuk@ifpan.edu.pl, ^bksobczak@ifpan.edu.pl, ^ckaminska@ifpan.edu.pl, ^djeziers@inmat.pw.edu.pl,

^eayamamoto@u-fukui.ac.jp, ^fdavid.schenk@soitec.com, ^gtadek@unipress.waw.pl

Indium segregation in high In content InAlN layers grown on GaN/sapphire templates was investigated by high-resolution transmission electron microscopy (HRTEM). Low In content samples show no indication of preferential incorporation of indium, proving that compositionally uniform layers and structures could be grown. For high content of indium, above 20 at% on average, the growth becomes unstable, leading to a preferential incorporation of In at some orientations. The V-shaped In-rich structures were observed, resulting in a preferential indium segregation at the sides of the structures.

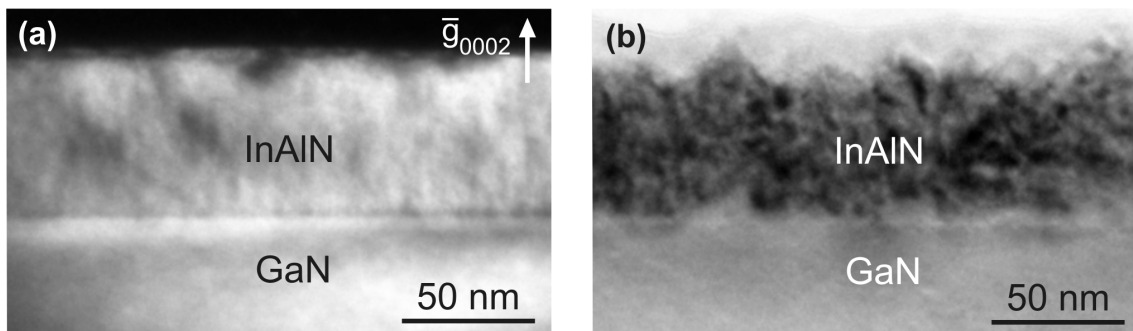


Fig. Cross-sectional TEM images of InAlN layers with indium content of 25% (a) and 28% (b)

This work has been partially financed by the National Science Centre (Poland) support by grants: DEC-2011/03/B/ST5/02698 and DEC-2012/05/B/ST3/03113.

Effect of electron energy on the structural evolution of functional perovskite $\text{La}_{0.6}\text{Ca}_{0.4}\text{CoO}_3$ thin films produced by pulsed electron deposition (PED) technique

Łukasz Cieniek

AGH University of Science and Technology, Faculty of Metals Engineering and Industrial Computer Science,
al. A. Mickiewicza 30, 30-059 Krakow, POLAND

lukasz.cieniek@agh.edu.pl

Introduction

The Pulsed Electron Deposition (PED) known also as an channelspark (CS) deposition is a highly efficient and low cost technique using ablation for producing stoichiometric thin films of complex oxides, alloys and novel polymers on desired substrates. The process is similar to the UV-laser ablation but it is initiated by a pulsed high current and magnetically self pinched electron beam. Typical PED system consists of two main components: vacuum chamber and the electron source (gun) which is equipped with a special type of the hollow cathode. Construction details and principle of operation of this solution are explained elsewhere [1]. Operating parameters are as follows: energy of electrons $8 \div 20$ kV, pulse width ~ 100 ns, pulse repetition rate max. 10 Hz, single pulse energy $0.1 \div 0.8$ J, beam cross section min. 6×10^{-2} cm², pulse power density max. 1.3×10^8 W/cm² and working gas pressure $5 \div 20$ mTorr ($6 \times 10^{-3} \div 3 \times 10^{-2}$ mbar). With the high power density generated at the target surface its thermodynamic properties such as the melting point and specific heat become unimportant for the evaporation process. Compared with the laser ablation system the capital costs of the PED system are 10 to 20 times lower. The possibility of ablation of laser-transparent target materials (glass, hydrocarbon or fluorocarbon polymers etc) is also a significant advantage of the electron deposition. The schematic diagram of the PED system used in this study is shown in the Fig. 1.

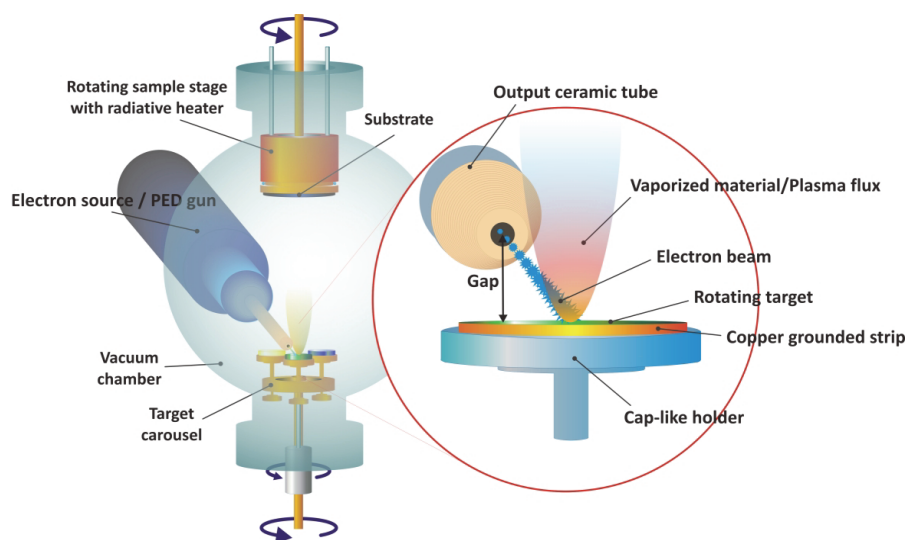


Fig. 1. Neocera's PEBS-20 electron source with the Pioneer 180 vacuum chamber setup

Experimental results

LaCoO_3 based perovskites are known as multi functional materials with unique electrical, catalytic and mechanical properties described in numerous publications [2, 3]. In this study thin films of $\text{La}_{0.6}\text{Ca}_{0.4}\text{CoO}_3$ were deposited on the [001] MgO substrates by PED technique. Each sample was prepared in oxygen atmosphere ($\sim 7 \times 10^{-3}$ Torr) using parameters summarized below.

Table 1. Parameters of $\text{La}_{0.6}\text{Ca}_{0.4}\text{CoO}_3$ thin films pulsed electron deposition process

| Sample | A | B | C |
|---------------------------|--------|-------|-------|
| Electron energy | 10 kV | 12 kV | 14 kV |
| Gap | ~ 3 mm | | |
| Target-substrate distance | 70 mm | 70 mm | 80 mm |
| Repetition rate | 5 Hz | | |
| Number of shots | 72 000 | | |

For structural characterisation of obtained thin films the scanning electron microscopy (FEI Nova NanoSEM 450 equipped with EDAX Energy Dispersive Spectroscopy Detector), transmission electron microscopy (Jeol 200CX and JEM-2010ARP with EDX INCA Oxford Instruments) and X-ray diffraction (XRD system EMPYREAN, working with $\lambda_{\text{Cu}} = 0.154$ nm and constant take off angle $\alpha = 3^\circ$) investigations have been used to reveal the microstructural details, chemical point/area microanalysis and phase composition. The atomic force microscopy (Bruker Dimension Icon SPM System with NanoScope V Controller) and scratch tests (CSM Instruments NHT-NST) have been performed to specify the surface topography, roughness parameters and the adhesion forces of the deposited perovskite thin films.

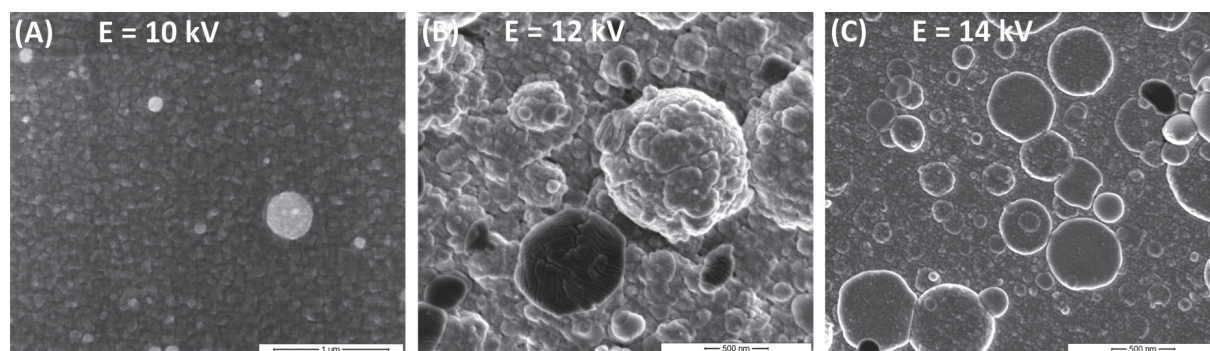


Fig. 2. SEM images of $\text{La}_{0.6}\text{Ca}_{0.4}\text{CoO}_3$ thin films

As can be seen in the Fig. 2 the structure of perovskite thin films is highly influenced by the energy of electrons. Thin films thickness and their smoothness can be controlled by increasing the target-substrate distance. Thorough analysis of the PED process parameters allows to determine the optimal conditions for the deposition of high quality $\text{La}_{0.6}\text{Ca}_{0.4}\text{CoO}_3$ thin films.

References

- [1] G. Müller, M. Konijnenberg, G. Krafft, C. Schultheiss: Deposition by means of pulsed electron beam ablation, Science and Technology of Thin Films, edited by F. C. Maticotta, G. Ottaviani, World Scientific (1995), p. 89 -119.
- [2] R.M. Navarro, M.C. Alvarez-Galvan, J.A. Villoria, I.D. González-Jiménez, F. Rosa, J.L.G. Fierro: Appl. Catal. B: Environ. 73, 3–4 (2007), p. 247.
- [3] V. Øyngarden, H. L. Lein, T. Grande: J. Sol. St. Chem. 192 (2012), p. 246.

Microstructure of annealed AA3003 alloy after constrained groove pressing

Miroslav Cieslar^{1,a}, Jan Bajer^{1,b}, Michaela Poková^{1,c}, Mariia Zimina^{1,d},
Jozef Zrník^{2,e}

¹Charles University in Prague, Faculty of Mathematics and Physics, Ke Karlovu 5, CZ-121 16 Prague 2, Czech Republic

²COMTES FHT a.s., Průmyslová 995, CZ-334 41 Dobřany, Czech Republic

^acieslar@met.mff.cuni.cz, ^bJanBajer69@seznam.cz, ^cpokova@karlov.mff.cuni.cz, ^dm.zimina@seznam.cz, ^ejzrnik@comtesfht.cz

Introduction

Different severe plastic deformation processes (SPD) have been developed for imposing high strain into a metal [1] and several methods have been developed for the SPD of plate or sheet materials. They are mainly the accumulative roll-bonding (ARB), repetitive corrugation and straightening (RCS) and constrained groove rolling (CGR) or its discontinuous modification constrained groove pressing (CGP) [2-4]. The effectiveness of CGP process in reducing the grain size from tens of micrometers to sub-micrometers has been demonstrated in several conventionally cast and rolled aluminum materials [5]. The basic principle of the SPD process consists in inducing the extremely high plastic strain into the material resulting in a substantial grain refinement and improved strengths. The homogeneity and final thermal stability of the grain structure depends on the processing temperature, number of CGP cycles but also on the grain size of the initial material and the size and distribution of coarse primary particles which are generally present in the ingot cast and cold-rolled sheets. Therefore the thermal stability and homogeneity is improved in materials with fine particles and small grain size which is typical for continuously twin-roll cast (TRC) aluminium alloys.

Results

TRC sheets from the AA3003 alloy modified by a small addition of Zr were CGP processed and the homogeneity of as-prepared materials and their thermal stability were studied by light optical microscopy and electron microscopy. Microhardness mappings were used for the correlation of non-uniformity of mechanical properties and observed microstructure. Fig. 1 shows light optical micrograph and microhardness distribution in the material after 3 CGP passes, Fig. 2 shows the evolution of deformation substructure in the specimen after 1 and 3 CGP passes, respectively. In-situ TEM in the heating stage was used for the study of recovery and recrystallization in the material.

Summary

Remarkable inhomogeneity of mechanical properties mapped by microhardness measurements was observed in aluminum sheets after CGP processing. This distribution of microhardness corresponds with non-uniform distribution of pure shear strain and bending which is characteristic for this type of SPD processing. The observed inhomogeneity of mechanical properties is always closely related to the resulting microstructure, which undergo significant changes during annealing.

Acknowledgment

The authors are grateful to the financial support from the Czech Science Foundation under the project P107-12-0921 and to the grant SVV-2014-260091.

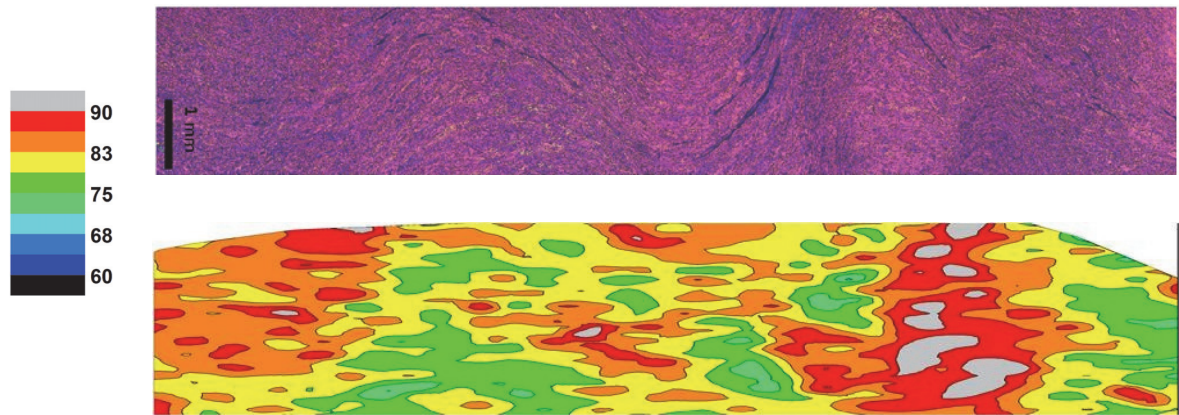


Fig. 1. Light optical micrograph of the AW3003 sheet after 3 CGP cycles (top) and distribution of microhardness HV0.1 (in MPa) in the same specimen (bottom)

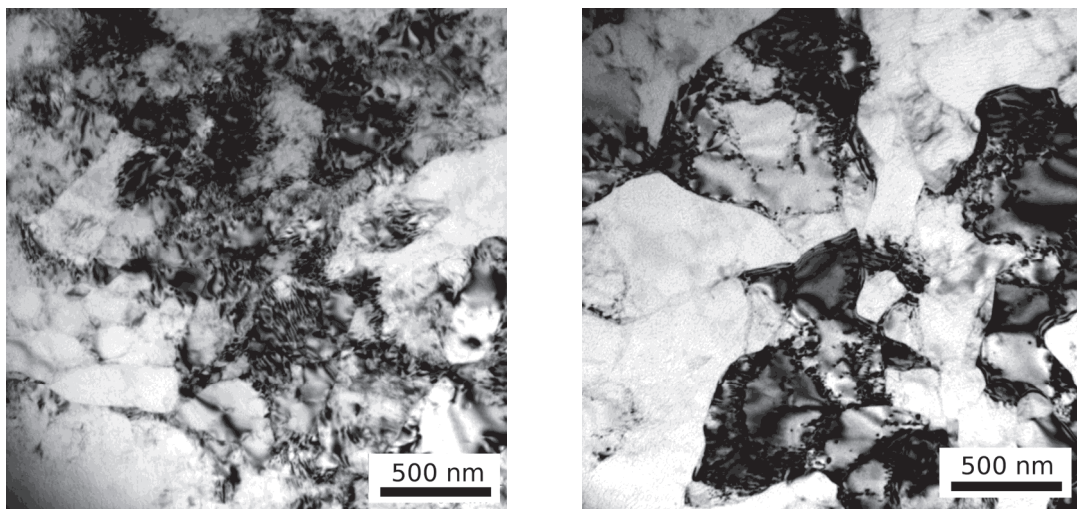


Fig. 2. Substructure in the specimen after 1 (left) and 3 (right) CGP passes

References

- [1] R. Z. Valiev, A. V. Korznikov, and R. R. Mulyukov: *Mater. Sci. Eng. A* 168 (1993), p.141.
- [2] N. Tsuji, Y. Saito, H. Utsunomiya, S. Tanigawa: *Scr. Mater.* 40 (1999), p. 1221.
- [3] Y.T. Zhu, H. Jiang, J.Y. Huang, T.C. Lowe: *Mater. Trans. A* 32 (2001), p. 1559.
- [4] D.H. Shin, J.-J. Park, Y.-S. Kim, K.-T. Park: *Mater. Sci. Eng. A* 328 (2002), p. 98.
- [5] J. Zrník, J. Kovařík, Z. Nový, M. Cieslar: *Mater. Sci. Eng. A* 503 (2009), p. 126.

Phase composition and microstructure of the alloys from Ni₃Al-Ni₃Sn system after rapid quenching and decomposition

Tomasz Czeppe^a, Lidia Lityńska-Dobrzyńska^b, Anna Sypień^c, Grzegorz Garzeł^d, Zbigniew Świątek^e, Anna Wierzbicka-Miernik^f, Anna Góral^g

Inst. of Metallurgy and Materials Sciences, PAS, Reymonta 25 St. 30-059 Krakow, Poland

^at.czeppe@imim.pl, ^bl.litynska@imim.pl, ^ca.sypien@imim.pl, ^dg.garzel@imim.pl, ^ez.swiatek@imim.pl, ^fa.wierzbicka@imim.pl, ^ga.goral@imim.pl

Introduction

From the basic knowledge point of view there is some interest concerning formation of the low-temperature equilibrium phase composition and microstructure in case of the alloys containing two high temperature intermetallic compounds, connected by the continuous phase field at the room temperature cross-section through phase diagram. The examples are alloys of the composition Ni₇₅(Al, V)₂₅ decomposing at 1273K into mixture of Ni₃Al and Ni₃V phases [1]. After the eutectoid decomposition, characteristic microstructure results, formed by the equilibrium of the highly ordered, dens packed, phases of L₁₂ and D0₂₂ with structures, reviling high degree of coherence at the interfaces as well [1, 2]. The path of the formation of such microstructures remains not completely clear, depending on the long time annealing, which finally leads to the lamellar type microstructure [1], revealing also good creep properties [2]. The present paper concentrates on the scanning and electron microscopy studies, supported also by the X-ray phase analysis of the phase composition and microstructure in case of the Ni₇₅(Al, Sn)₂₅ alloys achieved by high rate cooling from the liquid state and annealed. The papers concerning decomposition process in alloys of such composition are mostly absent in the available literature.

Experimental and results

The composition of the investigated alloys was Ni₇₅(Al_{25-x}Sn_x), x: 5, 10, 15, 20. The alloys were prepared by the cold crucible levitation melting (CCLM) followed by direct cooling down in the copper levitator at purified Ar atmosphere. Later samples were re-melted and rapidly cooled down in water or subdued to the long homogenization at 773K. As the respectful temperature cross section through phase equilibrium diagram is not known, thermal analysis (TA) in heating was performed. Microstructure, chemical and phase composition of the samples were studied with the Scanning Electron Microscopy (SEM) and X-ray phase analysis (XRD) and transmission electron microscopy (TEM).

In case of the samples cooled with very high (about 4800K/min) and moderate rate, the XRD phase identification and SEM microstructures suggested that Ni₃Al phase crystallizes at higher temperatures and remains in equilibrium with the high temperature solid solution Ni(Al, Sn). Under conditions of rapid and moderate cooling rates the solid solution remains stable down to RT. The EDX composition analysis showed that Ni₃Al phase remains enriched in Sn up to 2 at.%, while Ni(Al, Sn) may contain up to 10 at.% Al, much more than RT solubility of Al in Ni₃Sn phase. In both cases of moderate and rapid cooling the microstructure remains similar that is consisting on dendritic morphology of Ni₃Al phase, transforming into dendritic-equiaxial grains and grain boundary phase with the increase of the Sn content. The main difference in case of the rapidly cooled sample was more dispersed elements of the microstructure (Fig.1).

After annealing of the samples at 773K by 670 hours complete decomposition into mixture of the Ni₃Al and Ni₃Sn phases, slightly enriched in Sn and Al respectively should be expected [3]. However, much more complicated phase composition and microstructure was discovered. In case of the alloys with the high Al content, except Ni₃Al(Sn) phase two different phases of similar composition, but

enriched in Sn, of regular and hexagonal symmetry were noticed. In the case of Sn rich samples solid solution of the regular structure and Al content up to 16 at.% and a second Ni_3Sn phase, of hexagonal structure but different lattice parameters existed (Fig.1). The presence of the minor metastable phases caused more complicated microstructure in the micrometer scale, which may strongly influence mechanical properties of the alloys.

Conclusions

The $\text{Ni}_{75}(\text{Al}, \text{Sn})_{25}$ alloys, both crystallized with relatively high rate and annealed revealed some amount of metastable phases, predominantly of the $\text{Ni}_3(\text{X}, \text{Y})$ ($\text{X}, \text{Y}=\text{Al}, \text{Sn}$) structure and composition, but much more enriched in unexpected element than results from the equilibrium phase diagram. This leads to the complicated microstructure in the SEM and TEM scale.

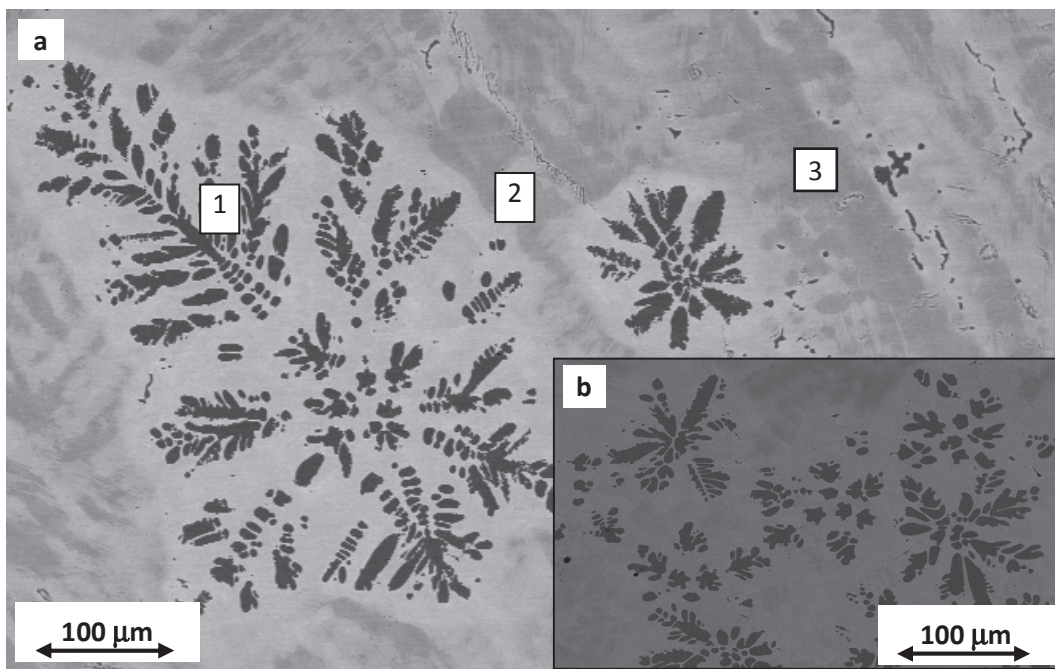


Fig. 1. SEM microstructures of the $\text{Ni}_{75}\text{Sn}_{15}\text{Al}_{10}$ alloy a) sample annealed (phases: 1 - Ni_3Al , 2 - Ni_3Sn , 3 - $\text{Ni}_3(\text{Al}, \text{Sn})$); b) sample quenched in water – the elements of microstructure smaller 4 times

Acknowledgement

The work was financed by the Research Program of IMMS PAS Krakow, as the project Z-9/2012,2013; The measurements were performed in the Accredited Testing Laboratories of the Institute of Metallurgy and Materials Sciences of the Polish Academy of Sciences.

References

- [1] M. Takeyama, M. Kikuchi: Intermetallics Vol. 6 (1998), p. 573.
- [2] S. Shibuya, Y. Kaneno, M. Yoshida, T. Shishido T. Takasugi: Intermetallics Vol. 15 (2007), p. 119.
- [3] A. Prince: in: Ternary Alloys, A Comprehensive Compendium., edited by G. Petzow, G. Effenberg, vol. 4 p. 478 VCH Publishers New York (USA)(1991).

Identification of phases in bearing steel 67SiMnCr6-6-4 on the basis of the transmission electron microscopy study

Karolina Dudzińska^{1,a}, Julita Smalc-Koziorowska^{2,b}, Emilia Skolek,
Wiesław Światnicki^{3,c}

¹Warsaw University of Technology, Faculty of Materials Science and Engineering,
Wolosa 141,02-507 Warszawa, Polska

^akarolina.dudzinska@nanostal.eu, ^bjulitasmalc@wp.pl, ^cemilia.skolek.@nanostal.eu,
^dwieslaw.swiatnicki.@nanostal.eu

Introduction

The microstructure of alloy steels after various thermal treatment processes is hardly definable and identifiable by typical metallographic examinations with use of light microscopy or scanning electron microscopy. The problem is even more complex in the case of steels with nanocrystalline structure. In present study a transmission electron microscopy (TEM) methods have been used to obtain detailed data on the structure of 67SiMnCr6-6-4 bearing steel submitted to 3 variants of nanostructuring processes. As a results a nanobainitic microstructures were produced with various structural characteristics.

Test methodology and results

Steel samples were subjected to austenitizing followed by quenching with isothermal annealing performed at three different temperatures in bainitic transformation range. The obtained structures were examined using the light microscope and transmission electron microscope operating at 120 kV. The stereological analysis of the obtained structures was conducted on the basis of the collected photographic documentation.

The use of light microscopy permitted us to characterise steel microstructure only generally and pictorially. TEM examination allowed us to determine the detailed structural features.

It was revealed that steel samples subjected to nanostructuring heat treatment processes had a nanobainitic structure containing residual austenite. After isothermal annealing with a temperature plateau at 220°C the structure is composed of thin bainitic ferrite plates separated by residual austenite layers. Exact phase identification revealed also fine lamellar carbides inside the plates of ferrite (Fig. 1).

The microstructure observed after isothermal annealing with a temperature plateau at 260°C contained wider but still nanometric plates of bainitic ferrite. Residual austenite layers were present between the ferrite plates. After such heat treatment we found also residual austenite in form of small blocks with an average area of $0.51 \mu\text{m}^2$.

A sample annealed isothermally at 300°C had a nanobainitic structure composed of ferrite plates separated by layers of a residual austenite which does not contain any carbide precipitations (Fig. 2). The larger areas of austenite blocks (of $2.79 \mu\text{m}^2$) were observed in the structure.

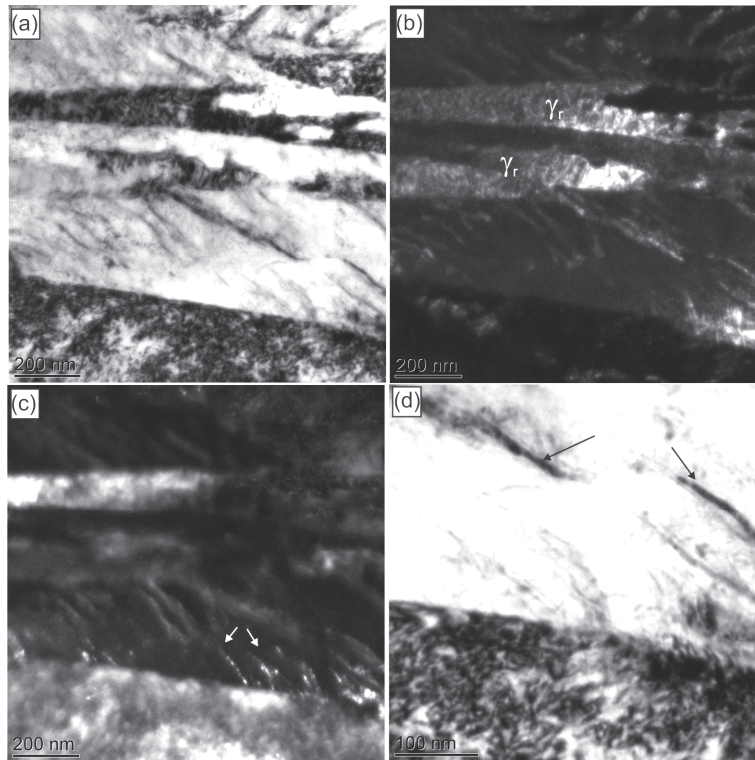


Fig. 1. (a) Microstructure of the 67SiMnCr6-6-4 steel after isothermal hardening with a temperature plateau at 220°C, observed in a bright field; (b) dark field image of the γ_r residual austenite grains; (c) dark field image of carbide separations (marked with arrows) in ferritic grains; (d) zoomed bright field picture of carbide separations

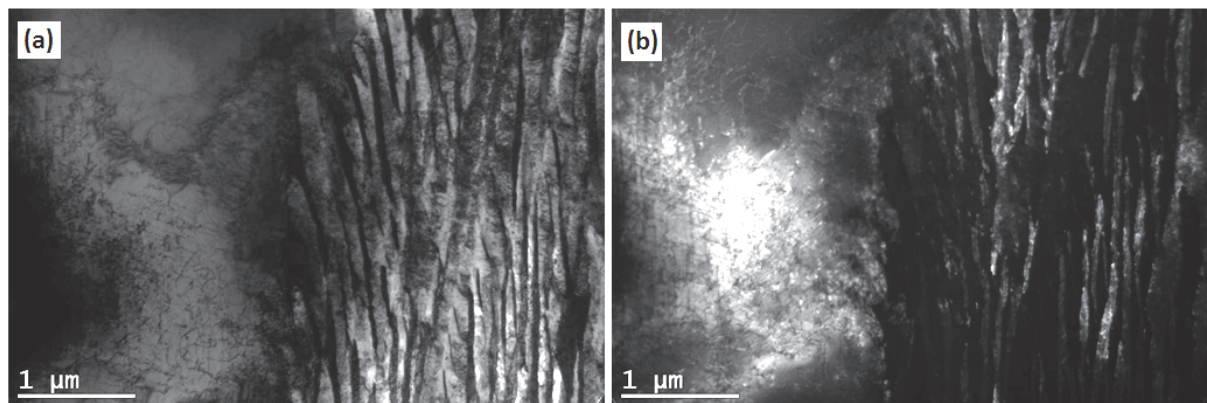


Fig. 2. Microstructure of the 67SiMnCr6-6-4 steel after isothermal hardening with a temperature plateau at 300°C, observed in a bright field; (b) dark field image of the γ_r residual austenite block

Conclusions

TEM examination allowed us one to carry out a detailed identification and exhaustive characterization of phases presented in the isothermally annealed 67SiMnCr6-6-4 bearing steel. Utilization of heat treatment consisting in austenitizing and subsequent isothermal annealing at 220°C, 260°C and 320°C led to nanobainitic structure composed of thin bainitic ferrite plates separated by nanometric austenite layers. Samples hardened isothermally at 220°C exhibited the presence of thin lamellar carbids inside the ferritic zones. This effect has not been observed for samples hardened isothermally at higher temperatures: 260°C and 300°C.

TEM-based pair distribution function study of bimetallic nanoparticles

Dung Trung Tran^{1,a}, Cheuk-Wai Tai^{1,b} and Gunnar Svensson^{1,c}

¹Department of Materials and Environmental Chemistry, Arrhenius Laboratory, Stockholm University, S-10691, Stockholm, Sweden

^adung.tran@mmk.su.se, ^bcheuk-wai.tai@mmk.su.se, ^cgunnar.svensson@mmk.su.se

Introduction

The *atomic pair distribution function* (PDF) method is particularly useful for significantly structurally-disordered materials on which the structure determination by measuring the position and intensity of the Bragg peaks may disappoint. PDF, which is often denoted as $g(R)$, represents the probability density of finding a pair of two atoms separated by the distance R . Atomic PDF analysis has been developed since 1930s, conventionally obtained by the *Fourier transformation* of the *structure function* which can be derived from synchrotron X-ray or neutron scattering data [1].

The electron-scattering-based PDF method has been proposed in 1990s, using the scattering data extracted from the ring patterns of *electron powder diffraction* acquired using a laboratory-standard *transmission electron microscope* (TEM) [2]. Physically, the major difference between TEM-based and synchrotron-based PDFs is that the atomic form factors for electron $f_e(Q)$ (with Q as the magnitude of the scattering vector) decrease much more quickly than those for X-rays $f_x(Q)$ do. As a result, the electron scattering intensity will attenuates in a shorter Q -range and thus TEM-based PDFs require lower Q_{max} (which is achievable) compared with synchrotron-based PDFs. The important advantage of the TEM-based PDF method is its feasibility and convenience in giving a quantitative structure analysis, which can compensate to and/or be consistently combined with other well-known TEM-based techniques.

Our work is reported here as a continuation of developing TEM-based PDF method in which we demonstrate its application for crystalline bimetallic nanoparticles. We show here the quantitative PDFs achieved from the electron powder diffraction of bimetallic nanoparticles, allowing measurement of not only interatomic distances but also coordination numbers and assessment of disordering.

TEM-based PDF for Cu-Au alloy nanoparticles

FCC-like crystalline Cu-Au alloy nanoparticles of which the size is roughly 1-5 nm [3] were characterised. Electron powder diffraction was performed for the nanoparticles (deposited on an amorphous carbon film) using a 200 kV JEOL JEM-2100 field-emission microscope equipped with a CCD camera (Gatan Ultrascan 1000) [4]. The major treatments for the data were the subtraction of the contribution of the carbon supporting films (with a recorded scattering data for a blank area of the carbon film) and the subtraction of the fitted background, which is mainly built up from the direct-beam tail, inelastic and incoherent multiple scatterings. The data treatments and the derivation of experimental PDF were done using a code written by our group (SUEPDF). A model of Cu₃Au cuboctahedral nanoparticles was adopted for the simulation of PDF corresponding to the scattering of 200 keV electrons. Our simulation, which was also performed by another home-written code (SimUePDF), takes into account the Q -dependence of the form factors $f_e(Q)$ to avoid the error caused by the large difference in atomic numbers of Cu (29) and Au (79).

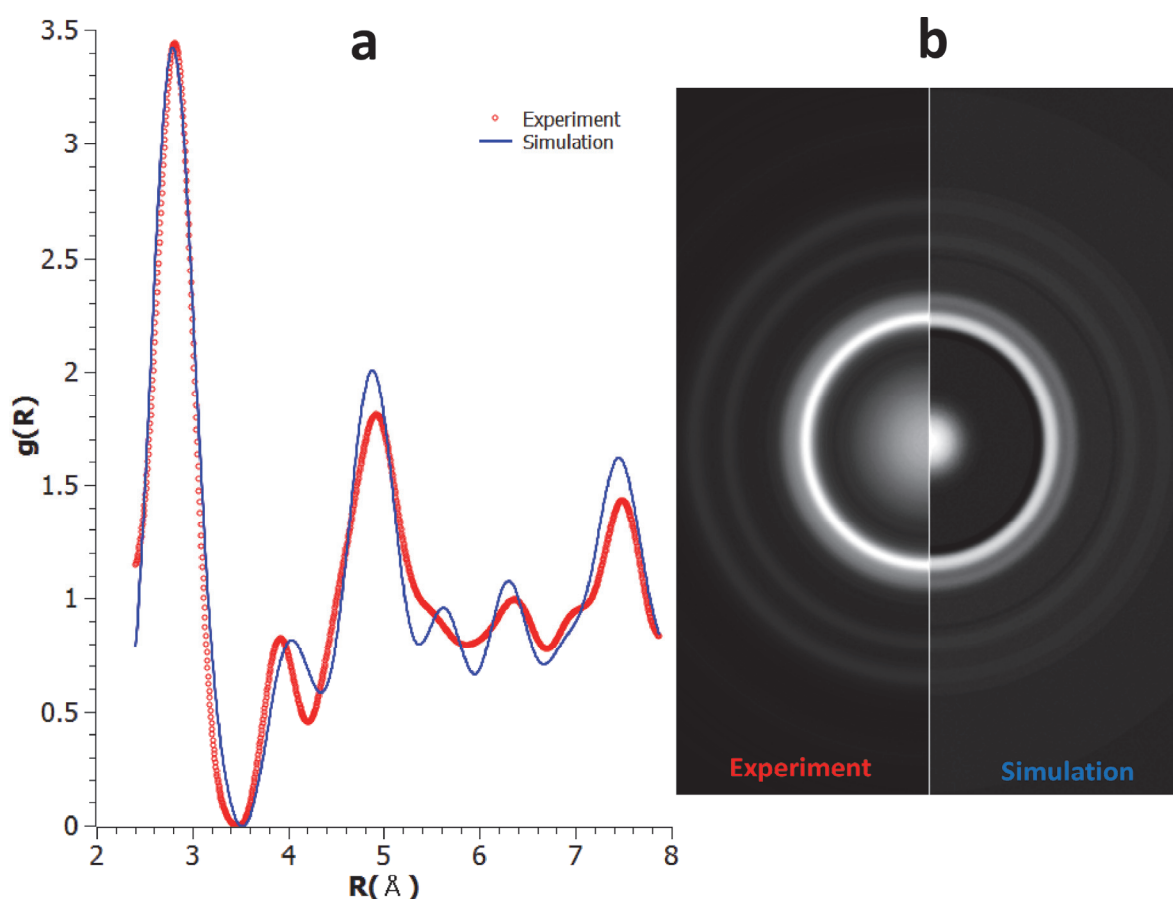


Fig. 1. (a) PDFs: experiment (red circles) in comparison with simulation (blue solid line); (b) patterns for electron powder diffraction: reconstructed experimental data (left) in comparison with simulation (right)

The experimental and simulated TEM-based PDFs, together with the corresponding diffraction patterns, are shown in Figure 1, confirming the fcc-like structure of the Cu-Au alloy nanoparticles with the first three peaks corresponding to the three interatomic distances of the 1st, 2nd and 3rd shells. The averaged 1st coordination number is ~ 9.57 for the experiment, compared with ~ 10.45 for the simulation. It is well known that, for a perfect bulk fcc structure, the 1st coordination number is 12. The reduction of average coordination numbers in cases of nanoparticles is mainly due to the increased surface-area to volume ratio and the truncated shapes. The disorder of the real nanoparticles is another reason for the variation of coordination number. The disorder means lowering structure coherence and loosing long-range order; therefore decreasing the probability of finding atom-atom pairs of expected distances. The lowered structure coherence explains why the experimental PDF has lower peaks at long distances, compared with the simulation. By comparing the averaged 1st coordination numbers between experiment and simulation, the short-range disorder level of the experimental nanoparticles has been quantified as a value of $\sim 8.4\%$.

References

- [1] T. Egami and S.J.L. Billinge: *Underneath the Bragg-Peaks: Structural Analysis of Complex Materials* (Elsevier Science, Amsterdam, 2002).
- [2] M. Tewes, J. Zweck and H. Hoffmann: *J. Phys.: Condens. Matter*. Vol. 6 (1994), p. 835.
- [3] D.T. Tran, I.P. Jones, J.A. Preece, R.L. Johnston and C.R. van den Brom: *J. Nanopart. Res.* Vol. 13 (2011), p. 4229.
- [4] The Knut and Alice Wallenberg (KAW) Foundation is acknowledged for providing the electron microscopy facilities and financial support under the project 3DEM-NATUR.

TEM & AFM - complementary techniques for structural characterization of nanobainitic steel

Julita Dworecka^{1,a}, Elżbieta Jezierska^{1,b}, Janusz Rębiś^{1,c},
Krzysztof Roźniatowski^{1,d}, Wiesław Świątnicki^{1,e}

¹Warsaw University of Technology, Faculty of Materials Science and Engineering,
Wołoska 141, 02-507 Warsaw, Poland

^ajulita.dworecka@nanostal.eu, ^bejez@inmat.pw.edu.pl; ^cjrebis@meil.pw.edu.pl
^dkrozn@inmat.pw.edu.pl; ^ewieslaw.swiatnicki@nanostal.eu

Keywords: transmission electron microscopy, atomic force microscopy, nanobainite, dilatometric tests, bearing steel

The aim of this study was the analysis and identification of phases formed in bearing steel during the austempering heat treatment. In order to precisely investigate the microstructure formed after heat treatments two advanced microscopy techniques were used: transmission electron microscopy (TEM) and atomic force microscopy (AFM).

The study was focused on a sample of bearing steel after isothermal hardening process. The process parameters have been specially designed in order to obtain nanobainitic structure (excluding carbides present in virgin material). The obtained structure consists of alternating plates of nanometric bainitic ferrite and austenite which was confirmed by electron diffraction (phase analysis). TEM observations of bainitic ferrite and austenite structures were carried out to determine the thickness of plates. Moreover, AFM analysis of the surface topography was performed to compare the results obtained by TEM. It was revealed that the chosen methods of structural analysis affect the results of plate thickness measurements. In both studies the structure meets the criteria of nanocrystalline structure.

The electron microscopic measurements of the multiphase microstructure in 35CrSiMn5-5-4 steel

Adam Gołaszewski^{1,a}, Jerzy Szawłowski¹ and Wiesław Świątnicki¹

¹ Faculty of Materials Engineering, Warsaw University of Technology, Wołoska 141 Street, 02-507 Warsaw, Poland

^aadam.golaszewski@nanostal.eu

Introduction

The properties of steels stem directly from their phase composition and their microstructure. The refinement of the grains to nanometric sizes, through phase transformations, is one of the ways of improving the properties of modern steels. It enables to achieve high strength as well as to keep good plasticity of the steel. Electron microscopy technique is necessary to characterise such structures as it guarantees high enlargement and high resolution.

The main subject of this study was to analyse the highly refined multiphase microstructure of 35CrSiMn5-5-4 steel after the applied heat treatments. In order to fully characterise the steel, light microscopy, electron microscopy (SEM and TEM) and the electron diffraction analysis were used. On the basis of the conducted observations, the microstructure of the steel after the two processes of heat treatment was described.

Isothermal quenching in the temperature higher than martensite start temperature (M_s) after annealing in the range of ferrite and austenite stability (between A_1 i A_3 temperatures) was used in two different variants of the treatment. In one of the variants, preliminary heat treatment was additionally applied in order to refine the initial microstructure. Two different types of the microstructure were obtained as a result of the applied heat treatments. They both consisted of carbide-free bainite with retained austenite in the ferritic matrix, however they differed in terms of the refinement of the grains.

Results

The analysis of the microstructure indicated higher grain refinement after applying the treatment with preliminary heat treatment (Fig. 1b) in comparison to the one without preliminary heat treatment (Fig. 1a). In both cases, significant differences in the morphology of the microstructure were observed.

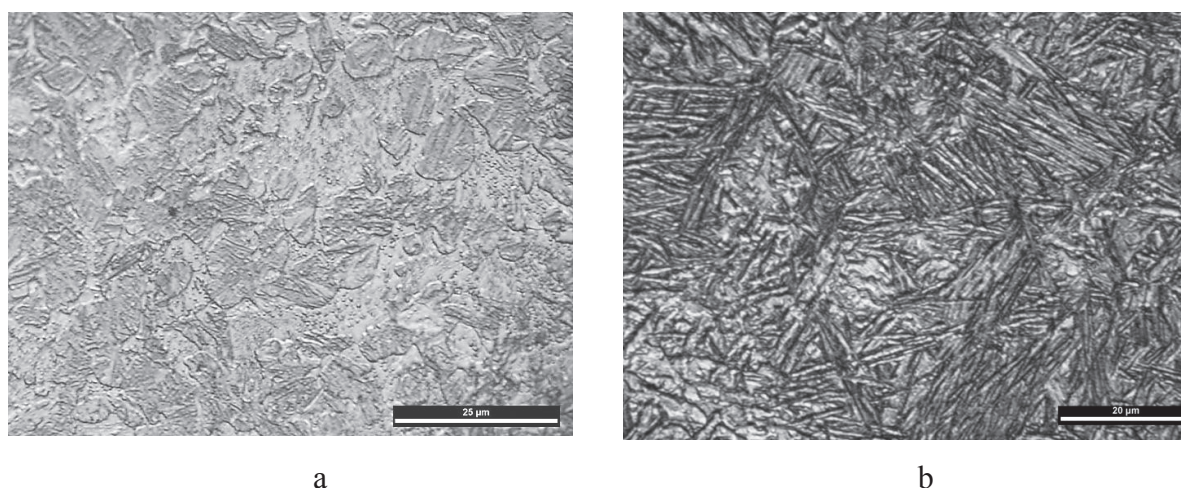


Fig. 1. The light microscope images of the microstructure of 35CrSiMn5-5-4 steel obtained after two variants of heat treatment; without (a) and with preliminary heat treatment (b)

The electron microscopic measurements revealed that both bainitic and ferritic grains were elongated (Fig. 2a), whereas the TEM analysis indicated the presence of austenite (Fig. 2b).

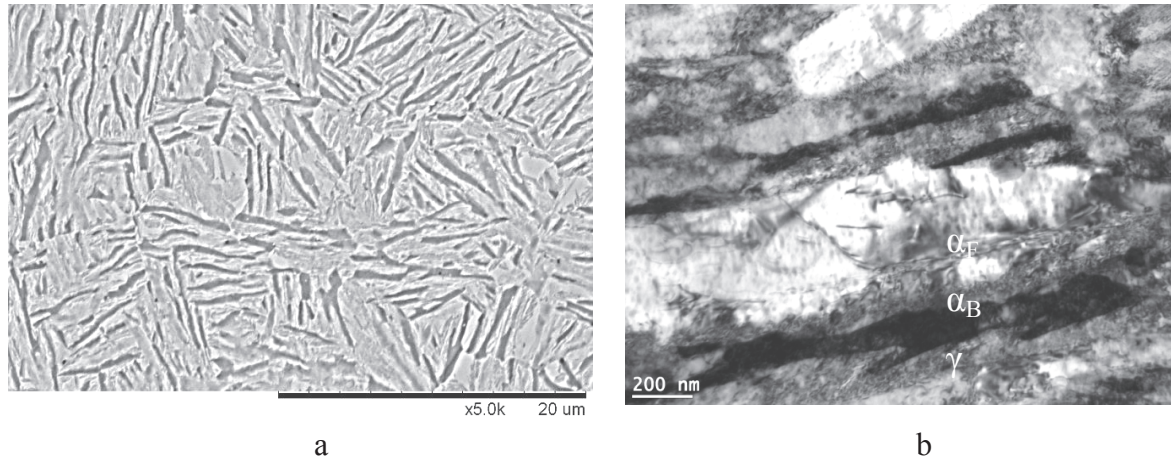


Fig. 2. The microstructure of 35CrSiMn5-5-4 steel after applying the preliminary heat treatment (a – SEM; b – TEM)

In case of the treatment without the preliminary heat treatment, bainitic areas with retained austenite were surrounded by ferrite. Additionally, in bainitic areas, bainitic ferrite plates were separated from each other by thin austenitic layers. After the other treatment (with preliminary heat treatment) bainitic plates did not grow in clusters. The presence of two bainite plates separated from each other with a thin austenite layer between the elongated ferritic grains is typical for this kind of treatment.

In both cases bainitic areas were carbide-free, whereas the small amounts of carbides were present in ferrite. This may indicate that the carbides did not fully dissolve during the annealing in the intercritical range.

Conclusion

Applied heat treatments resulted in developing the structures which consisted of carbide-free bainite with retained austenite in the ferritic matrix.

The preliminary heat treatment conducted before isothermal quenching from the incomplete austenitization led to the greater refinement of the structure, in which the width of ferritic areas was in the range of 200-700 nm.

The thickness of bainite plates was about 100-200 nm in both cases, while the average thickness of the austenite layers was about 100 nm.

Effect of dispersed α -Al₂O₃ particles on the morphology and tribological properties of nickel-alumina coatings

Anna Góral^a, Lidia Lityńska-Dobrzyńska^b, Katarzyna Berent^c

Institute of Metallurgy and Materials Science of the Polish Academy of Sciences,
30-059 Krakow, 25 Reymonta St., Poland

^aa.goral@imim.pl, ^bl.litynska@imim.pl, ^ck.berent@imim.pl

Introduction

In the last years a considerable progress is observed in the fabrication of composite coatings and the understanding of relations between processing, microstructures and properties. The possibility of producing coatings with better properties (e.g. mechanical, tribological, anti-corrosion) compared to the pure metal coatings opens up a wide range of research opportunities for different materials. Improved properties mainly derive from the presence of particles dispersed in the metallic matrix and thus depend on the content and nature of particles in the coatings. Among many methods of preparing such materials, electrodeposition is a simple and economic method of producing composite coatings. The microstructure of these coatings depends on many process parameters, including electrolyte composition, current density, hydrodynamics and characteristics of particles added to an electrolyte. The paper presents the study of the effect of the Al₂O₃ dispersed nano-particles on microstructure and mechanical (e.g. microhardness) and tribological (e.g. wear resistance) characteristics of the obtained composite coatings.

Methodology

Details regarding the electrodeposition of Ni/alumina coatings on steel substrates have already been published [1]. Analysed coatings were formed from the Watts bath containing 60 g/l α -Al₂O₃ nano-particles at the current density of 5 A/dm². In order to identify the effect of the ceramic particles on the Ni deposit properties, Ni/Al₂O₃ and Ni coatings were deposited under the same conditions. The scanning (SEM – FEI QUANTA 3D FEG) and transmission (TEM - FEI TECNAI G²) electron microscopy were applied to study the morphology changes of nickel matrix coatings developed by co-deposition of hard α -Al₂O₃ nano-particles. Microhardness of coatings was measured using MCT-CSM Instruments with Vicker's geometry diamond and load 50 mN. Eight different places on the samples surface were measured, and the values were then averaged. The friction coefficient and wear properties of coating-substrate systems were evaluated on a ball-on-disk apparatus.

Results

The solid particles present in the electroplating bath, and then as a dispersive phase in the coating, change the structure of the latter and therefore determines its mechanical, tribological and anti-corrosion properties. SEM observations revealed that the obtained coatings were smooth and compact without any pores or fissures on the surface (Fig. 1). Ni coatings presented evident pyramidal structure, whereas the Ni/Al₂O₃ composites developed a nodular surface structure, they were more fine and possessed a smaller surface roughness grade. The particle distribution observed in the macro scale was found to be approximately uniform on the cross sections of coatings. Although the particles showed a tendency to form agglomerates, from TEM images it seemed that the particles were not closely joined to each other, but rather deposited in loose groups. It is apparent that an introduced ceramic phase significantly affects the microstructure of deposited Ni. As can be seen in Fig. 1c Ni/Al₂O₃ composites showed columnar grains in the cross section. The smallest grains were observed near the steel substrate and as the distance from the substrate increased the size of the grains became significantly larger.

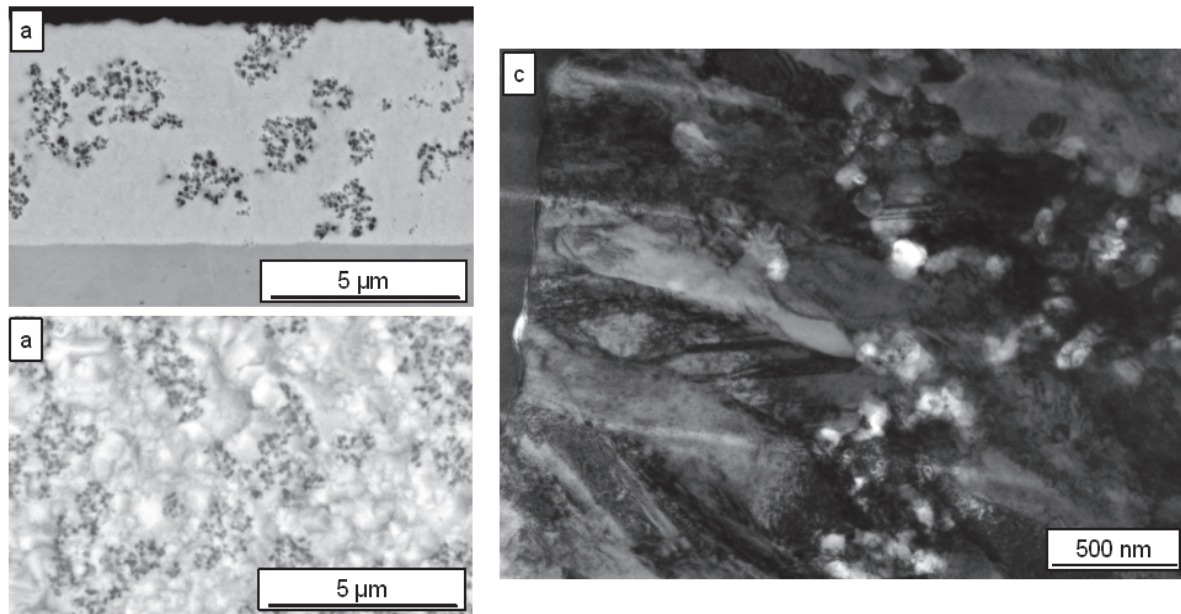


Fig. 1. SEM (backscattered electrons) microstructure of Ni/Al₂O₃ coatings a) cross section, b) surface, c) TEM (bright field) microstructure of cross section showing nickel grains with marked twins

The Ni grains were found to grow until they came in contact with the dispersed phase and then the growth stopped. In this way the incorporated nano-particles led to the decrease in the average grain size of Ni. This is explained in relation to the restraint to the growth of columnar grains of nickel imposed by dispersed particles, which also provoked nucleation of new sites. Nickel changed its microstructure from the coarse grained columnar to the fine grained one. Additionally, the formation of twinned nickel grains, which can enhance the mechanical properties of coatings was also observed (Fig. 1c). The microhardness measured on surfaces of Ni/Al₂O₃ deposits was about 40% higher than microhardness of pure nickel ones. The composite coatings revealed elastic - plastic deformation during scratch testing, their wear resistance and a friction coefficients were $2.7 \cdot 10^{-6} \text{ mm}^3/\text{Nm}$ and 0.3, respectively.

Summary

The resent study presents the attempt to explain the effect of $\alpha\text{-Al}_2\text{O}_3$ nano-particles co-deposited in Ni matrix on the morphological changes and to correlate them with mechanical and tribological characteristics of the obtained coatings. The addition of alumina particles effectively refined the size of nickel matrix grains, which stopped growing when they encountered the dispersed phase. Composite coatings with ceramic phase revealed a significant increase in the microhardness in comparison to the pure nickel. They also revealed good parameters in tribological tests.

Acknowledgements

This work is supported by National Science Centre of Poland (Project No 2011/01/D/ST8/05318).

References

- [1] A. Goral, M. Nowak, J. Wojewoda-Budka: Sol. St. Phenom. 203-204 (2012), p. 133.

Microstructural features of strain-induced martensitic transformation in advanced ultra-high strength medium-Mn steels

Adam Grajcar^{1,a}, Andrzej Kilarski^{2,b}, Krzysztof Radwański^{3,c}
and Radosław Swadźba^{3,d}

¹Institute of Engineering Materials and Biomaterials, Silesian University of Technology,
18a Konarskiego Street, 44-100 Gliwice, Poland

²General Motors Manufacturing Poland, 1 Adama Opla Street, 44-121 Gliwice, Poland

³Institute for Ferrous Metallurgy, 12-14 K. Miarki Street, 44-100 Gliwice, Poland

^aadam.grajcar@polsl.pl, ^bandrzej.kilarski@gm.com, ^ckradwanski@imz.pl, ^drswadzba@imz.pl

Introduction

The beneficial combination of high strength, ductility and technological formability of steel sheets for the automotive industry can be achieved by using advanced high-strength steels (AHSS). They consist of different soft and hard structural constituents in various volume fractions, which enable to obtain a very wide range of mechanical and technological properties. AHSS include Dual Phase (DP), Transformation Induced Plasticity (TRIP) and Complex Phase multiphase steels. New demands of the automotive industry for relatively low-cost steel sheets characterized by tensile strength above 1000 MPa require further searching of new chemical composition strategies. Advanced ultra-high strength steels contain a higher fraction of hard phases, i.e., acicular ferrite, bainite or martensite [1] compared to AHSS containing polygonal ferrite as a matrix. A key microstructural constituent of advanced multiphase steels is retained austenite with the amount from 10% to 30%. This phase ensures a required ductility level by its strain-induced martensitic transformation during cold forming. Recently, a high amount of retained austenite is obtained in bainitic alloys containing from 1.5 up to 8 wt.% Mn, being a main austenite stabilizer [2,3].

Multiphase steels are characterized by high grain refinement. In this regard, the identification of individual microstructural constituents is especially important. Recently, the EBSD technique in scanning electron microscope (SEM) has gathered essential significance for determination of the amount and morphological features of retained austenite as well as polygonal ferrite, bainitic ferrite and martensite [4]. Retained austenite can be distinguished from the A2-based phases by electron diffraction. A problem is to further distinguish the bcc phases into ferrite, bainite and martensite, which are crystallographically identical. Main factors serving to identify these structural constituents are the Image Quality (IQ) factor and Confidence Index (CI). The identification of strain-induced martensite formed from lamellar austenite requires using transmission electron microscope (TEM).

Methodology

The work deals with the microstructural analysis of the thermomechanically processed and subsequently cold-deformed 5Mn-1.5Al multiphase steels showing a TRIP effect. The thermomechanically processed sheet samples were subjected to 5%, 10% and 15% elongation in uniaxial tension. The evolution of the bainitic microstructures containing nanoscale lamellar retained austenite and especially the identification of strain-induced martensite was carried out using electron transmission microscopy and electron scanning microscopy equipped with EBSD (Electron Backscatter Diffraction). Morphological details affecting the mechanical stability of retained austenite were indicated. The EBSD technique was performed by the use of the Inspect F SEM equipped with Shottky's field emission. The thin foils investigations were carried out by the use of the JEOL JEM 3010 at the accelerating voltage of 200 kV.

Results

Applying the thermomechanical processing allows to obtain the fine-grained bainitic matrix containing uniformly distributed lath austenite regions. The amount of retained austenite determined by EBSD is about 14%. The carbon content of this phase determined using the X-ray analysis equals to 1.1 wt.%. Utilization of TEM allows to reveal the finest regions of retained austenite with a size from 50 to 200nm. The γ phase content decreases after applying cold tensile straining. Figure 1 shows the evidence of strain-induced martensite transformation using EBSD (a-c) and TEM (d). The inverse pole figure (Figure 1c) shows the crystal direction parallel to the specimen normal using colour-coding according to the unit triangle. The IQ factor (Figure 1a) represents a quantitative description of the sharpness of the EBSD pattern. A lattice distorted by crystalline defects such as dislocations, subgrain boundaries and strain-induced martensite has a distorted Kikuchi pattern, leading to lower IQ values. Formed martensite has a plate morphology (Figure 1d) and it contributes to fragmentation of untransformed austenite fostering its further stabilization.

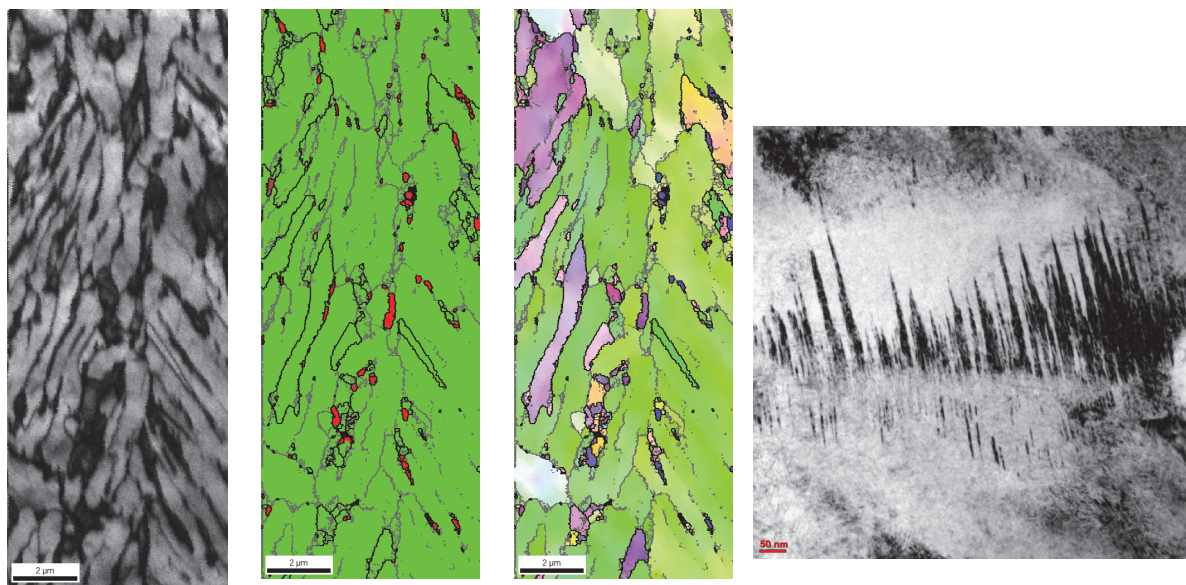


Fig. 1. Evidence of strain-induced martensite using EBSD (a-c) and TEM (d): a) IQ map, b) high-angle (thick lines) and low-angle (thin lines) boundaries, retained austenite in red, c) inverse pole figure map, d) plates of strain-induced martensite

Conclusions

The detailed identification of morphological features of individual microstructural constituents of thermomechanically processed medium-Mn steels is a challenging problem due to high dispersion of particular phases. The problem complicates even more during cold deformation, when highly dispersed retained austenite transforms into strain-induced martensite. The proper identification of multiphase microstructures requires the combined application of SEM-EBSD and TEM.

References

- [1] P.J. Gibbs, E. De Moor, M.J. Merwin, B. Clausen, J.G. Speer and D.K. Matlock: Metall. Mater. Trans. Vol. 42A (2011), p. 3691.
- [2] A. Grajcar, R. Kuziak and W. Zalecki: Arch. Civ. Mech. Eng. Vol. 12 (2012), p. 334.
- [3] F.G. Caballero, J. Chao, J. Cornide, C. Garcia-Mateo, M.J. Santofimia and C. Capdevila: Mater. Sci. Eng. A. Vol. 525 (2009), p. 87.
- [4] R. Petrov, L. Kestens, A. Wasilkowska and Y. Houbaert: Mater. Sci. Eng. A. Vol. 447 (2007), p. 285.

Microstructural features of Cu-Zn single crystals deformed at elevated temperature

Barbara Grzegorzczuk^{1,a}, Wojciech Ozgowicz^{1,b}
and Elżbieta Kalinowska-Ozgowicz^{1,c}

¹Institute of Engineering Materials and Biomaterials, Silesian University of Technology,
18a Konarskiego Street, 44-100 Gliwice, Poland

^abarbara.grzegorzczuk@polsl.pl, ^bwojciech.ozgowicz@polsl.pl, ^celzbieta.kalinowska-ozgowicz@polsl.pl

Introduction

Plastic deformation is the basic process of changing the geometrical features of solid bodies affected by external or internal forces, on which the technology of plastic working is based. The knowledge of the mechanisms of plastic deformation is, therefore, of essential importance both cognitively and with respect to its application. The development of crystallography and the methods of investigations, and mainly the techniques of utilizing the diffraction of X-rays, electrons and neutrons, contributed considerably to the development of materials engineering, particularly the knowledge concerning plastic deformation of metals and commercial alloys.

Due to the rather high interest in non-homogeneous deformation a considerable amount of investigations has been started, dealing with the influence of those factors which are responsible for this phenomenon. Most experiments were carried out on polycrystalline alloys. There are only few cases of investigations, in which the heterogeneity of plastic deformation concerned monocrystalline alloys. More recent methods of describing and recording the achieved results provide new information about the nature of this effect. The presently suggested theories describing this phenomenon are, however, not explicit enough, and none of them permits to explain sufficiently and to predict the occurrence of heterogeneities of plastic deformation in the given material. Every plastic deformation is a complex process, consisting in the not homogeneous and often also in a specific cooperation and organization of elementary sliding of twinning. The continuous development of the theory of dislocations, supported by modern techniques of investigations allow to understand the fundamental features of this process [1-4].

Methodology

The scope of investigation enclosed production of testing single crystals, determination of their crystallographic orientation, deformation of selected single crystals by compression in a temperature range from 20°C÷400°C, applying strain rate from 10⁻⁵s⁻¹ to 10⁻¹s⁻¹ as well as microstructure observations. The alloy CuZn30 is monocrytallized by means of the method of crystallization with a controlled temperature gradient in laboratory conditions making use of an electrical tubular furnace permitting a displacement of the zone of the temperature gradient of the furnace towards the crucible containing the charge. Compression tests of selected single crystals with some defined orientations were carried out within the temperature range of 20°C ÷400°C, at a strain rate of 10⁻⁵ s⁻¹ to 10⁻¹ s⁻¹, applying the testing machine INSTRON 3382. The values of strength were recorded with an accuracy of up to 0.5. The final deformation of the sample during the compression test amounted to about 50%. Transmission electron microscopy investigations were carried out with the technique of thin foils using JEOL JEM 3010 transmission electron microscope, at the accelerating voltage of 300kV and magnification of 30000 up to 50000x. Microstructural features were also revealed with the SUPRA 25 scanning electron microscope using the EBSD (Electron Backscatter Diffraction) technique.

Results

The analysis of the results of these investigations permitted to prove a considerable influence of the temperature, the strain rate and the crystallographic orientation on the metallographic effects of the

work hardening of the CuZn30 alloy. In the microstructures of the investigated monocrystals typical effects of plastic deformation were observed in the form of parallel cruciform lines and slip zones with locally intensified densities in various ranges of the cross-section of the sample and bands of deflection with weakly visible slip lines in the original system. At elevated temperature the respective slip lines integrate forming clusters – slip bands, between which irregular effects of strain do occur. These phenomena indicate that sliding is a heterogeneous process, because the plastic deformation takes place in the region of the paths of shear where dislocations may be extended to considerable distances.

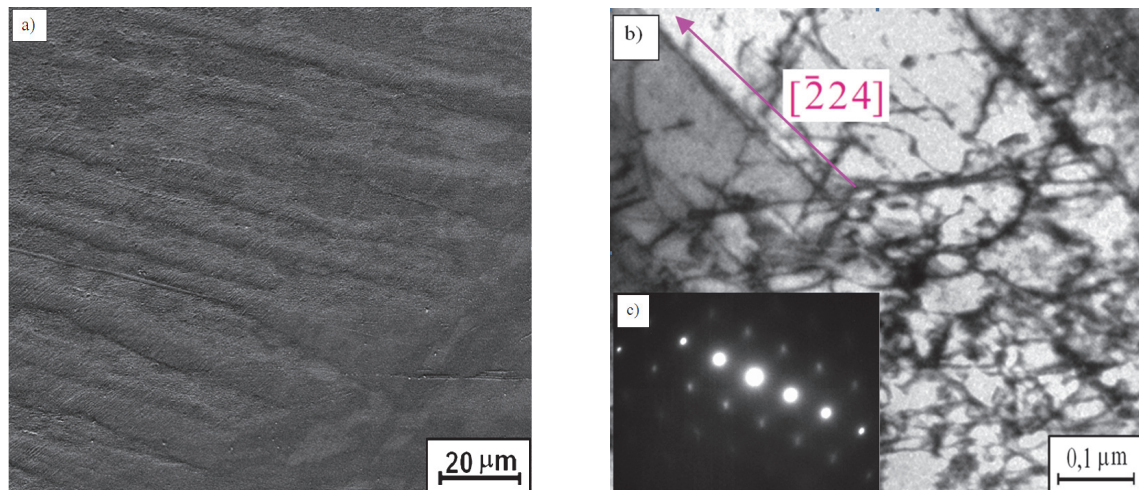


Fig. 1. Microstructure of a CuZn30 single crystal with the crystallographic orientation $[\bar{1}39]$ after deformation with a draft of 50 % at 400°C and $\dot{\epsilon} = 10^{-4}\text{s}^{-1}$: a) SEM - bands of deflection and criss-crossing slip of multiple lines, b) TEM - cellular systems and traces of dislocation slip plane in the direction of $[\bar{2}24]$ matrix, c) – diffraction pattern of the α -solution area

Conclusions

The analyzed microstructures of compressed monocrystals prove that the main mechanism of plastic deformation is the slide. Of essential influence on the structure of plastically deformed monocrystals are both the temperature and the strain rate.

References

- [1] C. Zhou, I. J. Beyerlein, R. LeSar: Acta Mat. 59 (2011), p. 7673.
- [2] G. Franz, F. Abed-Meraim, M. Berveiller: Int. J. Plast. 48 (2013), p.1.
- [3] A. Cuniberti, M. Ahlers, R. Romero: Mater. Sci. Eng. A. Vol. 234 (1997), p. 893.
- [4] W. Ozgowicz, B. Grzegorzcyk, A. Pawełek, A. Piątkowski, Z. Ranachowski: Arch.of Metall. and Mat. Vol.59 (2014), p.182.

Microstructure of niobia-stabilized bismuth oxide thin films deposited by PLD technique

Sławomir Kaç^a, Tomasz Moskalewicz^b and Grzegorz Szwachta^c

AGH University of Science and Technology, al. Mickiewicza 30, 30-059 Krakow, Poland

^aslawomir.kac@agh.edu.pl, ^btmoskale@agh.edu.pl, ^cgjs@agh.edu.pl

Introduction

Bismuth oxides are used in various domains, such as microelectronics, sensor technology, optical coatings, transparent ceramic glass manufacturing, etc. Ceramic films are essential for devices because the intrinsic properties of the material, rather than its grain boundaries, can be exploited. γ -Bi₂O₃ (body-centered cubic; bcc) and δ -Bi₂O₃ (face-centered cubic; fcc) bismuth oxides have the highest known oxide ion mobility, which makes it useful, electrolyzers and ceramic membranes for high-purity oxygen separation and partial oxidation of hydrocarbons [1, 2]. Bismuth oxides have a relevant importance for modern solid-state technology, owing to their peculiar properties such as energy band gap, refracting index, dielectric permittivity and photoconductivity [2]. These properties have made Bi₂O₃ thin films suitable for large range of applications, such as optical coatings, photovoltaic cells, microwave integrated circuits. Along with these applications, recently introduced applications of Bi₂O₃ films are oxygen sensors and oxygen pumps of fuel cells. Bismuth oxide has four main crystalline phases with two non-stoichiometric phases [3]. They are monoclinic α -Bi₂O₃, tetragonal β -Bi₂O₃, cubic (bcc) γ -Bi₂O₃, cubic (fcc) δ -Bi₂O₃ and non-stoichiometric phases are Bi₂O_{2.33}, Bi₂O_{2.75}, α -Bi₂O₃ and δ -Bi₂O₃ are more stable at normal atmospheric conditions but β -Bi₂O₃ and γ -Bi₂O₃ are the metastable phases for temperature less than 750 K [2, 4 - 7]. Each phase possess the distinct crystal structure and physical properties.

The aim of this paper was to characterize the microstructure and phase composition of the Nb-doped Bi₂O₃ thin films deposited by PLD technique.

Abstract

The several studies have suggested that pure, face-centered cubic δ -Bi₂O₃ phase, which have good ion conductivity could exist through adding oxide stabilizers. This research is the new approach to obtaining thin films from Bi₂O₃-Nb₂O₅ system via pulsed laser deposition method.

It appears that the threshold concentration of the dopant for the stabilization of δ -phase is a function of atomic number of the pentavalent metal (V, Nb, Ta). Thus, for the chosen niobia-stabilized bismuth oxide system the proper range of niobium oxide in mixture is 15 to 25 mol%.

The microstructure, chemical composition as well as morphology of deposited thin films were examined by means of diverse techniques like scanning, and transmission electron microscope as well as atomic force microscope. Nonetheless, the X-ray diffraction of the as-deposited specimens showed them to be multi-phase microstructure with presence of CaF₂ - type δ -Bi₂O₃ phase. Thereafter, the transmission electron microscopy investigation confirmed aforementioned results, since the face-centered cubic δ -Bi₂O₃ phase was detected. The columnar growth in as-deposited samples was observed, furthermore the diameter of columns was in the range from 30 to 60 nm. The thin films were deposited with the rate about 0,3 Å/s. The thickness measurements as well as scratch tests (adhesion) were performed and the investigation show that the thickness of obtained thin films was about 300-400 nm, nevertheless, the decohesion phenomenon on thin film-substrate interface was not observed.

We found that the crucial parameters of PLD process and the niobia dopant concentration have significantly influence on the morphology and properties of the thin films. The entire obtained results confirmed that the stoichiometric composition of niobia-stabilized bismuth oxide target was maintained, moreover was successfully deposited onto the single crystal substrate.

Summary

The investigations show that it is possible to transport stoichiometrically the complex material (oxides) from target to substrate by PLD technique. The deposited films are compact and the cracks or porosity, delamination, and decohesion aren't observed on the cross-sections. Thin films growth velocity is about 0,3 Å/s. Obtained thin films have columnar and grain morphology.

Acknowledgement

This work is financially supported by National Science Center, grant no 2011/03/B/ST8/05152.

References

- [1] M.T. Le, M. Kovanda, V. Myslik, M. Vrnata, I. Van Driessche, S. Hoste: *Thin Solid Films* Vol. 497 (2006), p. 284.
- [2] P. Shuk, H.-D. Wiemhofer, U. Guth, W. Gopel, M. Greenblatt: *Solid State Ionics* Vol. 89 (1996), p. 179.
- [3] M. Mehring: *Coord. Chem. Rev.* Vol. 251 (2007), p. 974.
- [4] H. Weidong, Q. Wei, W. Xiaohong, N. Hailong: *Mater. Lett.* Vol. 61 (2007), p. 4100.
- [5] T.P. Gujar, V.R. Shinde, C.D. Lokhande: *Mater. Res. Bull.* Vol. 41 (2006), p. 1558.
- [6] V. Fruth, A., Ianculescu, D. Berger, S. Preda, G. Voicu, E. Tenea, M. Popa: *J. Eur. Ceram. Soc.* Vol. 26 (2006), p. 3011.
- [7] L. Cieniek, S. Kac: *Acta Phys. Pol., A* Vol. 117 (2010), p. 803.

EDS technique appliance for investigation of laser remelted and alloyed aluminium cast alloys

Jaroslav Konieczny^{1,a} and Krzysztof Labisz^{2,b}

¹ Division of Metal and Polymer Materials Processing, Institute of Engineering Materials and Biomaterials, Silesian University of Technology, Konarskiego 18A, 44-100 Gliwice, Poland

² Division of Biomaterials Engineering, Institute of Engineering Materials and Biomaterials, Silesian University of Technology, Konarskiego 18A, 44-100 Gliwice, Poland

^ajaroslav.konieczny@polsl.pl, ^bkrzysztof.labisz@polsl.pl

In this paper there are presented results of EDS chemical composition investigation concerning the structure of the AlSi7Cu4 cast aluminium alloy after feeding with ceramic particles with the appliance of the high power diode laser (HPDL). In this work there are presented especially the changes of the chemical composition of the particle/precipitation as well as the Al α matrix. The reason of this work was also to present the EDS investigation method directly on new engineering materials like laser surface treated light Al alloys, which will be used for further alloying and remelting with ceramic powders – especially carbides and oxides.

Introduction

Laser surface treatment is used for improvement of hardness by changing the structure and improvement of the abrasion wear resistance, mostly by introduction of carbide or other ceramic particles to the material matrix. Rapid mixing is leading to development of the surface layer, with cross-section, from the remelted materials occurs during the alloying process with the sufficiently high laser power [1, 2].

Laser alloying and remelting was performed using high-power diode laser HPDL - High Power Diode Laser for the reason of a purposeful changes in the surface structure of the surface of the element and reduce the cost of materials.

Among all known metals, aluminum is widely used as the matrix due to its low density combined with high rigidity [3]. These characteristics decide about its widespread use in aerospace and aviation. The other hand the aluminum matrix composites (AMC) have the ability to withstand high tensile and compressive stresses, by the transfer and distribution of the load applied matrix to the reinforcing phase [4, 5].

Material for investigations

The aluminium alloy AlSi7Cu4 was used for investigations, supplied in form of moulds, with a standard heat treatment carried out, including solution heat treatment at 505°C for 600 min and ageing at 170°C for 720 min.

Table 1. Ion milling parameters using for polishing

| Angle [°] | Energy [KeV] | Time [min] |
|-----------|--------------|------------|
| 5.5 | 3.6 | 190 |
| 3.5 | 3.0 | 10 |

The examinations of thin foils microstructure and phase identification were carried out on the S/TEM Titan 80/300 transmission electron microscope (TEM), at the accelerating voltage of 300 kV. TEM specimens were prepared by cutting thin plates from the material. The specimens were ground down to foils with a maximum thickness of 80 μ m before 3 mm diameter discs were punched from the specimens. The disks were further thinned by ion milling method with the Precision Ion Polishing

System (PIPS™), used the ion milling device model 691 supplied by Gatan until one or more holes appeared. The ion milling was done with argon ions, accelerated by a voltage of 15 kV, energy and angle are presented in Table 1.

Investigation results

X-ray microanalysis based on an analysis of X-ray characteristic emission of the chemical composition makes it possible to examine the microregions of laser remelted and alloyed aluminium cast alloys.

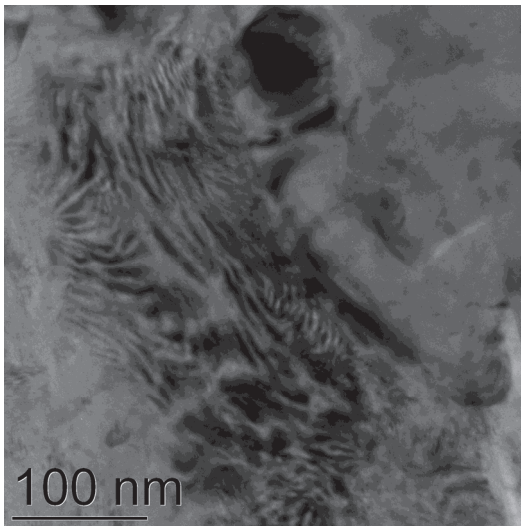


Fig. 1. Al α -matrix after HPDL feeding/alloying

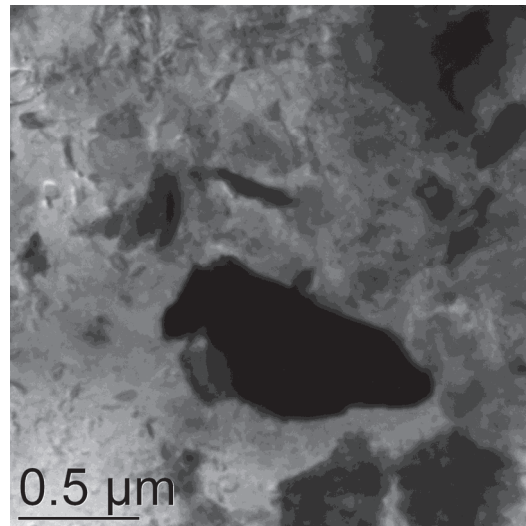


Fig. 2. Ceramic particle embedded in the Al α -matrix after HPDL laser treatment

Summary

The metallographic investigations performed on the transmission electron microscope using the EDX analysis confirm the occurrence of alloying additives like Si, Fe, Mn as well as the carbon and other ceramic powders compounds distributed in the Al matrix.

Acknowledgements

This research work was financed partially within the framework of the Polish State Committee for Scientific Research Project (NCN) No. 2011/01/B/ST8/06663 headed by Dr Krzysztof Labisz.

References

- [1] W. Ozgowicz, K. Labisz: *J. Iron Steel Res. Int.* Vol. 18/1 (2011), p. 135.
- [2] T. Tański, K. Labisz: *Sol. St. Phenom.* Vol. 186 (2012), p. 192.
- [3] J. Konieczny, L.A Dobrzański, K. Labisz, J. Duszczyk: *J. Mater. Proc. Technol.* Vol. 157-158 (2004), p. 718.
- [4] A. Włodarczyk-Fligier, L. A. Dobrzanski, J. Konieczny: *J. Achiev. Mater. Manuf. Eng.* Vol. 51/1 (2012), p. 22.
- [5] M. Adamiak: *J. Achiev. Mater. Manuf. Eng.* Vol. 31/2 (2008), p. 290.

Shape, size and distribution of metal particles embedded into ceramic matrix

Katarzyna Konopka

Faculty of Materials Science and Engineering, Warsaw University of Technology
kako@inmat.pw.edu.pl

Introduction

The combination of ceramics and metals creates new composite materials (cermets). Cermets are attractive for many applications as cutting tools, parts of machines and engines. Different systems of ceramics and metals are investigated. Among of them are Al_2O_3 with metals like Ni, Fe, Mo, Cu, Al [1-5]. Moreover, various types of their microstructures are fabricated. Cermets with metal particles incorporated into ceramic matrix are one of the most intensively elaborated. There are some processes responsible for improving the fracture toughness of composites. Cracks can be deflected by metal particles or bridging effect can be operating [6,7]. The new phases which can appeared during processing of composite forming also influence on crack propagation and as a consequence on crack energy dissipation [8,9].

Size, shape and distribution of metal particles embedded into ceramic matrix are the crucial factors which crates the properties of cermets [3,5,10]. The size, shape and distribution of metal particles can be controlled by the fabrication methods and as a result various microstructures of composites are tailored.

Paper presents the various type of cermets microstructures, homogeneously distributed metal particles and nonuniform, gradiented concentration of metal particles. Moreover, different shapes and size of metal particles obtained as result of processing are analyzed. The various cermets microstructures are considered in aspect of their mechanical properties.

One type of cermets microstructure is characterized by homogenous distributed metal particles in ceramic matrix. According to the parameters of cermet forming, especially atmosphere of sintering in ceramic matrix new phase can appeared. For example in system Al_2O_3 -Fe or Al_2O_3 -Ni the spinel phases FeAl_2O_4 and NiAl_2O_4 can be formed. Such uniform distribution of metal phase, or spinel in ceramic matrix represent the uniform properties. However, the process of agglomeration of metal particles give as a result not separate individual metal particles but the agglomerates of the few or even several particles surrounded by ceramic grains (Fig. 1A).

The nonuniform distribution of metal particles leads to gradiented structures. Such a structures can be obtained by using powder metallurgy processes or by colloidal methods as slip or tape casting. In these methods the distribution of metal particles can be achieved by sedimentation or by using magnetic field (Fig. 1B). The properties as hardness and the fracture toughness of such microstructures are changed together with the change of metal particles concentration.

Other microstructures, with specific morphology of metal particles are also result of processing. Sintering above melting point of metal creates the characteristic morphology of metal particles. Moreover, the size and the shape of metal phase embedded into ceramic matrix differ from the initial metal powder particles. Especially, the characteristic oval shape with hole inside ("doughnut") (Fig. 1C) is observed as result of the difference in the values of the thermal expansion coefficient of ceramic, metal or spinel phase.

As a conclusion it should be underlined that the size, morphology and distribution of metal particles or spinel phases are determined by the method of forming. Even in one method by changing the parameters of processing various microstructures can be obtained. Because of that the needed properties of the cermets can be tailored.

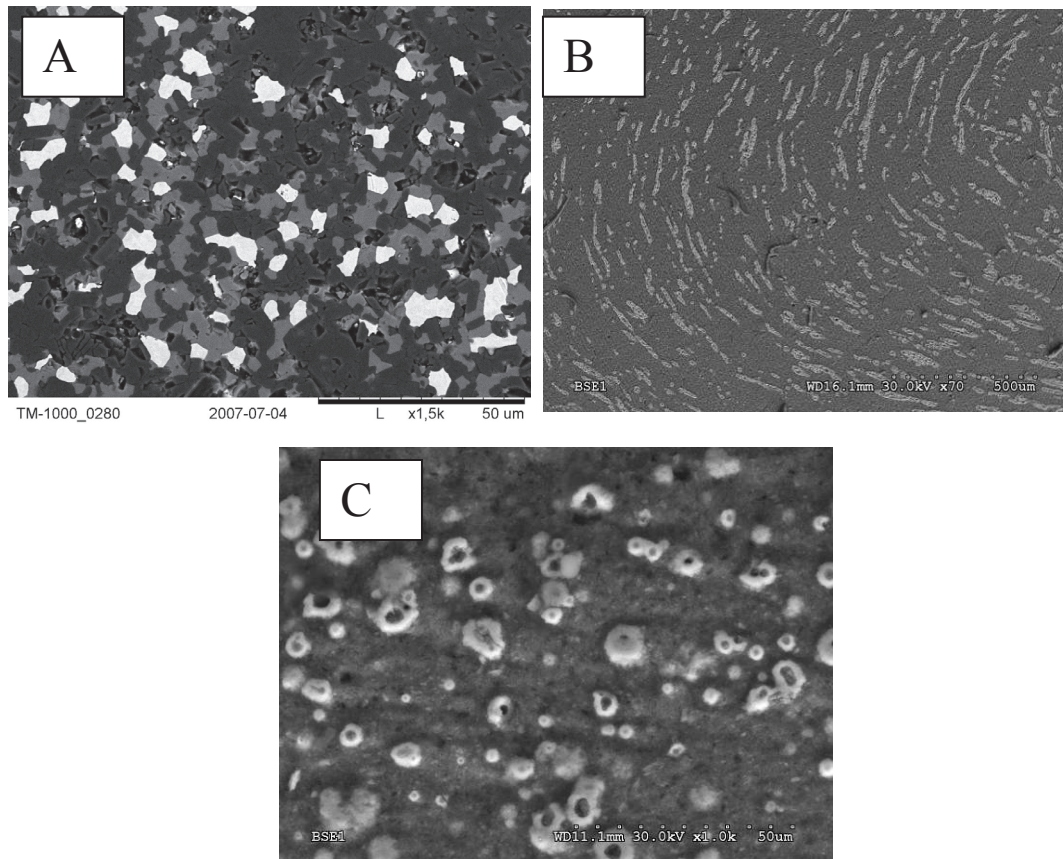


Fig. 1. SEM images of $\text{Al}_2\text{O}_3\text{-Fe}$ composites: A) composite obtained by slip casting method with uniform distribution of Fe spherical particles (white areas) and spinel FeAl_2O_4 phase (light-grey areas) in ceramic matrix; B) composite obtained by slip casting method with using magnetic field, elongated FeAl_2O_4 spinel grains distributed according to the magnetic forces; C) FeAl_2O_4 phase- shape of “doughnuts”

References

- [1] M. Aldridge, J.A. Yeomans: *J. Eur. Ceram. Soc.* Vol.19 (1988), p. 1769.
- [2] W.H. Tuan, H.H. Wu, T.J. Yang: *J. Mater. Sci.* Vol. 30 (1995), p.855.
- [3] J.S. Moya, S. Lopez-Esteban, C. Pecharroman: *Prog. Mater. Sci.* Vol. 52 (2007), p. 1017.
- [4] Z. He, J. Ma, G. E. B. Tan: *J. Alloys Compd.* Vol. 486 (2009), p. 815.
- [5] K. Konopka: *Sol. St. Phenom.* Vols. 101-102 (2005), p. 139.
- [6] L.S. Sigl, P.A. Mataga, B.J. Dalgleish, R.M. Mc Meeking, A.G. Evans: *Acta Metall.* Vol. 36 (1989), p. 1847.
- [7] S. Schicker, T. Erny, D.E. Garcia, R. Janssen, N. Claussen: *J. Eur. Ceram. Soc.* Vol. 19 (1999), p. 2455.
- [8] M. Lieberthal, W.D. Kaplan: *Mater. Sci. Eng. A302* (2001), p. 83.
- [9] X. Sun, J. Yeomans: *J. Am. Ceram. Soc.* Vol.79 (1996), p. 2701.
- [10] K. Konopka: *Solid Mech. Appl.* Vol. 135 (2005), p. 261.

Microstructural investigation of Sr doped LaCoO₃ thin films deposited by pulsed laser deposition

Agnieszka Kopia^{1,a}, Łukasz Cieniek^{1,b} and Kazimierz Kowalski^{1,c}

¹ AGH-University of Science and Technology, al. Mickiewicza 30, 30-059 Cracow, Poland

^akopia@agh.edu.pl, ^blukasz.cieniek@agh.edu.pl, ^ckazimierz.kowalski@agh.edu.pl

Cobaltites LaCoO₃ are compounds crystallising in the perovskite structure that is formed as a result of a chemical reaction between cobalt oxide Co₃O₄ and La₂O₃. Substitution of Sr²⁺ ions with a La³⁺ in LaCoO₃ structure results in a considerable change of the magnetic and electric properties of LaCoO₃. Strontium-doped cobaltites are produced in the form of powders [2, 3] that are used, for instance, in catalytic applications. The research carried out by Y. Xiaomao [2] showed that CO undergoes total oxidation into CO₂ already at the temperature of 260 °C. The powders obtained by the author were characterised by large-sized grain (120 nm). La_{1-x}Sr_xCoO₃ compounds in the form of thin films are produced by the laser ablation method or by chemical methods and they are used as electrodes in fuel cells [4,5]. The relevant literature does not provide any data on thin films produced by the laser ablation method for applications as gas sensors. The aim of the research was the microstructure characterization of pure and 10% Sr doped LaCoO₃ thin films deposited by pulsed laser deposition (PLD). Both films were grown by pulsed laser deposition (PLD) using the Nd:YAG Continuum (λ= 266 nm) and Excimer KrF (λ= 248 nm) lasers on Si [100] substrates. To characterize the structure and morphology of the surface SEM, AFM, XRD and XPS techniques were used. The SEM analysis of the layers showed the drops on the surface the thin films grown by using an Nd:YAG laser. The surface of the thin films deposited using excimer laser was almost free from the drops and totally free of cracks. Observed crystallites are much smaller and the topography of the thin film is much more developed (as observed by AFM). X-Ray analysis showed respectively LaCoO₃ in the thin film not doped and LaSrCoO₃ in the thin films doped by Sr.

References

- [1] Y. Xiaomao: Appl. Mech. Mater. Vol. 55-57 (2011), p. 1957.
- [2] Y. J. Yoo, K. K. Yu, Y. P. Lee, J. Y. Kim Chung Jong, Y. K. W. Kim: J. Korean Phys. Soc., Vol. 49 (2006), p. 2397.
- [3] K.H. Wong, W.Wu, P.W. Chan. J.T. Cheung: Thin Sol. Films Vol. 312 (1998), p. 7.
- [4] K.S. Hwang, H.M. Lee, S.S Min B.O Kang: J. Sol-Gel Sci. Technol. Vol. 18 (2000), p. 175.

Electron microscopy characterization of a multi-run friction stir processing cast AlSi9Mg aluminum alloy

Mateusz Kopyściański^{1,a}, Marek Stanisław Węglowski^{2,b}, Stanisław Dymek^{3,c}

^{1,3} AGH University of Science and Technology, Faculty of Metal Engineering and Industrial Computer Science, Krakow, Poland

² Institute of Welding, Department of the Testing of Materials Weldability and Welded Construction, Gliwice, Poland

^amateusz.kopyscianski@gmail.com, ^bmarek.weglowski@is.gliwice.pl, ^cgmdymek@cyfronet.pl

Introduction

Friction Stir Processing (FSP) is a novel technology that modifies microstructure and properties in surface layers of metallic materials through intense, localized plastic deformation. This deformation is produced by forcibly inserting a non-consumable tool into the workpiece, and revolving the tool in a stirring motion as it is pushed laterally through the workpiece. FSP uses the same methodology as Friction Stir Welding (FSW), however, it is aimed at changing microstructure rather than joining metals together. This process mixes the material without melting and creates a microstructure with fine, equiaxed grains [1,2]. Furthermore, FSP, when applied to cast alloys, may eliminate casting defects and simultaneously may refine other constituent phases and produce a homogenous distribution of these phases in the dispersed form [3].

In the present research, the FSP was utilized to produce a dispersion strengthened material from a cast AlSi9Mg aluminum alloy. This dispersion strengthened material was friction stir processed in the multi-run action according to three different schemes: a) the plate was subjected to the FSP on both sides of the plate with adjacent beads overlapped by 50% b) the material was processed on one side of the plate and adjacent beads were not overlapped c) the material was processed on one side of the plate in a cross run (Fig. 1). The investigation was aimed at characterization of microstructure by scanning and transmission electron microscopy.

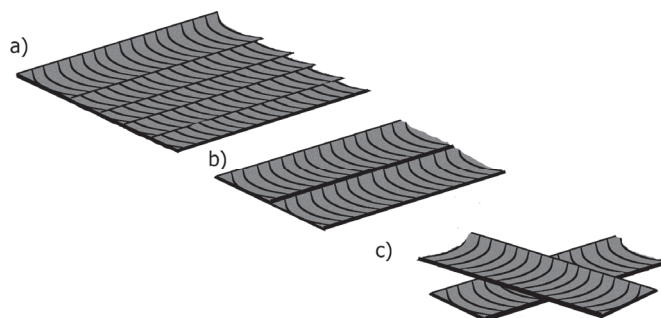


Fig. 1. Schematic drawing of multi-run FSP

Results and conclusions

Figure 2a presents typical microstructure of the as-cast alloy with dendritic solidification, intermetallic phases and shrinkage porosity. The stirring action during FSP closed porosity, fractured large second-phase particles reducing both their average size and aspect ratios (Fig. 2b). Transmission electron microscopy revealed additional features of the modified microstructure: high dislocation density, formation of subgrains and fine second phase particles (precipitates) – Fig. 3.

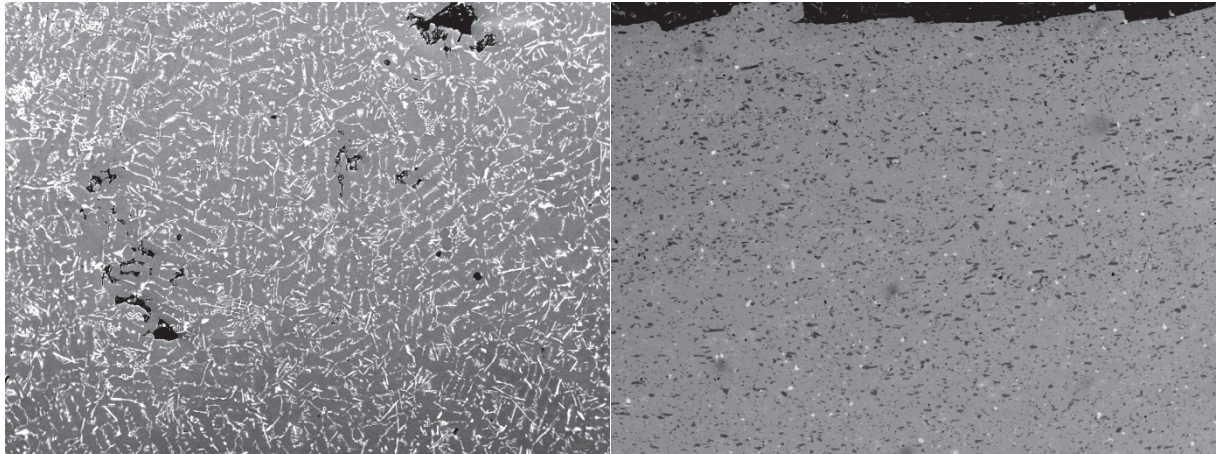


Fig. 2. SEM micrographs: a) as-cast alloy b) friction stir processed material

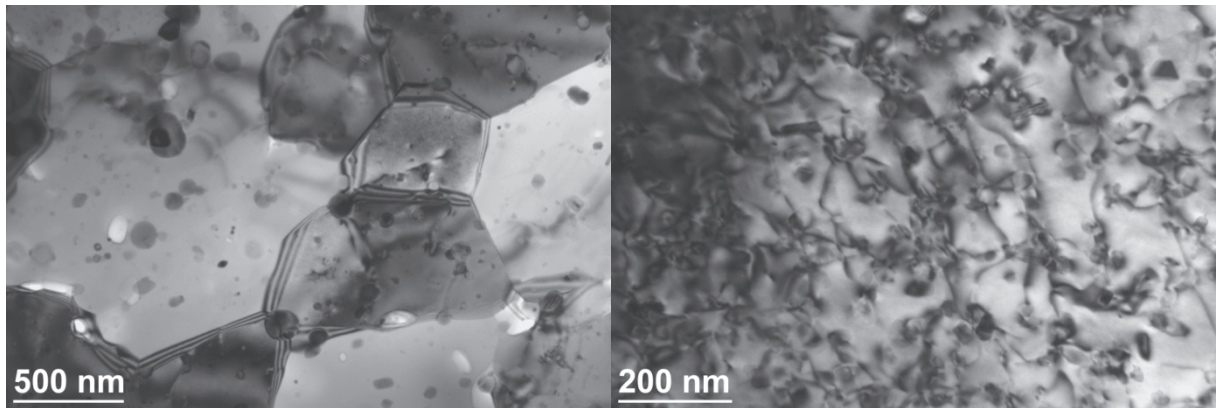


Fig. 3. TEM picture of the friction stir processed material

The microstructure at the TEM scale is showed a bimodal distribution of constituent particles. Next to large Si particles, small particles (precipitates) were also present.

Summary

FSP was used to modification of microstructure in as-cast AlSi9Mg aluminium alloy. In contrast to the as-cast condition, the microstructure in the processed material was characterized by a relatively uniform distribution of second-phase particles. The size and aspect ratio of these particles decreased significantly. The size distribution exhibited bimodal character. The porosity and dendritic microstructure was eliminated.

References

- [1] R.S. Mishra, M.W.Mahoney: Friction Stir Welding and Processing. ASM Int. (2007).
- [2] Z.Y. Ma: Metall. Mat. Trans. 39A (2008), p. 642.
- [3] M. Kopyscianski, M.St. Weglowski, A. Pietras, A. Weglowska, C. Hamilton, S. Dymek: Mat. Eng. Vol. 194 (2013), p. 303.
- [4] A.G. Rao, K.R. Ravi, B. Ramakrishnarao, V.P. Deshmukh, A. Sharma, N. Prabhu, B.P. Kashyap: Metall Mater. Trans. 44A (2013), p. 1519.

Electron microscopy of pressure torsion deformed Cu–10 wt.% In alloy

Anna Korneva^{1,a}, Boris Straumal^{2,3,b}, Paweł Zięba^{1,c}, Askar Kilmametov^{4,d}

¹Institute of Metallurgy and Materials Science, Polish Academy of Sciences, Reymonta St. 25, 30-059 Cracow, Poland

²Institute of Solid State Physics, Russian Academy of Sciences, Ac. Ossipyan str. 2, 142432 Chernogolovka, Russia

³Laboratory of Hybrid Nanomaterials, National University of Science and Technology «MISIS», Leninskii prosp. 4, 119049 Moscow, Russia

⁴Karlsruher Institut für Technologie, Institut für Nanotechnologie, Hermann-von-Helmholtz-Platz 1, 76344 Eggenstein-Leopoldshafen, Germany

^aa.korniewa@imim.pl, ^bstraumal@issp.ac.ru, ^cp.zieba@imim.pl, ^daskar.kilmametov@kit.edu

The Cu–10 wt.% In alloy was subjected to high pressure torsion (HPT) deformation at the room temperature in a Bridgman anvil-type unit. Before deformation the alloy was annealed at 380 °C for 400 h in order to obtain α solid solution (Cu) with precipitations of intermetallic δ phase (Cu₇In₃). Detailed study of microstructure of the alloy before and after deformation were performed using different techniques of scanning and transmission electron microscopy. The microstructure studies showed that HPT resulted in strong grain refinement of Cu matrix (to the nm range), while there was no refinement or dissolution of δ phase. The volume fraction of δ phase after deformation being almost identical as in the initial state (before HPT) indicates strong stability and probably high hardness of this phase.

Introduction

Cu-In based alloys have attracted interest as materials for production of semiconductors [1] as well as thin-film solar cells [2]. However, several intermetallic phases such as Cu₇In₃, Cu₂In, Cu₁₁In₉ present in the Cu–In equilibrium phase diagram makes difficult formation of films with uniform structure. The use of severe plastic deformation (SPD) which can induce dissolution of phases, formation or decomposition of a supersaturated solid solution, disordering of ordered phases, amorphization of crystalline phases [4] etc among with substantial grain refinement can help to overcome such obstacles. In the present paper the results of SPD by HPD method application for Cu–10 wt.% In alloy in the (α + δ) state will be described using scanning and transmission electron microscopy techniques.

Experimental

As cast Cu–10 wt.% In alloy was annealed at 380 °C for 400 h, and then quenched in water. The annealed samples (0.6 mm thick discs) were subjected to HPT at room temperature under a pressure of 5 GPa in a Bridgman anvil-type unit (5 rotations of the anvil with the rate of 1 rpm). The prior inspection of obtained material was carried out on a Philips XL30 scanning electron microscope (SEM) equipped with a LINK ISIS an energy-dispersive X-ray spectrometer (EDS) produced by Oxford Instruments. The details of the phases, especially in nanoscale, were revealed using a TECNAI G2 FEG super TWIN (200 kV) transmission electron microscope (TEM) equipped with an energy dispersive X-ray (EDX) spectrometer manufactured by EDAX.

Results and discussion

The microstructure of examined alloy after annealing at 380 °C for 400 h consists of elongated particles of intermetallic δ phase (Cu₇In₃) in the Cu matrix (Fig. 1a). The average size of δ phase in cross section is about 500 nm. The volume fraction of δ phase reaches almost 25 %. Some dislocations are also observed in the Cu matrix. After HPT process the strong grain size refinement (to the nm

range) of Cu matrix was observed (Fig. 1b), whereas the HPT did not result in refinement or dissolution of δ phase although its boundaries became poorly visible. The chemical composition of this phase before and after deformation did not change. It is possible that this unusual behavior of the δ phase is related to its significant hardness in comparison with Cu-based solid solution in the surrounding matrix. Unfortunately due to small sizes and poorly visible boundaries of δ phase it was not possible to measure the microhardness. However, in the Cu–22 wt. % In alloy (subjected to annealing at 520 °C for 553 h and the same HPT process) the δ phase particles were larger and the measurement of microhardness showed that microhardness of the δ phase was about 278 HV, while this of the nanograined Cu was about 202 HV [5].

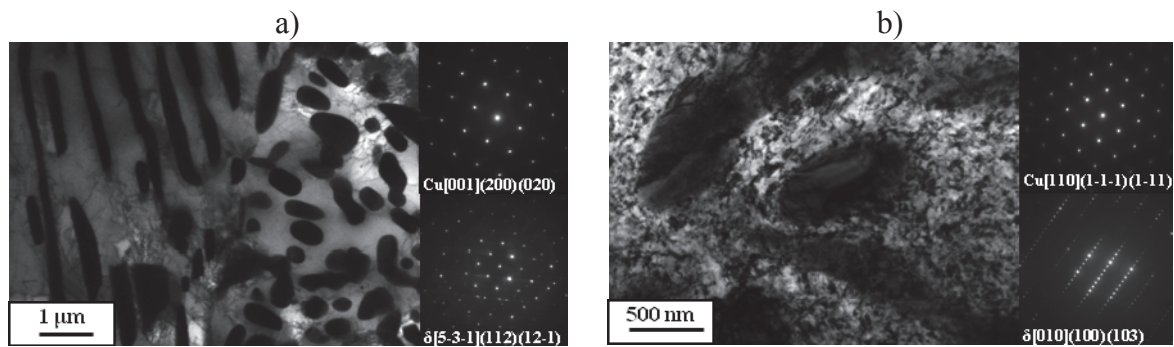


Fig. 1. TEM micrographs of Cu–10 wt. % In alloy after annealing at 380C for 400h (a) and after subsequent deformation by HPT (b) showing dark particles of δ phase (Cu_7In_3) in the Cu matrix (see also inserted electron diffraction patterns)

Summary

Based on the microstructure investigations by SEM and TEM techniques it was found that HPT of Cu-10 wt.% In alloy resulted in strong grain refinement of Cu matrix (to the nm range), while it did not result in refinement or dissolution of δ phase. The chemical composition of this phase after deformation did not also change. Probably such strong stability of δ phase is caused by its high microhardness.

Authors thank Russian Federal Ministry for Education and Science (grant 14.A12.31.0001), EraNet.Rus programme (grant STProjects-219) and the Polish National Science Centre for the financial support (grant DEC-2011/01/M/ST8/07822).

References

- [1] T. Nakano, S. Sato, S. Baba: Vacuum Vol. 74 (2004), p. 591.
- [2] D-W. Kima, H-T. Sona, J-H. Leeb: J. Alloy Compd. Vol. 528 (2012), p. 146.
- [3] X. Sauvage, A. Chbihi and X. Quelebec: J. Phys. Vol. 240 (2010), p. 012003.
- [4] B. B. Straumal, A. R. Kilmametov, Y. Ivanisenko, L. Kurmanaeva, B. Baretzky, Y. O. Kucheev, P. Zięba, A. Korneva, D. A. Molodov: Mater Lett Vol. 118 (2014), p. 111.
- [5] B. Straumal etc: will be published.

Microstructure and texture evolution during cold rolling in the Fe-23Mn-3Si-3Al alloy

Joanna Kowalska^{1,a}, Wiktoria Ratuszek^{1,b}, Małgorzata Witkowska^{1,c},
Anna Zielińska-Lipiec^{1,d}

¹AGH University of Science and Technology, Faculty of Metals Engineering and Industrial Computer Science,
Av. Mickiewicza 30, 30-059 Cracow, Poland

^ajoannak@agh.edu.pl, ^bratuszek@agh.edu.pl, ^cwitkowsk@agh.edu.pl, ^dalipiec@agh.edu.pl

High-manganese austenitic steels constitute an attractive material for the applications in the automotive industry. They exhibit high strength and exceptional plasticity. These properties are obtainable in high-manganese steels, in which plastic deformation induces martensitic transformation (TRIP-effect) and mechanical twinning (TWIP-effect). These requirements could also be met by metastable austenitic chromium-nickel stainless steels during cold deformation [1-6], however, this is non-feasible due to economical reasons.

Stainless steel and high manganese steel are similar in that they both contain ϵ and α' martensite. Martensite ϵ having a hexagonal structure is formed if the chemical composition of the steel is compatible with the formula: $\%Mn < 33\%Cx20$, whereas martensite α' having a regular structure is formed if $\%Mn < 22\%Cx10.5$ [7].

Fe–Mn–C alloys have relatively low stacking fault energies [8]. The addition of Al and Si to the Fe–Mn alloys affects their stacking fault energies and phase stability, and gives rise to various properties in Fe–Mn alloys, such as strain hardening associated with deformation twinning, strain-induced $\gamma_{fcc} \rightarrow \epsilon_{hcp}$ and $\gamma_{fcc} \rightarrow \epsilon_{hcp} \rightarrow \alpha'_{bcc}$ martensitic transformations. Formation of ϵ and α' martensite depends on the chemical composition, temperature and amount of strain. The results of some research has indicated that the alloy mainly reveals the TRIP effect when the manganese content is lower than 15%, while TWIP effect is dominant when manganese content is higher than 25%. For manganese content between 15% and 25%, both effects coexist [9-13].

Most work devoted to high manganese steels has been concentrated on the alloy, which either has TRIP or TWIP effect. In the present work, an alloy was designed with manganese content of 23% to see if both TRIP and TWIP effects could coexist.

Fe–23wt.%Mn–3wt.%Si–3wt.%Al alloy was cast, homogenized at 1150°C, hot-rolled at temperatures between 1200°C and 900°C and cold-rolled from 7% to 40% reductions in thickness. Microstructure and texture of this alloy, which has a low stacking fault energy, were evaluated after cold-rolling. Investigation of X-ray diffraction and transmission electron microscopy showed that mechanical twinning and martensitic transformations ($\gamma_{fcc} \rightarrow \epsilon_{hcp}$ and $\gamma_{fcc} \rightarrow \epsilon_{hcp} \rightarrow \alpha'_{bcc}$) took place during cold-rolling. The crystallographic Burgers relations $\{0001\}\epsilon \parallel \{111\}\gamma$ and $\langle 1120 \rangle \epsilon \parallel \langle 110 \rangle \gamma$ between martensite (ϵ) and austenite (γ), were found in the cold-rolled material.

References

- [1] E. Nagy, V. Martinger, F. Tranata, J. Sólyom: *Mat. Sci. Eng. A378* (2004), p. 308.
- [2] T. Suzuki, H. Kojima, K. Suzuki, T. Hashimoto, S. Koike, M. Ichihara: *Scripta Metall.* Vol. 10, no. 4 (1976), p. 353.
- [3] S. M. Tavares, D. Gunderov, V. Stolyarov, J. M. Neto: *Mat. Sci. Eng. A358* (2003), p. 32.
- [4] H. Oettel, U. Martin: *Int. J. Res.* 97 (2006), p. 1642.
- [5] W. Ratuszek, J. Kowalska, A. Bunsch, M. Rumiński, A. Zielińska-Lipiec: *Arch. Metall. Mater.* Vol. 53 (2008), p. 167.
- [6] A. Bunsch, J. Kowalska, K. Chruściel: *Arch. Metall. Mater.* Vol. 53 (2008), p.125.
- [7] Y. Lü, B. Hutchinson, D. A. Molodov, G. Gottstein: *Acta Mater.* 58 (2010), p. 3079.
- [8] H. Ding, H. Ding, D. Song, Z. Tang, P. Yang: *Mat. Sci. Eng. A528* (2011), p. 868.
- [9] O. Grässel, L. Krüger, G. Frommeyer, L. W. Meyer: *Int. J. Plasticity* 16 (2000), p. 1391.
- [10] G. Frommeyer, U. Brück, P. Neumann: *ISIJ International*, Vol. 43, no. 3 (2003), p. 438.

- [11] J. Kowalska, W. Ratuszek, M. Witkowska, A. Zielińska-Lipiec: *J. Alloys Compd.* in press, <http://dx.doi.org/10.1016/j.jallcom.2013.12.059>.
- [12] J-B Soel, J. E. Jung, Y. W. Jang, C. G. Park: *Acta Mater.* 61 (2013), p. 558.
- [13] H. Idrissi, K. Renard, L. Rueland, D. Schyvers, P. J. Jacques: *Acta Mater.* 58 (2010), p. 2464.

EBSD and X-ray topography in analysis of single-crystalline turbine blades root

Jacek Krawczyk^{1,a}, Maciej Zubko^{1,b}, Włodzimierz Bogdanowicz^{1,c},
Jan Sieniawski^{2,d}, Krzysztof Kubiak^{2,e} and Marzena Szczepkowska^{1,f}

¹University of Silesia, Institute of Materials Science, 75 Pułku Piechoty 1A, 41-500 Chorzów, Poland

²Rzeszów University of Technology, Department of Material Science, W. Pola 2, 35-959 Rzeszów, Poland

^ajacek.krawczyk@us.edu.pl, ^bmaciej.zubko@us.edu.pl, ^cwlodzimierz.bogdanowicz@us.edu.pl,

^djansien@prz.edu.pl, ^ekrkub@prz.edu.pl, ^fmszczepkowska@us.edu.pl

Introduction

The turbine blades of aircraft jet engines are subjected to high loads under high temperatures during operation [1, 2]. This is one of the reasons why they must possess good structural quality and high strength properties under operating conditions. The main parameter that affects the quality of turbine blades is structural perfection which describes the microstructure defects and deviations of crystal orientation [3]. The single-crystalline CMSX-4 nickel-based superalloy is a material compliant with the mechanical and thermal requirements and widely used in production of turbine blades i.a. for aircraft engines.

Due to superalloys specific structure, complex chemical composition and shape of the blades more frequent formation of cast defects occurs. Generated microstructure defects are related to local changes of crystal orientation [4]. The real structure analysis of as-cast blades allows to modify production process for prevent the defects creating and improve the structural quality.

The aim of the study was to analyze the crystal orientation and structure defects of as-cast single-crystalline turbine blades root, using scanning electron microscope technique of Electron Backscatter Diffraction (EBSD) and X-ray topography.

Material and methodology

Five analyzed turbine blades were produced in Research and Development Laboratory for Aerospace Materials in Rzeszów University of Technology. The withdrawal rate of the Bridgman technique was 3 mm/min. The samples for investigations were obtained by cutting blades root parallel to the vertical growth direction. Vertical planes of samples were prepared for further investigations.

The CMSX-4 nickel-base superalloy contain about 70% of cubic γ' phase (Ni_3Al) and the crystallites have almost the same crystal orientation. Therefore the investigation methods used usually for single-crystals can be applied. The JEOL JSM-6480 scanning electron microscope, equipped with backscattered electrons detector, was used for local crystal orientation analysis by EBSD technique. The SEM macro images were performed for analyzing the dendritic structure of the blades root. The Laue method and the crystal orientation mapping method, based on the modern automatic X-ray OD-EFG diffractometer [5] were used for analysis the crystal orientation in macro scale. Analysis of subgrain structure was conducted by classical X-ray diffraction topography, using Panalytical micro-focus source (Cu radiation), coupled with an Auleytner camera.

Summary

The sharp parallel contrast bands were visible on the X-ray topograms. This bands were related with dendrite cores, arranged with the same direction. Additionally the analysis of the topograms showed that, the low angle boundary were formed in certain samples, and it was visible on the topograms as a contrast shifts. The crystal orientation was determined by the Laue method and the specified direction was approximately consistent with preferred $[001]\gamma'$ crystallographic orientation. Local crystal orientation in selected areas of each sample were determined and the maps were created by EBSD technique. Minor variations of crystal orientation in specific areas were observed. Based on

the studies, low angle boundaries and local misorientation were analyzed. Similar investigations were performed by EFG orientation diffractometer. The orientation maps of whole samples were created. The defined α misorientation angle have values up to 10° and were within the limits considered in the standards as critical for use in applications. The crystal orientation maps obtained by EBSD technique were related to the maps, created by EFG diffractometer and the topograms. Not all changes in the crystal orientation of the micro-areas can be visualized by X-ray topography or modern automatic mapping. Local orientation changes can be analyzed only by the EBSD technique. Those methods are mutual complementary.

References

- [1] J.C. Williams and E.A. Strake: *Acta Mater.* Vol. 51 (2003), p. 577.
- [2] R.C. Reed: *The Superalloys: Fundamentals and Applications* (Cambridge University Press, UK 2006).
- [3] A. Onyszko, W. Bogdanowicz and J. Sieniawski: *Sol. St. Phenom.* Vol. 186 (2012), p. 151.
- [4] W. Bogdanowicz, R. Albrecht, J. Sieniawski, K. Kubiak: *J. Cryst. Growth* (2014), in press.
- [5] A. Onyszko, J. Sieniawski, W. Bogdanowicz, H. Berger: *Sol. St. Phenom.* Vol. 203-204 (2013), p. 177.

Superstructuring in the garavellite-berthierite solid solution series $\text{FeSbBiS}_4 - (\text{Fe}_2\text{Sb}_2\text{Bi}_2\text{S}_8 - \text{Fe}_2\text{Sb}_3\text{BiS}_8)$, a TEM and XRD micro diffraction study

Henryk Kucha¹, Heinz Mali², Władysław Osuch¹, Oskar Paris²

¹AGH University of Science and Technology, al. Mickiewicza 30, 30-059 Cracow, Poland

²Mining University Leoben, Austria

Introduction

Superstructuring occurring in various solid solution series is an attractive research target because it is often connected with new and valuable electronic properties. FeSbBiS_4 and FeSb_2S_4 are known in nature as mineral garavellite and berthierite respectively. No superstructuring has been reported so far therefore a statistical occupancy of the Sb-Bi site in the structure is assumed.

Materials and methods

Samples has been collected in the underground Mariengrube mine workings in 1991. The chemical composition of minerals was determined with an ARL SEMQ microprobe at the Institute of Geological Sciences, Mining University Leoben, Austria, at 25 kV. Grain of $\text{Fe}_2\text{BiSb}_3\text{S}_8$ had size 90 μm , grain of $\text{Fe}_2\text{Bi}_2\text{Sb}_2\text{S}_8$ had size of 35 μm .

The X-ray micro-diffraction instrument used was a GADDS (General Area Detector Diffraction System) at Physics Department, Uni Leoben, Austria. The instrument was equipped with a two dimensional detector (HI-STAR, Bruker, Karlsruhe, Germany) and monocapillary tube with hole 50 μm in diameter. The detection parameters of the instrument were as follows: Bruker D8 DISCOVER with GADDS, Cu K α 1.54056 Å radiation working at 40 kV and 40 mA, 150 mm HI-STAR two-dimensional detector, scanning angle 8–32, step size 0.02, scan step time 1800 s.

Superstructuring

On XRD micro diffraction patterns a few superstructure d-values has been detected only for $\text{Fe}_2\text{BiSb}_3\text{S}_8$ and all are weak. XRD system did not show superstructure diffractions in $\text{Fe}_2\text{Bi}_2\text{Sb}_2\text{S}_8$ probably due to too small grain size. However, on TEM diffractions superstructure dots are clearly visible. In $\text{Fe}_2\text{BiSb}_3\text{S}_8$ they occur at 1/3 of distance between main dots (Fig. 1) forming formidable superstructure. The super cell of $\text{Fe}_2\text{BiSb}_3\text{S}_8$ has size (Table 1, Å): $a=11.426\pm 0.009$, $b=14.13\pm 0.007$, and $c=11.45\pm 0.009$.

In $\text{Fe}_2\text{Bi}_2\text{Sb}_2\text{S}_8$ they are less spectacular and occur as weak spots at a half distance between main nodes. The super cell of $\text{Fe}_2\text{Bi}_2\text{Sb}_2\text{S}_8$ has size (Table 1, Å): $a=11.390\pm 0.041$, $b=14.16\pm 0.044$, and $c=7.50\pm 0.041$.

It appears that superstructuring is closely connected with chemistry or stoichiometry of the studied minerals. The a and b parameters of the unit cell are very close to garavellite FeSbBiS_4 and berthierite FeSb_2S_4 (Table 1). The difference occurs in c parametr, which is 3 times larger in FeSbBiS_4 and 2 times larger in $\text{Fe}_2\text{Bi}_2\text{Sb}_2\text{S}_8$ (Table 1).

These results may suggest that more superstructuring controlled by Sb to Bi ratios may be present in the solid solution studied offering an interesting new electronic properties. TEM diffraction appears to be the most suitable method to detect and characterize superstructuring in sold solutions.

Table 1. Crystallographic parameters of minerals related or close to garavellite

| | a | b | c | Method |
|--|--------------|--------------|--------------|----------|
| Fe ₂ BiSb ₃ S ₈ new mineral | 11.426±0.009 | 14.130±0.007 | 11.452±0.009 | XRD, TEM |
| Fe ₂ Bi ₂ Sb ₂ S ₈ new mineral | 11.390±0.041 | 14.16±0.44 | 7.50±0.041 | TEM |
| FeSbBiS ₄ garavellite | 11.439 | 14.093 | 3.754 | XRD |
| FeSb ₂ S ₄ berthierite | 11.44 | 14.12 | 3.76 | XRD |

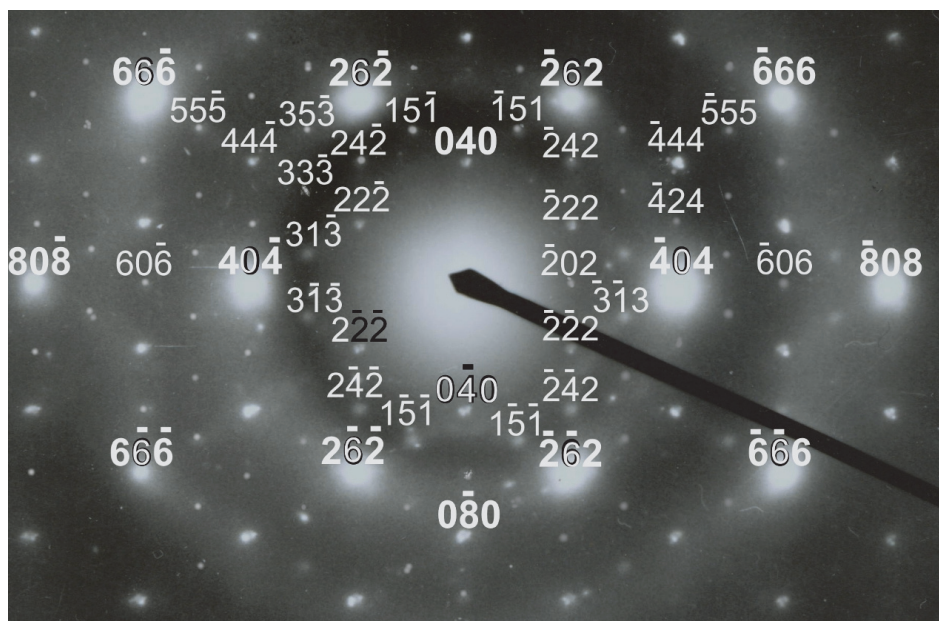


Fig. 1. The 101 electron diffraction pattern of Fe₂BiSb₃S₈ showing two types of diffraction dots: i) basic very strong with $(h+k+l)=2^2 2(n+1)$, and ii) subsidiary, weak nodes forming hexagonal superstructure with $(h+k+l)=\text{odd}$ around basic strong nodes and connected with ordered substitution of Bi for Sb in the structure

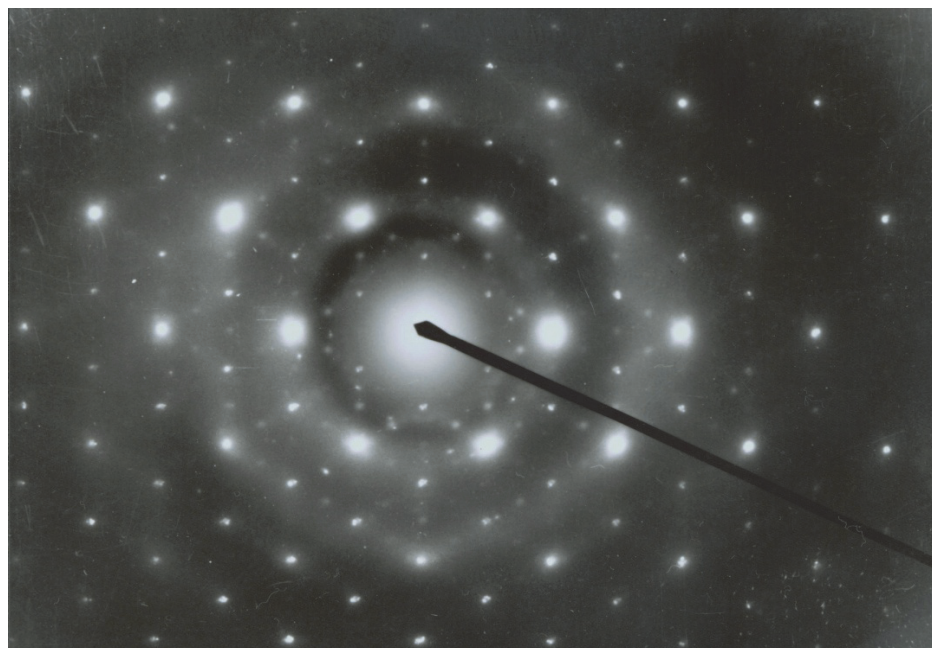


Fig. 2. The 101 electron diffraction pattern of Fe₂BiSb₃S₈ free of Miller indices to show a clear picture of superstructuring around main nodes (compare to Fig. above)

Electron microscope investigation of cast aluminium alloy after laser feeding with ceramic powder

Krzysztof Labisz^{1,a}, Tomasz Tanski^{2,b} and Jaroslaw Konieczny^{3,c}

¹Division of Materials Processing Technologies, Management and Computer Techniques in Materials Science, Institute of Engineering Materials and Biomaterials, Silesian University of Technology, Konarskiego 18A, 44-100 Gliwice, Poland

²Division of Biomaterials Engineering, Institute of Engineering Materials and Biomaterials, Silesian University of Technology, Konarskiego 18A, 44-100 Gliwice, Poland

³ Division of Metal and Polymer Materials Processing, Institute of Engineering Materials and Biomaterials, Silesian University of Technology, Konarskiego 18A, 44-100 Gliwice, Poland

^akrzysztof.labisz@polsl.pl, ^btomasz.tanski@polsl.pl, ^cjaroslaw.konieczny@polsl.pl

In this paper there are presented results of Transmission Electron Microscope investigation concerning the structure of the AlSi7Cu2 cast aluminium alloy after alloying and remelting with the high power diode laser (HPDL). In this work especially the changes of the particle/precipitation type, size and shape were determined. The reason of this work was also to present the laser treatment technology, which will be used for further alloying and remelting with ceramic powders – especially carbides and oxides. Particularly the overview will be directed on the laser power to achieve good layer hardness for protection of this hot work tool steel from losing their work stability and to make the tool surface more resistant to action in external conditions.

Introduction

Laser surface alloying using HPDL laser is well established method of surface properties improvement for many materials. Improvement of surface layer in respect of wear resistance can be obtained by alloying of the surface with hard particles such as carbides to locally reinforce the surface of steel. The surface hardening can be achieved with different manners - feeding of hard particles of TiC, WC, VC, SiC, WC as well as alloying with Si₃N₄ nitrides or oxides like Al₂O₃, ZrO₂ resulting in the modification of their resistance to pitting or intergranular corrosion.

Aluminium alloys are widely used structural materials group and particularly interesting due to their wide application possibilities and low weight as well a very good application properties and huge range of investigations. Laser alloying and remelting was performed using high-power diode laser HPDL - High Power Diode Laser for the reason of a purposeful changes in the surface structure of the surface of the element and reduce the cost of materials.

Material and investigations methods

The aluminium alloy AlSi7Cu2 was used for investigations, supplied in form of moulds, with a standard heat treatment carried out, including solution heat treatment at 505°C for 600min and ageing at 170°C for 720 min.

The examinations of thin foils microstructure and phase identification were carried out on the S/TEM Titan 80/300 transmission electron microscope (TEM), at the accelerating voltage of 300 kV. TEM specimens were prepared by cutting thin plates from the material. The specimens were ground down to foils with a maximum thickness of 80 µm before 3 mm diameter discs were punched from the specimens. The disks were further thinned by ion milling method with the Precision Ion Polishing System (PIPS™), used the ion milling device model 691 supplied by Gatan until one or more holes appeared. The ion milling was done with argon ions, accelerated by a voltage of 15 kV, energy and angle are presented in Table 1.

Table 1. Ion milling parameters using for polishing

| Angle [°] | Energy [KeV] | Time [min] |
|-----------|--------------|------------|
| 6 | 3.8 | 180 |
| 3 | 3.2 | 15 |

Investigation results

The examined layers consists of three subzones – the remelted zone, the heat influence zone and the substrate material. In the remelted zone based on TEM investigations it was found that, the SiC (Fig. 1, 2) powder particles occurs in the Al matrix as small grains with the size of ca. 2-3 micrometers, that is tenth of times smaller than the original powder used for feeding, where the size was in the range of ca. 100 μm . Further investigations will be needed to revealed the morphology and nature of these particles occurred in the remelting zone, occurring after alloying with different process parameters and different ceramic powders.

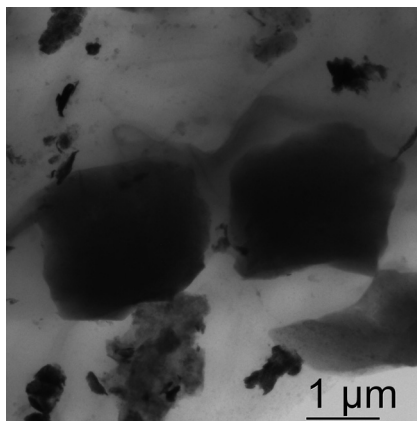


Fig. 1. SiC particles in Al α -matrix after HPDL feeding/alloying

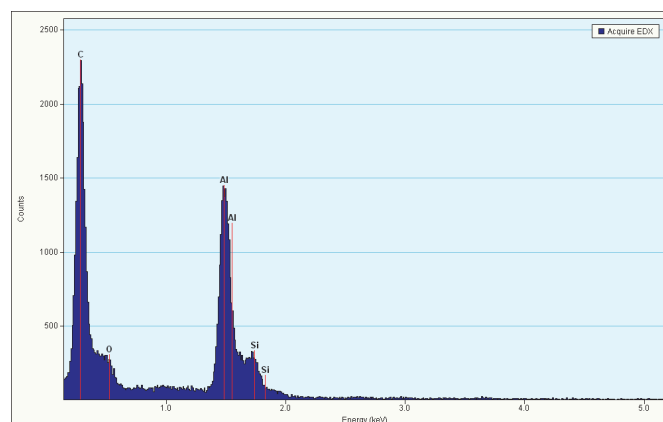


Fig. 2. EDS point-wise analysis performed in the marked point in Fig. 1

Summary

The analysis of the thin foils after the ageing process has confirmed that the structure of the aluminium cast alloy consists of the solid solution α – Al (matrix) with embedded secondary phases, mainly Al_2Cu or Mg_2Si evenly distributed in the structure. Furthermore, the examinations of thin foils of aluminium cast alloys after ageing confirm the appearance of a high density of defects of the crystal structure in the material. As the most often occurred phase, despite to Si needle, the SiC particles were found using transmission electron microscope, but in size of few microns only, what can lead to the conclusion, that beside feeding also alloying occurs during the laser treatment of the Al cast alloy surface layer.

Acknowledgements

This research work was financed partially within the framework of the Polish State Committee for Scientific Research Project (NCN) No. 2011/01/B/ST8/06663 headed by Dr Krzysztof Labisz.

References

- [1] W. Ozgowicz, K. Labisz: J. Iron Steel Res. Int. Vol. 18/1 (2011), p. 135.
- [2] T. Tański, K. Labisz: Sol. St. Phenom. Vol. 186 (2012), p. 192.

The effect of additions of Zn and Zr on the structure and texture of cast and wrought Mg alloys with different content of Ca

Sonia Boczkal^{1a}, Marzena Lech–Grega^{1b}, Janusz Żelechowski^{1c}

¹Institute of Non-Ferrous Metals, Light Metals Division, Skawina, Poland

^asboczkal@imn.skawina.pl, ^bmlechgrega@imn.skawina.pl, ^cjzelechowski@imn.skawina.pl

Introduction

New lightweight materials characterised by specific properties are currently enjoying the great interest of the industry. Such materials include magnesium and its alloys. Pure magnesium, although characterised by low density and satisfactory mechanical properties, is not as extensively used as a construction material as other pure metals. Despite this, magnesium plays the fundamental role in the biological system. Magnesium is a natural ion and component of the bone tissue [1, 2]. Additionally, compared with other commonly used implants, it was found to offer the mechanical properties approaching most the natural mechanical properties of the bone [3]. Alloying elements such as Ca, Zn, Y, and Zr play quite a special role in the magnesium characteristics such as biodegradability and biocompatibility in living organisms. Therefore, at present, a wide-scale research is carried out on an impact of these elements on the properties of magnesium for applications such as implants and surgical sutures [1, 3].

In this study, an attempt has been made to characterise magnesium alloys by electron microscopy and X-ray diffractometry. Of particular interest as regards the cognitive aspect of the study was phase and texture analysis of Mg-Ca alloys and Mg-Ca alloys with constant addition of 6% Zn and 0.4% Zr in as-cast and as-extruded condition.

Results

The study makes analysis of seven alloys, i.e. three Mg alloys containing Ca at a level of 1%, 2.5% and 5%, two Mg6%Zn alloys and two Mg6%Zn0.4%Zr alloys containing Ca at a level of 1% and 2.5%. Phase and texture analysis was carried out using SEM with EDS and EBSD starters, TEM with EDS chemical analysis and X-ray diffractometry. The structure of the MgCa2.5 alloy was observed to comprise Mg₂Ca phases, which were arranged along the grain boundaries, and their content was increasing along with the increasing content of Ca in Mg (Fig. 1).

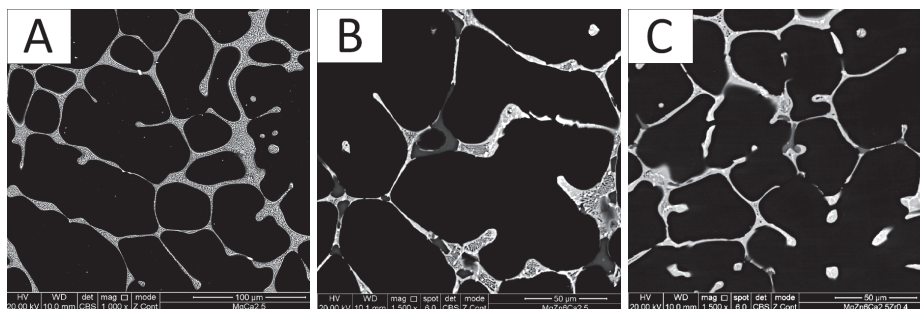


Fig. 1. As-cast structure of the MgCa2.5 alloy examined by: a) SEM and b) TEM

After the extrusion process, at a temperature of 400°C, it was observed that the additions of Zn and Zr in the presence of a variable content of Ca had varied effect on the structure of the examined alloys. With the increasing content of Ca in Mg, the average grain size of the recrystallised grains increased up to 15 μm in the MgCa5 alloys. The addition of Zn increased further the grain size, making it much larger than in the same alloy without Zn (Fig. 2). In contrast, the addition of Zr to the

MgCa2.5Zn alloy at a level of 0.4% arrested the migration of the recrystallised grain boundaries and induced a strong refinement of the structure in as-extruded condition.

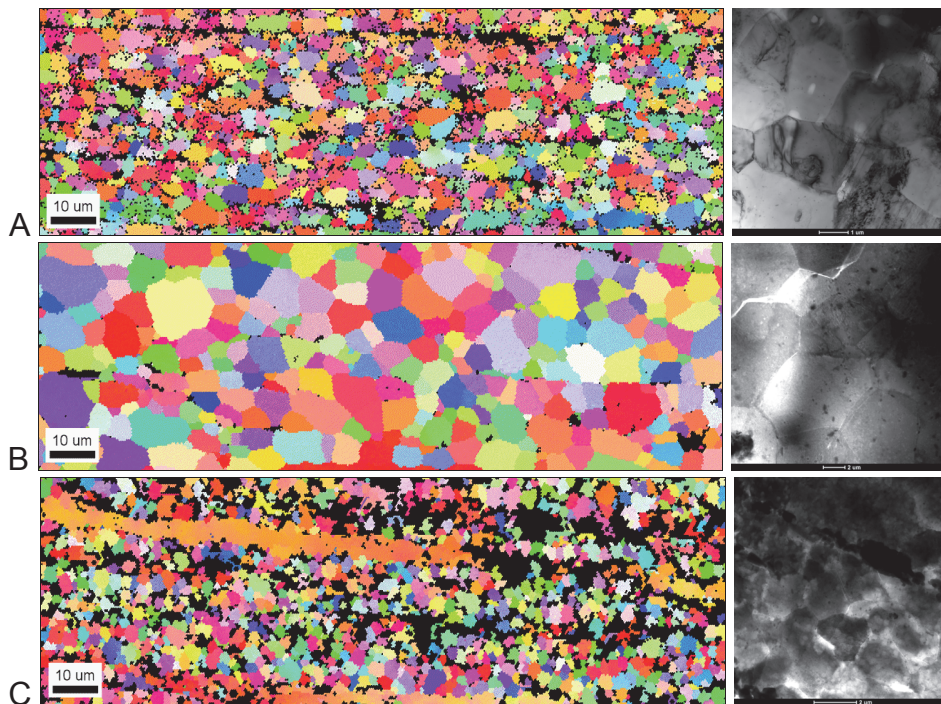


Fig. 2. Confirmed by TEM examinations, EBSD analysis of the following as-extruded alloys: a) MgCa2.5; b) MgCa2.5Zn; c) MgCa2.5ZnZr

Summary

The phase analysis of as-cast alloys carried out by the X-ray diffractometry has showed that the structure of Mg with varying content of Ca includes an Mg_2Ca phase, while Mg6% Zn alloys with different content of Ca contain a $Ca_2Mg_6Zn_3$ phase present in the form of eutectic at grain boundaries. Additionally, applying SEM analysis, the Mg6%Zn2.5%Ca alloys were found to contain an Mg_2Ca phase, occurring mainly at the multi-grain contact boundaries. The EBSD analysis of alloys subjected to plastic forming revealed an impact of Zr on structure refinement, although the structure of castings was observed to contain some non-dissolved compounds of Zr. The grain size in alloys containing Zr was the smallest and amounted to about 3 μm . TEM observations confirmed the results of analysis. The graphs of inverse pole figures indicate that the network planes most often parallel to the cross-sections of the examined magnesium rods are the network planes $(1\ 0\ 0) = (1\ 0\ \bar{1}\ 0)$.

References

- [1] J.F.Nie, B.C. Muddle: Scripta Mater. Vol. 37 (1997), p. 1475.
- [2] N. T. Kirkland, M.P. Staiger, D.Nisbet, Ch.H.J. Davies, N. Birbilis: Performance-driven design of biocompatible Mg alloys: JOM, June 2011, p. 28.
- [3] Y. Li, P. D. Hodgson, C.Wen: J. Mater. Sci. 46 (2011), p. 365.

Microstructure characterization of $ZrO_2 - Y_2O_3$ coatings deposited by thermal spraying process

Maria W. Richert^{1,a}, Beata Leszczyńska - Madej^{1,b}, Ilona Nejman^{1,c},
Paulina Zawadzka^{1,d}

¹AGH University of Science and Technology, Faculty of Non Ferrous Metals, Mickiewicza 30 Av., 30 – 05 Kraków, Poland

^amrichert@agh.edu.pl, ^bbleszcz@agh.edu.pl, ^cinejman@agh.edu.pl, ^dpauzaw@agh.edu.pl

The microstructure, phase composition wettability and microhardness of three types plasma spraying coatings: $ZrO_2 - Y_2O_3$, $ZrO_2 - Y_2O_3 + 10\%C$ and $ZrO_2 - Y_2O_3/Cr_3C_2 - NiCr$ deposited on graphite substrate were investigated. The thickness of coatings was found of about $200 \pm 20 \mu m$. The plasma spraying parameters are presented in Table 1.

Table 1. Plasma spraying parameters

| Ar, l/h | H ₂ , l/h | Voltage, V | Current, A | Distance, mm |
|---------|----------------------|------------|------------|--------------|
| 2500 | 160 | 50 | 450 | 80 |

The microstructure of coatings was observed by using optical microscopy (MO), scanning electron microscopy (SEM) and transmission electron microscopy (TEM). The obtained coatings are typical for plasma spraying technique. It contains some pores and discontinuities which locate between the grains (fig. 1, 2). Two types of grains morphologies were observed in the microstructure: almost equiaxial (fig. 2a) and elongated in the direction of heat extraction (fig. 2b). Both of them have nanometric size.

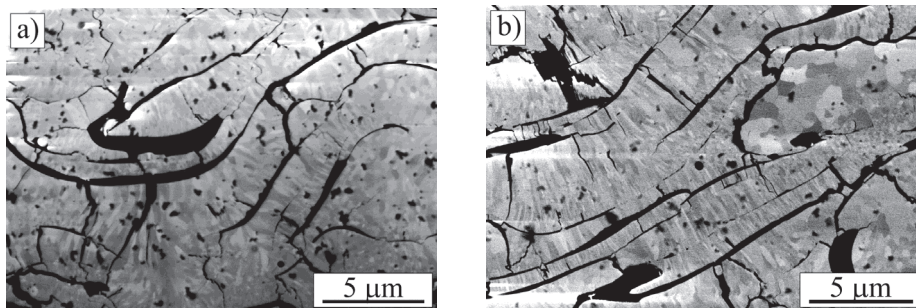


Fig. 1. Microstructure of: a) $ZrO_2 - Y_2O_3$, b) $ZrO_2 - Y_2O_3 + 10\%C$ coatings deposited by thermal spraying process, SEM

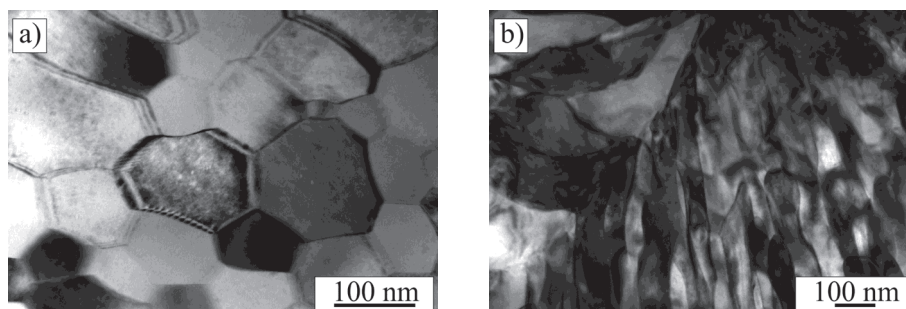


Fig. 2. Microstructure of $ZrO_2 - Y_2O_3/Cr_3C_2 - NiCr$ coating deposited by thermal spraying process, TEM

Microhardness of the investigated coating was in the range of 550 – 600 HV0.2. Addition of glassy carbon and Cr_3C_2 – NiCr increase microhardness level of about 5 - 10% compared to ZrO_2 – Y_2O_3 . All the coatings show poor wettability, wetting angle is about 127 – 131°.

Acknowledgements

The work was financially supported by polish project No: INNOTECH – K2/IN2/62/181851/NCBR/13.

Microstructure of rapidly and conventionally solidified quasicrystalline Al-Cu-Fe alloys

Lidia Lityńska-Dobrzyńska^a, Joanna Wojewoda-Budka^b, Anna Góral^c,
Katarzyna Stan-Głowińska^d, Mikołaj Mitka^e and Jan Dutkiewicz^f

Institute of Metallurgy and Materials Science Polish Academy of Sciences, 30-059 Krakow, 25 Reymonta St.,
Poland

^al.litynska@imim.pl, ^bj.wojewoda@imim.pl, ^ca.goral@imim.pl, ^dk.stan@imim.pl, ^em.mitka@imim.pl,
^fj.dutkiewicz@imim.pl

Introduction

Al-Cu-Fe quasicrystalline alloys exhibit unique combination of physical, thermal and mechanical properties [1]. Stable icosahedral quasicrystalline phase (I-phase) lies in a very narrow composition range [2, 3] and usually coexists with other phases in the as cast alloys. The phase composition in these alloys depends on chemical composition and solidification rates. A broader area of quasicrystalline phase can be observed in rapidly solidified alloys [5, 6] and in this case quasicrystals solidify directly from the melt as primary phase and crystalline phases formed at the inter-dendritic region from the remaining melt [7].

In the present study, the microstructural characteristic of conventionally cast and melt spun ribbons of Al-Cu-Fe alloys at a composition range 20 to 25.5 at.% Cu and from 12 to 15 at.% Fe have been investigated.

Experimental

The Al₆₅Cu₂₀Fe₁₅, Al₆₅Cu₂₃Fe₁₂, Al₆₈Cu₂₀Fe₁₂ and Al₆₂Cu_{25.5}Fe_{12.5} (in at.%) alloys were prepared by induction melting under argon atmosphere using Al, Cu and Fe elements of purity 99.99%. Ribbons were produced using a melt-spinning technique. The obtained ribbons were in the form of fragmented, brittle flakes. The microstructure of the conventionally cast alloys and melt spun ribbons was examined using Philips PW 1840 X-ray diffractometer (XRD), FEI scanning electron microscope E-SEM XL30 (SEM) and FEI transmission electron microscope Tecnai G² (TEM).

Results

All alloys cast as conventional ingot contained quasicrystalline phase of icosahedral structure (I-phase). Besides I-phase, cubic τ (AlCu) and monoclinic λ (Al₁₃Fe₄) were found in the Al₆₅Cu₂₀Fe₁₅ and Al₆₂Cu_{25.5}Fe_{12.5} alloys. In alloys containing more Al as compared to Fe (Al₆₅Cu₂₃Fe₁₂, Al₆₈Cu₂₀Fe₁₂), the I-phase and λ (Al₁₃Fe₄) coexist mainly with Θ (Al₂Cu) instead τ (AlCu). In all investigated alloys the small amount of η (AlCu) was also detected. EDX microanalysis results confirmed presence of phases identified by X-ray experiments. Based on the SEM images it could be conclude that the I-phase solidified peritectically from the λ and liquid in all alloys.

In the rapidly solidified ribbons the amount of phases were reduced as compared to the alloys cast as ingots. The I-phase was dominant in all ribbons and was observed as small cell or dendrite. Between them the τ (AlCu) phase were identified in the Al₆₅Cu₂₀Fe₁₅ and Al₆₂Cu_{25.5}Fe_{12.5} ribbons, while in the Al₆₅Cu₂₃Fe₁₂ and Al₆₈Cu₂₀Fe₁₂ this phase was replaced by Θ (Al₂Cu). The microstructures of ribbons were not homogenous and the area of small grains contained I-phase located near the wheel side. The identification of the phases inside the ribbons was done made by EDX microanalysis in TEM and electron diffraction patterns. In the ribbons the quasicrystal solidified from the melt as a primary phase and the crystalline phases formed at the inter-dendritic regions from the remaining melt. The example of the microstructures of cast Al₆₂Cu_{25.5}Fe_{12.5} alloy and the ribbon was presented in Figure.

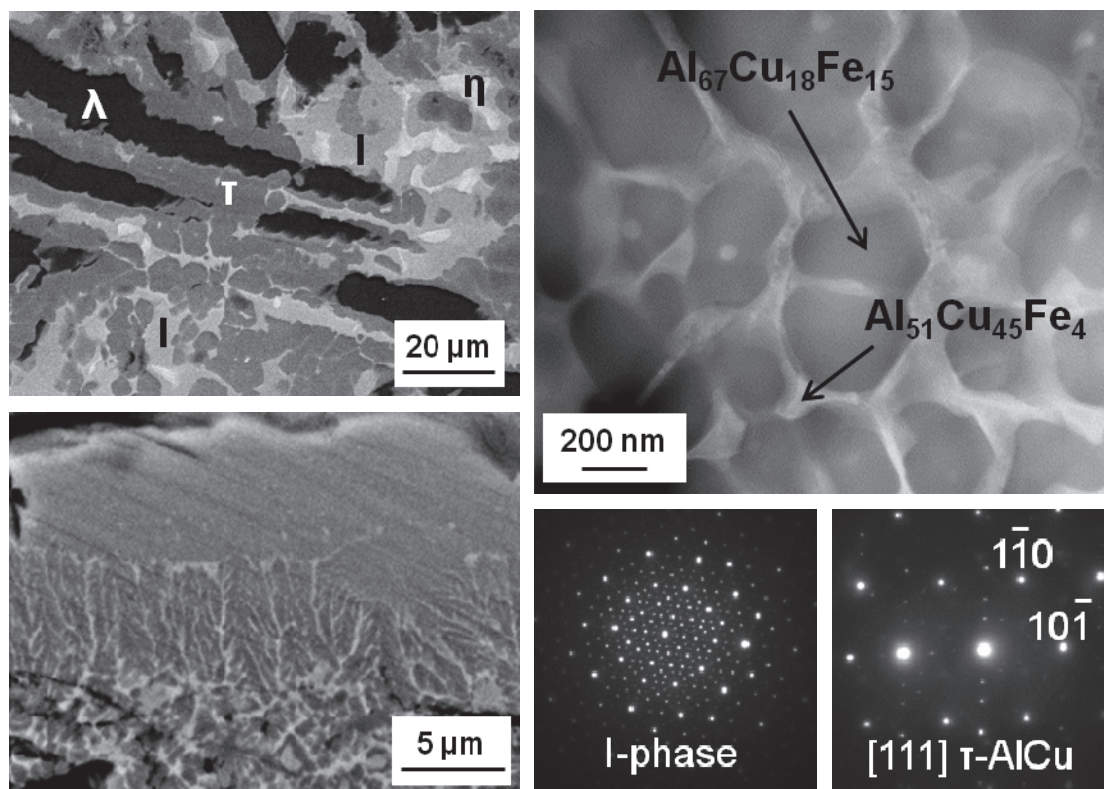


Fig. SEM images of the $\text{Al}_{62}\text{Cu}_{25.5}\text{Fe}_{12.5}$ cast alloy and the cross-section of the ribbon; STEM-HAADF image of the ribbon and electron diffraction patterns from the dendrite of I-phase (5-fold symmetry) and τ -AlCu phase located at interdendritic areas

Summary

In the conventionally cast alloys icosahedral I-phase formed as a product of peritectic reaction and coexist with λ ($\text{Al}_{13}\text{Fe}_4$), cubic τ (AlCu), Θ (Al_2Cu) and η (AlCu) crystalline phases.

The I-phase dominated in the ribbons of $\text{Al}_{65}\text{Cu}_{20}\text{Fe}_{15}$, $\text{Al}_{65}\text{Cu}_{23}\text{Fe}_{12}$, $\text{Al}_{68}\text{Cu}_{20}\text{Fe}_{12}$ and $\text{Al}_{62}\text{Cu}_{25.5}\text{Fe}_{12.5}$ and solidified in the form primary of cells or dendrites. In interdendritic areas τ or Θ occurred depending on the content of Al and Fe.

Acknowledgments

Financial support from the Polish National Science Centre NCN (research projects no 2011/03/B/ST8/05165) is gratefully acknowledged.

References

- [1] J.M. Dubois: Chem. Soc. Rev. Vol. 41 (2012), p. 6760.
- [2] E. Huttunen-Saaivirta: J Alloys Compd. Vol. 363 (2004), p.150.
- [3] F. Faudot, A. Quivy, Y. Calvayrac, D. Gratias and M.Harmelin: Mater. Sci. Eng. Vol. A133 (1991), p. 383.
- [4] L. Zhang and R. Lück: Z. Metallkd. Vol. 94 (2003), p. 774.
- [5] E. Huttunen-Saarivita and J. Vuorinen: Intermetallics Vol. 13 (2005), p. 885.
- [6] B. Avar, M. Gogebakan and F. Yilmaz: Z. Krystallogr. Vol. 223 (2008), p. 731.
- [7] S.M. Lee, H.J. Jeon, B.H. Kim, W.T. Kim and D.H. Kim: Mater. Sci. Eng. Vol. A 304-306 (2001), p. 871.

Characterization of the high potential carbon supports predicted as efficient materials for hydrogen storage

Mirosława Pawłyta^{1,a}, Dariusz Lukowiec^{2,b} and Barbara Liszka^{3,c}

¹ Institute of Engineering Materials and Biomaterials, Silesian University of Technology, Konarskiego 18A, 44-100 Gliwice, Poland

² Institute of Engineering Materials and Biomaterials, Silesian University of Technology, Konarskiego 18A, 44-100 Gliwice, Poland

³ Centrum Materiałów Polimerowych i Węglowych Polskiej Akademii Nauk (CMPW/PAN), M. Curie-Skłodowskiej 34, Zabrze 41-819, Poland

^amirosława.pawlyta@polsl.pl, ^bdariusz.lukowiec@polsl.pl, ^cbarbara.liszka@cmpw-pan.edu.pl

Nanostructural carbon materials have amazing potential for humanity and can in future change our life, to enable to make use of energy source and storage, in way friendly to the environment and economically justified. Theoretical works confirmed the high potential of Ti on carbon supports as new and efficient materials for hydrogen storage [1,2]. The aim of presented paper is to characterise selected carbon materials – modified Carbon Blacks, predicted for such application.

For well ordered carbon materials the method of choice for structure characterisation during graphitisation is Raman spectroscopy [3]. If an average diameter of graphitic-like domains L_a is larger than 5 nm, it can be determined by classical Tuinstra and Koenig's formula (1):

$$L_a = \frac{4.35nm}{I_D / I_G} \quad (1)$$

More universal relation $I_D / I_G \propto 1/L_a$ can be applied only for comparison of carbonaceous materials characterised by sufficiently high degree of organization ($L_a > 2$ nm), otherwise $I_D / I_G \propto L_a^2$ have to be used [4]. Carbon Blacks are classified as non-graphitizing carbons (which not convert easily into graphite). Quantitative information about L_a can be obtained from Raman spectroscopy only if correct fitting procedures are applied [5] (Fig.1) but even in such case it have to be verified with transmission electron microscopy.

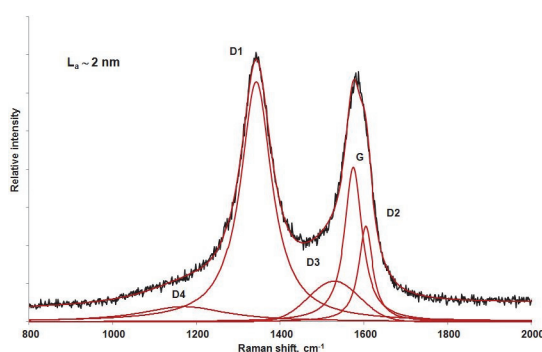


Fig. 1. Raman spectrum of Carbon Black sample heated at 1500°C - the extend of the 'graphitic-like' domains can not be determined using Tuinstra and Koenig's formula (1)

Two grades of commercial Carbon Blacks (a post oxidized gas black and a super conductive carbon black, achieved in specific confidential post-treatment) were used in conducted researches. The advantages of selected Carbon Blacks are: high specific surface area value (S_{BET} between 500 and 1000 m^2/g), accessibility, low price, low harmfulness (in contradiction to commonly applied carbon nanotubes) and possibility to modify their structure on atomic level at simple heat process. The result of functionalization and next metal nanoparticles deposition depend on the development of

surface area and density of remained structure defects. Heat treatment of Carbon Blacks enables removing of structure defects but final size of resulted ordered domains L_a are limited by primary particle diameter ($d_p = 20\text{-}30\text{ nm}$). Correct selection of used Carbon Blacks as well as temperature of heat treatment make possible to adequately adjust density of remained structure defects.

Structure changes during heat treatment are directly visible on TEM images – carbon layers are connecting, become parallel arranged and flat (Fig. 2). In microscopy researches of carbon materials challenging factor is weak contrast. Difficulties at imaging carbon materials result from the fact that light elements like carbon ($Z=6$) poorly scatter high energy electrons. An additional factor is that electron beam destroys the structure of these materials (knock-on damage) [6]. For that reasons imaging were conducted with lower accelerating voltage (80 kV) and in STEM mode. Final stage of presented work is comparison of preliminary results of deposition of selected metal nanoparticles on the such obtained and characterised carbon supports predicted as materials for hydrogen storage.

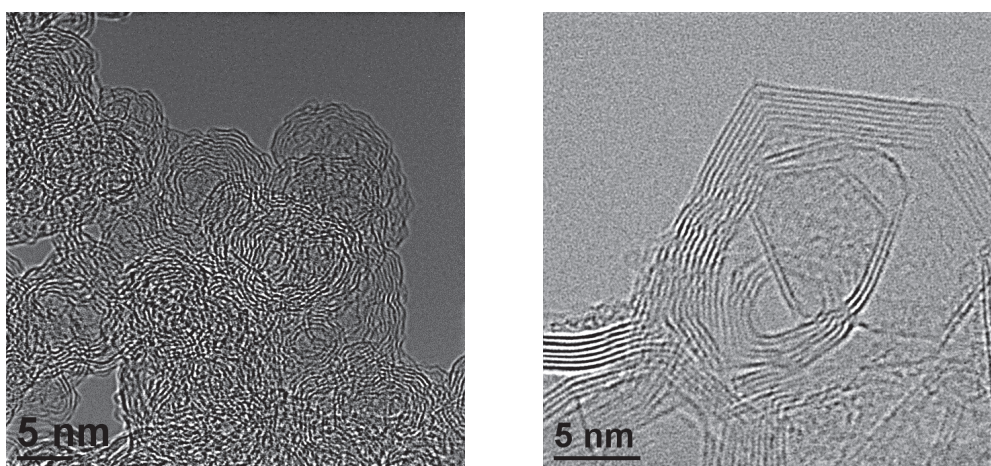


Fig. 2. TEM and STEM images of Carbon Black samples on different carbonization/graphitization stages

References

- [1] T. Yildirim and S. Ciraci: *Phys. Rev. Lett.* 94 (2005), p. 175501.
- [2] F. Zuliani, L. Bernasconi, E. J. Baerends: *J. Nanotech.* Vol. 2012 (2012), <http://dx.doi.org/10.1155/2012/831872>.
- [3] F. Tuinstra, J. L. Koenig: *J. Chem. Phys.* 53 (1970), p. 1126.
- [4] A. C. Ferrari, J. Robertson: *Phys. Rev. B: Condens. Matter Mater. Phys.* 61 (2000), p. 14095.
- [5] A. Sadezky, H. Muckenhuber, H. Grothe, R. Niessner, U. Pöschl: *Carbon* 43 (2005), p. 1731.
- [6] J.R. Jinschek, E. Yucelen, H.A. Calderon, B. Freitag: *Carbon* (2011), p. 556.

Microstructure of novel multilayer nano- composite, protective coatings for medical tools application

Łukasz Major^{1,a}, Roman Major^{1,b}, Jurgen M. Lackner^{2,c}, Jerzy Morgiel^{1,d}

¹ Institute of Metallurgy and Materials Science; Polish Academy of Sciences, 30-059 Cracow, 25 Reymonta Street, Cracow, Poland

² JOANNEUM RESEARCH- Materials- Institute for Surface Technologies and Photonics; Leobner Strasse 94; 8712 Niklasdorf, Austria

^al.major@imim.pl, ^br.major@imim.pl, ^cjuergen.lackner@joanneum.at, ^dj.morgiel@imim.pl

Introduction

Nanotechnology is the ability to manipulate atoms and molecules to produce nano- structured materials and functional nano- coatings on biomedical devices and surgical tools. Medical devices and surgical tools that contain micro and nano- scale features allow surgeons to perform clinical procedures with greater precision and safety in addition to monitoring physiological and bio-mechanical parameters more accurately. Transition metal nitrides films deposited by physical vapor deposition (PVD) process have now been used in a range of engineered application because of their desirable properties including high hardness and chemical inertness, thus they are often used as a protective coatings. Multilayers can lead to benefits in performance over comparable single- layer coatings and can combine the attractive properties of different materials in a single protective layer [1, 2]. The introduction of a number of interfaces parallel to the substrate surface can act to deflect cracks increasing the toughness and hardness of the coating.

The aim of the present work was to develop and characterize a novel type of nano- composite, multilayer, bio- tribological coatings. They were consisted of two parts. The first part, from the metallic substrate, was conventional chromium/ chromium nitride (Cr/CrN) multilayer. It is characterized by an appropriate crystallographic adjustment of subsequent constituent layers of Cr and CrN [3, 4] and by the creation of a transition layer between them with a thickness of several dozen of nanometers [5]. This ensures a good connection between particular constituent layers and as a result also good maintenance properties: high adhesion [6], wear [7] and corrosive [8] resistance. The second part of the coating was consisted of chromium/ amorphous carbon (Cr/a-C:H) multilayer which was deposited on Cr/CrN. Amorphous carbon coatings have been attracting great interest due to their excellent properties such as biocompatibility, hemocompatibility, low friction and chemical inertness [9, 10]. The amorphous nature of a-C:H opens the possibility to introduce certain amounts of additional elements. In the presented paper nano- Cr crystallites were also inserted into a-C:H structure forming pure a-C:H/ a-C:H implanted by Cr nano- crystals multilayer. The preliminary experiments confirmed very good coating adhesion to the substrate as well as showed that nano- Cr crystallites were distributed in a-C:H structure in the form of very thin layers with a thickness equal to one Cr crystallites size.

Methodology

A hybrid PLD system (Pulsed Laser Deposition connected with magnetron sputtering) equipped with chromium (99.9% Ti) and carbon (graphite) targets were used for multilayer coatings deposition. The microstructure of coatings was studied with TECNAI G² F20 FEG (200 kV transmission microscope). Chemical analysis was performed using Energy Dispersive X-ray Spectroscopy (EDS). Thin foils for these observations were prepared using QUANTA 200 3D Dual Beam Focused Ion beam (FIB) equipped with OmniProbe in-situ lift out system.

Results

The microstructure characterization was presented in the bright field TEM image (Fig. 1).

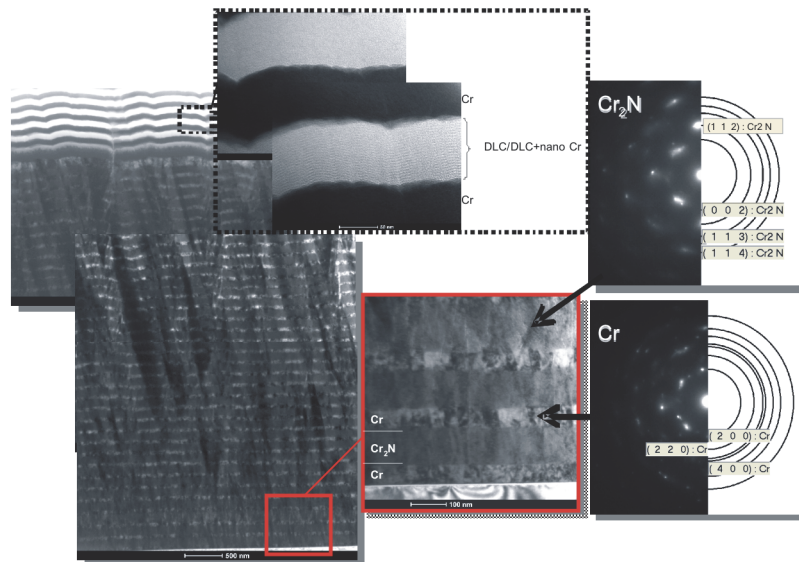


Fig. 1. Cross-section microstructure of nano- composite, multilayer coating, and accompanying electron diffraction patterns

In the Cr/CrN part, the same diffraction contrast went through several interfaces. This ensures a good connection between particular constituent layers. The role of Cr/DLC part was to enhance the bio- compatibility and reduce friction coefficient. Additionally DLC part was implanted by Cr nano-crystals, in the form of few nanometer thick layers

Conclusions

The novel type of nano- composite, multilayer coatings for medical tools application has been design and deposited. The hybrid PLD technique allowed to produce complex structure, with uniform layers thickness up to several nanometers. The detailed microstructure analysis has been performed using transmission electron microscopy technique. This method allowed to define and describe each part of such structure, present chemical composition and elements distribution, as well as showed the crystallographic dependency in between layers, phases and parts. In the Cr/CrN part, the same diffraction contrast passed through several interfaces. This ensures a good connection between particular constituent layers. The investigations confirmed high quality adhesion of the coating to the substrate as well as in between the Cr/CrN and the Cr/a-C:H parts.

Acknowledgement

Research project was financed by the National Science Centre (Polish- Narodowe Centrum Nauki, abbr. NCN) No: 2012/07/B/ST8/03396

References

- [1] L. Major, W. Tirry, G. Van Tendeloo: Surf. Coat. Technol. Vol. 202 (2008), p. 6075.
- [2] J. M. Lackner, L. Major, M. Kot: Bull. Pol. Ac.: Tech. Vol. 59 (2011), p. 343.
- [3] P. Wicinski, J. Smolik, H. Garbacz, K. J. Kurzydowski: Thin Solid Films Vol. 519 (2011) p. 4069.
- [4] J. Romero, J. Esteve, A. Lousto: Surf. Coat. Technol. Vol. 188- 189 (2004), p. 338.
- [5] S. Han, J.H. Lin, X.J. Guo, S.H. Tsai, Y.O. Su, J.H. Huang, F.H. Lu, H.C. Shih: Thin Solid Films Vol. 377-388 (2000), p. 578.
- [6] L. Major, J. Morgiel, B. Major, J.M. Lackner, W. Waldhauser, R. Ebner, L. Nistor, G.Van Tendeloo, Surf. Coat. Technol. Vol. 200 (2006), p. 6190.
- [7] M. Berger, U. Wiklund, M. Eriksson, H. Enqvist, S. Jacobson: Surf. Coat. Technol. Vol. 116- 119 (1999), p. 1138.
- [8] H.A. Jehn: Surf. Coat. Technol. 125 (2000), p. 212.
- [9] A. Grill: Wear Vol. 168 (1993), p. 143.
- [10] R. Hauert: Diamond Relat. Mater. Vol. 12 (2003), p. 583.

Characterization of nanometric-sized carbides formed during tempering of carbide-steel cermets

Krzysztof Matus^a, Mirosława Pawlyta^b and Grzegorz Matula^c

Institute of Engineering Materials and Biomaterials, Silesian University of Technology,
Konarskiego 18A, 44-100 Gliwice, Poland

^akrzymat899@student.polsl.pl, ^bmirosława.pawlyta@polsl.pl, ^cgrzegorz.matula@polsl.pl

The aim of this article is to present issues related to characterization of nanometric-sized carbides, nitrides and/or nitrocarbides formed during tempering of carbide-steel cermets. Closer examination of those materials is important because of hardness growth of carbide-steel cermets after tempering. The results obtained during research show that the upswing of hardness is significantly higher than for high-speed steels. Another interesting fact is the displacement of secondary hardness effect observed for this material to a higher tempering temperature range. This could be explained by influence of nanometric-sized carbides, nitrides and/or nitrocarbides contained inside the steel matrix. In order to conduct particles' analysis in proper way, they were extracted by dissolving the metal matrix with acids and then washing in distilled water, which operation was repeated several times (fig. 1) [1–3].

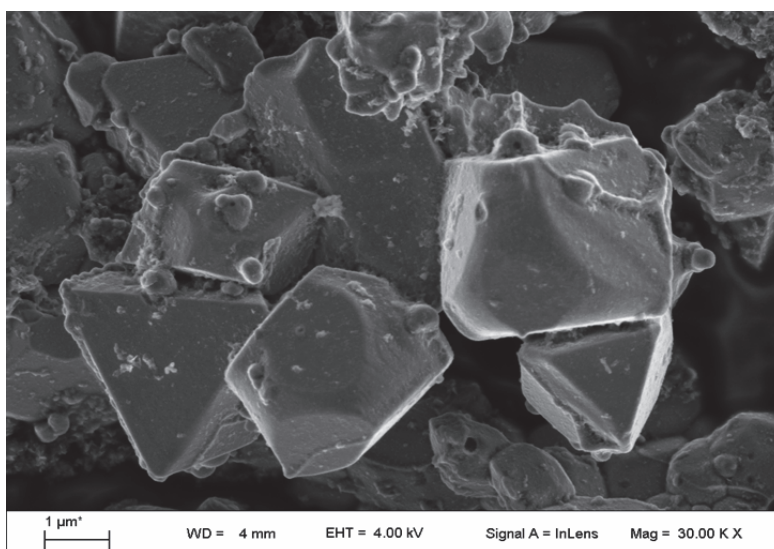


Fig. 1. SEM image of carbides extracted by dissolving the metal matrix with acids

Proper description of nanosized particles is both important and difficult as achievements of nanoscience and nanotechnology confirm significant influence of nanocrystalline particles on material properties even if its mass fraction is undetectable by standard methods. Hence, in order to correctly describe nanosized carbides and nitrides, it was necessary to apply techniques offering nanometric resolution. Scanning transmission electron microscope (STEM) and HRTEM (High Resolution Transmission Electron Microscopy) imaging were used as a primary research techniques. The diffraction pattern were collected by exploiting both Selected Area Diffraction (SEAD) and micro- or nanodiffraction, known as Small-angle Convergence Beam Electron Diffraction (SCBED). Chemical composition examination were carried out by energy dispersive spectrometry (EDS) and Electron Energy Loss Spectroscopy (EELS). Diffraction patterns recorded during the research were compared to the results of X-ray diffraction measurements. This made possible to identify material precipitates that occurred in the sample. To supplement the results, additional research were performed, using a scanning electron microscope [4–6].

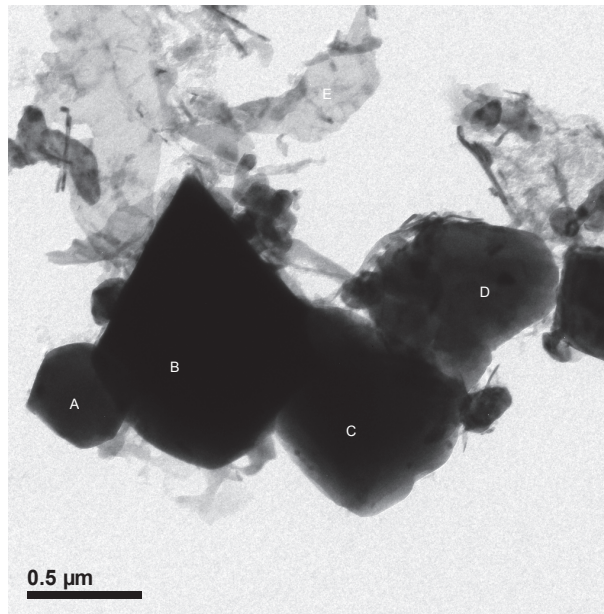


Fig. 2. TEM image carbide (point B - M₆C phase (mixture of carbides Fe₄Mo₂C and Fe₃W₃C), points A, C and D - MC phase (nonstoichiometric VC containing dissolved Mo and W))

References

- [1] G. Matula: Archives of Materials Science and Engineering, AMSE, vol. 43/2 June 2010.
- [2] G. Matula, *Gradient surface layers from tool cermets formed pressurelessly and sintered*, vol. 7 (13). Open access library, 2012.
- [3] P. Echlin, *Handbook of sample preparation for scanning electron microscopy and x-ray microanalysis*. New York: Springer, 2009.
- [4] L. A. Dobrzański and K. Gołombek: J. Mater. Proc. Technol. Vol. 164-165 (2005), p. 805.
- [5] S. Kuimalee, T. Chairuangstri, J. T. H. Pearce, D. V. Edmonds, A. P. Brown, and R. M. D. Brydson: Micron Vol. 41 (2010), p. 423.
- [6] *Science of microscopy*. New York: Springer, 2007.

Microstructure and martensitic transformation in $\text{Ni}_{48}\text{Mn}_{39.5}\text{Sn}_{12.5-x}\text{Si}_x$ metamagnetic Heusler alloy ribbons

Wojciech Maziarz^{1,a}, Paweł Czaja^{1,b}, Tomasz Czeppe^{1,c}, Maciej Szczerba^{1,d},
Anna Wójcik^{1,e}, Katarzyna Wańkowicz^{1,f} and Jan Dutkiewicz^{1,g}

¹Institute of Metallurgy and Materials Science, Polish Academy of Sciences, 25 Reymonta St.,
30-059 Kraków, Poland

^aw.maziarz@imim.pl, ^bp.czaja@imim.pl, ^ct.czeppe@imim.pl, ^dm.szczerba@imim.pl, ^ej.dutkiewicz@imim.pl

Introduction

Since the early reports by Suto *et al.* [1] on the discovery of the magnetic field induced reverse martensitic transformation (RMT) Ni-Mn-Z (Z=In, Sn, Sb) alloys have gained significant interest worldwide [2]. In principle the RMT is comparable to the conventional shape-memory effect induced by the reverse transformation due to heating. In this instance however in addition to temperature the reverse transformation may be induced by a magnetic field and hence such alloys are termed metamagnetic shape memory alloys (MSMA)[3]. The first order forward (MT) and RMT in these systems takes place between the cubic $L2_1$ ferromagnetic austenite and the weakly magnetic martensite with various structures: $10M$, $14M$, $L1_0$ or $4O$ depending on composition [4]. The magnetization difference (ΔM) between these two phases is the thermodynamic driving force for the metamagnetic transition [5]. What is more the first order structural transformation often coincides with the second order magnetic transition, which renders these alloys promising for environmentally friendly magneto caloric applications [6]. Several alloy systems from this group have been studied to date [7]. It has been established that MT temperatures in these alloys are sensitive to composition and may be altered in a wide range by changing the ingredients and/or substituting atoms by other elements [8]. Early reports have found that MT temperatures in $\text{Ni}_{50}\text{Mn}_{50-x}\text{Z}_x$ (Z=Sn, Sb, In) alloys generally decrease with increasing Z content. This has been linked primarily to the valence electron concentration per atom e/a [9]. Nevertheless MT temperature is also sensitive to other factors such as atomic ordering, internal stresses in the matrix, grain size, the formation of γ -precipitates due to aging, electronegativity of substituting elements and chemical pressure effect [10]. The latter has even been suggested by Chatterjee [11] to dominate the e/a factor in $\text{Ni}_2\text{MnGa}_{1-x}\text{Sn}_x$, which resulted in lowering of MT. Similar reports has been provided by Chen who studied $\text{Ni}_{43}\text{Mn}_{46}\text{Sn}_{11-x}\text{Al}_x$ [12]. Recently Liu [13] investigated the effect of isoelectronic substitution of Sn by Si in $\text{Ni}_{43}\text{Mn}_{46}\text{Sn}_{11-x}\text{Si}_x$ alloys in order to exclude the e/a influence on MT and determine the influence of the other related effects. An increase of MT was observed with increasing Si content.

Results

In this paper the combined effect of Si substitution and microstructure refinement on MT temperature and martensite structure is studied in melt spun $\text{Ni}_{48}\text{Mn}_{39.5}\text{Sn}_{12.5-x}\text{Si}_x$ ($x=1, 2, 3$) Heusler alloy ribbons. It is demonstrated by differential scanning calorimetry (DSC) studies that in accordance with literature reports the increase in Si concentration leads to an increase in MT. The average grain size regardless of composition is estimated by means of transmission electron microscope (TEM) at $1.4 \mu\text{m}$. The chemical composition appears homogenous throughout the ribbons samples. Selected Area Diffraction Patterns (SADPs) and XRD profiles taken at room temperature allow to confirm the $L2_1$ austenite and the $4O$ martensite structures. Considering the fact that melt spinning technique has been employed to produce Ni-Mn-Sn alloys with enhanced magnetocaloric properties [14] the present study may help to further advance the development of these materials for practical applications.

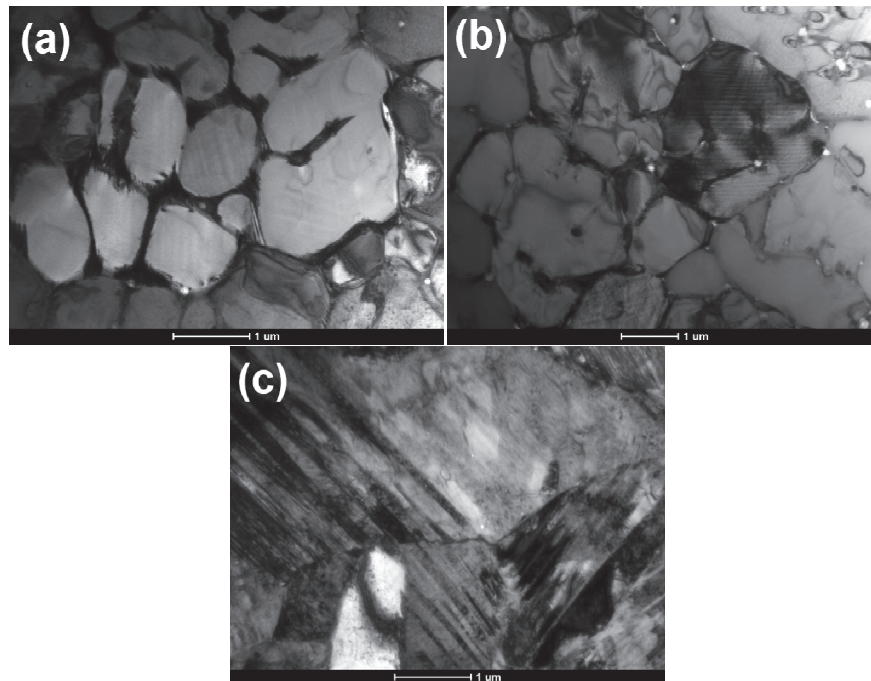


Fig. 1. Experimental BF images of the $\text{Ni}_{48}\text{Mn}_{39.5}\text{Sn}_{11.5}\text{Si}_1$ (a), $\text{Ni}_{48}\text{Mn}_{39.5}\text{Sn}_{10.5}\text{Si}_2$ (b) and $\text{Ni}_{48}\text{Mn}_{39.5}\text{Sn}_{9.5}\text{Si}_3$ (c) ribbons taken at room temperature

References

- [1] Y. Sutou, Y. Imano, N. Koeda, T. Omori, R. Kainuma, K. Ishida, K. Oikawa: *Appl. Phys. Lett.* Vol. 85 (2004), p. 4358.
- [2] H. C. Xuan, D. H. Wang, C. L. Zhang, Z. D. Han, H. S. Liu, B. X. Gu, Y. W. Du: *Appl. Phys. Lett.* 142 (2007), p. 591.
- [3] R. Kainuma, Y. Imano, W. Ito, Y. Sutou, H. Morito, S. Okamoto, O. Kitakami, K. Oikawa, A. Fujita, T. Kanomata and K. Ishida: *Nature Letters* Vol. 439 (2006), p. 957.
- [4] H. C. Xuan, D. H. Wang, C. L. Zhang, Z. D. Han, B. X. Gu and Y. W. Du: *Appl. Phys. Lett.* 92 (2008), p. 102503-1.
- [5] T. Krenke, M. Acet and E. F. Wassermann: *Phys. Rev. B* 73 (2006), p. 174413.
- [6] Z. D. Han, D. H. Wang, C. L. Zhang, H. C. Xuan, B. X. Gu and Y. W. Du: *Appl. Phys. Lett.* 90 (2007), p. 042507-1.
- [7] Y. Feng, J. H. Sui, H. B. Wang, W. Cai: *J. Magn. Magn. Mater.* 324 (2012), p. 1982.
- [8] N. V. Rama Rao, V. Chandrasekaran and K. G. Suresh: *J. Appl. Phys.* 108 (2010), p. 043913.
- [9] R. L. Wang, J. B. Yan, H. B. Xiao, L. S. Xu, V. V. Marchenkov, L. F. Xu, C. P. Yang: *J. Alloys Compd.* 509 (2011), p. 6834.
- [10] L. S. Barton, R. T. Lazott and E. R. Marsten: *J. Appl. Phys.* 115 (2014), p. 17A908.
- [11] S. Chatterjee, S. Giri, S. Majumdar, S. K. De, and V. V. Koledov: *J. Magn. Magn. Mater.* 324 (2012), p. 1891.
- [12] J. Chen, Z. Han, B. Qian, P. Zhang, D. Wang, Y. Du: *J. Magn. Magn. Mater.* 323 (2011), p. 248.
- [13] Z. Liu, Z. Wu, H. Yang, Y. Liu, W. Wang, X. Ma, G. Wu: *Intermetallics* 19 (2011), p. 1605.
- [14] X. G. Zhao, M. Tong, C. W. Shih, B. Li, W. C. Chang, W. Liu and Z. D. Zhang: *J. Appl. Phys.* 113 (2013), p. 17A913.

Recrystallization nucleation in plane strain deformed Al-Mn-Mg-Sc-Zr aluminium alloy

Magdalena Maria Miszczyk^{1,a}, Henryk Paul^{2,b}

¹Institute of Metallurgy and Materials Science, PAS, Krakow, Poland

^am.miszczyk@imim.pl, ^bh.paul@imim.pl

Introduction

During primary recrystallization the orientations of the new grains are thought to originate from the set of orientations within the as-deformed state, e.g. [1]. However, the nature of this relation has been the subject of major discussion over the last few decades. One of the main controversies concerns the lack of a well-defined selection system for the rotation axes and angles in the disorientation relation between recrystallized nuclei and as-deformed areas and, more generally, the frequently observed failure of the $40^\circ\langle 111 \rangle$ -type relations across recrystallization front. For a particular case of partially annealed pure Al and Al-alloys the primary nuclei were rotated approximately $25\text{--}35^\circ$ ($\sim\langle 111 \rangle$) with respect to the nearest as-deformed neighbourhood. In some cases these rotation axes were grouped near $\langle 012 \rangle$, $\langle 221 \rangle$ or $\langle 110 \rangle$ directions [2]. A more detailed analysis of the growth directions indicates the privileged role of $\{111\}$ planes at the initial stages of recrystallization. However, the nature of this relation still is the subject of major discussions.

The aim of the present study is to examine the microtextural aspects of the formation of recrystallization nuclei giving particular attention to the disorientations developed at the recrystallization front. Specimens composed of the polycrystalline material enables the analysis of strain concentration near the grain boundaries or their triple junctions with respect to recrystallization nucleation. The use of Al-alloy as a high stacking fault energy (SFE) model metal excludes mechanical and recrystallization twinning and facilitates identifying the mechanisms responsible for texture transformation during the initial annealing stages.

Experimental

The TeflonTM lubricated samples of polycrystalline Al-Mn-Mg-Sc-Zr alloy were plane strain compressed up to 60% in a channel-die rig at room temperature and a nominal strain rate of $\sim 0.02\text{ s}^{-1}$. Recrystallization was observed to occur at temperatures between 100 and 450°C for 3600s. Microstructure observations and local orientation measurements were made on the longitudinal plane using SEM (FEI Quanta 3D) equipped with a field emission gun and facilities for electron backscattered diffraction (EBSD). Microscope control, pattern acquisition and solution were carried out with the HKL Channel 5 system. In all cases a step size of 0.1 μm was applied.

Results

It turns out that during the initial recrystallization stages the grain boundary can play a double role, i.e. initial grain boundaries may facilitate nucleation or hinder growth. On the one hand, observations indicate that the first nuclei appear preferentially in the vicinity of the grain boundary and then grow into both as-deformed grains. On the other hand, a grain boundary may be a barrier for the growth of nuclei. New recrystallized grains that appear at the grain boundary is stopped at boundary if the new grains possess the disorientation with respect to the deformed structure of neighbouring grain different than $\alpha\langle 111 \rangle$ -type rotation. If the crystal lattice of the new grains possesses a common $\langle 111 \rangle$ pole with both as-deformed areas and represents the same type of disorientation described by $\alpha\langle 111 \rangle$ rotation (i.e. the growing grain is rotated around the common pole for both as-deformed areas or its orientation represents a 'symmetrical' position with respect to both deformed areas) the grain can cross the boundary. The present work confirmed the idea that triple junctions are not so important as

nucleation sites. However, in some cases they can play an important role in stress concentration near the grain boundaries that favours the nucleation of new grains.

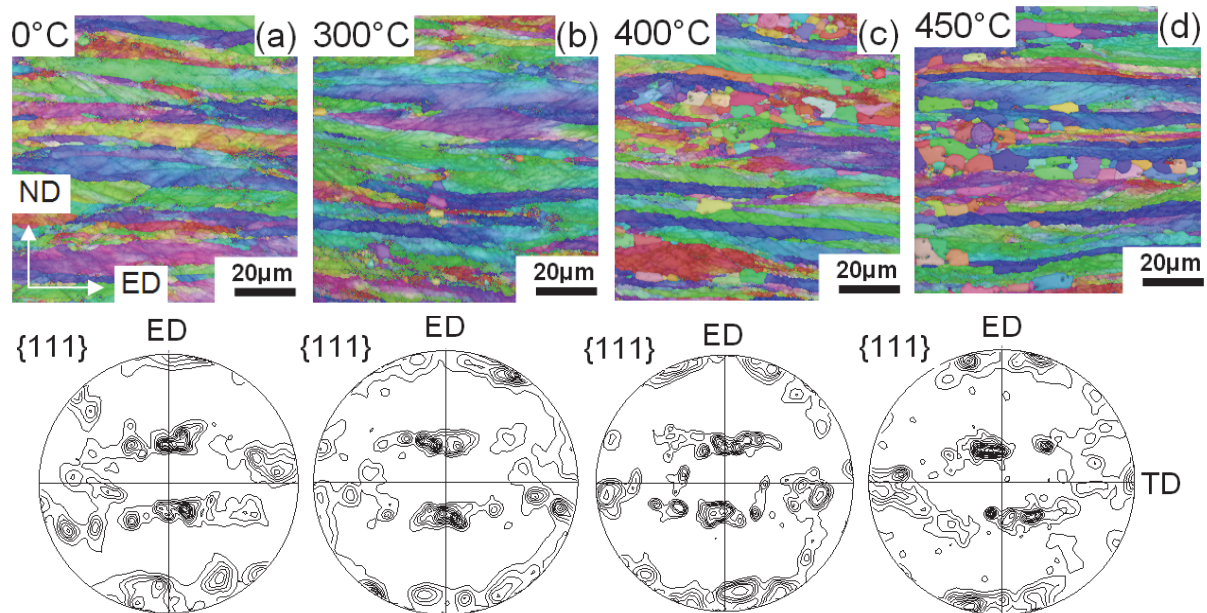


Fig.1. Microstructure and texture changes in deformed and recrystallized state after 1h annealing at temperatures ranged between at 150°C and 450°C. SEM/EBSD measurements on ND-ED section

Conclusions

In polycrystalline aluminium alloy this work has confirmed that triple junctions are not so effective nucleation sites as compared to the grain boundaries or band-like strain inhomogeneities of deformation. Most of the new grains are formed at pre-existing grain boundaries with a simultaneous, clearly marked, tendency to ‘consume’ both as-deformed areas. In accordance with earlier works one part of nuclei fall within the spread of orientations measured in the deformed state. The other appears to have been formed with new orientations rotated about a pole close to $\langle 111 \rangle$ or $\langle 112 \rangle$ relative to one (or two) of the deformed grain(s). The strong tendency to cross the boundary is demonstrated by the growing nuclei of new grains with crystal lattice orientation that possess a common $\{111\}$ plane with the crystal lattice of the deformed state.

References

- [1] R. D. Doherty et al: Mater. Sci. Eng. A Vol. A238 (1997), p. 219.
- [2] M. Miszczyk, PhD thesis, *Microstructure and texture evolution during annealing of plane strain compressed fcc metals*, Krakow, 2013.

Acknowledgements

This work was supported in part by the Polish Ministry of Science and Higher Education, projects: ‘Iuventus Plus’ IP2011 036471 and 3010/B/T02/2011/40.

Microstructure and morphology of composite polymer-based coatings on metallic substrates for medical applications

Tomasz Moskalewicz^{1,a}, Sigrid Seuss^{2,b}, Aldo R. Boccaccini^{2,c},
Grzegorz Cempura^{1,d}, Adam Gruszczyński^{1,e}
and Aleksandra Czyrska-Filemonowicz^{1,f}

¹ AGH University of Science and Technology, Faculty of Metals Engineering and Industrial Computer Science, Al. A. Mickiewicza 30, 30-059 Kraków, Poland

² University of Erlangen-Nuremberg, Institute of Biomaterials, Cauerstr. 6, 91058 Erlangen, Germany

^atmoskale@agh.edu.pl, ^bsigrid.seuss@ww.uni-erlangen.de, ^caldo.boccaccini@ww.uni-erlangen.de,
^dcempura@agh.edu.pl, ^egruszc@agh.edu.pl, ^fczyrska@agh.edu.pl

Introduction

Bioactive composite bioceramic/polymer coatings produced by electrophoretic deposition (EPD) are important materials used for improving the performance of metallic implants [1-3]. Bioglass is well-known coating component that exhibits high bioactivity. The properties of composite coatings and their functionalities might be tailored by the combination of polymeric and inorganic bioactive phase. In addition, the presence of the polymer enables also a good coating adhesion to the metallic substrate at low temperature, avoiding the problems associated with high temperature sintering of ceramics. PEEK is a bioinert, non-toxic and stable polymer finding applications in the biomedical field [2,3]. Chitosan is also a potential coating material for orthopedic and dental implants due to its osteogenic and biodegradable properties [4].

The goal of the present study was to characterise the microstructure and surface morphology of Bioglass/PEEK and Bioglass/chitosan coatings deposited by EPD on metallic substrates, Ti6Al7Nb alloy and model austenitic stainless steel.

Materials and methods

The Bioglass/PEEK and Bioglass/Chitosan coatings were deposited by EPD. Bioglass 45S5 particles (chemical composition: 45 SiO₂, 24.5 Na₂O, 24.5 CaO, 6 P₂O₅, in wt %) were used as a coatings component. A two phase ($\alpha+\beta$) Ti6Al7Nb titanium alloy and model austenitic steel were used as substrate materials for coatings deposition.

Microstructure of the coatings was characterised by light microscopy (LM), scanning- and transmission electron microscopy (SEM, TEM) as well as by X-ray diffractometry (XRD). The surface topography of coatings was examined with use of an atomic force microscope (AFM).

Results

Bioglass/PEEK coatings. The coatings, about 25-45 μm thick, were uniform and highly porous (Fig. 1a). The coatings were composed of an amorphous Bioglass particles embedded in a semi-crystalline PEEK matrix. The size of Bioglass particles was in the range of 2-50 μm , what allows to obtain high microporosity of the coating. The diameter of open pores was evaluated up to 40 μm . STEM-EDS microanalyses revealed diffusion of Na from the Bioglass particles into surrounding PEEK matrix. This is a result of coating sintering at temperature of 355 °C.

Bioglass/chitosan coatings. Thickness of Bioglass/chitosan coatings was evaluated as up to 3 μm . The coatings were composed of Bioglass particles with size in the range 0.5-3.5 μm embedded in an amorphous chitosan matrix (Fig. 1b). Both, surface morphology investigated by SEM and surface topography investigated by AFM indicate that the coating exhibited high surface development.

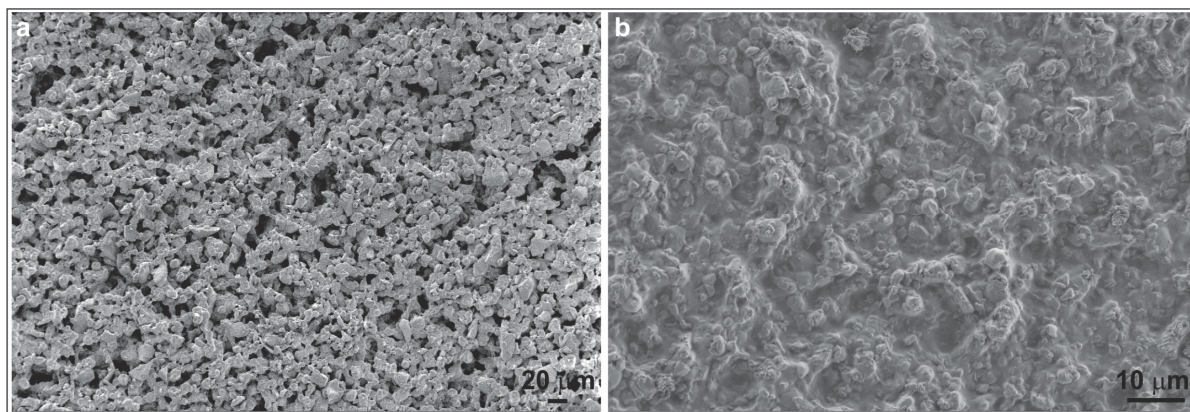


Fig. 1. Surface of the Bioglass/PEEK (a) and Bioglass/chitosan (b) coatings on Ti6Al7Nb titanium alloy. SEM plan-view

Summary

Composite Bioglass/polymer-based coatings were deposited by EPD on titanium alloy and austenitic stainless steel. The coatings microstructure was investigated by SEM, TEM and XRD. It was found that Bioglass/PEEK was highly microporous and consisted of an amorphous Bioglass particles in semi-crystalline PEEK matrix. The Bioglass/Chitosan coating was consisted of Bioglass particles embedded in an amorphous chitosan matrix. The coating revealed high surface development.

Acknowledgements

This work was supported by the EU COST MP1005 project „From nano to macro biomaterials (design, processing, characterization, modeling) and applications to stem cells regenerative orthopedic and dental medicine” (NAMABIO).

A part of this study was supported by the National Science Centre of Poland (project nr 2013/08/M/ST8/00332).

References

- [1] A. R. Boccaccini, S. Keim, R. Ma, Y. Li and I. Zhitomirsky: *J. R. Soc. Interface* Vol. 7 (2010), p. S581.
- [2] L. Petrovic, D. Pohle, H. Munstedt, T. Rechtenwald, K.A. Schlegel, S. Rupprecht: *J. Biomed. Sci.* Vol. 13 (2006), p. 41.
- [3] T. Moskalewicz, S. Seuss, A.R. Boccaccini: *Appl. Surf. Sci.* Vol. 273 (2013), p. 62.
- [4] A. Di Martino, M. Sittinger, M.V. Risbud: *Biomaterials* Vol. 26 (2005), p. 5983.

Microstructure and properties of TiN/Si₃N₄ nanocomposite coating on Vanadis 23 HS steel

Tomasz Moskalewicz^{1,a}, Sławomir Zimowski^{2,b}, Ivan Progalskiy^{3,c},
Bogdan Wendler^{3,d} and Aleksandra Czyrska-Filemonowicz^{1,e}

¹ AGH University of Science and Technology, Faculty of Metals Engineering and Industrial Computer Science,
Al. A. Mickiewicza 30, 30-059 Kraków, Poland

² AGH University of Science and Technology, Faculty of Mechanical Engineering and Robotics,
Al. A. Mickiewicza 30, 30-059 Kraków, Poland

³ Lodz University of Technology, Institute of Materials Science and Engineering, 1 Stefanowskiego St.,
90-924 Lodz, Poland

^amoskale@agh.edu.pl, ^bzimowski@imir.agh.edu.pl, ^cprogalskiy@gmail.com, ^dbowe@p.lodz.pl,
^eczyrska@agh.edu.pl

Introduction

The hard ceramic coatings are important group of materials used for improving the wear resistance of cutting, drilling and metal forming tools. The wear resistant of the coated material is related to the coating hardness and to the ability of the material to accommodate internal stresses resulting from the pressure of the cutting tool against the workpiece [1]. Therefore, the coating microstructure exhibits a crucial influence on hardness and tribological properties. The TiN/Si₃N₄ coatings are produced by different methods [2]. In this work, the coating was deposited by a new gas pulsed magnetron sputtering technique (GPMS) elaborated in the Lodz University of Technology based on an intermittent delivery of Ar to the vacuum chamber connected to an incessantly working high speed vacuum pumping system [3]. The aim of the present study was to characterise the microstructure as well as micromechanical properties of the TiN/Si₃N₄ coating deposited by the GPMS technique onto Vanadis 23 HS steel.

Materials and methods

The TiN/Si₃N₄ coating was deposited onto Vanadis 23 HS steel (1.27C, 0.3Mn, 0.3Si, 4.2Cr, 5Mo, 3.1V, 6.4W, 0.03P+S, in wt %) by GPMS magnetron sputtering similar to that described in Ref. [2]. The specimen was annealed at 450 °C after coating deposition in order to reduce residual stresses. Microstructure of the coatings was characterised by light microscopy (LM), scanning- and transmission electron microscopy (SEM, TEM). The TEM analyses were carried out using a Titan Cubed G2 60-300 microscope on FIB lamellas. Phase identification was performed by means of selected area electron diffraction (SAED). The SAED and fast Fourier transformation (FFT) patterns were interpreted with the help of a JEMS. The phase identification was supplemented by energy dispersive X-ray spectroscopy (STEM-EDS).

Hardness and Young's modulus were measured by instrumented indentation method. The adhesion of the coating to the Vanadis 23 steel was investigated by means of scratch test method.

Results

LM and SEM investigation revealed that the coating exhibits an uniform thickness of 13.5 µm (Fig. 1a). The coating was composed of two zones, which exhibited a nanocrystalline microstructure. Outer zone had a thickness in the range 200 nm-250 nm and consisted mainly of δ-TiN (face-centered cubic, fcc) nanocrystallites with columnar shape (Fig. 1b). Sporadically also some α-Si₃N₄ (trigonal primitive; tp) and β-Si₃N₄ (hexagonal) nanocrystallites were found in this zone. The size and spatial distribution of the nanocrystallites in the coating were investigated with use of HRTEM technique. The width of the nanocrystallites was in the range 4 nm - 15 nm, while their length was in the range 20 nm - 40 nm.

The inner zone was consisted mainly of δ -TiN (fcc) nanocrystallites and α -Si₃N₄ (tp). Sporadically β -Si₃N₄ (hexagonal) nanocrystallites were found in this zone also. The nanocrystallites exhibited an equiaxed shape and were smaller than in the outer zone; their size was in the range of 4 nm -12 nm.

A 2.5 μ m thick intermediate layer consisting of Cr and CrN zones occurred between the coating and the substrate.

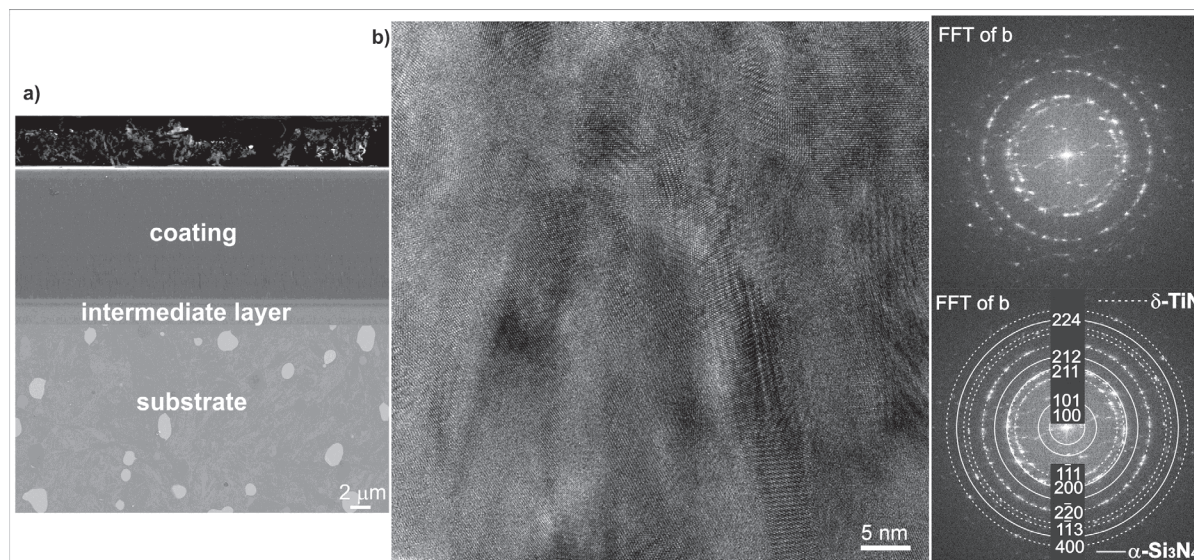


Fig. 1. SEM (a) and HRTEM (b) micrographs of the TiN/Si₃N₄ coating on Vanadis 23 HS steel as well as a corresponding FFT pattern calculated from the area of Fig. 1b and its identification (the most important rings of δ -TiN and α -Si₃N₄ are marked)

The coating showed a high hardness of 40 GPa and a high stiffness. The penetration depth of the Vickers indenter at 20 mN was 175 nm and the elastic modulus obtained from indentation load-displacement analysis was approx. 500 GPa. The coating showed a very good adhesion to the substrate. In the scratch test when the indenter was loaded with 30 N, there was not observed any destruction of an adhesive nature. Only the cohesive cracks appeared at load of 20 N.

Summary

The TiN/Si₃N₄ nanocomposite coating was composed of two zones. Both zones consisted of a mixture of δ -TiN, α -Si₃N₄ and β -Si₃N₄ nanocrystallites. A 2.5 μ m thick intermediate layer consisting of Cr and CrN zones occurred between the coating and the substrate surface. The coating exhibited a high hardness of 40 GPa and the elastic modulus of 500 GPa. Despite the high rigidity of the coating, their adhesion to the substrate was very good.

References

- [1] A.G. Dias, J.H. van Breda, P. Moretto, J. Ordelman: J. de Phys. IV Vol. 5 (1995), p. C5-831.
- [2] B. Wendler, T. Moskalewicz, I. Progalskiy, W. Pawlak, M. Makówka, K. Włodarczyk, P. Nolbrzak, A. Czyska-Filemonowicz, A. Rylski: J. Achiev. Mat. Manuf. Eng. Vol. 43 (2010), p. 455B.
- [3] B. Wendler et al.: Polish patent application P-399605, P-399606, P-399607 (2012).

Intermetallic phases examination in AlCu₄Ni₂Mg₂ aluminium alloy

Grażyna Mrówka-Nowotnik^{1,a}, Małgorzata Wierzbńska^{1,b}, Jan Sieniawski^{1,c},
Andrzej Nowotnik^{1,d}

¹Department of Materials Science, Rzeszow University of Technology, W. Pola 2, 35-959 Poland

^amrowka@prz.edu.pl, ^bmwierzb@prz.edu.pl, ^cjansien@prz.edu.pl, ^dnowotnik@prz.edu.pl

Introduction

Al-Cu-Ni-Mg aluminium alloys due to their excellent properties have a widespread application, especially in the aircraft, marine structures and automotive industry [1]. The main alloying elements – Cu, Ni and Mg, partly dissolve in the primary α -Al matrix, and to some amount present in the form of intermetallic phases. A range of different intermetallic phases may form during solidification, depending upon the overall alloy composition and crystallization condition. Their relative volume fraction, chemical composition and morphology exert significant influence on a technological properties of the alloys [1-3]. In the aluminium alloys besides the alloying elements, transition metals such as Fe, Mn and Cr are always present. Even small amount of these impurities causes the formation of a new phase component [2-4]. Therefore, the particle characterization is essential not only for choosing the best processing routes, but also for designing the optimized alloy composition. The main objective of this study was to analyze morphology and composition of the complex microstructure of intermetallic phases in AlCu₄Ni₂Mg₂ aluminium alloy in as-cast state and recommend accordingly, the best experimental techniques for analysis of the intermetallic phases occurring in the aluminium alloys.

Material and methodology

The investigation was carried out on the AlCu₄Ni₂Mg₂ casting aluminium alloy (composition: 4.3%Cu, 2.1%Ni, 1.5%Mg, 0.3%Zn, 0.1%Fe, 0.1%Si, Al-ball). The microstructure of examined alloy was observed using an optical microscope - Nikon 300, scanning electron microscope (SEM) HITACHI S-3400, and the transmission electron microscopes (TEM) Tesla BS-540 and Jeol-2100. The intermetallic particles from investigated AlCu₄Ni₂Mg₂ alloy were extracted chemically in phenol [3,4]. The intermetallic particles from the powder extract were identified by using X-ray diffraction analysis. The X-ray diffraction analysis of the powder was performed using ARL-XTR's diffractometer - Cu K α radiation at 40kV. DSC measurements were performed using a SETARAM Setsys Evolution 1200 with a sample weight of approximately 80-90 mg. Temperature scans were made from room temperature \sim 25°C to 800°C with constants heating rates of 5°C in a dynamic argon atmosphere. The heat effects associated with the transformation (dissolution/precipitation) reactions were obtained by subtracting a super purity Al baseline run and recorded.

Results and discussion

DSC curves obtained by heating (Fig.1a) and cooling (Fig.1b) of as-cast AlCu₄Ni₂Mg₂ alloy are shown in Fig. 1. DSC curves demonstrate reactions which occurred during heating and solidification process of the alloy. During cooling of the samples the recorded peaks were shifted to the lower values (Fig. 1b). The solidification sequence of this alloy can be quite complex. Possible reactions which followed during solidification of AlCu₄Ni₂Mg₂ alloy are presented in Tab. 1. Aluminum rich (α -Al) dendrites are formed at the beginning of solidification process. Additional alloying elements into the alloys (Ni, Cu, Mg) as well as impurities (eg. Fe) change the solidification path and reaction products. Therefore, as-cast microstructure of the tested alloy exhibit the appearance of mixture of intermetallic phases (Fig. 2a,b). The solidification reactions (the exact value of temperature) obtained during DSC investigation presented in Tab. 1. The analyzed microstructure in as- cast state contains of primary

aluminium dendrites and substantial amount of different intermetallic phases constituents varied in shape, size and distribution. They are located at the grain boundaries of α -Al and form dendrites network structure. The results of the SEM/EDS analysis of the particles extracted with boiling phenol from AlCu4Ni2Mg2 alloy were compared with X-ray diffraction pattern. The observed peaks confirmed SEM and TEM results. The majority of the peaks were from intermetallic phases: Al₇Cu₄Ni, Al₆Fe, S-Al₂CuMg, and Al₃(CuFeNi)₂.

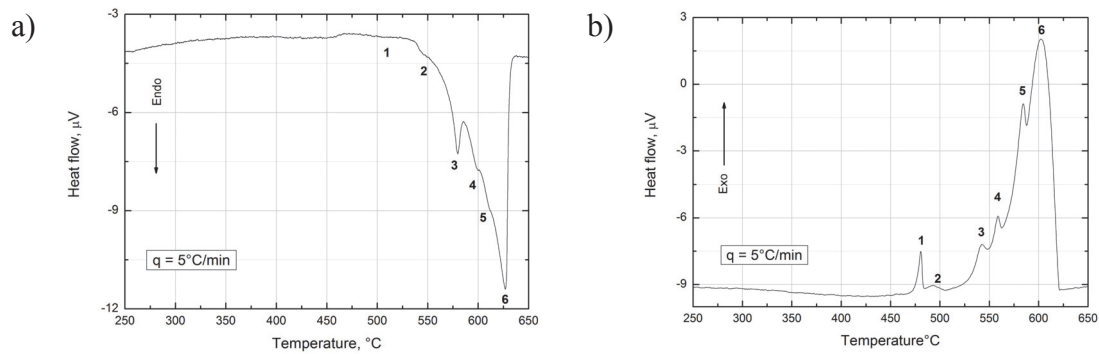


Fig. 1. DSC thermograms obtained during a) heating and b) cooling at a rate of 5°C/min

Table 1. Possible solidification reactions during nonequilibrium conditions in investigated AlCu4Ni2Mg2 alloy, at a heating rate 5°C/min

| | |
|---|-----|
| $L \rightarrow (Al) + Al_6Fe$ | 612 |
| $L \rightarrow (Al) + Al_4CuMg$ | 584 |
| $L \rightarrow (Al) + Al_2Cu + Al_2CuMg$ | 558 |
| $L \rightarrow (Al) + Al_2Cu + Al_7Cu_4Ni$ | 542 |
| $L \rightarrow (Al) + Al_2Cu + Al_2CuMg + Al_3(CuFeNi)_2$ | 493 |
| Solidus | 480 |

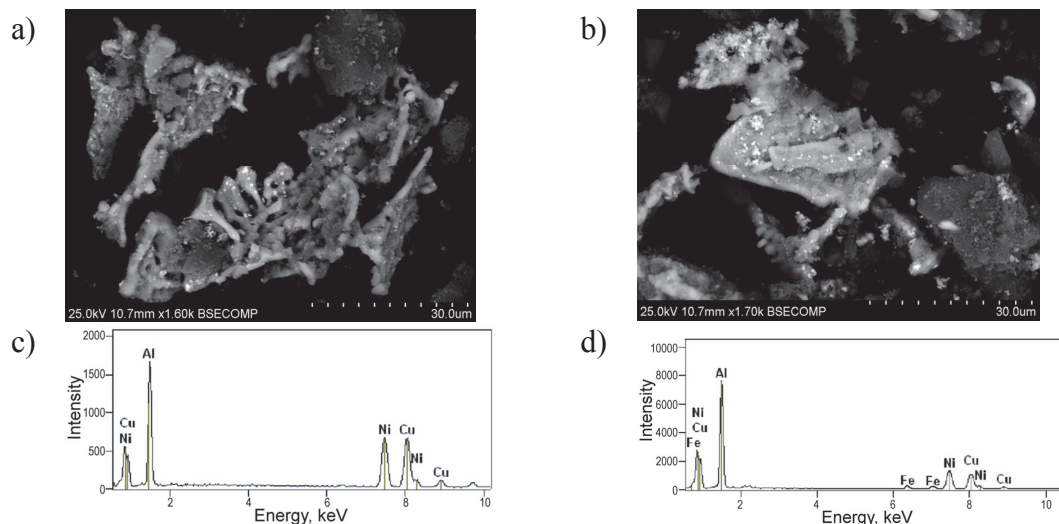


Fig. 2. SEM micrographs of the particles Al₇Cu₄Ni (a) and Al₃(CuFeNi)₂ (b) extracted from the AlCu4Ni2Mg2 alloy along with EDS spectra (c,d)

References

- [1] S. D. MacKenzie, G.E. Totten: Analytical characterization of aluminium, steel, and superalloys. Taylor & Francis Group, Boca Raton (2006).
- [2] F. King: Aluminium and its alloys. John Wiley and Sons, New York, Chichester, Brisbane, Toronto (1987).
- [3] G. Mrówka - Nowotnik, J. Sieniawski: Sol. St. Phenom. Vol. 186 (2012), p. 319.
- [4] G. Mrówka - Nowotnik, J. Sieniawski: Sol. St. Phenom. Vol. 197 (2013), p. 238.

Effect of isothermal annealing on the structure (XRD), microstructure (SEM, TEM) and magnetic properties of classical and bulk nanocrystalline alloys

Marcin Nabiałek^{1,a}, Paweł Pietrusiewicz^{1,b}, Katarzyna Błoch^{1,c}, Michał Szota^{2,d}

¹Czestochowa University of Technology, Faculty of Production Engineering and Materials Technology, Institute of Physics, 19 Armii Krajowej Av., 42-200 Czestochowa, Poland

²Czestochowa University of Technology, Faculty of Production Engineering and Materials Technology, Materials Engineering Institute, 19 Armii Krajowej Av., 42-200 Czestochowa, Poland

^anmarcell@wp.pl, ^bpietrusiewicz@wip.pcz.pl, ^c23kasia1@wp.pl, ^dmszota@wp.pl

One of the latest groups of functional alloys are nanomaterials, which are generally produced on the basis of amorphous alloys, as the results of their thermal treatment, carried out at specific (closely defined) temperature and time [1]. Knowledge of the structure and microstructure of these alloys is very important, because it gives the opportunity to design their properties, both magnetic as well as mechanical [2]. In this paper a nanocrystalline materials obtained by isothermal annealing of a conventional and bulk amorphous samples at a temperature near the crystallization temperature (770 K) was studied. The classical amorphous materials were obtained in the form of ribbon of thickness in about 35 microns, while the samples of the bulk amorphous alloys were produced in the form of plates with 0.5 mm thickness diameter. The study of a structure and microstructure was performed using: X-ray diffractometer, scanning and transmission electron microscope. The magnetic studies were performed in the low and high magnetic fields according to the H. Kronmüller theory, which gave possibility to verify of the real microstructure of investigated alloys [3, 4]. It was found that in the nanocrystalline alloys after adequate heat treatment nanometer grains and defects of the amorphous matrix are present, known as free volumes and quasidislocation dipoles. On the basis of these study, it can be concluded that not only the nanometric size grains located in the amorphous matrix are affecting the properties of the nanocrystalline alloys. Moreover, it was found that the magnetic studies can be very helpful in the assessment of the structure and properties of nanocrystalline alloys, and provide the opportunity to design their optimum performance.

References

- [1] M.E. McHenry, M.A. Willard, D.E. Laughlin: Prog. Mater. Sci. Vol. 44 (1999) p. 291.
- [2] M. Nabiałek, P. Pietrusiewicz, M. Dośpiał, M. Szota, J. Gondro, K. Gruszka, A. Dobrzańska-Danikiewicz, S. Walters, A. Bukowska: J. Alloys. Compd. <http://dx.doi.org/10.1016/j.jallcom.2013.12.236>.
- [3] H. Kronmüller: J. Appl. Phys. Vol. 52 (3), (1981) p. 1859.
- [4] H. Kronmüller, M. Fähnle: *Micromagnetism and the microstructure of ferromagnetic solids*, Cambridge University Press (2003).

Dynamic precipitation of nickel based superalloys undergoing sever deformation below solvus temperature

Andrzej Nowotnik^{1,a}, Paweł Rokicki^{1,b}, Paweł Pędrak^{1,c}, Sławomir Kotowski^{1,d},
Jan Sieniawski^{1,e}, Grażyna Mrówka-Nowotnik^{1,f}

¹Rzeszow University of Technology, The Faculty of Mechanical Engineering and Aeronautics, Department of Material Science, ul. Powstancow Warszawy 12, 35-959 Rzeszow, Poland

^anowotnik@prz.edu.pl, ^bprokicki@prz.edu.pl, ^cpedrak@prz.edu.pl, ^dskot@prz.edu.pl, ^ejansien@prz.edu.pl, ^fmrówka@prz.edu.pl

Keywords: microstructure, nickel based superalloy, CMSX-4, dilatometry

Variations of a true stress vs. true strain illustrate behaviour of materials during plastic deformation. Stress-strain relationship is generally evaluated by a torsion, compression and tensile tests. Results of these tests provide crucial information pertaining to the stress values which are necessary to run deformation process at specified temperature and cooling rate. Uniaxial compression tests at temperatures below the γ' solvus were conducted on nickel based superalloys – single crystal CMSX-4 and precipitation hardened – Inconel 718 and X750 to study the effect of temperature and strain rate on its flow stress and microstructure development. On the basis of received flow stress values activation energy of a high-temperature deformation process was estimated. Mathematical dependences ($\sigma_{pl} - T$ i $\sigma_{pl} - \dot{\epsilon}$) and compression data were used to determine material constants. These constants allow to derive a formula that describes the relationship between strain rate, deformation temperature and true stress. Microstructural observations of the deformed samples at high temperatures, previously solution heat treated and followed by aging CMSX-4 and Inconel's alloys revealed non uniform deformation effects. Distribution of either molybdenum- and niobium-rich carbides were found to be affected by localized flow within the investigated strain range at relatively low deformation temperatures 720 - 850°C. Microstructural examination of the alloys also shown that shear banding, cavities growth and intergranular cracks penetrating through the whole grains were responsible for decrease in the flow stress and a specimen fracture at larger strains.

Methodology and Results

In order to investigate the effect of the hardening phases on hot deformation behaviour, the uniaxial, isothermal compression tests at different temperatures and two strain rates were conducted on the heat treated precipitation hardenable nickel based superalloy CMSX-4 and Inconel 718 and X750. Heat treatment of the superalloys have been performed using a furnace in 10^{-5} mbar vacuum. Annealing was performed in the temperature range of 1287°C to 1316°C for 19 hours. The heat treated samples of the alloy have been compressed at two relatively low constant strain rates (10^{-4} , $4 \times 10^{-4} \text{s}^{-1}$) within the temperature range corresponding to temperatures of precipitation of the hardening phase (900-1200°C) up to a true strain of 0.5. The effect of deformation temperature on the true stress-true strain curves for the heat treated CMSX-4 superalloy deformed at each of the two strain rates (10^{-4} ; $4 \times 10^{-4} \text{s}^{-1}$) and temperature of 900-1200°C is shown in figure 1. Microstructure of the deformed alloys were observed using scanning electron microscopy SEM and transmission TEM.

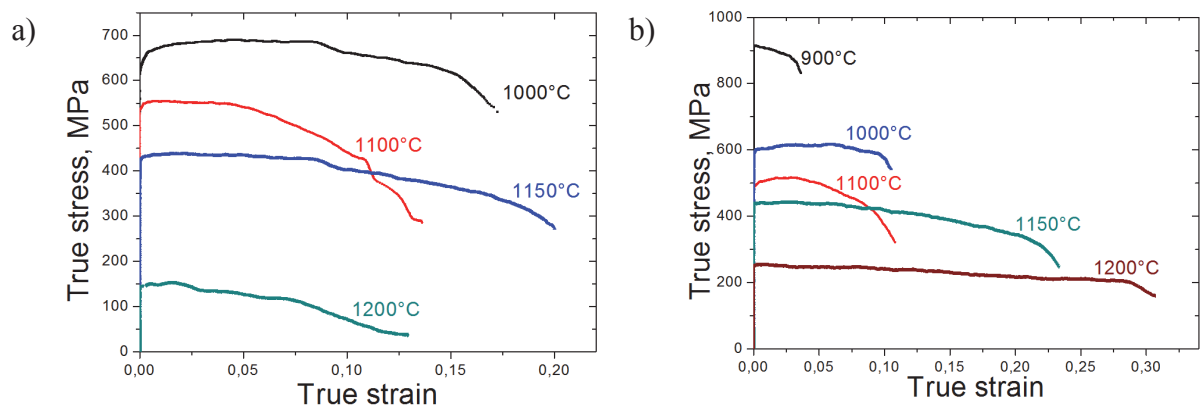


Fig. 1. True stress-true strain curves for CMSX-4 superalloy in after annealing deformed at different strain rates of a) 10^{-4} s^{-1} and b) $4 \times 10^{-4} \text{ s}^{-1}$ (the deformation temperature was indicated in the figure)

True stress-true strain curves (Fig. 1-3) confirmed, that increasing deformation temperature, or strain rate decreasing result in decreasing of flow stress value σ_{pl} . Decreasing the value of strain rate from 4×10^{-4} to 10^{-4} s^{-1} results in a 15% flow stress reduction. Increase of deformation temperature was found to have a greater influence on the flow stress value reduction.

The results of high-temperature deformation of the examined superalloys may possibly find some practical use in the workshop practice to predict a flow stress values, but only within particular temperature and strain rate ranges. Dissimilar energy activation values obtained under various conditions (depending on a research centre) or for a variety of materials make impossible to do a direct comparison of measurements, e.g. by means of plotting them on one common graph $\sigma_{pl}=f(Z)$.

Acknowledgements

The authors would like to thank Polish Ministry of Science and Higher Education for its financial support - this work was carried out under grant No. N N507 300640.

References

- [1] H. MC Queen: Zeszyty naukowe AGH, Metalurgia i Odlewnictwo 3 (1979), p. 421.
- [2] T. Sakai, J.J. Jonas: Acta Metal. 32 (1984), p.189.
- [3] F. Grosman: Problemy doboru naprężenia uplastyczniającego do programów komputerowej symulacji procesów przeróbki plastycznej. Materiały Konferencyjne „Plastyczność materiałów”, Ustroń (1996) 11-18.
- [4] F. Grosman: Kryteria doboru charakterystyk technologicznej plastyczności materiałów do symulacji procesów obróbki plastycznej. Mat. XVI Międzynarodowej Konf. Naukowo-Technicznej „Konstrukcja i technologia wytłoczek i wyprasek”. Poznań-Wąsowo (2004)157-168.
- [5] A. Nowotnik, L. Błaż, J. Sieniawski: Defect and Diffusion Forum 237-240 (2005), p. 1240.

An influence of casting procedure on microstructure and properties of Mg alloy-glassy carbon particles composite

Anita Olszówka-Myalska^{1,a*}

¹ Silesian University of Technology, Faculty of Materials Science and Metallurgy,
Kraśińskiego 8, 40-019 Katowice, Poland

^aanita.olszowka-myalska@polsl.pl

Keywords: magnesium matrix composite, glassy carbon particles, stir casting, pressure die casting

A magnesium matrix particulate composite can be obtained by casting an Mg alloy-particle suspension, but the applied casting procedure influences among others the formation of microdefects and the microstructure of matrix-particle bonding, and that determines their final properties. Composites reinforced by glassy carbon particles (Gcp), where magnesium alloys without aluminium are applied that exclude the formation of a hydrophilic Al_4C_3 carbide, are a new type of material dedicated to technical applications. However, the different matrix composition must change the effects at the alloy-GCp interface. The object of the study was a composite with a matrix of an Mg alloy with Zn 0.7 wt%, Zr 0.06wt.%, Nd 0.41wt%, Gd 0.21wt% and Mn 0.03wt% reinforced with GCp of 0.07-0.1 μm fabricated in industrial conditions by two methods - the mechanical mixing of a suspension followed by pressureless solidification, and by remelting a gravity cast composite and then pressure die casting. The microstructure of both types of composites was characterized with an FE-SEM with EDS electron microscope using cross-sectioned and polished composite samples, and fractured in tensile stress tests as well as the GCp extracted from the composite. The main focus was on the characteristics of the interface region morphology. The results of hardness measurements, tensile strength tests and sliding friction tests were presented and they showed the influence of the casting procedure on the final properties of the investigated composite. The reason for that was explained by the structural effects occurring at the interface, where a thin continuous oxide type layer was formed on all the particles and phases containing alloying elements that accumulated (Fig. 1) independent of the casting procedure. However, the elimination of micropores thanks to quick pressure crystallization seems to be the most important factor in changing the properties of the composite.

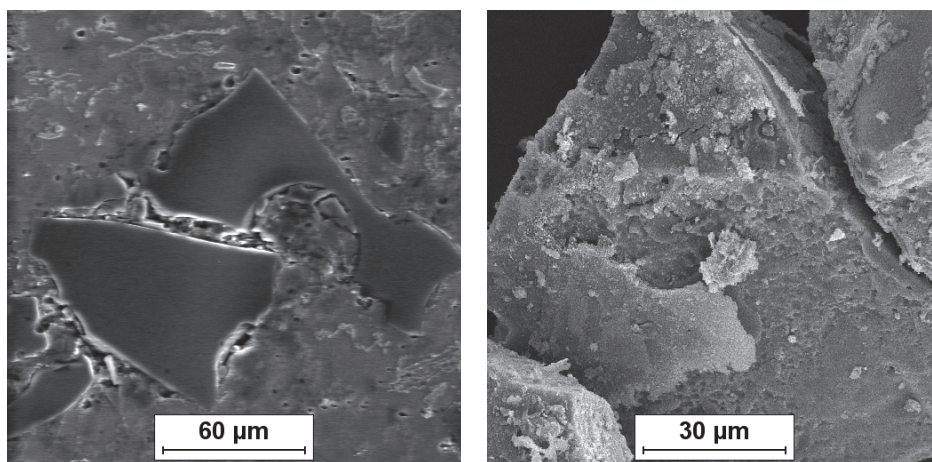


Fig. 1. SEM micrographs of gravity casted Mg alloy-GCp composite (a) and extracted GCp (b)

This work was supported by the Polish Ministry of Science and Higher Education (project N NR 15-0077-10/2010).

The influence of martensite transformation induced by plastic deformation on the microstructure of metastable austenite in X5CrNi18-10 stainless steel

Agnieszka Kurc-Lisiecka^{1a}, Wojciech Ozgowicz^{1b},
Elżbieta Kalinowska-Ozgowicz^{2c}, Wojciech Maziarz^{3d}

¹Institute of Engineering Materials and Biomaterials, Silesian University of Technology,
18A Konarskiego Str., 44-100 Gliwice, Poland

²Fundamentals of Technology Faculty, Lublin University of Technology, 38 Nadbystrzycka Str., 20-618 Lublin,
Poland

³Institute of Metallurgy and Materials Science of the Polish Academy of Sciences, 25 Reymonta Str., 30-059
Krakow, Poland

a agnieszka.kurc@polsl.pl, b wojciech.ozgowicz@polsl.pl,
c kalinowska-ozgowicz@tlen.pl, d w.maziarz@imim.pl,

Keywords: austenitic stainless steels, cold-rolling, microstructure, phase transformation, strain-induced martensite

The performed investigations concerned the influence of the degree and temperature of deformation on the microstructure of metastable austenite in stainless steel X5CrNi18-10 after its strain-induced martensitic transformation. Samples of steel strip were cold-rolled within the degree of deformation from 20 to 70% and stretched at a low temperature of -196°C . The microstructure was observed by means of a scanning electron microscopy (SEM) and transmission electron microscopy (TEM, HREM). It has been found that after cold-rolling with a little degree of deformation (20%) in the tested steel generally a single-phase microstructure of the matrix γ is found with a high density of dislocation and numerous deformation bands morphologically characteristic for stainless steel with a low stacking fault energy. After rolling with a 50% thickness reduction, however, the microstructure displayed deformation twins as well as refined morphologic formations of the phase α' , mostly localized in the vicinity of the grain boundaries of the metastable matrix γ , and also trace amounts of precipitations of carbides. In samples stretched at a temperature of -196°C the microstructure of the matrix displayed a considerable density of dislocations with lath areas of the martensite α' and precipitations of carbides M_{23}C_6 . Moreover, the tested steel revealed a crystallographic dependence of the planes and directions on the identified phases γ and α' , corresponding to the dependences of the Kurdjumov-Sachs type, independently of the method and temperature of plastic deformation. Tests carried out in TEM proved that typical sites of nucleation induced by the plastic deformation of martensite are the shear bands, particularly their intersection. The preferred mechanism of transformation, observed in the conditions of cold-rolling is, however, a direct transformation of the type γ (fcc) \rightarrow α' (bcc).

Microstructure and interfacial reactions during explosive bonding of carbon or stainless steels to zirconium

Henryk Paul^{1,a}, Jerzy Morgiel^{1,b}, Marek Faryna^{1,c}, Mariusz Prażmowski^{2,d}

¹Polish Academy of Sciences, Institute of Metallurgy and Materials Science, Krakow, Poland

²Opole University of Technology, Faculty of Mechanics, Opole, Poland

ah.paul@imim.pl, bj.morgiel@imim.pl, cm.faryna@imim.pl, dm.prazmowski@po.opole.pl

Introduction

Explosive bonding is a solid state metal joining process used to create a bond between two similar or dissimilar metals, especially those metals that cannot be joined by any other welding technique. At the *collision point*, the perfectly clean surfaces are brought together (if the impact angle and the impact velocity are within the range required for bonding) under very high pressure. The high velocity oblique collision ‘produces’ high temperature and high shear strain near the collision point in a very short time. This causes local melting of the bonded metals, simultaneously with the local plastic deformation in adjoining areas. Since the process occur under high pressure and at extremely fast cooling rates (due to the high thermal conductivity of the metals), the solidification terms are far from equilibrium, and the occurrence of non-equilibrium phases is expected. In some cases, the melted metals are ‘transformed’ into brittle metastable phases. The rate of the heat transfer, the severe plastic deformation and the high pressure are the most important factors which induce the melting of the material close to the weld interface, and more generally, control the reactions occurring at the boundary between the solid and the liquid phase. The present study is focused on the structural changes and the phase transformations occurring at the micro-/nano- scales near the interface; the identification of the intermetallic phases inside the melted zones, the possible interdiffusion between the bonded metals and the changes in the dislocation structure of base plates, were at the heart of interest. Particular attention was paid on the description of the interfaces *without macroscopically visible melted zones* between the bonded plates.

Experimental

The explosion welding of P265GH (carbon steel) and 10CrMo9-10 (stainless steel) sheets to Zr700 sheet was performed by High Energy Technologies Works ‘Explomet’ (Opole, Poland). The layers near the interface of clad were investigated by means of microscopic observations, with the use of scanning (SEM) and transmission (TEM) electron microscopy equipped with energy dispersive spectrometry. The focus ion beam technique for the thin foils preparation was applied.

Results

The performed investigations showed that amorphous and/or fine-grained crystalline volumes near the interface were formed within broad values of the technological parameters of bonding. The nano-grains ‘plunged’ within the rapidly solidified liquid was the most frequently observed inside the intermetallic inclusions. The internal microstructures of the broad of few μm inclusion and the extremely thin (<50nm) layer were qualitatively similar. The diameter of the nano-grains only rarely exceeds a few tens of nanometers. They were observed as single isolated grains ‘plunged’ in the solidified melt or as compact chains of grains. However, the crystallization process preferentially starts from both - (pure metal)/(solidified melt) - types of interfaces. The chemical composition of the phases that form within the melted zone is strongly diversified; e.g. starting from $\text{Zr} \rightarrow \text{Fe}$, in the case of the CS/Zr clad - Zr_3Fe , Zr_2Fe , ZrFe_2 or ZrFe_3 and for SS/Zr clad - $\text{Fe}_{21.8}\text{Zr}_{75.0}\text{Ni}_{1.8}\text{Cr}_{1.4}$ and $\text{Fe}_{72.0}\text{Zr}_{26.4}\text{Ni}_{0.0}\text{Cr}_{1.6}$.

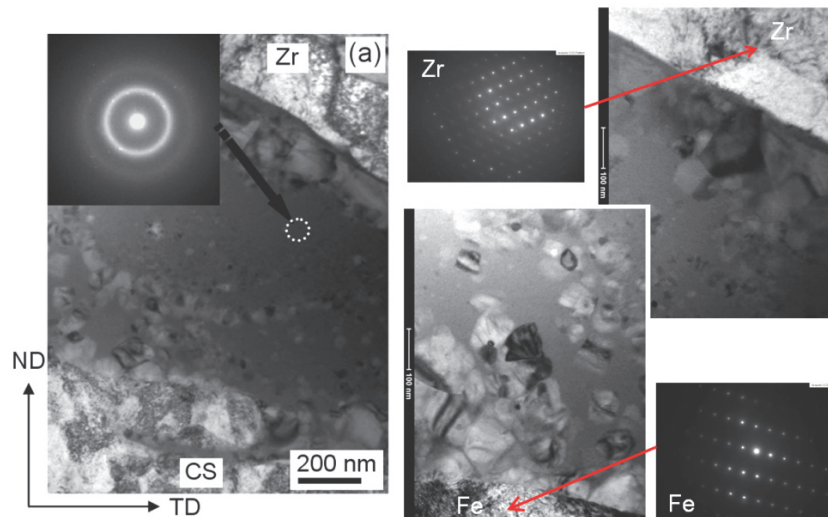


Fig. 1. Microstructure presenting the weld interface between carbon steel and zirconium sheets. The case of thin ($\sim 1 \mu\text{m}$) melted zone is presented. ND-TD section. TEM/BF imaging

Conclusions

Application of the SEM and TEM for investigations of the microstructure and the chemical composition changes near the interface of explosively welded carbon steel and zirconium sheets allowed to explain the mechanism of formation of good reliable bonding of such materials. Both the amorphous phases and the nano-crystallites were identified in the bonding zone of the (carbon or stainless steel)/Zr700 clads. The elongated shape of the (sub)grains and the randomly distributed dislocations inside them, observed in the plates near the interface of all the metal compositions, clearly indicated that, during welding, the deformation processes were prevailing over the softening ones. Observation proved that the proper explosion weld was always formed with a thin layer of remelted zone, which might be invisible for other than TEM observation methods.

References

- [1] T.Z. Blazynski: *Explosive Welding, Forming and Compaction*, Applied Science Publishers LTD, New York, 1983.
- [2] Y. Yang, B. Wang, J. Xiong: *J. Mat. Sci.* Vol. 41 (2006), p. 3501.
- [3] J. Song, A. Kostka, M. Veehmayer, D. Raabe: *Mat. Sci. Eng. A528* (2011), p. 2641.
- [4] H. Paul, L. Lityńska-Dobrzyńska, M. Prazmowski, *Metall. Mater. Trans. A 44A* (2013), p. 3836.

Acknowledgements

This work was supported by the National Science Centre (*in polish* - Narodowe Centrum Nauki, *abbr. NCN*) projects no: UMO-2012/05/B/ST8/02522 and UMO-2012/04/M/ST8/00401.

Characterization of multilayer (Ti,Al,Si)N coating by transmission electron microscopy

Mirosława Pawlyta^{1,a}, Klaudiusz Gołombek^{1,b}

¹Institute of Engineering Materials and Biomaterials, Silesian University of Technology, Konarskiego 18A, 44-100 Gliwice, Poland

^amirosława.pawlyta@polsl.pl, ^bklaudiusz.golombek@polsl.pl

Introduction

High importance of nano-multilayer coatings results from the possibility of wear reduction of tool materials. Their properties, like hardness, oxidation resistance and thermal stability are directly related to microstructure as well as crystal structure of phases formed during the deposition process [1]. It is expected that. The aim of presented work was to characterize crystallographic and electron structure the extremely hard multilayer (Ti,Al,Si)N coating.

Methodology

Multilayer nanostructural coating was synthesized on cemented carbides substrates by cathodic arc evaporation method (LARC-CAE) from pure titanium and aluminum/silicon targets in a mixture of Ar and N₂. FIB milling was done in a dual beam microscope for site-specific TEM specimen preparation. Cross sectional TEM imaging, diffraction and EDS study were performed in a S/TEM Titan 80-300 transmission electron microscope.

Results and conclusions

Fig. 1 shows images of the multilayer coating which consist of parallel wide (marked as A) and narrow (marked as B) layers. Wide layers are 200 nm while narrow are about 120 nm thick. HAADF-STEM image showing Z-contrast across the layers indicates differences in their chemical composition – confirmed by energy dispersive spectroscopy (Fig. 2). BF-STEM image showing diffraction contrast – confirmed by SAED patterns (Fig. 3). Narrow layer is characterized by columnar structure (Fig 4). It consists on about 5 mol% of Al and about 0.5 mol% of Si. Low content of Al determines cubic structure [2-3], identified as Ti₃AlN (ICSD#52642, Pm-3m) [4]. Evidence of the TiN (ICSD#64905, Fm-3m) phase was also confirmed. Wide layer is consists on small crystal domains, few nm in diameter (Fig. 4a). It contains about 20 mol% of Al and 1.5 mol% of Si. As the amount of Al is too small (theoretically predicted value is about 65 mol%) for phase transition to hexagonal structure [5], still only cubic Ti₃AlN is present. The bilayer period thickness, the grain structure and composition determine the extreme hardness of (Ti,Al,Si)N coating.

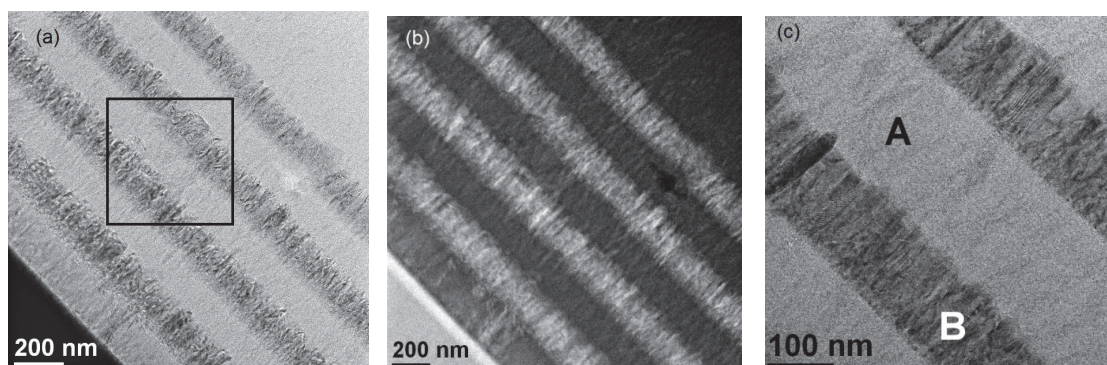


Fig. 1. BF-STEM (a) and HAADF-STEM image (b) of (Ti,Al,Si)N coating. BF-STEM image (c) of the part marked by square on Fig. 1a

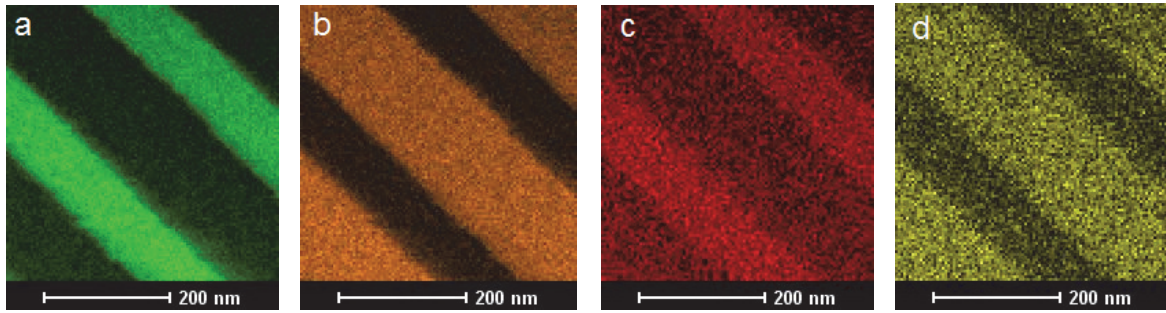


Fig. 2. Ti(a), Al(b), N(c) and Si(d) distribution maps of region visible in Fig.1c

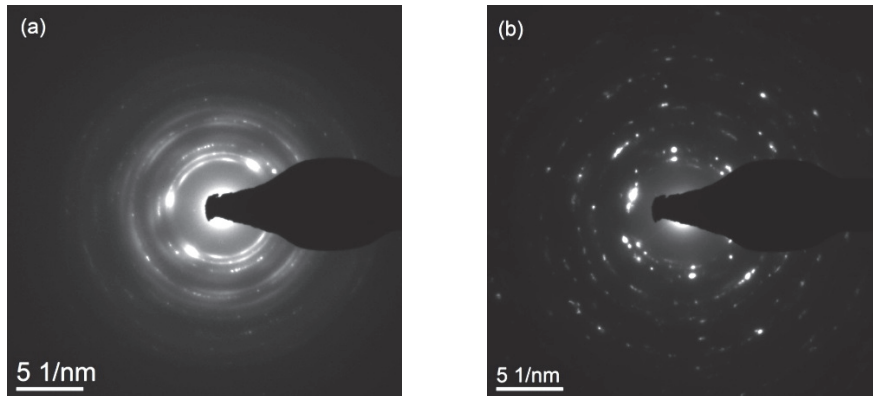


Fig. 3. SAED diffraction patterns obtained for wide (a) and narrow (b) layer

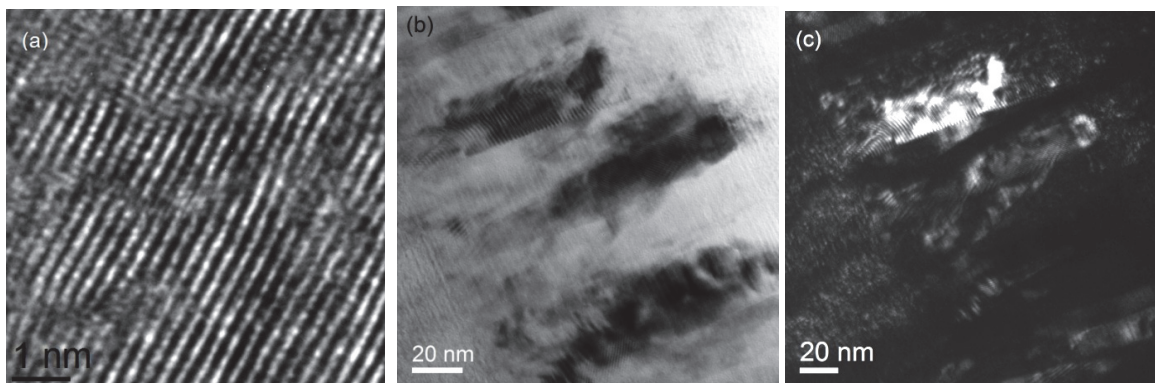


Fig. 4. HRTEM image (a) of wide layer showing small crystalline domains. TEM-BF (b) and TEM-DF (c) images showing crystalline structure of narrow layer (marked as B at Fig. 3)

References

- [1] S. PalDey, S.C. Dee: *Mat. Sci. Eng. A* 342 (2003), p. 58.
- [2] S.P. Pemmasani, K.V. Rajulapati, M. Ramakrishna, K.Valleti, R.C. Gundakaram, S.V. Josh: *Mater. Charact.* Vol. 81 (2013), p. 7.
- [3] Y.H. Zhao, L.Hu, G.Q. Lin, J.Q. Xiao, C. Dong, B.H. Yu: *Int. J. Refract. Met. Hard Mater.* Vol. 32 (2012), p. 27.
- [4] A. Czyrska-Filemonowicz, P.A. Buffat, M. Łucki, T. Moskalewicz, W. Rakowski, J.Lekki, T. Wierzchoń: *Acta Mater.* Vol. 53 (2005), p. 4367.
- [5] M. Zhou, Y. Makino, M. Nose, K. Nog, *Thin Solid Films* Vol. 339 (1999), p. 203.

The influence of solidification rate on the structure (XRD) microstructure (SEM, TEM) and magnetic properties of amorphous Fe₆₁Co₁₀Y₈W₁B₂₀ alloy

Paweł Pietrusiewicz^{1,a}, Marcin Nabiałek^{1,b}, Katarzyna Błoch^{1,c}, Michał Szota^{2,d}

¹Czestochowa University of Technology, Faculty of Production Engineering and Materials Technology, Institute of Physics, 19 Armii Krajowej Av., 42-200 Czestochowa, Poland

²Czestochowa University of Technology, Faculty of Production Engineering and Materials Technology, Materials Engineering Institute, 19 Armii Krajowej Av., 42-200 Czestochowa, Poland

^apietrusiewicz@wip.pcz.pl, ^bnmarcell@wp.pl, ^c23kasia1@wp.pl, ^dmszota@wp.pl

The paper presents the results of the structure, microstructure and magnetic properties of the amorphous Fe₆₁Co₁₀Y₈W₁B₂₀ alloy obtained in the form of plates with thickness 0.5 mm, belonging to the group of the bulk amorphous alloys. Secondary, samples in the form of a ribbons with a thickness of about 35 microns, known as classical amorphous alloys were prepared. The test specimens were produced using a suction-casting method from liquid alloy into copper- mold cooled with water and with use of melt-spinning method (Fig. 1).

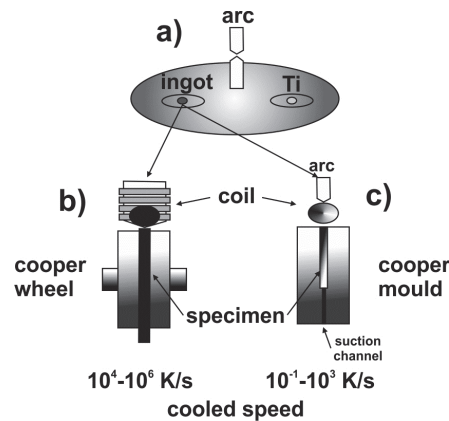


Fig. 1. A schematic description of the production cycle of conventional and bulk amorphous materials: (a) initial preparation of polycrystalline ingots using arc melting, (b) amorphous strip casting process, (c) the process of production of massive tiles using the suction casting method

All studies: X-ray diffraction, Mössbauer spectroscopy, scanning and transmission electron microscopy, as well as study the magnetic properties were carried out for samples in the state after solidification. As is clear from the conducted research, structure and microstructure of the samples produced at different cooling rates, directly affect on the magnetic properties. This means that the atomic structure of amorphous materials depends on the cooling rate during their production, which has also influence on the magnetic properties of these materials. Studying magnetization saturation of ferromagnetic alloys it is possible to indirectly investigate the influence of structural defects on the process of magnetization in the area known as the approach to ferromagnetic saturation [4]. Magnetization of the amorphous and nanocrystalline alloys in high magnetic fields may be described by the equation:

$$\mu_0 M(H) = \mu_0 M_s \left[1 - \frac{a_{1/2}}{(\mu_0 H)^{1/2}} - \frac{a_1}{(\mu_0 H)^1} - \frac{a_2}{(\mu_0 H)^2} \right] + b(\mu_0 H)^{1/2}, \quad (1)$$

where: μ_0 is vacuum permeability, M_s – saturation magnetization, H – magnetic field, a_i and b coefficients, $i = 1$ or 2 . The obtained results indicate that the magnetization process in high magnetic

fields is caused by rotation of the magnetic moments in the vicinity of free volumes and structural defects called quasi-dislocation dipoles, as well as damping of thermally excited spin waves.

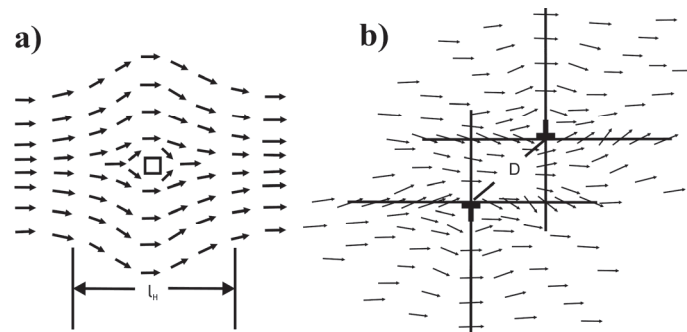


Fig. 2. Rotation of the magnetic moments in the vicinity of free volumes (a) and structural defects called quasi-dislocation dipoles (b) [3]

These defects are a source of internal stresses and areas of reduced density. Therefore, the complementary studies using the methods described in this work give information about the real structure of the amorphous alloys.

References

- [1] M.G. Nabialek, P. Pietrusiewicz, M.J. Dospial, M. Szota, K. Błoch, K. Gruszka, K. Ożga, S. Garus: *J. Alloys Compd.*, in Press <http://dx.doi.org/10.1016/j.jallcom.2013.12.163>
- [2] M. Nabialek, M. Szota, M. Dośpiał, P. Pietrusiewicz, S. Walters: *J. Magn. Magn. Mater.* Vol. 322, (21), (2010), p. 3377.
- [3] H. Kronmüller, M. Fähnle: *Micromagnetism and the microstructure of ferromagnetic solids*, Cambridge University Press (2003).
- [4] T. Holstein, H. Primakoff: *Phys. Rev.* Vol. 58 (1940), p.1098.

The influence of equal channel angular pressing on microstructure evolution during in-situ heating in transmission electron microscope

Michaela Poková^a, Miroslav Cieslar^b and Mariia Zimina^c

¹Charles University in Prague, Faculty of Mathematics and Physics, Department of Physics of Materials, Ke Karlovu 5, 121 16, Praha 2

^apokova@material.karlov.mff.cuni.cz, ^bcieslar@met.mff.cuni.cz, ^cmariia.zimina@mff.cuni.cz

Introduction

Equal channel angular pressing (ECAP) is a promising method of severe plastic deformation, which leads to grain refinement. Ultrafine-grained materials exhibit enhanced mechanical properties and are under intensive research [1].

AA3003 aluminium alloys are commonly used in automobile industry. The type, size and distribution of second phase particles in the aluminium matrix influence the mechanical properties of the final product [2]. To tailor the required properties, the microstructure changes occurring during thermo-mechanical treatment are to be understood.

In the present study the influence of ECAP processing and heat pre-treatment on the precipitation processes during in-situ annealing in transmission electron microscope (TEM) were studied.

Results

The studied material was prepared by twin-roll casting [3] in industrial conditions. After casting the material was annealed in an air furnace for 8 hours at 450 °C. Subsequently both annealed and non-annealed materials were subjected to 4 passes of ECAP at room temperature. This process led in both materials to substantial reduction of grain size – from original hundreds of μm to 0.5 μm (Fig. 1).

The evolution of mechanical properties was monitored by measurement of relative resistivity changes during isochronal annealing (Fig. 2), which is closely connected with precipitation processes [4]. The main changes in resistivity spectra were observed in the as-cast material around temperature 400 °C. In the non-annealed material after ECAP the main resistivity change started around 300 °C. In the pre-annealed material no significant peak in positive values was detected. At temperatures above 500 °C a drop in the resistivity spectra was measured in all materials.

Observations in TEM during in-situ heating (Fig. 3) revealed the formation of precipitates and their dissolution at higher temperatures. In the as-cast material the precipitation took place firstly at the grain boundaries, later also in the grain interior. In the non-annealed material, which had much higher number of grain boundaries, the precipitates were formed only on grain boundaries. In the pre-annealed material no new particles were formed during the heating, only the coarsening and later dissolution of existing ones was observed.

Summary

The ECAP processing led to development of high number of high-angle grain boundaries. These boundaries served as preferential sites for precipitation. Thus the temperature of precipitation was shifted to lower temperatures as compared to the as-cast material. The newly formed precipitates dissolved back to solid solution after annealing at temperatures above 500 °C. In the material which was annealed before ECAP the precipitates were already present in the matrix before ECAP and therefore no new ones were formed during post-ECAP annealing in TEM.

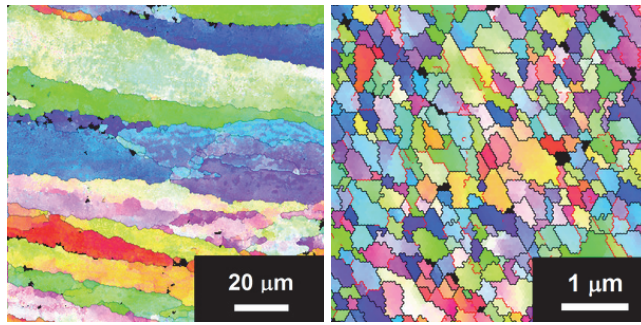


Fig. 1. Electron back-scatter diffraction image of the as-cast structure (left) and after 4 ECAP passes (right)

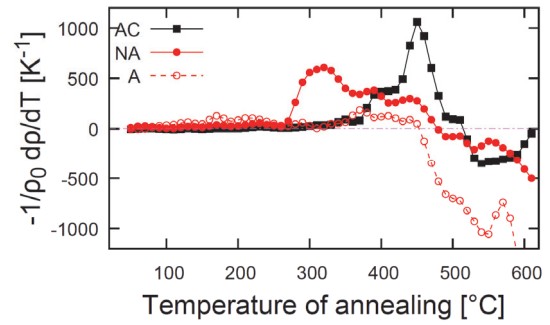


Fig. 2. The evolution of resistivity during annealing. “AC” = as-cast, “NA” = non-annealed and 4 ECAP passes, “A” = annealed and 4 ECAP passes

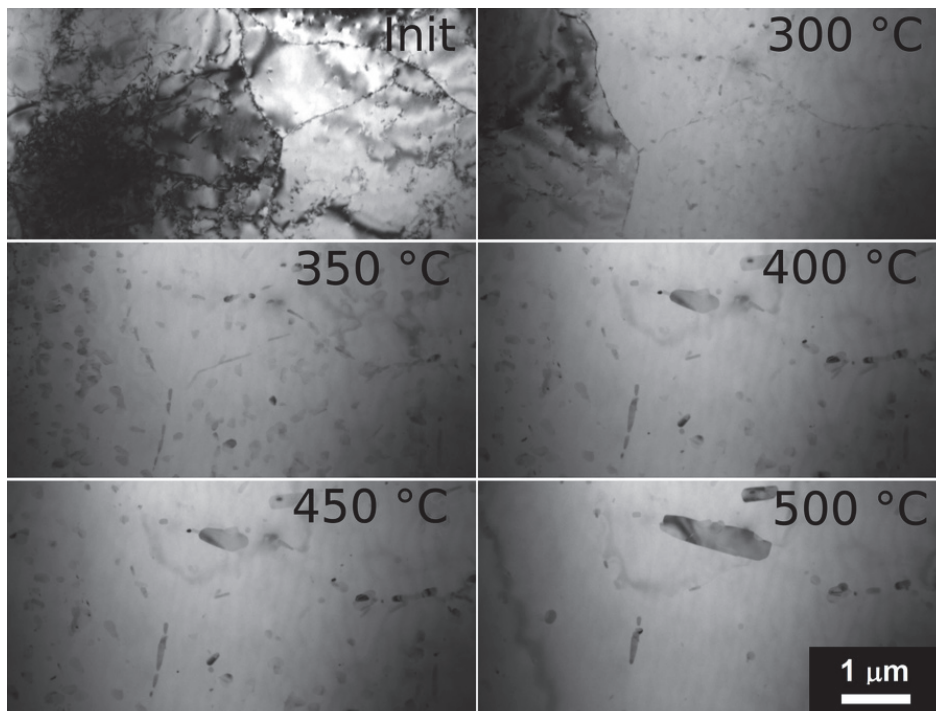


Fig. 3. Precipitates formation and dissolution during in-situ annealing in TEM of the as-cast material. Precipitates are formed preferentially on grain boundaries

Acknowledgement

The financial supports of grants GAUK 1428213, GAČR P107-12-0921 and SVV-2014-269303 are gratefully acknowledged by the authors.

References

- [1] M. Poková and M. Cieslar: submitted to Kovove Mater. (2014).
- [2] M. Karlík, T. Mánik and H. Lauschman: J. Alloys Compd. Vol. 515 (2012), p. 108.
- [3] Y. Birol: Scripta Mater. Vol. 59 (2008), p. 611.
- [4] M. Vlach, I. Stulikova, B. Smola, J. Piesova, H. Cisarova, S. Danis, J. Plasek, R. Gemma, D. Tanprayoon, V. Neubert: Mat. Sci. Eng. A Vol. 548 (2012), p. 27.

Effect of substrate on the morphology of electrodeposited ZnO nanostructures

Alina Pruna^{1,a}, Daniele Pullini^{2,b}, Dimitrios Tamvakos^{2,c}, Athanasios Tamvakos^{2,d} and David Busquets-Mataix^{3,e}

¹ University of Bucharest, 405 Atomistilor Str., 077125 Bucharest-Magurele, Romania

² Fiat Research Centre, 50 Torino Str., 10043 Orbassano, Italy

³ University Politecnica of Valencia, Camino de Vera s/n, 46022 Valencia, Spain

^aapruna@itm.upv.es, ^bdaniele.pullini@crf.it, ^ctamvakos@gmail.com, ^dathanasis_tamvakos@yahoo.gr, ^edbusquets@mcm.upv.es

Surface studies are reported for the deposition of ZnO nanostructures by an electrochemical deposition process. The electrosynthesis was performed in the absence of any buffer layer directly on the surface of ITO-coated glass substrates. The growth of ZnO nanostructures was investigated with the morphology of ITO films. The nucleation, growth, morphology and density of the ZnO nanostructures are reported to depend greatly on the quality of ITO substrates.

Introduction

Nanostructured ZnO has received increased research interest lately as transparent conductive oxide material for optoelectronic devices thanks to the benefit of tailoring its properties by morphology [1]. Amongst the techniques applied for the synthesis of ZnO nanostructures, electrochemical deposition detaches in terms of cost, conditions and process control [1] being well recognized as a nanostructuring technology for a wide range of materials with various potential applications [2-6]. In order to explain the properties of nanostructured doped ZnO, one should take into account besides the size effect and the grain crystallographic orientation also the influence of the growth substrate. Here, we investigated the effect of ITO substrate on the properties of the electrodeposited ZnO nanostructures in the absence of any seed layer. It is expected that such results may enhance the knowledge on the mechanism of ZnO electrodeposition for increased device efficiency.

Experimental

A conventional three-electrode electrochemical cell was employed with a saturated calomel reference electrode and a Pt disk counter electrode. ZnO nanostructures were electrochemically deposited by constant potential mode and constant current mode from 7.5 mM Zn(NO₃)₂ at 70°C.

Results and discussion

Morphology analysis revealed an inhomogeneous morphology for ITO type 1 (fig. 1a) while the ITO type 2 (fig. 1b) shows high homogenous morphology and grain size. The morphology of ZnO is markedly affected by ITO morphology and the deposition mode as seen in figures 2 and 3: galvanostatic mode results in lower quality nanostructures – spherical morphology on ITO type 1 and rods on type 2 while potentiostatic mode results in rods with increased diameter and density on ITO type 2 with respect to the ITO type 1.

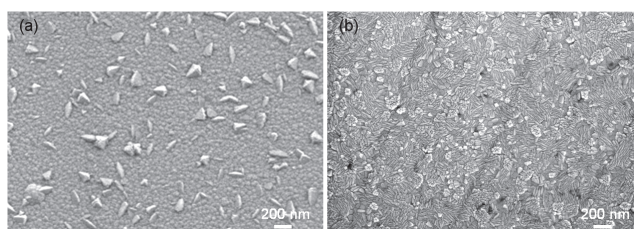


Fig. 1. Morphology of the ITO films: type 1 (a) and type 2 (b)

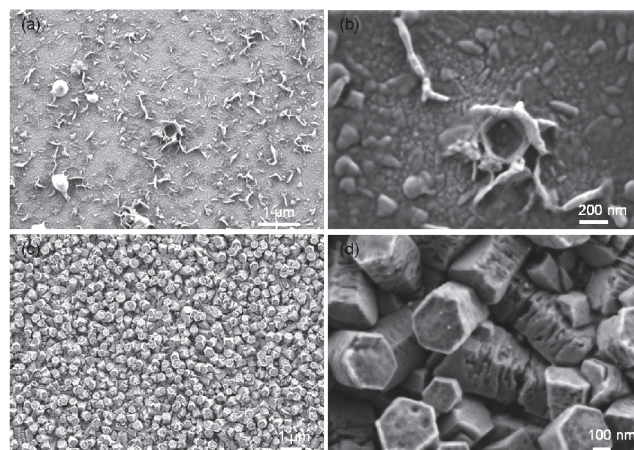


Fig. 2. Morphology of ZnO deposited by galvanostatic mode on ITO: type 1 (a, b) and type 2 (c, d)

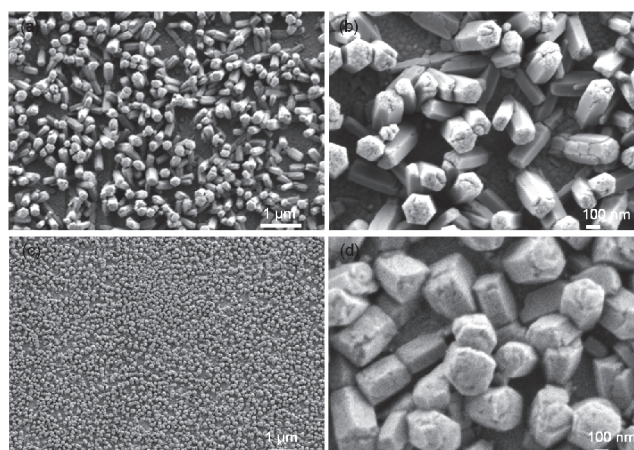


Fig. 3. Morphology of ZnO deposited by potentiostatic mode on ITO: type 1 (a, b) and type 2 (c, d)

Conclusions

Morphology properties of electrodeposited ZnO are greatly influenced by the deposition mode and ITO morphology. Sphere-like nanostructures were obtained by galvanostatic mode on ITO with irregular morphology while potentiostatic mode resulted in rods on both ITO substrates.

References

- [1] J. Cembrero, A. Pruna, D. Pullini and D. Busquets-Mataix: *Ceram. Int.* (2014) <http://dx.doi.org/10.1016/j.ceramint.2014.03.008>.
- [2] D. Pullini, A. Pruna, S. Zanin and D.B. Mataix: *J. Electrochem. Soc.* Vol. 159 (2012), p. E45.
- [3] A. Pruna, D. Pullini and D.B. Mataix: *J. Electrochem. Soc.* Vol. 159 (2012), p. E92.
- [4] A. Pruna, V. Brânzoi and F. Brânzoi: *J. Appl. Electrochem.* Vol. 41 (2011), p. 77.
- [5] A. Pruna and F. Brânzoi: *J. Pol. Res.* Vol 19 (2012), p. 9879.
- [6] A. Pruna, V. Brânzoi and F. Brânzoi: *Revue Roum. Chimie* Vol. 55 (2010), p. 293.

The microstructure and chemical composition of stainless steel after high temperature corrosion

Agnieszka Radziszewska^{1,a}, Axel Kranzmann^{2,b}, Ilona Dörfel^{2,c},
Maria Mosquera Feijoo^{2,d} and Monika Solecka^{1,e}

¹AGH University of Science and Technology, al. Mickiewicza 30, 30-059 Krakow, Poland

²BAM Federal Institute for Materials Research and Testing, Unter den Eichen 87, 12205 Berlin, Germany

^aradzisz@agh.edu.pl, ^baxel.kranzmann@bam.de, ^cilona.doerfel@bam.de, ^dmaria.mosquera-feijoo@bam.de,
^emsolecka@agh.edu.pl

Introduction

The high chromium content steels (e.g. X20Cr13-1.4021) are wide applied for the elements used in power plants [1]. These kinds of materials characterized the environment and high temperature resistance. Therefore are very often applied as the piping, shafts, injection pipe to transport the gasses from combustion processes which are then compressed into deep geological layers. After the contact of the tubes with damaging environment, on the steel surface the corrosion layers can be formed. Therefore nowadays are very important to study the growth mechanisms and microstructures of the corroded layers.

The present work was carried out to define the microstructure and chemical composition of layers on X20Cr13 steel obtained after high temperature corrosion.

Material and experiment details

The examined material was X20Cr13 steel (1.4021). The samples were exposed for 5 h to the distinct synthetic environment saturated with technical SO₂ at a flow rate >0,01 m/s. The samples were heat treated at 500 °C. After high temperature corrosion on steel surfaces the corrosion layers and in same places of samples the pits were observed. Therefore to determine the type of growing phases and the changes in distribution of elements in corroded layers the scanning and transmission electron microscopy (SEM, TEM-HREM) and energy dispersive spectroscopy (EDS) were preformed. The examinations of the microstructure and the chemical composition of corroded layers were obtained with the SEM, FEI Inspect S50, the TEM, JEM 2200FS (Jeol) at an acceleration voltage of 200 kV equipped with an energy dispersive X-ray spectrometer (EDX) [2]. The samples for TEM observations were performed as cross-sections normal to the surface of the corroded layer by focused ion beam (FIB) method. The investigations of phase composition of corroded layers were carried out in TEM by CBED (convergent beam electron diffraction) mode and nano beam diffraction (NBD) mode. The phase identification was supplemented by TEM-EDX analysis.

Results

The SEM and TEM observations showed that after high temperature corrosion of 13% Cr steel the thin corroded layer was formed (Fig 1). The obtained layer was about 30 nm thick. At the beginning of high temperature process grew the amorphous thin film with the dimension of 4-5 nm. This was followed by the growth of the next region which possessed crystalline structure. The transmission electron microscopy (TEM) studies revealed diffusion of elements from the metal substrate (X20Cr13) into the corroded layer. On the cross-section of the layer the distribution changes of oxygen, chromium, manganese and iron were visible.

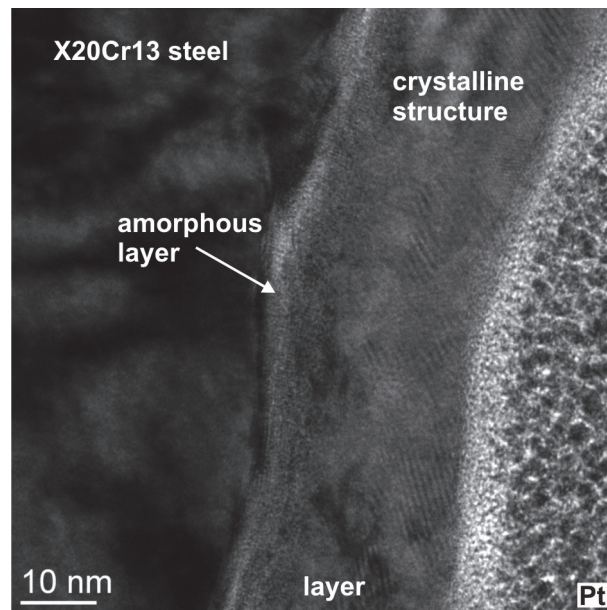


Fig. 1. HREM image showing corroded layer obtained on X20Cr13 steel after high temperature corrosion exposed by 5h in SO₂ atmosphere at 500 °C

Acknowledgment

The work was supported by the Ministry of Science and Higher Education of Poland under contract No. 11.11.110.936.

References

- [1] A. S. Ruhl and A. Kranzmann: Inter. J. Green. Gas Contr. Vol. 9 (2012), p. 85.
- [2] I. Dörfel, H. Rooch, W. Österle: Thin Solid Films Vol. 520 (2012), p. 4275.

Microstructural characterization of Laves phase in X10CrMoVNg9-1 and 12CrMoWCuVNB steels after long time exposure

Kinga Rodak^{1,a}, Adam Hernas^{1,b}

¹Silesian University of Technology, Institute of Materials Science, Katowice, Krasińskiego 8 str., Poland

^aKinga.Rodak@polsl.pl, ^bAdam.Hernas@polsl.pl

High alloy (9-12%Cr) creep resistance martensitic steels X10CrMoVNB9-1 and 12CrMoWCuVNB types after 100 000h of exposition at 550°C of steam have been studied regarding microstructural changes using Scanning Transmission Electron Microscopy (STEM) technique. Special attention was paid to the microstructural characteristics of Laves phase. The Laves phase is one of the most significant precipitates, which decided about structural stability and residual creep strength of heat-resistant steels. The results shows, that the favorable nucleation sites for Laves phase are lath boundaries and prior austenite grain boundaries. Moreover the particles are mainly located near the Cr-rich $M_{23}C_6$ carbide and are observed in contact with $M_{23}C_6$. These particles will facilitate the formation of Laves phase particles by providing nucleation sites. Laves phase particles in X10CrMoVNB9-1 and 12CrMoWCuVNB steels are recognized as: $(Fe,Cr)_2(Mo)$ and $(Fe,Cr)_2(W,Mo)$, $(Fe,Cr)_2(W)$, respectively.

Introduction

A continuous demand for energy production with limited pollution can be fulfilled only by higher thermodynamical efficiency of the power plants. This implies a higher temperature and pressure of the working media. The potential of many steels for power industry is limited by its structural stability. High chromium (9-12%Cr) creep resistant martensitic steels X10CrMoVNB9-1 and 12CrMoWCuVNB are one of the materials proposed for use in the superheater and reheater for supercritical boilers of new thermal power generation plants [1,2]. Despite differences in chemical compositions, the steels have the same microstructure of the as-tempered martensite.

The microstructural evolution in 9-12%Cr heat-resistant steels after long time exposure include: widening of martensitic laths, appearance of subgrains/grains, coarsening of precipitates, and formation of new precipitates, such as Laves-phase. Generally during long time service, degradation in dislocation structure occurs, but the most significant change in microstructure is the precipitation of intermetallic Laves phase particles of relatively large size. Tungsten, as the main alloying element, induces precipitation of intermetallic Laves phase during long-term exposure. Fe_2W is thermally more stable than Fe_2Mo . It is also suggest that the addition of W retards recovery of martensitic lath structure [3,4].

Experimental

Microstructural analysis of two creep resistance martensitic steels: X10CrMoVNB9-1 and 12CrMoWCuVNB types after 100 000h of exposure has been performed. For microstructure investigation a Hitachi HD-2300A scanning transmission electron microscopy (STEM) with a field emission type gun, was used. The energy dispersive X-ray analysis (EDS) of the precipitates was performed on thin foils.

Results

Figure 1 shows a comparison of the microstructure in X10CrMoVNB9-1 and 12CrMoWCuVNB after 100 000h of exposition. The steels undergo a recovery and recrystallisation of the matrix. It has been found that the phases presented in the serviced conditions are $M_{23}C_6$ carbides, Laves phase

(Fig. 2) and fine MX particles observed especially inside grain/subgrain. STEM – EDS analysis showed that the $M_{23}C_6$ carbides were enriched in Cr, Fe, Mn, Mo and . Whereas Laves phase for 12CrMoWCuVNb steel was enriched in W and Mo. Within the Laves precipitation, the stacking faults could be observed as a characteristic streaks on the electron diffraction pattern (Fig. 2).

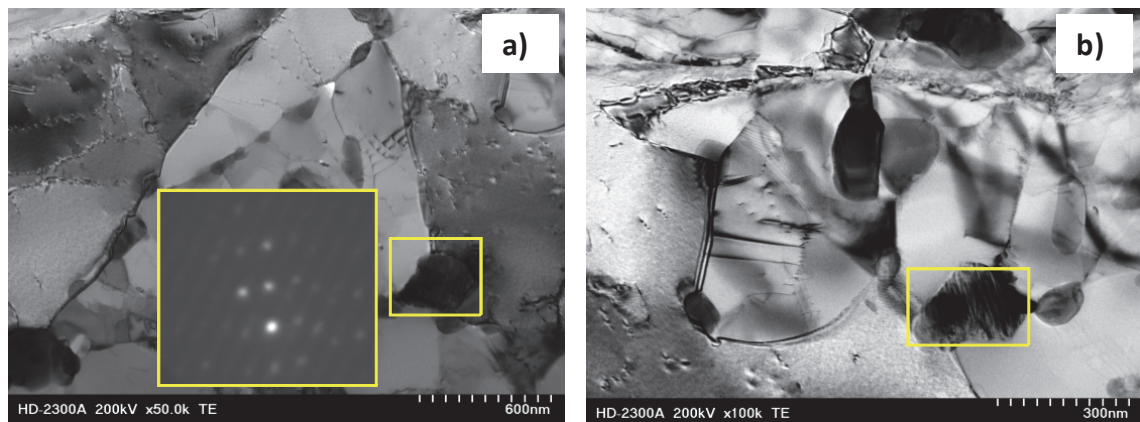


Fig. 1. Microstructure of creep resistance martensitic steels after 1000 000h of exposure, a) X10CrMoVNb9-1, b) 12CrMoWCuVNb

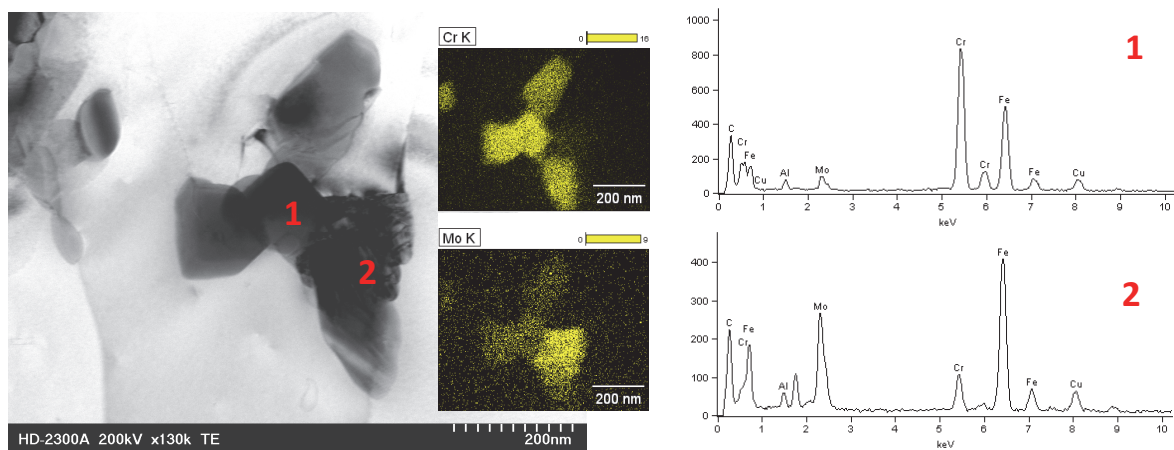


Fig. 2. STEM- EDX spectra and mapping of Laves phase particles in 12CrMoWCuVNb steel

Acknowledgements

This work was performed under the Strategic Research Project No SP/E/1/67484/10 supported by the National Centre for Research and Development.

References

- [1] J. Janovec et. al.: Mat. Sci. Eng. A249 (1998), p. 184.
- [2] W. Yan, et. al.: Front. Mater. Sci. 7 (2013), p. 1.
- [3] M. Hattestrand et al.: Mat. Sci. Eng. A250 (1998), p. 27.
- [4] J. Sawada et al.: Mat. Sci. Eng. A267 (1999), p. 19.

Application of scanning electron microscopy and EDS microanalysis for microstructural investigation of hypoeutectoid steels with 1% Ni

Edyta Rożniata^{1,a}, Dariusz Zasada^{2,b}

¹AGH University of Science and Technology, Faculty of Metals Engineering and Industrial Computer Science, 30 Mickiewicza Av., 30-059 Krakow, Poland

²Military Technical Academy, Division of New Technology and Chemistry, Gen. Sylwester Kaliski 2, 00-908 Warsaw 49, Poland

^aedyta.rozniata@agh.edu.pl, ^bdzasada@wat.edu.pl

Introduction

In order to achieve the required mechanical properties, the appropriate chemical composition and the microstructure (obtained as the result of the designed heat treatment) should be selected – in practice - individually for each alloy. From this point of view, the analysis of microgradients of the chemical composition of steels with a weak background of alloying elements such as: Mn, Mo, Cr, Ni, Co, Si and others, seems to be essential. Up to now, an influence of each element was considered separately, sometimes only indicating the group of alloys in which this influence was estimated [1 ÷ 5]. It should be noted, that the interaction of two or more alloying elements is significantly different from the sum of effects of these elements added separately. The most important can be the common effect of: molybdenum and chromium, molybdenum and nickel, chromium and nickel, manganese and chromium, manganese and nickel, manganese and molybdenum, manganese and cobalt. These mutual interactions of various elements on the effects of the others, may be the basis for the assessment of the impact magnitude of each of them on e.g. hardenability of steel under conditions of the presence of even one or several other elements in the above mentioned steels.

Methodology

The results of a microstructure, microanalysis of chemical composition and hardness investigations of the hypoeutectoid steels with 0.35% ÷ 0.40% C, imitating by its chemical composition toughening steels, are presented in the paper.

Metallographic examinations were carried out using a Carl Zeiss Axiovert 200 MAT light microscope and Quanta 3D FEG SEM-FIB scanning electron microscope of FEI. Polished sections were etched with a 3% Nital (3% HNO₃ solution in C₂H₅OH), or in some cases in an aqueous solution of picric acid to expose the former austenite grain boundaries.

Dilatometric tests were performed using L78R.I.T.A dilatometer of LINSEIS. Using dilatometer, the changes of elongation (Δl) of the samples with dimensions ϕ 3x10mm as a function of temperature (T) were registered. Obtained heating curves were used for precise determination of the critical temperatures (critical points) for the tested steels. The differentiation of obtained cooling curves allowed to precisely define the temperatures of the beginning and the end of particular phase transitions and thus to draw CCT diagrams.

EDS analyses were performed using Quanta 3D FEG SEM with EDAX spectrometer. For determination of the chemical composition in microareas, point, linear and a fixed area SEM-EDS microanalysis techniques were used.

Results and Conclusions

Developed CCT diagrams in accordance with the Rose and Wever classification are of type IV, what means that the diffusional transformations are separated by a stability range of the undercooled austenite and have the shape of the letter "C". After applying the cooling rate of about 50°C/s the microstructure of the steels investigated consists of martensite with small amount of bainite. However,

after applying cooling rates ranging from $25\text{ }^{\circ}\text{C/s} \div 1\text{ }^{\circ}\text{C/s}$, the microstructure of the tested hypoeutectoid steels consists of pearlite, ferrite and bainite in decreasing content. At the slowest cooling rates ($0.33\text{ }^{\circ}\text{C/s}$ and $0.16\text{ }^{\circ}\text{C/s}$) the microstructure of investigated steels is ferro – pearlitic.



Fig. 1. The microstructure of the investigated steel after $50\text{ }^{\circ}\text{C/s}$ cooling rate

The hardenability of tested steels is similar, but molybdenum acts much more effectively than nickel. Molybdenum occupies the 1st place among the effectiveness of alloying elements for the steels designed for low tempering, where the "background" of other elements is weak. For tested hypoeutectoid steels the EDS microanalysis revealed the precipitation of alloyed cementite at the grain boundaries.

References

- [1] R. Dziurka, J. Pacyna: Arch. Metall. Mater. 57/4 (2012), p. 943.
- [2] J. Krawczyk, E. Rożniata, J. Pacyna: J. Mater. Process. Technol. Vols. 162–163 (2005), p. 336.
- [3] R. Dąbrowski, E. Rożniata, R. Dziurka: Arch. Metall. Mater. 58/2 (2013), p. 563.
- [4] E. Rożniata, R. Dziurka: Arch. Mater. Sci. Eng. 58/2 (2012), p. 125.
- [5] E. Rożniata: Arch. Metall. Mater. 58/4 (2013), p. 1253.

Microstructure evolution in duplex stainless steels

Janusz Ryś^a, Anna Zielińska-Lipiec^b

AGH-University of Science & Technology, al. Mickiewicza 30, 30-059 Kraków, Poland

^ajrysjr@agh.edu.pl, ^balipiec@agh.edu.pl

Duplex type ferritic-austenitic stainless steels exemplify the group of steels very extensively examined in recent decades. Due to the two-phase character of these materials a development of microstructure and texture in the course of deformation differs from one-phase ferritic or austenitic steels [1-4]. Differences in microstructure evolution result first of all from the specific band-like morphology of ferrite-austenite structure. However the structural analysis performed by means of TEM, in cold-rolled duplex steels under examination, indicates at significant influence of few other factors on microstructure development. In the present paper two duplex steels were analyzed, which differed in chemical composition and the preliminary thermo-mechanical treatment. The first one was the commercial high-alloy super-duplex steel (X3CrNiMoCuN25-6-4) after hot-rolling [3]. The second material was a model chromium-nickel duplex steel (X1CrNi24-6), which was obtained by laboratory melt and then industrially hot-forged [4]. Both steels were subsequently solution treated and subjected to cold-rolling within a wide range of deformations.

Summary of the results

In the course of hot- and cold- plastic working both examined duplex steels developed a band-like ferrite-austenite morphology. Formation and subsequent reduction in thickness of ferrite and austenite bands resulted in so-called "pancake" structure at higher strains. As a consequence the (α/γ) phase interfaces, which are strong obstacles for dislocation motion, were arranged mostly parallel to the rolling plane. This specific two-phase structure imposed different conditions on plastic deformation in comparison to ferritic and austenitic steels [3, 4]. In spite of the fact, that basic mechanisms controlling deformation behavior within the bands of both constituent phases were essentially the same as in one-phase steels, it occurred that their contribution and the resulting structural effects were considerably changed upon deformation of two-phase banded structure [1-4].

Besides the banded morphology of two-phase structure the next crucial factor, from the viewpoint of ferrite and austenite co-deformation, were the starting orientation distributions (initial textures) after the preliminary treatment together with orientation relationships between both phases. In general the ferrite and austenite textures in duplex steels are not independent of each other since they are formed simultaneously upon the processes, which involve interactions of both phases. Preferential orientation relations between ferrite and austenite textures resulted in a specific mutual geometry of deformation systems (i.e. slip or twin systems) within the bands of both phases. Their symmetry with respect to rolling direction and the same or comparable values of the relative shear stresses ($m = \tau/\sigma$) resulted in plastically compatible deformation of ferrite and austenite bands [3,4]. In the course of plastic working the observed structural effects were limited to the areas (bands) of both phases and the "pancake" two-phase structure developed.

Strongly refined band-like morphology formed at higher deformation degrees influenced the strain localization and hindered formation of macroscopic shear bands. That is way structural features corresponding to macroscopic strain localization manifested themselves in various ways in both duplex steels under examination, depending on structural factors and deformation conditions. A wavy character of two-phase "pancake" structure (Fig.1) observed in the range of high deformations resulted from shearing of the (α/γ) phase-interfaces by micro-shear bands observed in super-duplex steel [3]. In the case of a model duplex steel (without addition of nitrogen), the instability of austenitic phase turned out to be of essential importance [4]. The phase instability, which stemmed from the chemical composition and the value of stacking fault energy (SFE) of austenite, resulted in deformation induced

($\gamma \rightarrow \alpha$) phase transformation affecting the final microstructure of the steel in the range of high deformations (Fig. 2).

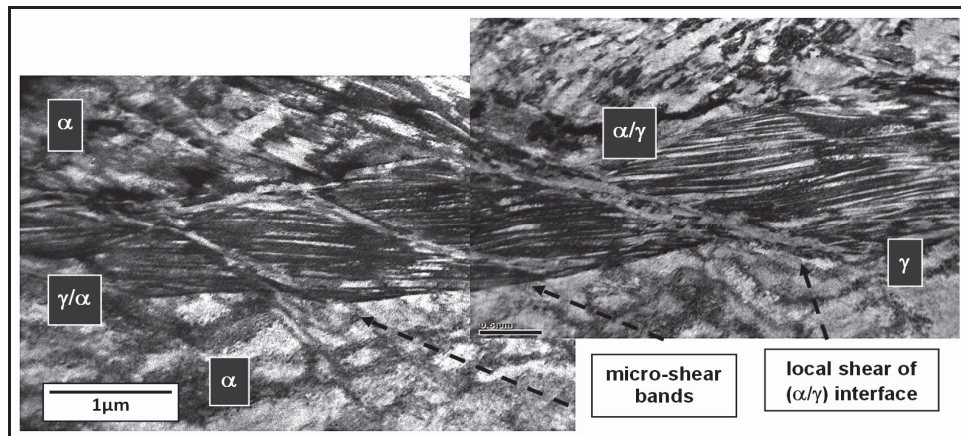


Fig. 1. Corrugated shape of the (α/γ) phase interface in super-duplex steel (X3CrNiMoCuN25-6-4) resulting from local shearing, after 80% of rolling reduction

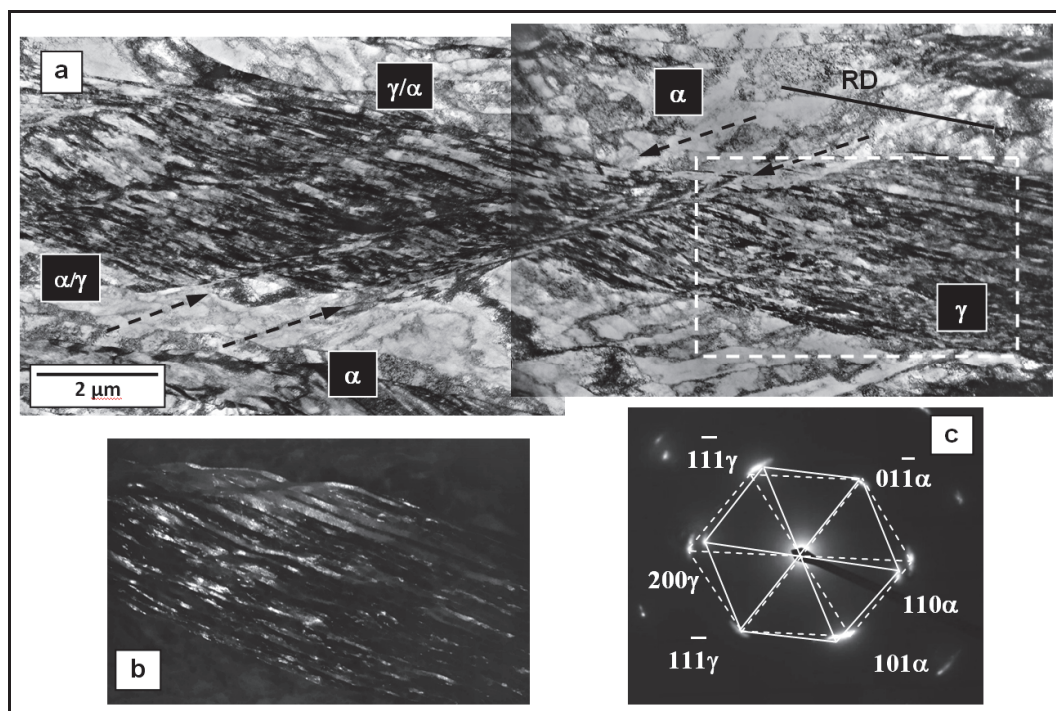


Fig. 2. Strongly refined microstructure within the austenite bands in model steel (X1CrNi24-6) after 80% of rolling reduction (a) and the dark field analysis indicating at the occurrence of the ($\gamma \rightarrow \alpha$) phase transformation (b, c)

References

- [1] N. Akdut, J. Foct: ISIJ International Vol. 36 (1996), p. 883.
- [2] J. Keichel, J. Foct, G. Gottstein: ISIJ International Vol. 43 (2003), p. 1781.
- [3] J. Ryś, M. Witkowska: Sol. St. Phenom. Vol. 163 (2010), p. 151.
- [4] J. Ryś, A. Zielińska-Lipiec: Arch. Metall. Mater. Vol. 57 (2012), p. 1041.

Electron diffraction study of layers obtained from ZnCrTe target by PLD method

Piotr Sagan, Grzegorz Wisz, Mariusz Bester, Marian Kuzma

Faculty of Mathematics and Natural Sciences, Department of Experimental Physics,
University of Rzeszow, Pigoia 1, 35-959 Rzeszow, Poland

Introduction

Pulsed laser deposition (PLD) is a promising technique for growing thin films of unique materials such as ceramic superconductors, semiconductors, ferroelectrics, polymers, biomaterials, and many others [1,2]. In this work we have used PLD for growth of thin films of Cr:ZnTe on KCl, and Si substrates at room temperature. ZnTe solid solution is base material for optoelectronic application. Particular interest is focused on ZnTe doped with chromium [3-8].

Experimental

CrZnTe films were grown by PLD with Nd:YAG laser operating at first harmonic (1064 nm, 20ns, 0.6 J) at different energy density of laser beam (controlled by diameter of laser beam spot at the target). The pulse repetition rate was 1 s. The deposition process was carried out at pressure of 5×10^{-5} torr in a vacuum chamber equipped with a turbomolecular pump. The films were deposited onto Si(001), glass, KCl (cleaved), and quartz plates. The distance between target and substrate was 4,5 cm. Temperature of substrate was room temperature. As a target, pressed tablets of CrTe and Zn (40%) powder were used.

The morphology of the films (SEM), and determination of the composition (EDS) were carried out using VEGA3 TESCAN electron microscope and electron diffraction measurements (THEED) were realized on JEOL JEM 6A microscope.

Results and discussion

The layers were obtained at two different values of energy density of the laser beam, i.e. at 34 J/cm^2 and 16 J/cm^2 . In both cases the films contain a large number uniformly deposited particles which are oval in shape. In the case of the layer deposited at energy density of 34 J/cm^2 the diameter of particles is approximated to $2 \mu\text{m}$ while in the case of lower fluence (16 J/cm^2) this diameter is $1 \mu\text{m}$ or $0.5 \mu\text{m}$ (there are two kinds of particles, greater and smaller ones). These results point on a different mechanism of layer growth. In both cases the rate of deposition was the same. Therefore we have deduced that the different mechanism of target ablation causes various morphology of layers. In the aim to verify this hypothesis, we have tested the morphology of targets after ablation with the fluence of 34 J/cm^2 and 16 J/cm^2 . Indeed, there are two modes of ablation: the "strong" ablation is observed in the first case (34 J/cm^2) while the irradiated target with the lower fluence is smooth, although it is damaged as well by thermal interaction of laser beam with the surface.

We present THEED patterns of films deposited on KCl substrate. This substrate was predicted to have the best adjustment of crystal lattice constant to the crystal lattice constant of cubic phase of CrTe [8, 9]. In case of the fluence of 34 J/cm^2 , a large number of continuous Debye rings is observed. The rings are sharp which confirms the polycrystalline structure of the film. The calculated crystal spaces result in two phases of ZnTe in films, i.e. cubic and hexagonal. The cubic phase is a predominant one. It is interesting that there are not additional rings arising from a third phase or from defects e.g. from the twinning.

The diffraction pattern of second layer differs considerably from the first one. There are few diffused Debye rings. This confirms the amorphous structure of the layer. Moreover, we were not able to determine the composition and phase from crystal spaces calculated while they did not fit any phases collected in crystal tables.

EDS measurements confirm results of electron diffraction studies . The first layer contains the same atomic amount of Zn and Te components. In the second layer the ratio of Zn to Te atoms is as 1:10. This results in a nonstoichiometric alloy obtained with a glass structure.

Acknowledgement

This work was supported by a grant No. NN507264740 from The Polish National Science Centre.

References

- [1] D. B. Chrisey, G. K. Hubler, G. K. Hubler: Pulsed Laser Deposition, A Wiley-Interscience Publication, New York, (1994),
- [2] M. N. R. Ashford, F. Claeysens, G. M. Fuge, S. J. Henley: Chem. Soc. Rev. 33 (2004), p. 23.
- [3] W. Mac, A. Twardowski, P. J. T. Eggenkamp, H. J. M. Swagten, Y. Shapira, M. Demianiuk: Phys. Rev. B 50 (1994), p. 19.
- [4] D. Soundararajan, P. Peranathan, D. Mangalaraj, D. Nataraj, L. Dorosinski: J. Alloys Compd. 509 (2011), p. 80.
- [5] D. Soundararajan, D. Mangalajar, D. Nataraj, L. Dorosinskii, J. Santoyyo-Salazar, M. J. Riley: J. Mag. Mag. Mater. 321 (2009), p. 4108.
- [6] G. Krishnaiah, N. M. Rao, B. K. Reddy, D. R. Reddy, T. M. Babu, S. Sambasivam, P. S. Reedy: Phys. Let. A 372, (2008), p. 6429.
- [7] M. G. Sreenivasan, K. L. Teo, X. Z. Cheng, M. B. A. Jalil, T. Liew, T. C. Chong, A. Y. Du, T. K. Chan, T. Osipowicz: J. Appl. Phys. 102 (2007), p. 053702.
- [8] S. Kuroda, N. Ozaki, N. Nishizawa, T. Kumekawa, S. Marcet, K. Takita: Sci. Techn.. Adv. Mater. 6 (2005), p. 558.
- [9] M. G. Sreenivasan, J. F. Bi, K. L. Teo, T. J. Liew: J. App. Phys. 103 (2008), p. 043908.

Preparation and characterization of silicon nanowires using SEM/FIB and TEM

Sayanti Banerjee^{1,a}, Uwe Muehle^{2,b}, Markus Löffler^{1,c}, Andre Heinzig^{3,4,d}, Jens Trommer^{4,e} and Ehrenfried Zschech^{1,2,f}

¹Technische Universität Dresden, Center for Advancing Electronics Dresden, Dresden Center for Nanoanalysis, 01069 Dresden, Germany

²Fraunhofer-Institut für Keramische Technologien und Systeme - Institutsteil Material Diagnostik Maria-Reiche-Str. 2, 01109 Dresden, Germany

³Technische Universität Dresden, Institute for Materials Science, 01062 Dresden, Germany
4NaMLab gGmbH, Nöthnitzer Str. 64, 01187 Dresden, Germany

^aSayanti.Banerjee@tu-dresden.de, ^bUwe.Muehle@izfp-d.fraunhofer.de, ^cMarkus.Loeffler@tu-dresden.de, ^dAndre.Heinzig@namlab.com, ^eJens.Trommer@namlab.com, ^fEhrenfried.Zschech@izfp-d.fraunhofer.de

Introduction

Due to their extraordinary physical properties, silicon nanowires have a great potential in application as nanoscale transistors and sensors. In this study, silicon nanowires as designed for reconfigurable field effect transistors (RFETs) are studied using SEM and TEM after precise FIB-based target preparation with particular concentration on Schottky junctions.

Experimental methods

The silicon nanowires were grown using the Vapor-Liquid-Solid (VLS) method as described by Weber et al. [1]. They were then deposited on a silicon/silicon oxide substrate and oxidized at an elevated temperature, forming a dielectric oxide shell around the nanowires. Then the oxide shell was selectively etched at each end to deposit nickel on the exposed silicon core by using electron beam lithography. During a heat treatment, nickel interdiffused into silicon and formed silicon/nickel silicide Schottky junctions within the nanowires [1].

In this study, nanowires after several steps of the fabrication process - starting from as-grown nanowires and after forming the Schottky junctions - were analyzed. Cross-sections of the silicon nanowires were prepared to determine the thickness of the oxide layer and to localize the silicon/nickel silicide interface using SEM and TEM.

Longitudinal cross-sections of the nanowires were prepared for studying the crystallography of silicon and nickel silicide, the materials forming the Schottky junction in the nanowire devices. The nanowires were also investigated with respect to crystallographic differences between wires with and without the junctions. The sample preparation for the TEM studies included the preparation of longitudinal sections of individual nanowires. Lift-out lamellae were prepared using FIB using Kleindiek[®] [2] or Easylift[®] [3] manipulator systems.

The nanowires were protected by electron induced deposition of carbon to avoid ion beam damage during FIB milling. The energy and the dose of the Ga ions were varied during the FIB studies to investigate the effect of amorphization during the thinning of the lamellae, with the goal to determine optimum parameters for the preparation process.

Results and Discussion

Figure 1 shows SEM images of a Silicon nanowire with the focus on the Si/NiSi_x Schottky junction. The oxide layer surrounding the structure is clearly visible.

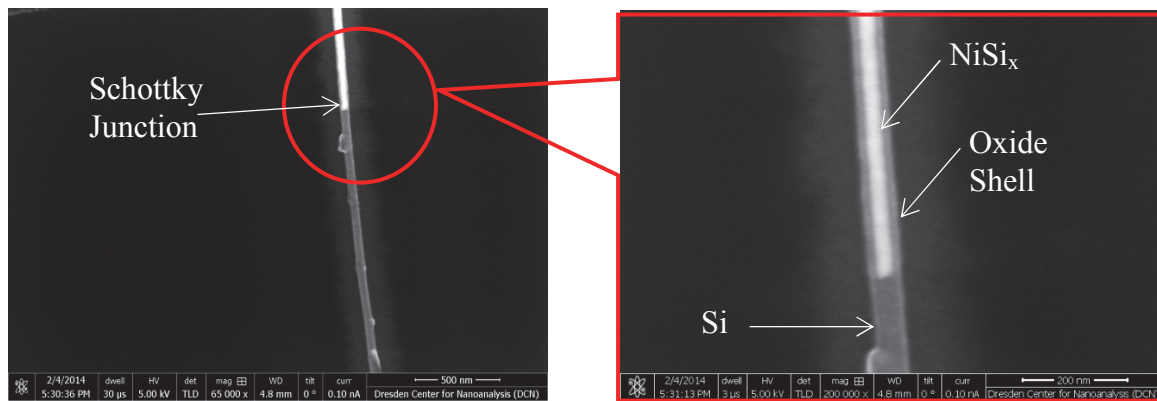


Fig. 1. SEM images showing Schottky junction between silicon (dark area) and nickel silicide (bright area). The different parts are labelled in the figure

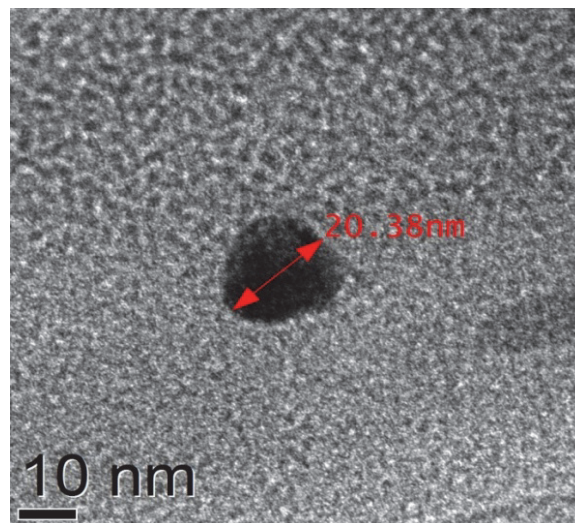


Fig. 2. A bright field TEM image of the cross-section of a single nanowire showing the loss of facets due to oxidation

The TEM studies show that after oxidation the facets of the nanowires before oxidation are completely lost as displayed in the high resolution image of the cross-section of a single nanowire in Figure 2.

Acknowledgments

The author would like to acknowledge Yvonne Standke from Fraunhofer-Institut für Keramische Technologien und Systeme for her assistance.

This work is partly supported by the German Research Foundation (DFG) within the Cluster of Excellence ‘Center for Advancing Electronics Dresden’.

References

- [1] Weber, W.M., et al.: Nano Lett. 6(12) (2006), p. 2660.
- [2] Kleindiek[®] is a registered product of Kleindiek Nanotechnik GmbH.
- [3] Easylift[®] is a registered product of FEI instruments.

Changes in the microstructure and phase composition of the steel 35HGSA depending on the quenching and partitioning parameters

Emilia Skolek^{1,a}, Krzysztof Wasiak^{2,b}, Wiesław A. Świątnicki^{3,c}

^{1,2,3}Warsaw University of Technology, Faculty of Materials Science, Wołoska 141, 02-507 Warsaw, Poland

^aemilia.skolek@nanostal.eu, ^bkrzysztof.wasiak@nanostal.eu, ^cwieslaw.swiatnicki@nanostal.eu

In recent years, a lot of research was dedicated to produce carbide free structures in steels, for example containing bainite or tempered martensite and retained austenite enriched with carbon. Heat treatment that allows obtaining the structure composed of martensite and carbon enriched austenite is called quenching & partitioning. During the "quenching" step the desired content of martensite is achieved. The second step – "partitioning" is intended to stabilize the rest of austenite. The stabilization of austenite is obtained by enriching it in carbon, which diffuses from martensite laths to austenite at elevated temperature. The carbon partitioning occurs during the austempering of steel immediately after the quenching stage. Austempering can be done at the quenching temperature or higher. "Quenching & Partitioning" treatment is provided for steels containing elements that inhibit the precipitation of carbides, whereby precipitation processes do not interfere with the partitioning of carbon. Metastable austenite content in the steel structure is very advantageous because of the TRIP effect.

The 35CrSiMn5-5-4 steel was subjected to quenching and partitioning heat treatment. The parameters of the treatment were chosen on the basis of computer simulations and dilatometric measurements which indicate that carrying out the process of quenching at 235 °C will produce 79 % martensite. In order to stabilize the rest of the untransformed austenite, the process of carbon partitioning between martensite and austenite was carried out at a temperature of 400° C for 60 s and 260° C for 900 s. According to the previous calculations the time and temperature of applied treatments were chosen so that it remain 20% of retained austenite in steel samples after cooling down to room temperature. In this work the influence of time and temperature of partitioning process on the retained austenite content was determined. The microstructure observations were carried out using the scanning electron microscope and transmission electron microscope (observation in bright and dark field) combined with electron diffraction patterns analysis.

Observation of the microstructure of the steel after partitioning treatment revealed the presence of martensite as well as significant amount of retained austenite in form of layers between the martensite laths. The rod-like carbides in the ferritic areas were also observed, which indicates the presence of lower bainite in the structure. The amount of retained austenite evaluated with the use of microscopic observations was about 28% for partitioning performed at 400°C and 25% for partitioning at 260°C. The electron microscopy observations are consistent with the results of the computer simulations.

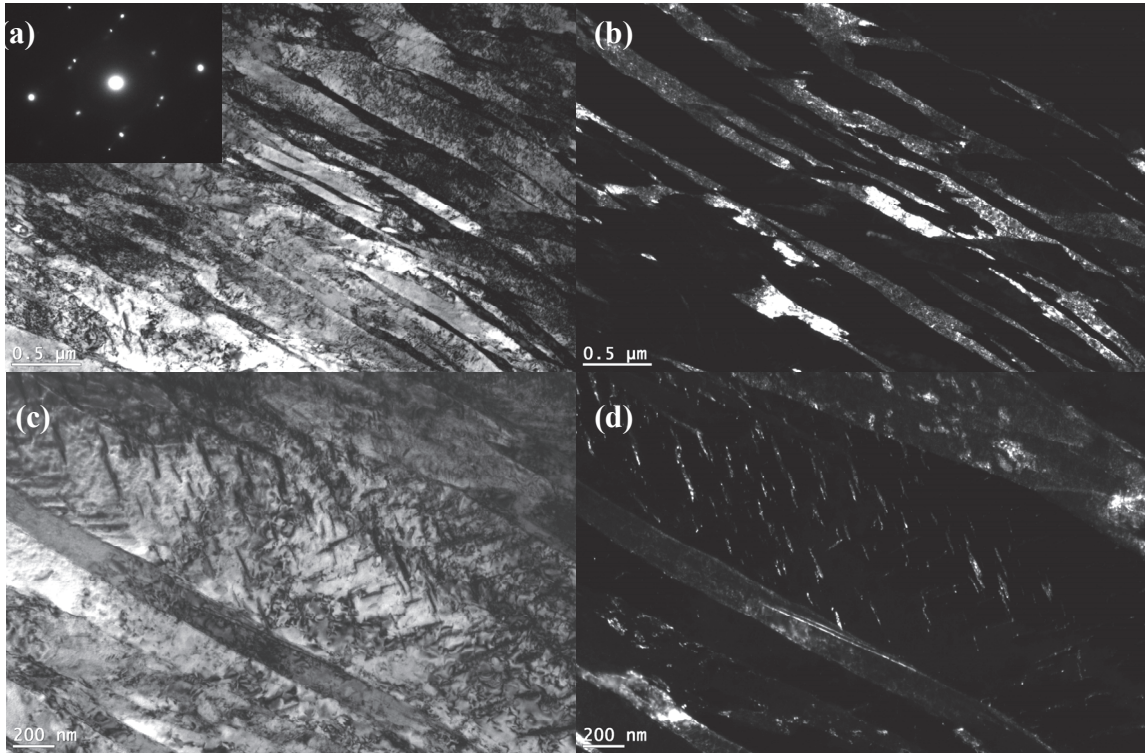


Fig. 1. Microstructure of steel after quenching and partitioning heat treatment at 235/400 °C for 60 s (b) – dark field image for austenite reflection, (d) – dark field image for Fe₃C carbide reflection

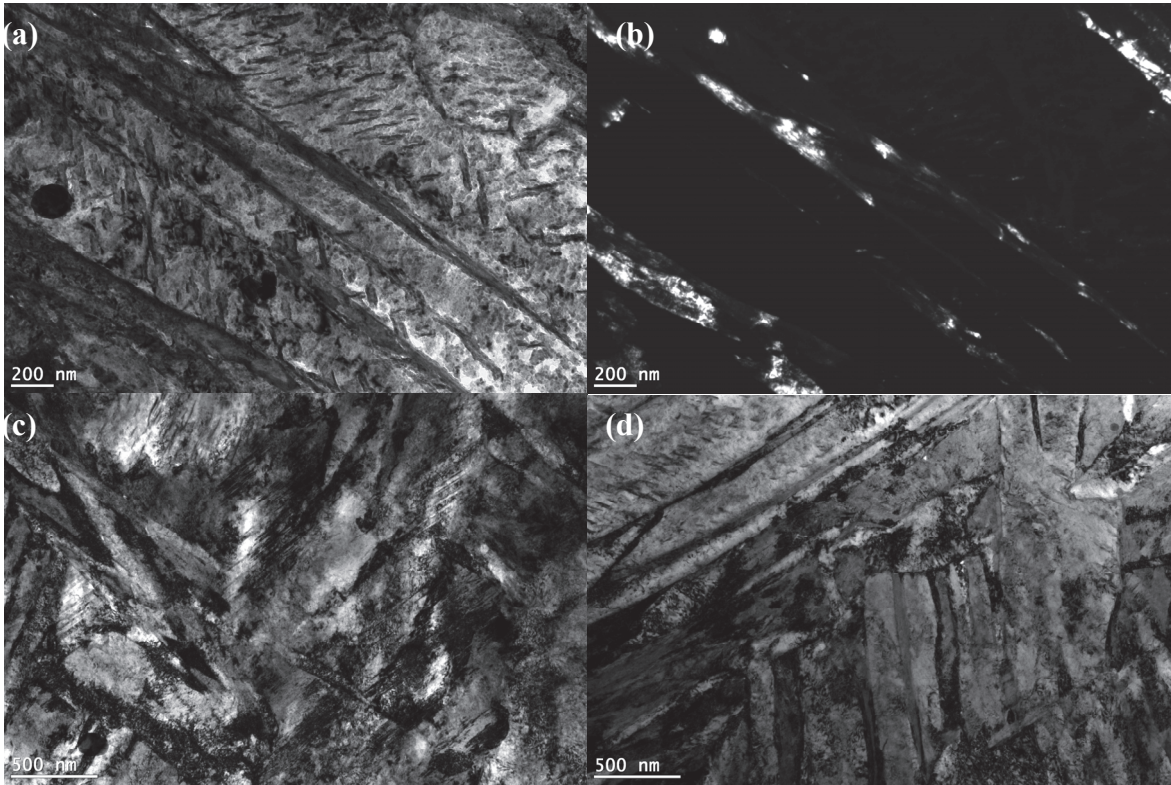


Fig. 2. Microstructure of steel after quenching and partitioning heat treatment at 235/260 °C for 900 s (b) – dark field image for austenite reflection

Determination of temperature stability of steel X37CrMoV5-I based on the electron microscopy observations

Emilia Skolek^{1,a}, Szymon Marciniak^{2,b}, Wiesław A. Świątnicki^{3,c}

^{1,2,3}Warsaw University of Technology, Faculty of Materials Science, Wołoska 141, 02-507 Warsaw, Poland
^aemilia.skolek@nanostal.eu, ^bszymon.marciniak@nanostal.eu, ^cwieslaw.swiatnicki@nanostal.eu

Introduction

A new method of obtaining high strength parameters and beneficial service characteristics in steels is producing a nanobainitic structure by means of a properly designed heat treatment. Such a structure ensures a better compromise between plasticity and strength of steel than a conventional heat treatment. Until now a nanobainitic structure was obtained in steels of a specially designed chemical composition. However, it has been shown that nanobainitisation can improve strength and cracking resistance of some standard steels, e.g. X37CrMoV5-I hot work tool steel. This study aims at determining whether and to what extent the structure of nanocrystalline bainite is resistant to increased temperature. In order to achieve this objective the methods of scanning electron microscopy (SEM) and transmission electron microscopy (TEM) were applied, with the use of bright and dark field observations combined with diffraction image analysis among others.

Methodology

X37CrMoV5-I hot-work tool steel of the following chemical composition: C-0,37% Si-1,01% Mn-0,38% Cr-4,91% Mo-1,2% V-0,34% Ni-0,19% was subjected to austempering at 300 °C, which produced a structure of carbide-free bainite of nanometric plate width separated by layers of retained austenite. In order to determine thermal stability of the nanostructure, the steel was annealed in a protective atmosphere at 400, 500 and 600 °C for 8 hours. During the annealing the changes in sample length as a function of time and temperature were recorded using a dilatometer. All the samples were observed with a scanning electron microscope and a transmission electron microscope using bright and dark field observations as well as the analysis of electron diffraction patterns. In order to determine the phase composition and to characterise the microstructure (grain size, content of austenite), the methods of stereological analysis were used. The obtained results were compared with the results of the analysis of dilatograms obtained during the steel annealing processes.

Results

Isothermal quenching of X37CrMoV5-I steel at 300 °C allowed us to produce a structure of carbide-free bainite of average plate width of 89 nm ± 6 nm with layers of residual austenite of average thickness of 31 nm ± 2 nm placed between the bainitic ferrite plates [1]. The content of ferrite in the structure is 57 % vol., the rest being austenite both in the form of layers and of blocks partially undergoing a martensitic transformation. Subjecting the X37CrMoV5-I steel samples to annealing at 400-600°C causes structure changes. The temperature of the process is higher, the changes of the structure are the greater,.. The analysis of dilatograms of steel annealed at 400 °C showed only small dilatational changes meaning minimal modifications of the structure of the annealed material [2]. Increasing the temperature to 500 °C leads to a significant shrinkage of the sample related to the precipitation of carbides. Increasing the temperature even further to 600 °C leads to a shrinkage twice as big as at 500 °C during the initial stage of annealing, which stops after 2 hours of treatment and to a subsequent elongation of the sample, caused most probably by austenite decay, during the next stage of annealing. Also positive dilatational effects related to a martensitic transformation of retained austenite in case of treatment at 500 °C and to a bainitic transformation in case of the sample annealed at 600 °C were recorded during the cooling of the samples from 500 °C and 600 °C. The above confirms that in X37CrMoV5-I steel as the annealing temperature grows, the destabilisation of

austenite also grows as a result of the decrease of carbon content in the austenite caused by its diffusion and precipitation of carbides.

The electron microscopy observations are consistent with the results of the dilatometric research. It was found that increased temperature causes carbides, mainly cementite to precipitate. Very fine carbide precipitates form at lower annealing temperatures. Their content and size grow with the annealing temperature. In the material processed at 600 °C large, spherical precipitates of Fe₇C₃ carbide were observed alongside fine-dispersed Fe₃C carbide. The precipitation leads to a decrease in the carbon content of austenite and consequently in a reduction of the austenite stability. Therefore, during cooling down to room temperature the austenite transforms to martensite or bainite. As a result of structural transformations there are less and less regions typical of a nanobainitic structure (ferrite plates separated by layers of austenite) in the observed structure and the content of ferrite in steel as well as the size of ferrite grains grow with the increasing temperature of the treatment.

Summary

The observations of microstructure and the dilatometric research we have carried out revealed that temperatures above 400 °C have a degrading effect on the nanobainitic structure in X37CrMoV5-1 steel. Therefore steels containing such a structure cannot be used as hot-working steels. However, they can well be used for manufacturing reliable constructions working in increased temperatures, i.e. below 400 °C. Both the microscopic observations and the dilatometric research showed that the changes occurring in nanobainite during annealing are due to the decrease in the stability of austenite and its transformation during cooling down to room temperature.

The results presented in this paper have been obtained within the project “Production of nanocrystalline steels using phase transformations” – NANOSTAL (contract no. POIG 01.01.02-14-100/09 with the Polish Ministry of Science and Higher Education). The project is co-financed by the European Union from the European Regional Development Fund within Operational Programme Innovative Economy 2007-2013.

References

- [1] W.A. Świątnicki, K. Pobiedzińska, E. Skołek, A. Gołaszewski, Sz. Marciniak, Ł. Nadolny, J. Szawłowski: Inżynieria Materiałowa 6 (2012), p. 524.
- [2] Sz. Marciniak, W.A. Świątnicki: Dylatometryczne badania stabilności temperaturowej mikrostruktury otrzymanej po hartowaniu izotermicznym stali X37CrMoV5-1, Materiały Konferencyjne XLI Szkoły Inżynierii Materiałowej, Kraków-Krynica 24-27.IX.2013.

Scanning and transmission electron microscopies as a techniques for the hybrid silica and silicone structures characterization

Magdalena Staszewska^{1,a}, Joanna Lewandowska-Łańcucka^{2,b},
Małgorzata Wierzbińska^{1,c}, Maria Nowakowska^{2,d}

¹Department of Materials Science, Rzeszow University of Technology, Pola 2, 35-959 Rzeszów, Poland

²Faculty of Chemistry, Jagiellonian University, Ingardena 3, 30-060 Kraków, Poland

^astaszews@prz.edu.pl, ^blewandow@chemia.uj.edu.pl, ^cmwierzb@prz.edu.pl ^dnowakows@chemia.uj.edu.pl

Introduction

Nowadays the requirements concerning the new materials are very demanding. To meet this expectations scientists create the hybrid materials - which are defined as composed of inorganic, organic or both types of these components with the fragmentation less than 1 μm . Taking into account the fact that the properties and potential applications of the material depend strongly on the morphology, the precise characterization is necessary. For this purpose the most appropriate is scanning and transmission electron microscopy. These techniques ensure not only imagining with high magnification, but also other analyses, e. g. energy dispersive X-ray spectroscopy or diffraction.

This work describes preparation and characterization of the new hybrid materials, in which silica or polysiloxanes served as a matrix. These substances were chosen due to their unique properties. Silicon dioxide is chemically, mechanically and thermally resistant, and exhibits the UV-Vis permeability. Additionally, occurring on the surface Si-OH groups provide with further modification. Whereas silicones are composed of polysiloxanes – high-molecular compounds whose main chain is built by alternating connected silicon and oxygen atoms. To silicon atoms might be attached hydrogen atoms or organic groups. In comparison with the typical organic polymers silicones possess exceptional properties such as: high chemical and thermal resistance, permeability for gases and vapors and in most cases biocompatibility.

Materials and methods

Above mentioned materials were combined with 5,10,15,20 - tetrakis(4-hydroxyphenyl)porphyrin. Porphyrines are group of compounds, which have very strong absorption and emission properties, very interesting for industry and medicine as well. Unfortunately, their applications are limited by low mechanical and thermal stability. In order to solve this problem, we have proposed the synthesis of the new hybrid material with silica and silicone as a matrix [1]. The second group of the investigated materials were superparamagnetic iron oxide nanoparticles modified with cationic chitosan (SPION-cchit). SPIONs are applied in medicine, e. g. as MRI contrast agent, or carriers in drug delivery systems. Unfortunately the pristine SPIONs are not very stable and exhibit the tendency for aggregation which considerably limits their potential applications. We prepared the silica shell on the surface of the SPION-cchit and thus obtained the hybrid core-shell type particles, to improve their stability and make possible their further modification [2]. In both cases SEM and TEM techniques were employed to examine the morphology and quality of the resulted structures.

SEM observations were performed using a cold field emission scanning electron microscope (FESEM) Hitachi S-4700 equipped with a Noran Vantage energy dispersive spectrometer. Samples were prepared by placing a drop of a dispersion on a silicon plate. The solvent was allowed to evaporate at room temperature and subsequently the thin film of gold or carbon was deposited on the sample by sputtering. TEM observation were carried out on a JEOL 100 SX (at an accelerating voltage of 80 kV) and JEOL Jem-2100 (at an accelerating voltage of 200 kV). A 200 mesh copper grid coated with Formvar/carbon film was dipped in the sample dispersion and left for 10 min (the excess of the sample was blotted with filter paper) or 12 h to allowed solvent evaporate at room temperature.

Results and discussion

Information on the structures formed was obtained on the basis of SEM and TEM observation. For silica-porphyrin materials morphology was strongly dependent on the concentration of the chromophore used in the synthesis. In the case of sample with lower content of porphyrin ribbon-like features were observed (Fig. a). The ribbons were present as discrete objects or, more frequently, they were organized into clusters of several ribbons forming double ‘brooms’. In the case of sample with higher concentration of chromophore rhombus-like features were observed (Fig. b). In both of the samples a small amount of spherical particles with the diameter of 400-500 nm was also noticed [1]. Micrographs obtained for polysiloxanes-porphyrin material (Fig. c, d) reveal similarity to morphology of silica-porphyrin with higher content of chromophore: rhombus-like structures and spherical particles, which was assigned to pristine silica that are usually obtained in the synthesis applied. SEM micrographs of SPION-cchit-SiO₂ was performed to investigate the morphology of the obtained material. The structures are round in shape, with diameter about 200 nm, but they are rather not smooth. SPION-cchit-SiO₂ particles show tendency for aggregation (Fig. e).

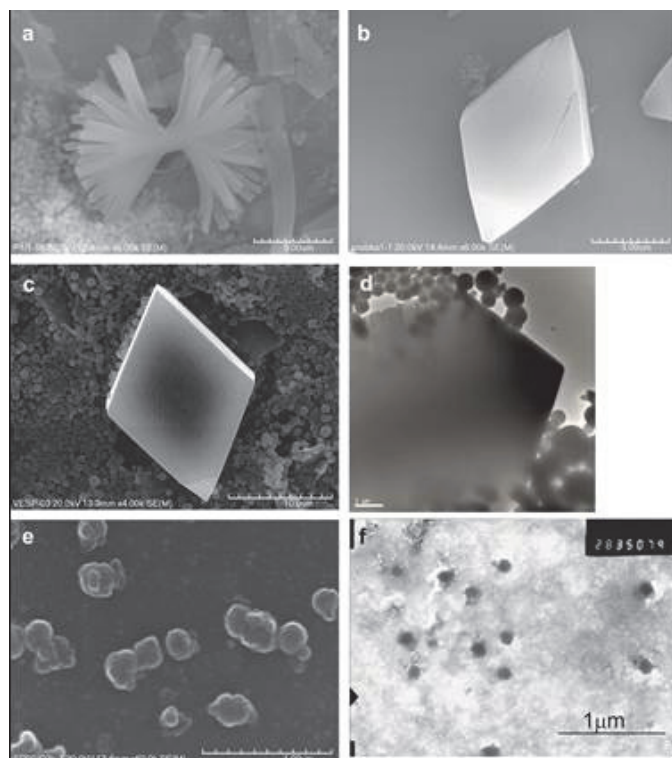


Fig. SEM and TEM micrographs of hybrid materials: a, b silica-porphyrin, c, d polysiloxanes-porphyrin, e, f SPION-cchit-SiO₂

In order to gain more insight into the morphology of the obtained particles TEM measurements were performed (Fig. f). The darker part in individual particles can be evidently distinguished and might assigned to iron oxide nanoparticles which have been coated with silica. It should be noted that iron oxide particles are not homogenously distributed into the volume of single SPION-cchit-SiO₂ particles [2].

References

- [1] M. Staszewska, M. Dzieciuch, J. Lewandowska, M. Kępczyński, S. Zapotoczny, M. Oszejca, A. Łatkiewicz, M. Nowakowska: *J. Sol-Gel. Sci. Techn.* Vol. 59 (2011), p. 276.
- [2] J. Lewandowska-Łańcucka, M. Staszewska, M. Szuwarzyński, M. Kępczyński, M. Romek, W. Tokarz, A. Szpak, G. Kania, M. Nowakowska: *J. Alloys Compd.* Vol. 586 (2014), p. 45.

TEM study of the multistage process of the TiZrCuPd BMG's partially isothermal crystallization

Anna Sypien^{1,a}, Tomasz Czepe^{1,b} Zbigniew Świątek^{1,c}
and Lidia Lityńska-Dobrzyńska^{1,d}

¹Institute of Metallurgy and Materials Science, Polish Academy of Sciences,
Reymonta St. 25, 30-059 Krakow, Poland

^aa.sypien@imim.pl, ^bt.czepe@imim.pl, ^cz.swiatek@imim.pl, ^dl.litynska@imim.pl

Introduction

Titanium alloys play an important role in many modern branches of industry, particularly in the aerospace and heat exchangers with a strong corrosion resistance, due to their highly desirable performance characteristics, such as low density, good strength, fatigue and corrosion resistance, and good strength-to-density ratio. For example for the last half of the twentieth century, Ti-6Al-4V has been accounted for about 45% of the total weight of all titanium alloys produced and its application in aerospace industries was about 33% because of good combinations of strength, toughness, corrosion and compatibility with polymer composite materials in case of this alloy [1-4]. However, the major disadvantages of titanium and its alloys are problems in joining [5]. The Ti-based alloys may be also produced as bulk metallic glasses with relatively low rates of cooling. The investigations of the effect of the increasing addition of Pd to the Ti-Zr-Cu amorphous alloys on the crystallization process are presented. Palladium addition has an influence on the glass formation, because of its atomic radius between Cu and Ti ($\text{Cu} < \text{Pd} < \text{Ti}$) and large heats of mixing with Ti and Zr [6].

Experimental and Resulted

The Ti-Zr-Cu based alloys compositions were prepared with additions of 10, 14 and 20 atomic Pd % by cold crucible levitation melting from high purity elements in an argon atmosphere. The bulk metallic glasses in the form of rods 3mm in diameter and 45mm in length were obtained by injection casting method, with use of the copper mould in a purified argon atmosphere.

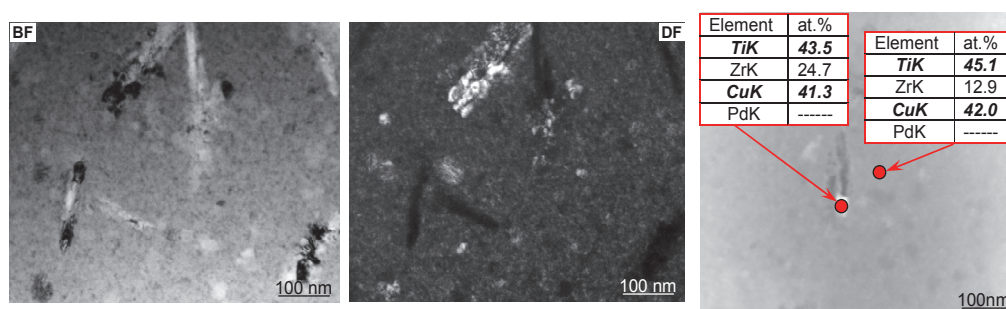


Fig. 1. TEM BF image, DF image and STEM-HAADF image of the $\text{Ti}_{40}\text{Zr}_{10}\text{Cu}_{36}\text{Pd}_{14}$ alloy annealed at 753K with the points of chemical composition analyses (in at.%) marked

The structure of the obtained samples were investigated with x-ray diffraction phase analysis (XRD) and with transmission electron microscopy techniques (TEM).

As was observed on the TEM micrographs and by XRD and electron diffraction methods, the structure of the as quenched BMG's was amorphous. Three characteristic temperature ranges of crystallization were determined with differential scanning calorimetry (DSC). The samples for the TEM investigations were prepared accordingly to the defined procedure, partially isothermal in each temperature range. The procedure was as follows: the samples were rapidly heated up to the start of the exothermic process to avoid preliminary nano-crystallization. Then, heated slowly with the rate of 2 degrees per minute in the proper temperature range. Finally, the samples were isothermally treated

for 10 minutes at the end of crystallization temperature to achieve more visible phase composition and microstructure changes.

Summary

The investigation proved that the crystallization process is multi-stage and very complex. It may be summarized as follows: at temperature range of the first thermal effect two processes take place, decomposition of the amorphous phase into two slightly different but still amorphous phases and the nucleation of a very small amount of the nano-crystallites, enriched in Cu.

Between the first and the second thermal effect the growth and the changes in composition of the existing crystals were observed which did not contain Pd (Fig. 1). However, still a very small amount of the crystalline phase was present. In the second and third thermal effect the amount of the crystalline phase drastically increased. The mixture of the plate-like and lenticular crystals formed. At 980 K the crystallization process was nearly completed, but still some amorphous phase remained.

Conclusion

For the future application it is very important to understand all the processes which may lead to the changes in general properties of the proposed material. The observed complexity of the crystallization process in the potentially biocompatible TiZrCuPd bulk metallic glasses may critically influence mechanical properties of these alloys depending on the temperature.

References

- [1] E. Ganjeh, H. Sarkhosh: *Mat. Sci. Eng. A* 559 (2013), p. 119.
- [2] M. J. Donachie: *Titanium, A technical Guide*, second ed. ASM, USA, 2000.
- [3] B. Cantor, H. Assender, P. Grant: *Aerospace materials*, IOP, 2001.
- [4] V. N. Moiseyev: *Titanium Alloys Russian Aircraft and Aerospace Applications*, Taylor & Francis Group, 2006.
- [5] A. Elrefaey, W. Tillmann: *J. Alloy. Compd.* 487 (2009), p. 639.
- [6] C.J. Smithells, E.A. Brandes, *Metals Reference Book*, 5th ed., Butterworths, London, 1976.

Acknowledgements

Research was financially supported by the Ministry of Science and Higher Education in Poland under the Grant No. NN507303940. The studies were performed in the Accredited Testing Laboratories at the Institute of Metallurgy and Materials Science of the Polish Academy of Sciences.

Correlation between withdrawal rate and microstructure of single crystalline superalloys CMSX-4

Marzena Szczepkowska^{1,a}, Włodzimierz Bogdanowicz^{1,b}, Robert Albrecht^{1,c},
Józef Lełatko^{1,d}, Jan Sieniawski^{2,e} and Krzysztof Kubiak^{2,f}

¹University of Silesia, Institute of Materials Science, 75 Pułku Piechoty 1A, 41-500 Chorzów, Poland

²Rzeszów University of Technology, Department of Material Science, W. Pola 2, 35-959 Rzeszów, Poland

^amszczepkowska@us.edu.pl ^bwlodzimierz.bogdanowicz@us.edu.pl, ^cralbrecht@us.edu.pl,

^djozef.lelatko@us.edu.pl, ^ejansien@prz.edu.pl, ^fkrkub@prz.edu.pl

Introduction

Development of aircraft engines leads a modern materials with high – temperature creep resistance. Turbine blades are critical for flight safety, so the attention should be given for preventing casting defects. In this article single crystal turbine blades made of CMSX-4 have been studied.

Material and methodology

The single – crystalline casts were obtained from an industrial alloy CMSX-4 in an ALD Vacuum Technologies furnace by the Bridgman technique. The process of the single crystals growth was carried out at rates of 1 mm/min, 3 mm/min and 5 mm/min. The samples were cut as a longitudinal sections of the turbine blade. The crystal orientation and microstructure were characterized by Laue method, X-ray topography, scanning electron microscope and novel X-ray diffraction mapping. Typical Laue method was used for examination of crystal orientation.

Summary

It was observed, that with increasing of the withdrawal rate results in increase of the direction deviation of the blade axis from the [001] direction. The X-ray topograms reveals that the increasing withdrawal rate affects the creation of the low angle boundaries. X-ray topography obtained from the blades with 5 mm/min showed a strongly depleted areas of contrast with low boundary (0.6 degree misorientation). The macroscopic deformation of some parts of the blade were revealed on the topograms. It is possible to determine the inclination of growth direction from X-ray topograms. The scanning electron microscope were used to for a visualization of the entire surface of the sample and determine dendrites arrangement. It was compare with X-ray topograms. The new mapping technique of X-ray diffractometer made by EFG company (Germany, Berlin) was also used for visualization orientation and lattice parameter at the same time. It was also found that misorientation changes in cast during crystallization depend on inclination of growth direction, airfoil shape (wall thickness, inclination and rotation about Z axis), withdrawal rate.

Investigation of TEM *in-situ* heating of Ni/Al multilayers

Jerzy Morgiel^{1,a}, Marta Marszałek^{2,b}, Maciej Szlezynger^{1,c}, Tomasz Czeppe^{1,d},
Konstanty Marszałek^{3,e}

¹ Institute of Metallurgy and Materials Science PAS, 30-059 Krakow, 25 Reymonta St., Poland

² Institute Nuclear Physics PAS, 31-342 Krakow, 152 Radzikowskiego St., Poland

³ AGH University of Science and Technology, 30-059 Krakow, 30 Mickiewicza st., Poland

^aj.morgiel@imim.pl, ^bmarta.marszalek@ifj.edu.pl, ^cm.szlezynger@imim.pl, ^dt.czeppe@imim.pl,
^emarszalek@agh.edu.pl

Introduction

The reaction of Ni/Al multilayers may either help to join heat sensitive metallic elements or form coatings of nano-crystalline NiAl intermetallic. Such reaction is strongly exothermic, so started with a heat pulse, it should propagate along the coating at a self propagating high temperature synthesis (SHS) manner [1]. The reaction rate accelerates with lowering the multilayer period only to slow down at nano-layer range [2]. It was suggested, that the latter is a manifestation of a reciprocal contamination as well as an increasing volume ratio of intermixed interfaces to that of the layers.

The double target magnetron systems with rotating table applied for deposition of the multilayer metallic coatings are efficient, but due to overlap of plasma streams their inter-layer interfaces are usually significantly intermixed. The electron beam deposition (EB) method gives lower deposition rates, but properly executed help to produce cleaner inter-layer interfaces. Therefore, materials produced with the EB should be better suited for studies of reactivity of nano-layer metallic coatings. The experiments with magnetron deposited Ni/Al multilayers confirmed, that their heat treatment did allow to produce an equiaxed nano-crystalline coating of NiAl intermetallic [3]. However, the mechanism of this reaction, i.e. whether it was controlled by inter-layer interfaces diffusion or via a reaction rate at the front advancing along the multilayer remains unknown.

The aim of this work was to characterize the EB Ni/Al multilayer of period in nano-meter range and next investigate the mechanism of their reaction during the TEM *in-situ* heating.

Experimental

The Ni/Al multilayers of nominal period of 10 nm (4:6) of total thickness of 200 nm (20x10) were deposited on silicon mono-crystalline substrates using EB method. The microstructure was characterized using TECNAI F20 FEG (200 kV) equipped with integrated EDAX detector. Thin foils were cut out with QUANTA 200 Dual Beam FIB equipped with OmniProbe *lift-out* system. The *in-situ* heating experiments were performed using Gatan heating holder.

Results

The microstructure observations of the as-deposited EB multilayer showed that they are built of fine crystallites of the size lower than the thickness of the individual Al/Ni layers (Fig. 1). The high resolution observations, as well as the selected area diffractions (presented as the inset) confirmed that they are of α -Al and Ni-Al phases, respectively. The interfaces of two near substrate layers show smooth interfaces, but higher up roughness of respective interfaces visibly increases.

The elemental profile acquired on a section of the multilayer proved, that the centers of respective layers are practically free from contamination by neighboring layers, what means that that indeed the eventual intermixing is limited to the interlayer interfaces.

The heating of such Al/Ni multilayer at 450°C/1h resulted in visible loss of contrast of nominal Al layer and darkening of nominal Ni layer indicating direction of net material transfer (Fig. 1b). The selected area electron diffraction patterns obtained after such treatment (again presented as inset) shows diminishing of intensity of ring corresponding to $\{111\}$ α -Al lattice spacing and increasing that

of $\{111\}\alpha\text{-Ni}$, as compared with the intensities of as-deposited multilayer, indicating that the reaction was not completed. The changes in rings intensities is most probably caused by nucleation and growth of NiAl intermetallic phase, as $\{110\}\text{AlNi}$ is superimposed on that of $\{111\}\alpha\text{-Ni}$.

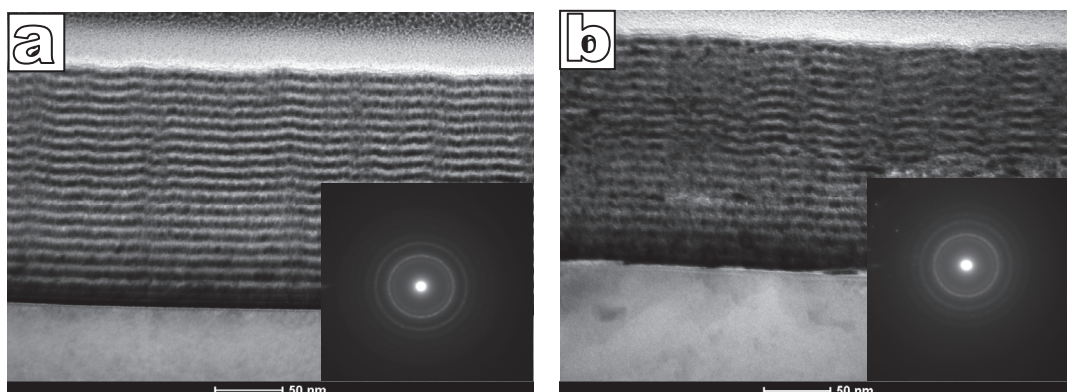


Fig. 1. Al/Ni multilayer: a) *as-deposited* and b) TEM *in-situ* heated up to 450°C/1h (ramp 100°C/min)

The application of higher heating rates, i.e. 200 and 300°C/min. ramps, resulted in similar results, but overall control over the experiment was relaxed due to increasing temperature overshoot over the planned final 450°C (by 20 and 50°C, respectively). Neither, the rising the heat treatment above the 450°C, nor extending time of this treatment seems possible due to reaction of multilayer with the substrate or fast reaction of tungsten - used to weld FIB thin foils to copper grid - with silicon substrate.

Summary

The performed investigations confirmed very good de-segregation of elements in as-deposited Al/Ni multilayer of nano-meter period produced with the EB method. Observations of *in-situ* reaction indicated, that it starts via inter-interface diffusion of aluminium to Ni layer and proceeds through formation of NiAl intermetallic. Obtaining a self sustained reaction in the *in-situ* heating experiments with such Al/Ni multilayers might be possible only by applying still higher heating rates.

Acknowledgments

The research was performed in a frame of the project no DEC-2012/05/B/ST8/01794 supported by National Science Centre (NCN) of Poland.

References

- [1] J.C. Trencle, L.J. Koerner, M. W. Tate, S.M. Gruner, T.P. Weihs T.C. Hufnagel: Appl. Phys. Lett. 93 (2008), p. 081903.
- [2] K.J. Blobaum, D. Van Heerden, A.J. Gavens, T.P. Weih: Acta Mater. 51 (2003), p. 3871.
- [3] A.S. Ramos, M.T. Vieira, J. Morgiel, J. Grzonka, S. Simões, M.F. Vieira: J. Alloys Compd. 484 (2009), p. 335.

On the wear of $TiB_x/TiSi_yC_z$ coatings deposited on 316L steel

Agnieszka Twardowska^{1,a}, Jerzy Morgiel^{2,b} and Boguslaw Rajchel^{3,c}

¹ Pedagogical University of Krakow, 2 Podchorazych Str., 30-084 Krakow, Poland

² Institute of Metallurgy & Materials Science, Polish Academy of Sciences, 25 Reymonta Str., 30-059 Krakow, Poland

³ The Henryk Niewodniczański Institute of Nuclear Physics, Polish Academy of Sciences, 152 Radzikowskiego Str., 31-342 Krakow, Poland

^aatwardow@up.krakow.pl, ^bj.morgiel@imim.pl, ^cboguslaw.rajchel@ifj.edu.pl

Introduction

Titanium diboride is a hard, refractory material, characterized by relatively low density, good both electrical and thermal conductivity, as well as corrosion and wear resistance, i.e. a set of properties desirable for surface engineering applications [1]. Unfortunately, TiB_2 coatings are characterized by high level of stress and therefore susceptible to brittle cracking [2]. Additionally, adhesion of TiB_2 coatings to metal substrates is poor [3]. These disadvantages may be overcome by combining TiB_2 with a relatively soft and damage tolerant phases like Ti [4] or a-C [5]. The aim of this work was to analyze the possibility of deposition of TiB_x with softer $TiSi_yC_z$ interlayer on AISI 316L steel used in medical applications, analyze its microstructure and dominating damage mechanisms operating in case of such system.

Experimental

Bilayered $TiB_x/TiSiC$ coatings were deposited on AISI 316L steel substrates by dual beam (DB) IBAD method from TiB_x and $TiSi_yC_z$ targets, respectively. Two Ar⁺ ion beams were applied of energy close to 10 keV. DB IBAD process was conducted in vacuum, without substrates kept at ambient temperature. Coatings were subject to single-pass scratch-test under non-lubricated sliding conditions. OM, SEM and AFM were used to examine the surface of coated substrate before and after the scratch-test. Thin foils for TEM and HRTEM observations were cut perpendicularly to the sample surfaces from scratch tracks by FIB technique.

Results

$TiB_x/TiSi_yC_z$ coatings deposited by DB IBAD were dense, smooth (Ra 8 nm) and well adherent to steel substrates. Friction coefficient of coated substrates was in the range 0.12 - 0.23, i.e. almost one fourth value of uncoated steel. OM, SEM and AFM examination of scratched tracks indicated that the main wear mechanism of analyzed coating-substrate system was an abrasive one. TEM and HRTEM observations revealed intensive plastic deformation of steel substrate under critical loads and its adverse impact on coating damage process. $TiSi_yC_z$ interlayer was effective in absorbing the energy of propagating cracks, as shown at Fig.1. In TiB_x layers the TiB_2 nano-crystalline phase was identified, while in $TiSi_yC_z$ layers $TiSi_2$ and $Ti_5Si_3C_x$ nano-crystallites were embedded in amorphous matrix (Fig. 1).

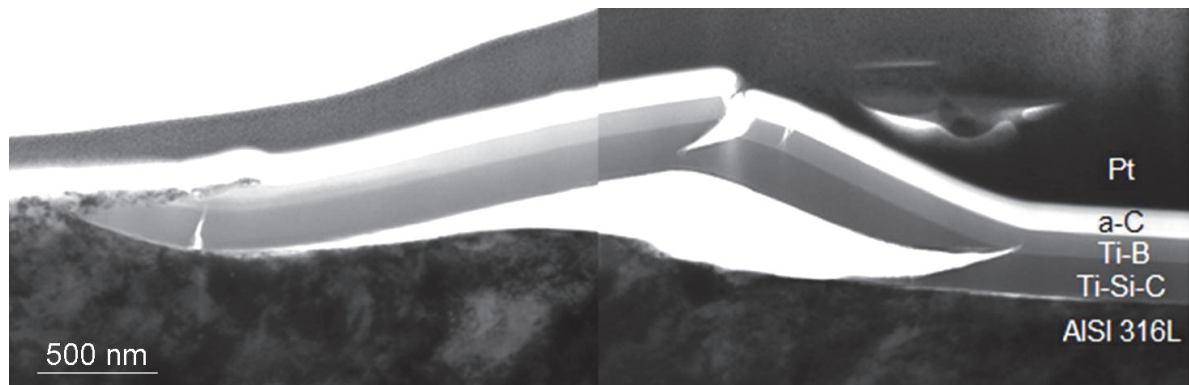


Fig. 1. Adhesive and cohesive cracking observed by TEM in Ti-B/Ti-Si-C coating (cross-section) under critical load

Summary

The bi-layer $TiB_x/TiSi_yC_z$ coatings deposited by DB IBAD method on AISI 316L steel were continuous, dense and smooth. In TiB_x layers the only identified crystalline phase was nc- TiB_2 , while in mostly amorphous $TiSi_yC_z$ interlayer, a small number of Ti_5Si_3 and $TiSi_2$ nano-crystallites was observed. The friction-wear mechanism of produced coating - substrate system was a complex abrasive one and depended both on applied load and actual thickness of the coating. It was shown that above critical load L_{C1} , the coating is already highly thinned and steel substrate is subject of significant plastic deformation, i.e. the diamond pin pushes the substrate material ahead and to the sides. Material displacement generates strong tensile stresses which in effect induces cohesive cracks in nano-crystalline TiB_2 outer layer of the coating. Under critical load L_{C2} adhesion cracking at coating-substrate interface also started to form. The performed observations indicate that the $TiSi_yC_z$ interlayer was effective in absorbing the energy of both cohesive and adhesive cracks.

References

- [1] R.G. Munro: J. Res. NIST 105, 5 (2000), p. 709.
- [2] M.K. Ferber, P.F. Becher, C.B. Finch: J. Am. Ceram. Soc. 66, 1 (1983), p. C2.
- [3] W. Dai, T. Zhang, J. Yang, R. Sun, J. Xu: Journal of Wuhan University of Technology - Materials Science 23, 5 (2008), p. 666.
- [4] N. Panich, P. Wangyao, S. Hannongbua, P. Sricharoenchai, Y. Sun: J. Met. Mater. Min. 16, 1 (2006), p. 45.
- [5] J.C. Sanchez-Lopez, M.D. Abad, A. Justo, R. Gago, J.L. Endrino, A. Garcia-Luis, M. Brizuela: J. Phys. D: Appl. Phys. 45 375401 (2012), p. 1.

Microstructural evolution in AISI 316LN + 0.1wt.%Nb steel during creep at 600 and 625°C

Vlastimil Vodárek^{1a}, Jan Holešinský^{1b}, Anastasia Volodarskaja^{1c}
and Adam Hernas^{2d}

¹VSB – TU Ostrava, 17. listopadu 15, Ostrava, Czech Republic

²Politechnika Slaska, Krasinskiego 8, Katowice, Poland

^avlastimil.vodarek@vsb.cz, ^bjan.holesinsky@vsb.cz, ^canastasia.volodarskaja@vsb.cz, ^dadam.hernas@polsl.pl

Introduction

Promoting of steam parameters in fossil fuel fired power plants to USC parameters presents a challenge for development of advanced materials exhibiting improved creep strength and steam oxidation resistance. Creep resistance of austenitic steels can be improved by small additions of strong carbide and nitride forming elements [1]. Additions of such elements to steels have to be followed by detailed investigations on microstructural stability and surveys of creep failure mechanisms. This paper deals with the effect of a small niobium addition to the wrought AISI 316LN steel on creep rupture behaviour and microstructural evolution during long-term creep exposure at 600 and 625°C.

Material and Experimental Procedures

Chemical composition of the AISI 316LN steel modified by a small addition of niobium is shown in Table 1. Solution annealing of the steel was carried out at 1050°C.

Table 1. Chemical composition of the steel investigated, wt. %

| Cast | C | N | Mn | Si | P | S | Cr | Ni | Mo | B | Nb |
|------|-------|-------|------|------|-------|-------|------|------|------|--------|-------|
| B | 0.023 | 0.161 | 1.34 | 0.48 | 0.014 | 0.013 | 18.1 | 12.5 | 2.82 | 0.0012 | 0.106 |

Creep rupture tests with a constant tensile load were carried out in air at temperature of 600°C. Microstructural evolution in the creep ruptured specimens was studied by light microscopy (LM) and transmission electron microscopy (TEM) using both carbon extraction replicas and thin foils.

Results

Results of long-term creep rupture tests at 600 and 625°C are shown in Fig. 1. Specimens for microstructural characterisation are marked B1, B2, B3 and B4. A small addition of niobium to the AISI 316LN steel resulted in a reduction of the minimum creep rate and shortening of the tertiary creep stage [2].

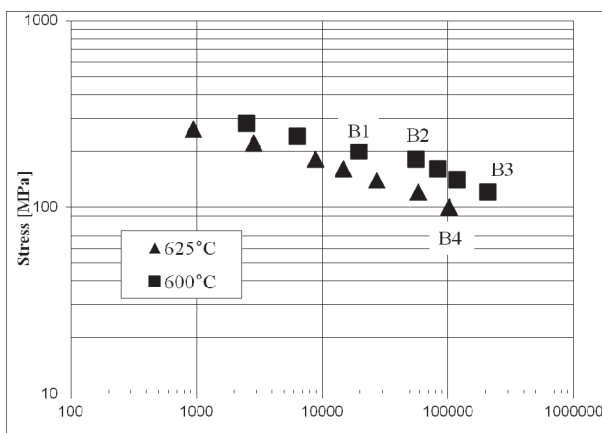


Fig. 1. Stress versus time to rupture dependence

Solution annealing at 1050°C was accompanied by precipitation of primary Z-phase (NbCrN) particles, which inhibited the austenite grain growth. The average grain size was about 20 μm. Results of studies on the minor phase evolution in specimens B1 to B4 are summarised in Table 2. The following precipitation sequence was determined: fine secondary Z-phase particles, chromium rich M₂₃C₆ particles which were gradually replaced by M₆X (Cr₃Ni₂SiX type), η-Laves and σ-phase. Fig. 2 shows precipitation of very fine particles of secondary

Z-phase on dislocations and a needle like intragranular particle of η -Laves phase in the specimen B1. Dimensional stability of Z-phase particles during long-term creep exposure was very high. Fig. 3 demonstrates pinning of dislocations by very small particles of secondary Z-phase (the average size of particles was less than 10 nm) and intensive intragranular precipitation of η -Laves phase in the specimen B3. Niobium addition to the AISI 316LN steel accelerated the formation of η -Laves and σ -phase. Coarsening of σ -phase particles was very fast. Coarse σ -phase particles at austenite grain boundaries facilitated the formation of creep cavities and contributed significantly to relatively poor creep ductility of long-term testpieces.

Table 2. Summary of minor phase evolution at 600 and 625°C

| Specimen | Temperature [°C] | Time to Rupture [h.] | Minor Phases |
|----------|------------------|----------------------|--|
| B1 | 600 | 19,508 | prim. Z-phase, σ -phase, sec. Z-phase, η -Laves, $M_{23}C_6$, M_6X , |
| B2 | 600 | 55,320 | σ -phase(\uparrow), M_6X (\uparrow), η -Laves(\uparrow), prim. Z-phase, $M_{23}C_6$ (\downarrow), sec. Z-phase |
| B3 | 600 | 223,603 | σ - phase(\uparrow), M_6X (\uparrow), η -Laves(\uparrow), prim. Z-phase, sec. Z-phase |
| B4 | 625 | 102,602 | σ - phase(\uparrow), M_6X (\uparrow), η -Laves(\uparrow), prim. Z-phase, sec. Z-phase |

Arrows indicate increasing (\uparrow) or decreasing (\downarrow) of a number density of minor phase particles

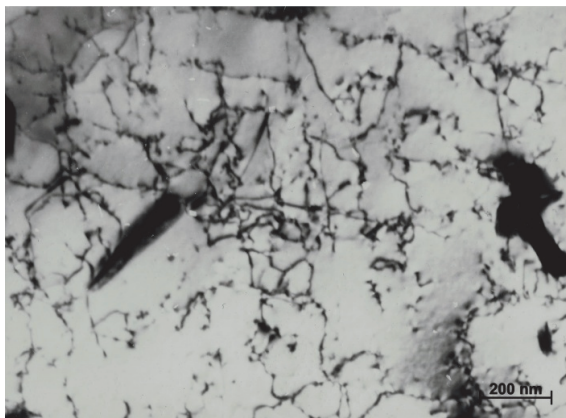


Fig. 2. Particles of sec. Z-phase on dislocations and a needle of η -Laves, specimen B1

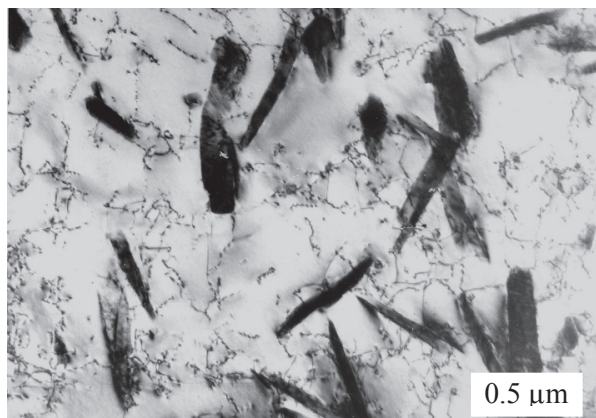


Fig. 3. η -Laves needles and fine sec. Z-phase particles on dislocations, specimen B3

Conclusions

A small addition of niobium to the AISI 316LN steel resulted in a reduction of the minimum creep rate and shortening of the tertiary creep stage. The minimum creep rate reduction can be related to precipitation of fine particles of Z phase. The positive effect of niobium on the creep resistance in the first and second stages of creep was gradually surpassed by its effect on acceleration of the σ -phase, M_6X and η -Laves formation. Coarse σ -phase particles at austenite grain boundaries promoted the formation of creep defects.

References

- [1] C. Chi, H. Yu, X. Xie: Advanced Austenitic Heat-Resistant Steels for Ultra-Super-Critical (USC) Fossil Power Plants, in: Alloy Steel - Properties and Use, edited by E. V. Morales, InTech China, (2011), p. 171, ISBN 978-953-307-484-9.
- [2] V. Vodárek: Mat. Sci. Eng. A, Vol. A528 (2011), p. 4232.

Study of zinc oxide nanopores structure on powder medium for TDG

Anna Wassilkowska^{1,a} and Rashid Galin^{2,b}

¹Cracow University of Technology, Faculty of Environmental Engineering, Warszawska 24, Cracow 31-155, Poland

²Vika-Gal2 Ltd., Molodogvardeyev 7, Chelyabinsk 454138, Russia

^aawassilkowska@pk.edu.pl, ^bvika-gal.chel@rambler.ru

Introduction

Nanostructures of zinc oxide (ZnO) constitute a wide topic in many fields of science [1]. Developed over the past 20 years, the method for preparing oxide film on fine-dispersed zinc powders [2] has rationalized the process of thermal diffusion galvanizing (TDG) in solid matter [3]. When TDG is carried on steel elements using modified powder, the duration of carrying out the process is reduced by a factor of 1.5. The increase in wear and corrosion resistance imparted to coated substrates [4], indicates a favorable phase composition of the galvanized surface [5]. The lack of wetting of the zinc powder particles by metallic zinc results in savings of powder and elimination of dust emissions. The study of the oxide film structure serves to provide a better understanding of the unusual properties of the zinc powders used in TDG.

Experimental methods

The evolution of the elemental composition of zinc powders was investigated in dependence on the TDG conditions, after annealing at various temperatures in the range 350-600°C. Particles size distribution was determined using Fritsch Particle Sizer ANALYSETTE 22. Isolated powder particles were examined at intermediate magnifications using a Hitachi HD-2300A STEM (Fig. 1a). The specimen preparation involves shaking a small amount of zinc powder in ethanol, then sprinkling the solution on a standard mesh support with a carbon film. X-ray energy dispersive spectra (Fig. 1b) and electron diffraction patterns were produced using a focused electron beam FEG 200kV on the edge of spherical particles, where the specimen was sufficiently thin (Fig. 2). Studies of the porous surface structure of the powder particles was performed by mercury porosimetry. The radii of the pores were determined from a plot of the differential:

$$V' = f(\lg r) \quad (1)$$

where: V is the volume of a pore to the total particle volume [cm^3/cm^3]; r - the pore radius in [Å].

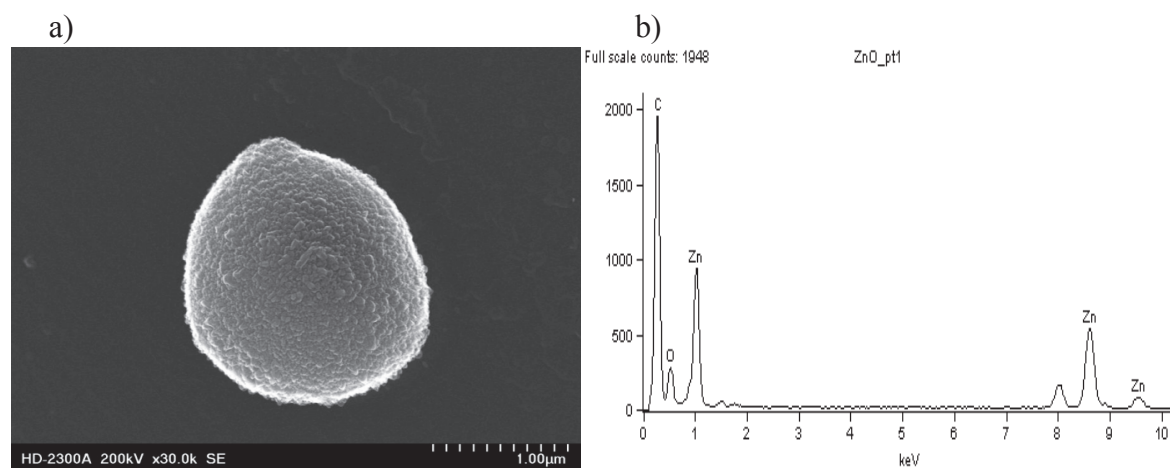


Fig. 1. STEM micrograph of modified zinc particle (a) and EDX spectrum from a shell (b)

Results

Fig. 2 illustrates the particle surface with clear nanocrystalline structure of the zinc oxide film obtained by modification of zinc powders [2]. Key data were obtained from porosimetry of particles, including size of pores belonging to the thermodynamically active interface surface. The minimal pore size yields about 6 nm for a typical oxide structure shown in Fig. 2a. Electron diffraction patterns obtained in Z-contrast mode (Fig. 2c) are representative of oxide grains on the edge of the particle shell (Fig. 2b). Due to the specimen support film (Fig. 1a) and extensive carbon contamination of the imaged areas in the focused high energy beam, the EDX spectrum provides only qualitative information on elemental composition of a nanocrystalline shell (Fig 1b).

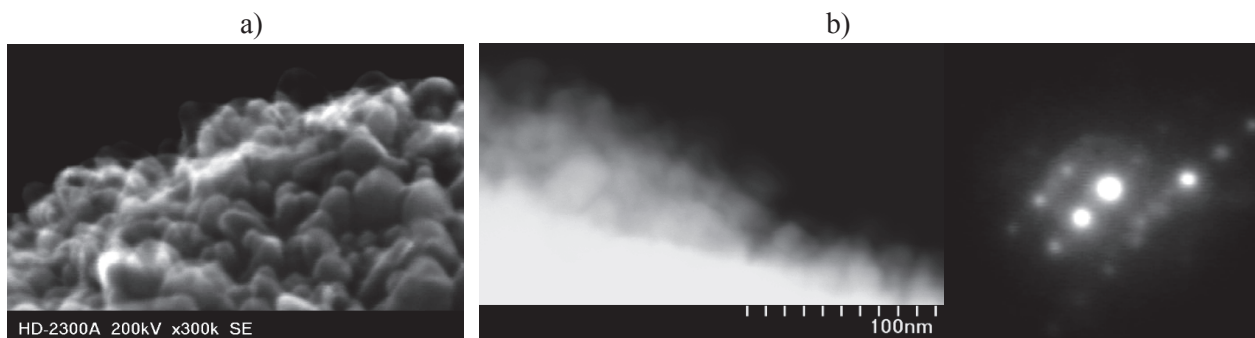


Fig. 2. STEM micrograph of the zinc oxide crystals (a), dark field image from the thinnest area of the particle (b) and a single-crystal spot electron diffraction pattern for the shell structure (c)

Summary

Nanostructure of zinc oxide has influence on the transport of metallic zinc to the TDG surface in powder medium. Unmodified zinc powders have weak pores. This is important as it should be taken into consideration that powder shells with large pore formation are ideal structures for thermal diffusion galvanizing due to their lack of interfacial wetting. Thus, specialised equipment used for the galvanizing of tape, wire, pipes and metal parts works without significant breaks to enable separation of the galvanized parts from the zinc powder. STEM is a powerful tool for observing the morphology of ZnO grains, however both the lattice structure and stoichiometry of the crystalline film are difficult to observe on a micrometer scale for particle substrates. The behavior of modified zinc powders during solid-state TDG provides an opportunity for further detailed investigation into the nanostructure of zinc oxide films.

Acknowledgement

We are greatly thankful to Dr K. Rodak from Silesian Technical University (Kinga.Rodak@polsl.pl) for permitting us to access the STEM used in the investigation.

References

- [1] Z.L. Wang: *Materials Today* (2004), p. 26.
- [2] R.G. Galin, Russian Patent Nr 2170643 (2000).
- [3] R. Galin, Y. Atanassova and S. Fiskuchev, in: *Machines, Technologies, Materials, MTM virtual Journal Vol. 2-3* (2007), p. 146.
- [4] R.G. Galin, D.A. Zakharyevich, S.V. Aleksandrov, O.V. Demidova and M.V. Fominykh: submitted to *Journal of Hardening Technologies and Coatings*, ISSN 1813-1336 (2013).
- [5] E.V. Proskurkin, I.V. Petrov, A.Yu. Zhuravlev, O.V. Ivanov and D.A. Sukhomlin: *Steel in Translation Vol. 42* (2012), p. 600.

Microstructure and stress evolution in multilayered structures under external load

Piotr Wieciński^{1,a}, Jerzy Smolik^{2,b}, Halina Garbacz^{1,c},
Krzysztof J. Kurzydłowski^{1,d}

¹ Faculty of Materials Science, Warsaw University of Technology, 141 Woloska Str., 02-507 Warsaw, Poland

² Institute for Sustainable Technology – National Research Institute, 6/10 Pulaskiego, 26-600 Radom, Poland

^a piotr.wiecinski@gmail.com, ^b jerzy.smolik@itee.radom.pl, ^c hgarbacz@inmat.pw.edu.pl, ^d kjk@inmat.pw.edu.pl

Introduction

In the past decade, a lot of attention has been paid to multilayer PVD coatings, since they demonstrate higher wear and erosion resistance compared to single layer coating. The properties of multilayer coatings are particularly impressive when the layers are composed of materials with profoundly different properties, for example ductile metals and hard ceramics [1]. Mechanical and tribological properties of the multilayer coatings depend strictly on their structure, in particular the thickness ratio of the constituent layers [2]. However, the currently available literature data have not resulted in the elaboration of comprehensive, quantitative relationships which allow to predict and optimize the properties of the multilayer coatings. The aim of this work was to investigate the influence of the structure of multilayer coatings on their mechanical and tribological properties, as well as on the deformation and failure mechanisms during external loading.

Experimental

The multilayer Cr/CrN coatings were deposited on titanium alloy Ti6Al4V using the PVD vacuum arc method. Several types of Cr/CrN layer coatings were deposited, which differed in the thickness ratio of Cr and CrN layers ($Q_{Cr/CrN}$ parameter). Nanoindentation tests were performed using HYSITRON Triboscope 950. The erosion resistance of the Cr/CrN multilayer coatings was investigated using sandblasting equipment. Spherical silica particles (40-80 μm) were used as a erodent. In order to investigate plastic deformation and fracture behaviour, the microstructure after indentation and erosion tests were characterized using Cs-corrected STEM. Samples for observation and cross sections were prepared using a Hitachi NB500 dual-beam system. The experimental investigations were supported by FEM.

Results

The observation of cross sections of the indentation zone prepared by FIB evidences that a large part of the plastic deformation induced by the indenter was transferred through the coating to the substrate material (Fig. 1a). Although the coatings underwent permanent deformation, no lateral cracks and delamination between coating and substrate, or between Cr and CrN layers were found in the observations of sections across indentation zones. This can be attributed to the effect of interfaces and to the presence of the ductile Cr layer, which accommodates the plastic deformation. Small cracks were observed in the microstructure, which did not penetrate the entire thickness of the coating and were observed only in CrN layers, whereas ductile Cr layers were free of cracks (Fig. 1). They were initiated and arrested at the interfaces between CrN and Cr layers. The cracks are stopped at the interfaces between CrN and Cr because of the shielding of crack propagation by plastic deformation and dislocation motion in Cr layers [3].

The performed investigation reveals the Cr/CrN multilayer coatings significantly improved erosion properties of the Ti6Al4V alloy. The degree of erosion protection depends of thickness ratio of constituent Cr and CrN layers. STEM observations of the sample after erosion test showed, that cracks were blocked at the interface between the constituent layers (Fig. 2b). The mechanism of this phenomenon is composed of two stages. At first, the propagating crack is divided into two smaller at

the interface between CrN and Cr₂N layers. Then, the smaller cracks are blocked at the interface between Cr₂N and Cr layers. penetrated the interface and were blocked at grain boundary of Cr grains and divided into two cracks which propagated along the grain boundaries in two directions. This phenomenon elongates the distance of the cracks propagation and thus, increases the resistance to failure of the Cr/CrN coatings.

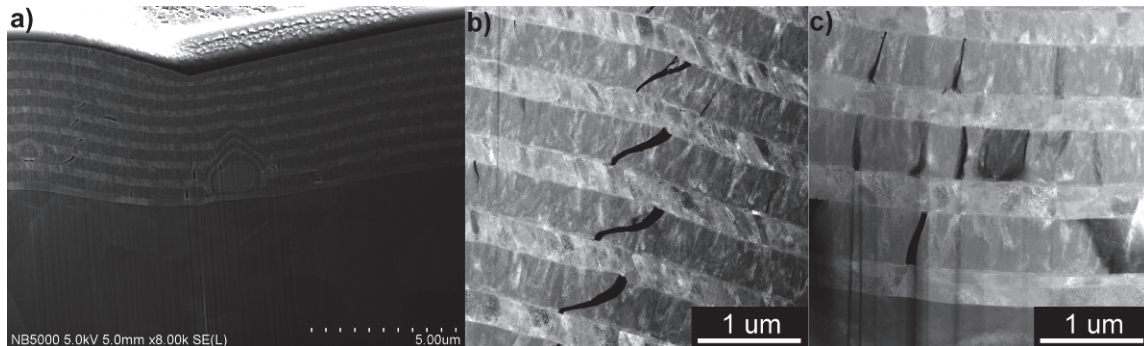


Fig. 1. Cross section of the indentation zone: a) SEM; b) STEM (dark field)

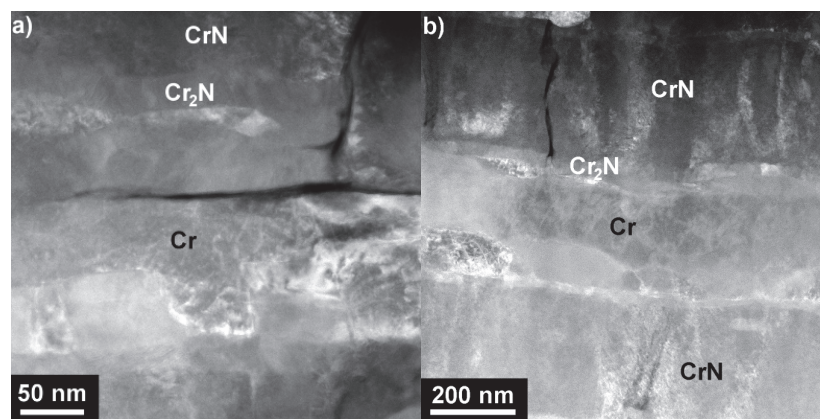


Fig. 2. Crack blocking at grain boundaries in Cr layers (a) and at the interfaces of sublayers (b)

Summary

- Multilayer Cr/CrN coatings significantly improved hardness and erosion properties of the Ti6Al4V titanium alloy
- The presence of transition layer Cr₂N between Cr and CrN layers provides a good adhesion between constituent layers and pay an important role in blocking cracks propagation
- The Cr layers accommodate plastic deformation and ensure no lateral cracks or delamination during mechanical loading
- The STEM observations revealed the mechanisms of the effective cracks blocking at the interfaces between the layers as well as in the microstructure of the ductile Cr layers during hardness and erosion test

Acknowledgements

This work was supported by the National Centre for Research and Development in Poland, Grant No. PBS1/A5/1/2012

References

- [1] B. Borawski, J. Singh, J.A. Todd, D.E. Wolfe: *Wear* 271 (2011), p. 2782.
- [2] P. Wieceński, J. Smolik, H. Garbacz, K.J. Kurzydłowski: *Thin Solid Films* 519 (2011), p. 4069.
- [3] J.Y. Zhang, X. Zhang, R.H. Wang, S.Y. Lei, P. Zhang, J.J. Niu, G. Liu, G.J. Zhang, J. Sun: *Acta Mater.* 59 (2011), p. 7368.

Morphology and chemical characterization of the Cu/(Sn,Ni) diffusion couples annealed at 220 °C

Anna Wierzbicka-Miernik^{1,a}, Krzysztof Miernik^{2,b}, Joanna Wojewoda-Budka^{1,c}, Lidia Lityńska-Dobrzyńska^{1,d}, Anna Korniewa-Surmacz^{1,e}

¹ Institute of Metallurgy and Materials Science, Polish Academy of Sciences, 25 Reymonta St., 30-059 Cracow, Poland

² Institute of Materials Engineering, Cracow University of Technology, 37 Jana Pawła II Av., 31-866 Cracow, Poland

^aa.wierzbicka@imim.pl, ^bkmiernik@pk.edu.pl, ^cj.wojewoda@imim.pl, ^dl.litynska@imim.pl, ^ea.korniewa@imim.pl

The preliminary studies of the Cu/Sn diffusion couples showed that the Ni addition into the copper pads changes not only the morphology but also the sequence of the intermetallic phases (IP) growing in the diffusion couples [1]. The chemical composition analyses revealed the presence of only the $(\text{Cu,Ni})_6\text{Sn}_5$ phase in the reaction zone. No $\epsilon\text{-Cu}_3\text{Sn}$ was detected as opposed to conventional Cu/Sn diffusion couples, where both phases were observed.

The purpose of the present study was investigation of the nickel addition into the tin and its influence on the morphology and chemical composition of the IPs growing in the Cu/(Sn,Ni) diffusion couples with the 1 and 5 at.% of Ni content, annealed in vacuum at 220 °C after 48, 120, 168 and 225 hours. The optical microscope (OM, Nikon Eclipse ME600) was applied for the preliminary microstructure observations of prepared samples. The intermetallic phases formed in the reaction zone between Cu and (Sn,Ni) were examined using the scanning (SEM, JEOL JSM5510LV) and transmission (TEM, TECNAI G2 FEG) electron microscopes equipped with an energy dispersive X-ray (EDX) spectrometer. The samples for TEM investigations in the form of thin foils were cut out from the accurately selected regions using a Quanta 3D focused ion beam instrument.

The OM observations revealed the presence of the three phases formed in the reaction zone between Cu and (Sn,Ni) pads (Fig. 1).

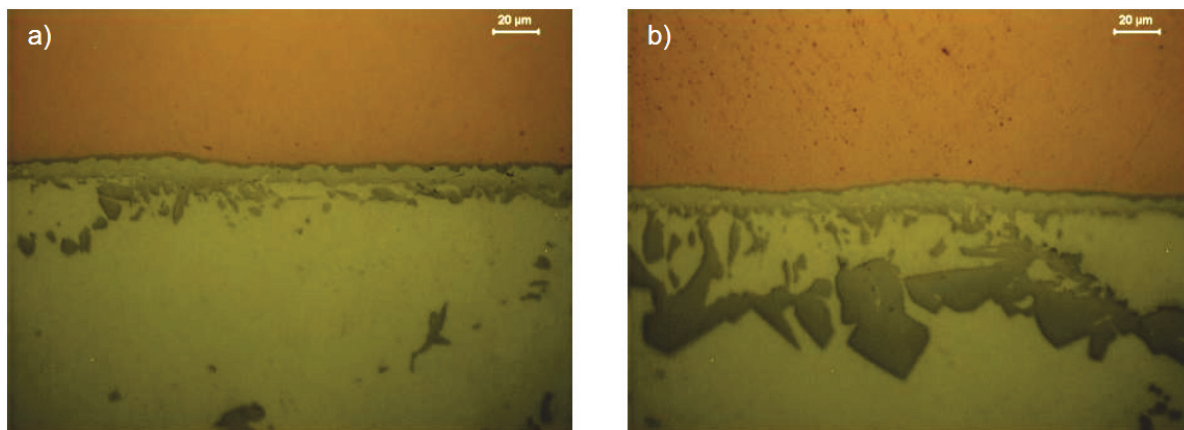


Fig. 1. OM images of the Cu/(Sn,Ni) diffusion couples annealed at 220 °C for 48 hours: a) with addition of 1 at.% Ni, b) with addition of 5 at.% Ni

The SEM microstructure examinations and the EDS analysis identified two intermetallic phases: $(\text{Cu}_{1-x}\text{Ni}_x)_3\text{Sn}$ and $(\text{Cu}_{1-x}\text{Ni}_x)_6\text{Sn}_5$ in two variants: rich and poor in Ni concentration. The $(\text{Cu}_{1-x}\text{Ni}_x)_3\text{Sn}$ phase was formed as thin, continuous layer near to the Cu pad (Fig. 2). Whereas the $(\text{Cu}_{1-x}\text{Ni}_x)_6\text{Sn}_5$ phase was of dual morphology. From the (Sn,Ni) side the phase formed as detached grains (of high Ni content) while closer to $(\text{Cu}_{1-x}\text{Ni}_x)_3\text{Sn}$ phase as continuous layer (of low Ni content), (Fig. 2).

The increase of the Ni addition to the Sn caused that much more $(\text{Cu}_{1-x}\text{Ni}_x)_6\text{Sn}_5$ phase grew within the reaction zone. In contrary to $(\text{Cu}_{1-x}\text{Ni}_x)_6\text{Sn}_5$ phase, a smaller amount of the $(\text{Cu}_{1-x}\text{Ni}_x)_3\text{Sn}$ was observed with nickel increasing concentration in tin (Fig. 2).

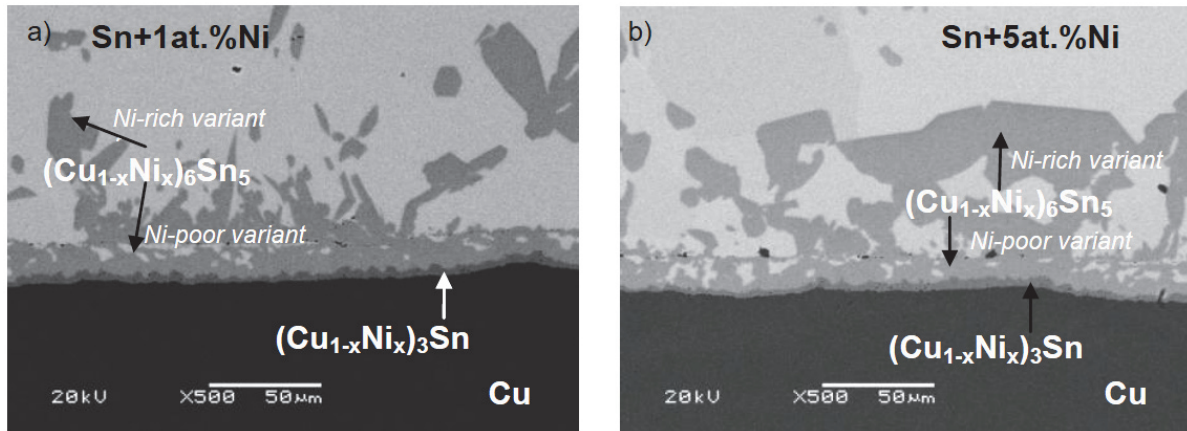


Fig. 2. SEM images of a) Cu/(Sn+1at.%Ni) and b) Cu/(Sn+5at.%Ni) diffusion couples annealed at 220 °C for 168 hours

The selected area diffraction patterns made in the Cu/(Sn,Ni) diffusion couples confirmed the presence of both $(\text{Cu}_{1-x}\text{Ni}_x)_6\text{Sn}_5$ and $(\text{Cu}_{1-x}\text{Ni}_x)_3\text{Sn}$ phases.

The presented research on the reactivity of Cu/(Sn,Ni) are innovating and contribute to a better understanding of the phenomena occurring at the interfaces during Cu-(Sn,Ni) interaction, which allow to improve the quality of the new lead-free joints used in the electronic industry.

References

- [1] Paul A.: The Kirkendall effect in solid state diffusion. PhD thesis, Eindhoven University of Technology, Eindhoven, The Netherlands, (2004) 85-88.

Acknowledgments

The research was financially supported by the National Science Centre under the grant No. 2011/03/B/ST8/06158. The TEM studies were performed in the Accredited Testing Laboratories at the Institute of Metallurgy and Materials Science of the Polish Academy of Sciences. The SEM research were carried on in the Institute of Materials Engineering, Cracow University of Technology.

Microstructural evolution of aluminium alloy 2024 during homogenization process

Grażyna Mrówka-Nowotnik^{1,a}, Małgorzata Wierzbińska^{1,b}, Jan Sieniawski^{1,c},
Andrzej Nowotnik^{1,d}

¹Department of Materials Science, Rzeszow University of Technology, W. Pola 2, 35-959 Poland

^amrowka@prz.edu.pl, ^bmwierzb@prz.edu.pl, ^cjansien@prz.edu.pl, ^dnowotnik@prz.edu.pl

Introduction

The pure aluminum and aluminum alloys are generally considered “soft engineering materials”. They are probably most commonly used in electrical and chemical applications since they are ideal materials for extrusion purpose. Most of commercially available aluminum alloys can be widely used for the production of extruded sections. Sections can be extruded from heat-treatable medium- and high-strength 2xxx series [1]. These multiphase alloys belong to the group of commercial, in which relative volume, chemical composition and morphology of structural constituents exert significant influence on their useful properties [1-3]. The microstructure of 2xxx aluminium alloys are usually complex because of the many additives used for strength, corrosion resistance or grain structure control. During solidification of 2xxx alloys containing Cu i Mg, intermetallics phases as product of eutectic reaction, often form at the edges of the dendrites. In as-cast state most of these intermetallics have different morphology [4]. However, among all stages of production of aluminium extrusion billets, the homogenization of them is a very important process since it gives significant changes in the microstructure and mechanical properties of the alloy. During the homogenization process of as-cast 2xxx alloys the interdendritic network of the plate-like phases transforming into multiple, more rounded discrete particles. The presence of globular particles in the homogenized microstructure improve the extrudability of the material and the surface quality of a product. During homogenization, other processes, eg. dissolution of Al_2Cu , Al_2CuMg , Mg_2Si and $\text{Q-Al}_5\text{Cu}_2\text{Mg}_8\text{Si}_6$ particles also occur [1-5]. Fe-containing intermetallics are also called “constituents” since they do not dissolve and remain as a separate phase in the Al-matrix even after long homogenization times, although they may have an effect on the phase composition and phase morphology [5].

Material and methodology

The material used in this investigation was AA2024 aluminium alloy (composition: 1.63%Mg, 0.50%Si, 4.5%Cu, 0.50%Fe, 0.59%Mn) in as-cast state and after homogenization. Homogenization treatment was performed at 480°C for 3, 10, 24, 48, 72 hours. Microstructure analysis was carried out on the as-cast condition and after different time of homogenization at 480°C. The microstructure of examined alloy was observed using an optical microscope - Nikon 300 on the polished sections etched in Keller solution (0.5 % HF in 50ml H₂O). The observation of specimens morphology was performed on deep etched samples (5gNaOH in 100ml H₂O) on the scanning electron microscope (SEM) HITACHI S-3400. The chemical composition of the intermetallics was analysed by energy dispersive spectroscopy (EDS) attached to the SEM manufactured by Thermo Noran. Quantitative analysis of the microstructure components was performed by X-ray diffraction (ARL XTR'A Thermo diffractometer).

Results

The microstructure of 2024 alloy in as-cast state (Fig.1) contains of primary aluminium dendrites and substantial amount of different intermetallic phases constituents namely: $\text{S-Al}_2\text{CuMg}$, $\theta\text{-Al}_2\text{Cu}$, $\text{Al}_7\text{Cu}_2\text{Fe}$, $\beta\text{-Mg}_2\text{Si}$, AlCuFeMnSi and $\text{Al}_3\text{Cu}_2\text{Mg}_8\text{Si}_7$ varied in shape, size and distribution located at the grain boundaries of $\alpha\text{-Al}$. This alloy besides the eutectic phases and primary intermetallics contains a large amount of the fine particles of hardening phases (Fig. 1). Large number of the fine

needle shaped strengthening phase are located in the boundary zone of the dendritic network structure. During the homogenization process many microstructural changes, such as dissolution of precipitates and transformation of intermetallics, which take place during heat-treatment of 2xxx aluminium alloys are controlled by diffusion of the alloying elements: Cu, Mg, Si, Fe and Mn in the aluminium matrix. Most of the θ -Al₂Cu, S-Al₂CuMg and Mg₂Si intermetallic phases are dissolved in the matrix. The continuous dendritic-network structure was broken with the increase of homogenization temperature and time.

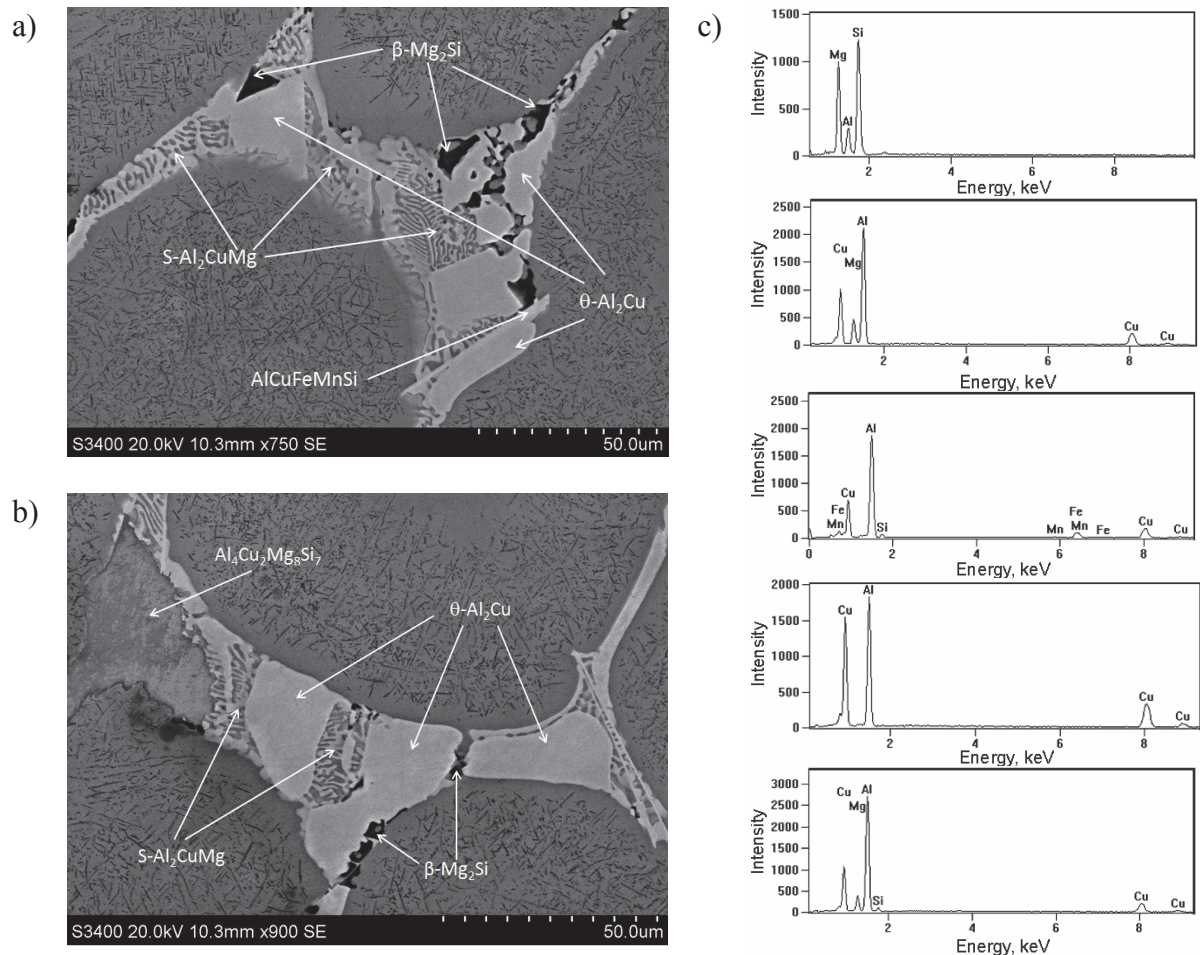


Fig. 1. SEM as-cast microstructure of 2024 alloy with particles of the intermetallic phases (a,b) and EDS spectra of the revealed particles (c)

Acknowledgment

This work was carried out with the financial support of the Ministry of Science and Higher Education under grant No. N N507 247940.

References

- [1] A. Boag, A.E. Hughes, N.C. Wilson, A. Torpy, C.M. MacRae, A.M. Glenn, T.H. Muster: Corros. Sci. 51 (2009), p. 1565.
- [2] G. Wang, B. Xiong, Y. Zhang, Z. Li, P. Li.: Int J. Min. Met. Mat. 16 (2009), p. 427.
- [3] Aluminium Handbook. vol.1 Fundamentals and Materials. Aluminium-Verlag Marketing & Kommunikation GmbH, Düsseldorf 1999.
- [5] L.F. Mondolfo: Aluminium Alloys: Structure and Properties. Butterworths, London-Boston, 1976.

Silver matrix composite reinforced by aluminum-silver intermetallic phases

Grzegorz Włoch^{1,a}, Tomasz Skrzekut^{1,b}, Jakub Sobota^{1,c} and Ludwik Błaz^{1,d}

¹AGH University of Science and Technology, Faculty of Non-Ferrous Metals, Al. Mickiewicza 30, PL-30059 Cracow, Poland

^agwloch@agh.edu.pl, ^bskrzekut@agh.edu.pl, ^csobkuba@agh.edu.pl, ^dblaz@agh.edu.pl

Powders of silver and aluminum in 82:18 mass % ratio were mixed for 1 hour using TURBULA T2F barrel. The mixed powders were preliminarily consolidated using 500 kN press to obtain a cylindrical charge of 40 mm diameter and 60 mm height. As compressed powders were extruded at 400 °C and a rod of 8 mm in diameter was received.

Structural analyses were performed using light microscopy (LM), scanning electron microscopy (SEM-EDS), transmission electron microscopy (TEM) and X-ray diffraction (XRD) methods. Tensile test and hardness measurements were performed to estimate mechanical properties of the material. Moreover, other physical properties such as the material density, electrical resistivity, thermal *expansion coefficient*, Young modulus and Poisson ratio were also evaluated. The results of mechanical and physical properties of as extruded material are shown in Table 1.

Table 1. Mechanical and physical properties of as extruded Ag-Al composite

| | |
|----------------------------------|--------------------------|
| Ultimate tensile strength, R_m | 490 [MPa] |
| Yield point, $R_{0,2}$ | 440 [MPa] |
| Elongation, A | 5 [%] |
| Young modulus, E | 80 [GPa] |
| Poisson ratio, ν | 0,3 |
| Hardness, HV2 | 135 |
| Electrical resistivity, ρ | 90,2 [nΩm] |
| Density, d | 6,8 [g/cm ³] |

Differential scanning calorimetry (DSC) tests, *thermomechanical* analysis (TMA) were also performed. Received data were analysed with respect to mechanical properties of annealed samples to evaluate a thermal stability of the material. Mechanical consolidation of powders by the hot extrusion processing was found to be a very effective method of the bulk material manufacturing that allows to obtain uniformly distributed structural components and negligible porosity of the material. XRD and SEM/TEM analyses confirmed the development of intermetallic phases (Ag_2Al -hcp and Ag_3Al -cubic, β -Mn type) in hot extruded material. Structural investigations revealed grains of mentioned phases at the silver-aluminium interface. Thermal analysis and hardness measurement of long term annealing samples revealed good thermal stability of the examined composite.

TEM microstructures formed due to the reactions in Al/metal oxide couples

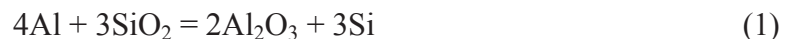
Joanna Wojewoda-Budka^{1,a}, Lidia Lityńska-Dobrzyńska^{1,b}, Katarzyna Stan^{1,c}, Jerzy Morgiel^{1,d}

¹Institute of Metallurgy and Materials Science, Polish Academy of Sciences, Cracow, Poland

^aj.wojewoda@imim.pl, ^bl.litynska@imim.pl, ^ck.stan@imim.pl, ^dj.morgiel@imim.pl

High temperature interaction between aluminum and various metal oxides such as SiO₂, Y₂O₃, ZnO and NiO have been studied as they lead to formation of metal-ceramic composites. This group of materials is considered as advanced engineering materials for aviation and ground transport industry due to their high modulus and high specific strength. Reaction performed at either 1173 K or 1273 K under vacuum resulted in formation of *Reaction Product Region* (RPR) zone at the (Al drop)/(MeO substrate) interface of complex morphology which can be successfully described only using Transmission Electron Microscopy (TEM) technique combined with the Focused Ion Beam (FIB) the only one technique suitable for the thin foil preparation.

The reaction between Al and SiO₂ at 1173 K takes place according to the equation (1):



It causes the formation of α -Al₂O₃ of various sizes and morphology: from relatively large, through the ones of medium size up to fine round or fibres. It was demonstrated that the orientation of these grains was not random and the surrounding matrix is composed of Si at the areas close to the drop/RPR interface and of Al away from it.

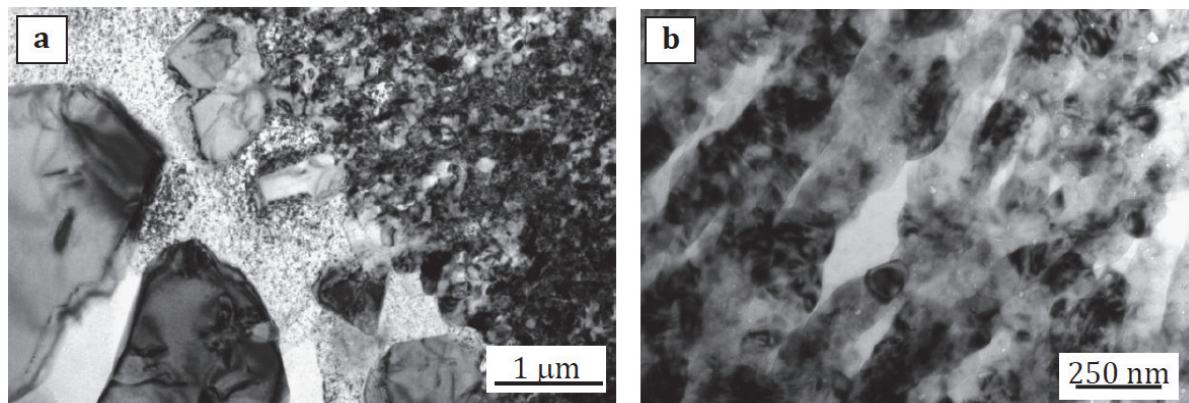


Fig. 1. TEM bright field images of the reactively formed α -Al₂O₃ of various sizes and morphology: large, medium and fine (a), fine fibres under higher magnification (b)

The structural observations of Al/Y₂O₃ couple formed at 1273 K allowed to identify the composition of the multi-layered structure of reaction product region extending into the oxide substrate: fine crystalline precipitates of Al₅Y₃O₁₂ (YAG) phase interspersed in the Al₃Y matrix, large AlYO₃ (YAP) crystals and elongated YAP surrounded by the Al₂Y metallic channels. This time the reaction between the Al and Y₂O₃ led to the formation of the YAP phase. The YAG phase formation could be a result of the reaction between the YAP and alumina or directly from Al₂O₃ and Y₂O₃ interaction [1,2].

The short time of interaction for 5 minutes at 1273 K between the ZnO single crystal and Al resulted in the formation of two layers of about 150-200 nm thick, which were identified as the Al₂O₃ and ZnAl₂O₄ spinel. The alumina type depended on applied ZnO single crystal orientation. The cubic

gamma, tetragonal delta or monoclinic lambda was detected and the information on their orientation with respect to the substrate and spinel was determined as well [3,4].

Application of various orientations of NiO single crystals as a substrate reacting with aluminium at 1273 K in each case resulted in the formation of the same phase composition: α -Al₂O₃, Al and Al₃Ni. However, the morphology and amount of particular components varied, depending on NiO crystallographic orientation [5,6].

References

- [1] J. Wojewoda-Budka, N. Sobczak, J. Morgiel: *J. Microsc.* Vol. 237(3) (2010), p. 253.
- [2] J. Wojewoda-Budka, N. Sobczak, B. Onderka, J. Morgiel, R. Nowak: *J. Mater. Sci.* Vol. 45(8) (2010) p. 2042.
- [3] J. Wojewoda-Budka, N. Sobczak, J. Morgiel, R. Nowak: *Sol. St. Phenom.* Vol. 172-174 (2011), p. 1267.
- [4] J. Wojewoda-Budka, N. Sobczak, K. Stan, R. Nowak: *Arch. Metall. Mater.* Vol. 58(2) (2013), p. 349.
- [5] J. Wojewoda-Budka: *Mater. Eng.* 4 (2013), p. 393.
- [6] J. Wojewoda-Budka, K. Stan, B. Onderka, R. Nowak, N. Sobczak: *J. Alloys Compd.* DOI: 10.1016/j.jallcom.2014.01.056.

Acknowledgments

Samples were prepared in the Centre for High-Temperature Studies at the Foundry Research Institute in Cracow and further examined in the Accredited Testing Laboratories at the Institute of Metallurgy and Materials Science of the Polish Academy of Sciences in Cracow.

The authors thank Prof. Natalia Sobczak and dr Rafał Nowak from Centre for High-Temperature Studies at the Foundry Research Institute in Cracow for useful discussion and suggestions.

The research was financially supported by The Ministry of Science and Higher Education of Poland within the Projects No. N N507 272836 (Al/SiO₂), Iuventus Plus No IP2011061071 (Al/ZnO, Al/NiO) and by Foundation for Polish Science within the grant for young researchers under the START programme (Al/Y₂O₃).

TEM investigations of a microstructure of 7CrMoVTiB10-10 steel weld metal

Krzysztof Pańcikiewicz^{1,a}, Anna Zielińska-Lipiec^{1,b}

¹Faculty of Metals Engineering and Industrial Computer Science, AGH University of Science and Technology, Al. Mickiewicza 30, 30-059 Kraków, Poland

^akrzysztof.pancikiewicz@agh.edu.pl, ^balipiec@agh.edu.pl

A progressive increase of the steam parameters calls for new requirements to the ferritic steels used in the boiler and piping system. Increased steam pressures and temperatures also have an impact on the conditions for operating water walls. A new 7CrMoVTiB10-10 (T24) steel is recommended for water membranes walls without post weld heat treatment (PWHT). The chemical composition of this steel and cooling conditions after welding influence the susceptibility to cracking in weld metal during and after welding [1,2]. The investigations of the microstructure of the weld metal were made for welded joints of T24 steel tube (OD 42.4 mm x 7.1 mm) made by Gas Tungsten Arc Welding.

TEM investigations were performed by JEM-200CX microscope using thin foils. The TEM results showed that in the as-welded microstructure the dominating microstructures were the mixtures of bainite and martensite. Four types of bainite morphology were observed. Figure 1a,b shows large areas of lower- and upper bainite, respectively. Moreover, the bainitic ferrite plates without precipitates and associated with inter-plate film of austenite have been observed, as shown on Fig 2. This morphology is similar to the carbide free bainite observed in CrMoV steel by C. Gupta et al. [3]. An the welded join a carbon free bainite associated with austenite- martensite islands (M-A) was also observed (Fig. 3). The presence of a large number of M-A islands reduced the ductility of the steel investigated.

In large areas of the specimens lath martensite with retained austenite on a subgrain was observed. If the martensite formed at temperature above, the autotempering effects were observed.

TEM investigations of the welded joints are necessary to assess the influence of formation various microstructural consistent during cooling of weld metal on properties of joints.

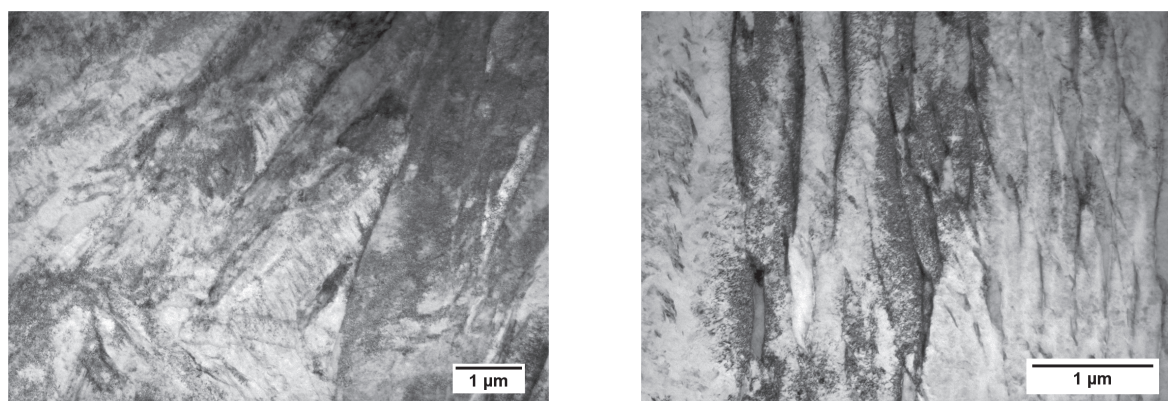


Fig. 1. TEM bright-field images of the packets of bainite, a) lower, b) upper

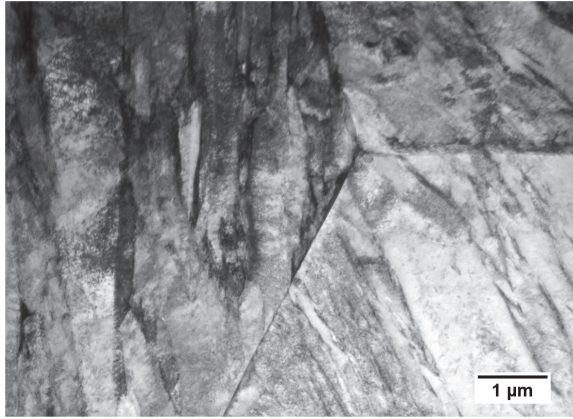


Fig. 2. Precipitate free ferrite associated with inter-plate films of austenite. TEM bright-field image

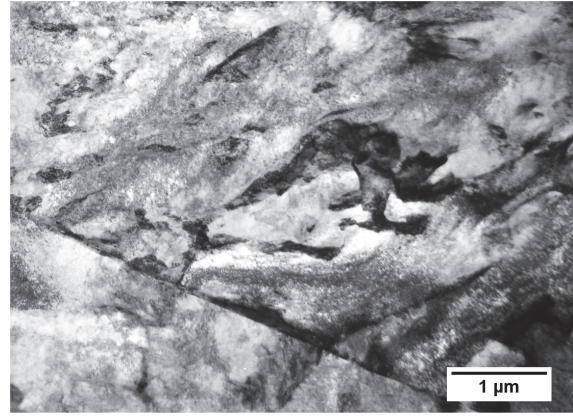


Fig. 3. M-A islands in a bainitic ferrite. TEM bright-field image

Acknowledgement

This work has been supported by National Science Centre NCN (2012/07/N/ST8/00630).

References

- [1] E. Tasak, A. Ziewiec, K. Pańcikiewicz: Metall. - Metall. Eng. News Vol. 79 (2012), p. 247.
- [2] K. Pańcikiewicz, A. Zielińska-Lipiec, E. Tasak: Adv. Mater. Sci. Vol. 13 (2013), p. 76.
- [3] C. Gupta, G.K. Chakravarty, D. Srivastav, S. Banerjee: Scripta Mater. Vol. 53 (2005), p. 259.

Effect of aging on twin-roll cast AZ31 magnesium alloy after constrained groove pressing

Mariia Zimina^{1,a}, Michaela Poková¹, Jozef Veselý¹, Jan Bohlen^{2,b},
Dietmar Letzig², Gerrit Kurz², Jozef Zrník³ and Miroslav Cieslar^{1,c}

¹ Charles University in Prague, Faculty of Mathematics and Physics, Ke Karlovu 5, 121 16 Prague 2, Czech Republic

² Magnesium Innovation Centre (MagIC) Helmholtz Zentrum Geesthacht, D21502 Max-Planck Str. 1, Geesthacht, Germany

³ COMTES FHT a.s., Průmyslová 995, Dobřany 334 41, Czech Republic

^am.zimina@seznam.cz, ^bjan.bohlen@hzg.de, ^ccieslar@met.mff.cuni.cz

Introduction

In recent years considerable attention has been paid to the development of new casting and deformation techniques and its application to structural materials, such as magnesium alloys. Continuous casting techniques are becoming more popular, because of more uniform microstructure with finer grains as compared to die-casting and wrought alloys [1]. Twin-roll casting (TRC) allows producing of magnesium alloy strips of the 5 mm thickness with high solid solution supersaturation and relatively large grains [2]. The refinement of microstructure using deformation is important for improving the mechanical properties of the magnesium alloys. Among other severe plastic deformation (SPD) techniques there is the constrained groove pressing (CGP) [3], which is well-established on aluminium alloys. The information about using CGP on magnesium alloy is limited. Combining TRC and CGP is believed to be the powerful tool to improve mechanical properties of magnesium alloys. In this paper microstructure and microhardness evolutions after heat treatment are considered.

Experimental

Twin-roll cast AZ31 magnesium alloy was used as a semi-product for CGP. The CGPed magnesium alloy was annealed at 450 °C for 10 h. The microstructure observations in as-CGPed and aged states using light microscopy were made. Vickers microhardness (HV 0.1) mapping was made along the cross-section of each sample. Electron back-scatter diffraction (EBSD) was applied to study the grain size and grain orientation in CGPed material. All observations were made in transverse direction (TD) of the specimens.

Results and Discussion

TRC AZ31 magnesium alloy exhibits heterogeneous microstructure along the strip width [2, 4]. It was shown [4], that homogenization at 450 °C for 10 h leads to the grain refinement of the TRC alloy and grain size achieves 50 µm instead of 200 µm in the as-cast TRC material. The microstructure observations of as-GCPed material showed the differences in structure along the rolling direction (RD) corresponding to the unequal deformation of different parts of the sample. The grain size decreased down to 20 µm in the regions of the highest deformation. Aging at 450 °C for 10 h leads to recrystallization and grain refinement of CGPed material. However, the inhomogeneity of the microstructure along RD still persists.

The EBSD measurements showed the basal texture respective to the surface in both materials accompanied by slight rotation of grains towards RD in the aged one (Fig. 1).

The evolution of local mechanical properties was studied using microhardness mapping of the specimen's cross-section. The maximum value of microhardness in the as-CGPed material was 110 MPa. After 10 h of aging softening of the alloy occurs and average microhardness drops to

55 MPa. Although the microstructure is more uniform, the distribution of the grain sizes along the RD is not the same. Thus, areas with small 10 μm grains alternates with larger grains of about 50-100 μm .

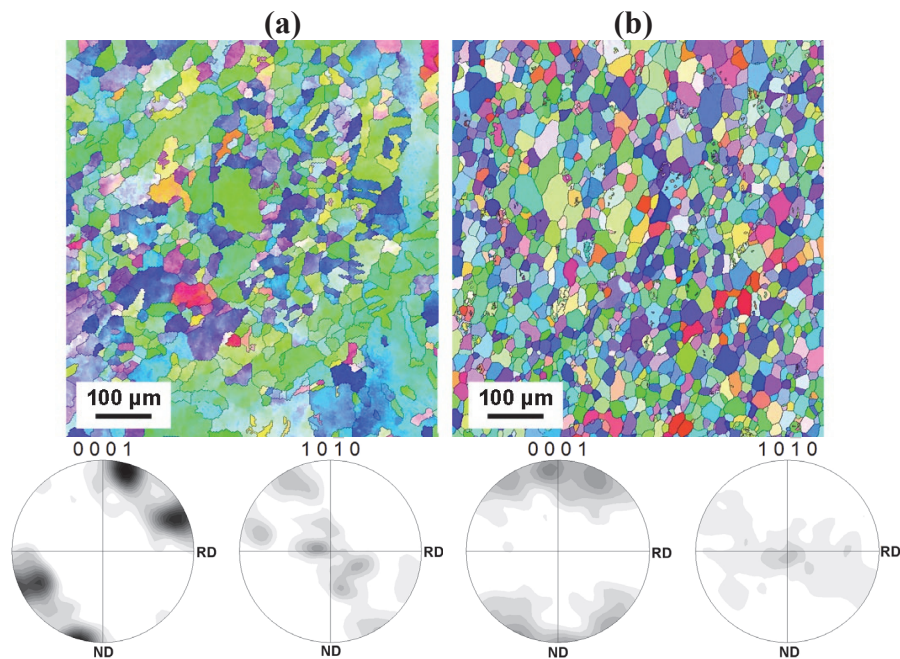


Fig. 1. Orientation maps of twin-roll cast AZ31 magnesium after constrained groove pressing: a) as-CGPed, b) after homogenization at 450 °C for 10 h

Summary

The new fine-grained material was produced using TRC technique followed by CGP. The microstructure investigations showed the inhomogeneity along the RD of the specimens. After aging at 450 °C for 10 h recrystallization occurs followed by significant change in the grain size and slight change in the grain orientation. The softening of the material was observed and microhardness decreases along the whole cross-section of the TRC AZ31 magnesium alloy.

Acknowledgements

Authors are grateful for the financial support of the Czech Science Foundation under the project P107-12-0921 and to the grant SVV-2014-269303 and GAUK 946213.

References

- [1] B.L. Mordike, T. Ebert: *Mat. Sci. Eng. A* Vol. 302 (2001), p. 37.
- [2] G. Kurz, J. Bohlen, L. Stutz, D. Letzig, K.U. Kainer: in: *Magnesium Technology 2013* (eds N. Nort, S.N. Mathaudhu, N.R. Neelameggham and M. Alderman), John Wiley & Sons Inc., 2013.
- [3] D. H. Shin, J.J. Park, Y.S. Kim and K.T. Park: *J. Mat. Sci. Eng. A* Vol. 328 (2002), p. 98.
- [4] M. Zimina, P. Malek, J. Bohlen, D. Letzig, G. Kurz, M. Cieslar: in: *Materials in Heat Treatment*, conference proceedings, pp. 218-225, 2013, Jihlava, Czech Republic.

Precession Electron Diffraction (PED) studies of grossular from the Wiluy River locality, Sakha-Jakutia Republic, Russia

Maciej Zubko^{1,a}, Krystian Prusik^{1,b}, Irina Galuskina^{2,c},
Joanna Wspaniała-Rak^{1,d}, Danuta Stróż^{1,e}

¹Institute of Materials Science, University of Silesia, 75 Pułku Piechoty 1a, 41500 Chorzów, Poland

²Faculty of Earth Sciences, University of Silesia, Będzińska 60, 41200 Sosnowiec, Poland

^amaciej.zubko@us.edu.pl, ^bkrystian.prusik@us.edu.pl, ^cirina.galuskina@us.edu.pl ^dj.wspaniala@gmail.com, ^edanuta.stroz@us.edu.pl

Introduction

Grossular is a member of the garnet group in the garnet supergroup [1]. The general crystal chemical formula for the garnet supergroup minerals is $\{X3\}\{Y2\}\{Z3\}\phi12$, where X, Y, and Z refer to dodecahedral, octahedral, and tetrahedral sites, respectively, and ϕ is O, OH, or F [1,2]. End-member formula of grossular is $\text{Ca}_3\text{Al}_2\text{Si}_3\text{O}_{12}$, it is cubic, space group $Ia\bar{3}d$.

Grossular crystal about 2 cm in size, representing by combination of trapezohedron $\{211\}$ and rhombododecahedron $\{110\}$, have been studied using electron diffraction methods with beam precession. Precession electron diffraction (PED) is a measurement technique with increasing interest and applications. The method was proposed in 1994 by Vincent and Midgley [3] for *ab initio* structure determinations from electron diffraction data. PED patterns usually contain more Bragg peaks than diffraction patterns collected without beam precession - conventional selected area diffraction (SEAD) patterns. This fact is explained by the geometrical consideration that during PED measurements bigger volume of the reciprocal space is sampled [4]. Using that technique also intensity of the diffracted beams is integrated over selected volume of reciprocal space. Due to these features PED pattern contain more complete data with more reliable intensities suitable for structural studies. Additional benefit of beam precession is the further reduction of dynamical interactions [5] so kinematical approximation can be successfully used during crystal structure determination and refinement.

Experimental

Green grossular crystals for the studies have been collected on the shores of the Wiluy River, Sakha-Yakutia Republic, Russia. Grossular have been studied by Electron Back Scattering Diffraction (EBSD) method using JEOL 6540 electron microscope with HKL detector. Afterwards crystals were crushed in agate mortar. The obtained fine powder was dispersed in ethanol and sonicated in ultrasonic bath for 3 hours. A drop of the solution was allocated on Cu mesh covered with amorphous carbon layers. Electron diffraction patterns with beam precession of 1.0° were recorded sequentially while tilting a crystal around an arbitrary crystallographic axis with 1° steps as described in [6]. After each rotation crystal was tracked in image mode to ensure that data collection is performed always from the same region. Studied samples are beam stable materials so no additional care have to be taken in order to obtain good quality diffraction data.

Data collection was performed on JEOL 3010 electron microscope with $2k \times 2k$ OriusTM 833 SC200D Gatan CCD camera within tilt range of 52° what is the maximum available tilt due to limitation of holder dimensions and the microscope pole piece. The high tension was set to 300 kV and Nanomegas DigiStar electron beam precession attachment was used.

Result summary

From the PED measurements three dimensional reciprocal space was reconstructed, unit cell parameters were determined and diffraction intensities were extracted from tilt series by means of

ADT3D software package. Visualization and analysis of reciprocal space was performed by means of *Chimera* program [7]. No additional features as satellite reflections or diffuse scattering were observed.

Crystal structure of the studied grossular was solved using direct methods and obtained results were refined using full matrix least square method by means of *SHELXL97* [8] software assuming kinematical approximation. No absorption correction was applied. That is main reason for relatively large agreement factors in comparison to those usually obtained from X-ray diffraction measurements [2]. Obtained data is in good agreement with the XRD single-crystal data on grossular structure that is allows to consider PED as perspective method for phase with unknown crystal structure.

References

- [1] E. S. Grew, A. J. Locock, S. J. Mills, I. O. Galuskina, E. V. Galuskin, U. Hålenius: *Am. Mineral.* 98 (2013), p. 785.
- [2] G. A. Novak, G. V. Gibbs: *Am. Mineral.* 56 (1971), p. 791.
- [3] R. Vincent, P. A. Midgley: *Ultramicroscopy* 53 (1994), p. 271.
- [4] E. Mugnaioli, T. Gorelik, U. Kolb: *Ultramicroscopy* 109 (2009), p. 758.
- [5] P. Oleynikov, S. Hovmoller, X. D. Zou: *Ultramicroscopy* 107 (2007), p. 523.
- [6] U. Kolb, T. Gorelik, C. Kübel, M. T. Otten, D. Hubert: *Ultramicroscopy* 107 (2007), p. 507.
- [7] E. F. Pettersen, T. D. Goddard, C. C. Huang, G. S. Couch, D. M. Greenblatt, E. C. Meng, T.E. Ferrin: *J. Comput. Chem.* 13 (2004), p. 1605.
- [8] G. M. Sheldrick: *Acta Crystallogr. A*64 (2008), p. 112.

SEM-EDS and X-ray micro computed tomography studies of skeletal surface pattern and body structure in the freshwater sponge *Spongilla lacustris* collected from Goczalkowice reservoir habit (Southern Poland)

Jagna Karcz^{1,a}, Andrzej Woźnica^{2,b}, Marcin Binkowski^{3,c}, Małgorzata Klonowska-Olejnik^{4,d}, Tytus Bernas^{5,e}, Jerzy Karczewski^{6,f} and Paweł Miguła^{7,g}

¹Laboratory of Scanning Electron Microscopy, Faculty of Biology and Environmental Protection, University of Silesia, 40-032 Katowice, Poland

²Department of Biochemistry, Faculty of Biology and Environmental Protection, University of Silesia, 40-032 Katowice, Poland

³Department of Biomedical Computer Systems, Institute of Computer Science, University of Silesia, 41-200 Sosnowiec, Poland

⁴Institute of Environmental Sciences, Faculty of Biology and Earth Sciences, Jagiellonian University, 30-387 Cracow, Poland

⁵Nencki Institute of Experimental Biology, Polish Academy of Sciences, Laboratory of Imaging Tissue Structure and Function, 02-093 Warszawa, Poland

⁶Department of Biophysics and Plants Morphogenesis, Faculty of Biology and Environmental Protection, University of Silesia, 40-032 Katowice, Poland

⁷Department of Animal Physiology and Ecotoxicology, Faculty of Biology and Environmental Protection, University of Silesia, 40-009 Katowice, Poland

^ajagna.karcz@us.edu.pl, ^bandrzej.woznica@us.edu.pl, ^cmarcin.binkowski@us.edu.pl,

^duxklonow@cyf-kr.edu.pl, ^eet.bernas@nencki.gov.pl, ^fjerzy.karczewski@us.edu.pl, ^gpawel.migula@us.edu.pl

Keywords: high-resolution scanning electron microscopy, energy dispersive X-ray spectroscopy, X-ray micro-computed tomography

Sponges represent a natural resource for their functional role in natural processes of water purification in freshwater ecosystems. Freshwater sponges are an important component of aquatic ecosystem filtering particles of a smaller size range than other benthic invertebrates. The study of freshwater sponges has become increasingly popular as more is known about their ability to filter large volumes of water together with their importance as bioindicators in diagnostic of aquatic environments [1, 2]. Here, we present a detailed study of the structure and elemental composition of the freshwater sponge *Spongilla lacustris*, which has not been previously studied in relation to the three-dimensional architecture of the skeleton.

The sponge material was obtained from Goczalkowice reservoir (Southern Poland) during its biological monitoring. In our study, we applied a combination of the SEM-EDS and X-ray micro-Computed Tomography (X-ray micro-CT) methods to visualize spatial architecture of sponge body. Scanning electron microscopy (FE-SEM Hitachi SU 8010) enabled visualization of external and internal pattern of sponge skeleton at the large area with excellent resolution of topographic features. For SEM examination, small pieces of fresh *S. lacustris* were cut out from different areas of the sponge body and prepared according to chemical fixation protocols followed by CPD drying and lyophilization. The X-ray micro-CT was used to provide non-invasive visualization of large volumes of the sponge body in a label-free manner.

Detailed SEM-EDS and X-ray micro-CT analyses revealed that sponge skeleton was not homogenous in composition and comprised several forms of skeleton organization: (1) Dermal membrane was delicate and transparent with the arrangement of the jutting sponge spicules; (2) Ectosomal skeleton occurred as spicular brushes at apices of primary fibres with cementing spongin material; (3) The choanosomal skeletal architecture was isotropic alveolate with pauci- or multispicular fibres, made by siliceous megascleres embedded in a scanty spongin matrix both in the choanosome and at the sponge surface. Microscleres were scattered in the sponge mesohyle and

appear to be involved in the main skeletal network; (4) Siliceous microscleres were irregularly scattered in choanosome and skeletal surface; (5) In megascleres and microscleres the distribution of silica was observed along the spicules and sponge surface areas. Such a spatial arrangement of the skeleton spicules allows sponges to grow upwards and facilitate water exchange with minimal metabolic cost.

In conclusion, the combination of these microscopy techniques allowed to obtain a complete picture of the sponge structure and organization. *S. lacustris* secrete siliceous elements, which can subsequently fuse, interlock with each other, or form three-dimensional structures connected by spongin. This form of the spatial structure of the skeleton allows sponges to grow upwards and facilitate water exchange with minimal metabolic cost. Understanding the structure and chemical composition of the sponge skeleton may prove to be a novel model for applications in modern materials science and biotechnology.

Acknowledgment

This research was co-financed by the European Regional Development Fund within the Innovative Economy Operational Programme 2010-2014 entitled “Integrated system supporting management and protection of dammed reservoir (ZiZoZap)”, No POIG 01.01.02-24-078/09).

References

- [1] M.J. Uriz, X. Turon, M.A. Becerro, and G. Agell: *Microsc. Res. Techniq.* Vol. 62 (2003), p. 279.
- [2] R. Manconi, R. Pronzato: *Hydrobiology* Vol. 595 (2008), p. 27.

The ultrastructural comparison of plants infected with different pathotypes of *Pepino mosaic virus* (PepMV)

Julia Minicka^{1,a}, Katarzyna Otulak^{2,b}, Grażyna Garbaczewska^{2,c},
Beata Hasiów-Jaroszewska^{1,d}

¹Department of Virology and Bacteriology, Institute of Plant Protection – National Research Institute, Wł. Węgorzka 20, 60-318 Poznan, Poland

²Department of Botany, Faculty of Agriculture and Botany, Warsaw University of Life Sciences –SGGW (WULS-SGGW), Nowoursynowska 159, 02-776, Warsaw, Poland

^aJ.Minicka@iorpib.poznan.pl, ^bkatarzyna_otulak@sggw.pl, ^cgrazyna_garbaczewska@sggw.pl,
^dB.Hasiow@iorpib.poznan.pl

Introduction

The *Pepino mosaic virus* (PepMV) from *Potexvirus* genus is one of the most important pathogens infecting tomato worldwide nowadays. PepMV was first identified in Peru in 1974 [1] and since then has spread in Europe and both Americas, causing significant economic losses. Four genotypes of the virus have been described so far: European (EU), Peruvian (LP), Chilean (CH1) and Chilean 2 (CH2). In Poland, currently the CH2 genotype is dominant. Virus causes a wide range of symptoms, which intensity depends on many factors, such as genotype [2], climate [3] and cultivar [4]. Moreover, it has been shown that single nucleotide substitutions in viral genome are responsible for the development of disease symptoms: necrotic and yellowing, respectively [5,6]. Virus particles are filamentous, about 508 nm length.

The aim of the study was detailed ultrastructural comparison of plants infected with different isolates of PepMV: mild (PepMV-P22), yellowing (PepMV-P5) and necrotic (PepMV-P19), using transmission electron microscope (TEM).

Methodology

The study was performed on *Solanum lycopersicum* var. Beta Lux under greenhouse conditions. Plants were inoculated mechanically with three isolates from CH2 genotype: mild (PepMV-P22), necrotic (PepMV-P19) and yellowing (PepMV-P5). After 3, 7 and 14 days post inoculation (dpi) samples were collected from apical leaves of infected plants, then fixed, dehydrated through a series of acetones and embedded in Spurr Low-Viscosity Embedding Kit (Polysciences). Ultrathin sections were cut and stained with uranyl acetate and lead citrate.

The observations were performed in Department of Virology and Bacteriology IPP-NRI using HT7700 transmission electron microscope (Hitachi, Japan) and in Department of Botany WULS-SGGW using Morgani 268D transmission electron microscope (FEI, The Netherlands).

Results

A high concentration of viral particles (about 508 nm in length) was observed in ultrathin section of infected leaves. A particularly large number of viral particles in the infected cells was observed for the necrotic isolate. PepMV particles were located in various compartment (cytoplasm, vacuoles) of mesophyll and phloem cells. Occasionally for mild and necrotic isolates, virus-like organized inclusions were present in cells.

In the later stage of infection (about 14 dpi) strong damages of organelles structure were observed for necrotic isolates. The most disorganized were mitochondria (Fig. 1A) and chloroplasts (Fig. 1B). Also, two weeks after inoculation with PepMV-P19 isolate formation of groups of necrotic cells were visible. For all virus variants, an increased activity of the rough endoplasmic reticulum (Fig. 1C) and the Golgi apparatus was noticed. In addition, secretion of proteins towards cell wall was observed (Fig. 1D).

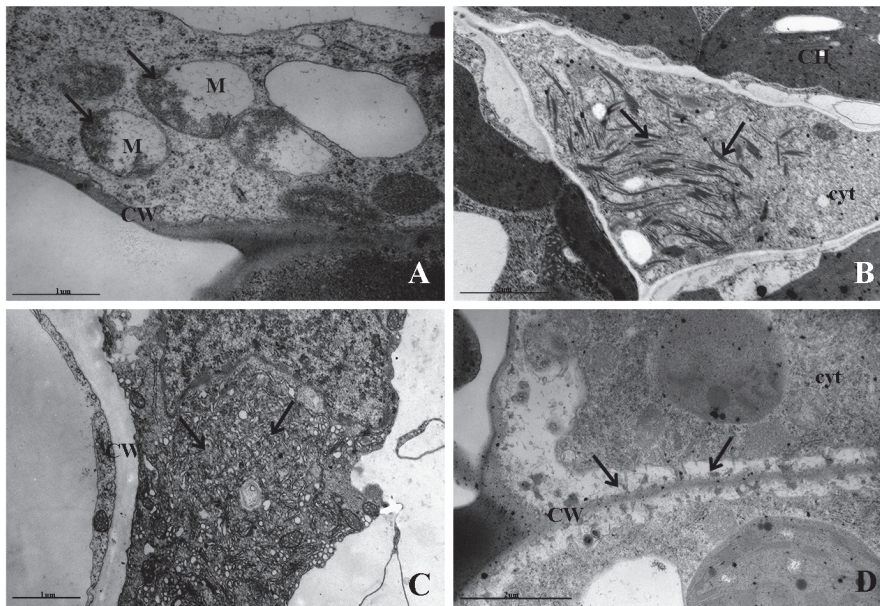


Fig. 1. Ultrastructural alteration induced by PepMV isolates: A) degeneration of mitochondria with reduced density of stroma and number of cristae [arrows], B) degradation of chloroplast [arrows], C) extended rough endoplasmic reticulum [arrows] D) secretion of proteins of unknown origin into the cell wall

Conclusions

The largest number of viral particles were visible in a case of necrotic isolate, indicating a faster rate of replication of these variants. Also, the strongest changes in ultrastructure of the organelles were observed as a result of PepMV-P19 infection. Strong secretion of the proteins to the cell wall was noticed. In addition, a numerous viral proteins were localized in the plants conductive elements, confirming their role in the movement of the virus and the systemic infection.

References

- [1] R.A.C. Jones, R. Koenig and D.E. Lesemann: *Annals of Applied Biology* 94 (1980), p. 61.
- [2] B. Hasiów-Jaroszewska, P. Jackowiak, N. Borodynko, M. Figlerowicz and H. Pospieszny: *Virus Genes* 41 (2010), p. 260.
- [3] N.J. Spence, J. Basham, R.A. Mumford, G. Hayman, R. Edmondson and D.R. Jones: *Plant Pathol.* 55 (2006), p. 595.
- [4] S. Villemson, R. Hunt and L. Jarvekulg: *Plant Protect. and Quarantine* 11 (2003), p. 37.
- [5] B. Hasiów-Jaroszewska, H. Pospieszny and N. Borodynko: *J. Phytopathol* 157 (2009), p. 494.
- [6] B. Hasiów-Jaroszewska, A. Paeleman, N. Ortega-Parra, N. Borodynko, J. Minicka, A. Czerwoniec, B.P.H.J. Thomma and I.M. Hanssen: *Molec. Plant Pathol.* 14 (2013), p. 923.

A desk-top low voltage TEM for high quality imaging of biological specimen

Ida-Maria Sintorn^{1&2,a}, Martin Ryner^{2,b}, Gustaf Kylberg^{1,a}, Rickard Nordström^{2,b},
Mats Uppström^{2,b}, Jan Fulin^{2,b}, Petr Stepan^{3,c}, Vladimir Kolarik^{3,c},
Michal Drsticka^{3,c}, Eva Coufalova^{3,c}

¹Centre for Image Analysis, Uppsala University, Sweden

²Vironova AB, Gävlegatan 22, Solna, Sweden

³Delong Instruments, Brno, Czech Republic

^a[ida.sintorn, gustaf]@it.uu.se, ^b[martin.ryner, rickard.nordstrom, mats.uppstrom, jan.fulin]@vironova.com,
^c[petr.stepan, vladimir.kolarik, michal.drsticka, eva.coufalova]@dicomps.com

Traditional transmission electron microscopes are bulky and complex machines that are mostly operated by trained specialists. The miniTEM is a new desktop-top low-voltage TEM with a high degree of automation in the microscope alignment, image acquisition, and analysis process. The microscope runs at 25 keV, which enables imaging of biological samples with a thickness up to at least 100 nm. We briefly introduce the miniTEM, and illustrate the imaging possibilities and compare and contrast the image quality it produces with traditional TEMs.

Introduction

In this paper, we introduce the miniTEM, shown in Fig. 1 (left), a desk-top instrument designed for imaging of biological samples, with a high degree of automation regarding instrument alignment, image acquisition and analysis. Our goal is a small, cheap, robust, and easy to use system that requires no more training than any simple lab equipment, and can be hosted in any office or lab (even mobile).

The miniTEM Instrument

The Microscope

The miniTEM runs at 25 keV which, according to our tests (in high voltage microscopes operated at lower voltage than designed for) and simulations, will enable to achieve resolution sufficient for tasks as virus identification for biological samples with a thickness of at least 100 nm. In addition to TEM functionality, the miniTEM can also run in STEM (scanning transmission electron microscopy) mode.

We present here the achieved parameters of resolution, applicable sample thickness and image signal collection efficiency in both operating modes. Two of the first images acquired in the miniTEM in the TEM and STEM mode, respectively are shown in Fig. 1 (middle and right).

The Graphical User Interface

The GUI is divided into three main views: live, edit, and analysis. It is developed for Windows 8, and designed for a touch screen, allowing convenient scrolling over the sample and zooming in (changing magnification). The live view is used when manually investigating the sample by moving around, changing magnification and acquiring images. The edit view is for manually marking, drawing, measuring and annotating objects in the images. In the edit view the user can also manually correct analysis results, i.e., remove, add, and rename objects. The analysis view is where the user creates and applies automated image acquisition and/or image processing and analysis scripts. A graph-based interface is used to create scripts, which can be saved for future use and applied to multiple images.

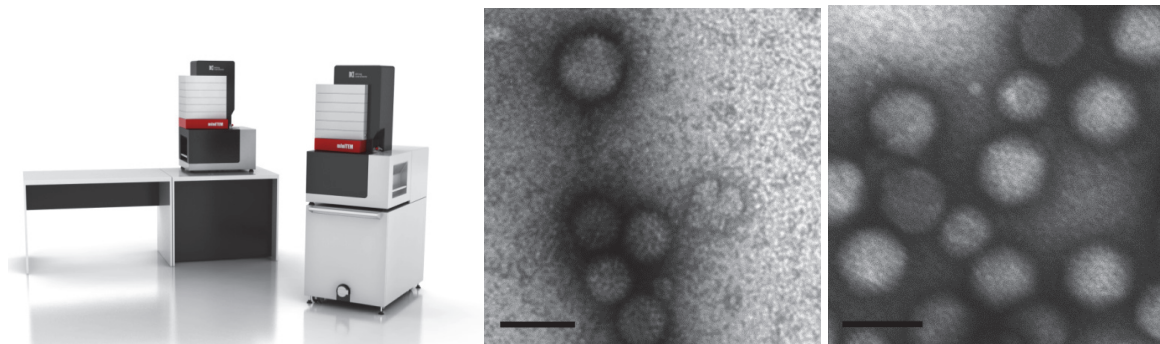


Fig. 1. The desktop and mobile version of the miniTEM instrument (left). Close up of negatively stained Adeno and Rota viruses in images acquired with the miniTEM in TEM mode (middle) and STEM mode (right). The scalebars correspond to 100 nm (right)

Cytopathology of barley plants infected with Barley stripe mosaic virus (BSMV) different strains

Aleksandra Zarzyńska-Nowak^{1,a}, Małgorzata Jeżewska^{1,b},
Beata Hasiów-Jaroszewska^{1,c}

¹Institute of Plant Protection-National Research Institute, Wł. Węgorzka 20, 60-318 Poznań, Poland

^aa.zarzyńska@iorpib.poznan.pl, ^bm.jezewska@iorpib.poznan.pl, ^cb.hasiow@iorpib.poznan.pl

Introduction

Barley stripe mosaic virus (BSMV) is a very important seed-transmitted pathogen which has been reported from nearly all barley producing regions worldwide [1]. BSMV is represented by different strains which induce wide range of symptoms on infected plants [2]. The most commonly observed symptoms for aggressive isolates are yellow or white chlorotic striping and necrosis while mild isolates are symptomless. Infected plants are also stunted and poorly developed. BSMV particles are rod-shaped, with a central canal, 20 nm in diameter, and length between 110-160 nm [1].

The aim of this study was to observed the localization of virus particles in barley plant cells infected with different strains of BSMV as well as to compared the cytopathological changes.

Methodology

The two BSMV isolates used in this study were the Polish aggressive isolate (BSMV-R) and the German mild isolate (BSMV-De-M) (obtained from Julius Kühn Institut in Quedlinburg).

Inoculated with BSMV-R and BSMV-De-M barley plants var. Annabell and healthy plants, used as control, were maintained under greenhouse conditions. 7, 14 and 32 days post inoculation leaf samples were collected. To confirm presence of virus particles in plant tissues, small pieces of apical leaves were crushed in water and negatively stained with phosphotungstic acid for 30 s.

For the cytological studies, pieces of leaves were fixed in 3% glutaraldehyde in 0.025 M phosphate buffer (pH, 7.5) for 3 h at room temperature, washed four times for 1 h in the same buffer, treated with 2% osmium tetroxide in phosphate buffer at 4°C for 2 h and again washed in buffer. Leaf fragments were dehydrated in ethyl alcohol and acetone series. Pieces were then embedded in Spurr Low-Viscosity Embedding Kit (Polysciences). Ultrathin section were cut with diamond knife on a EM UC7 (Leica) ultramicrotome, placed on coated cooper grids and stained with uranyl acetate and lead citrate. The observations were performed using Hitachi HT7700 transmission electron microscope at 80 kV accelerating voltage.

Results

Virus particles of both observed isolates were found in various compartments, mostly in parenchyma cells. Virions were observed mainly in the cytoplasm and the vacuoles of mesophyll cells, and also in the intercellular space. Predominantly BSMV-De-M particles were loosely scattered (Fig. 1A) whereas BSMV-R particles occurred in the aggregates (Fig. 1B). BSMV-R virions were also found in the chloroplast and occasionally in the nucleus.

Additionally, electron microscopy observation showed ultrastructural changes occurring in infected cells. As the result of BSMV-R infection vesiculo-membranous inclusions (Fig. 1C), microbodies, accumulation of membranous structure between cell membrane and cell wall and chloroplast destruction were noticed. Microbodies were also observed in the case of BSMV-De-M infection. Additionally presence of the mild isolate in cells caused changes of lamellae pattern in the chloroplasts (Fig. 1D). Furthermore for both isolates, symptoms of the cell necrosis were observed.

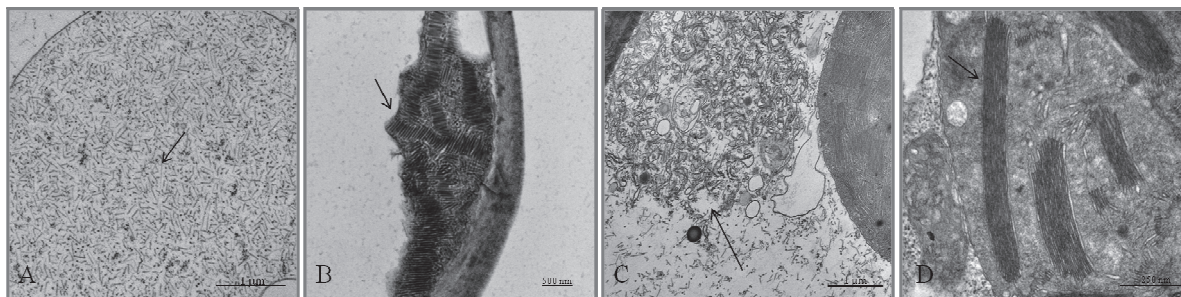


Fig. 1. A - loosely scattered virus particles (arrow) of BSMV-De-M, B - BSMV-R virus particles occurred in aggregates (arrow), C - vesiculo-membranous inclusions (arrow) in the cytoplasm, D - chloroplast with changed lamellae pattern (arrow)

Conclusions

Compared BSMV isolates differed in term of virus particles concentration, arrangement of particles, occurrence in various compartments and caused ultrastructural changes.

References

- [1] J.N. Bragg, A.O. Jackson in: *Viruses and Virus Diseases of Poaceae (Gramineae)*, edited by H. Lapierre and P.A. Signoret. Paris, chapter, 4 of *Virus diseases of Poaceae*, INRA (2004).
- [2] A.O. Jackson, H-S. Lim, J. Bragg, U. Gunesan, M.Y. Lee: *Annu. Rev. Phytopathol.* Vol. 47 (2009), p. 385.

Influence of grain refinement on microstructure and martensitic transformation in $\text{Ni}_{48}\text{Mn}_{39.5}\text{Sn}_{10.5}\text{Al}_2$ metamagnetic shape memory alloy powders

Paweł Czaja^{1,a}, Wojciech Maziarz^{1,b}, Tomasz Czeppe^{1,c}, Maciej Szczërba^{1,d},
Anna Wójcik^{1,e}, Robert Chulist^{1,f}, Jan Dutkiewicz^{1,g}

¹Institute of Metallurgy and Materials Science, Polish Academy of Sciences, 25 Reymonta St.,
30-059 Kraków, Poland

^ap.czaja@imim.pl, ^bw.maziarz@imim.pl, ^ct.czeppe@imim.pl, ^dm.szczërba@imim.pl, ^ea.wojcik@imim.pl,
^fr.chulist@imim.pl, ^gj.dutkiewicz@imim.pl

Ferromagnetic shape memory alloys are an important class of materials because of their potential impact on energy saving and environmental concerns [i]. Among them the full Heusler Ni_2MnGa is the most studied alloy to date [ii]. Recently a new series of Ni-Mn-Z (Z=In, Sn, Sb) alloys have received significant attention [iii]. For some critical ranges of concentration on cooling these alloys undergo a reversible first order martensitic transformation from the high temperature austenite phase to a low temperature martensite phase. This transition is often accompanied by an abrupt change of magnetization (ΔM) [iv]. ΔM change is linked to fact that the magnetic moment in the high temperature phase (m_H) is reported to be larger than the magnetic moment in the low temperature phase (m_L) as in $\text{Ni}_{50}\text{Mn}_{50-y}\text{X}_y$, which is contrary to Ni_2MnGa , where $m_H < m_L$ [v]. This phenomenon may then be responsible for a large difference in Zeeman energy ($\mu_0\Delta M \cdot H$) between austenite and martensite phases leading to a magnetic field induced reverse martensitic transformation [vi,vii]. Owing to the latter as well as to a large magnetic entropy changes (ΔS_M), due to ΔM , these alloys, termed metamagnetic shape memory alloys (MSMA), offer interesting functional properties including the magnetocaloric effect [viii], large magnetoresistance [ix], exchange bias [x] and giant barocaloric effect.

Some new research has focused on MSMA alloy powders with the view of improving considerable brittleness of typical polycrystalline materials produced by conventional metallurgy. Another important consideration is the thermal hysteresis, which limits the use of MSMA [xi]. Recently Ito *et al.* [13] observed that with increasing annealing time (1173 K) the transformation interval, defined as the difference between the martensite start and martensite finish temperatures, decreases as a result of microstructural change in the gas atomized $\text{Ni}_{43}\text{Co}_7\text{Mn}_{39}\text{Sn}_{11}$ particles. Alves *et al.* investigated the influence of grain refinement and induced crystal defects on the magnetic properties of $\text{Ni}_{50}\text{Mn}_{36}\text{Sn}_{14}$ Heusler alloy and demonstrated that 90 s high energy ball milling may change the cubic L2₁-B2 type disordered structure into a simple cubic B2 disordered structure. Moreover, extended milling times impose reduction in the crystalline grain size and facilitate formation of point defects, which result in formation of strains in the crystalline lattice and overall lead to a decrease in the net magnetization of the alloy [xii]. Grain refinement is also shown to have an effect on martensitic transformation temperature [xiii] and exchange bias in MSMA [xiv].

This paper is focused on the effect of extended milling and subsequent annealing times on microstructure and martensitic transformation temperature in $\text{Ni}_{48}\text{Mn}_{39.5}\text{Sn}_{10.5}\text{Al}_2$ powders. The powders under scrutiny were produced from melt spun ribbons of the same composition. To our knowledge this is a novelty since most of the literature reports on MSMA powders are concerned with materials produced from polycrystalline bulk alloys. Subsequently, the powders were subjected to high energy ball milling at varying milling times. Then powders were sealed in quartz ampules under argon gas and annealed at 1173 K for varying lengths of time followed by water quenching. Differential Scanning Calorimetry was employed to determine the characteristic transition temperatures. It is shown, that with increasing milling times the martensitic transition temperatures decrease in accordance with the literature reports, which is related to the grain size refinement. X-ray diffraction,

Scanning Electron Microscopy and Transmission Electron Microscopy techniques were used for the analysis of grain size, morphology and structure of the obtained powders.



Fig. 1. SEM micrograph taken from ball milled $\text{Ni}_{48}\text{Mn}_{39.5}\text{Sn}_{10.5}\text{Al}_2$ powders

References

- [i] J. Pons, E. Cesari, C. Segui, F. Masdeu, R. Santamarta: *Mater. Sci. Eng. A* 481-482 (2008), p. 57.
- [ii] M. Khan, I. Dubenko, S. Stadler, J. Jung, S. S. Stoyko, A. Mar, A. Quetz, T. Samanta, N. Ali and K. H. Chow: *Appl. Phys. Lett.* 102 (2013), p. 112402.
- [iii] Y. Feng, J. H. Sui, H. B. Wang, W. Cai: *J. Magn. Magn. Mater.* 324 (2012), p. 1982.
- [iv] R. L. Wang, J. B. Yan, H. B. Xiao, L. S. Xu, V. V. Marchenkov, L. F. Xu, C. P. Yang: *J. Alloys Compd.* 509 (2011), p. 6384.
- [v] K. Koyama, K. Watanabe, T. Kanomata, R. Kainuma, K. Oikawa and K. Ishida: *Appl. Phys. Lett.* 88 (2006), p. 132505.
- [vi] C. Jing, Y. J. Yang, Z. Li, X. L. Wang, B. J. Kang, S. X. Cao, J. C. Zhang, J. Zhu and B. Lu: *J. Appl. Phys.* 113 (2013), p. 173902.
- [vii] B. Zhang, X. X. Zhang, S. Y. Yu, J. L. Chen, Z. X. Cao and G. H. Wu: *Appl. Phys. Lett.* 91 (2007), p. 012510.
- [viii] Z. D. Han, D. H. Wang, C. L. Zhang, H. C. Xuan, B. X. Gu and Y. W. Du: *Appl. Phys. Lett.* 90 (2007), p. 042507.
- [ix] C. Jing, Y. J. Yang, Z. Li, X. L. Wang, B. J. Kang, S. X. Cao, J. C. Zhang, J. Zhu and B. Lu: *J. Appl. Phys.* 113 (2013), p. 173902.
- [x] M. Khan, I. Dubenko, S. Stadler and N. Ali: *J. Appl. Phys.* 102 (2007), p. 113914.
- [xi] I. Titov, M. Acet, M. Farle, D. Gonzalez-Alonso, L. Manosa, A. Planes and T. Krenke: *J. Appl. Phys.* 112 (2012), p. 073914.
- [xii] A. L. Alves, E. C. Passamani, V. P. Nascimento, A. Y. Takeuchi and C. Larica: *J. Phys. D: Appl. Phys.* 43 (2010), p. 345001.
- [xiii] A. Quintana-Nedelcos, J. L. Sanchez-Llamazares, D. Rios-Jara, A. G. Lara-Rodriguez and T. Garcia-Fernandez: *Phys. Status Solidi A* 210 (2013), p. 2159.
- [xiv] H. Endo, A. Hirohata, J. Sagar, L. R. Fleet, T. Nakayama and K. O'Grady: *J. Phys. D: Appl. Phys.* 44 (2011), p. 345003.

Transmission electron microscopy characterization of the clads' bonding interfaces manufactured using explosive welding

Dagmara M. Fronczek^{1,a}, Joanna Wojewoda-Budka^{1,b},
Lidia Lityńska-Dobrzyńska^{1,c}, Zygmunt Szulc^{2,d} and Paweł Zięba^{1,e}

¹Institute of Metallurgy and Materials Science Polish Academy of Sciences, Reymonta Street 25; 30-059 Kraków; Poland

²Explomet, Oświęcimska Street 100H; 45-641 Opole; Poland

a dfronczek@gmail.com, b j.wojewoda@imim.pl, c l.litynska@imim.pl, d zygmunt.szulc@explomet.pl, ep.zieba@imim.pl

Introduction

Explosive welding is a method of metals joining using energy of explosion. This process can be applied to join at least two different kinds of metals or alloys, which in many cases cannot be joined using other welding techniques such as friction or electrical welding. The obtained interconnections are characterized by good mechanical properties, high resistance to corrosion and to high temperatures [1]. In the present paper, electron microscopy techniques were used in order to characterize Al/Ti/Al clads manufactured by the Explomet Company.

Experimental

The Al/Ti/Al sandwich was joined using one act of detonation. The samples, sized 6 mm x 12 mm x 2.8 mm, were cut off from the center of the clad and grounded using abrasive papers (1000, 2000 and 4000) and diamonds pasts (3 μm , 1 μm and 0.25 μm). The prior inspection of the obtained cross-sections was carried out on a FEI Quanta 3D FEG scanning electron microscope (SEM) equipped with Trident energy-dispersive X-ray spectrometer (EDS) produced by EDAX. The details of the phases, in nanoscale, were revealed using a FEI TECNAI G2 FEG super TWIN (200 kV) transmission electron microscope (TEM) equipped with Phoenix EDS also manufactured by EDAX. The thin foils for TEM observation were cut from the properly selected regions of the bonds using a FEI Quanta 3D Dual Beam Focus Ion Beam (FIB).

Results and discussion

The characteristic wavy interconnection between joined metals were obtained only on the upper side of the clads in accordance with the condition of the collision (Fig. 1a). In few cases the slab of new phase adjacent was also observed (Fig. 1b). The use of EDS analysis revealed that the joined area is occupied by the solid solution of Ti in Al ($\alpha\text{-Al}$). In some places (see points 21 and 23 in Fig. 1b), the chemical composition was close to the TiAl_3 intermetallic compound as referred to Ti-Al equilibrium phase diagram. The interconnection between joined metals on the lower side of the titanium was quite different. The interface is rather planar without any new phases. Moreover, some cracks are clearly visible in titanium layer (Fig. 2).

The closer inspection of the upper side using TEM confirmed the SEM results (Fig. 3a). The crystalline $\alpha\text{-Al}$ dominated which has been confirmed by the selected area electron diffraction (SAED) (Fig. 3b). Between the rings of $\alpha\text{-Al}$ solid solution the additional weak spots could be visible. It may suggest that the Ti-rich phase is also present in this area.

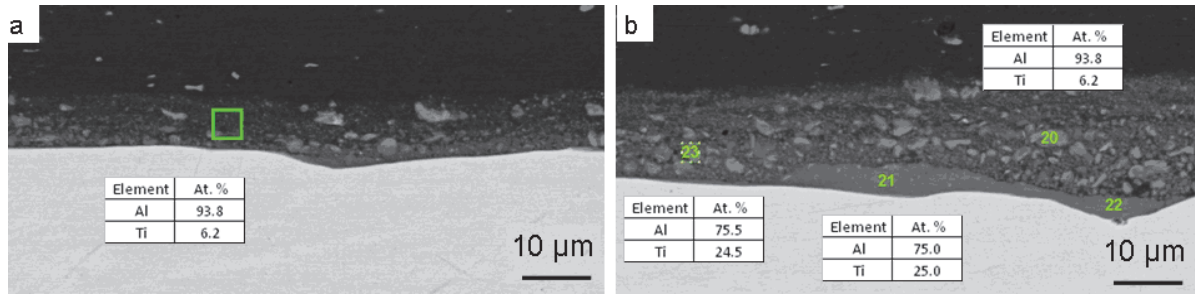


Fig. 1. SEM micrograph of the upper side of Al/Ti/Al clad. The characteristic wavy interconnection between titanium and aluminum (a); the area occupied by the intermetallic phase (b) and corresponding results of EDS analysis

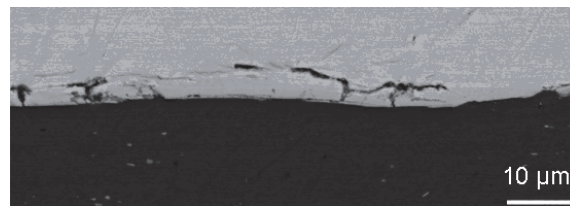


Fig. 2. SEM micrograph of the lower side of Al/Ti/Al clad with some cracks within Ti layer

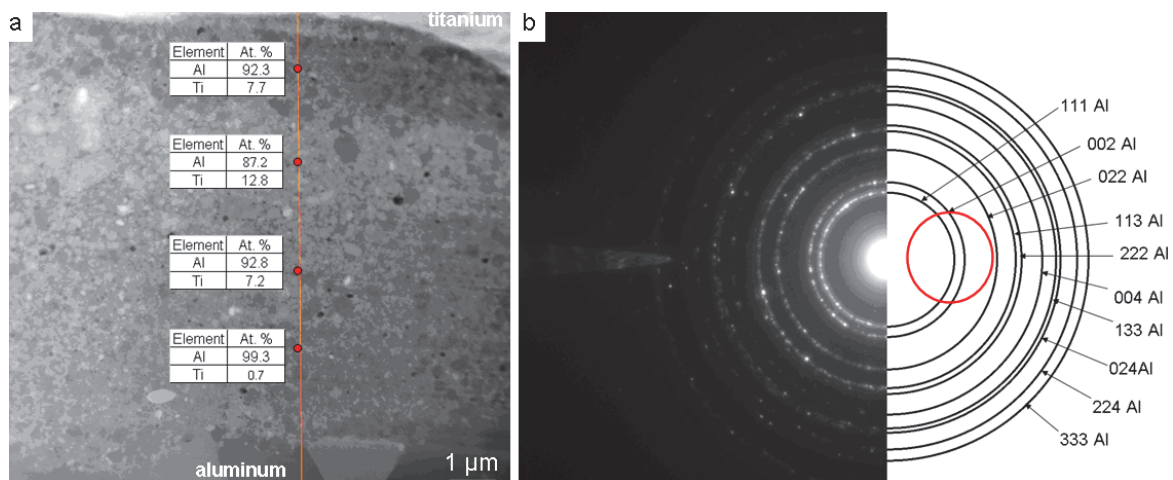


Fig. 3. (a) TEM micrograph showing fine crystalline microstructure within the upper side of Al/Ti/Al clad and corresponding results of EDS analysis, (b) selected area electron diffraction pattern taken from the region marked by red circle

Summary

The use of SEM and TEM techniques allowed to reveal that directly after explosive welding the upper side of Al/Ti/Al clads was composed mainly of fine crystalline (α -Al) solid solution. Only in few places the new intermetallic phase with the composition close to Al_3Ti was detected.

Acknowledgments

Samples were examined in the Accredited Testing Laboratories at the Institute of Metallurgy and Materials Science of the Polish Academy of Sciences in Cracow. The authors thank Dr Anna Korniewa-Surmacz for the thin foil preparation.

References

- [1] T.Z. Blazynski *Explosive welding forming and compaction* (Applied Science Publishers, London and New York 1983).

Microstructural investigation of *in situ* AMCs obtained via reactive sintering of Al with Mg₃N₂

Marta Gajewska^a, Jerzy Morgiel

Institute of Metallurgy and Materials Science, Polish Academy of Sciences, Reymonta 25,

30-059 Krakow, Poland

^am.gajewska@imim.pl

Introduction

Aluminium matrix composites (AMCs) have gained considerable interest in automotive and aerospace applications due to their better specific strength, thermal stability and wear resistance as compared with respective aluminium alloys. Reinforcing phases for AMCs are most often prepared separately, prior to composite fabrication and introduced into matrices via e.g. powder metallurgy, spray deposition or casting. These techniques, referred to as *ex situ*, usually result in relatively weak reinforcement-matrix bonding. On the other hand, *in situ* techniques, in which a reinforcement is produced directly in a metallic matrix, e.g. by chemical reaction between elements or compounds present in the material, routinely provide a strong bonding between a metal matrix and a reinforcing phase, which is a key factor for the efficient load transfer in composite materials [1-4].

High reactivity of aluminium with oxygen has already been used in *in situ* formation of Al/Al₂O₃ composites [1]. Experiments with injection of nitrogen into liquid aluminium alloys showed that obtaining an *in situ* AlN reinforcement is also possible, and that the occurring reaction proceeds efficiently through intermediate Mg₃N₂ phase [2-4]. Soon after, it was proven that Al/AlN composites could be also formed by introduction of Mg₃N₂ into aluminium melt. In that case magnesium, which is a by-product, does not pose any problem, as it serves as an alloying element in many aluminium alloys, markedly increasing their strength without a loss in ductility. An advantage of the latter of described processes of Al/AlN composites formation lies, among the others, in possibility of formation of void- and oxide- free bonding with the matrix, what should lead to significantly improved hardness and wear properties. However, up until now there is no detailed information concerning the microstructure of Al/AlN composites obtained through *in situ* reaction of aluminium with magnesium nitride.

Therefore, the aim of the present work was to characterize – with use of scanning and transmission electron microscopy – Al/AlN composites obtained by reactive heating of green compacts of Mg₃N₂ and aluminium powder mixtures.

Experimental procedure

Mg₃N₂ (Alfa Aesar, 99.7%, -325 mesh) and aluminium (Alfa Aesar, 99.7%, APS ~11 μm) powders were mixed in 1:2 weight ratio and then compacted at ~400 MPa. As prepared green compacts (5mm diameter, ~6mm height) were then sintered under protective atmosphere at different temperatures (900°C - 1300°C). Microstructure of the resulting materials was characterized using an FEI E-SEM XL30 scanning and a Tecnai F20 (200kV) transmission electron microscopes equipped with EDAX systems. Phase composition was confirmed by XRD measurements performed on BRUKER D2 PHASER diffractometer with Cu K α radiation ($\lambda = 1.5406 \text{ \AA}$). Thin foils for TEM investigations were prepared both by mechanical polishing, dimpling with Gatan Dimple Grinder (Model 656) and ion milling with Leica EM RES101 or by Quanta 3D focused ion beam (FIB).

Results and discussion

SEM (BSE) investigation combined with X-ray microanalysis (EDS) showed high density of aluminium- and nitrogen- rich microsized particles present in the material. The Al matrix, apart from some minor N and O content, was characterized by an average Mg content of ~3.5 at.%. TEM

investigations allowed to reveal that Al- and N- rich regions observed in SEM are in fact agglomerates of submicron AlN particles (as confirmed by electron diffraction) immersed in aluminium-magnesium solid solution. Al/AlN interfaces were found to be generally clean in a case of materials sintered at 1300°C, while in materials sintered at 900°C and 1000°C magnesium oxide and aluminium magnesium spinel intermediate layers at the component interfaces were often observed. It should be noted that Al powder particles tend to be superficially oxidised which could inhibit reaction between the components at lower temperatures. Detailed microstructure observations indicated that the defect content in the matrix regions both away from matrix/reinforcement interfaces as well as near them was negligible.

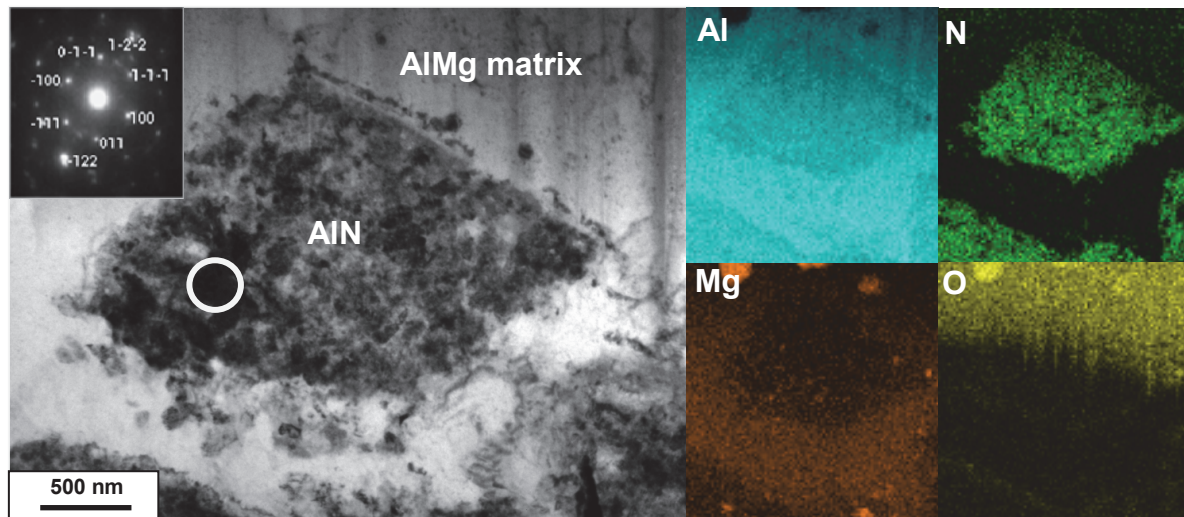


Fig. 1. Bright-field TEM micrograph of composite sintered at 1300°C with SAED inset from marked area (left) and EDS elemental maps of the region (right)

The accompanying X-ray diffraction investigation confirmed presence of only two main phases: aluminium and aluminium nitride. The lack of Mg_3N_2 diffraction lines indicates that all of it (or nearly all) was consumed in the reaction with aluminium resulting in the AlN phase formation.

Summary

The SEM and TEM investigations of the Al/ Mg_3N_2 green compacts subjected to high temperature treatment (900°C - 1300°C) proved that the interaction of aluminium with Mg_3N_2 particles leads to substitution of the latter with densely packed areas of fine AlN particles. That type of microstructure indicates that the Mg_3N_2 is first dissolved by liquid aluminium and only then the precipitation of AlN phase starts. Composites produced at lower of applied temperatures showed presence of minor amount of oxygen at Al/AlN interfaces, while that obtained at higher temperatures were free of such contaminants.

Acknowledgement

The work was supported through project no. POKL. 04.01.00-00-004/10 co-financed by the European Union within the European Social Fund.

References

- [1] T.G. Durai, K. Das, S. Das: Mater. Sci. Eng. A Vol. 445-446 (2007), p.100.
- [2] S.C. Tjong, Z.Y. Ma: Mater. Sci. Eng. Vol. 29 (2000), p. 49.
- [3] S.S. Kumari, U.T.S. Pillai, B.C. Pai: J. Alloy Compd. Vol. 509 (2011), p. 2503.
- [4] Q. Hou, R. Mutharasan, M. Koczak: Mater. Sci. Eng. A Vol. 195 (1995), p. 121.

Microstructure characterization of Cr/CrN+ a-C:H/a-C:H:Cr multilayer coatings on Carbon Fiber Composites (CFC)

Marta Janusz^{1,a}, Łukasz Major^{1,b}, Jurgen M. Lackner^{2,c}, Jerzy Morgiel^{1,d}

¹ Institute of Metallurgy and Materials Science; Polish Academy of Sciences, 30-059 Cracow, 25 Reymonta Street, Cracow, Poland

² JOANNEUM RESEARCH- Materials- Institute for Surface Technologies and Photonics; Leobner Strasse 94; 8712 Niklasdorf, Austria

am.janusz@imim.pl, ^bl.major@imim.pl, ^cjuergen.lackner@joanneum.at, ^dj.morgiel@imim.pl

Introduction

Carbon-based materials show significant oxidative degradation in air beginning at temperatures in the region of 400°C. The reinforcement of carbon with carbon fibers, complicates the anti-oxidative coating problem, due to the thermal and elastic anisotropy of the carbon fibers [1]. Therefore, a coating concept for carbon-carbon composites should consist of an inner part, which serves as structural link with stress compensation ability to the carbon substrate, and an outer part, which acts as a diffusion barrier. In the presented paper, as the inner part chromium/ chromium nitride (Cr/CrN) multilayer structure has been selected. The literature data [2– 5] indicates the particular meaning of Cr and CrN multilayer coatings. They are characterized by an appropriate crystallographic adjustment of subsequent constituent layers of Cr and CrN [2] and by the creation of a transition layer between them with a thickness of several dozen of nanometers [5]. This ensures a good connection between particular constituent layers and as a result also good maintenance properties: high adhesion [6], wear [3] and corrosive [4] resistance. The CrN and Cr lattice parameters, 4.14 and 2.88, respectively, allow a cube-on-cube, close to epitaxial growth with a low mismatch (1.6%). With this idea, Cr/CrN multilayers have been designed and deposited on CFC substrates. The outer part of the coating, in the presented paper, was a-C:H implanted by Cr nanocrystals. It is well-known that hydrogenated amorphous carbon (a-C:H) [7] coatings have low- friction coefficients and low-specific wear rates. Thus, the amorphous carbon coatings are very promising tribo-materials. However, the poor adhesion strength to substrate, high residual stress and weak thermal stability would limit the application of a-C:H coatings [7]. Currently, many metallic elements (Ti, W, Ag, Cr etc.) have been utilized to modify the structure of the coatings, and it has been proved that the metal doping is an effective method to reduce residual stress and enhance adhesion strength of the film [8]. Among those doping metals, Cr as one of carbide formed elements possesses an attractive combination of properties (corrosion resistance, wear resistance, etc.). Thus, in the presented paper Cr/a-C:H coatings was developed, deposited at the Cr/CrN part coating and characterized. The experiments confirmed very good adhesion of the coating to the CFC substrates as well as showed gradient distribution of Cr nanocrystals in a-C:H structure.

Methodology

Coatings were prepared using magnetron sputtering technique, using high purity chromium (99.9% at. Cr) and carbon (graphite) targets. Their microstructure was described by the application of TECNAI G² F20 FEG (200kV) transmission electron microscope (TEM). Phase analysis was done by electron diffraction pattern and confirmed by calculations of high resolution images (HRTEM). Energy Dispersive Spectroscopy (EDS) was done for chemical analysis of coatings. Thin foils for TEM were prepared using Focused Ion Beam (FIB) (QUANTA 200 3D) with OmniProbe in- situ lift-out system.

Results

The initial microstructure characterization was presented in the bright field TEM image (Fig. 1).

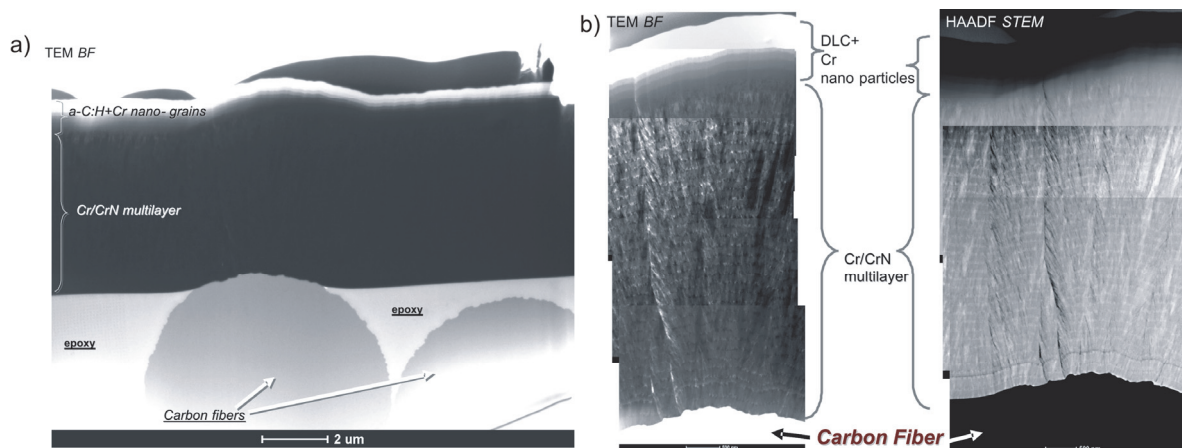


Fig. 1. Microstructure characterization of nano- composite, multilayer coating, performed on the cross- section by transmission electron microscopy technique- Bright Field Image and diffraction patterns; a). image of coating and carbon fibers- lower magnification; b). image in the higher magnification

Cr/CrN part caused very good coating adhesion to Carbon- Fiber- Composite substrate. The a-C:H part of the coating contained the gradient concentration of Cr nano- grains. The higher the distance from the Cr/CrN part, the lower Cr concentration in a-C:H.

Conclusions

The microstructure analysis by transmission electron microscopy technique allowed to characterize in detail two parts of the coating. It confirmed strong crystallographic dependence in between Cr and CrN layers and exhibited Cr nano- crystals distribution in a-C:H part. The investigations confirmed high quality adhesion of the coating to the CFC substrate as well as in between the Cr/CrN and the a-C:H parts. The analysis also showed that presented coatings deposited by hybrid PLD technique, reproduce substrates roughness on coating surfaces.

Acknowledgement

Research project was financed by the National Science Centre (Polish- Narodowe Centrum Nauki, abbr. NCN) No:2012/06/M/ST8/00408.

References

- [1] E. Fitzer: Carbon 16 (1977), p. 3.
- [2] L. Major, W. Tirry, G. Van Tendeloo: Surf. Coat. Technol. Vol. 202 (2008), p. 6075.
- [3] M. Berger, U. Wiklund, M. Eriksson, H. Enqvist, S. Jacobson: Surf. Coat. Technol. Vol. 116-119 (1999), p. 1138.
- [4] H.A. Jehn: Surf. Coat. Technol. Vol. 125 (2000), p. 212.
- [5] S. Han, J.H. Lin, X.J. Guo, S.H. Tsai, Y.O. Su, J.H. Huang, F.H. Lu, H.C. Shih: Thin Solid Films Vol. 377-388 (2000), p. 578.
- [6] L. Major, J. Morgiel, B. Major, J.M. Lackner, W. Waldhauser, R. Ebner, L. Nistor, G. Van Tendeloo: Surf. Coat. Technol. Vol. 200 (2006), p. 6190.
- [7] H. Ronkainen, S. Varjus, K. Holmberg: Wear Vol. 222 (1998), p. 120.
- [8] Q. Wang, F. Zhou, X. Ding, Z. Zhou, C. Wang, W. Zhang, L. Kwok- Yan Li, S.-Tong Li: Tribol. Int. Vol. 67 (2013), p. 104.

In-situ recrystallization and orientation imaging of commercially pure titanium deformed plastically by complex loading

Jakub Kawałko^{1,a}, Magdalena Bieda^{1,b}, Krzysztof Sztwiertnia^{1,c}

¹Institute of Metallurgy and Materials Science, Polish Academy of Sciences,
25 Reymonta St., Krakow, Poland

^akuba.kawalko@gmail.com ^bnmbieda@imim-pan.krakow.pl ^ck.sztwiertnia@imim.pl

Introduction

Thermal stability and evolution of structure and texture of plastically deformed hexagonal metallic samples have been investigated. The material was commercial purity (CP) grade 2 titanium after plastic deformation in process with complex loading scheme. Deformation technique utilized for production of samples was KoBo type extrusion, where deformation occurs under conditions of cyclically changing deformation path [1]. Changes of deformation path induced by oscillating rotations of the extrusion die, causes increase of plasticity and allows for high straining of material in a single step of the process.

Thermal stability and character of evolution during subsequent thermal treatment of heavily deformed structure is one of the most important aspects in SPD (severe plastic deformation) material processing. Recrystallization behavior is governed by the stored accumulated energy and structure of defects created during deformation process [2]. Morphology of deformed structure in KoBo extruded titanium bears some resemblance with structures of cold rolled titanium sheets [3]. On the other hand KoBo-ed titanium differs in distribution of grain boundaries character (no twin boundaries have been observed) and texture (strong 0001 axial texture). Therefore effect of KoBo-specific structure and texture on thermal treatment evolution and resulting microstructure have been investigated.

Experimental procedure

Investigations were carried out on high resolution FEI Quanta 3D FEG SEM microscope with integrated EDAX TSL system for high speed EBSD patterns acquisition, equipped with Gatan hot-stage allowing for high precision *in-situ* EBSD mapping. Additionally thermal analysis of recrystallization process was performed on TA Instruments Q1000 and Q600 differential scanning calorimeters, and hardness measurements were carried on Zwick/Roell ZHU250 universal hardness tester.

Plastic deformation was performed on grade 2 titanium with mean diameter of 30 μm . Titanium ingot in form of 35 mm diameter rod was hot extruded in KoBo process at 400 °C (charge was pre-heated to 450 °C) with extrusion ratio $\lambda = 19$ (final product was in form of 8 mm diameter rod). During deformation process extrusion die was oscillated by an angle of $\pm 6^\circ$ at the frequency of 8Hz and extrusion rate was 0.5 mm/s.

In-situ EBSD observations were carried out for samples prepared from transverse (perpendicular to extrusion direction - ED) and longitudinal sections of extruded rod. Initial EBSD maps were collected for both types of samples at room temperature. Separate samples were then heated up to suitable temperature and annealed for specific period of time (10, 20, 30, 50, 60, 90 minutes). After each annealing interval sample was cooled down in order to collect EBSD map at given recrystallization stage (in function of temperature and time). Temperatures and time intervals of in-situ thermal treatment were selected based on DSC analyses performed in order to identify recrystallization processes start and finish points. Additionally classic annealing and hardness testing were used for approximation of recrystallization dynamics at different annealing temperatures.

Results and discussion

Titanium structure after KoBo is characterized with elongated grains parallel to ED and additionally curled in transverse section. Two main types of grain morphology is present – fine elongated grains with no internal structure and lamellar like strongly elongated ones with internal orientation gradients, dislocation walls and small angle grain boundaries.

Recrystallization proceeds at several distinct stages related to different types of structural defects being activated. These stages are apparent from DSC analyses with two thermal effects at approximately 580 °C and 650 °C. Respective temperatures are related to recrystallization onset in areas with fine crystal structure and high density of stored energy related to high amount of HAGBs, and to following recovery of areas characterized with low rate of misorientations inside elongated lamellae.

After annealing in 650 °C structure composes of recrystallized equiaxed grains with distribution of grain diameter from one to 13.5 microns and homogenous internal structure. Grain boundaries structure is significantly changed with broad distribution of misorientations in HAGB range and substantially decreased amount of low angle grain boundaries. Axial texture is retained and no meaningful changes compared to deformed state are observable at this stage of recrystallization.

Conclusions

In-situ heating combined with high resolution EBSD measurements proved to be suitable tool for recrystallization investigations of materials after complex loading deformation process.

Recrystallization of titanium proceeds in several distinct stages with different rates of process for two types of microstructure. This behavior allows broad range of possibilities for tailoring of microstructure morphology with specific thermal treatment after KoBo deformation process.

References

- [1] A. Korbel and W. Bochniak 1998, U.S. Patent 5.737.959, 2000 European Patent 0.711.210.
- [2] F.J. Humphreys, M. Hatherly Recrystallization and Related Annealing Phenomena Elsevier Science, New York (2004).
- [3] N. Bozzolo, N. Dewobroto, H. R. Wenk, F. Wagner: J. Mater. Sci. Vol. 42 (2007), p. 2405.

Effect of carbides on creep resistance of master heat ingot of IN-713C nickel superalloy

Barbara Kościelniak^{1,a}, Maria Sozańska^{1,b} and Jan Cwajna^{1,c}

¹Silesian University of Technology, Faculty of Materials Science and Metallurgy,
Kraśińskiego 8, 40-019 Katowice, Poland

^abarbara.koscielniak@polsl.pl, ^bmaria.sozanska@polsl.pl, ^cjan.cwajna@polsl.pl

The quality assurance system is central to a process of the investment casting of turbine blades which are made of IN-713C superalloy. This system requires the evaluation of creep resistance of samples fabricated from casted master heat ingot. If the results of the tests are positive, the master heat alloys are allowed for production. One of the most distinctive features of the material characterized by creep resistance is a change of microstructure. In case of polycrystalline nickel superalloys, the most important points are the nucleation of discontinuities on carbides and their phase transformation. *The influence* of carbides on the creep behavior of alloys depends on their morphology, arrangement of carbides in matrix, chemical and phase composition. The following paper presents the results of an analysis of carbides characteristics and their effect on creep resistance of master heat ingot of IN-713C alloy. The correlation between the carbides and creep properties of master heat ingot was investigated at the temperature of 982°C and stress of 151.7 MPa. The evaluation of structure and carbides morphology was performed with the use of light microscope (LM) and scanning electron microscope (SEM). Chemical and phase composition of carbides was described by using an energy dispersive X-ray spectroscopy (EDS), electron backscatter diffraction techniques (EBSD) and electron diffraction techniques with scanning transmission electron microscope (SAED and STEM). The results show that primary carbides MC are the most prone to cracking during the process of creep (Fig.1). Some MC carbides decompose into secondary carbides $M_{23}C_6$ and γ' phase (Fig. 2 and 3), mainly at the grain boundaries. The $M_{23}C_6$ and γ' might facilitate cracks propagation (especially at the grain boundaries), but do not contribute to the process of their formation.

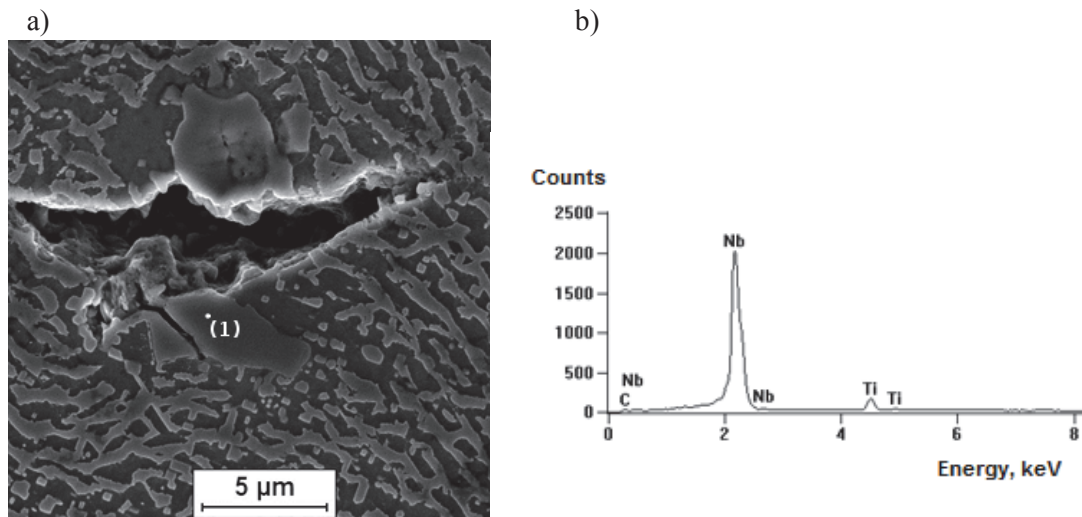


Fig. 1. Nucleation of discontinuities on primary carbide MC in master heat ingot of IN-713C alloy after creep: (a) SEM micrograph and (b) EDS spectrum of MC carbide

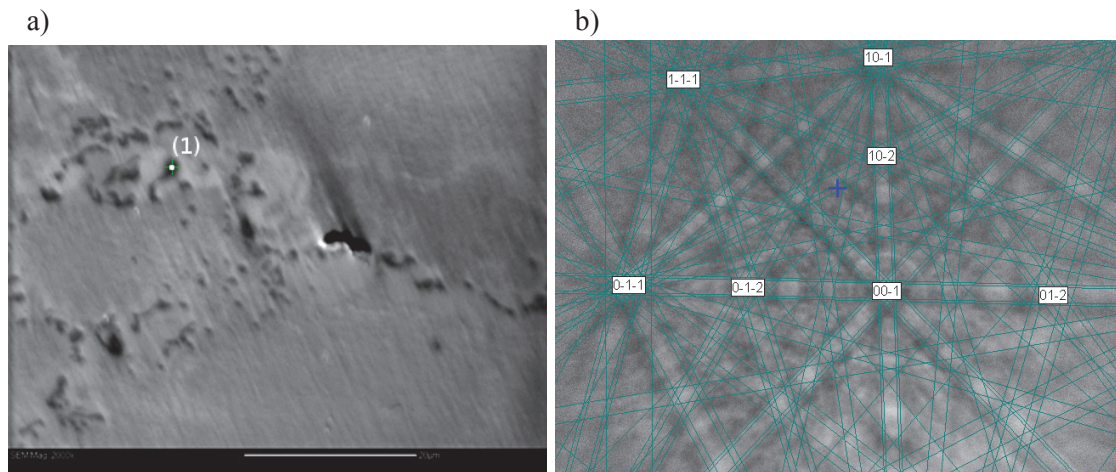


Fig. 2. The secondary carbides $M_{23}C_6$ at the grain boundaries in master heat alloy of IN-713C after creep: (a) SEM micrograph and (b) indexed Kikuchi pattern of $M_{23}C_6$ carbide

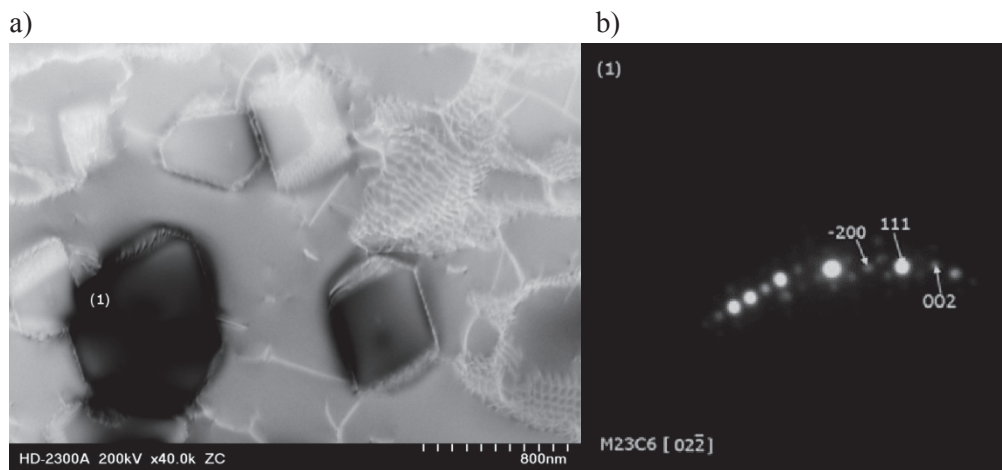


Fig. 3. Identification of small secondary carbides $M_{23}C_6$: (a) STEM micrograph and (b) electron diffraction patterns of $M_{23}C_6$ carbide

Acknowledgment

Financial support of Structural Funds in the Operational Programme - Innovative Economy (IE OP) financed from the European Regional Development Fund - Project "Modern material technologies in aerospace industry", Nr POIG.01.01.02-00-015/08-00 is gratefully acknowledged.

References

- [1] L.Z. He, Q. Zheng, X.F. Sun, H.R. Guan, Z.Q. Hu, A.K. Tieu, C.Lu, H.T. Zhu: Mater. Sci. Eng. A 397 (2005), p. 297.
- [2] X.Z. Qin, J.T. Guo, C. Yuan, C.L. Chen, J.S. Hou, H.Q. Ye: Mater. Sci. Eng. A 485 (2008), p. 74.
- [3] T.M. Maccagno, A.K. Koul, J.P. Immarrigeon, L. Cutler, R. Allem, G. L'Esperance: Metall. Trans. A, 21A (1990).
- [4] F. Zupanic, T. Boncina, A. Krizman, F.D. Tichelaargine: J. Alloys Compd. 329 (2001), p. 290.
- [5] M. Sozańska, B. Chmiela, Marta Kianicowá, J. Cwajna: Sol. St. Phenom. 186 (2012), p. 143.
- [6] A. Szczotok, K. Rodak: IOP Conf. Ser. Mater. Sci. Eng. 35 (2012), p. 012006.

TEM study of aged Mg-3Zn-3Ca wt.% alloy for biomedical applications

Katarzyna Kubok^a, Lidia Lityńska-Dobrzyńska^b and Anna Wierzbicka-Miernik^c

Institute of Metallurgy and Material Science Polish Academy of Sciences, Poland

^ak.kubok@imim.pl, ^bl.litynska@imim.pl, ^ca.wierzbicka@imim.pl

Introduction

Alloys from the Mg-Zn-Ca system are very attractive due to number of possible applications, such as orthopaedic implants [1, 2]. The main advantage of the Mg-Zn-Ca alloy over currently used materials is its biocompatibility and biodegradability combined with mechanical properties similar to that of cortical bone [1,3]. Unfortunately, the corrosion rate is too fast and rapid H₂ evolution may cause inflammation [1,2,3]. Therefore, the control of corrosion rate is the most important problem and may be solved by choosing proper chemical composition and designing appropriate heat-treatment procedure [4]. It is known that Mg-Zn alloys can be precipitation strengthened and addition of Ca enhances this effect [5,6,7,8]. Most of the authors focused their studies on alloys with low calcium content. Oh *et al.* [5] investigated the aged Mg-4.79Zn-0.5Ca wt.% alloy and observed no significant increase in hardness. Oshi-ishi *et al.* [7] associated the age-hardening response in the Mg-4.18-0.48Ca wt.% alloy with precipitation of $\beta 1'$ rods (Mg₄Zn₇ or MgZn₂ phase) and fine plates of Ca₂Mg₆Zn₃ phase. This study was performed to investigate if alloy with relatively high Ca and Zn content can undergo artificial age-hardening and design heat treatment for this type of alloy.

Experimental

Mg-3Zn-3Ca wt.% alloy was prepared from high purity elements under an argon atmosphere. The heat treatment was designed according to the results from differential scanning calorimetry (temperatures) and scanning electron microscopy (time). Thus the following procedure for the solution treatment was adopted: holding at 390 °C for 90 h followed by water quenching. Samples were examined by hardness tests after various stages of ageing at 175 °C in silicon oil. Detailed studies of distribution and types of phases during ageing were done by transmission electron microscopy (TEM) using a Tecnai G2 F20 (200 kV).

Results and conclusions

The aged microstructures of studied alloy contained uniform and dense distribution of fine precipitates in the α -Mg matrix. Sizes of precipitates and hardness remain relatively stable up to ~200 hours of ageing at 175 °C. The peak-age for the Mg-3Zn-3Ca wt.% alloy occurred at ~100 hours with value of 63 HV. Figure 1 shows types of precipitates in the Mg-3Zn-3Ca wt.% alloy aged for 66 hours (a, b) in under-age conditions and for 140 hours (c, d) in slightly over-aged conditions with corresponding diffraction patterns. Fine disc-shape precipitates with diameter below 10 nm and their habit planes parallel to the basal plane of α -Mg were found in all microstructures. For SADPs taken along $[2\bar{1}\bar{1}0]$ zone axis (Fig. 1b, d) the streaks parallel to $[0001]$ direction of the magnesium matrix are visible. Similar disc-shape precipitates have been reported by Oh *et al.* in Mg-0.8Zn-0.5Ca (wt.%) [5] and Oh-ishi *et al.* in Mg-0.8Zn-0.49Ca (at.%) [7] alloys.

Scanning transmission electron images and information from bright field images with corresponding SADPs indicate three types of precipitates: spherical, rod-like and very fine plate-like precipitates with a coherent strain contrast. EDX analysis of coarse precipitations in over-aged sample shows that these precipitates are enriched both in Ca and Zn. The fine precipitates are dominant, so they are considered to be the major contributor to the age-hardening in this alloy. Further studies on

this alloy are needed in order to investigate precipitation sequence and chemical compositions of present precipitates.

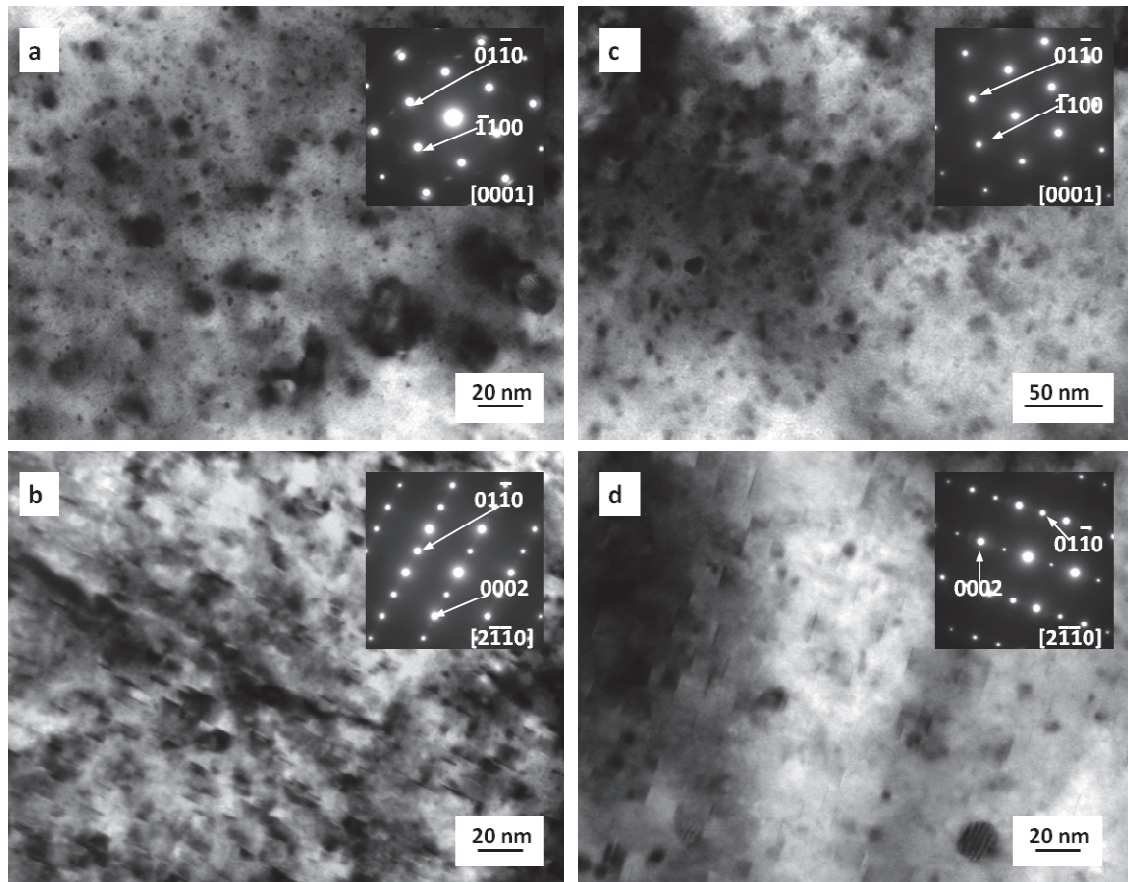


Fig. 1. TEM micrographs recorded from aged Mg-3Zn-3Ca wt% samples; (a, b) under-aged sample for 66 hours at 175 °C and (c, d) for slightly over-aged sample 140 hours at 175 °C with inset corresponding diffraction patterns taken along (a, c) [0001] α -Mg and (b, d) $[2\bar{1}\bar{1}0]$ α -Mg zone axes

Summary

The fine densely distributed plate-like precipitates in Mg-3Zn-3Ca wt.% alloy are considered to be the main straightening factor. The research shows the importance of interdisciplinary studies in designing biomaterials.

Acknowledgments

The authors acknowledge gratefully the financial support from the project no. POKL. 04.01.00-00-004/10 co-financed by the European Union within the European Social Fund.

References

- [1] N. Kirkland: Corros. Eng. Sci. Techn. Vol. 47 (2012), p. 322.
- [2] F. Witte, N. Hort, C. Vogt, S. Cohen, K.U. Kainer, R. Willumeit, F. Feyerabend: Curr. Opin. Solid State Mater. Sci. Vol. 12 (2008), p. 63.
- [3] N.T. Kirkland, N. Birbilis, M.P. Staiger: Acta Biomater. Vol. 8 (2012), p. 925.
- [4] J.W. Chang, X.W. Guo, P.H. Fu, L.M. Peng, W.J. Ding: Electrochim. Acta Vol. 52 (2007), p. 3160.
- [5] J.C. Oh, T. Ohkubo, T. Mukai, K. Hono: Scripta Mater. Vol. 53 (2005), p. 675.
- [6] C.J. Bettles, M.A. Gibson, K. Venkatesan: Scripta Mater. 51 (2004), p. 193.
- [7] K. Oh-ishi, R. Watanabe, C.L. Mendis, K. Hono: Mat. Sci. Eng. A Vol. 526 (2009), p. 177.
- [8] K. Kubok, L. Litynska-Dobrzynska, A. Wierzbicka-Miernik: Mater. Sci. Forum Vol. 765 (2013), p. 481.

Electron microscopy of quasicrystals in Al-Cu-Fe mechanically alloyed powder

Mikołaj Mitka^a, Lidia Lityńska-Dobrzyńska^b, Anna Góral^c and Łukasz Rogal^d

Institute of Metallurgy and Materials Science Polish Academy of Sciences, 30-059 Krakow, 25 Reymonta St., Poland

^am.mitka@imim.pl, ^bl.litynska@imim.pl, ^ca.goral@imim.pl, ^dl.rogal@imim.pl

Introduction

Quasicrystals in Al-Cu-Fe ternary system are frequently investigated in last years [1, 2]. They can be used as addition to aluminum based composite construction materials, as anti-friction and anti-adhesion coatings or as solar light absorbers [3]. Recent papers shows that mechanical alloying (MA) is a method in which range of existence Al-Cu-Fe quasicrystal is wider [1, 4]. Formation of quasicrystals depends on the composition of the alloy and milling conditions [4, 5]. Other articles shows dependence of annealing temperature and time on the formation of icosahedral phase in MA powder [5, 6].

The aim of current study was to investigated effect of milling time of MA process and subsequent annealing temperatures on the formation of quasicrystal in $\text{Al}_{62}\text{Cu}_{25,5}\text{Fe}_{12,5}$ (at. %) powder.

Experimental

Powder of pure elements of Al, Cu and Fe having a particle size 10-15 μm was used in experiment. Nominal composition of material was $\text{Al}_{62}\text{Cu}_{25,5}\text{Fe}_{12,5}$ (at. %). First, pure elements powder was ball milled using tungsten carbide vials and balls in planetary mill Fritsch 5 up to 10 hours at a rate of 250 rpm. 10 hours milled powders were closed in quartz ampules under vacuum and annealed at 600-800 °C for 4 hours. The powder were investigated using D2 Phaser Bruker diffractometer with Cu $K\alpha$ filtered radiation (XRD), FEI scanning electron microscope E-SEM XL 30 (SEM) and FEI transmission electron microscope Tecnai G² (TEM).

Results

XRD and SEM investigations shows that powder particles contain pure elements up to 6 hours of milling. Elemental particles started to mix with each other (particles were not homogenous and the layers of different composition are visible inside them). At this stage of milling morphology of particles changes from initial irregular to the shape of flakes. After 10 hours the particle size was greatly reduced and their shape changes to near spherical. It was also notice that apart of pure elements the cubic $\beta\text{-AlCu(Fe)}$ phase appear. EDX microanalysis results indicate that powders have areas of different elements ratio from assumed. The nanocrystalline structure was observed inside the powder particles. In Figure 1 the SEM and TEM images of the powder after 10 hours of milling were presented. The corresponding diffraction pattern contains reflections lying on the rings which were identified as pure elements.

Annealed powder for 4 hours at 600 °C contains mixture of $\beta\text{-AlCu(Fe)}$, $\lambda(\text{Al}_{13}\text{Fe}_4)$ and small amount of I-phase. Increase of annealing temperature cause the increase of the content of I-phase in the powder and reduce the amount of other phases. After annealing at 800 °C the I-phase is main phase, although β and λ phases are still present. TEM microstructure of the powder particle annealed for 4 hours at 800 °C contained I-phase and corresponding electron diffraction pattern with 5-fold symmetry is shown in Fig. 2. TEM microstructure show that I-phase particles are submicron size with irregular shape.

Summary

Mechanical alloying and subsequent annealing of $\text{Al}_{62}\text{Cu}_{25,5}\text{Fe}_{12,5}$ (at. %) powder were applied to obtain the quasicrystals. Increase of milling time up to 10 hours and temperature of annealing up to $800\text{ }^{\circ}\text{C}$ have impact on reaction in this ternary system and forming the quasicrystalline icosahedral phase in final product.

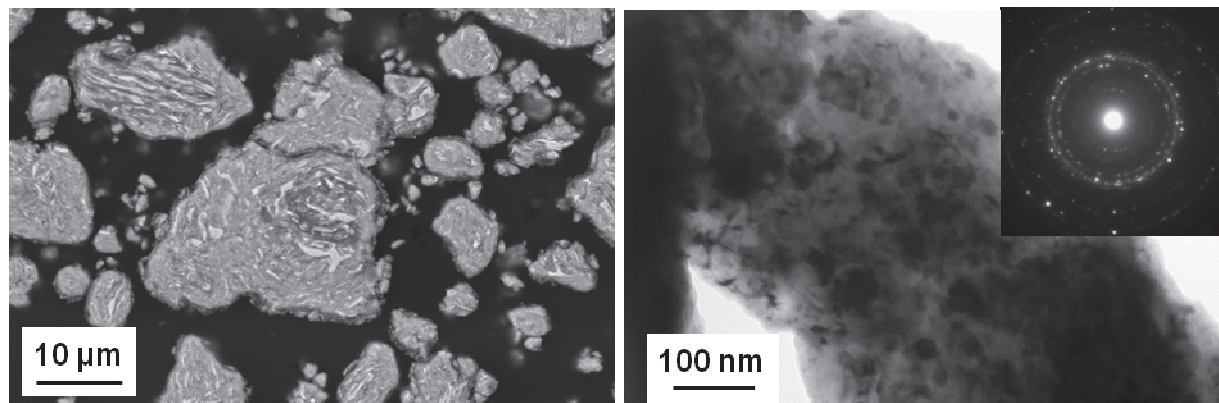


Fig. 1. SEM microstructure, TEM image and corresponding diffraction pattern of the $\text{Al}_{62}\text{Cu}_{25,5}\text{Fe}_{12,5}$ after 10 hours of mechanical alloying

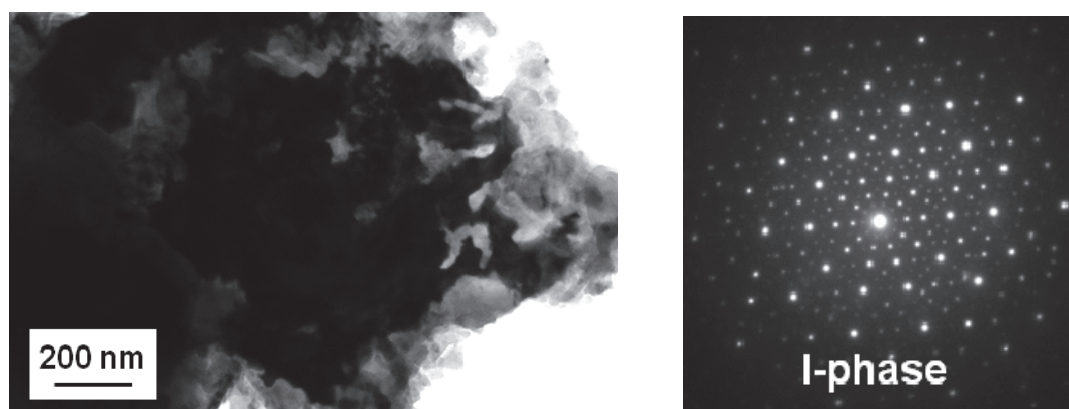


Fig. 2. TEM image and corresponding diffraction pattern of the icosahedral particle of $\text{Al}_{62}\text{Cu}_{25,5}\text{Fe}_{12,5}$ after 10 hours of mechanical alloying and annealing 4 hours at $800\text{ }^{\circ}\text{C}$

Acknowledgments

Financial support from the Polish National Science Centre NCN (research projects no 2011/03/B/ST8/05165) is gratefully acknowledged.

References

- [1] F. Ali et al.: *Acta Mater.* Vol. 61 (2013), p. 3819.
- [2] D.N. Travessa et al.: *Mater. Res.* Vol. 15 (2012), p. 749.
- [3] J.-M. Dubois: *Chem. Soc. Rev.* Vol.41 (2012), p. 6760.
- [4] E. Huttunen-Saarivirta: *J. Alloys Compd.* Vol. 363 (2004), p. 150.
- [5] B. Avar, M. Gogebakan: *J. Optoelectron. Adv. M.* Vol. 11 (2009), p. 1460.
- [6] M. Gogebakan, B. Avar: *Pramana - Journal of Physics* Vol. 77 (2011), p. 735.

Effect of the silicon carbide nanoparticles introduction on the biological properties of porous polymer coatings

Aldona Mzyk^{1,a}, Roman Major^{1,b}, Juergen M. Lackner^{2,c}, Łukasz Major^{1,d}

¹Institute of Metallurgy and Materials Science, Polish Academy of Sciences, 25 Reymonta Street, 30-059 Krakow, Poland

²Joanneum Research Forschungsges mbH, Institute of Surface Technologies and Photonics, Functional Surfaces, Leobner Strasse 94, A-8712 Niklasdorf, Austria

^aaldonamzyk@googlemail.com, ^br.major@imim.pl, ^cjuergen.lackner@joanneum.at, ^dl.major@imim.pl

Introduction

Multilayer polyelectrolyte films consist of chitosan/chondroitin sulfate polymers exhibit a fast biodegradability in the environment of human tissues. Lifetime extension of this material type could be implemented by its structure stabilization through the introduction of nanoparticles. Transmission electron microscopy (TEM) and high resolution transmission electron microscopy (HRTEM) methods were used to determine the microstructure and localization of the silicon carbide nanoparticles introduced to the extracellular like structure of the polymer coatings. Modified coatings biocompatibility was analyzed in cytotoxicity assay and microscopic observations of endothelial cells growth on the material surface.

Methodology

Multilayer (48 bilayers) polyelectrolyte chitosan/chondroitin sulfate films were prepared by “layer by layer” method on the silicon substrate. Coatings were cross-linked by mixture of 100 mM N-hydrosulfosuccinimide (NHS) and 260 mM 1-ethyl-3-(3-dimethylamino-propyl)carbodiimide (EDC) reagents. Nanoparticles were introduced to cross-linked and control non-cross-linked films by the physical vapor deposition technique (PVD), in 5-10s ongoing process. The main assumption of the PVD technique is described elsewhere [1].

A silicon disc was evaporated in an acetylene atmosphere. At first topography observations were done using Scanning Electron Microscopy technique (SEM) on Quanta 200 3D. Microstructure characterization was performed using Transmission Electron Microscopy technique (TEM), on cross-section. The Tecnai G² F20 (200kV) FEG was used for analysis [2]. Thin foils for TEM observations were prepared directly from the place of interest using Focused Ion Beam technique (equipped with in-situ micromanipulator). The Quanta 200 3D DualBeam was used for FIB preparation. Nanoparticles dispersion was theoretically simulated with ADINA software. Potential cytotoxic effect of coatings was determined according to the ISO 10993-5 2009 standards [3]. The morphology, adhesion and proliferation of endothelial cells on the surface of modified films was investigated through the confocal laser scanning microscopy observations (CLSM).

Results and Conclusions

Based on TEM analysis, it was found that SiC nanoparticles have penetrated through the polymer coating and have formed a phase directly on the substrate (Fig. 1). Only a small number of nanoparticles was located in the polymer multilayer.

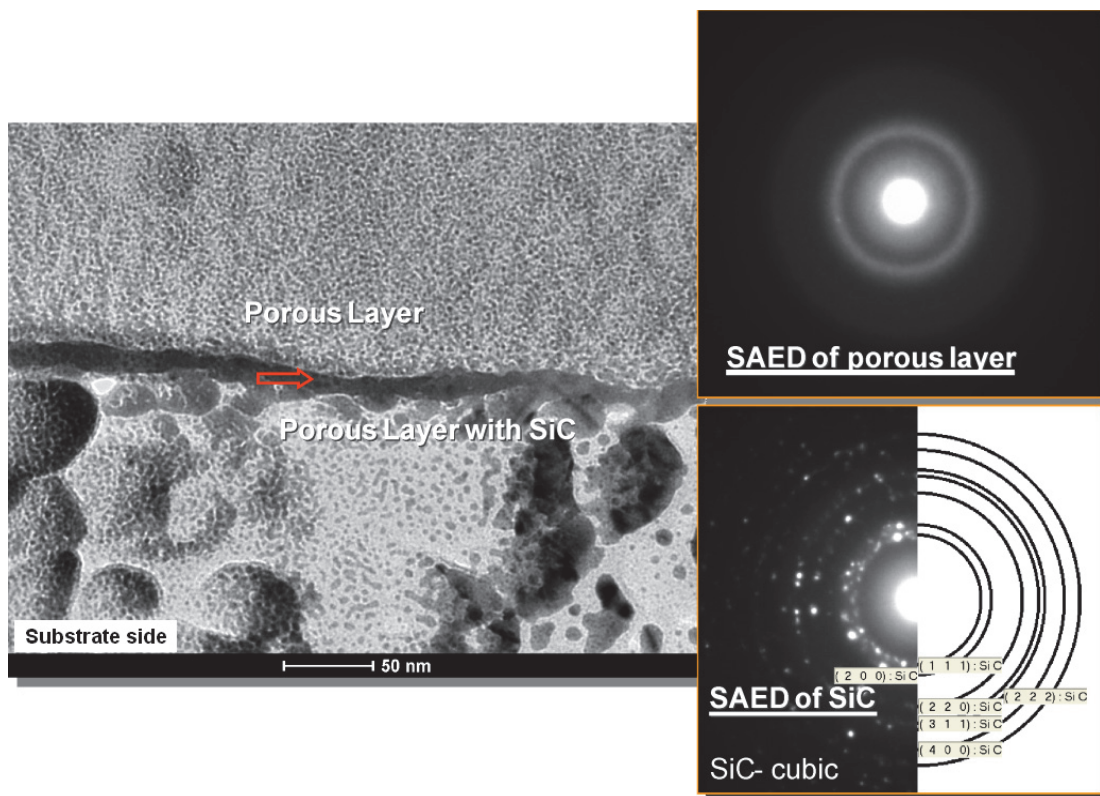


Fig. 1. Cross section TEM analysis of the silicon carbide nanoparticles introduction into porous polymer coatings - the red arrow indicates a border between polymer porous layers

Simultaneously theoretical model of the porous cross-linked/non-cross-linked coatings with or without introduced nanoparticles was prepared. Following the theoretical analysis SiC nanoparticles should be uniformly distributed in the multilayer. Experimental verification did not confirm the simulation thesis. Theoretical model demonstrated changes in mechanical properties after nanoparticles incorporation. The biological verification considered coatings cytotoxicity has shown higher necrotic effect of cross-linked films probably due to lower contribution of polymer - nanoparticles interaction sides and higher particles release rate. The mechanical properties of the material used for a biomedical application has a considerable effect on biological reaction. Porous coatings with varying degrees of rigidity were elaborated as a substrate for endothelial cell culture. More effective adhesion and proliferation was observed on cross-linked coatings.

Acknowledgments

The research was financially supported by the European Union under the European Social Found within Project No. POKL.04.01.00-00-004/10 and Project No. 2011/03/D/ST8/04103 “Self-assembling, biomimetic porous scaffolds in terms of inhibiting the activation of the coagulation system” of the Polish National Center of Science.

References

- [1] J.M. Lackner, Industrially-scaled hybrid Pulsed Laser Deposition at Room Temperature. Orecop sc. Krakow, 2005.
- [2] L. Major, W. Tirry, G. Van Tendeloo: Surf. Coat. Technol. Vol. 202 (2008), p. 6075.
- [3] ISO 10993-5 2009: “Biological evaluation of medical device - Part 5: “Tests for in vitro cytotoxicity“.

Electron microscopy investigation of Inconel 625 weld overlay on boiler steels

Paweł Petrzak^a, Marek Blicharski^b, Stanisław Dymek^c and Monika Solecka^d

AGH University of Science and Technology, Faculty of Metals Engineering and Industrial Computer Science,
30 Mickiewicza Av. 30-059 Kraków, Poland

^appetrzak@agh.edu.pl, ^bmablich@uci.agh.edu.pl, ^cdymek@agh.edu.pl, ^dmsolecka@agh.edu.pl

Introduction

The boiler elements that are exposed to elevated temperatures and aggressive corrosion environments (sulfides, chlorides) are currently weld overlaid by nickel-based alloys. Weld overlaying is a process of depositing a layer of a material on a surface of the base metal by welding methods. The strong metallurgical bonding produced by interdiffusion of elements across the interface develops during this process. However, during solidification the main constituents of the Ni-based alloy, like Mo, Nb and minor additions, like Ti, Si or C, segregate to the liquid giving rise to the expressive differences in their composition between dendrite cores and interdendritic spaces. In addition, mixing the steel and the Ni-based alloy within the bonding zone may result in precipitation of phases like intermetallics or carbides. These segregation and precipitation of secondary phases influence the mechanical properties of the alloy and decrease its resistance to corrosion. Moreover, the iron content on the overlay surface may increase and further reducing overlay properties.

The main goal of this study was to provide fundamental understanding of microstructural changes at the interface of commercially produced steel/Inconel 625 alloy weld overlays. In addition, a novel cladding method – Cold Metal Transfer (CMT) – was utilized in this study. Investigations of overlays produced with this method, developed by Fronius in 2002 as a variation of conventional welding technologies [1, 2], are not numerous on worldwide scale.

Material and methodology

The investigation focused on the characterization of microstructure and chemical composition within the bonding zone between the boiler steel (P235GH or 16Mo3) and CMT overlaid Inconel 625. Two layers of Inconel were clad on the steel surface. The analysis included a study of microstructure (considering weld quality and degree of overlapping of particular weld beads), chemical composition (iron content in the overlay near surface areas and microsegregation of alloying elements in weld overlay). The microstructure and chemical analysis were performed on a FEI Inspect S50 scanning electron microscope with a Noran energy dispersive spectrometer (EDS). The analysis of iron content was carried out on the surface and on the specimen cross-sections. Additionally, transmission electron microscopy was utilized for revealing substructure details in areas adjoining to the weld interface, both on the nickel-based and steel sides.

Results

The typical fusion boundary is shown in Fig. 1. The interface was free from pores or other welding defects. Both grades of steel in as-received condition exhibited typical ferritic-pearlitic structure, however, in the heat affected zone the microstructure changed to ferritic-bainitic in the P235GH steel and to bainitic (or tempered martensitic) in the 16Mo3 one. The Inconel overlay in regions adjoining the steel/Inconel interphase exhibited austenitic cellular microstructure. The qualitative and quantitative chemical analyses were conducted on metallographic samples by means of EDS in SEM. It was found that Nb and Mo in the Inconel weld overlay had a strong tendency to microsegregation (Fig. 2). Such a behavior is typical for cast microstructures of the 625 alloy [3]. This microsegregation produces differences in chemical composition between dendrite core and interdendritic spaces and deteriorate the overall properties of weld overlay. The EDS analyses were

also performed along a direction perpendicular to the weld interface. In this case, the determination of changes in the content of main constituent elements was of primary importance. It was shown that Fe content in the first layer was fairly high (about 20%), however, in the second layer it was kept below 3%. Thus, the basic requirement for the quality of the Inconel weld overlay was satisfied.

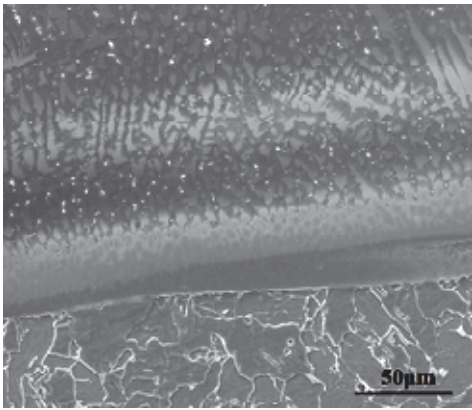


Fig. 1. Microstructure of fusion boundary (SEM)

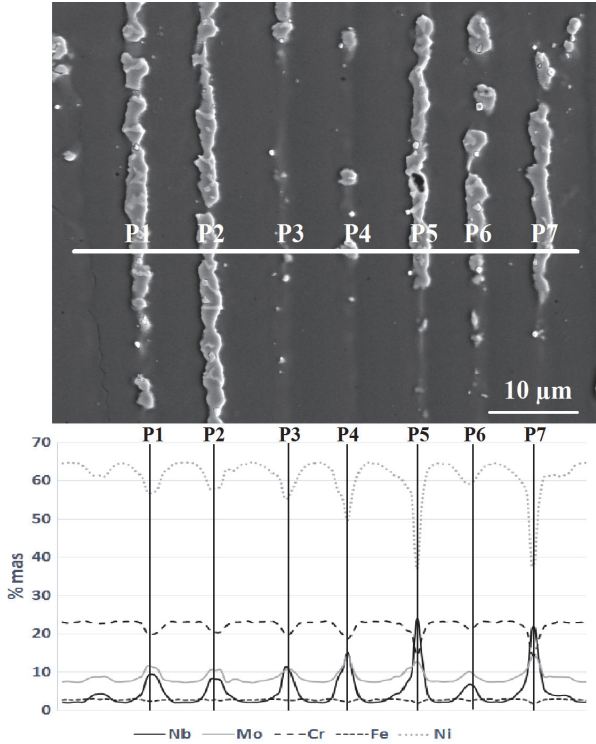


Fig. 2. Distribution of elements in overlay weld

References

[1] www.fronius.com [access: 16 January 2014].
 [2] C.G. Pickin, S.W. Williams, M. Lunt: J. Mater. Proc. Technol. 211 (2011), p. 496.
 [3] J.N. DuPont, J.C. Lippold, S.D. Kiser: Welding metallurgy and weldability of nickel-base alloys. John Wiley & Sons, New Jersey 2009.

Acknowledgements

The financial support from The National Centre for Research and Development, project No. PB51/B5/4/2012, is greatly appreciated.

Structural and mechanical features of mechanically alloyed AlMg-CeO₂ composite

Tomasz Skrzekut^{1,a}, Anna Kula^{1,b}, Ludwik Blaz^{1,c} and Makoto Sugamata^{2,d}

¹ Faculty of Non – Ferrous Metals, AGH-University of Science and Technology, 30-059 Cracow, Poland

² Department of Mechanical Engineering, College of Industrial Technology, Nihon University, 1-2-1 Izumi-cho, Narashino Chiba 275 – 8575

^a skrzekut@agh.edu.pl, ^b kula@agh.edu.pl, ^c blaz@agh.edu.pl, ^d sugamata@cit.nihon-u.ac.jp

Introduction

The special group of materials produced by powder metallurgy methods includes mechanically alloyed (MA) composites based on light metal matrix such as aluminum and magnesium that are strengthened with different metal oxides or silicides [1-3]. Application of light metal matrix provides relatively high strength to density ratio that fit commonly formulated demands of car and aviation industry. It is worth stressing that numerous MA composites, reinforced with heavy metal-oxide (MeO) particles, cannot be manufactured by means of common metallurgy processes because of a high reactivity of components. Application of MA method enables successful introduction of MeO particles into aluminum, or aluminum/magnesium matrix due to the low diffusion rate at solid state that effectively reduce the chemical reaction between MA composite components. Experiments on manufacturing MA composites have been carried out for over twenty years and a lot of different combinations of the system composition were researched [4]. General conclusions from the experiments are often related to the structural effect of chemical reaction between the composite components that usually proceeds at high annealing temperatures. The composite systems can be separated into two groups. The first group of composites is reinforced by means of MeO oxides that are reduced in aluminum or aluminum/magnesium matrix and released Me-metal does not form any intermetallic particles at Al-Me system. After prolonged annealing of mentioned composites that is needed to the chemical reaction finish, the material become reinforced solely by Me-particles and fine aluminum or aluminum/magnesium oxides [5]. The chemical reaction at the second group of composites leads to Al_xMe_y intermetallic grains growth and very fine aluminum or aluminum/magnesium oxides development.

One of the composites - Al(Mg)-CeO₂ - was used for experiments described in a present work. The composite reinforced with CeO₂ belongs to group of component systems, which are characterized by the intermetallic phase development if the reinforcement undergoes a chemical reaction in aluminum matrix. Attention was paid for the effect of temperature on the structure evolution and related properties of the material tested at high temperature range. The material structure and particles morphology was analyzed using SEM/TEM and EDX analysis method.

Structural observations revealed uniform distribution of CeO₂ reinforcement in as-extruded material as it is shown in Fig. 1a. Cerium oxide particles size were found to vary from tens nanometers to 500nm. Because of fine microstructure attained by MA, solid-state reactions at high enough temperatures are promoted due to increased reaction area, decreases diffusion distance and enhanced diffusivity of elements. As a result, decomposition of dispersed CeO₂ particles and growth of new structural components are observed. Typical microstructure of annealed sample is shown in Fig.1b. Long annealing time and favorable diffusion conditions were found to result in development of Al₄Ce intermetallic phase (Fig.1b). In spite of formation of extra phase in Al(Mg)-CeO₂ system, annealing of the composite at 773K results in reduction of the material hardness from 182HV to 137HV for as extruded material and the sample annealed at 773K/336h, respectively. In order to test the temperature effect on the composite mechanical properties, hot compression test were performed in the temperature range of 293K-823K. It is considered that high mechanical properties of Al(Mg)-CeO₂ composite result from an efficient refining of components due to mechanical alloying and advantageously selected conditions of MA-powders consolidation methods i.e. vacuum pressing and

following hot extrusion. The material softening during prolonged annealing was ascribed first of all to the structure transformation due to chemical reaction between CeO_2 particles and surrounding aluminum/magnesium matrix, which result in Al_4Ce intermetallic grains growth and very fine aluminum-magnesium oxides development.

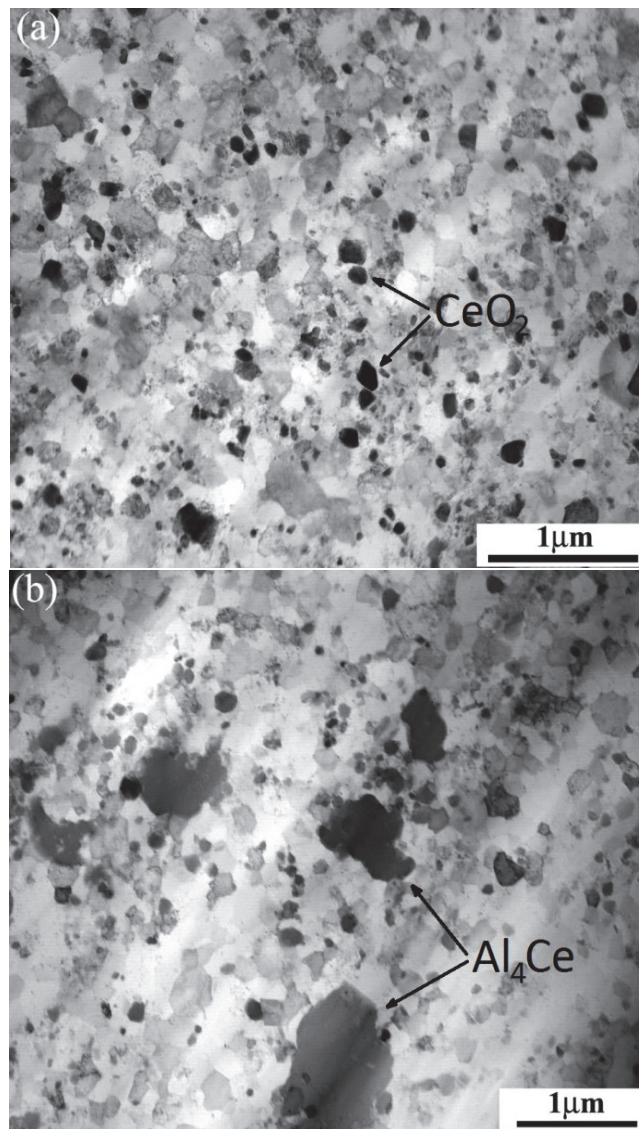


Fig. 1. STEM micrographs of Al(Mg)- CeO_2 composite: (a) as-extruded material, (b) annealed at 773K for 336h

References

- [1] A. Yamazaki, J. Kaneko, M. Sugamata, L. Blaz: Mater. Sci. Forum Vol. 419-422 (2003), p. 829.
- [2] J. Kaneko, M. Sugamata, L. Blaz and R. Kamei: Mater. Sci. Forum Vol. 396-402 (2002), p. 161.
- [4] A. Kula, L. Blaz, J. Kaneko, M. Sugamata: J. Microsc. Vol. 237, Pt 3 (2010), p. 421.
- [5] L. Blaz, J. Kaneko, M. Sugamata, Z. Sierpinski, M. Tumidajewicz: Mater. Sci. Tech., Vol. 21 (2005), p. 715.

The microstructure of weld overlay Ni-base alloy deposited on carbon steel by CMT method

Monika Solecka^{1,a}, Paweł Petrzak^{1,b}, Jan Kusiński^{1,c},
Agnieszka Radziszewska^{1,d}

¹AGH University of Science and Technology, 30 Mickiewicza Av. 30-059 Krakow, Poland
^amsolecka@agh.edu.pl, ^bppetrzak@agh.edu.pl, ^ckusinski@agh.edu.pl, ^dradzisz@agh.edu.pl

Introduction

Coatings are widely used in all modern power generation systems, including utility turbines for electric power production and gas turbines, since their improved efficiencies, lower emissions and reduced downtime of plant can be achieved with the higher temperature and corrosive resistances.

Nowadays, Ni-base alloys are used as a one of the most important coating material and can be applied in a different environments and elements of devices having various applications. Due to the excellent high temperature corrosion resistance and good strength at high temperatures [1, 2], the Inconel 625 can be applied in power boilers in the waste incineration plants.

Among a variety of hard facing techniques, cladding is another form of surface treatment, where the bulk material's surface is given a protective layer of another material having more superior properties than those of the bulk material. To perform the Ni weld overlays the newest weld technique called Cold Metal Transfer (CMT) is used. CMT is the method of submerged arc welding with a completely new way of droplet detachment from the wire detachment by means of the wire-motions incorporated in the digital process-control. In comparison with conventional GMA process, CMT reduces the thermal input by achieving almost current-free metal transfer from the wire to the coating. Indeed, what reduces the Fe content (coming from the remelted substrate) in a weld overlay. Characteristic and very important for a CMT method is that the coating is received in lower temperatures [3,4]. Even that, using this technique, good metallurgical bonding can be obtained between coating and substrate.

The Inconel 625 alloy was deposited on P235GH steel by using CMT technique. In the paper the microstructure (SEM, TEM) and chemical composition (EDS) of obtained weld overlays were investigated.

Materials and experimental details

For the experiments the external surface of boiler pipes made of P235GH steel was cladded with Inconel 625 alloy using CMT method. The chemical compositions of the investigated alloy and P235GH steel are shown in Table 1.

The microstructure investigations of Inconel weld overlays was carried out using scanning electron microscope (SEM) as well as transmission electron microscope (TEM). The metallographic microphotographs were taken using FEI Nova NanoSEM 450 microscope equipped with energy dispersive spectroscopy (EDS) EDAX analyzer. The TEM investigations were performed using JEM-2010 JEOL Company.

The microstructure and chemical composition investigations were carried out on the obtained cross-sections of the samples. The changes of the elements distribution were performed using the linear EDS analysis perpendicular to dendritic structure

Table 1. The chemical composition of Inconel 625 and P235GH alloys,% wt.

| Alloy | Ni | Cr | Mo | Nb | Fe | C | Mn | Si |
|-------------|---------|-------|------|------|---------|------|------|------|
| Inconel 625 | Balance | 23,20 | 9,45 | 3,46 | 0,30 | 0.12 | 0.40 | 0.40 |
| P235GH | 0.30 | 0.30 | 0.08 | 0.01 | Balance | 0.16 | 1.20 | 0.35 |

Results

Due to the segregation of Ni, Cr, Nb and Mo elements the Inconel 625 weld overlays deposited on carbon steel obtained the dendritic structure, with the formation of a second phases at the end of solidification (Fig. 1a). Presence of γ (with high dislocation density), Laves and Ti carbide phases was revealed by means of TEM examinations. The multipoint EDS analysis confirmed the presence of increased Fe concentration in the Inconel 625 alloy coatings. The concentration profiles of Ni, Cr, Mo and Nb performed across the dendritic structure (Fig. 1b,c) show segregation of these elements. The presence of significant concentration gradients would lead to preferential attack in the dendrite cores, since preferential corrosion often occurs at the dendrite cores in welds of Mo and Nb - bearing alloys due to microsegregation of Mo and Nb.

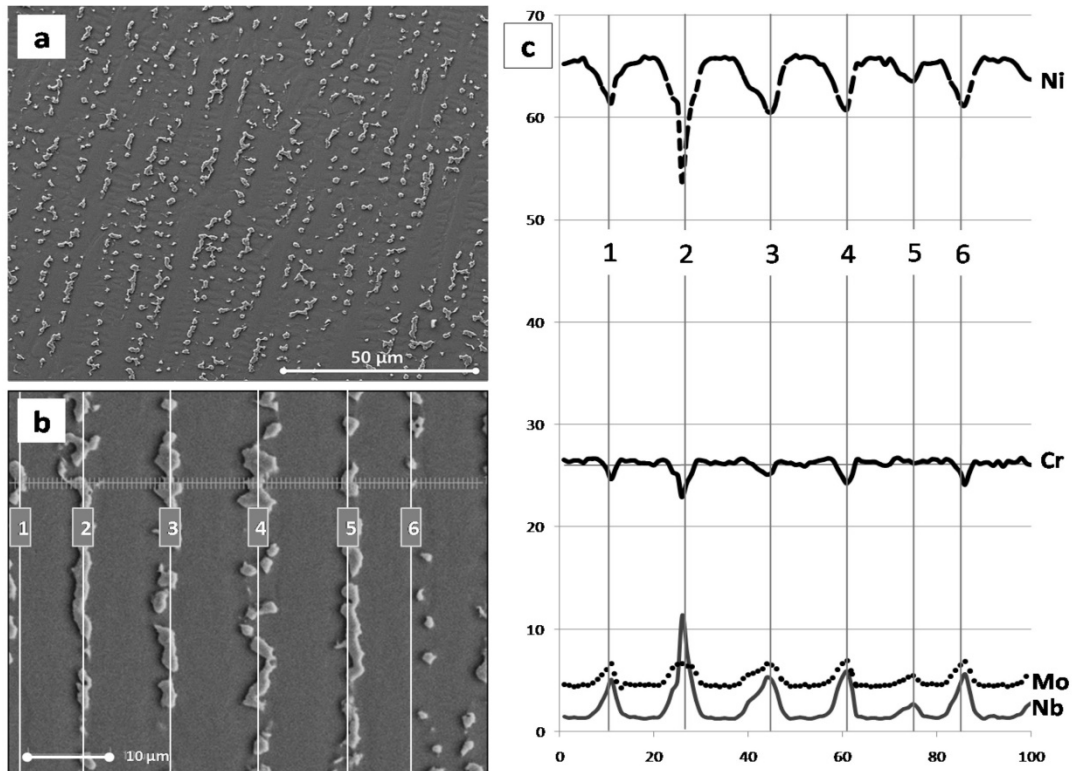


Fig. 1. The dendritic structure of the clad layer and line EDS analysis: a) microstructure Inconel 625 weld overlay, b) multipoint EDS analysis, c) distribution of elements in Inconel 625 clad layer

Conclusions

Inconel have a characterization dendritic structure. Revealed the presence of phases: γ , Laves and Ti carbides. The concentration profiles of Ni, Cr, Mo and Nb performed across the dendritic structure show segregation of these elements. Preferential corrosion attack in the dendrite cores of the Mo- and Nb based bearing alloys is caused by the significant concentration gradients of Mo and Nb due to microsegregation of these elements.

References

- [1] Information on www.specialmetals.com.
- [2] ASTM G-28-A.
- [3] C.G. Pickin, S.W. Williams, M. Lunt: J. Mater. Proc. Technol. 211 (2011), p. 496.
- [4] J. Bruckner: *Metoda CMT – rewolucja w technologii spawania* Przegląd Spawalnictwa Vol. 7-8 (2009), p. 24.

STEM-EDS and electron diffraction investigation of TCP phases in CMSX-4 single crystal nickel-base superalloy

Tomasz Ratajski^{1,a}, Beata Dubiel^{1,b}, Grzegorz Cempura^{1,c},
Aleksandra Czyska-Filemonowicz^{1,d}

¹AGH University of Science and Technology, International Centre of Electron Microscopy for Materials Science,
Faculty of Metals Engineering and Industrial Computer Science,
Al. A. Mickiewicza 30, 30-059 Kraków, Poland

^aratajski@agh.edu.pl, ^bbdubiel@agh.edu.pl, ^ccempura@agh.edu.pl, ^dczyska@agh.edu.pl

Additions of W, Mo and Re to single crystal superalloys have been introduced to increase the high temperature creep strength. However, the amount of these elements promote the formation of brittle topologically close-packed (TCP) phases. The crystal structure of TCP phases consists of close-packed layers of relatively smaller atoms, such as Ni and Cr, with the larger atoms, such as Re, W and Ta [1]. Frequently, the TCP phases exhibit plate-like morphology parallel to the four {111} planes. This results in the characteristic needle-like appearance when sectioned in the {100} plane.

Although TCP phases have been studied for many years, and their presence carefully monitored in a great number of alloys, data on the specific nature of the phases formed and their compositions in Re-containing single crystal superalloys are limited [2-4]. The difficulties in unambiguous phase identification disable the precise determination which phases are present.

In the present work phase analyses of TCP phases in CMSX-4 superalloy annealed at 1050 °C for 2500 hours have been performed. Chemical composition of CMSX 4 superalloy is as follows: Ni - 8.4 Co - 6.4 Cr - 6.5 Ta - 6.4 W - 5.68 Al - 2.8 Re - 1.04 Ti - 0.58 Mo (in wt %). Scanning-transmission electron microscopy (STEM) analysis were carried out in high angle annular dark field (HAADF) mode by means of a probe Cs-corrected Titan G2 60-300 microscope equipped with a ChemiSTEM™. Selected area electron diffraction (SAED) analysis was conducted using JEOL JEM-2010 microscope. Identification of precipitates performed by electron diffraction was supported by JEMS software.

STEM-HAADF investigation of high temperature annealed CMSX-4 superalloy revealed precipitates of TCP phases inclined by 45° versus <100> directions Figure 1 shows the STEM-HAADF image and the corresponding STEM-EDS maps of Ni, Re, Al, Ti, W, Cr, Mo, Co and Ta. The results of EDS microanalysis show that the TCP precipitates are enriched with Re, W and Mo.

SAED analysis revealed that the diffraction patterns of TCP precipitates in CMSX-4 give the best fit with calculated theoretical patterns of rhombohedral μ phase (R-3mH, Fe₇W₆ type) and orthorhombic P phase (Pbnm, Cr_{9.61}Mo_{25.12}Ni_{21.27} type). TEM-BF images showed the presence of planar defects within precipitates (Fig. 2a). The diffraction pattern and its solution with best fitting with the μ phase are given in Figs 2 b, c, respectively. The precipitates of μ phase are twinned, what is in agreement with Refs. [1, 3].

Uncertainty of the phase analysis by electron diffraction can be connected with the difference of the chemical composition of the investigated TCP phases in comparison with those ones, for which the crystallographic data are available. The more detailed analysis of TCP precipitates in CMSX-4 requires further investigations.

References

- [1] C.M.F. Rae, M.S.A. Karunaratne, C.J. Small, R.W. Broomfield, C.N. Jones, R.C. Reed, in: *Superalloys 2000*, edited by T.M. Pollock et al., The Minerals, Metals & Materials Society/TMS (2000) p. 767.
- [2] C.M.F. Rae, R.C. Reed: *Acta Mater.* Vol. 49 (2001), p. 4113.
- [3] R. Darolia, D.F. Lahrman, R.D. Field, in: *Superalloys 1988*, edited by D.N. Duhl et al., The Metallurgical Society (1988) p. 255.

[4] J.X. Yang, Q. Zheng, X.F. Sun, H.R. Guan, Z.Q. Hu: Mat. Sci. Eng. A Vol. 465 (2007), p. 100.

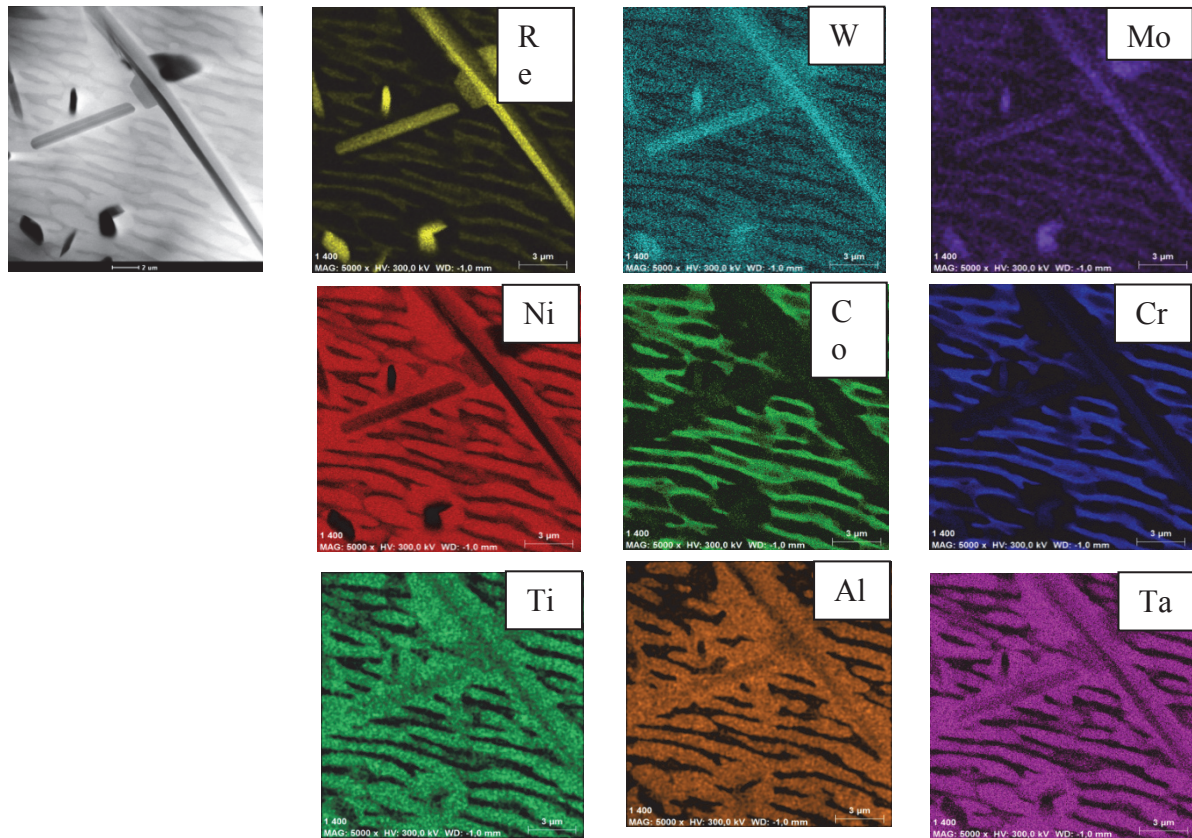


Fig. 1. STEM-HAADF image and STEM-EDS maps of Re, W, Mo, Ni, Co, Cr, Ti, Al and Ta in CMSX-4 superalloy after annealing at 1050 °C for 2500 h

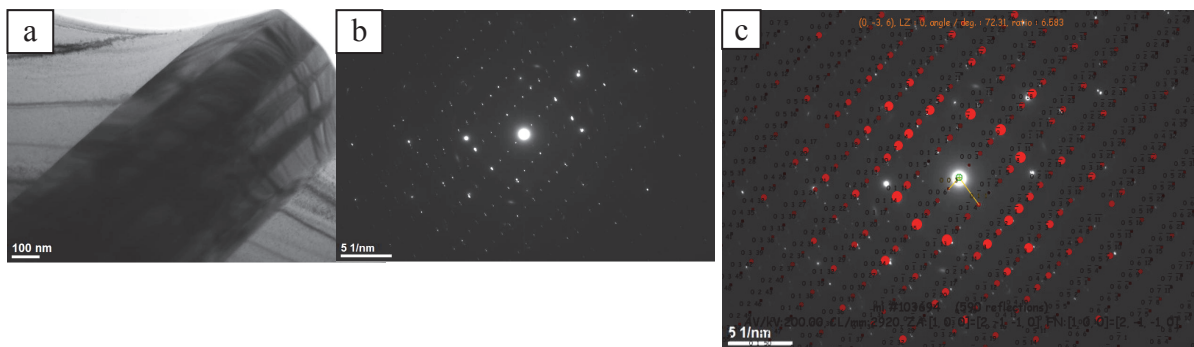


Fig. 2. a) TEM-BF image of the TCP precipitate, b) SAED pattern c) solution for μ phase $[2\bar{1}\bar{1}0]$ zone axis

Acknowledgements

The financial support by the European Union under the Framework 7 Program, contract for an Integrated Infrastructure Initiative. Reference 312483 ESTEEM2 is gratefully acknowledged. We also thank Mrs K. Płońska-Niznik (AGH-UST) for her assistance in TEM specimen preparation.

Influence of microstructure and mechanical properties of titanium carbonitride stabilized hydrogel coatings on haemocompatible properties

Klaudia Tembecka^{1,a}, Roman Major^{1,b}, Beata Butruk^{2,c}, Hanna Plutecka^{3,d}
and Łukasz Major^{1,e}

¹Institute of Metallurgy and Materials Science, Polish Academy of Sciences, 25 Reymonta Street, 30-059 Krakow, Poland

² Faculty of Cematic and Process Engineering Warsaw University of Technology. 1 Waryńskiego Street, 00-645 Warsaw, Poland

³ Department of Medicine, Jagiellonian University Medical College, 8 Skawinska Street, 31-066 Cracow, Poland

^aklaudia.trembecka@gmail.com, ^br.major@imim.pl, ^cB.Butruk@ichip.pw.edu.pl, ^dhankaz32@interia.pl, ^el.major@imim.pl

Introduction

Application of scanning electron microscopy (SEM), transmission electron microscopy (TEM), high resolution transmission electron microscopy (HREM) and confocal laser scanning microscopy (CLSM) methods were used to study the a-thrombogenicity of blood contacting materials as well as a blood material interaction.

Methodology

A medical-grade polyurethane applied in the heart assist system was covered by hydrogel layers in order to inhibit blood-clotting cascade activation. Hydrogel coatings were stabilized by the titanium carbonitride Ti(C,N) buffered layers deposited directly on the polyurethane (PU) substrate beneath the final hydrogel coating. Ti(C,N) coatings were deposited using a hybrid method comprising pulsed laser deposition (PLD) and magnetron sputtering (MS) in high vacuum conditions. Hydrogel layers were deposited by the dip-coating method. An influence of microstructure and mechanical properties were studied in respect to the blood cells activation. The influence of the buffer Ti(C,N) layer on the hydrogel coating were analyzed by means of the microstructure study in multi-scale (SEM, TEM, HREM, CLSM). The top view analysis and the cell-material interaction were analyzed in use of SEM. Thin foils for the microstructure analysis for the cross section analysis were prepared with focused the ion beam (FIB) technique. Selected area electron diffraction patterns confirmed Ti(C,N) phase of the buffer layer and the nanostructural character of the deposited coating. Physical vapor deposited (PVD) coatings do not diffuse to the substrate. Their adhesion is based on the mechanical anchoring and normally has a high proportion of structural defects, which was confirmed in TEM analysis. Mechanical tests were performed at an indentation load of 5 mN using the Berkovich indenter geometry. The loading and unloading rates were of order of 10 mN/min. The haemocompatible analysis were performed in vitro tests using a blood flow simulator. The protocol of the test is given elsewhere [1,2]. The blood-material interaction was analyzed in dynamic conditions. The quality of blood, cell activation, consumption and aggregation taken above the surface of the sample were analyzed by a flow cytometry technique. For the confocal microscopy analysis the dedicated antibodies: CD62P conjugated with FITC (platelets with the active receptor selectin P), CD45 conjugated with PE-Texas Red (active leucocytes) CD62P conjugated with FITC (platelets with the active receptor selectin P) for the fluorescence microscopy technique were applied. The co-localization function was applied to separate red and green channels in the confocal microscopy study.

Results and conclusions

It was concluded that the hydrogel coatings stabilized by the Ti(C,N) buffer layer had an insignificantly better a-thrombogenic performance and they were much more stable with time in comparison to the single hydrogel coatings.

Acknowledgments

This research was financially supported by project 2011/03/D/ST8/04103 “Self-assembling, biomimetic porous scaffolds in terms of inhibiting the activation of the coagulation system” of the Polish National Center of Science.

References

- [1] R. Major: *J. Mater. Sci. Mater. Med.* Vol. 24 (2013), p. 725.
- [2] M. Sanak, B. Jakiela, W. Wegrzyn: *B. Pol. Acad. Sci. - Tech.* Vol. 58(2) (2010), p. 317.

SEM study of the development of local texture and microstructure during asymmetric rolling of copper

Agnieszka Uniwersal^{1,a}, Tomasz Tokarski^{1,c}, Sebastian Wroński^{1,d},
Mirosław Wróbel^{1,b}, Krzysztof Wierzbowski^{1,e}

¹AGH University of Science and Technology, 30 Mickiewicza Av., 30-059 Kraków, Poland

^aa.uniwers@agh.edu.pl, ^bmwrobel@agh.edu.pl, ^ctokarski@agh.edu.pl,
^dwronski@fis.agh.edu.pl, ^ewierzbowski@fis.agh.edu.pl

Introduction

The grain refinement is the only known method of strengthening without detrimental influence on the material toughness. The thermo-mechanical processing (e.g. plastic deformation and recrystallization) is traditional way applied to control grain size in commercial metals. However, for technically pure metals such as aluminum or copper it is practically difficult to reduce the grain size below 5 μm . Fortunately a significant grain refinement can be obtain by an only slight modification of the conventional processes of plastic deformation e.g., asymmetric rolling (*AR*) [1-3].

The study of fine-grained materials requires research methods, which allow a precise determination of crystallographic orientations in small sample volumes. The most accurate currently known methods of determining the local orientations use patterns of the Kikuchi bands (*KB*) produced by electrons diffracted during passing through the sample thickness or reflected from the sample surface (Electron Backscatter Diffraction - *EBS*D). With *KB* one can reach an angular resolution up to 0.25° . Using convergent beam electron diffraction (*CBED*) in the transmission electron microscope (*TEM*) one can examine sample volumes of the size *around* 50 nm [4]. The *EBS*D technique in the scanning electron microscope (*SEM*) enables efficient testing of area size of the order of 1 mm², but spatial resolution of this technique ($> 0.1 \mu\text{m}$ [5]) is worse than of the *CBDE-TEM* one. This is due to both a much larger interaction volume of electrons with the sample and the sample tilt of 70° . The spatial resolution of *EBS*D-*SEM* can be *ca.* 3 time improved by changing measurement geometry (*i.e.*, using the transmission working mode with the specimen tilted of $10\text{-}20^\circ$) and adjusting measurement parameters. Such possibility was recently shown by Keller and Gaiss [6, 7] and they call it the transmission electron backscatter diffraction (*t-EBS*D). In this work we present some applications of the *EBS*D and *t-EBS*D methods for a study of the microstructure and texture of *AR* copper.

Experimental procedure

The material used in this study was a commercial copper in the form of plates with dimensions of $5 \times 25 \times 100 \text{ mm}^3$, annealed at $450^\circ\text{C}/1.5\text{h}$ and asymmetrically cold rolled on a laboratory mill by using different values of rotational speed of each roll (Fig. 1).

Thin foils perpendicular to the transverse direction (*TD*) of the rolled bar were investigated on the Hitachi S-3400N *SEM* using classical *EBS*D and *t-EBS*D.

Results and discussion

The material after low deformation was successfully investigated by classical *EBS*D. For higher deformations of copper *AR* produces a bi-modular distribution of grain size. As it was expected the classical *EBS*D worked well for bigger grains but its spatial resolution was not sufficient for measurement of the highly deformed material. The material was characterized by the *t-EBS*D measurement. A sample *EBS*D map is shown in Fig. 2.

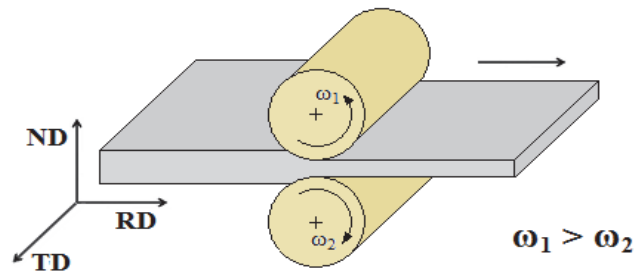


Fig. 1. Asymmetric rolling

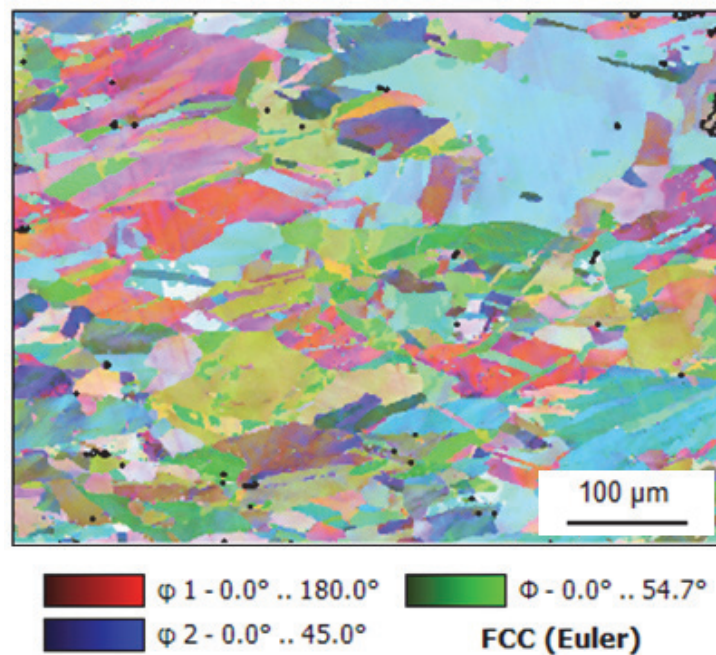


Fig. 2. EBSD map for asymmetrically cold rolled copper, deformation 17%

Conclusion

The grain size distribution and texture of the asymmetrically rolled copper can be successfully characterized by Scanning Electron Microscopy using combination of the classical electron backscatter diffraction technique and the transmission electron backscatter diffraction technique.

References

- [1] V.G. Sinicyn: Metallurgiya Moskva, (1986) p. 166, in Russian.
- [2] W. Polkowski, P. Jóźwik, M. Polański, Z. Bojar: Mat. Sci. Eng. A Vol. 564 (2013), p. 289.
- [3] Y.G. Ko Loorentz: J. Alloys Compd. Vol. 536 (2012), p. S122.
- [4] P.E. Champness: Mineral. Mag. Vol. 51 (1987), p. 33.
- [5] F.J. Humphreys: Scripta Mater. Vol. 51 (2004), p. 771.
- [6] R.R. Keller and RH Geiss: J. Microsc. Vol. 245 (2012), p. 245.
- [7] R.H. Geiss, K.P. Rice, R.R. Keller: Microscopy Today Vol. 21 (2013), p. 16.

Characterization of γ' and γ'' nanoparticles in Inconel 718 superalloy down to atomic level

Krzysztof Kulawik^{1,a}, Philippe André Buffat^{1-2,b}
and Aleksandra Czyska-Filemonowicz^{1,c}

¹AGH University of Science and Technology, International Centre of Electron Microscopy for Materials Science and Faculty of Metals Engineering and Industrial Computer Science,

Al. A. Mickiewicza 30, 30-059 Kraków, Poland

²Ecole Polytechnique Fédérale de Lausanne, Centre Interdisciplinaire de Microscopie Electronique, Station 12, CH-1015 Lausanne, Switzerland

^akulawik@agh.edu.pl, ^bphilippe.buffat@epfl.ch, ^cczyska@agh.edu.pl

Inconel 718 (IN718) is a nickel-iron based superalloy used for applications in aeronautics, aerospace and power generation. Its typical chemical composition is Ni-19Fe-18Cr-5Nb-3Mo-1Ti-0.5Al-0.04C (wt%). The IN718 microstructure consists of a γ matrix (Ni-based solid solution) strengthened by ordered face centred cubic γ' Ni₃(Al,Ti)-type and ordered body centred tetragonal γ'' Ni₃Nb-type nanoparticles (Fig. 1). The primary strengthening mechanism for this alloy is a precipitation hardening by the γ' and γ'' particles and therefore properly sized and distributed precipitates are critical for good alloy performance. The aim of this study was to describe IN718 micro- and nanostructure, identify γ' and γ'' precipitates and examine their shape, chemical element partitioning and metrology that influence its mechanical properties.

Microstructural investigation of Inconel 718 superalloy after various heat treatments was performed by electron microscopy (SEM, TEM, and STEM-HAADF-EDX) taking advantage of recent developments in quantitative electron microscopy. Electron microscopy analyses were performed using a Merlin Gemini II of Zeiss, Tecnai G2 Twin and a probe Cs-corrected Titan G2 60-300 with EDX ChemiSTEM technology (X-FEG, probe Cs-corrector and Super-X design detection system), both of FEI. The Super-X system gathers a five times enhanced X-ray generation using a new high brightness Schottky electron gun (X-FEG) design and a larger X-ray collection efficiency (0.7sr instead of 0.1 sr) using four windowless Silicon Drift Detectors (SDDs) symmetrically arranged around the specimen. Moreover, the probe Cs-corrector brings at the same time beam current and spatial resolution high enough to obtain STEM-EDX elemental maps at the atomic scale.

STEM-HAADF-EDX observation revealed γ' and γ'' particles with different morphology (prolate ellipsoid and disk - shaped γ'' particles and almost spherical γ' particles) in the matrix. In the alloy subjected to a specific heat treatment, beside isolated particles of γ' and γ'' , so-called γ'/γ'' co-precipitates were observed (Fig. 2d).

The distribution maps of the chemical elements collected by ChemiSTEM™ EDX system, especially Al and Ni maps, bring a clear contrast between γ' , γ'' and the matrix (Fig. 2). It allows not only to distinguish between γ' and γ'' phase precipitates but also to measure their size precisely. Moreover, the high map signal/noise ratio brought by the ChemiSTEM optimization makes possible to extract the actual composition of the γ' and γ'' nanoparticles though they are buried in the matrix using an ImageJ plugin developed for that purpose.

The study shows that the presence of γ'/γ'' co-precipitates contributes to better mechanical properties of Inconel 718 superalloy. Further investigation of these precipitates, their 3D morphology and metrology by electron tomography are in progress.

Acknowledgements: The financial support by the EU under the FP7, contract for an Integrated Infrastructure Initiative, Reference 312483 ESTEEM2 is gratefully acknowledged. We acknowledge also Pratt and Whitney, USA for providing the material for investigation and thank A. Gruszczyński, MSc. (AGH), Dr A. Carlsson and Dr I. Alexandrou (FEI) for their assistance in this research.

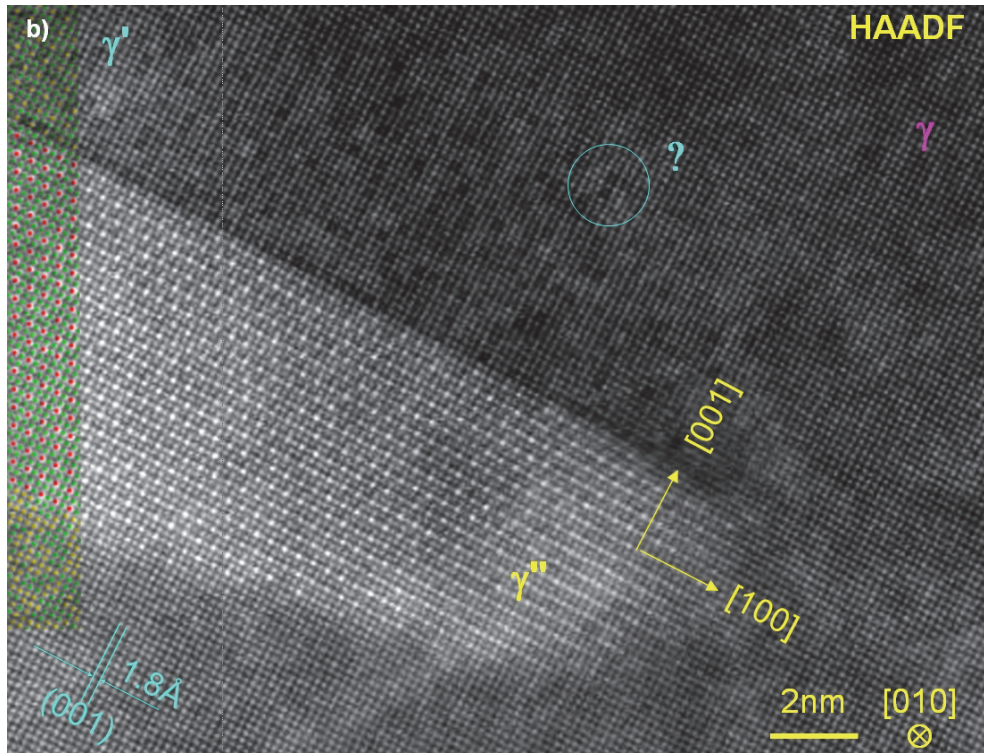


Fig. 1. HAADF high-resolution STEM image of γ' and γ'' precipitates in the γ matrix. All interfaces are coherent, but the γ'/γ'' one as well as the γ' precipitate contain defects at the atom column scale. Left b): ball model (Ni: green, Nb+Ti: red)

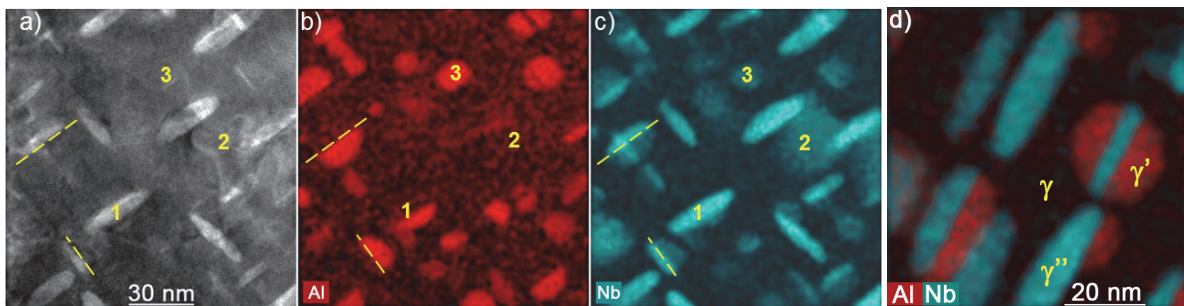


Fig. 2. a) HAADF image along $[100]_{\gamma}$ and EDX ChemiSTEM raw counts map of b) Al (red) and c) Nb (blue). A γ'' precipitate platelet (contains Nb but no Al) is seen edge-on as an elongated ellipse in 1 and in plan view as a disc in 2. The disc in 3 is a spherical γ' precipitate (Al + Nb). d) shows a γ'/γ'' co-precipitate made of a thin γ'' disc between two γ' hemispheres

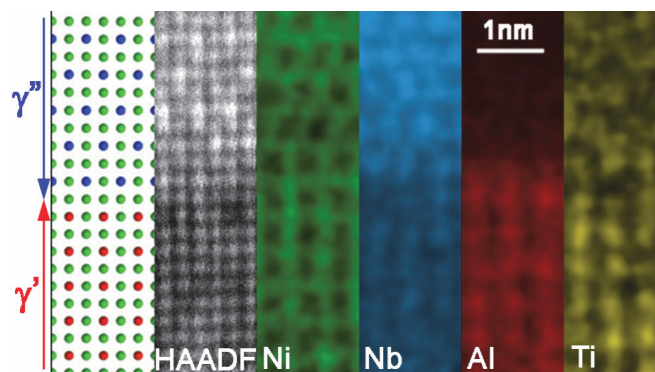


Fig. 3. EDX ChemiSTEM maps of a γ'/γ'' interface. Unexpectedly in comparison with the phase models, Nb and Ti substitute to Al and Nb in the γ' and γ'' phases, respectively

SEM investigation of cracks in turbine wheels in car engine turbochargers

Sebastian Krawiec, Łukasz Krawczyk

Borgwarner Poland Sp. z o.o. Rzeszow Technical Center
skrawiec@borgwarner.com, lkrawczyk@borgwarner.com

Introduction

Increasing requirements placed on reducing exhaust emission and cost reduction, while simultaneously maintaining the engines' performance, are forcing the automotive industry seek new solutions. Currently, the supercharging of the internal-combustion engine using a turbocharger is a widely applied practice.

Components of the turbochargers are exposed to high temperature vibration and corrosive effects of the exhausts. The turbine wheel is the most affected element.

To meet the increasing requirements of the turbine wheel failure analysis, in addition to the widely used light microscopy, scanning electron microscopy method is used. This allows for more detailed identification of the faults' development process and the mechanism of the turbine wheel cracking process [1].

Methodology

To analyze turbine wheel damage correlative microscopy was used. This method enables automatical location of defined regions of interest while moving the specimen from light to electron microscope. In the present work the Zeiss system consisting of Axio Imager Z2m light microscope and Ultra Plus scanning electron microscope was used. Microanalysis of chemical composition was performed using Energy Dispersive X-ray spectroscopy (EDX).

Results and conclusions

Stereomicroscopic view of the turbine wheel subjected to the turbocharger test is shown in Fig. 1a. The crack of the wheel is observed in the area marked by rectangle. More detailed analysis in the crack area were performed using SEM. Subsequently, the analysis of the cracking mechanism were.

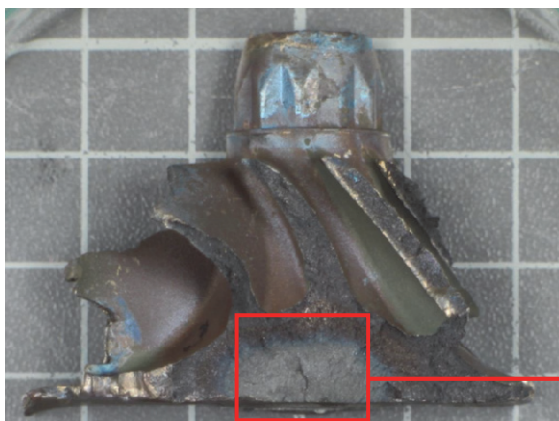


Fig. 1a) Turbine wheel after test. LM image

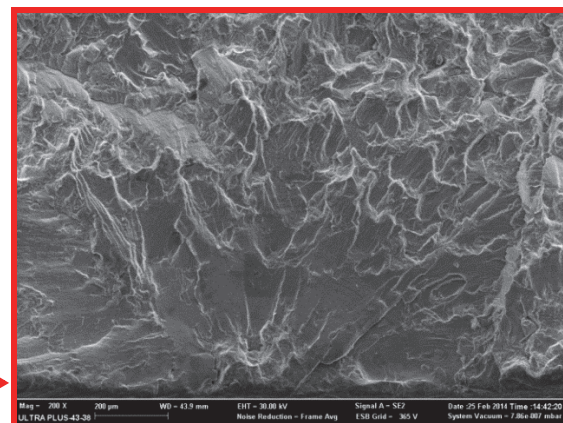


Fig. 1b) SEM image of the area marked by rectangle in Fig. 1a)

Figure 1b shows the SEM image of the crack initiation and its propagation.

Fractographic studies revealed that the cause of the turbine wheel destruction was fatigue cracking at low frequencies. The number of the fatigue slip bands ranges between 100 to 200 per 1 mm and depends on their distance from the location of the crack initiation (Fig. 2).

Cracks 1 and 2 shown in Fig. 3 start at the rear end of the turbine wheel surface. These cracks are also visible after removing the top layer of the material from the rear end of the wheel's surface, and their length ranges from 2 to 3 mm.

The Crack 1 shown in Fig. 3, occurring at the interdendritic region, has been subjected to a chemical microanalysis. SEM image and corresponding SEM-EDX line profiles are shown in Figs 4a, b. The drop of the nickel content associated with an enrichment with oxygen and chrome content was observed across the boundary between dendrites. This indicates that the chromium oxide is being formed at this boundary and that it is penetrated by the oxidizing environment of the exhaust gases.

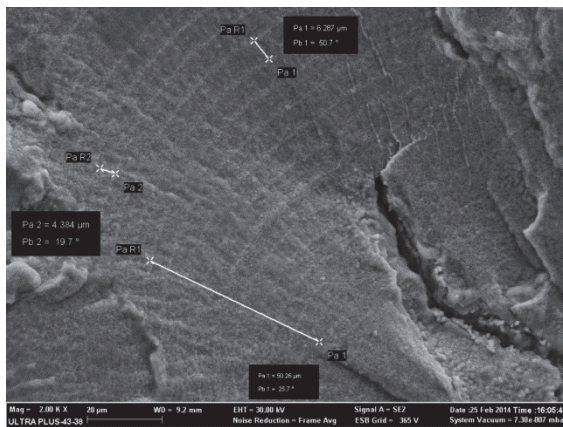


Fig. 2. Fatigue slip marks. SEM image

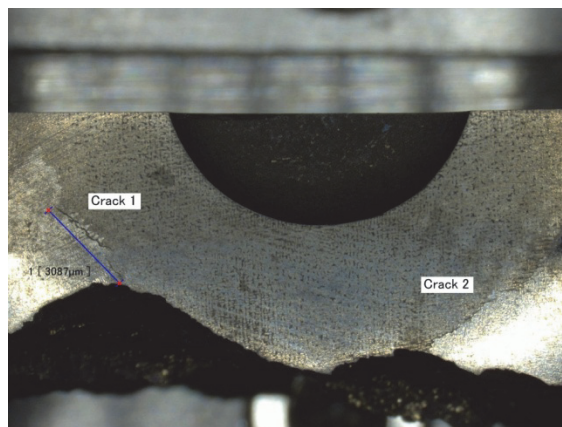


Fig. 3. Cracks on the turbine wheel rear end. LM

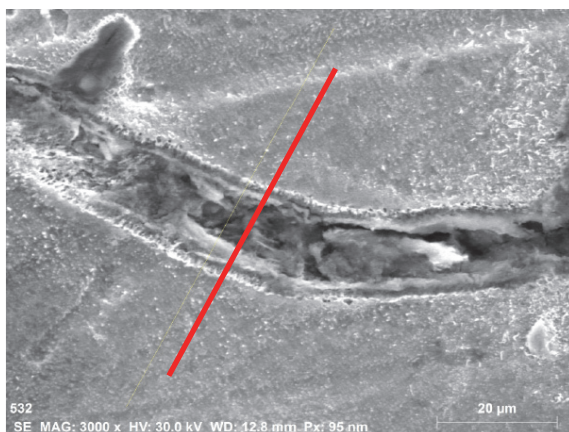


Fig. 4a) Magnified SEM image of Crack 1 shown in Fig. 3

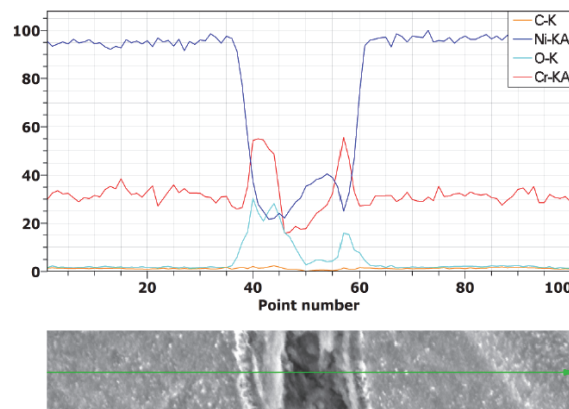


Fig. 4b) SEM-EDX line profiles of C, Ni, O and Cr across the crack

References

- [1] Lothar Engel, Herman Klingele. An Atlas of Metal Damage: surface examination of scanning electron microscope, Wolfe Publishing, London .

The influence of high temperature annealing on the γ' precipitates morphology in CMSX-4 single-crystalline nickel-base superalloy

Tomasz Ratajski^{1,a}, Beata Dubiel^{1,b}, Adam Kruk^{1,c}, Adam Gruszczyński^{1,d},
A. Czyrska-Filemonowicz^{1,e}

¹AGH University of Science and Technology, Faculty of Metals Engineering and Industrial Computer Science, Al. A. Mickiewicza 30, 30-059 Kraków, Poland

^abdubiel@agh.edu.pl, ^bkruczek@agh.edu.pl, ^cratajski@agh.edu.pl, ^dgruszcz@agh.edu.pl, ^eczyrska@agh.edu.pl

The SEM and TEM studies of CMSX-4 single-crystalline nickel-base superalloy were performed to examine microstructural changes during high temperature annealing at temperature 1000 °C. Microstructural analyses were focused mainly on evolution of the morphology and chemical composition of γ and γ' phases. The development of dislocation substructure was also examined.

SEM analysis were carried out by means of Merlin Gemini II of ZEISS. TEM investigation was conducted using JEOL JEM-2010 ARP microscope. Chemical composition was examined by EDS microanalysis using INCA system of Oxford Instruments. Ion beam milling of thin foils for TEM analysis was performed using a Gatan PIPS.

Based on the SEM and TEM analyses it was shown that the microstructure of CMSX-4 superalloy is unstable during annealing at 1000 °C. Figure 1 shows the microstructure after 200 and 500 hours exposure. Although the external load was not applied, the tendency for directional coarsening of γ' precipitates called rafting was observed. Preferentially-oriented plate development of the γ' precipitates without applied stress in CMSX-4 superalloy was reported previously in [1-3]. This phenomenon was attributed to local heterogeneities in chemical composition related with the dendrite structure, which causes the presence of internal dendritic stresses [2].

EDS microanalysis have shown that the thickening of the horizontal γ channels was associated with the decrease of the Co and Cr concentration and slight increase of the Al and Ti content. TEM analysis revealed that with the prolongation of high temperature annealing the dislocation networks were formed on γ - γ' interfaces (Fig. 2). Formation of the dislocation networks on the γ - γ' interfaces relieves the misfit stresses and thus the diffusion between γ and γ' phases is initiated what leads to coalescence of cuboidal γ' precipitates [4].

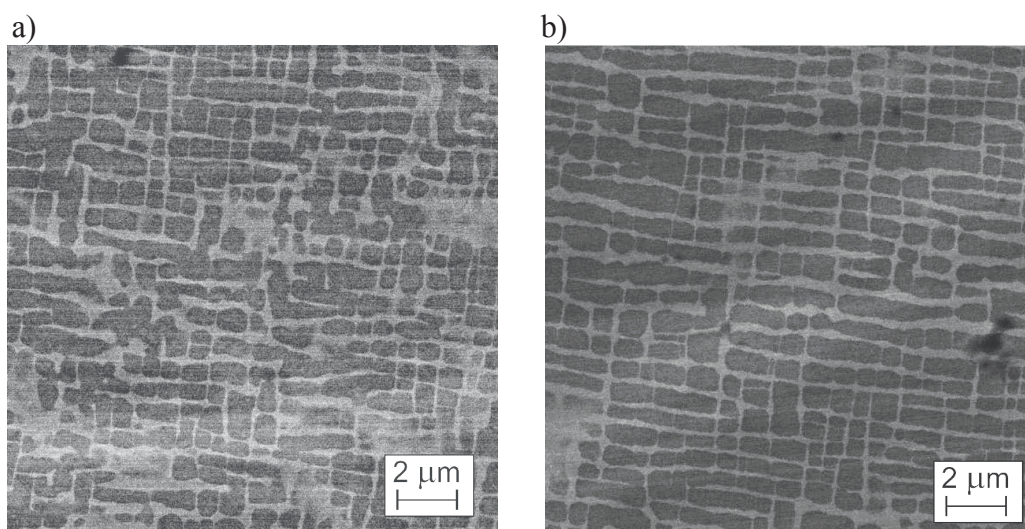


Fig. 1. Microstructure of CMSX-4 superalloy after annealing at 1000 °C for a) 200 h, b) 500 h. SEM

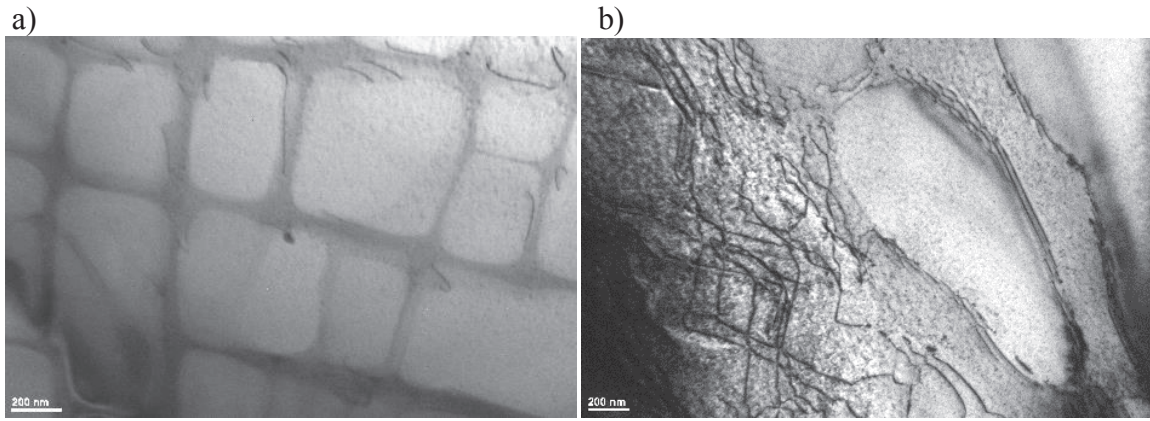


Fig. 2. Dislocation in CMSX-4 superalloy annealed at 1000 °C for a) 200 h, b) 1000 h. TEM

References

- [1] A. Hazotte, J. Lacaze: *Scripta Metall.* Vol. 23 (1989), p. 877.
- [2] A. Epishin, T. Link, U. Brückner, B. Fedelich, P. D. Portella in: *Superalloys 2004*, edited by Kenneth A. Green et al., The Minerals, Metals and Materials Society (2004) p. 537.
- [3] K.Y. Cheng, C.Y. Jo, D.H. Kim, T. Jin, Z.Q. Hua: *Mater. Charact.* Vol. 60 (2009), p. 210.
- [4] R.C. Reed, N. Matan, D.C.Cox, M.A. Rist, C.M.F.Rae: *Acta Mater.* Vol. 47 (1999), p. 3367.

Acknowledgements

The financial support by the National Science Centre, project 2012/07/B/ST8/03392 is gratefully acknowledged. We also thank Mrs K. Płońska-Niżnik (AGH-UST) for her assistance in specimen preparation and Howmet, Exeter, UK for providing the CMSX-4 material.

The structure of the weld layer on stainless X50CrMnNiNbN21-9 steel

Władysław Osuch^a, Grzegorz Michta^b, Adam Kruk^c

AGH University of Science and Technology, Faculty of Metals Engineering and Industrial Computer Science,
International Centre of Electron Microscopy for Materials Science,
Al. A. Mickiewicza 30, 30-059 Kraków, Poland

^aosuch@agh.edu.pl, ^bgmichta@agh.edu.pl, ^ckruczek@agh.edu.pl

This paper describes the examination results of the microstructure of the stellite weld layer on austenitic stainless steel. Microscopic examination was performed with a light microscope (LM), scanning electron (SEM) and transmission (TEM) microscopes. The identification of phases which occurring in the base material, in the weld zone and heat affected zone were performed using electron diffraction and XEDS analysis.

The γ phase was a matrix of base material, in which occurred precipitation of $M_{23}C_6$ and M_6C carbides. In weld zone dendritic structure was present and the basic hardening elements were M_7C_3 carbides. In the heat affected zone were presented both M_7C_3 and $M_{23}C_6$ carbides.

Introduction

The main materials used in the valves of combustion engines are martensitic and austenitic steels. The valves head exposed to the highest temperatures are made of austenitic stainless steel. The valve stem more mechanically loaded, of martensitic stainless steel for engine valves. In addition, to enhance the durability of the valve seat face, austenitic valves head are padded of hard alloy layer - stellite. Stellites are mainly the cobalt-base alloys, less often nickel or iron. In the present study valves head was made of steel X50CrMnNiNbN21-9, and padded layer was made from stellite with the cobalt matrix. The studies performed covered analysis of the microstructure of the weld layer performed using electron microscopy SEM and TEM. The basic phase of imparting high hardness of weld was M_7C_3 carbide. The M_7C_3 carbides are widely and extensively studied and were found that, depending on the chemical composition and crystallization method may be present in alloy in different crystallographic forms [1, 2]. It is assumed that may crystallize in the hexagonal, orthorhombic and trigonal systems. Last form, which occurs most often, is orthorhombic system. Diffraction distinguish these forms it is practically impossible, reciprocal lattice images frequently are not different.

The structure of the weld layer

The microstructure of the valve head is the matrix, which was a γ phase, and isolated carbides, mainly $M_{23}C_6$. In the structure of the stellite weld layer, was also present γ phase (with a different chemical composition) and carbide forming dendritic layouts. In Figure 1 shows the microstructure of the weld layer, observed on a scanning electron microscope and chemical composition spectrum made from selected area, using XEDS analysis method. Has been identified elements in the stellite, such as Cr, Ni, Mo, Si, Fe, W, and of course cobalt.

The basic method of the study was to transmission electron microscopy. Fig. 2 shows the image of the microstructure of the weld layer with the diffraction pattern and its solution. Occurring predominantly carbides is M_7C_3 type carbides. Besides M_7C_3 carbide in the microstructure MC-type carbides were found.

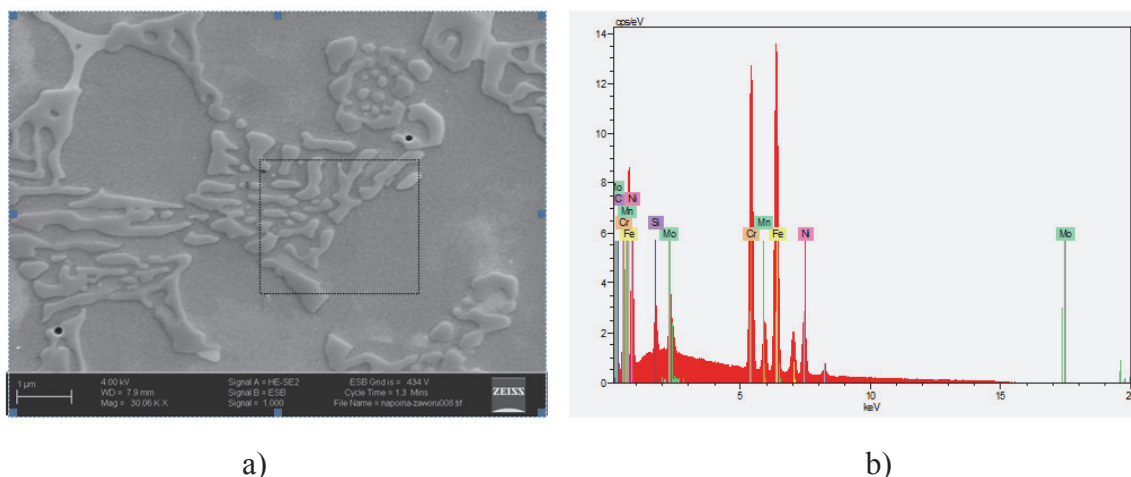


Fig. 1. The microstructure of the weld layer (a) and results of chemical composition XEDS analysis (b), SEM

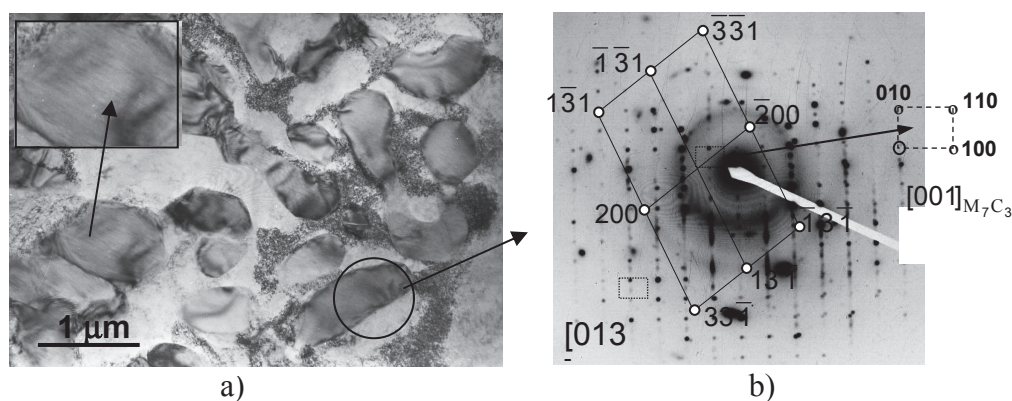


Fig. 2. The microstructure of the weld layer, a microscopic image (a), the diffraction pattern (b) TEM

Summary

Based on the survey, it was found that:

- the welded steel microstructure was a γ phase, in which were present large M_6C and much finer $M_{23}C_6$ carbides precipitate,
- in the weld zone of characteristic dendritic structure occurred, and the basic occurring carbide was M_7C_3 , but MC -type carbides also be found,
- heat affected zone characteristic phases for both the base material and weld zone were observed,
- identification of present phases was made on the basis of diffraction studies and research carried out by the chemical composition XEDS analysis.

References

- [1] W. Dudziński: *Structure defects in the carbides of the type M_7C_3* . Prace Naukowe Instytutu Materialoznawstwa i Mechaniki Technicznej Politechniki Wrocławskiej – nr 45, Monografie nr 17, Wrocław 1986, in polish
- [2] F. Ernst, D. Li, H. Kahn, G.M. Michal, A.H. Heuer: *Acta Mater.* 59 (2011), p. 2268.

Acknowledgement

The authors acknowledge the financial support from the AGH-UST statutory project 2014.

Pad welding of Inconel 625 layer on structural steel used in the power industry

Władysław Osuch^a, Grzegorz Michta^b, Adam Kruk^c

AGH University of Science and Technology, Faculty of Metals Engineering and Industrial Computer Science,
International Centre of Electron Microscopy for Materials Science,

Al. A. Mickiewicza 30, 30-059 Kraków, Poland

^aosuch@agh.edu.pl, ^bgmichta@agh.edu.pl, ^ckruczek@agh.edu.pl

The paper presents the results of microstructure investigation of Inconel 625 padding weld layer on the tight wall elements for steam boiler designed for biomass combustion. The dislocation structure and analysis of the phases present in the layer, using light microscope (LM), and scanning as well as transmission electron microscopes (SEM, TEM) was performed.

In the weld layer the dendritic structure was observed. Main structural element of the weld layer was γ phase with increased dislocation density and stacking faults. In alloy matrix also occurred titanium nitrides TiN, niobium-titanium carbides (Nb, Ti) C, and the Laves phase with a high content of niobium.

Introduction

Tight walls, is one the main structural element of a power boiler. Prefabricated panels are constructed of pipes and flat bars welded alternately and made of steel designed to operate at high temperature in environment of aggressive gases, during combustion.

Particularly aggressive gases are produced during biomass combustion, therefore the water walls in boilers for biomass burning are covered on one side with a layer of material with a particularly high corrosion resistance. The commonly used materials are expensive: nickel based alloys, ie. Inconel 625 alloy

There are developed several methods of nickel alloys pad welding on boiler steel [1-3]. Inconel 625 alloy microstructure constitutes of γ phase as the matrix, γ' phase as precipitations, carbides MC, M_6C , $M_{23}C_6$, Laves and δ phases [4]. In the examined alloy exists, in addition to the matrix γ phase also titanium nitride precipitates of TiN, titanium and niobium (Nb, Ti), C carbides and Laves phases.

This paper presents, results of a comprehensive microstructural investigations, with a particular attention to the complete studies of the microstructure using advanced methods of transmission electron microscopy technique.

Structure of pad welding layer

Figure 1 shows the microstructure of the pad welding layer observed using a scanning electron microscope. Pad welding layer may be characterized by a dendritic structure with precipitates of foreign phases. Figure 2a shows selected examples of phases present in the microstructure. Figure 2a shows group of titanium nitride and niobium carbides. Carbide precipitation varied in size: large primary carbides of size 0.5-1 μm and the small with the size of 20-50 nm were observed. Phase identification based on the selected area electron diffraction technique (SAED). Carbides analysis was carried out using double extraction replica technique. Replicas allow to isolate carbides from the matrix and give clear and legible diffractograms. It was also possible to very accurately determine their shape and size. Fig.2b presents complex of particles, the primary titanium nitride (rectangular) and precipitated on it niobium titanium carbide with compatible orientation. The exact determination of the shape would require tomographic analysis using electron tomography techniques.

In the microstructure Laves phase was present. Some chosen results of investigations conducted on thin foils are shown in Fig. 2c, d. Laves phases particles had the size of about 1 μm , and with characteristic internal substructure. Phase identification was performed using SAED technique.

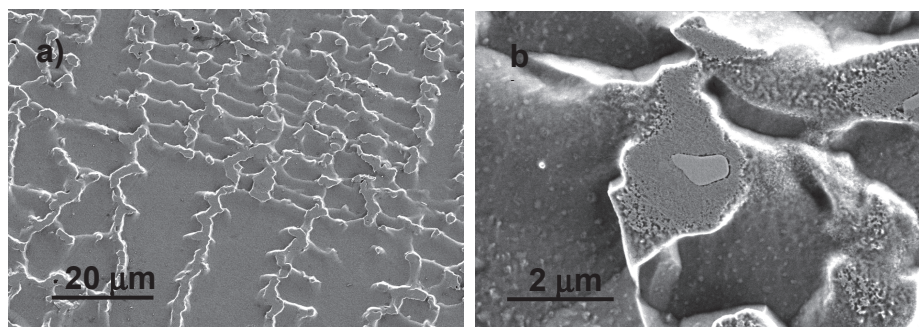


Fig. 1. The microstructure of the pad welding layer observed in SEM

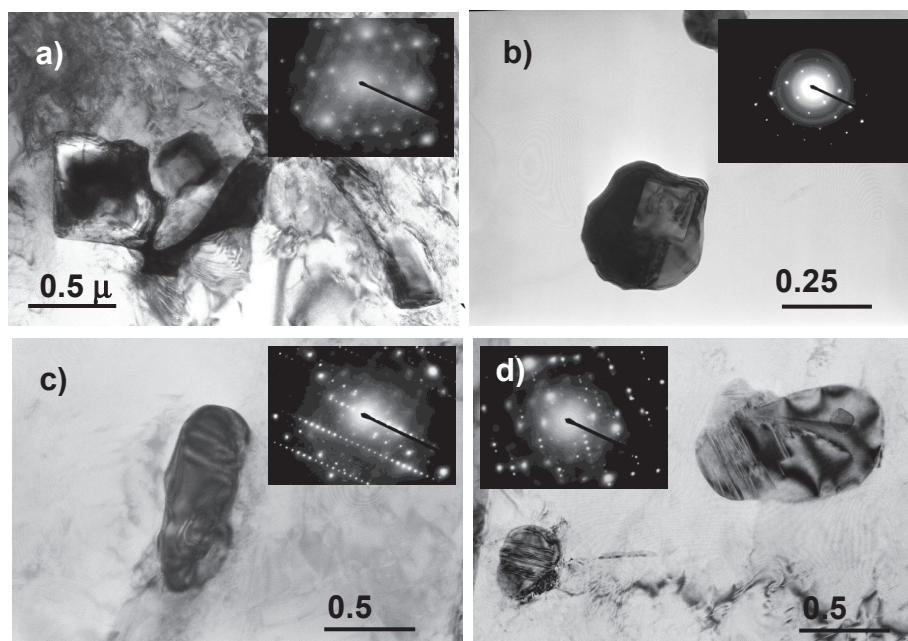


Fig. 2. The microstructure elements observed in TEM; a) the carbides and nitrides within the grains; TEM - a thin foil, b) nitride TiN (inside) and boron carbide (Nb, Ti) C (outside); TEM - double extraction replica, c, d) particles of Laves phase

References

- [1] P. Adamiec, J. Adamiec: *Przegląd Spawalnictwa* 5-6 (2006), p. 11.
- [2] P. Pietrzak, M. Blicharski, S. Dymek: *Hutnik-Wiadomości Hutnicze* 4 (2014), p. 204.
- [3] M. Rozmus, M. Blicharski, J. Kusiński, M. Pako, L. Kusiński, S. Marszycki: *Hutnik-Wiadomości Hutnicze* 4 (2012), p. 260.
- [4] K.H.Chung, J. Lee, R. Rodriguez, E.J. Lavernia: *Metal. Mater. Trans. A* 33A (2002), p. 125.

Acknowledgement

The authors acknowledge the financial support from the AGH-UST statutory project 2014.

Comparative microstructure analysis of the plastically deformed alloy Inconel[®] 718, manufactured by plastic working and Direct Metal Laser Sintering

Krzysztof Żaba^{1,a}, Sandra Puchlerska^{1,b}, Michał Kwiatkowski^{1,c},
Tomasz Tokarski^{1,d}, Maciej Nowosielski^{1,e}

¹AGH University Of Science And Technology, Faculty Of Non-Ferrous Metals, 30-059 Cracow,
Mickiewicza 30 Av., Poland

^akrzyzaba@agh.edu.pl, ^bsandrapu@wp.pl, ^cmkwiat@agh.edu.pl, ^dtokarski@agh.edu.pl, ^emnowosie@agh.edu.pl

Introduction

Nickel superalloys as INCONEL[®] are materials widely used in the aerospace industry among others for diffusers, combustion chamber, shells of gas generators and other [1-3]. In most cases, manufacturing process this type of parts metal strips are used, produced by conventional plastic processing techniques, and thus by either hot and cold rolling. An alternative technology allowing for manufacturing components for jet engines is the technique of 3D printing (additive manufacturing), and most of all Direct Metal Laser Sintering, which is one of the latest achievement in field of additive technologies [4, 5].

The paper presents a comparative analysis of the microstructure of the alloy INCONEL[®] 718 manufactured plastic working methods (PW), and using technology Direct Metal Laser Sintering (DMLS) in the initial state and after deformation.

Methodology

The starting materials for the study were: sheet of INCONEL[®] 718 with thickness 2.15mm manufactured by rolling (condition O) and a plate made of INCONEL[®] 718 with thickness 2.15mm made from a powder with a grain size ~36µm by DMLS technology, with use of printer EOSINT M 280 (EOS company) [4]. During the research the chemical composition analysis was performed by use of Inductively Coupled Plasma (ICP). Then from both materials were cut in a mechanical way samples with dimensions of 2.15mm x 4mm x 20mm and plastic deformed by cold rolling. Rolling was conducted on four-high reversing mill (Fig. 1), in which is equipped the Department of Metal Working and Physical Metallurgy of Non-Ferrous Metals at the Faculty of Non-Ferrous Metals AGH UST.

Rolled samples PW and DMLS were subjected to deformation of 15%, 30%, 45%, 60%. Samples before and after rolling were stretched according to PN-EN ISO 6892-1:2010 P, in order to determine the technological hardening curves. Then at samples of the PW and DMLS in the initial state and after deformation microstructure analysis was performed using analytical scanning electron microscope (SEM) Hitachi SU-70. Based on observations defined grain size and porosity of the tested materials. Were also made a linear analysis of the chemical composition and mapping. In addition, to the samples in the initial state and after rolling surface roughness tests were performed according to PN-EN 10049:2008 P using an optical profilometer Veeco Wyko NT9300 and testing of microhardness Vickers method acc. to PN-EN ISO 6507-1:2007P using microhardness tester Wolpert-Wilson Tukon 2500.

Results

Table 1 presents the results of ICP analysis the chemical composition of the sample PW and chemical composition of the powder EOS NickelAlloy IN718 from which made the plate.

Table 1. Chemical composition of INCONEL[®]718

| Material | S | P | Cu | C | Si | Mn | Co | Al | Ti | Mo | Nb | Cr | Fe | Ni |
|----------|-------|-------|------|------|------|------|------|------|------|-----|------|------|------|------|
| PP | 0,002 | 0,007 | 0,03 | 0,05 | 0,05 | 0,09 | 0,16 | 0,56 | 1,00 | 2,0 | 5,02 | 18,0 | 19,6 | bal. |
| DMLS | 0,015 | 0,015 | 0,25 | 0,08 | 0,35 | 0,32 | 0,2 | 0,61 | 0,95 | 3,0 | 5,10 | 19,0 | 20,1 | bal. |

Example results SEM observations of samples PW and DMLS of alloy Inconel[®]718 in the initial state shown in Fig. 1.

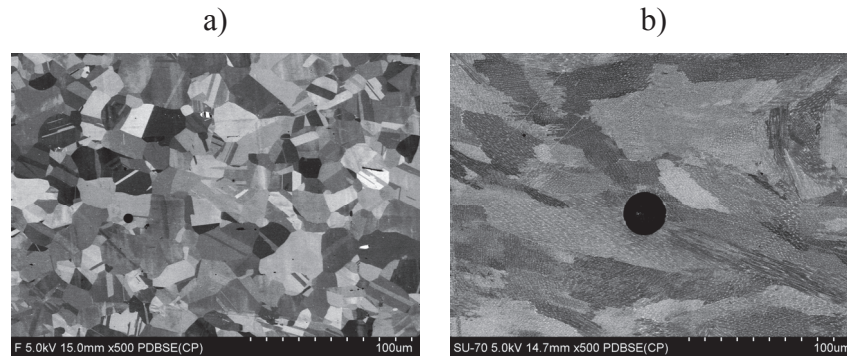


Fig. 1. Results SEM observations of Inconel[®]718 samples in the initial state a) sample PW, b) sample DMLS

Characteristic is the variation of the microstructure for tested materials. The average grain size in the initial state of the PW material is $9.5 \mu\text{m}^2$, while for the material DMLS is $82.9 \mu\text{m}^2$. In the structure of the tested materials was also observed porosity. The average pore size of the material are respectively $5 \mu\text{m}$ for PW and $25 \mu\text{m}$ for DMLS material.

Summary

On the basis of completed research may be provide the following conclusions:

1. Characteristic is the variation of microstructure and grain size of materials made by classic plastic working (sheet) and using DMLS.
2. The material made by DMLS in the initial state has a higher porosity than the material of the PW.

References

- [1] Q.I. Huan: J. Mater. Eng. 8 (2012), p. 92.
- [2] D. Dudzinskia, A. Devilleza, A. Moufkia, D. Larrouquèreb, V. Zerroukib, J. Vigneaub: Int. J. Mach. Tools Manuf. Vol. 44, Issue 4 (2004), p. 439.
- [3] D.F. Paulonis, J. J Schirra, Alloy 718 at Pratt & Whitney – Historical Perspective and Future Challenges, Superalloys 718, 625, 706 and Various Derivatives, The Minerals, Metals & Materials Society (2001).
- [4] Information on <http://www.eos.info/>
- [5] C. Cazmei, F. Caloian: Economics and Finance 3 (2012), p. 457.

Disorientation angles of single-crystal superalloy turbine blades defined by X-ray topography, X-ray and EBSD mapping

Włodzimierz Bogdanowicz^{1,a}, Robert Albrecht^{1,b}, Jan Sieniawski^{2,c},
Krzysztof Kubiak^{2,d}

¹Institute of Material Science, University of Silesia, Bankowa 12, 40-007 Katowice, Poland

²Department of Material Science, Rzeszów University of Technology, W. Pola 2, 35-959 Rzeszów, Poland

^awlodzimierz.bogdanowicz@us.edu.pl, ^bralbrecht@us.edu.pl, ^cjansien@prz.edu.pl, ^dkrkub@prz.edu.pl,
^eonyszko@prz.edu.pl

Introduction

Single-crystal nickel-based superalloys are widely used as material for turbine blades in advanced aircraft engines and stationary gas turbines. As these elements are critical for flight safety much attention should be given for preventing the casting defects. However, dendritic structure and complex shape of turbine blades tend to create many growth defects. The macroscopic investigation of the whole turbine blade especially the crystal orientation is fundamental for preventing damage during service.

Methodology

The single-crystal turbine blade made of CMSX-4 have been investigated. Material for research was produced in Research and Development Laboratory for Aerospace Materials at Rzeszów University of Technology. Casts were obtained in ALD Vacuum Technologies by the Bridgman technique.

In the casts the predominant phase was γ' . The disorientation angle α which describes the deviation of $[001]\gamma'$ crystallographic direction from axis of blade (axis of pulling out) is the key parameter of blade crystal perfection. Angle α can be determined using the X-ray diffractometer by mapping the cross-section surface. Angle β , which describes rotation of γ' phase around blade axis, is an additional parameter of crystal orientation.

Turbine blades airfoil possesses characteristic surface which generally can be described as having spiral shape with leading and trailing edges also spirally shaped. Therefore arrangement, described by angle β , of γ and γ' phases boundaries relative to the leading and trailing edges should play an important role in turbine blade strength. Angle β is even more important in the case of cooled turbine blades with thin walls.

Results and conclusions

X-ray topography study was conducted to obtain maps and measurements of the *mutual* disorientation of the blade root subgrains. Disorientation angles α and β were defined for subgrains from X-ray diffraction maps obtained by using diffractometer of EFG company and by EBSD method. Angle of the subgrains mutual disorientation ξ were measured from topograms obtained by Auleytner topography method with divergent beam (micro-focus X-ray source).

The relationship of angle ξ in respect to α and β was determined analytically and then verified with the use of experimentally defined value of α , β and ξ .

An applied methodology of 1 mm foil preparation for TEM studies on neutron irradiated austenitic stainless steels used in nuclear power plants

**Petra Bublíková¹, Vít Rosnecký¹, Jan Michalička¹, Hygreeva Kiran Namburi¹,
Miroslava Ernestová², Eliška Keilová², Jan Kočík²**

¹Research Centre Rez, 250 68 Husinec-Řež, Czech Republic

²ÚJV Rez, 250 68 Husinec-Řež, Czech Republic

bui@cvrez.cz

Austenitic stainless steels are being mostly used for decades as materials for structural applications in industries, constructions etc. In this paper, we would like to present our work related to the application of austenitic steels as a structural material in nuclear power plants. The investigated material is 300-series austenitic stainless steel commonly used for Reactor Vessel Internals (RVI) of Pressurized Water Reactor (PWR) nuclear plants. During the reactor operation period, which can exceed 60 years, the reactor internals are exposed to a high neutron irradiation dose. The irradiation conditions lead to a change in microstructure of the material at nanometric scale. It includes radiation-induced defects (e.g. dislocation loops, precipitates, cavities, “black-dots”) and solutes radiation-induced segregation at microstructure sinks (e.g. grain boundaries, dislocations, precipitates).

Due to the effect of radiation damage, the materials may turn out to be hardened, swelled and/or to be sensitive to Irradiation Assisted Stress Corrosion Cracking (IASCC). Hence, there is a prominent research interest to characterize the materials and to understand the physical basis of the radiation degradation mechanisms using Transmission Electron Microscopy (TEM).

Microstructural characterization of neutron irradiated materials by TEM requires enhanced sample preparation methodologies. In our study, the tailored methodology based on preparation of small thin foils for TEM analysis was developed and applied on a miniaturized tensile specimen with shank diameter of 2 mm. Actual foil size of diameter 1 mm has to be smaller compared to the classical TEM foil size, because of the small shank diameter and high activity of the studied material.

The paper describes whole process from bulk sample handling, remote-controlled material cutting in shielded hot-cells, polishing in glove-boxes and final procedure of electrolytic polishing of transparent 1 mm foils. Finally, the results of TEM microanalysis of radiation-induced defects observed at small foils are illustrated.

Degradation analysis of Thermal Barrier Coatings and modified aluminide coatings using S/TEM

Radosław Swadźba^{1,a}, Jerzy Wiedermann^{1b}, Lucjan Swadźba^{2c},
Marek Hetmańczyk^{2d}

¹Institute for Ferrous Metallurgy, ul. K. Miarki 12-14, 44-100 Gliwice, Poland

²Silesian University of Technology, ul. Krasinskiego 8, 40-019 Katowice, Poland

^arswadzba@gmail.com, ^bjwiedermann@imz.pl, ^clucjan.swadzba@polsl.pl, ^dmarek.hetmanczyk@polsl.pl

High temperature coatings such as Thermal Barrier Coatings (TBC) with diffusion aluminide coatings are applied on blades and vanes of modern jet engines in order to provide significant temperature reduction as well as oxidation resistance leading to prolonged lifetimes and efficiency. The most advanced TBCs consist of yttria stabilized zirconia (YSZ) top coating which is deposited using electron beam physical vapor deposition (EB-PVD) method providing a unique strain tolerant columnar structure. The most common bond coatings for these TBCs are platinum modified aluminide coatings that provide excellent high temperature oxidation resistance. However, due to high prices of Pt new alternatives are sought for. Since Pd is two times cheaper than Pt it is currently considered as a beneficial and cost-effective replacement for Pt. The role of the bond coating is to provide excellent high temperature oxidation resistance by forming a slow growing thermally grown oxide (TGO – usually α -alumina) which is considered as the most crucial component of the whole TBC system since it ensures a good adhesion between the ceramic top coat (YSZ) and the metallic bond coating.

The results presented in this paper concern the evolution of Pt and Pd-Pt-aluminide bond coating's microstructure during high temperature oxidation at 1100 °C. Due to its low thickness (up to 4-7 μm) the microstructure of the Al_2O_3 TGO can only be studied in detail using high resolution S/TEM method. The phenomena including the growth of protective Al_2O_3 oxide scale, phase transformation of θ to α -alumina and ionic segregation of Reactive Elements (Hf, Zr and Y) to the grain boundaries of Al_2O_3 are presented. In addition, the diffusion processes of elements such as Ta from the metallic bond coating through the grain boundaries of β phase to the oxide scale are analyzed and their influence is studied. The samples for S/TEM analysis were prepared from the triple interface between the bond coating, TGO and YSZ using Focused Ion Beam (FIB) method.

Structure (XRD) and the microstructure (TEM, SEM, AFM) analysis of bulk amorphous and nanocrystalline alloys based on FeCoB

**Anna Bukowska^{1,a}, Konrad Gruszka^{2,b}, Marcin Nabiałek^{2,c}, Katarzyna Błoch^{2,d},
Adrian Łukaszewicz^{1,e}, Michał Szota^{1,f}**

¹Czestochowa University of Technology, Faculty of Production Engineering and Materials Technology, Materials Engineering Institute, 19 Armii Krajowej Av., 42-200 Czestochowa, Poland

²Czestochowa University of Technology, Faculty of Production Engineering and Materials Technology, Institute of Physics, 19 Armii Krajowej Av., 42-200 Czestochowa, Poland

^aabukowska@wip.pcz.pl, ^bkgruszka@wip.pcz.pl, ^cnmarcell@wp.pl, ^d23kasia1@wp.pl, ^ealukaszewicz@wip.pcz.pl, ^fmszota@wp.pl

The diffusion processes in amorphous materials cause changes in their microstructure. These processes occur during isothermal annealing, and have a direct impact on the properties of amorphous and nanocrystalline alloys. The control of the evolution of amorphous materials and lowering their internal energy as a result of atoms transition through subsequent potential barriers describing metastable states, is a direct factor in designing functional properties of modern materials. The paper presents the results of tests carried out for the group of five alloys $\text{Fe}_{62-x}\text{Co}_{10}\text{Y}_8\text{Me}_x\text{B}_{20}$ (where Me = Cr, Be and Cu $x = 0$ or 1), obtained by a suction-casting method. The bulk amorphous samples were obtained in the form of plates with a thickness of 0.5 mm. The structure and microstructure of the investigated plates in the as-quenched and after annealing state, were studied using: scanning and transmission electron microscopy, atomic force microscopy, a computer tomography and X-ray diffractometry. Moreover, for samples after heat treatment Rietveld's analysis was performed and crystalline phases were determined. On the basis of studies carried out, there is opportunity to observe the structure and microstructure of amorphous and nanocrystalline alloys. Additionally microscopic studies combined with X-ray studies and computer tomography, allowed the observation of the diffusion effects occurring in the material.

Investigation of pressure induced whisker formation on pure tin electroplated copper and brass surfaces

Anna Sycheva^{1,a}, Adam Radanyi^{2,b} and Zoltan Gacsi^{3,c}

¹ MTA-ME Materials Science Research Group, Miskolc, Hungary

²Institute of Physical Metallurgy, Metal Forming and Nanotechnology, University of Miskolc, Miskolc, Hungary

³Institute of Physical Metallurgy, Metal Forming and Nanotechnology, University of Miskolc, Miskolc, Hungary

^aa.sycheva@uni-miskolc.hu, ^bdzsorden@gmail.com, ^cfemtangz@uni-miskolc.hu

Introduction

In the last decade, the traditional tin-lead solders in electronics have been gradually replaced by lead-free soldering technologies. Along with this it is necessary to develop alternative solders; these are lead-free ones based on tin. Tin possesses excellent properties such as ductility, electrical conductivity and corrosion resistance. Even at room temperature on the surface of some low melting metals including tin, cadmium and zinc, whiskers formation is observed. The whiskers formed on the tin surface are single crystals of several micrometers in diameter and up to several millimeters long, and they are electrically conductive. These properties pose a serious risk to small electronic devices causing a short circuit that may lead to the component/device failure. For decades, the formation of whiskers on tin has been prevented by lead alloying. But due to the strict EU regulations the use of lead for this purpose is not allowed any longer [1]. *The aim of this work* is the investigation of tin whisker formation under operation conditions of electrical contacts maximally close to the real ones, i.e. under mechanical load on the contact surface. The present work also reports the effect of substrate composition and tin plating thickness on pressure induced whisker formation.

Experimental

Pure Cu and brass substrates were electroplated with pure Sn using methane sulfonic acidic industrial bath obtained from a printed circuit board (PCB) manufacturer (Eurocircuits Co. Ltd. Eger). For this purpose, a specially shaped container “Hull cell” was used having the cathode at a pre-defined angle to the anode to produce a range of current densities. As a result, the thickness of Sn film obtained varied from 7 to 37 μm . Under ambient conditions, the films were fixed on a stage and compressed by on a steel bearing ball forming imprint on the surface of the sample. A total of 20 imprints on the copper and brass samples were produced applying 2 and 24 hours exposure time and pressure of 3000 MPa at different Sn deposit thicknesses (7, 11, 14, 28 and 37 μm). The device produces the mechanical stress to be measured on the surface of the contacts by loading it with force F via a steel ball (radius $r_l = 1.5$ mm). In this case the mechanical stress arising at the loading (sphere-plain contact) point is the Hertz stress, which can be calculated by the following equation:

$$\sigma = (1/\pi)\{[1.5 F E^2]/[r(1-\lambda^2)]^2\}^{1/3} = (F^{1/3})(1/\pi)\{[1.5 E^2]/[r(1-\lambda^2)]^2\}^{1/3} \quad (1)$$

where F – compressing force; $E = 2 [E_1 E_2 / (E_1 + E_2)]$ – harmonic mean of the elastic modulus, if the elastic moduli of the materials in contact are E_1 and E_2 ; r – radius of the ball; λ – Poisson coefficient of the materials in contact (in this case it is that of the contact coating, i.e. tin). The imprints were of a regular circle shape and in most cases whiskers are formed along the imprint boundary. The microstructure of tin whiskers obtained, their length and number at the boundary of each imprint were studied using Zeiss EVO MA Correlative Light Electron Microscope (CLEM). To calculate the formation and growth rates of whiskers, the number of whiskers was related to exposure time and average whisker length accordingly.

Results and discussion

The experimental results showed that mechanical stress induced the formation of whiskers, while their growth depended on the grain microstructures and the grain-boundary distribution. After compression recrystallization in the mechanically deformed region creates many new grain boundaries. New grain boundaries provide faster diffusion routes of atoms, to which effect whiskers are formed at the boundary between the deformed and non-deformed surface (Fig. 1).

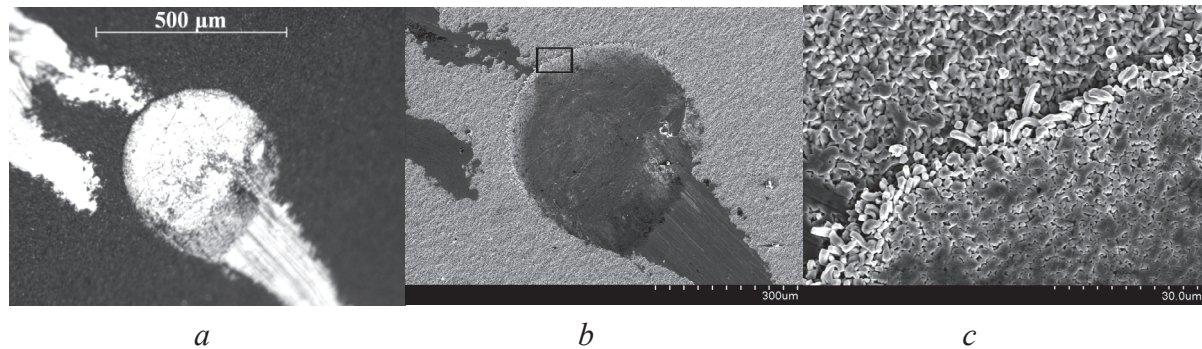


Fig. 1. Light (a) and Scanning Electron Microscope micrographs (b) of the imprint obtained after 24 hours at 3000 MPa on a 7 micrometer thick Sn-layer with copper substrate and its boundary with tin whiskers (c)

It has been shown that increasing the thickness of tin plating both the length and number of the formed whiskers decrease. This is due to that a thicker tin layer better distributes and neutralizes the mechanical stress and thereby suppresses the whisker growth. A current density of 2.7 A/dm^2 proves to be the most optimal to decrease the risk of whisker formation under the given experimental conditions and corresponds to an $11 \text{ }\mu\text{m}$ thick tin plating on both substrates.

It has been established that in the case of brass substrates the whiskers are longer but their number is smaller than in the case of copper (for copper: average length – $4.5 \text{ }\mu\text{m}$, number – 1150, for brass: average length – $12 \text{ }\mu\text{m}$, number – 600). For this reason, the industrial use of brass is not recommended. This observation can be explained by higher hardness of brass, which does not neutralize but rather induces additional mechanical stress in the tin plating. However, it is believed in literature that the presence of Zn in the brass substrates suppresses the formation of Cu-Sn intermetallic compounds, thereby reducing the risk of growth of long whiskers. In our case, the formation of intermetallide is not observed because the plating has been obtained at room temperature.

Acknowledgements

The authors would like to express their gratitude to Dr. A. Rónaföldi for the experimental setup.

Anna Sycheva: This research was realized in the frames of the highly important „National Excellence Program - working out and operating an inland student and researcher support, identification number TÁMOP 4.2.4.A/2-11-1-2012-0001. The project is realized with the help of European Union and Hungary subsidy and co-financing by the European Social Fund.

Adam Radanyi, Zoltan Gacsi: The research work presented in this paper (partially) based on the results achieved within the TÁMOP-4.2.1.B-10/2/KONV-2010-0001 project and carried out as part of the TÁMOP-4.2.2.A-11/1/KONV-2012-0019 project in the framework of the New Széchenyi Plan. The realization of this project is supported by the European Union, and co-financed by the European Social Fund.

References

- [1] A. Sycheva, A. Radanyi and Z. Gacsi: Mater. Sci. Forum 790-791 (2014) p. 271.

Applications of electron microscope in infectious diseases

Virendra Kumar

National JALMA Institute for Leprosy & Other Mycobacterial Diseases, (ICMR)

Taj ganj Agra-282004 (INDIA),

e-mail: vksjalma@gmail.com

Introduction

Electron microscopy used to investigate the detailed structure and configuration of the mycobacteria which may lead to an understanding the role of infections and in transmitting the diseases. *Mycobacterium tuberculosis*, and *Mycobacterium leprae* is a slightly curved [1] or straight rod-shaped. *M. tuberculosis* causes tuberculosis which is a major global health problem. In 2011, there were 8.7 million new cases of active tuberculosis (TB) worldwide and 1.4 million deaths, plus 430,000 deaths among HIV-infected patients. While India is the second-most populous country in the world, having more new TB cases annually than any other country. However in leprosy patients the presence of *M. leprae* has been shown by electron microscopy in Schwann cell of unmyelinated nerve fibres, macrophages, endothelial cells [2] and perineurial cells of leprosy patients.

Methodology

Small pieces of nerve biopsy were fixed in glutaraldehyde for 6 hrs. followed by OsO₄ for post fixation. The fixed tissues were then dehydrated in ascending grades of alcohol. Later, these were immersed in propylene oxide and embedded in Spurr's resin. Finally, the tissues were polymerized overnight at 70°C and blocks were made. 1µm thick semithin sections of the entire fascicle were cut and examined in light microscope (LM) after staining in toluidine blue. The ultrathin sections were cut in an ultramicrotome and stained in uranyl acetate & lead citrate solutions to observe in electron microscope. On the other hand, the development of biofilms in different Mycobacteria has been reported to form on solid substrates in contact with moisture, on soft tissue surfaces in living organisms, and at liquid air interfaces. Attachment of mycobacteria involved in biofilm formation in the liquid air interface is a complex process, with many variables such as pH, nutrient levels, iron, oxygen, ionic strength and temperature, affecting the outcome. The standard Microtiter plate assay was used in the present study to observed the effect of pH, temperature, and OADC (oleic acid albumin dextrose catalase) enrichment in Sauton's medium slow grower and fast grower mycobacteria like *M. smegmatis*, *M. fortuitum*, *M. avium* and *M. tuberculosis*. The genes responsible for biofilm formation has been identified by micro array hybridisation techniques and the homologous genes were confirmed by Real Time PCR.

Results and conclusion

A systematic ultrastructural of peripheral nerves across the spectrum of leprosy was studied with an aim to better understanding the pathogenesis of bacilli and nerve involvement in leprosy by light and electron microscope. Therefore, we conducted an ultra-structural study for understanding the changes in architecture of the bacilli, Schwann cells and endothelial cell in peripheral nerves of treated leprosy patients. The pathogenesis of nerve destruction varies in leprosy considerably along the spectrum. The study has begun to shed new light on some aspects of the infection of *Mycobacterium leprae* and phenomenon has opened new avenue of research and possible mechanism of pathogenesis in borderline tuberculoid (BT) / lepromatous leprosy (LL). It was observed that in BT cases hypertrophy of the endothelial cells to such an extent that the lumen of the vessels becomes narrower and completely closed causing ischemia in patients. In tuberculoid type and BT leprosy, the degenerative changes of Schwann cells and presence of perineurial and perivascular cuffing by mononuclear cells. The endoneurial blood vessels showed thickening of basement membrane with

hypertrophy of endothelial cell leading to narrowing or complete occlusion of lumen and patient causing ischemia. On the other hand in LL patients many intact bacilli was observed in endothelial cell of endoneural blood vessels, the lumen of the blood vessels is open and vascular leakage facilitating entry of *M. leprae* into the nerves.

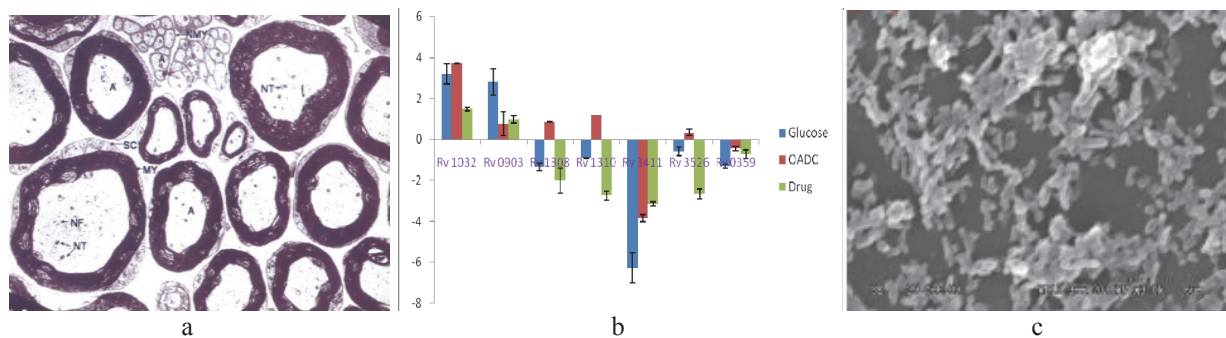


Fig. 1. Ultrastructure of peripheral nerves showing Myelinated and Unmyelinated fibres in leprosy patients. Quantitative real time PCR profiling of selecting genes in *M. tuberculosis* (Fig. b). Ultrastructure of Biofilm in *M. tuberculosis* (Fig. c)

Electron microscopic study of Biofilm forming Mycobacteria

On the other hand all the Mycobacteria are formed biofilms to protect from host defences, antibiotics and from harsh environmental conditions. In the natural world more than 99% of bacteria exist as biofilms. According to NIH report about 65% of all human infections are associated with biofilms formation. The development of biofilms has been reported to form on solid substrates in contact with moisture, on soft tissue surfaces in living organisms, and at liquid air interfaces.

We had taken four Mycobacteria species such as *M. fortuitum*, *M. avium* and *M. tuberculosis*. *M. smegmatis* subcultured and developed into biofilm at laboratory conditions, characterized biochemically and molecularly. Antibiotic susceptibility of biofilms at ultrastructural level was also studied in fast growing clinical isolates of *M. smegmatis* in presence of Streptomycin, Isoniazid Rifampicin, Ethambutol and Pyrazinamide [3]. *M. smegmatis*, a non-pathogenic species which was homologous with *M. tuberculosis*, was commonly used as a surrogate host for pathogenic *M. tuberculosis* [4]. However, many mycobacterial species are known to form biofilms, little is known about either the genetic requirements, patterns of gene expression, or the nature of the extracellular matrix of mycobacteria. In micro array hybridisation we have found that six genes were expressed in *M. avium*. In *M. tuberculosis* MDR isolates, seven genes were expressed and two genes Rv0359 and Rv3526 were homologous as confirmed by RT-PCR and reported earlier in *P. areuginosa* and *M. avium*. Therefore, these two genes Rv0359 and Rv3526 might be responsible for biofilm formation in *M. tuberculosis* MDR isolates.

A more comprehensive understanding of processes connected with biofilm development in different stress conditions will lead to new knowledge that would help in developing novel and effective control strategies for prevention of biofilms in clinically relevant situations and hence in improvement in patient management.

References

- [1] V. Kumar: Micro. Res. Tech. 71 (2008), p. 614.
- [2] D.M. Scollard: Microb. Infect. 2 (2000), p. 1835.
- [3] J.W. Costerton, P.S. Stewart, E.P. Greenberg: Science 284 (1999), p. 1318.
- [4] R.M. Donlan and J.W. Costerton: Clinical Microbiology Reviews 15 (2002), p. 167.

Advanced study of the atomic and electronic structure of the defects in metal nitride films

Zaoli Zhang¹, Rostislav Daniel², Christian Mitterer², Gerhard Dehm^{1,#}

¹Erich Schmid Institute of Materials Science, Austrian Academy of Sciences, Leoben, Austria

²Department of Physical Metallurgy and Materials Testing, Montanuniversität Leoben, Austria

Now: Max-Planck-Institut für Eisenforschung, Düsseldorf, Germany

e-mail: zaoli.zhang@oeaw.ac.at

Introduction

Transition metal nitrides (TMN) have found wide-spread applications in the cutting- and machining-tool industry due to their extreme hardness, thermal stability and resistance to corrosion. The increasing demand of these nitrides requires an in-depth understanding of their structures at the atomic scale. This has led to numerous experimental and theoretical researches. Among TMNs, CrN exhibits fascinating structural, magnetic, and electronic properties that are of fundamental importance to condensed-matter physics [1-6]. Detailed studies of the structure of CrN will definitely reveal its unique property. On the other hand, it is inevitable to generate structural disorders during film deposition, where various defects can be introduced. Apparently, these defects will obviously influence the properties of CrN films. Recently available aberration corrected TEM enables quantitative characterization and evaluation of materials atomic structure. In this study, we apply C_s -corrected HRTEM, quantitative electron diffraction, and EELS analysis to understand the atomic and electronic structure of defects in CrN films.

Experimental

The films used in this study were deposited by reactive direct current magnetron sputtering of a Cr target in an Ar+N₂ atmosphere at a constant total pressure of 1 Pa, a target power of 6 kW, and a temperature of 350°C. A TEM/STEM JEOL 2100F operated at 200 kV and equipped with an image-side C_s -corrector and a Gatan imaging filter (Tridiem) was used to characterize the film structure. The specimen consisting of three sublayers deposited under different substrate bias voltages, i.e. -40, -120 and -40 V, and having each 1 μm thickness was also grown.

Results

The first part of this paper will be ordered defects, i.e. nitrogen (N) vacancies, which were often found at the interface and well distributed at the {111} planes. These ordered N vacancies result in the formation of numerous stacking faults, which are accompanied by strongly distorted interface regions (a defective layers, Figure 1), and lead to a reduced lattice constant. The strain measurement by geometrical phase analysis shows an isotropic distribution within the defective layer (Figure 1). Spectrum analysis reveals that triggered by N vacancy change the core-loss and low-loss spectra can dramatically change, i.e. N-K and L_{2,3} edges, which are comparable to the recently calculated results by *ab-initio* method. Combining the independent image analysis and spectra analysis, some further conclusions are drawn: i) a generalized relationship between the lattice constant and N vacancy concentration in CrN is established [5], ii) the ionicity change in CrN crystal with the N vacancy is shown; iii) most interestingly, a relation between electronic structure changes and elastic deformation has been derived, revealing that the elastic deformation may lead to a detectable change in L₃/L₂ ratio of Cr-L edge.

Randomly distributed defects in the films are also explored in a quantitative way using quantitative electron diffraction, HRTEM and spectrum analysis. Quantitative electron diffraction analysis reveals that the intensity ratios of (111), and (200) reflections (I_{111}/I_{200}) sensibly varies with the defect density. It is seen that the ratio noticeably increase from the layer (-40 V) to the -120 V

layer. A high defect density also results in a slight variation in electronic structure which might be detected by EELS measurements on the layers grown at different bias voltage. It is noted that a higher randomly distributed defect density in the film can also give a detectable change in the near edge fine structure of N-K and Cr-L_{2,3}.

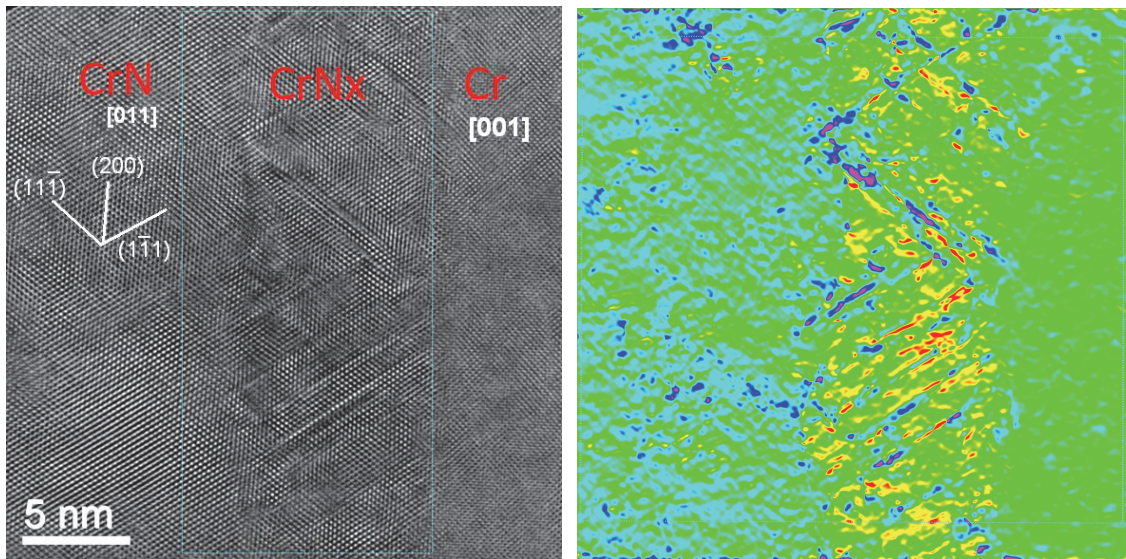


Fig. 1. Left: a typical HRTEM image of the CrN/Cr interface along CrN [011] direction (Wien filtered), a defect layer between Cr and CrN originates from the ordered N-vacancies on {111} planes. Right: a strain map (e_{yy}) obtained by geometrical phase analysis, demonstrating the anisotropic distribution of strain within the defective CrN_x layer

References

- [1] B.Alling et al: Physical Review B 82 (2010), p.184430.
- [2] R. Daniel et al: Acta Mater. 58 (2010), p. 2621.
- [3] X.Y. Zhang et al: Physical Review B 83 (2011), p. 165205.
- [4] SM Wang et al: Physical Review B 86 (2012), p. 064111.
- [5] Z.L. Zhang et al: Physical Review B 87 (2013), p.014104.
- [6] A.S. Botana et al: Physical Review B 85 (2012), p. 235118.
- [7] Acknowledgements: Gabriele Moser and Herwig Felber are gratefully acknowledged for their help with sample preparation, thanks are given to Dr.Hong Li for *ab-initio* calculations. B. Sartory, Materials Center Leoben Forschung GmbH, Leoben, Austria.

Effect of hydrogen on corrosion of RE-containing magnesium alloys in sodium sulfate solution

Bartosz Chmiela^{a*}, Adrian Mościcki^b, Maria Sozańska^c

Silesian University of Technology, Faculty of Materials Science and Metallurgy,
Kraśińskiego 8, 40-019 Katowice, Poland

^abartosz.chmiela@polsl.pl, ^badrian.moscicki@polsl.pl, ^cmaria.sozanska@polsl.pl

Keywords: magnesium alloys, corrosion, hydrides, hydrogen

Introduction

Modern magnesium alloys containing rare-earth elements from the Mg-Y-RE-Zr and Mg-Al-RE systems are characterized by low density and good mechanical properties. Therefore these alloys are used in automotive and aerospace industries. However, magnesium alloys offer insufficient corrosion resistance in environments containing electrolyte solutions. Hydrogen is the main corrosive factor appearing during chemical reactions between magnesium and water in electrolyte solution. Selecting rare-earth-containing magnesium alloys allows to analyse the various effects of hydrogen on these materials. The microstructure of WE43 magnesium alloy consists of α -Mg matrix and precipitates of various intermetallic phases: $Mg_{12}NdY$, $Mg_{14}Nd_2Y$, MgY . But the microstructure of AE44 alloy consists of precipitates of other phases ($Al_{11}RE_3$, Al_2RE , $Al_{10}RE_2Mn_7$) in α -Mg matrix.

Microstructure of the alloys before and after corrosion was observed using scanning electron microscope (SEM) and scanning transmission electron microscope (STEM), equipped with energy dispersive X-ray spectrometer (EDS). Phase identification was performed by XRD and EBSD analysis.

The results showed that when samples were immersed in 0.1M sodium sulfate solution, hydrogen atoms diffused into the material and enriched in intermetallic phases. With the increase of immersion time, magnesium hydride would be brittle fractured when the inner stress caused by hydrogen pressure and expansion stress of formation of magnesium hydride was higher than fracture strength. The solubility of hydrogen in magnesium alloys increases for alloys containing yttrium, zirconium and rare-earth elements. Precipitates of these phases can be hydrogen traps and the hydrides ZrH, ZrH₂, YH₂ and NdH₂ can form in these alloys.

Authors Index

Albrecht R. 66, 233, 307
 Altskär A. 53
 Andrzejczuk M. 124, 132
 Apel P. 110

Bailey R.J. 32
 Bajer J. 140
 Bała P. 102
 Bala P. 93
 Bals S. 49
 Banerjee S. 223
 Barber A.H. 32
 Baretzky B. 90
 Barthel J. 17, 59
 Bazarnik P. 95, 124
 Beanland R. 85
 Beigmohamadi M. 17
 Berent K. 97, 151
 Bernáš T. 257
 Bester M. 221
 Bieda M. 97, 133, 273
 Bigaj M. 135
 Binkowski M. 257
 Błaż L. 75, 285, 248
 Blicharski M. 283
 Błoch K. 96, 198, 207, 310
 Blomqvist C.H. 53
 Bobrowski P. 55, 97
 Boccaccini A.R. 192
 Boczek S. 135, 176
 Bogdanowicz W. 66, 99, 170, 233, 307
 Bohlen J. 253
 Bonollo F. 98
 Borysiuk J. 88, 137
 Brabetz M. 73
 Brisset F. 97
 Brunetti G. 8
 Bubliková P. 308
 Buffat P.A. 41, 295
 Bukowska A. 310
 Busquets-Mataix D. 211
 Butruk B. 291

Caron J. 38
 Carter C. Barry 3
 Cempura G. 51, 61, 192, 289
 Chin R. 23
 Chmiela B. 68, 317
 Chromiński W. 63
 Chulist R. 265
 Chuvilin A. 6
 Ciecierska E. 95
 Cieniek Ł. 83, 138, 163
 Cieslar M. 140, 209, 253
 Cimenoglu H. 61
 Clemens H. 73
 Cobden D.H. 85
 Cora I. 131
 Coufalova E. 261
 Cwajna J. 275
 Czaja P. 188, 265
 Czepe T. 142, 188, 231, 234, 265

Czerwiński A. 124
 Czulak A. 95
 Czyska-Filemonowicz A. 25, 41, 51, 61, 126, 192, 194,
 289, 295, 299

Dahmen U. 36
 Daniel R. 315
 Datta R. 57
 Dehm G. 315
 Delille D. 6
 Dercz G. 99
 Dijkstra J.M. 12
 Dileep K. 57
 Dimitrakopoulos G. 120
 Dłużewski P. 67, 88, 130
 Dódony I. 131
 Dörfel I. 213
 Dosta S. 25
 Drsticka M. 261
 Dubiel B. 25, 289, 299
 Dubiel M. 27
 Dudek J. 125
 Dudek M. 34
 Dudzińska K. 144
 Dunin-Borkowski R.E. 38
 Dutkiewicz J. 180, 188, 265
 Dworecka J. 148
 Dymek S. 25, 100, 164, 283

Eggeman A.S. 19
 Ernestová M. 308

Fabrizi A. 98
 Fahrnbauer F. 128
 Faryna M. 55, 97, 203
 Ferraro S. 98
 Frank L. 76
 Fraunhofer C. 128
 Frocisz Ł. 102
 Fronczek D.M. 267
 Fulin J. 261

Gacsi Z. 311
 Gajewska M. 269
 Galanis A.S. 10
 Galin R. 240
 Galuskina I. 255
 Garbacz H. 242
 Garbaczewska G. 259
 Garzel G. 142
 Gautam A. 36
 Gawlik M. 135
 Georgiou E. 25
 Gerlach J.W. 47
 Giorgio S. 83
 Gluch J. 72
 Gołaszewski A. 149
 Gołombek K. 205
 Góral A. 142, 151, 180, 279
 Goris B. 49
 Goryczka T. 79
 Grajcar A. 153

- Grobler H. 113
 Grogger W. 43
 Gruszczyński A. 192, 299, 301
 Gruszka K. 310
 Gryboś J. 59, 122
 Grzegorzczak B. 155
 Guedj C. 115
 Gurdziel W. 99
 Gustafsson S. 53
- Haider M. 4
 Hasiów-Jaroszewska B. 259, 263
 Hébert C. 45
 Heinzig A. 223
 Hermansson A.-M. 53
 Hernas A. 215, 238
 Hetmańczyk M. 309
 Hofer F. 43
 Holešínský J. 238
 Houben L. 17
 Huang C. 85
 Hufenbach W. 95
 Hýtch M. 40
- Illig S. 19
 Indyka P. 119, 122
 Ivaldi F. 88
- Jäger W. 87
 Jaksch H. 93
 Janik E. 117
 Janovszky D. 131
 Janusz M. 271
 Januszka A. 104
 Jany B. 119
 Jeżewska M. 263
 Jezierska E. 69, 137, 148
 Jurczyk-Kowalska M. 95
- Kaç S. 25, 157
 Kaczmarczyk J. 59
 Kalembe I. 100
 Kalinowska-Ozgowicz E. 155, 202
 Kamińska A. 137
 Karbowniczek J. 61
 Karcz J. 257
 Karczewski J. 257
 Kawałko J. 97, 273
 Kawasaki M. 24
 Keilová E. 308
 Kempen P. 23
 Kilariski A. 153
 Kilmametov A. 166
 Kilmametov A.R. 90
 Klonowska-Olejniak M. 257
 Kočík J. 308
 Kogtenkova O.A. 90
 Koh A.L. 23
 Kolarik V. 261
 Konieczny J. 159, 174
 Konopka K. 161
 Konvalina I. 76
- Kopia A. 83, 163
 Kopyściański M. 100, 164
 Korneva A. 90, 166
 Korniewa-Surmacz A. 244
 Kościelniak B. 275
 Kotarba A. 122
 Kothleitner G. 43
 Kotowski S. 199
 Kovács A. 38
 Kowalska J. 168
 Kowalski K. 25, 83, 163
 Kowalski M. 95
 Krakow R. 19
 Kranzmann A. 213
 Krauze S. 95
 Krawczyk J. 99, 102, 170
 Krawczyk Ł. 297
 Krawiec S. 297
 Kret S. 88, 117
 Krok F. 119
 Kruk A. 30, 51, 299, 303
 Kubiak K. 66, 170, 233, 307
 Kubok K. 277
 Kucha H. 30, 172
 Kula A. 75, 285
 Kulawik K. 295
 Kumar V. 313
 Kurc-Lisiecka A. 202
 Kurz G. 253
 Kurzydłowski K.J. 132, 242
 Kusiński J. 25, 287
 Kusiński J.
 Kuzma M. 221
 Kwiatkowski M. 305
 Kylberg G. 261
- Lábár J.L. 64
 Labisz K. 159, 174
 Lackner J.M. 184, 271, 281
 Lech-Grega M. 176
 Legutko P. 122
 Lelątko J. 79, 233
 Leroux C. 83
 Lesz S. 104
 Leszczyńska-Madej B. 178
 Letzig D. 253
 Lewandowska M. 63, 95, 124, 132
 Lewandowska-Łańcucka J. 229
 Li T. 88
 Lichte H. 15
 Lipińska L. 124
 Liszka B. 182
 Lityńska-Dobrzyńska L. 64, 142, 151, 180, 231, 244,
 249, 267, 277, 279
 Löffler M. 223
 Lopatin S. 6
 Lopez Moriyama A.-L. 83
 Lorén N. 53
 Lotnyk A. 47
 Loukya B. 57
 Łukaszewicz A. 310
 Lukowiec D. 182

Madigou V. 83
 Madsen S. 23
 Major L. 184, 271, 281, 291
 Major R. 184, 281, 291
 Mali H. 172
 Marciniak S. 227
 Marszałek A. 29
 Marszałek K. 234
 Marszałek M. 234
 Matteazzi P. 25
 Matula G. 186
 Matus K. 186
 Mayer J. 17
 Mayer S. 73
 Maziarz W. 188, 202, 265
 Mazilkin A.A. 90
 Michalička J. 308
 Michalska M. 124
 Michta G. 301, 303
 Midgley P.A. 19
 Miernik K. 106, 244
 Migula P. 257
 Migunov V. 38
 Mikmeková Š. 76
 Minicka J. 259
 Miszczyk M. 190
 Mitka M. 135, 180, 279
 Mitterer C. 315
 Morawiec K. 67
 Morgiel J. 70, 184, 203, 234, 236, 249, 269, 271
 Mościcki A. 68, 317
 Moskalewicz T. 157, 192, 194
 Mosquera Feijoo M. 213
 Mrówka-Nowotnik G. 196, 199, 246
 Muehle U. 223
 Muhaffel F. 61
 Mzyk A. 281

 Nabiałek M. 96, 104, 198, 207, 310
 Nakafushi Y. 24
 Namburi H.K. 308
 Nejman I. 178
 Nikiel M. 119
 Nobuchi T. 24
 Nocuń-Wczelik W. 108
 Nordström R. 261
 Nose M. 24
 Nowak R. 70
 Nowakowska M. 229
 Nowosielski M. 305
 Nowosielski R. 104
 Nowotnik A. 196, 199, 246

 Ochín P. 79
 Oeckler O. 128
 Olsson E. 44, 53
 Olszówka-Myalska A. 201
 Ophus C. 36
 Orelovitch O. 110
 Osuch W. 30, 172, 301, 303
 Otulak K. 259

 Ozgowicz W. 155, 202

 Pańcikiewicz K. 251
 Pańczyk E. 125
 Paris O. 172
 Paul H. 190, 203
 Pawłowski B. 102
 Pawlyta M. 182, 186, 205
 Pechlivani E.M. 66
 Pędrak P. 199
 Pędzich Z. 55
 Pekker P. 131
 Pereira de Souza C. 83
 Peters J.J.P. 85
 Petrzak P. 283, 287
 Pietrusiewicz P. 96, 198, 207
 Pisarek M. 132
 Plutecka H. 291
 Poková M. 140, 209, 253
 Pomorska M. 70
 Poppitz D. 47
 Pozzi G. 38
 Prażmowski M. 203
 Presz A. 110
 Progalskiy I. 194
 Pruna A. 211
 Prusik K. 255
 Puchlerska S. 305
 Pullini D. 211

 Radanyi A. 311
 Radetic T. 36
 Radmilović V. 21
 Radwański K. 153
 Radziszewska A. 213, 287
 Rajchel B. 236
 Rapacz-Kmita A. 34
 Rashkova B. 73
 Ratajski T. 289, 299
 Ratuszek W. 168
 Rauschenbach B. 47
 Rębiś J. 148
 Richert M.W. 178
 Rodak K. 215
 Rogal Ł. 279
 Roguska A. 132
 Rokicki P. 199
 Röntzsch L. 72
 Rosenthal T. 128
 Rosnecký V. 308
 Roźniata E. 217
 Roźniatowski K. 148
 Różycka A. 34
 Rutkowski B. 30, 126
 Ryner M. 261
 Ryś J. 219

 Sagan P. 221
 Sanchez A.M. 85
 Sartowska B. 110, 125
 Schenk H.P.D. 137
 Schlegel R. 128

Schmidt F. 43
 Schneider S. 45
 Seuss S. 192
 Shiojiri M. 24
 Sieniawski J. 66, 170, 196, 199, 233, 246, 307
 Sinclair R. 23
 Sintorn I.-M. 261
 Sirringhaus H. 19
 Skierbiszewski C. 120
 Skołek E. 144, 225, 227
 Skrzekut T. 248, 285
 Smalc-Koziorowska J. 120, 144
 Smolik J. 242
 Sobczak K. 88, 130, 137
 Sobczak N. 70
 Sobota J. 248
 Sojka Z. 59, 122
 Solecka M. 213, 283, 287
 Solórzano G. 22
 Sozańska M. 68, 78, 275, 317
 Spiradek-Hahn K. 73
 Stachewicz U. 32
 Stan K. 249
 Stan-Głowińska K. 64, 180
 Staszewska M. 229
 Stelmachowski P. 122
 Stepan P. 261
 Stodolak-Zych E. 34
 Stone C.A. 32
 Straumal B. 90, 166
 Stróż D. 255
 Sugamata M. 75, 285
 Suski T. 137
 Svensson G. 146
 Swadźba L. 309
 Swadźba R. 153, 309
 Świątek Z. 142, 231
 Światnicki W. 144, 148, 149
 Świątnicki W.A. 225
 Świątnicki W.A. 227
 Sycheva A. 311
 Sypień A. 142, 231
 Szawłowski J. 149
 Szczepkowska M. 170, 233
 Szczerba M. 188, 265
 Szlązak K. 96
 Szlezynger M. 234
 Szota M. 198, 207, 310
 Sztwiertnia K. 97, 133, 273
 Szule Z. 267
 Szwachta G. 157

 Tai C.-W. 146
 Tamvakos A. 211
 Tamvakos D. 211
 Tang D. 88
 Tanski T. 174
 Tembecka K. 291
 Teresa Krawczyńska A. 124
 Timelli G. 98
 Tokarski T. 81, 102, 293, 305
 Tran D.T. 146

 Trommer J. 223
 Trybalska B. 108
 Tsyruilin K. 93
 Turski H. 120
 Twardowska A. 236
 Tylko G. 27

 Uhlemann S. 4
 Uniwersał A. 293
 Uppström M. 261
 Urban K.W. 13, 17
 Urban P. 128

 van Tendeloo G. 49
 van Wyk P.W.J. 113
 Veselý J. 253
 Vodárek V. 238
 Volodarskaja A. 238

 Wagner G. 128
 Waliś L. 125
 Wańkiewicz K. 188
 Wasiak K. 225
 Wassilkowska A. 111, 240
 Węglowski M.S. 164
 Weker W. 125
 Wendler B. 194
 Widawski M. 125
 Wיעiński P. 242
 Wiedermann J. 309
 Wierzbanowski K. 293
 Wierzbička-Miernik A. 142, 244, 277
 Wierzbińska M. 196, 229, 246
 Willis C.R. 32
 Wisz G. 221
 Witkowska M. 168
 Włoch G. 248
 Wójcik A. 188, 265
 Wojewoda-Budka J. 180, 244, 249, 267
 Wojnar P. 117
 Wojtowicz T. 117
 Woźnica A. 257
 Wróbel M. 293
 Wroński S. 293
 Wspaniała-Rak J. 255
 Wu S. 85

 Xu X. 85

 Yamamoto A. 137

 Żaba K. 305
 Zamkotowicz Z. 135
 Zarzyńska-Nowak A. 263
 Zasada D. 217
 Zasada F. 59
 Zawadzka P. 178
 Żelechower M. 78
 Żelechowski J. 135, 176
 Zhang H. 32
 Zhang Z. 73, 315
 Ziąbka M. 34

Zięba P. 90, 166, 267
Zielińska-Lipiec A. 168, 219, 251
Zimina M. 140, 209, 253
Zimowski S. 194
Zrník J. 140, 253
Zschech E. 72, 223
Zubko M. 66, 170, 255

